

Mag.rer.nat. Martin Felix PICHLER, MSc

**MODEL PREDICTIVE CONTROL FOR  
HEATING IN RESIDENTIAL BUILDINGS**  
**PV-led heat pump operation in a single family house**

**PhD Thesis**

For obtaining the academic degree of

Doctor of Technical Sciences

submitted to

**Graz University of Technology**

Supervisor

Ao.Univ.-Prof. Dipl.-Ing. Dr.techn. René Rieberer

Institute of Thermal Engineering

Secondary supervisor

Ao.Univ.-Prof. Dipl.-Ing. Dr.techn. tit.Univ.-Prof. Anton Hofer

Institute of Automation and Control

Graz, August 2016

This document is set in Palatino, compiled with [pdfL<sup>A</sup>T<sub>E</sub>X2<sub>ε</sub>](#) and [Biber](#).

The L<sup>A</sup>T<sub>E</sub>X template from Karl Voit is based on [KOMA script](#) and can be found online: <https://github.com/novoid/LaTeX-KOMA-template>

## Affidavit (Eidesstattliche Erklärung)

I declare that I have authored this thesis independently, that I have not used other than the declared sources/resources, and that I have explicitly marked all material which has been quoted either literally or by content from the used sources. The text document uploaded to TUGRAZonline is identical to the present PhD thesis.

Ich erkläre an Eides statt, dass ich die vorliegende Arbeit selbstständig verfasst, andere als die angegebenen Quellen/Hilfsmittel nicht benutzt, und die den benutzten Quellen wörtlich und inhaltlich entnommenen Stellen als solche kenntlich gemacht habe. Das in TUGRAZonline hochgeladene Textdokument ist mit der vorliegenden Dissertation identisch.

Graz, \_\_\_\_\_

Date

\_\_\_\_\_

Signature



# Abstract

Title: MODEL PREDICTIVE CONTROL FOR HEATING IN RESIDENTIAL BUILDINGS

Subtitle: PV-led heat pump operation in a single family house

Author: Martin Felix PICHLER

1<sup>st</sup> keyword: thermally activated building system (TABS)

2<sup>nd</sup> keyword: thermal energy storage (TES)

3<sup>rd</sup> keyword: weather forecast

The aim of this thesis is the development of a versatile model predictive control (MPC) scheme for a heat pump (HP) with variable speed compressor supplying a thermal energy storage (TES) mainly for domestic hot water (DHW) purpose and a space heating (SH) system of a single family house (SFH), with thermally activated building systems (TABS) as heat emission system. The whole system is extended by a PV-system installed on the roof of the house. The motivation for this research is mainly the maximization of PV-generated electricity use. This thesis represents the scientific part of the research project TheBat, the Appendix includes also an account on the related research project MPC-Boxes.

The whole reference system is implemented and simulated with TRNSYS, which serves as test environment to investigate various MPC approaches. The final MPC concept relies on a number of empirical functions, which describe all necessary characteristics of the HP. Practically, these characteristics may be obtained through lab measurements. The whole MPC concept is subdivided into two separate MPC's, with higher priority given to that which is responsible for the TES heating. The used controller models are derived from first principles. The thesis gives also emphasis to the important subject of system identification. In addition to simulation, real measurement data from the project MPC-Boxes are facilitated to investigate various procedures for validation of the derived controller model. The final model for the SFH is a 4th order linear state space model. The TES in connection with the HP requires a non-linear hybrid model approach. However, one global linearization of the non-linear model is sufficient, finally leading to an affine hybrid model for the TES within the MPC. The derived MPC's lead to a constrained quadratic and a mixed integer quadratic problem both implemented in MATLAB by means of YALMIP. The subject optimization algorithm is only briefly touched in this work. For clarity the topic state estimation – which might be important in this context – is explained in detail for non-control people towards the end of this thesis.

Results are graphically illustrated and summarized in detail in various tables. A PV electricity self-consumption between 46 % and 62 % is possible with the suggested MPC concept. By comparison a standard system may use only  $\approx 20$  % directly by coincidence. The HP-consumed and directly PV-generated energy ranges between 55 % and 60 %. During the heating season from October to April the average self-consumption reaches 84 %. In this time 65 % of the HP-consumed electricity originates from the PV. These numbers do not consider the ordinary household electricity consumption. Further the MPC concept is viable to strive for HP operation at maximum efficiency. In this case the seasonal performance factor of the HP may be increased by 5 %. A detailed analysis of the results for the relevant TABS temperatures shows supply water temperatures reduced by more than 2 K and return temperatures reduced by more than 1 K for the MPC scenarios compared to the reference scenarios.



# Kurzfassung

Title: MODELL PRÄDIKTIVE REGELUNG FÜR HEIZZWECKE IM WOHNBAU

Untertitel: PV-geführter Wärmepumpenbetrieb im Einfamilienhaus

Autor: Martin Felix PICHLER

1. Stichwort: thermisch aktivierte Bauteilsysteme (TABS)
2. Stichwort: thermischer Energie Speicher (TES)
3. Stichwort: Wettervorhersage

Ziel der Arbeit ist die Entwicklung und Untersuchung einer Modellbasierten prädiktiven Regelung (MPC) für eine Wärmepumpe (WP). Die unmittelbare Aufgabe der Regelung ist die Heizung eines thermischen Energiespeichers (TES) überwiegend für Brauchwasserzwecke und die Raumheizung mittels thermisch aktivierter Bauteile (TABS) in einem Einfamilienhaus. Das Einfamilienhaus ist außerdem mit einer Photovoltaikanlage ausgestattet, für die es gilt den Eigenverbrauch durch optimale Regelung der WP zu maximieren. Diese PV Eigenverbrauchsmaximierung stellt das globale Regelungsziel der MPC dar. Diese Arbeit repräsentiert den wissenschaftlichen Hintergrund zum Forschungsprojekt TheBat, eine Zusammenfassung zum verwandten Projekt MPC-Boxes befindet sich im Anhang.

Als Prüfstand für unterschiedliche MPC Ansätze dient eine TRNSYS Simulation in der das thermische und das elektrische System modelliert sind. Der MPC basiert auf einer Reihe von empirischen Funktionen die alle notwendigen Eigenschaften der WP wiedergeben. Für die reale Anwendung können diese Funktionen im Rahmen von Labormessungen ermittelt werden. Die MPC basiert auf zwei individuellen MPC, wobei die Priorität des MPC für die TES Heizung höher ist als jene für den Raumheizungs MPC. Die Reglermodelle fußen auf physikalischen Modellen. Das Kapitel über System Identifikation befasst sich mit unterschiedlichen Verfahren zur Validierung und Bewertung verschiedener Modelle; dafür verwendet werden Simulationsdaten und reale Gebäude-Messdaten vom Versuchsaufbau des Projekts MPC-Boxes. Im Rahmen der Regelung wird das thermische Verhalten des Einfamilienhauses über ein lineares Zustandsraummodell 4ter Ordnung abgebildet. Der TES in Verbindung mit der WP erfordert einen nichtlinearen hybriden Modellansatz für den MPC. Als Optimierungsprobleme erhält man schließlich ein quadratisches- und ein nichtganzzahlig gemischt quadratisches-Programm, implementiert jeweils in MATLAB unter Zuhilfenahme von YALMIP. Lösungsalgorithmen für die Optimierungsprobleme stehen nicht im Mittelpunkt der Arbeit. Das in diesem Kontext zentrale Thema Zustandsschätzung wird allgemein verständlich mittels einfachem Beispiel heuristisch erklärt.

Der optimierte PV Eigenverbrauch variiert je nach Szenario zwischen 46 % und 62 % für die MPC. Circa 20 % erhält man für eine gewöhnliche Standardregelung, wo der PV Eigenverbrauch rein auf Zufall basiert. Der Anteil des direkten PV Stromverbrauchs der WP liegt zwischen 55 % und 60 %. Während der Heizsaison von Oktober bis April erreicht man einen durchschnittlichen Eigenverbrauch von 84 % und einen PV Stromverbrauch der WP von 65 %; ohne Berücksichtigung des gewöhnlichen Haushaltsstroms. Neben der Maximierung des Eigenverbrauchs wurde auch ein optimaler Betrieb im Sinne der WP Effizienz untersucht, wobei die Jahresarbeitszahl der WP um 5 % gegenüber dem Referenzfall erhöht werden konnte. Eine detaillierte Analyse der TABS Temperaturen zeigt eine um mehr als 2 K geringere Vorlauftemperatur und eine um mehr als 1 K geringere Rücklauftemperatur für die MPC im Vergleich zum Referenzfall.



## Foreword

The reported work was conducted between January 2013 and June 2016. Prior and closely related research of the author is also reported in five journal publications and six conference publications, for details see Appendix A. Another two journal and two conference publications are planned.

This thesis principally reports on work related to the research project TheBat (FFG Project-Number 838657). However, especially concerning the building controller model, it is impossible to imagine the reported work without the prior steps in system identification made whilst working on the project MPC-Boxes. In addition, the gained experience with real measurement data and the successful evaluation of the building controller model approach based on this data gives certainty on that subject. An introduction to the project MPC-Boxes (FFG Project-Number 840675) is provided in Appendix D, and a few results from the project MPC-Boxes are reported towards the end of sec. 6.

## Guide to the reader

The thesis consists of seven chapters, it opens with a general introduction including a literature review and the basics on model predictive control, and it concludes with a summary and the implications.

Chapter 2 describes the reference system which is implemented and simulated with TRNSYS, Klein et al. (TRNSYS 17). This system simulation is used to evaluate the developed model predictive control concepts. However, the explanations in this chapter provide also the basis for the controller models developed in sec. 3.1 and chapter 4.

Chapter 3 deals with general aspects on system identification. Sec. 3.1 outlines the transition from an initially physical building model to a structured state space model. Sec. 3.2 describes the principal concept of parameter estimation methods and it exemplifies the procedure with linear regression applied to a simple second order state space model. The topics: model performance, stability and experiment design are discussed in sec. 3.3 and sec. 3.4 as far as necessary. This chapter may be skipped initially and consulted only if required.

Chapter 4 reports on the model performance achieved for different controller model structures. The first two sections 4.1 and 4.2 deal with the MPC-Box building model

which is simpler – compared to the TheBat building model – and a good preparation for getting into this topic. Reported results for the MPC-Box controller model include also a model validation based on real measurement data. The sections 4.3 and 4.4 elaborate on the developed TheBat building model and on the hybrid model approach, which is required for the thermal storage when heated through the heat pump.

Chapter 5 describes the model predictive control tasks and required ingredients. Starting with a simple temperature control in sec. 5.1, the control task related objective or cost functions gradually become more complicated until reaching the most challenging control task formulated in 5.3. The topic state estimation is explained in sec. 5.4.

Chapter 6 outlines the evaluation strategy and reports on the results for various scenarios with different parametrizations or boundary conditions. Results are graphically illustrated and summarized in detail in various tables.

The Appendix includes a short summary addressing related publications of the author, and an account on the research project MPC-Boxes. In addition, mathematical preliminaries, numerous graphical illustrations and quantitative simulation results and further supplementary material is appended.

## Acknowledgments

My supervisors during this work have been Associate Professor René Rieberer and Professor Anton Hofer. I would like to thank both for the thorough reading and the valuable feedback.

My thanks go to “my” master students Daniel Gerstgrasser and Alexander Arnitz for their excellent work.

To my colleagues at the institute of thermal engineering, especially to those from the third floor, thank you all for the numerous discussions we had and our lunch time together. Special thanks goes also to the seniors on the third floor, thank you all for the numerous discussions we had and I am very grateful that you trusted me and “let me do my thing”.

My thanks go also to all people working with me together on the projects TheBat and MPC-Boxes; special thanks to Gregor Görtler for all discussions we had and to Michael Herzlieb for the smooth and constructive collaboration. Thanks to Alex Thür, Andreas, Franz, Richard, Hermann, Thomas, Heinz, Markus R. and Markus S.

Thanks go also to Markus G. and Viktor O. from Bioenergy for the discussions we had and the indication of relevant literature.

Redzo, I am very grateful for the friendship we made and our time together as we talked about God and the world.

Tom, I am very glad I got to know you.

Finally, but especially I want to thank my wife Ana and my daughter Sophia for the continuous support and the patience over the last few years to get the reported work done. Thanks for the freedom you gave me and your occasional appearance at work, which made me very happy.

I also gratefully acknowledge the financial funding of the reported scientific work, which was supported by the project TheBat and the project MPC-Boxes. Special thanks goes also to the participating companies Heliotherm, REHAU and EAM for their financial contribution and the collaboration.

The project "The thermal battery in the smart grid in combination with heat pumps – an interaction optimization (TheBat)" is sponsored by the Austrian Climate and Energy Fund and conducted within the framework of the program „ENERGY MISSION AUSTRIA“ (Project-Number 838657).



The project "MPC-Boxes", is supported by the program BUILDING OF TOMORROW (Haus der Zukunft) which is a research and technology funding program of the Austrian Ministry for Transport, Innovation and Technology (Project-Number 840675).





# Contents

<b>Abstract</b>	<b>v</b>
<b>Foreword</b>	<b>ix</b>
<b>Notational conventions and nomenclature</b>	<b>xix</b>
<b>1. Introduction</b>	<b>1</b>
1.1. Background	2
1.2. Literature review	2
1.2.1. Model based predictive control (MPC) – principle	2
1.2.2. Methodological aspects and chronology on predictive control	5
1.2.3. Model predictive control applied for heat pump operation	6
1.2.4. Model predictive control related to building automation	7
1.3. Optimization – potential savings and different approaches	8
1.3.1. Optimization schemes for predictive controls	9
1.3.2. Benefits for related technologies and beneficiaries	10
1.4. Synthesis and challenges in research	11
1.5. Thermal comfort	12
1.5.1. A short review	12
1.5.2. Comfort violation measurements	13
<b>2. Heat pump, PV system and building</b>	<b>15</b>
2.1. Demand side management	15
2.2. System description	16
2.2.1. Heat pump description	17
2.2.2. Hydraulic system and thermal energy storage	19
2.2.3. Building characterization – TABS	22
2.3. Control criteria and control functions	24
2.3.1. Control criteria description	24
2.3.2. Control functions and derived operating-states	26
2.4. Heat pump characteristic functions	30
2.4.1. General aspects and prototypical functions and graphs	30
2.4.2. MPC relevant HP characteristics – SH with TABS ( $CF_4$ )	33
2.4.3. MPC relevant HP characteristics – TES heating, ( $CF_1$ )	35
2.4.4. Fit results for characteristic functions	36

## Contents

2.5. Modelling of photovoltaic components . . . . .	39
2.5.1. Efficiency coefficient model . . . . .	40
2.5.2. Cell temperature . . . . .	41
<b>3. System identification and modeling</b>	<b>43</b>
3.1. Model design and selection . . . . .	43
3.1.1. Physical models from first principles . . . . .	44
3.1.2. Structured state space models with lumped parameters . . . . .	47
3.1.3. Mathematical formalization of the modeling . . . . .	49
3.1.4. Prototypical constrained structured SSM . . . . .	50
3.2. Parameter estimation methods . . . . .	52
3.2.1. Linear regression and least square estimate . . . . .	52
3.2.2. Short account on more advanced estimation methods . . . . .	55
3.3. Model performance and stability . . . . .	58
3.3.1. Output trajectories and physical model errors . . . . .	58
3.3.2. Model fitness value . . . . .	61
3.4. Identification data and experiment design . . . . .	64
3.4.1. Properties of input and output data . . . . .	65
3.4.2. Relevant temperature range – excitation . . . . .	66
3.4.3. Model evaluation through self- and cross-validation . . . . .	67
<b>4. Models for control purpose – system identification results</b>	<b>69</b>
4.1. MPC-Boxes linear building model . . . . .	69
4.1.1. Final model structure and constraints . . . . .	70
4.1.2. Parameter estimation and numerical results . . . . .	70
4.1.3. Model performance and error analysis – based on simulation data . . . . .	73
4.2. MPC-Boxes controller model based on real measurements . . . . .	76
4.2.1. Models from real measurement data with $\dot{q}_{gi} = 0$ . . . . .	76
4.2.2. Models from real measurement data with full excitation . . . . .	77
4.2.3. Investigation on the importance of selected disturbance variables . . . . .	78
4.2.4. Reflection on the S-SSM for the MPC-Boxes . . . . .	80
4.3. TheBat linear building model . . . . .	82
4.3.1. Initial physical RC model structure – $\mathcal{M}^{n4}$ . . . . .	83
4.3.2. Third order models – $\mathcal{M}^{n3}$ S-SSM estimation . . . . .	85
4.3.3. Fourth order model with virtual wall – $\mathcal{M}^{n4w}$ . . . . .	85
4.3.4. Final model structure . . . . .	90
4.4. Thermal storage with heat pump – controller model . . . . .	90
4.4.1. General non-linear storage model . . . . .	91
4.4.2. Linearization of the general non-linear model . . . . .	93
4.4.3. Hybrid approach for the TES-HP model . . . . .	95
4.4.4. Discretization and valid model range . . . . .	96
4.4.5. Model performance and validation . . . . .	97
4.4.6. Linearization point and $\hat{C}$ -model . . . . .	100

<b>5. Model predictive control</b>	<b>105</b>
5.1. Simple temperature control – MPC-Boxes . . . . .	105
5.1.1. Objective function and constraints . . . . .	106
5.1.2. An optimization run in slow motion . . . . .	107
5.2. PV-led heat pump control for space heating (TABS-MPC) . . . . .	108
5.2.1. Objective function and constraints . . . . .	109
5.2.2. Reference function for tracking a certain PV power . . . . .	110
5.3. PV-led heat pump control for TES heating (TES-MPC) . . . . .	111
5.3.1. Objective function and constraints . . . . .	111
5.4. State estimation – Kalman Filter . . . . .	113
5.4.1. Heuristic explanation and basic examples . . . . .	114
5.4.2. Kalman Filter equations and explanations . . . . .	115
5.4.3. Summary of the Kalman Filter equations and recursion . . . . .	117
5.5. Optimization problem . . . . .	119
5.5.1. General aspects . . . . .	119
5.5.2. A prototypical MPC problem solved with a QP . . . . .	121
5.5.3. Numerical complexity . . . . .	123
5.6. The complete MPC control task – overview . . . . .	124
5.6.1. Realization and coding of the MPC . . . . .	126
<b>6. Results and controller performance</b>	<b>127</b>
6.1. Evaluation strategy and performance indicators . . . . .	127
6.1.1. Penalties for comfort violation . . . . .	127
6.1.2. Heat pump- and system-performance indicators . . . . .	128
6.1.3. Control related performance indicators . . . . .	129
6.2. PV yield and boundary conditions . . . . .	130
6.3. DHW(TES) and SH(TABS) – BC results, scenario 0.0 . . . . .	130
6.4. DHW(TES) and SH(TABS) – MPC results, scenario 1.0 . . . . .	133
6.4.1. Control system trajectories . . . . .	133
6.4.2. Energy flow and induced PV self consumption . . . . .	134
6.5. DHW(TES) and SH(TABS) – scenario overview . . . . .	136
6.5.1. Scenarios 1.1 - 1.3 . . . . .	136
6.6. DHW(TES) and SH(TABS) – MPC results 1.3a . . . . .	137
6.7. DHW(TES) and SH(TABS) – base case results 0.1 . . . . .	138
6.8. DHW(TES) and SH(TABS) – MPC results 1.4 . . . . .	139
6.9. Results overview and histograms . . . . .	140
<b>7. Summary and conclusion</b>	<b>147</b>
7.1. What can be learned from the MPC . . . . .	149
7.2. Possible future work . . . . .	150
<b>Bibliography</b>	<b>151</b>

<b>Appendix</b>	<b>163</b>
<b>A. Overview on related publications</b>	<b>165</b>
<b>B. Mathematical preliminaries</b>	<b>167</b>
B.1. State space model representation . . . . .	167
B.1.1. Solution for $x$ in the time domain and discrete time SSM . . . . .	168
B.1.2. Properties of the dynamic matrix $A$ . . . . .	169
B.1.3. Interpretation of the eigensolutions – eigenvalues and $-$ directions	171
B.1.4. Matrix algebra . . . . .	173
B.2. Jacobi-matrix . . . . .	174
B.3. Observability and controllability . . . . .	174
B.4. Positive and semi-positive definiteness . . . . .	175
<b>C. HP PV system and building</b>	<b>177</b>
C.1. Control of $V_4$ and $V_{4a}$ . . . . .	177
C.2. Climate data . . . . .	178
C.3. CF minimal terms based on Karnaugh maps . . . . .	179
C.4. Modelling of photovoltaic components . . . . .	181
C.4.1. PV equivalent circuit diagram . . . . .	181
C.4.2. Four-parameter model . . . . .	182
<b>D. The Project MPC-Boxes</b>	<b>189</b>
D.1. Test-Box construction and thermal characteristics . . . . .	190
D.1.1. Detailed geometry and material properties . . . . .	190
D.1.2. TRNSYS building model deficiency – compensation . . . . .	193
D.1.3. Heating and cooling demand . . . . .	193
D.1.4. Maximum heating and cooling load . . . . .	193
D.2. Measurement equipment and accuracy . . . . .	194
D.2.1. Temperature sensors . . . . .	194
D.2.2. Heat meter . . . . .	195
D.3. Evaluation and comparison of the two real Test-Boxes . . . . .	197
D.3.1. Comparison by means of a Blower Door Test . . . . .	197
D.3.2. Comparison by means of measurement data . . . . .	198
D.3.3. Calibration and validation of the TRNSYS simulation . . . . .	200
D.3.4. Thermally Activated Building System (TABS) . . . . .	204
D.3.5. TRNSYS-model interior – air-node . . . . .	206
D.4. Mechanical ventilation and related disturbance variables . . . . .	207
D.5. Further details on comfort models . . . . .	209
<b>E. Selected TRNSYS models and simulation details</b>	<b>213</b>
E.1. Building simulation . . . . .	213
E.1.1. Long-wave radiation exchange . . . . .	213
E.1.2. Short-wave radiation distribution . . . . .	214

E.1.3.	Convective heat transfer . . . . .	215
E.1.4.	Operative temperature . . . . .	215
E.1.5.	Mean radiant temperature . . . . .	215
E.2.	U value error in TRNSYS – ‘Cold-bridge correction’ . . . . .	216
E.2.1.	FEM-simulations for the TRNSYS layer construction . . . . .	217
E.2.2.	FEM-simulations for a real construction . . . . .	219
E.2.3.	Increased heat flux near an edge . . . . .	220
E.2.4.	Weighting scheme to obtain correction factors . . . . .	222
E.2.5.	Facilitation of the correction factors . . . . .	224
E.3.	Uncertainty . . . . .	225
E.4.	Climate data . . . . .	226
E.4.1.	virtual sky temperature . . . . .	226
E.4.2.	Effective sky temperature . . . . .	226
E.5.	TRNSYS results interpretation . . . . .	227
E.6.	Further details on the TRNSYS simulation . . . . .	227
<b>F.</b>	<b>Blower door test – complete measurement protocols</b>	<b>229</b>
<b>G.</b>	<b>System identification</b>	<b>235</b>
G.1.	Comments on the physical model from first principles . . . . .	235
G.2.	Multiple correlation coefficient . . . . .	235
G.3.	Model parameter values – MPC-Boxes . . . . .	236
G.4.	MPC-Boxes results based on simulation data . . . . .	238
G.4.1.	Residual analysis – MPC-Boxes . . . . .	238
G.4.2.	Ill-structured SSM from simulation – MPC-Boxes . . . . .	240
G.4.3.	Unconstrained case – MPC-Boxes . . . . .	242
G.4.4.	Parameters from another season – MPC-Boxes . . . . .	243
G.4.5.	Further results of sub-optimal model structures – MPC-Boxes . . . . .	244
G.5.	MPC-Boxes results based on real measurement data . . . . .	245
G.6.	TheBat – model structures and results . . . . .	247
G.6.1.	The model $\mathcal{M}^{n4}$ . . . . .	247
G.6.2.	The model $\mathcal{M}^{n3}$ . . . . .	247
G.6.3.	The model $\mathcal{M}^{n4w}$ – further internal parametrizations . . . . .	249
G.6.4.	The other eigensolutions of $\mathcal{M}^{n4w}$ . . . . .	250
G.6.5.	Parameter inspection . . . . .	255
<b>H.</b>	<b>Detailed simulation results</b>	<b>257</b>
H.1.	DHW(TES) and SH(TABS) results – BC scenario 0.0 . . . . .	257
H.2.	DHW(TES) and SH(TABS) results – BC scenario 0.1 . . . . .	259
H.3.	DHW(TES) and SH(TABS) results – MPC scenario 1.0 . . . . .	261
H.4.	DHW(TES) and SH(TABS) results – MPC scenario 1.3a . . . . .	263
H.5.	DHW(TES) and SH(TABS) results – MPC scenario 1.4 . . . . .	265
H.6.	DHW(TES) and SH(TABS) results – MPC scenario 1.5 . . . . .	267
H.7.	PV module data . . . . .	267



# Notational conventions and nomenclature

## List of variables

### Standard variable names

$a$	weighting factor for the operative temperature, –
$b, c$	constants, specific heat capacity
$c_{ta}$	TABS-area specific heat capacity of TABS node
$d$	thickness
$dmax_{v_1}$	max distance between a subset of dominating eigenvectors
$fit$	model fitness measure
$f$	frequency, HP compressor speed or sampling frequency
$\mathbf{f}_1$	dominating eigensolution
$g$	solar energy transmittance
$h_{ven}$	ventilation related disturbance input normalized wrt $A_{ta}$
$k$	discrete time index variable, Boltzmann constant
$m$	mass
$\dot{m}_{ta}$	mass flow rate in the TABS loop, kg/(h m <sup>2</sup> )
$\dot{m}_c$	mass flow of the HP condenser, kg/(h m <sup>2</sup> )
$\dot{m}_d$	mass flow of the HP desuperheater, kg/(h m <sup>2</sup> )
$n$	ideality factor or discrete variable used as index
$n_{inf}, n_{ven}$	infiltration, mech. ventilation rate, 1/h
$pdf$	general probability density function
$q$	elementary charge
$\dot{q}_{gi}$	internal gains, W/m <sup>2</sup>
$\dot{q}_{gs}$	solar gains, W/m <sup>2</sup>
$\dot{q}_{ta}$	heat flux supplied to the TABS, W/m <sup>2</sup>
$s, \sigma$	empirical standard deviation
$t$	continuous or discrete time (instant)
$\Delta t_s$	sampling time constant
$u, (\mathbf{u})$	manipulated variable (vector)
$\mathbf{v}_i$	$i$ -th eigenvector ( $i=1$ : dominating eigenvector)
$v_{1,xyz}$	$xyz$ -related component of the dominant eigenvector
$x, (\mathbf{x})$	state variable (vector)
$y, (\mathbf{y})$	output variable (vector)

## Notational conventions and nomenclature

### Standard variable names

$A$	area, $m^2$
$C$	thermal heat capacity, Wh/K
$C_A$	control criteria if 1 TES heating is required
$CF_1$	control function defining the TES heating operation
$COP$	coefficient of performance
$D$	diode diffusion factor
$D_{tf}$	simulation id-data set for the data indicated with $tf$
$\mathcal{F}$	general function
$E_F$	Fermi level
$F_{PV,use}$	Fraction of directly (by the HP) used PV-generated electricity
$F_{HP,PV}$	Fraction of HP electricity consumption with PV origin
$G_T$	total (global) irradiance, $W/m^2$
$H$	enthalpy
$H_{PV}$	solar irradiance on the PV surface integrated over time, $kWh/m^2$
$H_{tot,hor}$	solar irradiance on the horizontal integrated over time, $kWh/m^2$
$I$	current
$I_L$	light current (source)
$I_S$	saturation current
$J$	cost function or more precisely functional
$\dot{Q}_{ta,ra}$	heat flux between TABS and room air node (state)
$L$	linear filter
$\mathcal{M}_1$	linear free floating TES model
$\mathcal{M}_2$	linearized TES-HP model
$\mathcal{M}^{n4w}$	TheBat building model
$MRfit$	MPC relevant fit
$N_p, N_c$	prediction-, control horizon
$P$	(id-)data interval length
$R$	thermal resistance (RC models)
$R_s$	serial resistance (PV model)
$RH$	relative humidity in %
$T$	temperature in K
$T_c$	cell temperature, K
$U$	thermal transmittance, $W/m^2K$
$V$	volume, $m^3$ , or voltage, V
$V_N$	sum characterizing the average model error
$V_T$	thermal voltage, V
$V_D$	diode voltage, V
$W_{PV}$	total (specific) annual PV yield, $kWh$ or $kWh/m^2$
$Y_p^{1,N}$	time series vector of length $N$ for output $p$ , $[y_p(1), y_p(2), \dots, y_p(N)]$

## Greek letters

$\mu$	temperature coefficient
$\alpha, \alpha_1$	heat transfer coefficient, W/mK; predictor model parameter
$\beta_{ta}, \beta_1$	scaling factor for $C_{ta}$ or $c_{ta}$ ; predictor model parameter
$\gamma_{gs}, \gamma_{gi}$	fraction of solar, internal gains affecting the room air node (state)
$\mathcal{E}_N$	time series vector of residual
$\varepsilon$	prediction error or residual (difference) value
$\hat{\varepsilon}$	approximated residual value based on a model approach
$\bar{\varepsilon}$	bias error
$\epsilon$	emissivity
$\epsilon_G$	semiconductor material bandgap energy
$\eta$	efficiency
$\Theta$	parameter vector
$\theta$	element(s) of $\Theta$
$\vartheta$	temperature in °C , by contrast to $T$ which is in Kelvin
$\vartheta_{2m,t}$	ground temperature in 2 m depth
$\vartheta_{cell,>15W}$	solar cell temperature average based on all $P_{PV}(t) > 15$ W
$\vartheta_{d,o}$	desuperheater outlet temperature
$\vartheta_{S1}$	temperature of sensor 1 (2, 3)
$\vartheta_{fl}$	floor temperature (concrete)
$\vartheta_{grd}$	ground temperature (below XPS)
$\vartheta_{oa}$	outside ambient temperature
$\vartheta_{op}$	operative room (air) temperature
$\vartheta_{ra}$	room air temperature
$\vartheta_{ret}$	AL return water temperature
$\vartheta_{sw}$	AL supply water temperature
$\vartheta_{ta}$	TABS temperature at AL depth in the concrete
$\lambda$	thermal conductivity, W/mK
$\lambda_i$	$i$ -th eigenvalue of $\mathbf{A}$
$\tau$	time constant
$\mathcal{T}$	selected (simulation) time interval for identification
$\varphi$	regressor constituting $\Phi$
$\Phi_N$	regressor matrix with $N$ columns

## Sub- and superscripts

act	actual value
avg	average value
bui	building
c	condenser, convective or control related (horizon)
comp	compressor
cond	condenser
ctr	control related
d, desup	desuperheater, discrete model form
dif	diffuse
dp	double port connection of the TES
e, evap	evaporator
el	electrical (consumption)
env	environment related
gi, gs	internal- or solar gain
gla	glazing
grd	ground
hys	hysteresis
inf	infiltration
i, in	input, an input quantity of a balance
loss	attributed to losses
oa	outside air
op	operative room (air) temperature
opa	opaque
o, out	output, an output quantity of a balance
p, P	prediction related (horizon)
pen	variable considering penalty energies from comfort violations
ra	room air
ra2fl	room air temperature in the 2nd floor (TheBat)
racl	room air temperature in the 2nd floor (TheBat)
rad	radiative
ref	reference value
ret	return (water)
set	set value related
sw	supply (flow water)
sys	system related
ta	TABS related
tacl	TABS (temperature) of the ceiling in the 1st floor (TheBat)
ta2fl	TABS (temperature) of the ceiling in the 1st floor (TheBat)
th	threshold
trn	TRNSYS related

u	related to an input (controlled) variable
v	related to a disturbance input variable
ven	mechanical ventilation
w	virtual wall
win	window
zo	thermal zone related
F	filtered
H	high fit measure
L	lower (temperature) limit, low fit measure
N	length of data set
U	upper (temperature) limit

## Identification data abbreviations

Simulation data for model identification and validation purpose are termed wc, wm, ts, sh, sm and tf. These data set descriptors are used for data to identify the 3rd order building model (MPC-Boxes), as well as for data to identify the 4th order building model (TheBat). Although the data sets for MPC-Boxes and TheBat are not the same, the respective data share the following characteristic. The heating demand is always highest for the data wc (winter cold) followed by wm (winter moderate). The summer intervals sh (summer hot) and sm (summer moderate) require practically no heating and the transition intervals ts (transition spring) and tf (transition fall) only little.

Real identification (validation) data used only for the 3rd order MPC-Boxes model are termed wc1 (winter cold 1), wc2 (winter cold 2), wc1s (winter cold 1 short) and wc2s (winter cold 2 short), wc (winter cold), wcs (winter cold short), wcg1 (winter cold gains 1), wcg2 (winter cold gains 2) and wcgs (winter cold gains short). The data deviate in terms of their length and in terms of the excitation with respect to the shading and the internal gains.

## Mathematical symbols

=	equal
:=	left side is defined by the right
$\approx$	almost equal, asymptotic to
$\propto$	proportional to
$\iff$	equivalent to
$\Theta^*$	<i>starred</i> variables indicate an optimum
$\Sigma$	summation symbol
$\bar{y}$	time average value over all $y(i)$ , $i = 1, 2, \dots, N$
$\hat{\phantom{y}}$	a <i>hat</i> indicates a model related property examples follow:
$\hat{y}$	value of a SSM output opposed to a TRNSYS variable or real measurement
$\hat{U}$	a model parameter to be determined through estimation
$\dot{V}$	<i>dot</i> indicates a derivative wrt time
$\partial_x$	partial derivative wrt the variable $x$
$\nabla$	gradient
$\infty$	infinity
$\ \mathbf{x}\ _2$	(euclidean or 2) norm of $\mathbf{x}$
$\ \mathbf{x}\ _\infty$	maximum norm of $\mathbf{x}$ (select largest element)
$argmin$	minimize through variation of the given argument
$E[y]$	expectation value of the variable $y$
$\mathbf{x}^T$	transposition of vector $\mathbf{x}$
$b_{1,2}$	means the matrix element in the first row, second column
$B(1,2)$	alternative notation for $b_{1,2}$
$\mathcal{D}$	general set of data
$\mathcal{M}(\Theta)$	general (or MPC-Boxes) model $\mathcal{M}$ with parametrization $\Theta$
$\mathbb{R}$	set of all real numbers
$\mathbb{R}^+$	set of all positive real numbers
$\mathcal{S}_M$	set of model parameters
$\Phi$	regressor matrix

In general any *vector* for example  $\mathbf{y}$  is understood being a column vector, and alternatively this column vector may be written as a transposed row vector:

$$\mathbf{y} := \begin{bmatrix} \vartheta_{ta} \\ \vartheta_{ra} \\ \vartheta_{fl} \end{bmatrix}, \text{ or equivalently } \mathbf{y} = [\vartheta_{ta}, \vartheta_{ra}, \vartheta_{fl}]^T.$$

A real *matrix*  $\mathbf{B}$  is indicated by  $\mathbf{B} \in \mathbb{R}^{3 \times 5}$  which means that  $\mathbf{B}$  is of the form

$$\mathbf{B} = \begin{bmatrix} B(1,1) & B(1,2) & B(1,3) & B(1,4) & B(1,5) \\ B(2,1) & B(2,2) & B(2,3) & B(2,4) & B(2,5) \\ B(3,1) & B(3,2) & B(3,3) & B(3,4) & B(3,5) \end{bmatrix}, \text{ and } B(i,j) \in \mathbb{R}, \text{ that is all elements consti-}$$

tuting  $\mathbf{B}$  are real numbers.

The term *constrained* means that only a certain range of values is possible or allowed. For example a parameter  $B(1,2)$  constrained to positive values ( $\in \mathbb{R}^+$ ) may take only a positive value. Similarly *unconstrained* means that, in this context, any real number is possible.

## Nomenclature

**Actual value** Current value obtained via a proper measurement method.

**Closed-loop control** A closed-loop control uses direct feedback information to obtain one or more objectives.

**Controlled variable** The physical quantity ( $y$ ) that is controlled to match a specific set-value or to kept within given limits (e.g. room air temperature).

**Cross-validation** means the evaluation of a model with a different then the id-data or training data set.

**Data-assimilation, model-assimilation, model alignment** Assimilation of the model using actual real measurement data from sensors, weather forecast or plant sensors.

**Dynamic matrix** the A-matrix in the SSM determining the intrinsic model dynamic.

**Ensemble prediction** Weather forecast for the far future using averages over results originating from different models or different initial parameters.

**Future window** Prediction horizon for the control.

**id-data** data set used for identification purpose.

**Ideal prediction** Ideal prediction of all future disturbances such as weather, DHW draw-off, etc.

**Input matrix** the B-matrix in the SSM determining the input coupling.

**Manipulated variable** the manipulated or **actuating** variable ( $u$ ) is that physical quantity through which the system is driven in the intended direction to reach a specific set-value. In this context this is mostly a heating or cooling power.

**Node** in thermal modeling the term node is often used instead of **state** for an internal model variable

**Performance bound** Best control strategy or ideal case one can think of; this is a pure theoretical concept.

**Persistence prediction** Weather data from a certain past period are used as forecast for weather data for a future period.

**Residual** numerical difference (**error**) between real and model variable value

**Self-validation** means the evaluation of a model based on the id-data or training data

**Setpoint or set value** Certain physical value to be reached by a closed-loop control.

**State** a model state is an internal model variable (a node) changing over time

**valid-data** validation data set used for model validation.

## Acronyms and abbreviations

<b>dp</b>	double port
<b>fit</b>	model fitness (value)
<b>id-data</b>	identification data
<b>pp</b>	percentage points
<b>valid-data</b>	validation data for cross evaluation
<b>A</b>	valve port A or area
<b>AB</b>	valve port AB
<b>AL</b>	active (pipe) layer in the concrete
<b>ARX</b>	auto regressive model with extra input term
<b>ARMAX</b>	ARX with moving average
<b>B</b>	valve port B
<b>BC</b>	base case scenario
<b>BIBO</b>	bounded input bounded output stability criteria
<b>BMS</b>	building management systems
<b>DHW</b>	domestic hot water
<b>DSM</b>	demand-side-management
<b>EPBD</b>	energy performance directive for buildings
<b>FW</b>	fresh water
<b>FWS</b>	fresh water station
<b>FEM</b>	finite element method
<b>HP</b>	heat pump
<b>HVAC</b>	heating ventilation air conditioning
<b>LHS</b>	left hand side
<b>LQ</b>	linear quadratic
<b>LS</b>	least square
<b>MAE</b>	mean absolute error
<b>MIQP</b>	mixed integer quadratic program
<b>MLS</b>	multivariate least square
<b>MPC, MBPC</b>	model predictive control
<b>MP</b>	maximum power point
<b>MPPT</b>	maximum power point tracker
<b>MRI</b>	model predictive control relevant identification
<b>NCS</b>	number of cells in series
<b>NOCT</b>	nominal cell temperature operating conditions
<b>NRPE</b>	non renewable primary energy
<b>NP-hard</b>	non-deterministic polynomial-time hard (very complex and extremely difficult to solve or find the globally best solution)
<b>OE</b>	output error
<b>OP</b>	operating point
<b>P</b>	pumps
<b>PB</b>	performance bound

**PEM** predictor error method  
**PPD** predicted percentage of dissatisfied (persons)  
**PWM** pulse width modulation  
**QP** quadratic program  
**RBC** rule based control  
**RH** relative humidity  
**RHS** right hand side  
**RMSE** root mean square error  
**SFH** single family house  
**SH** space heating  
**SISO** single input single output  
**SIMO** single input multiple output  
**SPF** seasonal performance factor  
**SSM** state space model  
**S-SSM** structured state space model  
**STC** standard test conditions  
**TABS** thermally activated building system  
**TES** thermal energy storage  
**TABS-MPC** TABS controlling MPC  
**TES-MPC** TES controlling MPC  
**TES-HP** TES model with heat supply from the HP (linearized controller model)  
**V** valve



# 1. Introduction

The relevance of this research topic is probably best demonstrated by numerous recently finished or ongoing research projects and doctoral theses with emphasis on predictive control and (thermal) energy. In Europe quite a few research groups deal with model predictive control tasks concerning heating and cooling and related energy supply.

A proponent in this field is probably the Swiss Federal Institute of Technology (ETH Zurich) with first publications in the early 80s, e.g. Gruenenfelder and Toedtli (1985). Recently a six year lasting project – OptiControl (Gwerder et al., 2013) – and a PhD (Sturzenegger et al., 2012) have been conducted at this address. The Technical University in Prague hosts also a few people with special focus on building and energy related predictive control. In one of their projects the researchers achieved cost savings of approximately 20%. Privara (2013) finished a PhD dealing with relevant issues on system identification, and an ongoing doctoral theses is conducted by Žáčková. At Chalmers University of Technology (Sweden) Karlsson (2010) finished a doctoral thesis related to thermal models of floor heating systems with a strong connect to predictive control. Also Vienna University of Technology has undertaken real life projects recently, see e.g Mayer et al. (2015).

For sack of completeness a number of further institutions dealing with this topic is listed. Technical University of Denmark, Technological Educational Institute of Crete and Technical University of Crete - Greece, Katholieke Universiteit Leuven - Belgium, Loughborough University and University of Ulster - UK, eCampus University and Politecnica delle Marche - Italy. This is just a flavor and if an institution in Europe dealing with subject related research is missing it is probably due to the fact that the enormous number of ongoing research makes it impossible to cover all relevant institutions. More details are provided in the literature review in Sec. 1.2.

This thesis contributes to understanding of modeling and system identification related to a model predictive control framework for domestic hot water provision and space heating for a single family house. Further, the thesis introduces the incorporation of an optionally photovoltaic-driven heat pump with desuperheater and variable speed compressor into the predictive control scheme, and it indicates the related energetic implications. Finally, it briefly reports on important aspects of real implementations.

## 1. Introduction

### 1.1. Background

The energy consumption of buildings within the European Union (EU) amounts to 40% of total consumption. To meet the commitments initially made under the Kyoto protocol and to ensure security of energy supply the EU has introduced legislation to reduce the energy consumption.

A key part of this legislation is the Energy Performance of Buildings Directive (Directive 2002/91/EC, EPBD), which was first published in 2002 aiming at an improved energy efficiency for new and renovated buildings. The national Austrian action to this legislation may be found within "OIB-Richtlinie 6" (2007), "Standards for Energieeffizienz von Gebaeuden" (2005-2008) and the "Gesamtenergieeffizienz von Gebaeuden" (2007). A practical outcome of those is for example the compulsory energy labeling of buildings. In 2010 the EPBD was updated by Directive 2010/31/EU<sup>1</sup>. This recast of the former EPBD from 2002 defines further tough challenges such as retrofitted nearly-zero energy buildings by 2020 but it stresses also cost reductions for the building envelope and the technical systems<sup>2</sup>. In addition, it requires the building energy label to identify also primary energy demand and CO<sub>2</sub> emission data.

The European Standard, Energy Performance of Buildings - Impact of Building Automation, Controls and Building Management (EN 15232:2012) is a key indicator that automation and control are considered viable to improve the energy efficiency of buildings. This standard provides a method to estimate the cost effectiveness of new or replaced building automation. The standard divides buildings into classes from A – high degree of sensible automation – to D indicating no automation at all.

### 1.2. Literature review

This review tries to reveal influential research dealing with predictive control and heating applications. Preliminary questions which have been addressed in other theoretical and experimental research work might be answered in research introduced in this review. After an outline on predictive control basics and a brief historical account on this topic, a literature review on heating applications and (predictive) control follows.

#### 1.2.1. Model based predictive control (MPC) – principle

Fig. 1.1 shows a standard closed-loop control. Assume a heat emission system (radiators) with constant mass flow being the controlled system. Imagine this system, then typical physical pendants are the set-room-temperature as set-value, the flow-temperature as

---

<sup>1</sup> The pendant in Germany is the so called Energieeinsparverordnung (EnEV 2014).

<sup>2</sup> For details see <http://www.epbd-ca.eu/>.

manipulated variable, the actual-room-temperature as actual-value and any kind of external and internal “out of control actions” as disturbances. A standard feedback controller reacts only upon given deviations between set-value and actual-value.

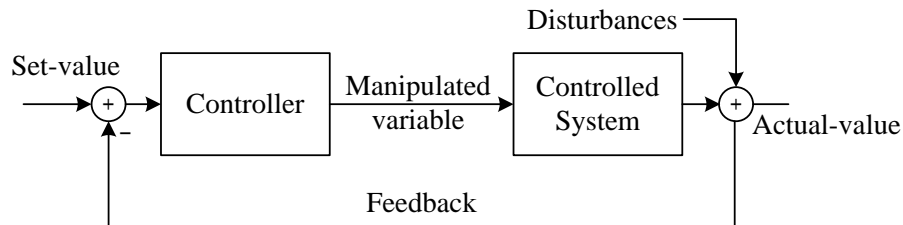


Figure 1.1.: Standard feedback controller scheme with disturbance at the output.

Model based predictive control MBPC or MPC does not refer to a certain control algorithm or structure, it is rather a strategy to determine an optimal manipulated variable given various boundary conditions – compare also Wimmer (2004) and Beigelboeck (2009). Fig. 1.2 shows a principal scheme for a predictive controller. In comparison to the standard control loop, the feedback might include more than just the actual-value of the controlled variable and the set-value could be also a trajectory set up of future set-values. MPC employs a mathematical, mostly physically based model of

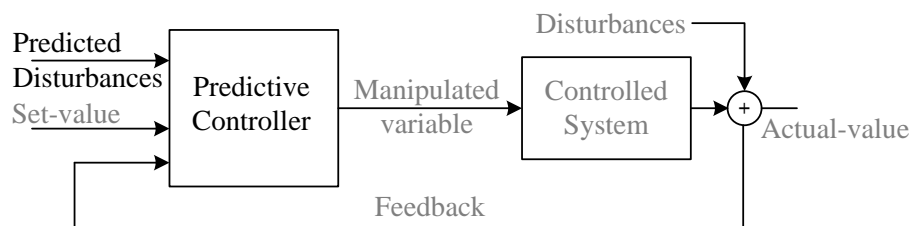


Figure 1.2.: Principal predictive controller scheme with disturbance prediction.

the controlled process or plant to determine a manipulated variable, and can thus pre-act rather than react such as a simple closed loop control does, (Gyalistras and Gwerder, 2010). The determination of the manipulated variable relies on some kind of simulation for a system – being at a defined initial state – over a certain finite future horizon considering possible disturbances and reference- or set-values. The simulation is repeated every sampling interval over this finite *prediction-* or *output horizon*. Each simulation leads to an optimal control trajectory over the *control-* or *input horizon*, which is the time frame for which the controller changes dynamically according to certain rules or constraints and remains constant after that. Thus, a sensible problem requires the prediction horizon to be greater than the control horizon, compare with Morari and Lee (1999).

## 1. Introduction

Fig. 1.3 illustrates the trajectory for a manipulated variable ( $u$ ) e.g. a heat flux and the trajectory for the controlled variable ( $y$ ) e.g. a specific temperature, given a constant set-value ( $y_{ref}$ ) for this variable. The optimal control trajectory obtained at instant  $k$  is given by  $u(k+1|k)$ ,  $u(k+2|k)$ , ...  $u(k+N_C|k)$ . Actually only the first value of this trajectory  $u(k+1|k)$  is employed as manipulated variable for the real plant. The right most argument  $k$  stands for the instant of time at which the optimal control trajectory was generated e.g. now. Consequently, one discrete time interval later the whole procedure restarts with the most recent update for the system states, which have evolved due to the manipulated variable  $u(k+1|k)$  or any disturbances that have meanwhile acted on the system.

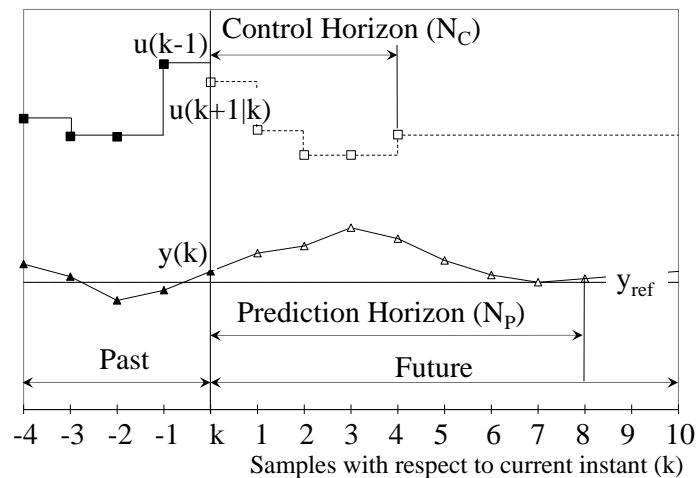


Figure 1.3.: Principal trajectories for a manipulated ( $u$ ) and controlled variable ( $y$ ) and illustration of the control and prediction horizon. For  $u$  one may imagine a *heat flux* and for  $y$  a specific *temperature*. The horizontal time axis is given in terms of samples or discrete time intervals with respect to the instant  $k$ .

## MPC – a few facts and preliminary literature

The model predictive control concept allows good control performance even for involved and complex control tasks and it is widely used in the process industries. Morari and Lee (1999) discuss a great number of research issues, including the justification and the difficulty of acceptance of on-line optimization for industrial purposes. Research areas addressed to be resolved are: general difficulties in modeling, sensing, state estimation, fault detection and *robustness*. The latter means preserving stability and the stated performance despite of indispensable model variations and other uncertainties. For a survey on industrial MPC's see Qin and Badgwell (2003). Two standard textbooks on MPC are Maciejowski (2002) and Camacho and Bordons (2004). However, the MATLAB toolbox user guide (Bemporad et al., 2010) provides also in a comprehensible manner the most important basics for the user.

### 1.2.2. Methodological aspects and chronology on predictive control

The three most relevant MPC development stages are: first, the *model building process*, second, the *model parameter identification*, and third, the *model validation*. These stages can occur in an iterative manner when the model is altered or refined until acceptable results are achieved. Morari and Lee (1999) indicate that modeling efforts require 90% of the total development time.

The availability of a model allows for the selection of a suitable cost or *objective function* (optimization criterion) and an according *optimization algorithm* or procedure. Finally, the MPC-specific parameters must be defined and tested and likewise for the process or plant specific parameters (constraints). Being at this stage one may also investigate convergence issues and think of a reasonable *fail-safe* solution in case of forecast data failure etc.

#### A short historical account

Model predictive control finds the way into industrial practice as a heuristic method, without a fully theoretical framework. C. E. Garcia et al. (1989) make out the first roots of receding horizon control (RHC) and model (based) predictive control (MPC or MBPC) in the 1960s. In Richalet et al. (1978) successful MPC-like but heuristic, practical applications in several plants have been reported. Some say the advent of MPC occurred in the refineries. Currently the *canonical MPC approach* employs a state space model in connection with a cost function – set up by linear and/or quadratic terms – and the optimization is solved through a suitable optimization algorithm.

Based on the initially moderately complex MPC approaches a number of other partly very complex approaches exist nowadays, possible due to the high computing power. One popular approach departed from offline plant or system optimization studies. Typically such studies allow for complex models to be studied with different candidate controllers and various parameters. It is a logical idea to drive this forward towards an on-line application. These approaches may be sub-summed under *co-simulation*, for building related approaches see for example Pichler et al. (2011), Schuss (2011), and Korkas et al. (2015), however, the complexity limits these approaches mostly to pure research applications.

The accuracy of weather forecast data has only in the last 10-15 years risen to an acceptable level to be considered for control purposes. Especially the accuracy of solar radiation forecasts has only in the last 5-10 years – motivated from a need of PV power forecasts – reached a level, that makes something like incorporation of these data in heating applications practically possible. These facts gave rise to a number of research projects with theoretical and practical focus (Wimmer, 2004; Bianchi, 2006; Karlsson, 2010; Rovas, 2011; Sturzenegger et al., 2012; Gwerder et al., 2013; Privara, 2013; Sourbron et al., 2013; Žáčková et al., 2014; Coninck, 2015).

## 1. Introduction

### 1.2.3. Model predictive control applied for heat pump operation

Since modeling efforts account for approximately 90% of the total MPC development time (Morari and Lee, 1999), in the context of heat pump applications the preliminary work of Reiner et al. (1998) on this must be highlighted. That research marks a root leading to further research which is discussed in the next paragraphs. In Reiner et al. (1998) it is stated that a physical model of the heat pump itself would be too complex to be used for an MPC approach. However, the on/off-behavior of a heat pump has been found to be sufficiently approximated by two simple low-pass filters.

Wimmer (2004) has investigated the model predictive control of a heat pump for a single family house with different approaches based on the preliminary work of Reiner et al. (1998). In this work the compressor speed is constant and a variation of the heat pump power is realized by means of pulse width modulation (PWM). That is, given a constant period – between 0.4 h and 3.2 h has been used – the on-time of the heat pump is varied to adjust the average heating power over that period. Wimmer analyzed building models of different complexity, from 2<sup>nd</sup> to 4<sup>th</sup> order. The models are physically motivated, but the estimated model parameters are a mixture of physical and lumped physical parameters. The derived state space model of 3<sup>rd</sup> order comprises the flow medium, the thermal mass of the floors, and the room air as heat capacities. Although, *solar radiation* entering the building was found to intensively interfere with the building, it was *neglected*. One year simulations have shown cost savings up to 13% – compared to a standard on/off controller – and an electricity consumption reduction up to 3.5%. Eventually, the simplest (least square optimization) of the three developed algorithms has been successfully employed in a real building. The author noted that any future application for other buildings would require an adaptation of the used building model, Wimmer (2004).

Bianchi (2006) continued the research of Wimmer and investigated an *adaptive* MPC approach for the purpose of heating a single family house. The main contribution of Bianchi is the introduction of an identification mechanism to automatically adjust the building model parameters during operation. This way, the MPC approach of Wimmer has been supplemented to be suitable for application in different single family houses. Principally, this approach should allow for plug-and-play application of model predictive heat pumps. Experience on real applications has not been reported.

A heat pump internal MPC is investigated in Wallace et al. (2012), where model predictive control is used to control the vapor compression cycle (*compressor speed* and *expansion valve*) in an air-conditioning system. Improved set-value tracking and significant energy savings have been reported.

In Ahmad et al. (2013) the performance of a combined solar system with heat pump for residential purposes has been investigated. However, this research misses a proper treatment of comfort violations – it is too tolerant concerning this.

Young (2013) deals with the topic demand side management (DSM) with heat pumps for single family houses with floor heating. In this article a prediction horizon of 24 h has been found to outperform smaller prediction horizons in terms of renewable energy utilization with nearly negligible impact on the comfort.

The electrical load shifting potential of a smart heat pump has been analyzed by Danny et al. (2014). It has been found, that the theoretical load shifting potential could be exploited by a fraction between 19% and 33%. However, at the same time the electricity consumption increases by approximately 9%. The numbers are on an annual base.

In the work of Li et al. (2015) the heat pump operation by means of MPC is only a minor task in light of the relatively complex system introduced – heat pump, thermal storage, PV-system, air handling unit, ventilation, floor heating . This research investigates also the impact of solar irradiation prediction inaccuracies, with the outcome that even inaccuracies  $> 70\%$  increase the energy consumption by only 3%, but cause an adverse effect on the comfort violations which increase significantly. Li et al. (2015) successfully rely on a *gray-box* modeling approach for the thermal storages involved – building envelope, room, floor and tank. Unfortunately, figures on energy savings which have been reported rely on a too short time interval to be representative for annual performance implications.

Coninck (2015) recently finished his PhD with the title “Grey-Box Based Optimal Control for Thermal Systems in Buildings – Unlocking Energy Efficiency and Flexibility”. This work deals also with optimal heat pump operation. The reported daily cost savings related to a real office building are claimed to be 30% to 40%, however, these figures are based on short term measurements rather than annual measurement data or simulations, which makes it difficult to extrapolate the savings on an annual base.

### 1.2.4. Model predictive control related to building automation

Many devices in buildings are controlled using simple difference controllers with hysteresis or PID-controllers<sup>3</sup>. One reason therefore is the simple numerical coding of these controllers. This section provides information on model predictive applications in the context of building automation and energy supply. Most predictive frameworks are based on the canonical approach explained in sec. 1.3.1, by contrast to co-simulation, which is shortly explained towards the end of this section.

Radiative heating through e.g. an activated ceiling involves huge time constants due to the thermal inertia, making it difficult to dynamically react to set-point changes. Further, the thermally activated building system (TABS) requires much power to drive the system from heating to cooling or vice versa. TABS are predestined for model predictive control. Once, weather prediction data are incorporated the data may be facilitated to include the blind control, domestic hot water provision or heat pumps and the like in a predictive control framework.

---

<sup>3</sup> The D-part of such a controller could be interpreted to imply a very simple predictive nature.

## 1. Introduction

Components of building management systems (BMS) and according predictive controllers have been investigated in Gyalistras and Gwerder (2010), Gwerder et al. (2010), Oldewurtel, Parisio, Jones, Morari, et al. (2010), Oldewurtel, Gyalistras, et al. (2010), Halvgaard et al. (2012), and Gwerder et al. (2013). In Oldewurtel et al. (2012) also the uncertainty of weather predictions is considered for the MPC design, resulting in a stochastic model predictive control.

A great deal of research on the *building model* and related parameter estimation has been published in recent years (Karlsson, 2010; Karlsson and Hagentoft, 2011; Žáčková et al., 2011; Privara et al., 2012; Sturzenegger et al., 2012; Sourbron et al., 2013; Privara, Cigler, Zdenek, et al., 2013; Coninck, 2015). The modeling approaches are dominated by physical first principle (white box) models (Sturzenegger et al., 2012) and gray-box models. Practical applications show to require more involved parameter estimation methods than pure simulation studies. Sensor misplacement or noise signals require methods such as model predictive control relevant identification (MRI) (Lauri et al., 2010; Žáčková et al., 2011).

Results on the performance and practical issues of model predictive control for BMS have been investigated in the last few years in a number of projects and simulation studies. Results from practice may be found for example in Gwerder et al. (2013), Žáčková et al. (2014), and Coninck (2015). The number of simulation studies is high, only a few are cited here Beigelboeck (2009), Kolokotsa et al. (2009), Oldewurtel et al. (2012), Sourbron et al. (2013), and Li et al. (2015).

A MPC scheme for residential cooling in connection with an ice storage has been investigated in Candanedo et al. (2013) – the found cost saving potential is quite attractive. Snoek and Kluiters (2011) investigated the performance improvement for incorporation of weather forecast data into the operation plan of a district heating system with seasonal and short term thermal storages.

### 1.3. Optimization – potential savings and different approaches

A number of MPC strategies with different optimization objectives have been already tested using simulations. The algorithms employed widely vary in complexity and only few were used and tested in practical applications.

In Oldewurtel, Gyalistras, et al. (2010) a theoretical non renewable primary energy (NRPE) saving potential with MPC applied for BMS, of up to 40% has been reported<sup>4</sup>. This hypothetical potential represents a performance bound (PB). The practical saving potential in Oldewurtel, Gyalistras, et al. (2010) was found to range from 9% to 28%, for certain cases with less than 70 Kh/a of comfort violations<sup>5</sup>. MPC with *persistence*

<sup>4</sup> Comfort violations are less than 300 Kh/a in this study.

<sup>5</sup> This practical potential can be calculated using the energy consumption of the rule-based control and that of the MPC.

### 1.3. Optimization – potential savings and different approaches

*weather predictions* – tomorrow as today – clearly showed less NRPE saving potential than MPC with real weather predictions – the NRPE savings halve with respect to the performance bound. A *robustness* analysis has shown changes of NRPE use within only a few percent, however, the amount and the numbers of comfort violations showed a greater but still agreeable sensitivity to altered building model parameters.

A theoretical saving potential of approximately 8% – compared to a standard PI-controller – with MPC applied for room temperature control was found in Beigelboeck (2009).

A MPC strategy with ideal predictions applied to cogeneration of heat and power lead to primary energy savings in the range from 20% to 25% as reported in Gaehler et al. (2007). A MPC-scheme applied for residential cooling in connection with an ice storage has been reported to lead to cost savings between 5% and 30% compare with Candanedo et al. (2013).

#### 1.3.1. Optimization schemes for predictive controls

In principal any optimization algorithm may be used in a predictive control scheme. Ideally, the desired optimum is found analytically but due to the optimization problem constraints in most cases this is infeasible. Hence, a numerical optimization is required. For such a scheme the requirement is to keep the number of numerical iterations as small as possible. The iterations, a numerical optimization requires to find an optimum – ideally the global – are closely entangled with the model properties (linear or non-linear).

##### The canonical MPC approach

A linear quadratic (LQ) optimization problem without constraints can be solved analytically. Consideration of constraints for the controller output requires a numerical optimization algorithm. This represents the canonical MPC-approach, a linear model, constraints and a suitable solver for a quadratic program. More details on this may be found in Maciejowski (2002).

##### The controller co-simulation

A controller co-simulation environment usually consists of a relatively complex non-linear simulation for the plant or process of interest and a very efficient numerical optimization algorithm. In Rovas (2011) such a scheme was developed and applied for a relatively complex office building.

## 1. Introduction

Concerning complexity, a controller co-simulation can be compared to a sophisticated plant analysis e.g. during the engineering or development stage of a process. However, in co-simulation the purpose is to find in some sense optimal control decisions.

A simple but mostly sufficient example for the controller is a P-controller, as used in Rovas (2011), or a set of alternatively operating P-controllers. An example for a single controller is given in eq. (1.1), where the P-factors, hidden in  $\Theta$ , together with a state vector  $x$  lead to the control output  $u$ .  $\Theta$  is updated after a predefined control period.

$$u(t) = \Theta(t) \cdot x(t) \quad (1.1)$$

A practical example is the determination of the supply water (flow) temperature  $\vartheta_{sw}$  as a function of the current ambient temperature  $\vartheta_{oa}$  and the current solar radiation  $G$ :

$$\vartheta_{sw}(t) = \theta_1 \vartheta_{oa}(t) + \theta_2 G(t), \quad (1.2)$$

with  $\theta_1$  being a positive and  $\theta_2$  being a negative number. Dealing with more than one controller at the same time,  $\Theta$  turns into a matrix and  $u$  becomes a vector.

A predictive simulation-based controller for systems in buildings was developed in Rovas (2011), and has been deployed e.g. by Schuss (2011). Controller co-simulation is also dealt with in Pichler et al. (2011), but not considered further within this thesis.

Schuss (2011) has conducted two practical controller co-simulation experiments for a few weeks. Mean overheating is approximately 1 K, and 2.1 K less compared to a rule-based controller and evaluation of comfort in terms of psychometric charts lead to 38% and 35% less comfort violations, respectively. Peak temperatures were up to 4 K less.

### 1.3.2. Benefits for related technologies and beneficiaries

A MPC control strategy can serve as a performance bound for rule-based controllers (RBC) and is likely to provide insight to aid developing suboptimal but simpler rule-based controllers with predictive features. That is, a careful study of MPC results, i.e. optimal solutions and found optimal strategies, can be exploited for partial utilization in RBCs, cf. Gyalistras and Gwerder (2010).

Weather forecast can also be used for district heating systems with seasonal storage and decentralized solar thermal energy supply to decide when not to deliver energy to the seasonal storage from short term thermal storages or vice versa, Snoek and Kluiters (2011).

Residential cogeneration is an emerging technology with a potential to reduce the primary energy consumption. Electricity and thermal energy generation in parallel may result in net primary energy (NPE) saving, only if intelligent control strategies are applied, Gaehler et al. (2007).

### 1.4. Synthesis and challenges in research

MPC belongs to the mostly implemented advanced process control technology with many industrial applications. At the building system control sector, MPC is very seldom used. The legislation directive to lower the energy consumption in the building sector and the related requirements on the automation sector are already defined. The number of recent and ongoing research projects indicate a clear movement in this matter in building automation, however, widespread practical implementations are not in sight at the very moment.

Influential research groups in building related MPC are at the Swizz Federal Institute of Technology and at the Technical University of Prague. The researchers in Prague report cost savings of approximately 20%, based on real experiments in the university building. The primary energy saving potential reported by Oldewurtel, Gyalistras, et al. (2010) is between 9% and 28%. In general MPC increases the thermal comfort compared to a standard controller.

A major challenge is the modeling part, concerning the MPC-development steps. The remaining questions are, how to standardize this process for buildings and how to design models with a high degree of re-useability. Finally, system identification based on real, often poor measurement data poses also a challenge.

#### Open questions and tasks

Based on the literature review, selected research questions and tasks are formulated. The content of this thesis should contribute to the following aspects.

- Development of a MPC-scheme incorporating a heat pump with variable speed compressor, a thermal storage, a photovoltaic-system and TABS as heat emission system for a single family house.
- Indication of the expected electricity self consumption.
- Energetic and comfort related implications for this system.
- Evaluation of the system performance based on annual simulation results.
- Gaining knowledge related to suitable, accurate enough building models for a single family house.
- Gaining knowledge related to the controller model for the thermal storage when heated with a heat pump with variable speed compressor.
- Extension of system identification related knowledge in connection with (linear) building models for the purpose of MPC.
- Extension of knowledge in system identification with real measurement data from a building.
- Report on practical problems when it comes to real implementation of a MPC-scheme in a building management system.

## 1. Introduction

### 1.5. Thermal comfort

This research deals with residential heating and cooling demand optimization through a smart control scheme. Thermal comfort is the constraining aspect which must be maintained for this optimization. Existing comfort standards determine HVAC<sup>6</sup> set point values and the upper and lower temperature bound as a function of a reference outdoor temperature.

#### 1.5.1. A short review

Thermal comfort is a very vague term, it is generally defined as "... that condition of mind which expresses satisfaction with the thermal environment" (ASHRAE 55:2004). However, given one and the same conditions the judgment varies among the individuals. For engineering purposes a few standards exist, which try to objectify thermal comfort.

The available standards deviate concerning the HVAC set point value, the minimum and maximum indoor temperature bound and the reference outdoor temperature. This *reference outdoor temperature*<sup>7</sup>  $\vartheta_{rm}$  may be an hourly-, daily-, monthly-, seasonal- or moving -average; or the maximum outdoor temperature. *Classical* and *adaptive* thermal comfort standards exist. A classical standard<sup>8</sup>, such as OENORM EN ISO 7730:2006 treats thermal comfort usually in a conservative manner. This means that humans adaptability to changing ambient conditions is considered to be very limited. In *adaptive* comfort standards, such as ASHRAE 55:2004 or OENORM EN 15251:2007, humans adaptability to the ambient conditions is extended beyond the classical theory of P. O. Fanger (1981). The theory of adaption incorporates the idea, that to some degree humans are able to adapt to the indoor conditions at specific outdoor conditions. For example, occupants in mechanically ventilated buildings are usually less tolerant to varying conditions compared to occupants in buildings where window ventilation is applied – this is an underlying assumption of adaptability-theory. A good review which backs the theory of adaption on behalf of real studies is given in Yang et al. (2014).

An energy demand analysis must be seen within the light of the selected comfort standard. The question which standard to choose is not straightforward to answer. Actually, there is no comfort standard to be preferred over all the other standards. OENORM EN 15251:2007 is designed such that the cooling demand in summer may be reduced significantly. Researchers often also choose national standards for their analysis. Apart from the existing comfort standards at the end the individuals and the building owners decide on the required level of thermal comfort. This evaluation is always a subjective one, and therefore the used comfort models in practice may also

---

6 HVAC is the common acronym for heating, ventilation and air conditioning.

7 The index  $rm$  in  $\vartheta_{rm}$  stands for running mean.

8 Concerning ventilation and cooling for buildings it is worth to mention also OENORM EN 13779:2007 which replaced the famous DIN 1946-2.

be tailored to the given requirements, combining aspects of the different standards. This highlights the importance of *pre-design discussions* between building designers and clients.

For further reading, Toedtli et al. (2009) provide a good overview and a discussion on that topic in the context of TABS. Sourbron and Helsen (2011) go further and investigate the impact of a few selected comfort models on the energy demand. A recent review on thermal comfort models for living space and vehicles, and indications for future developments are given in Croitoru et al. (2015). In temperate zones such as central Europe it is possible to avoid *humidity* as an explicit variable in a comfort model, however, this may not hold for arid or humid climate zones. Rana et al. (2013) conduct a feasibility analysis of using *humidex* indoor – originally humidex is used outdoors to predict the human thermal perception, it is expressed as a number and corresponds approximately to the temperature in °C . Consulting the corresponding journals one will find work striving to develop a homogenous comfort model, valid and suitable for all climate zones. To get a feeling for thermal perception and sensitivity from a physiological point of view, Herrmann et al. (1994) provides a good insight under the title "Humans under showers".

In this research comfort assessment is principally based on [OENORM EN ISO 7730:2006](#) office type buildings of Class B. That is, the (operative) temperature set-point and limits in winter (heating season) are  $22.0\text{ °C} \pm 2.0\text{ K}$  and in summer (cooling season) the limits are  $24.5\text{ °C} \pm 1.5\text{ K}$ . That is, in winter the lowest allowed temperature is  $20.0\text{ °C}$  and in summer the highest tolerated temperature is  $26.0\text{ °C}$  .

Tab. 1.1 provides further details on the selected comfort level *class B* as defined in [OENORM EN ISO 7730:2006](#) with a predicted percentage of dissatisfied (PPD) < 10%. Cooling or heating through a TABS is also limited by the *radiation temperature asymmetry* which is explained in Appendix D.5, and the maximum *vertical air temperature gradient*. The radiation temperature asymmetry limits are based on P. Fanger et al. (1985), but as is discussed in Appendix D.5 especially the heated ceiling limits may be relaxed.

Table 1.1.: Comfort requirements for the three comfort classes given in [OENORM EN ISO 7730:2006](#).

Class	vertical $\frac{\partial \vartheta_{ra}}{\partial x}$ <sup>a</sup> K/m	range $\vartheta_{floor}$ °C	radiation asymmetry in K			
			heat ceil	cool wall	cool ceil	heat wall
A, PPD < 6%	< 2	19-29	< 5	<10	<14	<23
B, PPD < 10%	< 3	19-29	< 5	<10	<14	<23
C, PPD < 15%	< 4	17-31	< 7	<13	<18	<35

<sup>a)</sup> this gradient refers to the length interval 0.1 m - 1.1 m above the floor.

### 1.5.2. Comfort violation measurements

Given the selected comfort model the question arises how to measure comfort violations. This may be done either purely by counting the time where the limits were violated or, more advanced, with an additional weight indicating the severeness of each violation.

## 1. Introduction

A prominent method to measure comfort violation is to count the absolute time of violations. Typically 3% and 5% of the occupation time are stated being acceptable. Assuming approximately 250 working days a year and 8 office hours a day, the number of accepted comfort violations equates to 60 h and 100 h per year. However, this violation measure does not indicate the severity of the violation.

An alternative to the hours with comfort violations is given in terms of *degree hours* separated for over- and undershoot of the comfort limits, compare with Appendix F in [OENORM EN 15251:2007](#). There exist no limits for these measures but the according number may be used as a performance indicator of a control. Very good total values are below 100 Kh/a but the range is very large up to approximately 1500 Kh/a, cf. Oldewurtel et al. (2012). However, Kh of the category cold are more critical than those of the category hot. The measures for undercooling and overheating may be calculated as

$$\text{undercooling} = \sum_{\text{undershoots}} \Delta t_{\text{undershoot}} * (\vartheta_{L,\text{limit}} - \vartheta_{\text{actual}}), \quad (1.3)$$

$$\text{overheating} = \sum_{\text{overshoots}} \Delta t_{\text{overshoot}} * (\vartheta_{\text{actual}} - \vartheta_{U,\text{limit}}). \quad (1.4)$$

That is, the undercooling measure is obtained through all violations of the lower temperature limit  $\vartheta_{L,\text{limit}}$  each weighted with the duration of the violation in h and similarly for the overheating above the upper temperature limit  $\vartheta_{U,\text{limit}}$ . Based on building standards a reasonable comfort violation level of 70 Kh/a is defined in Oldewurtel, Gyalistras, et al. (2010), which is rather strict, 200 Kh/a seems more realistic.

## 2. Heat pump, PV system and building

Chapter 2 describes the reference system which is implemented and simulated with TRNSYS 17. This system simulation is used to evaluate the developed model predictive control (MPC) concepts. The heat pump-characteristics outlined in sec. 2.4.1 provide the basis for the thermal energy storage with heat pump (TES-HP) controller model developed in chapter 4. Further, sec. 2.4.1 provides all HP-related functions used for the MPC objective functions. However, initially the topic demand side management is briefly introduced.

### 2.1. Demand side management

Electricity is probably the most relevant form of energy and characterizing our current age of mankind. Fighting against the artificial global warming is connected with many obstacles, two of them being volatile electricity generation and electricity storage. Variability at the grid demand side is mostly compensated by dynamic supply units, such as pumped-storage hydroelectricity plants (in mountainous regions) or generators, which can easily be turned up or down, but are mostly fossil-fueled. These dynamic supply units are also suitable to compensate variable, grid connected photovoltaic (PV) or wind power plants.

Dynamic fossil-fueled generators, as compensation for the variable grid demand or to assist volatile renewable sources, go against the trend of becoming independent of this source. An alternative approach represents demand-side management (DSM). DSM describes the timely adjustment of a given load to a specific (price) signal (Schaefer et al., 2015). Characterized by the imagination of a peak and valley shaped load profile three types are divided: reduction- (*peak clipping*), increase- (*valley filling*) and shifting- (*load shifting*) of consumption. That is, rather than providing any existing demand, DSM strives to shape the demand to fit the current supply. This is especially interesting in connection with volatile renewable energy sources.

It is clear, that energy generation from renewable sources must be maximized, rather than curtailed. This motivates the search for applications suitable for PV- or wind-led operation. Residential heating and cooling by means of a compression heat pump (HP) system in connection with a thermal storage constitute a prototypical case to develop and apply a load shifting strategy. Extending the system with a PV plant increases the scope also in the direction of power generation. Such a system poses an interesting prototype for detailed investigation of demand-side but also (renewable) electricity generation related aspects. The emphasis in this thesis is on the control part of a (compression) HP-PV-system for a single family house (SFH), cf. fig. 2.1.

## 2. Heat pump, PV system and building

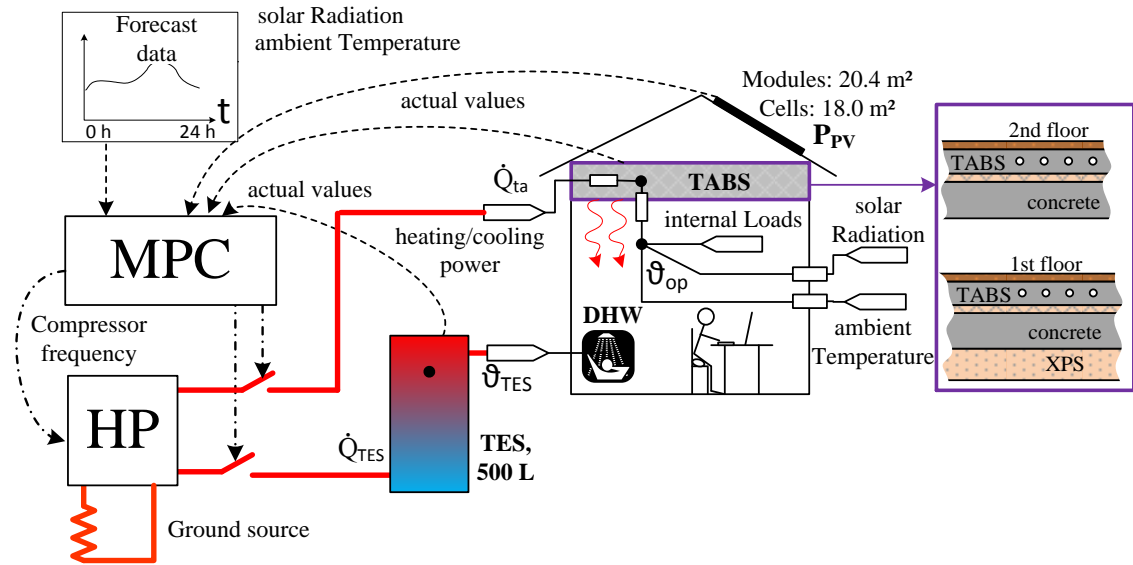


Figure 2.1.: Overview (simplified) on the overall system components and interfaces.

Concerning the terminology of load shifting and daily heating- or cooling-demand, one is confronted with *continuous load shifting*<sup>1</sup>. First, this allows for partial load shifting – that means the daily load must not be shifted as a whole – and second, it allows for repeated load shifting of different shares of the whole load and – depending on the existing thermal storage capacities – also at various times of a day.

The minimization of grid consumption or maximization of PV-generated electricity is only possible, if a thermal storage, either the water-storage (TES) or the building concrete-storage (TABS), is *thermally unsaturated* at times with high PV-power. The task of the MPC is to schedule the HP operation such, to prevent from grid-assisted heating at times with low PV-power in situ. Hence, the MPC requires an approximate trajectory or time series for the expected (future) PV-power.

## 2.2. System description

The investigated system comprises two *active* components: the ground source HP (thermal) and the PV-plant (electrical), and two *classical passive* components: the thermal energy storage (TES) and the thermally activated building system (TABS) as part of the single family house. The HP, the TES and the TABS are connected through a hydraulic system, cf. fig 2.3, electrical inter-connections are not relevant for the analysis, although, the grid consumption and feed-ins are determined.

<sup>1</sup> The counterpart is blockwise shifting, which is typical for an industrial process that is started at one time and must not be interrupted, until it is finished.

## 2.2. System description

The special feature about the whole DSM idea in this context is the fact, that through suitably scheduled supply management the classical passive TES and TABS may become *pseudo active* thermal components. A properly scheduled management of the pseudo active components reflects at the grid side with two main characteristics: first, damped electricity demand at times with thermal peak load, and second, limited feed-ins at times with high PV generation.

### 2.2.1. Heat pump description

Fig. 2.2 shows the HP set-up by means of the refrigerant cycle and a typical temperature-enthalpy ( $\theta$ -h) diagram. The main components are the evaporator (e), the scroll compressor, the desuperheater (d), the condenser (c) and the economizer (eco). The state changes during the refrigerant cycle are the following:

- $r_1 \rightarrow r_2$  polytropic compression
- $r_2 + r_9 \rightarrow r_3$  adiabatic mixing of  $r_2$  and  $r_9$
- $r_3 \rightarrow r_4$  polytropic compression
- $r_4 \rightarrow r_5$  isobaric heat transfer in the desuperheater
- $r_5 \rightarrow r_6$  isobaric heat transfer in the condenser
- $r_6 \rightarrow r_7$  isenthalpic expansion in valve  $V_{ex1}$
- $r_7 \rightarrow r_8 \rightarrow r_9$  isobaric heat transfer with superheating in the economizer (cold side)
- $r_6 \rightarrow r_{10}$  isobaric heat transfer in the economizer (hot side)
- $r_{10} \rightarrow r_{11}$  isenthalpic expansion in the valve  $V_{ex2}$
- $r_{11} \rightarrow r_{12} \rightarrow r_1$  isobaric heat transfer with superheating in the evaporator.

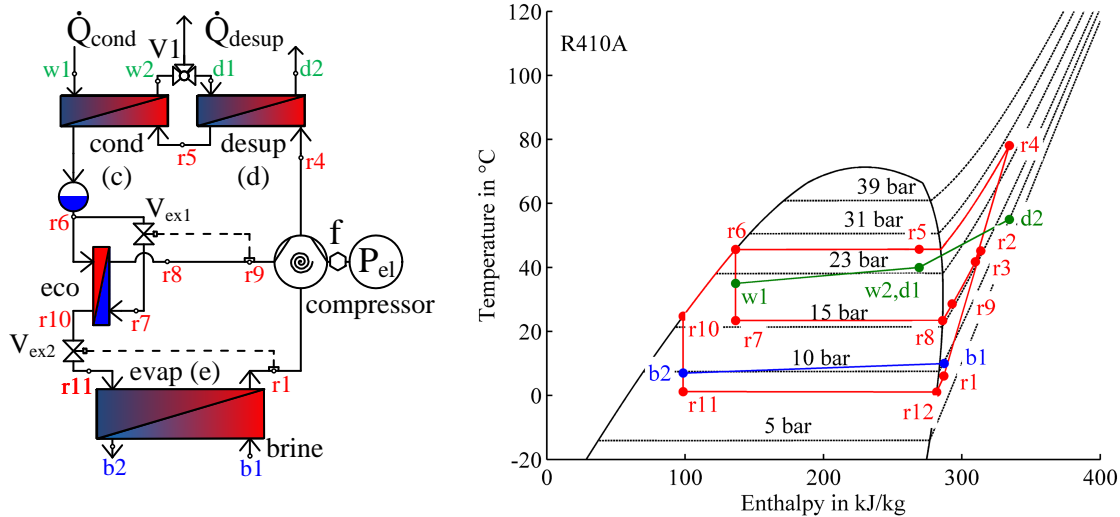


Figure 2.2.: Heat pump set-up (left) and exemplary temperature-enthalpy  $\theta$ -h diagram (right).

The used refrigerant R-410A is a zeotropic mixture although with close to zero temperature glide ( $< 0.2$  K), thus, it is a near-azeotropic mixture behaving similarly like

## 2. Heat pump, PV system and building

a pure component. R-410A is widely used as refrigerant in air conditioning applications. It has a relatively high vapor pressure (e.g. 8 bar at 0 °C ) leading to a high volumetric cooling capacity (4650 kJ/m<sup>3</sup> at<sup>2</sup> 0/40 °C ) which allows for smaller construction sizes – compared to former refrigerants (R22) – at the same cooling capacity. Although R-410A does not contribute to ozone depletion, a main drawback of R-410A is the relatively high global warming potential (GWP) of 2100, (Recknagel, 2013/2014, p. 1613 ff.), see also chapter 3 in Hundy et al., 2016 for more details.

The compressor operating limits are provided in fig. 2.4. The area inside the drawn polygons show the possible operating range as a function of evaporating- and condensing-temperature. Given a constant source temperature of 0 °C and a required desuperheater outlet temperature of 50 °C for TES heating, the possible operating range is from 30 Hz to approximately 110 Hz.

The simulation model for the HP in fig. 2.2 is a user defined TRNSYS type, which has been originally developed together at Graz University of Technology and SPF Rapperswil (Dott et al., 2012, p. 47 ff.). The parametrization of the model is based on extensive measurements, see Hengel et al. (2014) and Hengel et al. (2016).

The implementation of the HP characteristics in the MPC controller model is outlined in sec. 4.4. In principal it is based on extensive simulations and approximation of relevant physical relations through polynomial functions, presented in sec. 2.4.1. Concerning practical applications the extensive simulations may be replaced by HP specifications from the manufacturer.

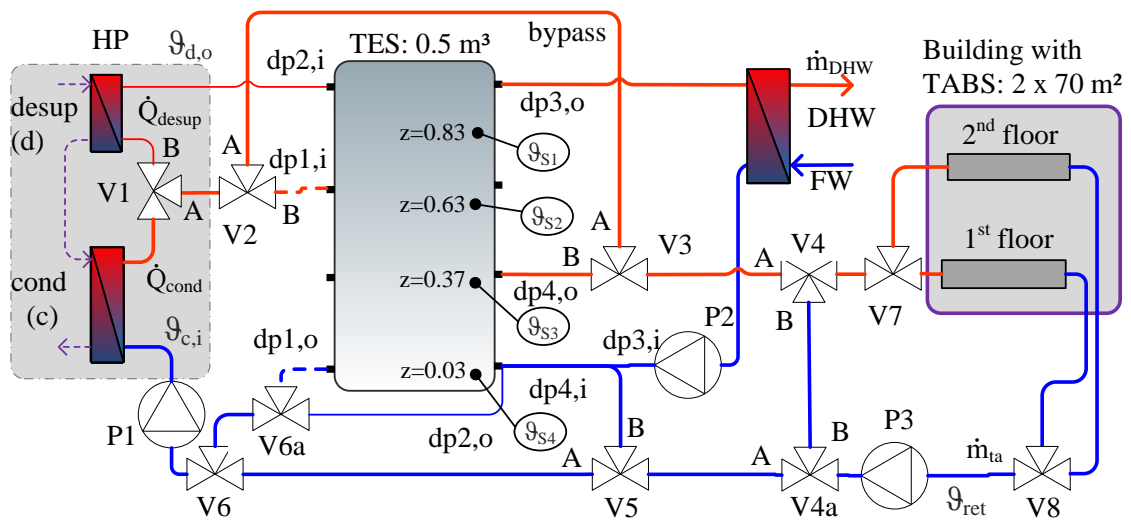


Figure 2.3.: Illustration of the hydraulic system with HP, TES and TABS.

2 The additional information 0/40 °C indicates evaporation at 0 °C and condensation at 40 °C , which define the two points to read the corresponding  $\Delta h$  in the  $\theta$ -h diagram; together with the density at the dew point at evaporation temperature this leads to the volumetric cooling capacity.

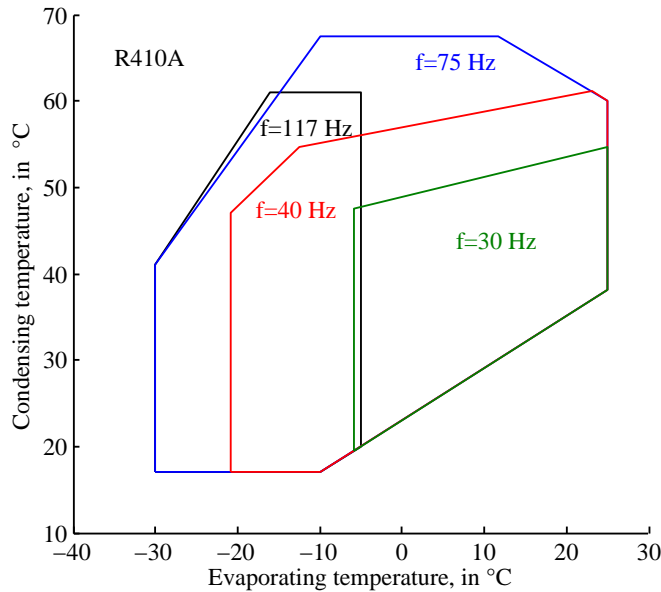


Figure 2.4.: Heat pump scroll compressor operating limits.

### 2.2.2. Hydraulic system and thermal energy storage

Fig. 2.3 shows the hydraulic pipe-system including valves (V) and pumps (P). Tab. 2.1 provides a simplified overview on the operation modes of the valves and the pumps for the different operating-states, which are described in terms of control functions (CF). CF<sub>1</sub> and CF<sub>4</sub> exclude each other and so do CF<sub>4</sub> and CF<sub>5</sub>, apart from these exclusions more than one CF may be active at the same time. Except for the double port 1 (dp1) connections to and from the TES in fig. 2.3 – drawn in dashed lines – all connections are used for the operating-states described in detail in sec. 2.3.

#### Operating conditions of the hydraulic components

Tab. 2.1 briefly summarizes the operating conditions for controlled elements for the *base case scenarios*. The logical part related to the operating conditions is described in sec. 2.3. For any MPC *scenario* the operating conditions deviate only with respect to the frequency set value. In addition, the control criteria (described in sec. 2.3) that trigger a CF are different for MPC scenarios.

The HP may either be switched on to heat the TES (for DHW purpose) – which means operation of the compressor at 60 Hz – or for direct space heating which results in an outside ambient temperature ( $\vartheta_{oa}$ ) dependent frequency control; see eq. (2.10). The *ground source brine pump*, which is not shown in fig. 2.3, is operated such to sustain a brine temperature difference of 3 K over the evaporator. If not stated otherwise, the ground is assumed as infinitely large reservoir being at a temperature of 0 °C .

## 2. Heat pump, PV system and building

Table 2.1.: Overview on the operating conditions of the controlled elements for CF<sub>1</sub>, CF<sub>3</sub>, CF<sub>4</sub>, CF<sub>5</sub>; all mass flows are given in kg/h.

controlled elements	CF <sub>1</sub> TES heating	CF <sub>3</sub> DHW draw-off	CF <sub>4</sub> space heating direct	CF <sub>5</sub> space heating from TES
HP comp. frequency	$f = 60 \text{ Hz}$	X <sup>a</sup>	$f(\vartheta_{oa})$	X
V <sub>1</sub>	$\dot{m}_A = 0$ $\dot{m}_B = \dot{m}_{AB}$	X X	$\dot{m}_A(\vartheta_{c,i}, \Delta\vartheta_c = 5 \text{ K})$ $\dot{m}_B(\vartheta_{d,o} = 50 \text{ }^\circ\text{C})$	X X
V <sub>2</sub>	X X	X X	$\dot{m}_A = \dot{m}_{AB}$ $\dot{m}_B = 0$	X X
V <sub>3</sub>	X X	X X	$\dot{m}_{AB} = \dot{m}_A$ X	$\dot{m}_A = 0$ $\dot{m}_{AB} = \dot{m}_B$
V <sub>4</sub>	X X	X X	$\dot{m}_{AB} \geq 700 \text{ kg/h}$ $\dot{m}_B = 0 \text{ OR } (700 \text{ kg/h} - \dot{m}_{V1,A})$	$\vartheta_{AB} = \vartheta_{ret} + 5 \text{ K}$ $\dot{m}_{AB} = 1031 \text{ kg/h}$
V <sub>5</sub>	X X	X X	$\dot{m}_A = \dot{m}_{V1,A}$ $\dot{m}_B = 0$	$\dot{m}_A = 0$ $\dot{m}_B = \dot{m}_{AB}$
V <sub>7</sub>	X	X	$\dot{m}_A = \dot{m}_B$	$\dot{m}_A = \dot{m}_B$
P <sub>1</sub>	ON	X	ON (master)	X
P <sub>2</sub>	X	ON	X	X
P <sub>3</sub>	X	X	ON (slave) OR ON	ON

<sup>a</sup> An X indicates that the controlled element does not depend on the respective CF.

V<sub>1</sub> is a continuously operating valve and determines the distribution of the condenser mass flow ( $\dot{m}_c$ ). The  $\dot{m}_c$  is a function of the condenser inlet temperature ( $\vartheta_{c,i}$ ) that is either dominated by the TES bottom temperature (see fig. 2.8 for active CF<sub>1</sub>) or the TABS return water temperature ( $\vartheta_{ret}$ ) (see fig. 2.9 for active CF<sub>4</sub>). During TES heating the whole condenser mass flow is directed also through the desuperheater. However, this is to exploit its heat exchange capacity, rather than using the real desuperheater functionality. For direct space heating operation the desuperheater mass flow is adjusted such to obtain an outlet temperature ( $\vartheta_{d,o}$ ) of 50 °C (if not stated otherwise).

The control of the switching valve V<sub>2</sub> is principally relevant to switch between direct space heating (port A) or storage heating via port B. However, in this thesis only port A is in use since a preliminary investigation showed that the HP performance decreases for CF<sub>1</sub> via V<sub>2</sub> port B and TES heating for space heating purpose is not considered cf. sec. 2.3.1.

The switching valve V<sub>3</sub> directs the bypass-mass flow towards V<sub>4</sub> for direct space heating (CF<sub>4</sub>), while during space heating from the TES (CF<sub>5</sub>)  $\dot{m}_A = 0$  and  $\dot{m}_{AB} = \dot{m}_B$ .

Mixing valve V<sub>4</sub> has two distinct functions. During direct space heating it (indirectly) assures a total TABS loop mass flow greater than<sup>3</sup> 700 kg/h and during heating from the

<sup>3</sup> This minimum value originates from the desired minimum specific mass flow of 5 kg/(h m<sup>2</sup>) for the TABS. It has to do with the partitioning (discretization) and the related accuracy of the TABS model in TRNSYS. Theoretically, the lower limit to ensure turbulent flow in the pipes ( $\approx 0.2 \text{ m/s}$ ) given  $d_i = 16 \text{ mm}$  is with  $\approx 145 \text{ kg/h}$  far below the 700 kg/h. The area specific minimum value is obtained through the area of the TABS.

## 2.2. System description

TES  $\dot{m}_B$  is adjusted such, that  $\vartheta_{AB} = \vartheta_{ret} + 5 \text{ K}$  given a constant mass flow<sup>4</sup>  $\dot{m}_{AB} = 1031 \text{ kg/h}$  maintained by  $P_3$ . The role of  $V_{4a}$  is to distribute the mass flow  $\dot{m}_{V_{4,AB}}$  accordingly. For more details see Appendix C.1.

The distribution valve  $V_5$  directs  $\dot{m}_{AB}$  such that the TABS loop is closed either via the HP ( $CF_4$ ) or through the TES ( $CF_5$ ).  $V_6$ ,  $V_{6a}$  and  $V_8$  are uncontrolled mixing valves with a T-piece function.  $V_7$  equally splits the total TABS mass flow for the first- and second building floor TABS.

The pump operation schedule is relatively straight forward.  $P_1$  is always switched on during HP operation and it is controlled such that the desired HP desuperheater- ( $CF_1$ ) or condenser ( $CF_4$ ) outlet temperatures are met, independently of the condenser inlet temperature.  $P_2$ , being part of the domestic hot water preparation through the continuous flow heater principle, is controlled such to met the desired DHW draw-off temperature for predefined  $\dot{m}_{DHW}$ .  $P_3$  operates in slave mode together with  $P_1$  (if  $CF_4$  is active and  $\dot{m}_{V_{1,A}} > 700 \text{ kg/h}$ , see fig. 2.9), or independently, to maintain either 700 kg/h in the TABS loop (if  $CF_4$  is active and  $\dot{m}_{V_{1,A}} < 700 \text{ kg/h}$ ) or 1031 kg/h (if  $CF_5$  is active, see fig. 2.10).

### Thermal energy storage (TES)

The TES in fig. 2.5/2.3 comprises four double port (dp) connections, however, dp1 is not in use herein. Double port 2 connects the HP (desuperheater) to the storage. The fresh water station (FWS) is connected via dp3 and SH from the TES is possible via dp4. Four sensors are installed for control purposes, with their relative installation height being indicated by  $z$ , which takes a value between 0 (for bottom 0 m) and 1 (for top 1.81 m).

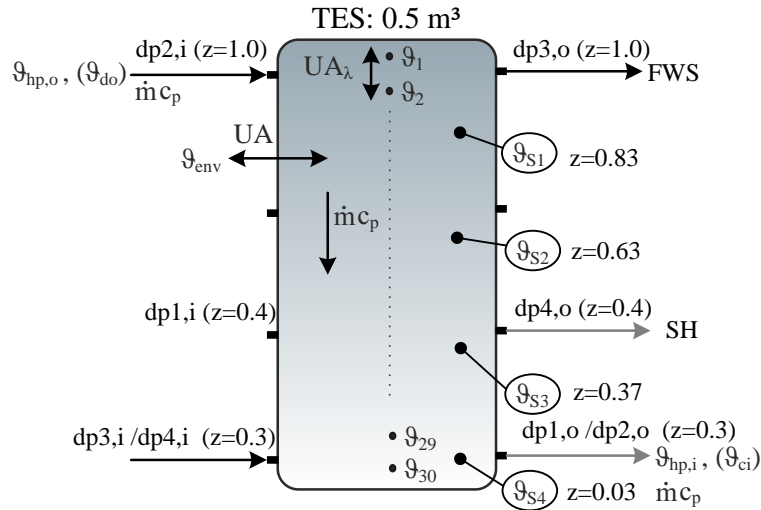


Figure 2.5.: Illustration of the TES-model with 30 nodes.

<sup>4</sup> This value was predefined in the reference system specifications from the HP manufacturer.

## 2. Heat pump, PV system and building

Tab. 2.2 provides an overview for the main simulation model parameters of the detailed TES model, cf. fig. 2.3 and fig. 2.5. The facilitated TRNSYS model is type 534. This model is parametrized such, that stratification is realized with 30 nodes and in case of inversion instantaneous adiabatic mixing occurs between adjacent nodes. Losses are calculated against a constant environment temperature of 20 °C. The complete description of the model equations may be found in Thornton et al. (2012).

Table 2.2.: Main model parameters and boundary conditions for the TES in fig. 2.5 and fig. 2.3.

Property <sup>a</sup>	Parameters and values
model	TRNSYS type 534, cf. Thornton et al. (2012), # of tank nodes=30
geometry	$V_S = 0.5 \text{ m}^3$ , $h = 1.81 \text{ m}$ , $r = 0.3 \text{ m}$
connections & sensors	see fig. 2.5
insulation	$U = 1.45 \text{ W}/(\text{m}^2\text{K})$ , $\vartheta_{env} = 20 \text{ }^\circ\text{C}$
int. heat conduction	$\lambda_z = 2 \text{ W}/(\text{m K})$
inversion	instantaneous mixing is activated

<sup>a</sup> Further properties and simulation boundary conditions are given in Appendix tab. C.1.

### 2.2.3. Building characterization – TABS

Fig. 2.7 illustrates the shape of the simulated building and tab. 2.3 provides the most important characteristics; for more details see SHC Task 44-Part B (Dott et al., 2013), Part B. The building has a nominal annual heating demand of 45 kWh/m<sup>2</sup>. Compared to the original TRNSYS set-up and facilitating type 56 as building model, a major modification was made for the heat emission system of the building.

The original simulation set-up used an approximation for the floor heating system. For this purpose an external room radiator model was parametrized such to mimic a floor heating system. In this research the *heat emission system* within the TRNSYS simulation is modeled through a functionality for TABS implementation which is directly supported by type 56. The so called active layer (AL) functionality has been developed by Koschenz and Dorer (1999); for an extensive description see Koschenz and Lehmann (2000) and for design aspects see Lehmann et al. (2007). *Heat transfer* related parameters are discussed in Appendix D.3.4. Fig. 2.6 illustrates the layer construction for the implemented first- (ground) and second floor-TABS.

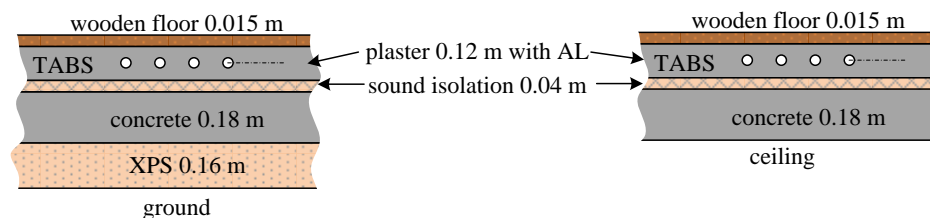


Figure 2.6.: Layer construction of the TABS – first (ground) floor (left) and second floor (right).

## 2.2. System description

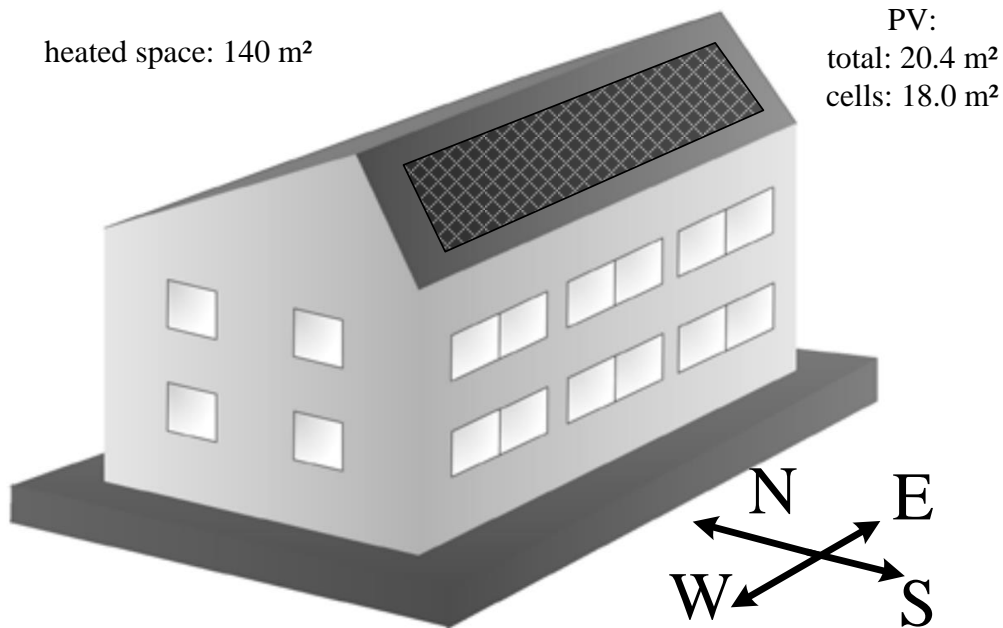


Figure 2.7.: Illustration of the simulated building model, cf. Dott et al. (2013), Part B.

Inclined surfaces irradiation is calculated using the Perez model, see Perez et al. (1990) assuming a standard ground reflectance of 0.2. This model is already implemented in TRNSYS type 15 or type 99. The approach of M. Martin and Berdahl (1984) is used for the effective sky temperature calculation to be used for the long-wave heat transfer calculations, see also Appendix E.4.1.

Concerning the possible control strategy for the heat emission, the first- and second floor TABS allow only for one unique supply water temperature ( $\vartheta_{sw}$ ) – as can be seen in fig. 2.3, and the mass flow in  $V_7$  is split equally. Since the control in the reference system foresees only one unique mass flow for the activation, the supplied heat flux to the TABS ( $\dot{Q}_{ta}$ ) is treated as one variable within the MPC concept.

Table 2.3.: Main building model parameters and boundary conditions.

Device	Parameters and values
model	TRNSYS type 56, cf. Klein et al. (TRNSYS 17); radiation modes: standard
outside measures	$(7.7 \times 10.7) \text{ m}^2$ ; total height $\approx 8 \text{ m}$ ; roof south: $28 \text{ m}^2$ , $45^\circ$
inside measures	room height $2.6 \text{ m}$ ; first- and second floor TABS $2 \times 70 \text{ m}^2$
glass area	N $2.6 \text{ m}^2$ ; E $3.4 \text{ m}^2$ ; S $10.2 \text{ m}^2$ ; W $3.4 \text{ m}^2$
infiltration	$0.4 \text{ h}^{-1}$
climate	Innsbruck, Austria for details see Appendix tab. C.2
heat demand	space heating $45 \text{ kWh/m}^2$ (nominal); domestic hot water $2133 \text{ kWh/a}$

## 2. Heat pump, PV system and building

### 2.3. Control criteria and control functions

Control criteria (C) and control functions (CF) define the operating-states of the hydronic system. Both, C and CF are Boolean variables, that is  $C, CF \in \{0, 1\}$ .

The values of  $CF_1 - CF_5$  define specific operating modes of elements in the hydraulic loop (cf. tab. 2.1), and all CF values together define an *operating-state* of the hydraulic loop. The *control functions* itself are determined based on the *criteria*  $C_A - C_D$  and the values of these criteria are directly related to the overall objective of sustaining the comfort conditions.

#### 2.3.1. Control criteria description

Control criteria may be simply understood as values of an abstract and virtual sensor. For example  $C_A = 1$  stands for the need to heat up the upper part of the TES which is the energy reservoir for the fresh water station (FWS). Each criterion results from a composition of real sensor measurements and the states of various (hysteresis) controllers. A detailed description of the criteria is also provided in Kofler (2016).

The decision tab. 2.4 provides an overview on the influence of the criteria on the control functions. Each CF forms a separate truth table in connection with all criteria. The simplest possible logical combination or minimal terms (*minterms*) for each  $CF(C_A, C_B, C_C, C_D)$  may be found by means of a *Karnaugh map*, see Appendix C.3. A control function value X in tab. 2.4 indicates that the CF may either be 0 or 1 depending on which value is more favorable wrt the minterm; e.g. the Karnaugh map in fig. C.2 results in a very simple logical relation for all X's in column CF1 being replaced with 0, if a 1 for one or the other X would be needed to simplify the logical relation one selects 1 instead of 0, it is a matter of choice. For all CFs the Karnaugh map shows that a 0 simplifies the minimal term, which is why 0 is chosen for all X's.

#### Request TES heating for DHW purpose – $C_A$

If the storage sensor temperature  $\vartheta_{S1}$  falls below  $41\text{ }^\circ\text{C} \rightarrow C_A = 1$ . This request for heating of the upper part in the TES directly triggers  $CF_1$ , cf. eq. (2.8). As the storage sensor temperature  $\vartheta_{S2}$  increases  $46\text{ }^\circ\text{C} \rightarrow C_A = 0$ .

#### Disable SH from the TES (request TES heating for SH) – $C_B$

The criterion  $C_B$  indicates that the temperature in the SH-volume of the TES (lower region of the TES) is too low for space heating from the TES ( $CF_5$ ). The sensor measurement  $\vartheta_{S3}$  represents the temperature in the upper part of the SH-volume. The criterion

## 2.3. Control criteria and control functions

Table 2.4.: Decision table for the values of  $CF_1 - CF_5$  as a function of the defined criteria  $C_A - C_D$ .

Criteria				Control functions			
$C_A$	$C_B$	$C_C$	$C_D$	$CF_1$	$CF_3$	$CF_4$	$CF_5$
TES heating "DHW""SH"		Demand DHW	SH	TES heating	DHW draw-off	SH direct	SH from TES
1	1	1	1	1	1	0	0
1	1	1	0	1	1	0	0
1	1	0	1	1	0	0	0
1	1	0	0	1	0	0	0
1	0	1	1	1	1	0	1
1	0	1	0	1	1	0	0
1	0	0	1	1	0	0	1
1	0	0	0	1	0	0	0
0	1	1	1	0	1	1	0
0	1	1	0	0	1	0	0
0	1	0	1	0	0	1	0
0	1	0	0	X <sup>a</sup>	X	X	X
0	0	1	1	0	1	1	0
0	0	1	0	0	1	0	0
0	0	0	1	0	0	1	0
0	0	0	0	X	X	X	X

<sup>a</sup> An X shows an irrelevant combination of criteria for the CF, hence one may replace X with 0 or with 1.

$C_B$  is determined through an outside ambient temperature dependent heating curve, see eq. (2.1). If the storage sensor  $\vartheta_{S3}$  falls below  $\vartheta_{S3,set} \rightarrow C_B = 1$ . This indicates that the temperature at dp4,0 is too low for space heating from the TES. If  $(\vartheta_{S4} > \vartheta_{S3,set}) \rightarrow C_B = 0$ . The return temperature set value  $\vartheta_{ret,set}$ , being defined in eq. (2.6), is the basis for the definition of  $\vartheta_{S3,set}$ :

$$\vartheta_{S3,set} = \vartheta_{ret,set} + 7 \text{ K.} \quad (2.1)$$

### Request DHW demand – $C_C$

This criterion stands for DHW demand and it is directly determined by the DHW profile according to Task44 Report C1 Part A: chapter 6 (Dott et al., 2013). If  $\dot{m}_{DHW} > 0 \rightarrow C_C = 1$ , if  $\dot{m}_{DHW} = 0 \rightarrow C_C = 0$ . This request directly triggers  $CF_3$ , cf. eq. (2.9).

### Request SH demand – $C_D$

The space heating demand criterion is composed of three sub-criteria:  $C_{season}$  being 1 during the heating season<sup>5</sup>,  $C_{oa,th}$  being an indicator if the average ambient temperature is below the heating-threshold temperature, and  $C_{ret}$  which indicates with 1 that the

<sup>5</sup> 01.01. ÷  $t = 0$  h, 31.12. ÷  $t = 8760$  h  $\rightarrow$  heating season ÷  $t = 0$  h ... 2880 h &  $t = 6528$  h ... 8760 h.

## 2. Heat pump, PV system and building

TABS return temperature is too low to suspend the heating, or with 0 that the AL return temperature is high enough to switch off the heating. The sub-criteria definitions read:

$$C_{season} = 1 \leftrightarrow (t \in [0, 2880] \text{ h OR } t \in [6528, 8760] \text{ h}), \quad (2.2)$$

$$C_{oa,th} = 1 \leftrightarrow (\bar{\vartheta}_{oa} < \vartheta_{oa,th}), \quad (2.3)$$

$$C_{ret} = 1 \stackrel{set}{\leftarrow} (\vartheta_{ret} < \vartheta_{ret,set}), \quad C_{ret} = 0 \stackrel{clear}{\leftarrow} (\vartheta_{ret} > \vartheta_{ret,hys}). \quad (2.4)$$

The temperatures involved in these sub-criteria are defined as follows:

$$\text{average } \vartheta_{oa}(\bar{\vartheta}_{oa}) = \frac{1}{24} \sum_t \vartheta_{oa}(t - \Delta t) \text{ with } \Delta t = 0 \text{ h}, 1 \text{ h}, \dots, 23 \text{ h}, \quad (2.5)$$

$$\vartheta_{ret,set} = \begin{cases} 30 \text{ }^\circ\text{C} & : \quad \bar{\vartheta}_{oa} \leq -16 \text{ }^\circ\text{C} \\ -0.294 \bar{\vartheta}_{oa} + 25.29 \text{ K} & : \quad -16 \text{ }^\circ\text{C} < \bar{\vartheta}_{oa} < 18 \text{ }^\circ\text{C} \\ 20 \text{ }^\circ\text{C} & : \quad \bar{\vartheta}_{oa} \geq 18 \text{ }^\circ\text{C}, \end{cases} \quad (2.6)$$

$$\vartheta_{ret,hys} = \begin{cases} \vartheta_{ret,set} + 2 \text{ K} & : \quad \bar{\vartheta}_{oa} \leq -16 \text{ }^\circ\text{C} \\ 0.088 \bar{\vartheta}_{oa} + 3.41 \text{ K} + \vartheta_{ret,set} & : \quad -16 \text{ }^\circ\text{C} < \bar{\vartheta}_{oa} < 18 \text{ }^\circ\text{C} \\ \vartheta_{ret,set} + 5 \text{ K} & : \quad \bar{\vartheta}_{oa} \geq 18 \text{ }^\circ\text{C}. \end{cases} \quad (2.7)$$

### Control criteria for MPC operation

For MPC scenarios  $C_A$ , and  $C_D$  are differently. TES heating (for DHW purpose) occurs if the defined MPC decides to heat up the upper TES volume  $\rightarrow C_A=1$ . Demand for SH may be given if the defined MPC decides to switch on the HP for space heating and  $C_{season}$  is true  $\rightarrow C_D = (\dot{Q}_{ta} > 0) C_{season}$ .

#### 2.3.2. Control functions and derived operating-states

This section describes the implications of  $CF_1$ ,  $CF_3$ ,  $CF_4$  and  $CF_5$  for operating the elements in the hydraulic loop, already introduced from a pure hydraulic point of view in sec. 2.2.2. The desired criteria-dependent values of the CFs are given in tab. 2.4, which is the basis for the derivation of the CFs, see Appendix C.3. The values of all CFs together at a specific instant of time define the *operating-state* of the complete hydraulic loop and the HP shown in fig. 2.3.

The control function  $CF_2$  is reserved for heating of the SH-part in the TES but this operation is not considered herein. Tab. 2.1 provides a simplified overview of valve and pump operation modes if a control function has the value 1, the complete hydraulic picture for each CF as a function of all C is given on the following pages.

### Heating of the TES for DHW purpose – CF<sub>1</sub>

This operating mode of the HP has the highest priority. Preliminary investigations by Kofler (2016) showed that heating of the TES with one mass flow through the condenser and the desuperheater ( $\dot{m}_d = \dot{m}_c$ ) feeding into the top part of the storage is the most efficient way for this purpose, see fig. 2.8.

For the base case scenario the HP operates at a compressor frequency of 60 Hz during this mode.  $\dot{m}_{V1,A} = 0$  and the condenser water mass flow  $\dot{m}_c$  is controlled such that the desuperheater outlet temperature is 50 °C . The hydraulic loop at the water side back to the HP is closed via V<sub>6a</sub> and V<sub>6</sub>, cf. fig. 2.8. For the results, the energy supplied to the TES during this operation mode is entirely attributed to  $Q_c$ .

$$CF_1 = C_A \quad (2.8)$$

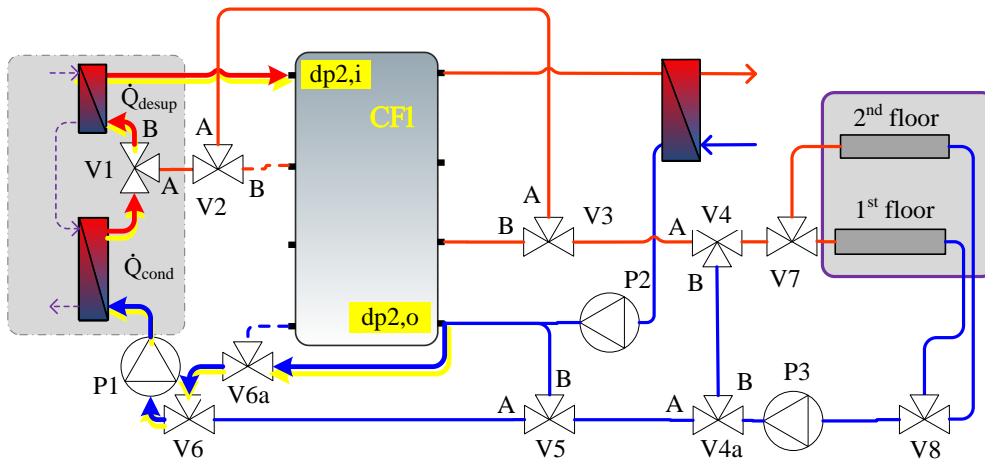


Figure 2.8.: CF<sub>1</sub> is active; illustration of the relevant connections.

### DHW draw off – CF<sub>3</sub>

This operating-state is always possible if  $\dot{m}_{DHW} > 0$ . The loop at the storage side of the FWS is driven with P<sub>2</sub> and the mass flow is adjusted such to obtain the required outlet temperature for the DHW, cf. fig. 2.10 connections highlighted in green. The system simulation uses a DHW-profile from Task44 Report C1 Part A: chapter 6 (Dott et al., 2013).

$$CF_3 = C_C \quad (2.9)$$

## 2. Heat pump, PV system and building

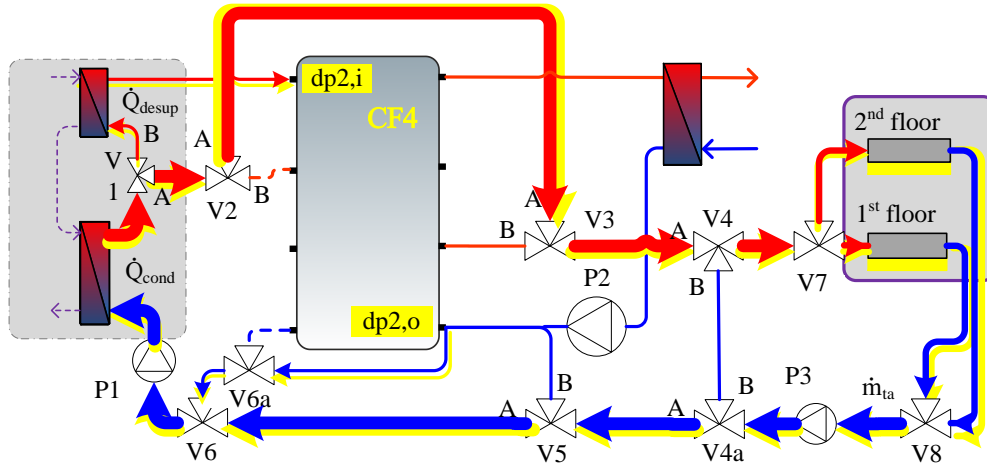


Figure 2.9.: CF<sub>4</sub> is active and  $\dot{m}_{V1,A} > 700$  kg/h; illustration of the relevant connections.

### Direct heating – CF<sub>4</sub>

During this operating-state the HP operates at an outside ambient temperature dependent frequency defined by:

$$\frac{f}{f_{nom}} = \begin{cases} 100\% & : \vartheta_{oa} \leq -16 \text{ }^\circ\text{C} \\ \left(\frac{19}{35} - \frac{1}{35}\vartheta_{oa}\right) \cdot 100\% & : -16 \text{ }^\circ\text{C} < \vartheta_{oa} < 12 \text{ }^\circ\text{C} \\ 0\% & : \vartheta_{oa} \geq 12 \text{ }^\circ\text{C} \end{cases} \quad (2.10)$$

For direct heating the TES is bypassed via  $V_{1,A}$  and  $V_{2,A}$ , however, a small mass flow through the desuperheater leads to parallel heating of the DHW-volume in the TES, cf. fig. 2.9 connections highlighted in yellow. The overview for valve positions and pump operations is given in tab. 2.1.

With the compressor frequency being the *reference variable* in the base case scenario, the condenser water mass flow  $\dot{m}_c$  is operated such to obtain a temperature difference of 5 K between the water inlet and outlet. The desuperheater water mass flow is adjusted such to obtain an outlet temperature of 50 °C fed into the TES at the top. The mass flow  $\dot{m}_{V1,A}$  directly reaches  $V_4$  via the bypass, and as long as<sup>6</sup>  $\dot{m}_{V1,A} \geq 700$  kg/h holds, for  $V_4$   $\dot{m}_{AB} = \dot{m}_A$ , that is, no return water is led back to the supply water side. Finally,  $\dot{m}_{V4,AB}$  is split equally in  $V_7$  to supply each TABS with the same amount. In case  $\dot{m}_{V1,A} < 700$  kg/h the missing amount to obtain 700 kg/h is added through  $\dot{m}_{V4,B}$  such that  $\dot{m}_{AB} = 700$  kg/h holds. Hence  $P_3$  may either be switched off in case  $\dot{m}_{V1,A} \geq 700$  kg/h, or it is operated such that  $\dot{m}_{P3} = 700$  kg/h. In direct heating mode  $\dot{m}_{V5,B} = 0$  is essential. Through  $V_{6a}$  and  $V_6$  the desuperheater mass flow  $\dot{m}_d$ , diverted at  $V_1$ , is added to the heating return mass flow, which closes the loop.

<sup>6</sup> The minimum total mass flow of 700 kg/h is derived from a predefined minimum specific TABS mass flow of 5 kg/(h m<sup>2</sup>).

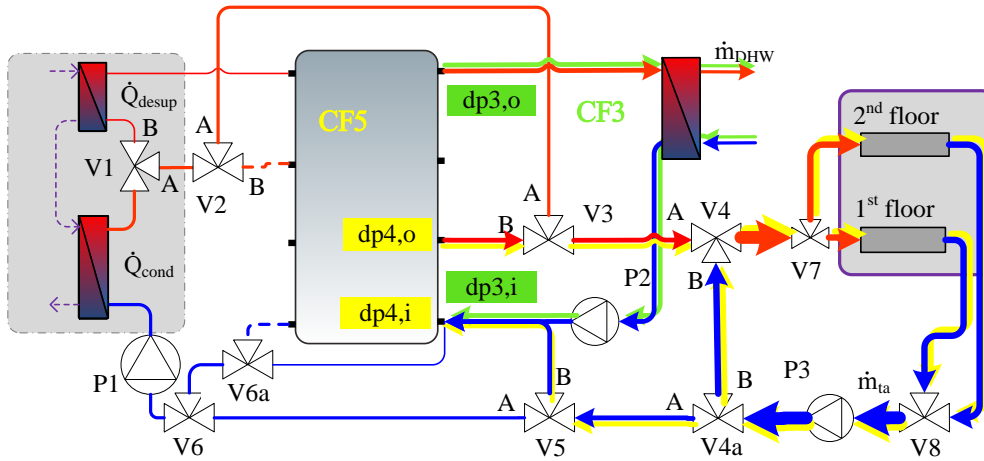


Figure 2.10.: CF3 and CF5 being active; illustration of the relevant connections.

In summary, as long as  $\dot{m}_{V1,A} \geq 700$  kg/h, which is indirectly determined by  $\vartheta_{oa}$  and  $\Delta\vartheta_c = 5$  K, the mass flow  $\dot{m}_{V4,AB}$  is the same as  $\dot{m}_{V1,A}$  – in this case P1 drives this one mass flow in the loop, see fig. 2.9. Once  $\dot{m}_{V1,A} < 700$  kg/h, the mass flow  $\dot{m}_{ta}$  in the TABS loop is kept constant at 700 kg/h through P3 and V4a.

$$\boxed{CF_4 = \text{NOT}(C_A) \text{ AND } C_D} \quad (2.11)$$

### Heating from the storage – CF5

This operating-state (indicated by  $CF_5=1$ ) represents a heating operation with the TES being the heat source, see fig. 2.10 connections highlighted in yellow. It may be active in case the HP is needed to heat up the TES (for DHW purpose, indicated by  $CF_1=1$ ) to sustain the temperature required for DHW preparation. The short description of valve positions and pump operations is given in tab. 2.1.

Given the temperature in the volume part of the TES below the dp4,o connection is high enough ( $C_B = 0$ ) and heating demand exists ( $C_D = 1$ ), V3 switches to  $\dot{m}_{AB} = \dot{m}_B$ . Pump P3 is operated such that  $\dot{m}_{ta} = 1031$  kg/h and V4 has to maintain a difference between flow- and return-temperature of 5 K. Finally  $\dot{m}_{V4,AB}$  is split equally to supply each TABS with the same amount. For V5  $\dot{m}_{V5,A} = 0$  is essential to close the hydraulic loop through V5,B with the TES.

$$\boxed{CF_5 = C_A \text{ AND } \text{NOT}(C_B) \text{ AND } C_D} \quad (2.12)$$

## 2. Heat pump, PV system and building

### 2.4. Heat pump characteristic functions

The heat pump (HP) simulation in TRNSYS is based on a very detailed model, cf. sec. 2.2.1, with parameters based on real measurement data, see Hengel et al. (2014) or (2016). This allows for simulation runs under various boundary conditions to generate data at different stationary operating points. These data are utilized to derive *simple characteristic functions* which describe the thermodynamic HP characteristic to be used for MPC.

This section addresses all relevant functions which are finally required for the MPC objective functional  $J$  or the controller model  $\mathcal{M}$ . The HP capacity flow rate at the sink or water side  $\dot{C}(\vartheta_{ci}, \vartheta_{sc}, \vartheta_{do})$  for example, is required in sec. 4.4 to derive the TES-HP *controller model*. In addition, other characteristic functions (e.g.  $\dot{Q}_{cond}$  as a function of the condenser inlet temperature and the power consumption of the compressor) are facilitated in the sections 5.2 and 5.3 as *reference functions*. Finally, specific characteristics are required for *constraints formulation* related to the MPC.

Tab. 2.1 in the first line shows the HP (reference) frequency required for TES heating for DHW purpose ( $CF_1 = 1$ ,  $f = 60$  Hz) and for direct SH ( $CF_4 = 1$ ,  $f = f(\vartheta_{oa})$  see eq. (2.10)), which relate to the base case scenario. HP operation based on MPC scenarios requires different HP frequency reference functions that are derived in this section.

#### 2.4.1. General aspects and prototypical functions and graphs

Simulations conducted for the purpose of characteristic function identification are based on approximately 100 distinct stationary operating points of the HP. These operating points represent the basis to derive characteristic functions, i.e. *curves*  $g(x)$  or *fields*  $h(x, y)$ ; e.g.  $g$  and  $h$  may be the COP and  $\dot{Q}_c$  and  $x$  is the compressor frequency ( $f$ ) and  $y$  is the condenser inlet temperature ( $\vartheta_{ci}$ ).

A general limitation for each characteristic concerns the validity or the definition range. Fig. 2.11 for example shows the COP values as function of  $f$  and  $\vartheta_{ci}$ , given  $\Delta T_c = 5$  K and four different  $\Delta T_d$  values. The fact, that the COP curves do not depend on  $\Delta T_d$  makes any derived curve or field independent of  $\Delta T_d$ , however, the main limitation is given by  $\Delta T_c = 5$  K. Hence, a function  $g = COP(f, \vartheta_{ci} = 25^\circ\text{C})$  holds only if  $\Delta T_c = 5$  K. Although this seems quite restrictive, it is reasonable due to pragmatic decisions related to the operation strategies. For example,  $\Delta T_c = 5$  K is a good compromise balancing pump power requirements – higher for lower  $\Delta T_c$  – and the drawback of increasing pressure ratio with increasing  $\Delta T_c$ . Decreasing  $\Delta T_c$  further requires a higher water mass flow rate through the condenser, however, improves the heat exchanger properties; at the same time the pressure ratio drops which increases the COP. This effect of changing COP value with  $\Delta T_c$  becomes stronger for decreasing  $\vartheta_{ci}$ .

## 2.4. Heat pump characteristic functions

Being aware of the valid range of derived characteristics two or more functions may be also composed to obtain a "new" function. The **source reservoir temperature** (temperature at b1 in fig. 2.2) **is assumed constant**  $\vartheta_{sc} = 0\text{ }^{\circ}\text{C}$  **if not stated otherwise**, which is rather pessimistic. The additional dependence of the COP or other characteristic functions on the source temperature  $\vartheta_{sc} = 0\text{ }^{\circ}\text{C}$  was not mentioned so far – this would require an additional parameter in all characteristic functions.

### Coefficient of performance (COP)

The HP COP in fig. 2.11 shows a significant sensitivity with respect to  $\vartheta_{ci}$  and  $f$ . However, a varying temperature increase across the desuperheater has nearly no effect on the COP (curves overlay).

The red line, connecting the COP maximum values for different  $\vartheta_{ci}$ , indicates an information that will be exploited in a specific manner to operate the HP at optimal conditions through tracking of a reference function.

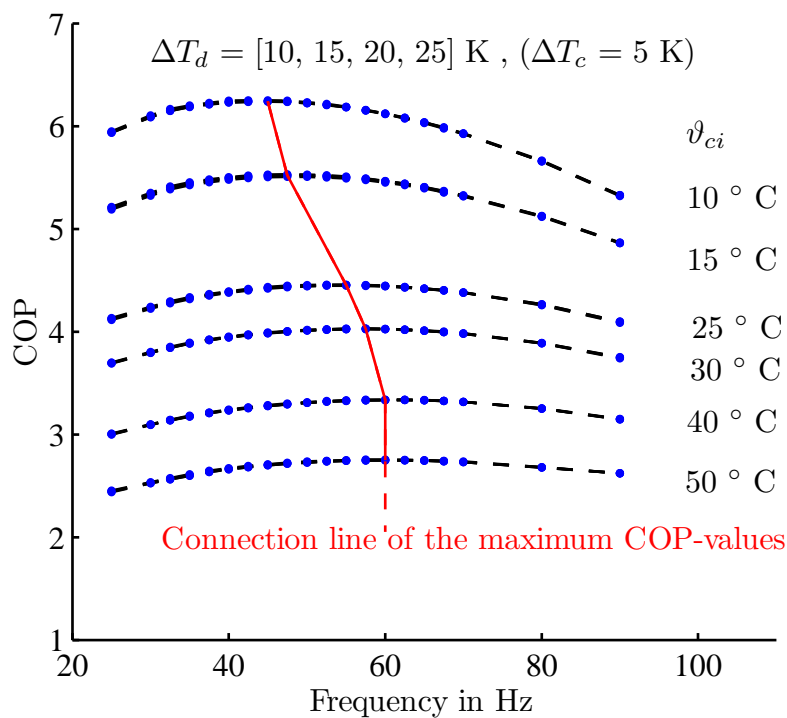


Figure 2.11.: HP TABS mode, COP as a function of  $f$  and the condenser water inlet temperature ( $\vartheta_{ci}$ );  $\Delta T_c = 5 \text{ K}$ , and for each  $\vartheta_{ci}$  four  $\Delta T_d$  are plotted – the COP values for different  $\Delta T_d$  but the same  $\vartheta_{ci}$  nearly overlap and appear as a single curve;  $\vartheta_{sc} = 0\text{ }^{\circ}\text{C}$ .

## 2. Heat pump, PV system and building

### Thermal and electrical power of the HP

The thermal capacity of the condenser ( $\dot{Q}_c$ ) and the desuperheater ( $\dot{Q}_d$ ) as a function of the compressor speed or frequency  $f$  and condenser water inlet temperature represent main characteristic functions for the MPC concept. These functions are more or less the pillar for the TABS and the TES-MPC. Fig. 2.12 shows exemplary simulation results for these variables. A *bilinear* approach with constant term:

$$\dot{Q}(f, \vartheta_{ci}) = k_1 + k_2 f + k_3 \vartheta_{ci} \quad \text{with } k_i \in \mathbb{R} \quad (2.13)$$

proved to be sufficient for both  $\dot{Q}_c$  and  $\dot{Q}_d$ . A very similar approach is sufficient for the calculation of the HP electricity consumption based on different variables.

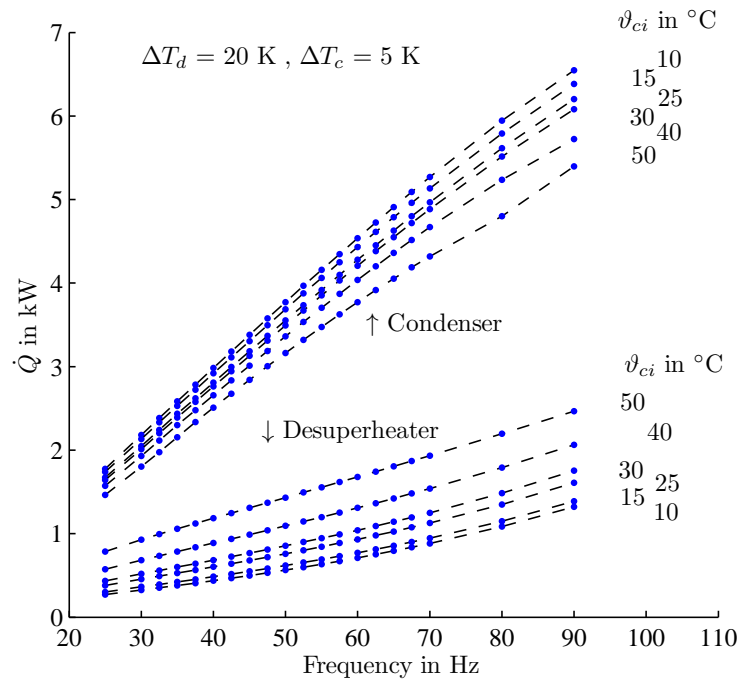


Figure 2.12.: HP in TABS mode,  $\dot{Q}_c$  and  $\dot{Q}_d$  at specific  $\vartheta_{ci}$ , as a function of  $f$ ;  $\Delta T_c = 5$  K,  $\Delta T_d = 20$  K.

### HP heat sink (water) mass flow rate

The HP heat sink mass flow rate in kg/h, or the heat capacity (flow) rate  $\dot{C}$  in W/K play an important role in the derivation of the TES-HP controller model in sec. 4.4. Fig. 2.13 shows the family of curves for  $\dot{m}(f)$  obtained through variation of  $\vartheta_{ci}$  ( $\vartheta_{do} = 50$  °C,  $\Delta T_c \neq 5$  K,  $\dot{m}_c = \dot{m}_d$ ). This graph shows also that  $\dot{m}(f)$  tends to become very high as  $\vartheta_{ci}$  approximates  $\vartheta_{do}$  ( $= 50$  °C = const.), theoretically  $\dot{m}(f) \rightarrow \infty$ . Definitely, an approach similar to eq. (2.13) is not suitable for a large definition range, however, it is difficult to judge based on this representation – more details on this in sec. 2.4.3. The mass flow rate of the desuperheater in TABS mode of the HP is shown in Appendix fig. C.6.

## 2.4. Heat pump characteristic functions

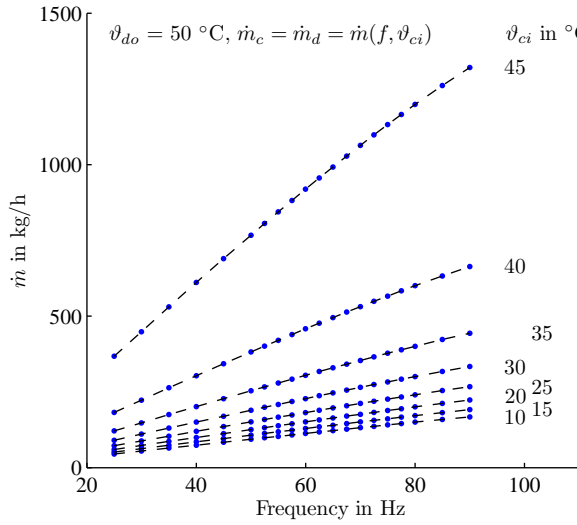


Figure 2.13.: HP TES mode, water  $\dot{m}$  as a function of the  $f$  and  $\vartheta_{ci}$ , for constant  $\vartheta_{do}=50\text{ °C}$ .

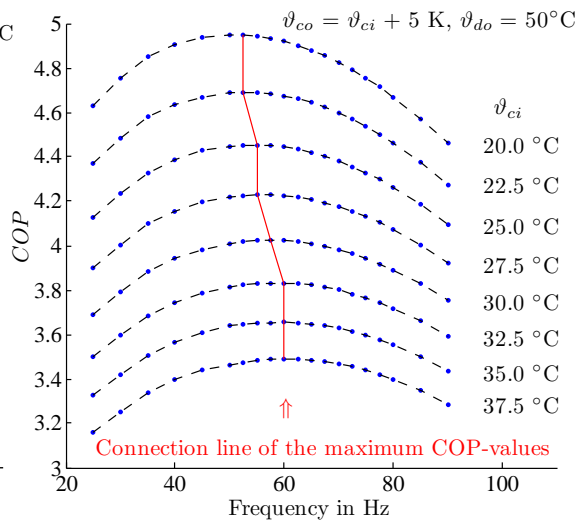


Figure 2.14.: HP TABS mode,  $COP(f, \vartheta_{ci})$ ,  $\Delta T_c=5\text{ K}$  with  $\vartheta_{sc} = 0\text{ °C}$ .

### 2.4.2. MPC relevant HP characteristics – SH with TABS ( $CF_4$ )

HP characteristic functions for implementation of the space heating controller (TABS-MPC) in sec. 5.2 are discussed and provided in this subsection. Any TABS-MPC scenario requires to replace the outside ambient temperature dependent compressor frequency set value of eq. (2.10) by an alternative. Apart from that, tab. 2.1 still holds.

Two guiding principles – or in MPC terminology *reference variables* – are defined in relation to the HP operation. The first being the PV-led operation and, the second being the operation with maximum efficiency which is explained in the following.

#### HP operation with maximum efficiency

This operation mode of the HP requires the implementation of the red line in fig. 2.14 as a reference variable in the MPC objective functional. During SH or TABS operation the values range of desuperheater mass flows  $\dot{m}_d$ , supplied to the TES in order to reach  $\vartheta_{do} = 50\text{ °C}$ , is relatively low. An alternative may be an approach with constant temperature difference over the desuperheater ( $\Delta T_d$ ), which led to fig. 2.11 where the COP values for different  $\Delta T_d$  but the same  $\vartheta_{ci}$  nearly overlap and are combined to a single curve.

## 2. Heat pump, PV system and building

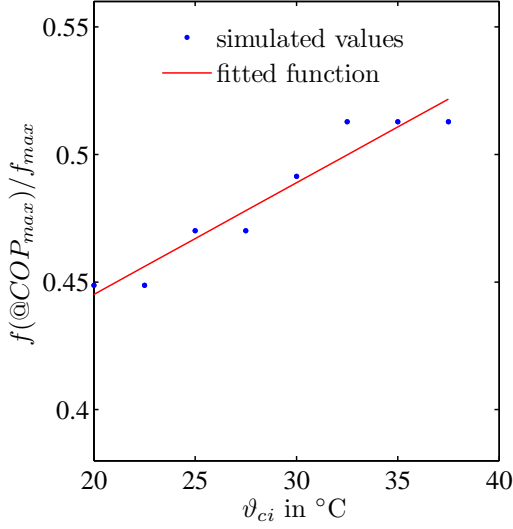


Figure 2.15.: HP TABS mode, relative frequency at  $COP_{max}$  as a fct. of  $\vartheta_{ci}$ ;  $\Delta T_c = 5$  K,  $\vartheta_{do} = 50$  °C,  $\dot{m}_c(\vartheta_{ci}, f)$ ;  $f_{max} = 117$  Hz.

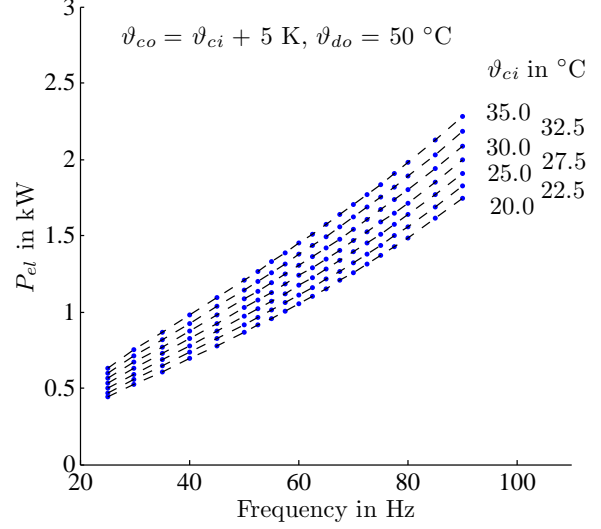


Figure 2.16.: HP TABS mode, HP power consumption as a function of  $f$  and  $\vartheta_{ci}$ ;  $\Delta T_c = 5$  K,  $\vartheta_{sc} = 0$  °C.

In a first step the dependence of the optimum compressor frequency on the condenser inlet temperature is derived – it is shown in fig. 2.15 normalized wrt  $f_{max}$ . The fitted solid line shows the graph of the optimum relative  $f$  as a function of  $\vartheta_{ci}$  for HP operation in TABS-MPC mode. This fitted function is based on a simple affine approach:

$$f(@COP_{max}) = d + k \vartheta_{ci} \quad \text{with } d, k \in \mathbb{R} \text{ to be determined.} \quad (2.14)$$

Based on a function for  $\dot{Q}_c(f, \vartheta_{ci})$ <sup>7</sup>, which looks similar to that shown in fig. 2.12, with the structure of eq. (2.13), a simple affine reference function for  $\dot{Q}_c(\vartheta_{ci})$  that holds for HP operation at optimal COP may be derived by replacing the variable  $f$  in  $\dot{Q}_c(f, \vartheta_{ci})$  with the expression from eq. (2.14):

$$\begin{aligned} \dot{Q}_c(f(@COP_{max}), \vartheta_{ci}) &= d_{Qc} + k_{Qc} \vartheta_{ci} && \text{with } d_{Qc}, k_{Qc} \in \mathbb{R} \\ \text{and } d_{Qc} &:= k_1 + k_2 d, && k_{Qc} := k_2 k + k_3. \end{aligned} \quad (2.15)$$

HP operation for SH purpose with the TABS, with a thermal output equal to the reference function in eq. (2.15) automatically leads to operation at maximum efficiency. If this operation mode is the only objective, it is in principal – except for some normalization – this function, which must be inserted in eq. (5.3) for  $u_{ref,i}$ . The values to be used for  $d_{Qc}$  and  $k_{Qc}$ :  $d$ ,  $k$ ,  $k_1$ ,  $k_2$  and  $k_3$  are listed in tab. 2.5.

<sup>7</sup> Precisely it should be  $(\dot{Q}_c - \dot{m}_d c_p 5 \text{ K})$  but  $\dot{m}_d$  is relatively small.

## 2.4. Heat pump characteristic functions

Transformation of the thermal output ( $\dot{Q}_c$ ) into the corresponding HP frequency value is possible through a specific transformation rule,  $f(\dot{Q}_c, \vartheta_{ci})$ . This may be a polynomial function up to second order elements, cf. eq. (2.19).

### HP operation depending on the PV generation

The other guiding principle for HP operation, in context of this thesis, is the PV-led operation. This mode means HP operation as a function of a given reference power consumption of the HP (compressor), see fig. 2.16 and for  $\vartheta_{do} = 65$  °C Appendix fig. C.7. The PV- or electricity led operation requires a function similar to that for  $\dot{Q}_c(f, \vartheta_{ci})$ , however,  $Q_c$  must be replaced by  $P_{el}$  standing for the total HP power consumption. It is intuitive to assume that a function  $P_{el} = k_1 + k_2 f + k_3 \vartheta_{ci}$  is the right approach, cf. fig. 2.16. However, the MPC formulation becomes simpler, if

$$P_{el} = k_1 + k_2 \dot{Q}_c + k_3 \vartheta_{ci} \rightarrow \dot{Q}_c = \tilde{k}_1 + \tilde{k}_2 P_{el} + \tilde{k}_3 \vartheta_{ci} \quad \text{with } k_i, \tilde{k}_i \in \mathbb{R} \quad (2.16)$$

is chosen. The desired electricity consumption level of the HP may be implicitly assigned through  $P_{el}$  in eq. (2.16). Employing  $\dot{Q}_c$  as a reference function within the MPC framework should ensure an operation of the HP such that the real power consumption matches  $P_{el}$ . In MPC PV-led operation mode,  $P_{el}$  in eq. (2.16) is replaced with the predicted PV power generation.

### 2.4.3. MPC relevant HP characteristics – TES heating, ( CF<sub>1</sub> )

HP characteristic functions for the TES-MPC implementation in sec. 5.3 are discussed and provided in this subsection. This MPC implementation is more complicated than the TABS-MPC, because the general controller model is a non-linear model. The non-linearity is due to the HP water mass flow rate entering the TES. Concerning the HP characteristics required for formulation of the reference functions the requirements and functions are more or less the same as in sec. 2.4.2, which is why this subsection deals mainly with the approximation of the mass flow rate only.

#### TES heating with maximum efficiency

The graph for the optimum compressor frequency for TES heating (for DHW purpose) is shown in the right graph of fig. 2.18. Compared to CF<sub>4</sub> this time the optimum frequency may be directly facilitated as a reference function for the MPC, because the controlled variable  $u$  is the compressor frequency itself in contrast to the thermal output as for CF<sub>4</sub>.

Fig. 2.19 provides the total thermal output of the HP as a function of  $f$  for various  $\vartheta_{ci}$  values. The HP inlet temperatures do not lead to distinct curves but tend to overlay,

## 2. Heat pump, PV system and building

that is, the  $\vartheta_{ci}$ -dependence may be neglected for this function. Assume a specific frequency say 70 Hz; the related thermal output from fig. 2.19 together with the various  $\vartheta_{ci}$ -dependent electrical consumptions from fig. 2.17 reveal the increase of the COP with decreasing  $\vartheta_{ci}$ .

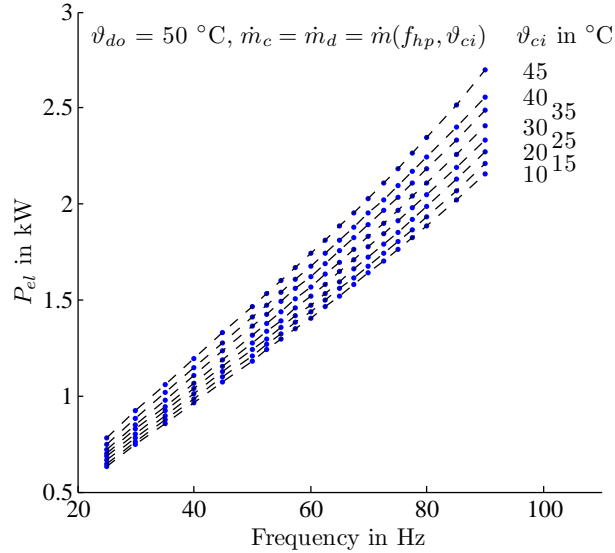


Figure 2.17.: HP TES mode, total HP power consumption ( $P_{el}$ ) as a function of the frequency and the condenser inlet temperature, for constant desuperheater outlet temperature ( $\vartheta_{do}=50\text{ }^{\circ}\text{C}$ ).

### HP operation depending on the PV generation (PV-led HP operation)

Fig. 2.17 shows the HP total power consumption as a function of the compressor frequency for various  $\vartheta_{ci}$ . This graph is the basis for the PV- or electricity-led HP operation for TES heating. The graph may be approximated by a function of the form

$$P_{el} = k_1 + k_2 f + k_3 \vartheta_{ci} \quad \text{with } k_i \in \mathbb{R}. \quad (2.17)$$

Solving eq. (2.17) for  $f(P_{el}, \vartheta_{ci})$  and inserting the predicted PV power instead of  $P_{el}$  leads to the reference frequency-function required in eq. (5.5) to track PV power.

#### 2.4.4. Fit results for characteristic functions

An important aspect in this matter is the selected range of parameter identification data. For example, ideally the  $f$  and  $\vartheta_{ci}$  values facilitated for the calculation of the function parameters in eq. (2.17) represent a relevant range of values. The selected range was approximately 10-20% above the minimum and 10-20% below the maximum numerical values. That is, e.g. to fit data to eq. (2.17) with the definition range being [0.5, 2.7] kW,

## 2.4. Heat pump characteristic functions

[25, 110] Hz and [10, 45] °C the range of selected data to obtain  $k_1, k_2, k_3$  was [0.7, 2.5] kW, [35, 90] Hz and [15, 38] °C. The parameter estimations given in tab. 2.5 were obtained through linear regression or with the MATLAB command *fmincon*, which allows also to set parameter constraints.

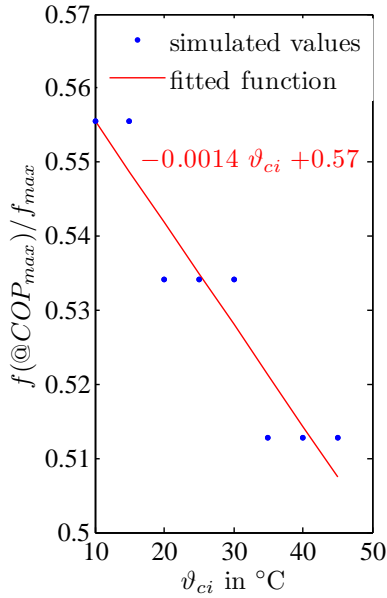


Figure 2.18.: HP TES mode, relative frequency at  $COP_{max}$  as a function of  $\vartheta_{ci}$ , for  $\vartheta_{do}=50$  °C and  $\dot{m}_c = \dot{m}_d = \dot{m}(f, \vartheta_{ci})$ ;  $f_{max} = 117$  Hz.

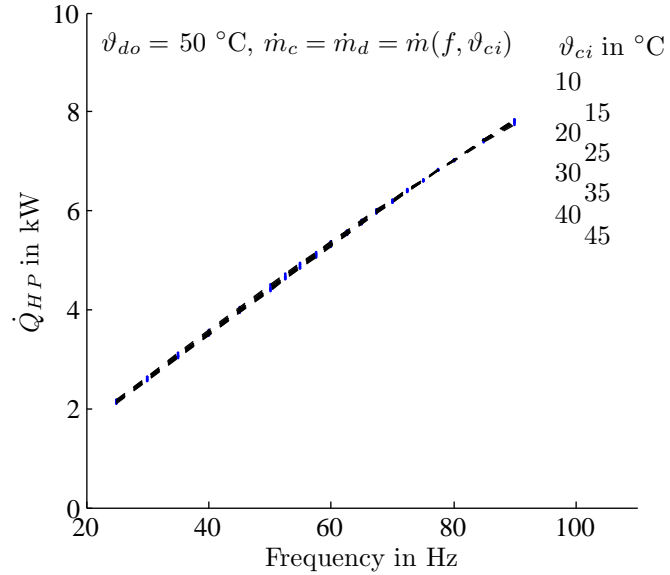


Figure 2.19.: HP TES mode, total thermal output  $\dot{Q}_{HP}$  as a fct. of the frequency and the condenser inlet temperature,  $\vartheta_{do}=50$  °C and  $\dot{m}_c = \dot{m}_d = \dot{m}(f, \vartheta_{ci})$ .

Table 2.5.: Coefficients for various approximation functions, given for  $\vartheta_{sc} = 0$ .

Function <sup>a</sup>	eq. no.	Model parameters						Boundary conditions
		$d$ or $k_1$	$k$ or $k_2$	$k_3$	$k_4$	$k_5$	$k_6$	
$f(@COP_{max})$ (2.14)		39.78	0.57	cf. also fig. 2.15				$\Delta T_c = 5, \vartheta_{do} = 50$
$\dot{Q}_c(f, \vartheta_{ci})$	(2.15)	0.78	0.071	-0.031	-	-	-	$\Delta T_c = 5, \vartheta_{do} = 50$
$P_{el}(\dot{Q}_c, \vartheta_{ci})$	(2.16)	-0.90	0.30	0.034	-	-	-	$\Delta T_c = 5, \vartheta_{do} = 50$
$f(\dot{Q}_c, \vartheta_{ci})$	(2.17)	-25.90	13.40	1.73	0.10	-0.02	-0.00	$\dot{m}_c = \dot{m}_d, \vartheta_{do} = 50$
$f(@COP_{max})$ (2.14)		66.57	-0.16	cf. also fig. 2.18				$\dot{m}_c = \dot{m}_d, \vartheta_{do} = 50$
$P_{el}(f, \vartheta_{ci})$	(2.17)	-0.27	0.026	0.01	-	-	-	$\dot{m}_c = \dot{m}_d, \vartheta_{do} = 50$
$\dot{m}(f, \vartheta_{ci})$	(2.19)	314.91	-0.21	-25.67	-0.01	0.47	0.16	$\dot{m}_c = \dot{m}_d, \vartheta_{do} = 50$

<sup>a</sup>  $\vartheta$  in °C,  $\Delta T$  in K, power or thermal output in kW, frequency in Hz, mass flow in kg/h.

### Modelling the HP mass flow rate

The general TES-HP controller model derived in sec. 4.4 for the TES-MPC requires an analytical expression for the mass flow rate ( $\dot{m}_c = \dot{m}_d$ ). A possible but simple approach

## 2. Heat pump, PV system and building

for the mass flow rate as a function of  $f$  and  $\vartheta_{ci}$ , given  $\vartheta_{do,set} = 50\text{ }^\circ\text{C}$  and  $\vartheta_{sc} = 0\text{ }^\circ\text{C}$  is

$$\dot{m} = k_1 + k_2 f + k_3 \vartheta_{ci}. \quad (2.18)$$

The accuracy of this relatively simple model for  $\dot{m}$  is illustrated in fig. 2.20, the blue dots are the 3D representation of fig. 2.13 with an additional axis for  $\vartheta_{ci}$ . Whether or not, this simple tangential plane approximation for  $\dot{m}$  is sufficiently accurate within the MPC framework, depends mainly on the required range for  $f$  and  $\vartheta_{ci}$ . In the drawn example the range of simulation data facilitated for the identification of the parameters  $k_i$  in eq. (2.18) is:  $f \in [40, 80]\text{ Hz}$ ,  $\vartheta_{ci} \in [20, 40]\text{ }^\circ\text{C}$ . As can be seen clearly, already for  $\vartheta_{ci} = 40\text{ }^\circ\text{C}$  the model is relatively poor, and for higher temperatures it fails.

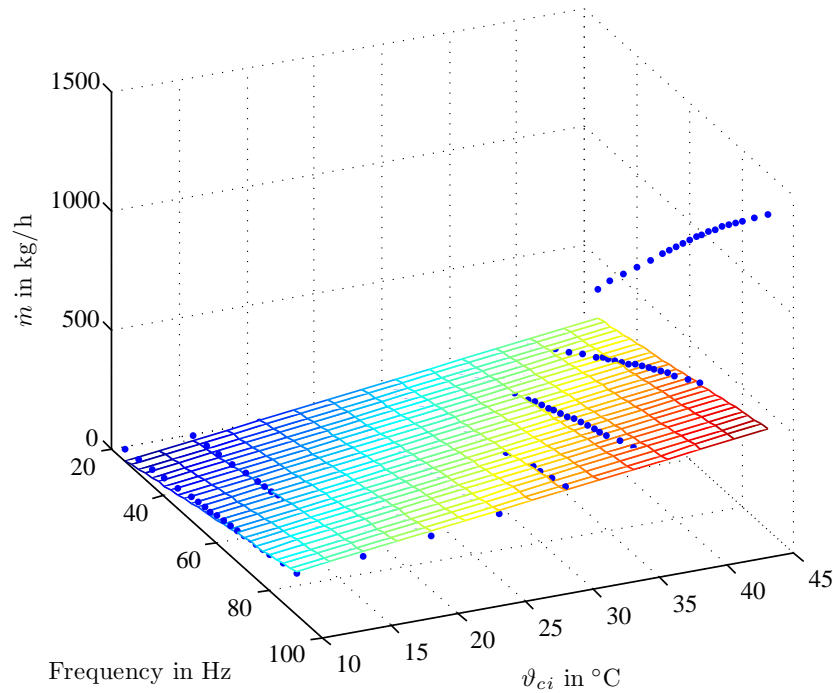


Figure 2.20.: HP TES mode, tangential plane approximation according to eq. (2.18) for  $\dot{m}(f, \vartheta_{ci}) = \dot{m}_c = \dot{m}_d$ , given  $\vartheta_{do} = 50\text{ }^\circ\text{C}$ ,  $\vartheta_{sc} = 0\text{ }^\circ\text{C}$ ; dots show simulated values.

The next higher level of approximation is the incorporation of quadratic terms for  $f$  and  $\vartheta_{ci}$ . This means already a significant improvement compared to eq. (2.18), however, only the consideration of a mixed term ( $f \vartheta_{ci}$ ) as in eq. (2.19) leads to relatively high accuracy over a sufficient range of data.

$$\dot{m} = k_1 + k_2 f + k_3 \vartheta_{ci} + k_4 f^2 + k_5 \vartheta_{ci}^2 + k_6 (f \vartheta_{ci}). \quad (2.19)$$

This is shown by the hyperplane in fig. 2.21, for which the range of simulation data facilitated for the parameter identification is:  $f \in [40, 80]\text{ Hz}$ ,  $\vartheta_{ci} \in [20, 40]\text{ }^\circ\text{C}$ . The main

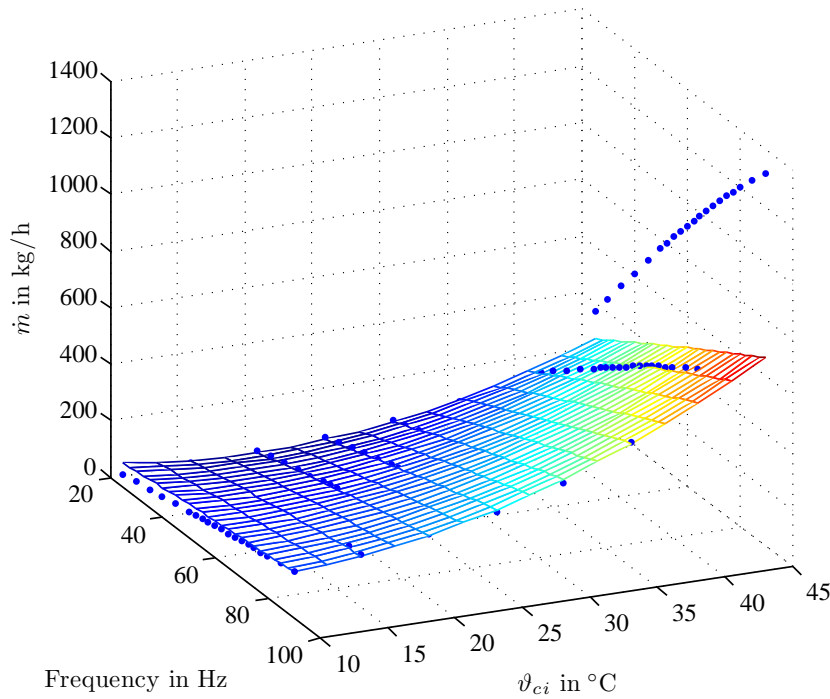


Figure 2.21.: HP TES mode, quadratic approximation with mixed terms according to eq. (2.19) for  $\dot{m}(f, \vartheta_{ci}) = \dot{m}_c = \dot{m}_d$ , given  $\vartheta_{do} = 50 \text{ }^\circ\text{C}$ ,  $\vartheta_{sc} = 0 \text{ }^\circ\text{C}$ ; dots show simulated values.

advantage of an increased accuracy for  $\dot{m}$  may be recognized during the parametrization of the MPC only. In principal a simple bilinear approach with constant term could be facilitated in a framework with repeated linearization of the generalized model. However, a problem arises with increasing prediction horizon, when the linearization point is so to say "far away". More precisely, the reliable and robust range is too small.

## 2.5. Modelling of photovoltaic components

A photovoltaic (PV) system must be modeled for two reasons. First, the simulation of the whole plant requires a model for the PV-system. Second, the predictive control framework, acting on the HP and the building operation, has the task to minimize the electricity consumption from the grid, and this requires a model for PV-power estimation based on predicted weather data to schedule the HP operation accordingly.

The accuracy of the simulation PV-model must be higher than the accuracy of the PV-model for MPC purpose. A few models with different degree of complexity may be found in literature. The difficulty is to derive and parametrize a model, suitable to describe the whole range of operational conditions, based on the limited PV manufacturer's information.

## 2. Heat pump, PV system and building

Townsend (1989) investigated various methods to calculate PV electrical characteristics from generally provided test data. Eckstein (1990) facilitated one method to implement a *four-parameter model* as routine in TRNSYS (type 94)<sup>8</sup>. Based on these initial works Fry (1998) elaborated on a more involved *five-parameter model*, see also Soto et al. (2006).

The physical basics related to a PV cell, and the explanation of the four-parameter model is included in Appendix C.4. This section describes the approach employed for the estimation of the PV power within the MPC concept for PV-led HP operation.

### 2.5.1. Efficiency coefficient model

The general efficiency of a PV module is given as the ratio of electrical power to the total solar irradiance ( $G_T$ ) on the module area  $A$

$$\eta(I, V) = \frac{I V}{A G_T}. \quad (2.20)$$

with  $I$  and  $V$  being the module current and the module voltage. The maximum power point (MP) efficiency  $\eta_{MP}$  generally depends on the cell temperature and the solar irradiance; for more details on the MP efficiency see Appendix C.4. However, it may be assumed to depend only on the cell temperature with a linear characteristic using the gradient  $\frac{d\eta_{MP}}{dT}$ , which is often approximated as  $\mu_{\eta,MP}$ . Using the first two terms of the Taylor series for  $\eta$  one gets

$$\eta_{MP}(T_c) = \eta_{MP,ref} + \left( \frac{d\eta_{MP}}{dT_c} \right)_{ref} (T_c - T_{c,ref}) \quad (2.21)$$

where  $T_c$  and  $T_{c,ref}$  stand for the cell temperature and the cell reference temperature in K, respectively. The index *ref* at the gradient indicates that its numerical value is calculated at some reference conditions (defined later). For irradiance levels above  $400 \text{ W/m}^2$  this approximation appears to be fairly accurate. At lower levels, the efficiency (coefficient) model clearly overestimates the efficiency. Assume a constant cell temperature,  $\eta_{MP}^{real}$  strictly drops with decreasing irradiance, reaching the minimum of  $\approx \eta_{MP}/2$  at zero irradiance. According to eq. (2.21)  $\eta_{MP}$  stays constant under the same conditions, which is not true in reality as mentioned before. However, low irradiance means also low PV power, which is why the annual overestimation of generated electricity when making use of eq. (2.21) is relatively low (1% to 5% have been found by Fry (1998)).

The derivation of eq. (2.21) and the linear temperature coefficient are based on a similarity assumption, see eq. (2.23), which requires to restrict  $\eta$  in eq. (2.20) to the

---

<sup>8</sup> The description in TRNSYS is very limited and currently faulty, for a full understanding the work of Eckstein is highly recommended.

maximum power point. The total change of  $\eta$  with varying temperature reads

$$d\eta(I_{MP}, V_{MP}) = \left( \frac{V_{MP}}{A G_T} \frac{\partial I_{MP}}{\partial T_c} + \frac{I_{MP}}{A G_T} \frac{\partial V_{MP}}{\partial T_c} \right) dT_c. \quad (2.22)$$

The partial derivatives in this expression are unknown, but a fairly good approximation is to set the current and the voltage at maximum power point in relation to the short circuit (sc) current and the open circuit (oc) voltage and use the partial derivatives at these operating conditions, respectively, which leads to

$$\begin{aligned} \frac{\partial I_{MP}}{\partial T_c} &= \left( \frac{I_{MP}}{I_{sc}} \frac{\partial I_{sc}}{\partial T_c} \right)_{T_c=T_{c,ref}}, & \left( \frac{\partial I_{sc}}{\partial T_c} \right)_{T_c=T_{c,ref}} &=: \mu_{sc} \\ \frac{\partial V_{MP}}{\partial T_c} &= \left( \frac{V_{MP}}{V_{oc}} \frac{\partial V_{oc}}{\partial T_c} \right)_{T_c=T_{c,ref}}, & \left( \frac{\partial V_{oc}}{\partial T_c} \right)_{T_c=T_{c,ref}} &=: \mu_{oc}. \end{aligned} \quad (2.23)$$

Replacing the partial derivatives in eq. (2.22) by  $\mu_{sc}$  and  $\mu_{oc}$  leads to an expression for the temperature coefficient  $d\eta_{MP}/dT_c$ . For many modules  $\mu_{sc}$  is an order of magnitude smaller than  $\mu_{oc}$  which is why practically the latter dominates and the former may be neglected. For calculation in eq. (2.23) and finally of eq. (2.21) the nominal operating cell temperature (NOCT) conditions are facilitated as *reference conditions*.

$$\left( \frac{d\eta_{MP}}{dT_c} \right)_{ref} = \eta_{MP,ref} \left( \frac{\mu_{sc}}{I_{sc,ref}} + \frac{\mu_{oc}}{V_{oc,ref}} \right). \quad (2.24)$$

### 2.5.2. Cell temperature

The cell temperature in eq. (2.21) may be derived from an energy balance on a unit area of module, (Eckstein, 1990; Duffie and W. A. Beckman, 2006):

$$(\tau\alpha)G_T = \eta G_T + U_L(T_c - T_{oa}). \quad (2.25)$$

The left hand side of this equation stands for the transmitted and absorbed irradiance ( $\tau\alpha \approx 0.9$  for normal incidence i.e.  $\alpha = 0$ ). On the right hand side the first term represents the part of irradiance that is converted to electricity and the last term gives the part which is thermally dissipated. The decisive loss coefficient  $U_L$  may be derived at *open circuit* ( $\eta = 0$ ) from the *nominal operating cell temperature* (NOCT) conditions:  $G_T = 800 \text{ W/m}^2$ , windspeed=1 m/s,  $T_{oa} = 20 \text{ }^\circ\text{C}$ .

$$U_L = \left( \frac{(\tau\alpha)G_T}{T_c - T_{oa}} \right)_{NOCT}. \quad (2.26)$$

Since the share of generated electricity is small compared to the dissipated heat, a constant efficiency value for  $\eta$  in eq. (2.25) is a sufficient approximation. Solving this

## 2. Heat pump, PV system and building

equation for the cell temperature and using  $\eta_{MP,NOCT}$ <sup>9</sup> leads to

$$T_c = T_{oa} + \frac{(\tau\alpha)G_T}{U_L} \left( 1 - \frac{\eta_{MP,NOCT}}{(\tau\alpha)} \right). \quad (2.27)$$

This equation together with eq. (2.26) may be used in eq. (2.21) to calculate  $\eta_{MP}(T_c)$ . More accurate values may be obtained through iteratively updating  $\eta$  and the cell temperature using eq. (2.21) and eq. (2.27).

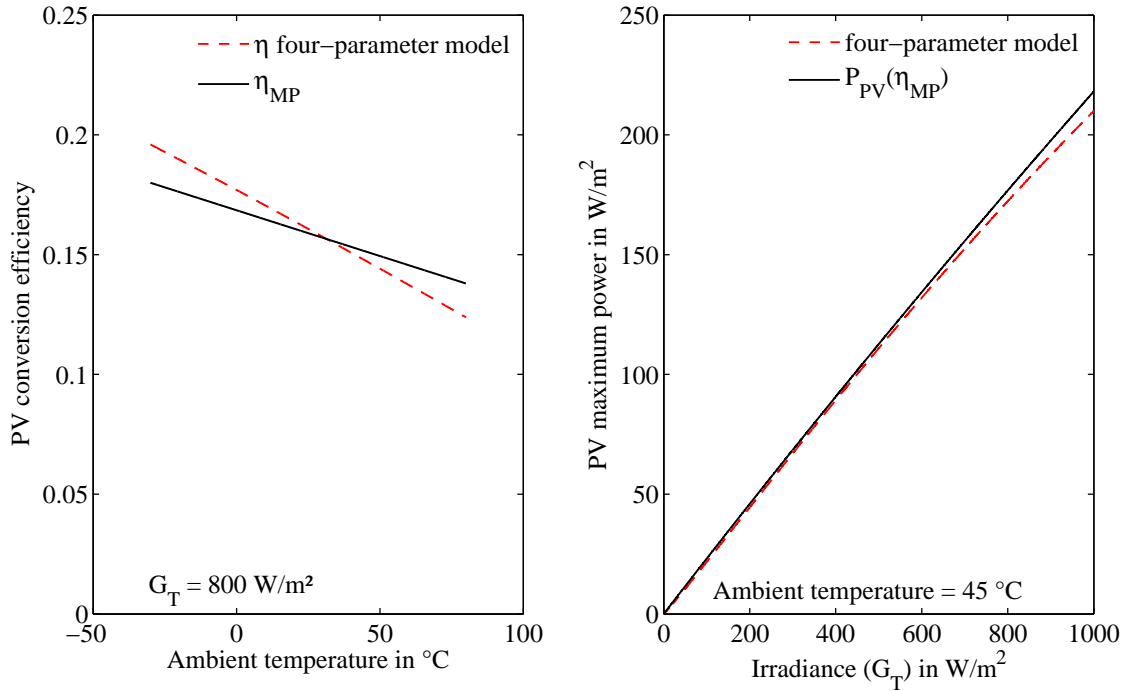


Figure 2.22.: PV module efficiency as a function of the ambient temperature (left) and PV power as a function of the radiation (right) – PV module Solarwatt 60P.

Fig. 2.22 on the left graph, shows the similarity of the efficiency model from eq. (2.21) ( $\eta_{MP}$ ) with the four-parameter model according to Appendix C.4.2, in terms of the conversion efficiency. The PV efficiency changes slightly less with the temperature for the efficiency model given  $800 \text{ W/m}^2$ . The right graph indicates a negligible difference for the two models for the PV power as a function of solar irradiance.

<sup>9</sup> One may find the suggestion to use  $\eta_{MP,STC}$ , which is the MP efficiency at standard test conditions (STC), in literature, but from a physical point of view it is more sensible to use the NOCT efficiency.

## 3. System identification and modeling

*An essential element in an MPC framework is the model of the controlled system or process. This chapter introduces the modeling strategy and provides basics on parameter estimation methods. Imagine a real spring-mass system; parameter estimation in this example means to estimate the numerical values of the mass, the spring constant, the friction term, etc. based on measurement data (velocity and position). In that simple example the model equation can be found in any text book on mechanics. If the required model equations are not trivial, which is the case e.g. for a thermal building model, effort on system modeling is needed. A white box first principle model for a simple building (project: MPC-Boxes) is derived in this chapter and the basic concept behind parameter estimation methods is outlined. Finally, this chapter includes the topics model performance evaluation and experiment design for the purpose of data acquisition.*

*The standard book on system identification is Ljung (1999), however, as introductory material Aarts (2012) is suggested. Thermal simulations conducted with TRNSYS require also some kind of parameter selection or estimation, this, however, is not the focus within this chapter.*

### 3.1. Model design and selection

The first task in system identification is the model selection. This means the choice for a more or less rigid system (of equations), which bears the potential to mimic the system or process of interest. Increasing with the degree of pre-definition black-box, gray-box or white-box models from first principles may be distinguished. Generally it is true that a sound understanding of the real physical relations of a system eases the modeling process. However, as will be seen later, the complete incorporation of known physical relations is not necessarily a wise decision.

Numerous articles and academic reports underline the variety of modeling approaches suitable for MPC in residential heating systems (Reiner et al., 1998; Karlsson and Hagentoft, 2011; Sturzenegger et al., 2012; Sourbron et al., 2013; Privara, Cigler, Zdenek, et al., 2013; Žáčková et al., 2014). The approaches are often complex and time-consuming which is a major obstacle in terms of practical applicability. The models are mostly unique, unsuitable to be applied a second time and the model parameters barely represent known physical quantities. A motivation for this research is also the idea to investigate the application of simple, physical models within a MPC. The modeling process starts with a linear physical model and all parameters should be understood from a practical point of view. This way the re-useability of the model should increase.

### 3. System identification and modeling

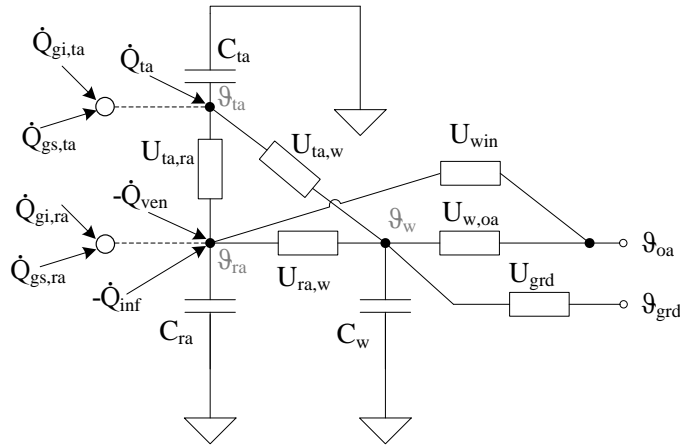


Figure 3.1.: Exemplary thermal RC model for a ground connected building zone, with Cs indicating thermal storages and Us indicating thermal resistances. Gains are indicated by  $\dot{Q}$ s and  $\theta$  are model internal or external temperatures.

Fig. 3.1 provides a schematic drawing for a thermal resistance (R) and capacity (C) network approach (RC-network) – the RC formalism is briefly explained in sec. 3.1.1, it is mere a visual aid to derive the required first order differential equations. The drawn model consists of three thermal nodes (states) and six thermal resistances, characterizing together one thermal zone. A similar model is finally implemented in state space model (SSM) form. The RC-network definition is referred to as *modeling*, model selection or model structure definition. By contrast to the term *parameter estimation* describing the identification of suitable numerical values for Cs and Us to optimally mimic the real process or system. Heat fluxes such as  $\dot{Q}_{gi}$  may (alternatively) be also connected to a different thermal node and likewise the disturbance variables outside ambient and ground temperature ( $\theta_{oa}$  and  $\theta_{grd}$ ). This is a typical example of a structural change which might violate the obvious physical intuition but at the same time improve the model performance.

#### 3.1.1. Physical models from first principles

This section exemplifies the derivation of a linear building model from first principles for one thermal zone. Each element in this model is physically reasoned and the according parameters have attributed physical values. The considered physical relations may be correct from a theoretical point of view, however, due to the general simplification one or the other structural element might turn out to be negligible, which can be seen when conducting a parameter estimation. Similarly, the parameter estimation may lead to a parameter value strongly deviating from a reasonable initial value, which is another typical phenomenon for an approximate model.

The RC approach is only a structured formalism of the first law of thermodynamics while neglecting the work term, i.e.  $dU = dQ$ . In the context of thermal modeling the

### 3.1. Model design and selection

RC approach relies on two elements: resistances – representing an overall heat transfer coefficient or more precisely the inverse of it – and capacities – representing a thermal heat capacity. The model drawn in fig. 3.1 requires three linear differential equations of first order. The derivation of these differential equations is based on a simple *formalism*. First, the heat flux balance ( $dQ$  =heat inputs minus heat outputs per unit time) must be established for each thermal heat capacity – the geometrical border constituting the heat capacity represents the system boundary in the sense of the first law. Second, the net value of this balance is set as the driving force and proportional to the temperature change at the according heat capacity ( $dU = C d\frac{\vartheta}{dt}$ ), cf. eq.(3.1).

#### Linear physical building model

The building model equations for fig. 3.1 with thermal heat capacities for the activated building system- ( $\vartheta_{ta}$ ), the room air node- ( $\vartheta_{ra}$ ) and a virtual wall temperature ( $\vartheta_w$ ) read

$$C_{ta} \beta_{ta} \frac{d\vartheta_{ta}}{dt} = \dot{Q}_{ta} + \dot{Q}_{gs,ta} + \dot{Q}_{gi,ta} - \dot{Q}_{ta,ra} - \dot{Q}_{ta,w} \quad (3.1)$$

$$C_{ra} \beta_{ra} \frac{d\vartheta_{ra}}{dt} = \dot{Q}_{ta,ra} + \dot{Q}_{gs,ra} + \dot{Q}_{gi,ra} - \dot{Q}_{ra,w} - \dot{Q}_{ra,oa} \quad (3.2)$$

$$C_w \beta_w \frac{d\vartheta_w}{dt} = \dot{Q}_{ra,w} + \dot{Q}_{ta,w} - \dot{Q}_{w,oa} - \dot{Q}_{grd}. \quad (3.3)$$

$C_{ta}$ ,  $C_{ra}$  and  $C_w$  are heat capacity values of the TABS, the air volume and the virtual wall volume, obtained from the raw geometry data (area and thickness) and material properties (density and specific heat capacity), i.e. the according values for  $A$ ,  $d$ ,  $\rho$  and  $c$ . The  $\beta$  factors relate the relevant model capacity to the theoretical physical capacity.  $\beta_{ta}$  and  $\beta_w$  represent something like a relative penetration depth and are expected to be  $< 1$ .  $\beta_{ra}$  represents the thermal coupling of adjacent objects to the room air in terms of multiple of the pure room air heat capacity, it is expected to be  $> 1$ .

Heat fluxes are defined for the heating case. A positive quantity contributes positively to the left hand side (LHS) of the balance equations (3.1) -(3.3) if accounted with a "+" in the balance equation and contributes negatively to the LHS if accounted with a "-" in the balance equation. The list of used heat fluxes and their computation is provided by tab. 3.1.

To obtain a normalized model with respect to the activated floor area the following area specific heat capacities are defined, to be used for the derivation of the state space model

$$c_{ta} := C_{ta}/A_{ta} \quad c_{ra} := C_{ra}/A_{ta} \quad c_w := C_w/A_w. \quad (3.4)$$

In addition, the area fractions of the glazed window area  $A_{gla}$  and the TABS area,

### 3. System identification and modeling

Table 3.1.: List of heat fluxes used to derive a physical building model from first principles.

Variable	computation and other required physical relations
$\dot{Q}_{ta} =$	$\dot{m} c_p (\vartheta_{sw} - \vartheta_{ret});$ supply heat into the TABS
$\dot{Q}_{gs,ta} =$	$(1 - \gamma_{gs}) \dot{Q}_{gs};$ solar gains affecting the TABS $\dot{Q}_{gs} = g A_{gla} G_{gla};$ solar gains into the zone
$\dot{Q}_{gi,ta} =$	$(1 - \gamma_{gi}) \dot{Q}_{gi};$ internal gains affecting the TABS $\dot{Q}_{gi}$ are internal gains according to e.g. a schedule
$\dot{Q}_{ta,ra} =$	$U_{ta,ra} A_{ta} (\vartheta_{ta} - \vartheta_{ra});$ heat emitted from the TABS into the zone
$\dot{Q}_{ta,w} =$	$U_{ta,w} A_{ta} (\vartheta_{ta} - \vartheta_w);$ heat flux from the TABS to the wall
$\dot{Q}_{gs,ra} =$	$\gamma_{gs} \dot{Q}_{gs};$ gains due to solar origin
$\dot{Q}_{gi,ra} =$	$\gamma_{gi} \dot{Q}_{gi};$ internal gains affecting the room air
$\dot{Q}_{ra,w} =$	$U_{ra,w} A_w (\vartheta_{ra} - \vartheta_w);$ heat flux from room air to the wall
$\dot{Q}_{ra,oa} =$	$\dot{Q}_{inf} + \dot{Q}_{ven} + \dot{Q}_{win};$ natural, ventilation (air renewal) and window losses $\dot{Q}_{inf} = c_{ra} \rho_{ra} V_{ra} n_{inf} (\vartheta_{ra} - \vartheta_{oa});$ infiltration losses $\dot{Q}_{ven} = \dot{H}(\vartheta_{ra}^*, RH_{ra}^*, \vartheta_{oa}, RH_{oa});$ ventilation losses or gains, see eq. (D.12) or $\dot{Q}_{ven} = n_{ven} V_{ra} \dot{H}(\dot{V} = 1 \text{ m}^3/\text{h});$
	$\dot{Q}_{win} = U_{win} (A_{gla} + A_{opa}) (\vartheta_{ra} - \vartheta_{oa});$ heat losses through window
$\dot{Q}_{w,oa} =$	$U_{w,oa} A_w (\vartheta_w - \vartheta_{oa});$ losses to ambient through heat conduction
$\dot{Q}_{grd} =$	$U_{grd} A_{ta} (\vartheta_w - \vartheta_{grd});$ losses to the ground through heat conduction.

between the total facade area  $A_{gla} + A_{opa}$  and the TABS area, and between the wall area  $A_w$  and the TABS area are defined

$$f_{A,gla} := A_{gla} / A_{ta} \quad f_{A,fac} := (A_{gla} + A_{opa}) / A_{ta} \quad f_{A,w} := A_w / A_{ta}. \quad (3.5)$$

Being precise  $A_{ta}$  should be replaced by the heated zone area  $A_{zo}$ , but since  $A_{ta} \approx A_{zo}$  (cf. fig. D.3 and fig. D.4) and the free parameters  $\beta$  exist it has no adverse effect – this approximation leads to slightly larger  $\beta$  values only.

Replacement of the heat fluxes in eq. (3.1)-(3.3) by the definitions given in tab. 3.1 and making use of the definitions from eq. (3.4) and eq. (3.5) after some rearrangement one gets eq. (3.6). Quantities with a hat symbol indicate variable parameters to be estimated or improved through a parameter estimation procedure unless known exactly, but even if a physical parameter is known it could be sensible to estimate the parameter rather than setting it to the known value.

$$\begin{aligned} \frac{d\vartheta_{ta}}{dt} &= -\frac{\hat{U}_{ta,ra} + \hat{U}_{ta,w}}{c_{ta} \hat{\beta}_{ta}} \vartheta_{ta} + \frac{\hat{U}_{ta,ra}}{c_{ta} \hat{\beta}_{ta}} \vartheta_{ra} + \frac{\hat{U}_{ta,w}}{c_{ta} \hat{\beta}_{ta}} \vartheta_w + \frac{f_{A,gla}(1 - \hat{\gamma}_{gs})\hat{g}}{c_{ta} \hat{\beta}_{ta}} G_{gla} + \frac{(1 - \hat{\gamma}_{gi})}{c_{ta} \hat{\beta}_{ta}} \dot{q}_{gi} + \frac{1}{c_{ta} \hat{\beta}_{ta}} \dot{q}_{ta} \\ \frac{d\vartheta_{ra}}{dt} &= \frac{\hat{U}_{ta,ra}}{c_{ra} \hat{\beta}_{ra}} \vartheta_{ta} - \left( \frac{\hat{U}_{ta,ra} + f_{A,w} \hat{U}_{ra,w} + f_{A,fac} \hat{U}_{win}}{c_{ra} \hat{\beta}_{ra}} + \frac{n_{inf}}{\hat{\beta}_{ra}} \right) \vartheta_{ra} + \frac{f_{A,w} \hat{U}_{ra,w}}{c_{ra} \hat{\beta}_{ra}} \vartheta_w \\ &+ \left( \frac{f_{A,fac} \hat{U}_{win}}{c_{ra} \hat{\beta}_{ra}} + \frac{n_{inf}}{\hat{\beta}_{ra}} \right) \vartheta_{oa} + \frac{f_{A,gla} \hat{\gamma}_{gs} \hat{g}}{c_{ra} \hat{\beta}_{ra}} G_{gla} + \frac{\hat{\gamma}_{gi}}{c_{ra} \hat{\beta}_{ra}} \dot{q}_{gi} + \frac{n_{ven} V_{ra}}{c_{ra} \hat{\beta}_{ra}} \dot{h}_{ven} \\ \frac{d\vartheta_w}{dt} &= \frac{\hat{U}_{ta,w} / f_{A,w}}{c_w \hat{\beta}_w} \vartheta_{ta} + \frac{\hat{U}_{ra,w}}{c_w \hat{\beta}_w} \vartheta_{ra} - \frac{\hat{U}_{ra,w} + (\hat{U}_{ta,w} + \hat{U}_{grd}) / f_{A,w} + \hat{U}_{w,oa}}{c_w \hat{\beta}_w} \vartheta_w + \frac{\hat{U}_{w,oa}}{c_w \hat{\beta}_w} \vartheta_{oa} + \frac{\hat{U}_{grd} / f_{A,w}}{c_w \hat{\beta}_w} \vartheta_{grd}. \end{aligned} \quad (3.6)$$

### 3.1. Model design and selection

With the following definitions for the states ( $\mathbf{x}$ ), the controlled variable input ( $\mathbf{u}$ ) and disturbance input ( $\mathbf{u}_v$ )

$$\mathbf{x} := [\vartheta_{ta}, \vartheta_{ra}, \vartheta_w]^T \quad \mathbf{u} := [\dot{q}_{ta}] \quad \mathbf{u}_v := [\vartheta_{oa}, \dot{q}_{gs}, \dot{q}_{gi}, \dot{h}_{ven}, \vartheta_{grd}]^T, \quad (3.7)$$

the state space parameters (cf. Appendix B for more details) of the model

$$\begin{aligned} \dot{\mathbf{x}}(t) &= \mathbf{A}\mathbf{x}(t) + \mathbf{B}_u\mathbf{u} + \mathbf{B}_v\mathbf{u}_v \\ \mathbf{y} &= \mathbf{C}\mathbf{x} \end{aligned} \quad (3.8)$$

are given as

$$\mathbf{A} := \begin{bmatrix} -\frac{\dot{U}_{ta,ra} + \dot{U}_{ta,w}}{c_{ta} \hat{\beta}_{ta}} & \frac{\dot{U}_{ta,ra}}{c_{ta} \hat{\beta}_{ta}} & \frac{\dot{U}_{ta,w}}{c_{ta} \hat{\beta}_{ta}} \\ \frac{\dot{U}_{ta,ra}}{c_{ra} \hat{\beta}_{ra}} & -\left( \frac{\dot{U}_{ta,ra} + f_{A,w} \dot{U}_{ra,w} + f_{A,fa} \dot{U}_{win}}{c_{ra} \hat{\beta}_{ra}} + \frac{n_{inf}}{\hat{\beta}_{ra}} \right) & \frac{f_{A,w} \dot{U}_{ra,w}}{c_{ra} \hat{\beta}_{ra}} \\ \frac{\dot{U}_{ta,w}/f_{A,w}}{c_w \hat{\beta}_w} & \frac{\dot{U}_{ra,w}}{c_w \hat{\beta}_w} & -\frac{\dot{U}_{ra,w} + (\dot{U}_{ta,w} + \dot{U}_{grd})/f_{A,w} + \dot{U}_{w,oa}}{c_w \hat{\beta}_w} \end{bmatrix} \quad (3.9)$$

$$\mathbf{B}_u := \begin{bmatrix} \frac{1}{c_{ta} \hat{\beta}_{ta}} \\ 0 \\ 0 \end{bmatrix}, \quad \mathbf{B}_v := \begin{bmatrix} 0 & \frac{(1-\hat{\gamma}_{gs})\hat{g}}{c_{ta} \hat{\beta}_{ta}} & \frac{(1-\hat{\gamma}_{gi})}{c_{ta} \hat{\beta}_{ta}} & 0 & 0 \\ \left( \frac{f_{A,fa} \dot{U}_{win}}{c_{ra} \hat{\beta}_{ra}} + \frac{\hat{n}_{inf}}{\hat{\beta}_{ra}} \right) & \frac{\hat{\gamma}_{gs}\hat{g}}{c_{ra} \hat{\beta}_{ra}} & \frac{\hat{\gamma}_{gi}}{c_{ra} \hat{\beta}_{ra}} & \frac{\hat{n}_{ven} V_{ra}}{c_{ra} \hat{\beta}_{ra}} & 0 \\ \frac{\dot{U}_{w,oa}}{c_w \hat{\beta}_w} & 0 & 0 & 0 & \frac{\dot{U}_{grd}/f_{A,w}}{c_w \hat{\beta}_w} \end{bmatrix} \quad (3.10)$$

$$\mathbf{B} := [\mathbf{B}_u, \mathbf{B}_v] \quad \mathbf{C} := \mathbf{1}^{3 \times 3}. \quad (3.11)$$

The state variables and the temperature inputs have the unit °C and each heat flux input represents the heat flux with respect to the TABS area, hence the unit is W/m<sup>2</sup>. That is,  $\dot{q}_{ta} := \dot{Q}_{ta}/A_{ta}$  and  $\dot{h}_{ven} := \dot{H}(1\text{ m}^3/h)/A_{ta}$  must be provided as input. Latent loads are disregarded in  $\dot{H}$  leading to  $\dot{h}_{ven}$ . The total solar gains are represented by  $\dot{q}_{gs} := f_{A,gl} \cdot G_{gl}$ ; through the inner product  $f_{A,gl} \cdot G_{gl}$  it is possible to obtain the sum over all boundary glass surfaces relevant for a thermal zone. The inner product turns into a simple multiplication for windows at one facade only – for the project MPC-Boxes it is the south facing one.  $G_{gl}$  represents the total irradiance on a plane parallel to the window – in case it is a vector each component refers to one facade.

#### 3.1.2. Structured state space models with lumped parameters

A framework slightly relaxed in comparison to a physical model from first principles as derived in sec. 3.1.1 is given by structured state space models (S-SSM). Such a model is based on lumped parameters, that means not the real imaginable physical parameter

### 3. System identification and modeling

values are adjusted via parameter estimation to improve the model performance, but the single elements of the **A**- and the **B**- and if required the **C**-matrix. Each element of a matrix represents a lumped parameter. In a pure physical model for example  $a_{1,1}$  in eq. (3.9) changes through adjustment of the parameters  $\hat{U}_{ta,ra}$ ,  $\hat{U}_{ta,w}$  and  $\hat{\beta}_{ta}$ , whereas in a S-SSM the value of  $a_{1,1}$  is directly adjusted or estimated.

With the S-SSM the parameter estimation probably becomes simpler, if the original physical model is complex. The model performance may likely improve, however, the detailed physical structure as depicted in fig. 3.1 gets lost<sup>1</sup>. Although, the rigid physical structure is finally lost, starting with the modeling from first principles is necessary to obtain a scaffolding for the S-SSM.

#### Linear structured state space building model

A prototypical definition of a complete model structure comprises the definition of a general structure (the size of the matrices) and constraints on the according matrix elements. Assume the same state, output and input definition as in eq. (3.7), but this time with disturbance inputs incorporated in **u**, that is, (**u**, **u<sub>v</sub>**) from eq. (3.7))  $\rightarrow$  **u**:

$$\mathbf{x} := [\vartheta_{ta}, \vartheta_{ra}, \vartheta_w]^T \quad \mathbf{u} := [\dot{q}_{ta}, \vartheta_{oa}, \dot{q}_{gs}, \dot{q}_{gi}, \dot{h}_{ven}, \vartheta_{grd}]^T \quad \mathbf{y} := \mathbf{x}. \quad (3.12)$$

With the six input and the three output components all possible input and output relations are predefined. Consequently the dimensions of the model matrices are fixed. For now, any further constraints on matrix elements are disregarded, then the *prototypical unconstrained* S-SSM with parameters  $a_{i,j}$ ,  $i, j = 1, 2, 3$  and  $b_{i,j}$ ,  $i = 1, 2, 3$  and  $j = 1, \dots, 6$  reads

$$\mathbf{A} = \begin{bmatrix} a_{1,1} & a_{1,2} & a_{1,3} \\ a_{2,1} & a_{2,2} & a_{2,3} \\ a_{3,1} & a_{3,2} & a_{3,3} \end{bmatrix}, \quad \mathbf{B} = \begin{bmatrix} b_{1,1} & b_{1,2} & b_{1,3} & b_{1,4} & b_{1,5} & b_{1,6} \\ b_{2,1} & b_{2,2} & b_{2,3} & b_{2,4} & b_{2,5} & b_{2,6} \\ b_{3,1} & b_{3,2} & b_{3,3} & b_{3,4} & b_{3,5} & b_{3,6} \end{bmatrix}, \quad \mathbf{C} = \begin{bmatrix} 1 & 0 & 0 \\ 0 & 1 & 0 \\ 0 & 0 & 1 \end{bmatrix}. \quad (3.13)$$

Comparing **B** with eq. (3.10) one can see that it is probably sensible to set a few elements of **B** zero, which is discussed in sec. 3.1.4. Different structures and their performances are analyzed in chapter 4.

#### Physical units of the matrix elements

The matrix elements in eq. (3.13) and in eq. (3.9)-(3.11), must share the same physical unit. Rather than analyzing the individual contributions for example in eq. (3.9), this problem is approached backwards.

The left hand side (LHS) in the first equation of the continuous time SSM ( $\dot{x}$  in eq. (3.8)) must have the dimension *temperature per time*. The relevant order of magnitude

<sup>1</sup> Although, introducing certain slack variables and utilizing a non linear equation solver the physical parameters probably may be regained.

of time constants involved ranges from an hour to 100 hours, which is why the preferred time unit in this context is  $h$ . The building model relates to a real environment dominated by temperature measurements in  $^{\circ}\text{C}$ , however, temperature increments may be expressed in K. This clarifies the selection of the unit  $K/h$  for the left hand side of the first SSM equation.

Based on the unit of the LHS and recalling the physical dimension of the state and the input variables it is straightforward to obtain the unit of the various matrix elements. The elements of  $\mathbf{A}$  and those elements of  $\mathbf{B}$  related to a temperature input ( $^{\circ}\text{C}$ ) must have the unit  $1/h$ . All elements of  $\mathbf{B}$  related to a heat flux input with the unit  $W/m^2$ , must have the unit  $K m^2/Wh$ .

Dealing with a *discrete (d) time model*, which may be obtained from the continuous model by a transformation as outlined in Appendix B, the units of the matrix components change. The new unit of dynamic matrix ( $\mathbf{A}^d$ ) elements becomes 1 and the units of the input matrix ( $\mathbf{B}^d$ ) elements are the units of the continuous time model matrix times  $h$ . That is, all elements of  $\mathbf{B}^d$  – the time discrete pendant to  $\mathbf{B}$  – related to a heat flux input with the unit  $W/m^2$ , must have the unit  $K m^2/W$ , and all inputs related to a temperature input ( $^{\circ}\text{C}$ ) must have the unit 1.

### 3.1.3. Mathematical formalization of the modeling

In this research linear SSM as described in detail in Appendix B are of special interest. Two modeling approaches, both leading to a linear SSM, were already discussed in this chapter. Fig. 3.2 visualizes a model  $\mathcal{M}$  – which stands e.g. for a thermal RC-network –

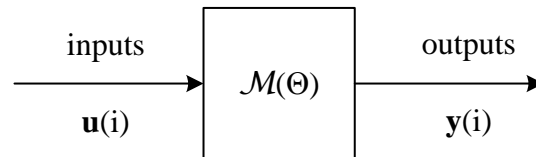


Figure 3.2.: Visualization of a model  $\mathcal{M}(\Theta)$  with inputs and outputs.

parametrized with  $\Theta$ . In this case the parameter vector  $\Theta$  incorporates the numerical values used for the *physical* parametrization of the matrices in eq. (3.9) and (3.10). That is  $\theta_1 = \hat{U}_{ta,ra}$ ,  $\theta_2 = \hat{\beta}_{ta}$ , etc. Alternatively, for a S-SSM  $\Theta$  incorporates the numerical values of the matrix elements for  $\mathbf{A}$  and  $\mathbf{B}$  in eq. (3.13). That is  $\theta_1 = a_{1,2}, \dots, \theta_9 = a_{3,3}$  and  $\theta_{10} = b_{1,1}, \dots, \theta_{27} = b_{3,6}$ .

Model inputs are abbreviated as  $\mathbf{u}(i)$  and outputs as  $\mathbf{y}(i)$ , with the argument  $i$  indicating the (discrete) time dependence. Different *model structures* throughout this work are distinguished by an upper index ( $\mathcal{M}^1$ ), and a specific parametrization with parameters  $\Theta_{init}$  is indicated as  $\mathcal{M}^1(\Theta_{init})$ . For a profound discussion and further details see Ljung (1999) Ch. 7.

### 3. System identification and modeling

In this thesis the *upper index* refers always to a model structure only, and the lower index refers to the set of parameters. This is important since – as explained in sec. 3.1.4 – constraints on  $\mathbf{A}$  and  $\mathbf{B}$  define the internal model structure of a S-SSM. A structured model may be named  $\mathcal{M}^1$  but this does not say anything about the internal model structure realized through  $\Theta$ . Hence, it is required to provide  $\Theta_{init}^a$ , where the superscript  $a$  refers to the structure relevant parametrization and *init* to the real parametrization. However, if not really necessary only one of the indices will be given. For example, when discussing the parametrization in context of one specific model structure, different parametrizations are just written as  $\Theta_{init}$ ,  $\Theta_{wc}$ , etc.

The required time for the development of detailed and optimally non-linear models, led to a trend to simplify the models, which has finally become a common practice. Strictly speaking the match between a real system or process and a model is termed *consistency* see Ljung (1999) Ch. 8, and an according test is the consistency test, however, in practice this is barely relevant (Aarts, 2012). The reason is that consistency is given up in favor of *approximate modeling* which inherently bears the assumption that only the purpose-relevant characteristics of a system or process are modeled.

#### 3.1.4. Prototypical constrained structured SSM

Fig. 3.3 is a more detailed version of fig. 3.2, restricting the potential models  $\mathcal{M}$  to linear SSM. Throughout this work, model names such as  $\mathcal{M}^{n4w}$  are assigned according to the following convention. The superscript is the order<sup>2</sup> of the system (n4...) and, if given, an additional acronym provides a unique indicator of the general model structure for example (...w). A *general structure*  $\mathcal{M}^{n4w}$  makes only sense in context of predefined input and output vectors. Assume all possibly relevant inputs are provided in  $\mathbf{u}$ , then the coupling of the system to a certain input  $u_i$  (e.g. for  $i = 1$  the first component or  $\dot{q}_{ta}$ ) is entirely determined by the input matrix  $\mathbf{B}$ . Similarly, the *state interactions* are determined by the dynamic matrix  $\mathbf{A}$ . Because  $\mathbf{A}$  and  $\mathbf{B}$  are functions of  $\Theta$ , although termed parameter vector,  $\Theta$  also describes the *internal model structure*. Assume  $\mathcal{M}^{n4w}$ , the entire model structure is not given unless the parameter vector  $\Theta$  is known. A certain internal structure  $\Theta^a$  is imposed with *structural zeros* in  $\mathbf{A}$  and  $\mathbf{B}$  – these zeros may be formulated simply through constraints on  $\Theta$  before the optimization. The *prototypical definition* of a complete model structure comprises the definition of the general structure (size, inputs and outputs) and the limitation of  $\Theta$  in terms of structural zeros, to define the internal structure.

Lets start with the definition of the general structure and assume the same state, output and input definition as in eq. (3.12) – explained already in detail for eq. (3.7) in sec. 3.1.1 – but this time extend by a virtual sky temperature ( $\vartheta_{sky}$ ):

$$\mathbf{x} := [\vartheta_{ta}, \vartheta_{ra}, \vartheta_w]^T \quad \mathbf{u} := [\dot{q}_{ta}, \vartheta_{oa}, \dot{q}_{gs}, \dot{q}_{gi}, \dot{h}_{ven}, \vartheta_{grd}, \vartheta_{sky}]^T \quad \mathbf{y} := \mathbf{x}. \quad (3.14)$$

<sup>2</sup> The order equals the number of states.

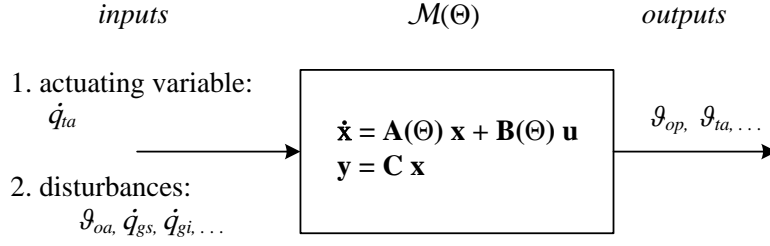


Figure 3.3.: Refined visualization of a model as box-object with defined model structure.

With the seven input and the three output components and a choice for the system order  $n := 3$ , all possible input and output relations are predefined. Consequently the dimensions of the matrices are fixed. Now it is possible to parametrize  $\mathbf{C}$  and after this stage the general structure definition  $\mathcal{M}^{n3}$  is complete

$$\mathbf{A} = \begin{bmatrix} \cdot & \cdot & \cdot \\ \cdot & \cdot & \cdot \\ \cdot & \cdot & \cdot \end{bmatrix}, \quad \mathbf{B} = \begin{bmatrix} \cdot & \cdot & \cdot & \cdot & \cdot & \cdot & \cdot \\ \cdot & \cdot & \cdot & \cdot & \cdot & \cdot & \cdot \\ \cdot & \cdot & \cdot & \cdot & \cdot & \cdot & \cdot \end{bmatrix}, \quad \mathbf{C} = \begin{bmatrix} 1 & 0 & 0 \\ 0 & 1 & 0 \\ 0 & 0 & 1 \end{bmatrix}. \quad (3.15)$$

Imposing zeros for specific elements of  $\mathbf{A}$  and  $\mathbf{B}$  for the optimization the internal structure is also fixed, see eq. (3.16). In case  $\mathbf{C}$  is not given explicitly, it is assumed  $\mathbf{C} = \mathbf{1}^{n \times n}$ . This leads directly to the definition of the parameter constraints.

A prototypical constrained S-SSM ready for optimization of initially provided parameters is given by

$$A = \begin{bmatrix} \mathbb{R} & \mathbb{R} & \mathbb{R} \\ \mathbb{R} & \mathbb{R} & \mathbb{R} \\ \mathbb{R} & \mathbb{R} & \mathbb{R} \end{bmatrix}, \quad B = \begin{bmatrix} \mathbb{R}^+ & 0 & 0 & 0 & X & 0 & 0 \\ 0 & \mathbb{R}^+ & \mathbb{R}^+ & \mathbb{R}^+ & X & 0 & \mathbb{R}^+ \\ 0 & 0 & 0 & 0 & X & \mathbb{R}^+ & 0 \end{bmatrix}, \quad C = \begin{bmatrix} 1 & 0 & 0 \\ 0 & 1 & 0 \\ 0 & 0 & 1 \end{bmatrix}, \quad (3.16)$$

where  $\mathbb{R}$  stands for the parameter range  $-\infty, \dots, \infty$  and  $\mathbb{R}^+$  indicates only positive numbers  $0, \dots, \infty$ . Parameter values such as 0 and 1 represent fixed values excluded from the optimization. The  $X$ 's indicate an irrelevant parameter – a parameter of the input matrix is irrelevant in case the input variable (trajectory) is neglected for a certain experiment, for the estimation such parameters may be set zero.

The conduction of the parameter estimation for the discrete time SSM requires an according transformation of the constraints. This may be understood consulting Appendix B and applying Euler's method from eq. (B.6) to the estimation prototype in eq. (3.16). Structural zeros or a zero constraint on the main diagonal in  $\mathbf{A}$  transform to a 1 in  $\mathbf{A}^d$  – this is the most important constraints transformation.

### 3. System identification and modeling

#### 3.2. Parameter estimation methods

Given a physical model structure  $\mathcal{M}$  as depicted in fig. 3.1 one may start to think on suitable numerical values for the according model parameters. Assume only one input and one output variable, and the model  $\mathcal{M}$  to be parametrized with some initial values  $\Theta_{init}$ . Now a time series of input data  $u(1), u(2), \dots, u(N)$  (say  $u \equiv \dot{Q}_{ta}$ ) may be used to qualitatively test whether the model does approximately what is expected, that is, if the reaction of the output is reasonable from a physical point of view. If this is the case, one may go further and ask for the best numerical parameters, which leads directly to some sort of parameter estimation method.

Any parameter estimation requires a set of experimental data for  $\mathbf{u}$  and  $\mathbf{y}$  in fig. 3.2. Assume, the following data  $\mathcal{D}^N$  are available from a detailed simulation or a real experiment:

$$\mathcal{D}^N = \{y(1), u(1), y(2), u(2), \dots, y(N), u(N)\}, \quad (3.17)$$

where  $N$  indicates the number of values or the length of the data set. Given these data the aim is to find an optimum set of estimated parameters  $\hat{\Theta}$  such that the experimental outputs  $y \in \mathcal{D}^N$  are reproduced as good as possible when feeding  $\mathcal{M}(\hat{\Theta})$  with the inputs  $u \in \mathcal{D}^N$ . The obtained model output is then indicated as  $\hat{y}$ . Formally the *parameter estimation method* is a mapping:

$$\mathcal{D}^N \rightarrow \hat{\Theta} \in \mathcal{S}_{\mathcal{M}}, \quad (3.18)$$

with  $\mathcal{S}_{\mathcal{M}}$  being the possible set of parameters<sup>3</sup>, compare with Ljung (1999). Ideally the optimum parameters  $\hat{\Theta}$  are unique, that is the optimum output  $\hat{y}$  may be reproduced by these parameters only and not also by another  $\hat{\Theta}_2 \in \mathcal{S}_{\mathcal{M}}$ .

Depending on the availability of data for inputs and outputs different methods may be employed to estimate an optimum set of model parameters  $\hat{\Theta}$ . For the following section it is assumed, that data are available for all model inputs and outputs.

##### 3.2.1. Linear regression and least square estimate

Assume the availability of a time series with  $N$  data for the input and the output as declared by eq. (3.17). Further, assume a single input single output (SISO) linear model with the parameters  $\Theta$ . The model output variable is written as  $\hat{y}$ , then the following sum provides a quantitative measure for the model accuracy

$$V_N(\Theta) = \frac{1}{N} \sum_{t=1}^N |y(t) - \hat{y}(t)|^2. \quad (3.19)$$

---

<sup>3</sup> This set may be restricted through a number of constraints based on physical insight.

The smaller this sum, the higher the accuracy of the model. In this equation,  $\hat{y}(t)$  is obtained by supplying the input  $u(t)$  to the model parametrized with  $\Theta$ . Now lets turn to the derivation of an expression for  $\hat{\Theta}$  (the optimum set of estimated parameters) for a linear multiple input multiple output (MIMO) model. Essentially this boils down to minimization of  $V_N$ , which has the form of eq. (3.22) in the MIMO case.

### Multivariate least square problem

An n-dimensional SSM with dynamic- and input-matrix  $\mathbf{A}$  and  $\mathbf{B}$  where  $\mathbf{C} = 1^{n \times n}$  may be written in time discrete form (*superscript*<sup>d</sup> for indication of the discrete model nature is neglected) as<sup>4</sup>

$$\hat{\mathbf{y}}(k+1) = \mathbf{A}\mathbf{x}(k) + \mathbf{B}\mathbf{u}(k). \quad (3.20)$$

A set of experimental data for the outputs and the inputs, similarly as given by eq. (3.17), allows for direct calculation of  $\mathbf{A}$  and  $\mathbf{B}$  through solving a multivariate least square (MLS) problem. This problem is the multivariate counterpart of an autoregressive model with external variables (ARX). The solution to the multivariate problem will be exemplified by means of a 2<sup>nd</sup> order SSM with two input variables, i.e.

$$\underbrace{\begin{bmatrix} \hat{y}_1(k+1) \\ \hat{y}_2(k+1) \end{bmatrix}}_{\hat{\mathbf{y}}(k+1)} = \underbrace{\begin{bmatrix} a_{11} & a_{12} \\ a_{21} & a_{22} \end{bmatrix}}_{\mathbf{A}} \underbrace{\begin{bmatrix} x_1(k) \\ x_2(k) \end{bmatrix}}_{\mathbf{x}(k)} + \underbrace{\begin{bmatrix} b_{11} & b_{12} \\ b_{21} & b_{22} \end{bmatrix}}_{\mathbf{B}} \underbrace{\begin{bmatrix} u_1(k) \\ u_2(k) \end{bmatrix}}_{\mathbf{u}(k)}. \quad (3.21)$$

By contrast to former formulations of the SSM  $\mathbf{y}$  in eq. (3.20) and (3.21) is written with a *hat* as  $\hat{\mathbf{y}}$  to distinguish the *model output* from the available measurement (simulation) data denoted as  $\mathbf{y}$ . With these data and the model output according to eq. (3.21) for each instant  $i$  from  $i = 1, 2, \dots, N$ , the cost functional may be written as<sup>5</sup>

$$V_N(\Theta) = \frac{1}{N} \sum_{i=1}^N \|\mathbf{y}(i) - \hat{\mathbf{y}}(i)\|_2^2. \quad (3.22)$$

The optimal solution for the model parameters in a least square sense is then given by

$$\hat{\Theta} = \arg \min_{\Theta} V_N(\Theta), \quad (3.23)$$

where the dependency of  $V_N$  on  $\mathbf{A}$  and  $\mathbf{B}$  is hidden in  $\Theta$ . The solution for  $\hat{\Theta}$ , given an experimental time-series for  $\mathbf{y}$  and  $\mathbf{u}$ , is derived in the following. Therefore it is convenient to define

$$\begin{bmatrix} \mathbf{a}_1^T \\ \mathbf{a}_2^T \end{bmatrix} := \begin{bmatrix} a_{11} & a_{12} \\ a_{21} & a_{22} \end{bmatrix}, \quad \begin{bmatrix} \mathbf{b}_1^T \\ \mathbf{b}_2^T \end{bmatrix} := \begin{bmatrix} b_{11} & b_{12} \\ b_{21} & b_{22} \end{bmatrix}. \quad (3.24)$$

<sup>4</sup> The time dependence may also be written using the index notation rather than the argument notation.

<sup>5</sup> The extension from a scalar residual as in eq. (3.19) to a residual vector  $\boldsymbol{\varepsilon}$  as in the multivariate case, requires to use the euclidean norm; in 2-D:  $\|\boldsymbol{\varepsilon}\|_2^2 = \varepsilon_1^2 + \varepsilon_2^2$ .

### 3. System identification and modeling

The full form of eq. (3.22) with  $\hat{\mathbf{y}}(i)$  according to the model from eq. (3.21) reads

$$V_N = \frac{1}{N} \sum_{i=1}^N \left( y_1(i) - \mathbf{a}_1^T \mathbf{x}(i-1) - \mathbf{b}_1^T \mathbf{u}(i-1) \right)^2 + \left( y_2(i) - \mathbf{a}_2^T \mathbf{x}(i-1) - \mathbf{b}_2^T \mathbf{u}(i-1) \right)^2. \quad (3.25)$$

The parameters to be determined are the elements of  $\mathbf{A}$  and  $\mathbf{B}$ , which are summarized by the parameter vector  $\Theta$ . The optimum values are obtained by  $\nabla_{\Theta} V_N = 0$ , that is the gradient of  $V_N$  with respect to  $\Theta$  must vanish. The partial derivatives with respect to an element  $a_{pq}$  are given by

$$\frac{\partial V_N}{\partial a_{pq}} = \frac{1}{N} \sum_{i=1}^N -2 \left( y_p(i) - \mathbf{a}_p^T \mathbf{x}(i-1) - \mathbf{b}_p^T \mathbf{u}(i-1) \right) x_q(i-1), \quad p, q \in \{1, 2\} \quad (3.26)$$

and similarly for  $b_{pq}$

$$\frac{\partial V_N}{\partial b_{pq}} = \frac{1}{N} \sum_{i=1}^N -2 \left( y_p(i) - \mathbf{a}_p^T \mathbf{x}(i-1) - \mathbf{b}_p^T \mathbf{u}(i-1) \right) u_q(i-1), \quad p, q \in \{1, 2\}. \quad (3.27)$$

Setting all partial derivatives to zero a necessary condition for an extremum is obtained, which – due to the convex character of the cost function – leads to the desired minimum  $V_N$  in eq. (3.23). From eq. (3.26) and eq. (3.27) one gets

$$\sum_{i=1}^N x_q(i-1) y_p(i) = \sum_{i=1}^N x_q(i-1) \left( \mathbf{a}_p^T \mathbf{x}(i-1) + \mathbf{b}_p^T \mathbf{u}(i-1) \right), \quad p, q \in \{1, 2\}, \quad (3.28)$$

$$\sum_{i=1}^N u_q(i-1) y_p(i) = \sum_{i=1}^N u_q(i-1) \left( \mathbf{a}_p^T \mathbf{x}(i-1) + \mathbf{b}_p^T \mathbf{u}(i-1) \right), \quad p, q \in \{1, 2\}. \quad (3.29)$$

For  $q \in \{1, 2\}$  one may write the left hand side (LHS) of the last two equations as

$$\begin{aligned} & x_1(0)y_p(1) + x_1(1)y_p(2) + \dots + x_1(N-1)y_p(N) \\ & x_2(0)y_p(1) + x_2(1)y_p(2) + \dots + x_2(N-1)y_p(N) \\ & u_1(0)y_p(1) + u_1(1)y_p(2) + \dots + u_1(N-1)y_p(N) \\ & u_2(0)y_p(1) + u_2(1)y_p(2) + \dots + u_2(N-1)y_p(N) \end{aligned} \Leftrightarrow \begin{bmatrix} x_1(0) & x_1(1) & \dots & x_1(N-1) \\ x_2(0) & x_2(1) & \dots & x_2(N-1) \\ u_1(0) & u_1(1) & \dots & u_1(N-1) \\ u_2(0) & u_2(1) & \dots & u_2(N-1) \end{bmatrix} \begin{bmatrix} y_p(1) \\ y_p(2) \\ \vdots \\ y_p(N) \end{bmatrix}$$

and summarizing the states and the inputs as vectors and the  $p^{\text{th}}$ -output in a time series (vector)  $Y_p^{1,N}$  this may be written as

$$LHS : \begin{bmatrix} \mathbf{x}(0) & \mathbf{x}(1) & \dots & \mathbf{x}(N-1) \\ \mathbf{u}(0) & \mathbf{u}(1) & \dots & \mathbf{u}(N-1) \end{bmatrix} \left[ Y_p^{1,N} \right]. \quad (3.30)$$

Similarly, the right hand side (RHS)<sup>6</sup> may be written as

$$\begin{bmatrix} \mathbf{x}(0) & \mathbf{x}(1) & \dots & \mathbf{x}(N-1) \\ \mathbf{u}(0) & \mathbf{u}(1) & \dots & \mathbf{u}(N-1) \end{bmatrix} \left[ \begin{bmatrix} \mathbf{x}^T(0) \\ \vdots \\ \mathbf{x}^T(N-1) \end{bmatrix} \mathbf{a}_p + \begin{bmatrix} \mathbf{u}^T(0) \\ \vdots \\ \mathbf{u}^T(N-1) \end{bmatrix} \mathbf{b}_p \right], \quad (3.31)$$

<sup>6</sup> The expression  $\mathbf{a}_p^T \mathbf{x}(i-1)$  is simply a scalar product, i.e. a number which may alternatively be written as  $\mathbf{x}^T(i-1) \mathbf{a}_p$ , and equivalently for  $\mathbf{b}_p^T \mathbf{u}(i-1)$ .

or

$$RHS : \underbrace{\begin{bmatrix} \mathbf{x}(0) & \mathbf{x}(1) & \dots & \mathbf{x}(N-1) \\ \mathbf{u}(0) & \mathbf{u}(1) & \dots & \mathbf{u}(N-1) \end{bmatrix}}_{\Phi_N :=} \begin{bmatrix} \mathbf{x}^T(0) & \mathbf{u}^T(0) \\ \vdots & \vdots \\ \mathbf{x}^T(N-1) & \mathbf{u}^T(N-1) \end{bmatrix} \underbrace{\begin{bmatrix} \mathbf{a}_p \\ \mathbf{b}_p \end{bmatrix}}_{\theta_p :=}. \quad (3.32)$$

With the definitions made for the *regressor matrix*  $\Phi_N$  and the parameter vector  $\theta_p$  the *LHS* and the *RHS* may be put together giving the so called matrix (normal) equations for the least square problem

$$\Phi_N Y_p^{1,N} = \Phi_N \Phi_N^T \theta_p. \quad (3.33)$$

The unconstrained least square solution of eq. (3.23) leads to the same regressor matrix for  $p = 1$  and  $p = 2$ , hence  $\theta_1$  and  $\theta_2$  may be obtained with the output time series matrix  $[Y_1^{1,N} Y_2^{1,N}]$ . The parameter vectors  $\theta_1$  and  $\theta_2$  result after applying the inverse of  $(\Phi_N \Phi_N^T)$  on eq. (3.33)

$$\left[ \left( \Phi_N \Phi_N^T \right)^{-1} \Phi_N \right] \left[ Y_1^{1,N} Y_2^{1,N} \right] = [\theta_1 \theta_2]. \quad (3.34)$$

The first expression of this equation on the left hand side, in square brackets is the famous *pseudoinverse* or *Moore-Penrose-Inverse*. For successful establishment of  $\Phi_N$  based on eq. (3.17) the indices must be shifted by  $-1$ .

### 3.2.2. Short account on more advanced estimation methods

The method described in sec. 3.2.1 is the beginner level in terms of parameter estimation methods. However, it shows the principal idea and concept hidden in some way in nearly all estimation methods. For this work the method is used to obtain the initial model parameters only. In the following the basic concepts behind the subspace method and the predictor error method are sketched. See Ljung (1999) and Ljung (2002) and Heusden et al. (2010) for more details.

#### Subspace method

The method in sec. 3.2.1 assumes all model input and output data to be available. Since  $\mathbf{C}$  was assumed to be the unity matrix even all internal model states were directly accessible. Assume a case where the number of model outputs is smaller than the number of internal states for a given model Ansatz. This situation leads directly to a slightly more advanced parameter estimation method, the subspace method.

### 3. System identification and modeling

The subspace estimation method is based on an *outer* model and a predictor or *internal* model. The outer model is the model in the sense of that shown in fig. 3.3, the internal model describes the relation, e.g. between the last two output and input variables to the current output variable, therefore also the name (internal) *predictor*.

$$\hat{y}(t|t-1) = \alpha_1 y(t-1) + \alpha_2 y(t-2) + \beta_1 u(t-1) + \beta_2 u(t-2) \quad (3.35)$$

where the argument  $(t|t-1)$  means estimated for the instant  $t$  based on data up to  $t-1$ , compare with Ljung (1999). The coefficients  $\alpha$  and  $\beta$ , both real numbers, refer to the predictor model parameters.

The predictor concept from eq. (3.35) is practically expanded, using more than two data steps from the past and predicting more than one step ahead. The estimated values from the predictor  $\hat{y}$  are then utilized to construct the model states of the outer model. With all model states given in terms of the internal predictor the least square method from 3.2.1 may be employed again to estimate the parameters of the outer model. For more details see Ljung (1999).

#### Prediction error method

Prediction error estimation methods (PEM) mark a common and versatile family of methods for system identification, Ljung (1999) and Ljung (2002). A PEM is also utilized in this research to arrive at the final controller models which required parameter estimation from real or simulation data.

Lets assume a model structure  $\mathcal{M}$  to be given, the aim is to find the optimum set of parameters  $\hat{\Theta}$ , such that for any output of the model the prediction error  $\varepsilon(t, \hat{\Theta})$  becomes as small as possible for  $t = 1, 2, \dots, N$ . It is sufficient to restrict to a single output system for the remaining explanations. The prediction error is defined by

$$\varepsilon(t, \Theta) = y(t) - \hat{y}(t, \Theta), \quad (3.36)$$

where  $y(t) \in \mathcal{D}^N$  stands e.g. for a measured temperature value and  $\hat{y}(t, \Theta)$  represents the corresponding output value of the model  $\mathcal{M}(\Theta)$  at the instant  $t$ . The vague phrase "as small as possible" may be mathematically expressed in various ways. For simplicity this term is qualified with a quadratic functional, that should become a minimum

$$V_N(\Theta) = \frac{1}{N} \sum_{t=1}^N |\varepsilon(t, \Theta)|^2. \quad (3.37)$$

The *structure* behind the PEM approach is important in order to understand the quality of the outcome. The freedom of the PEM structure in this context must not be confused with the internal (physical) structure of the model  $\mathcal{M}$  describing  $\hat{y}$ . The structure of the PEM may be understood only in a stochastic framework, where the

deviation between the real and the model output is compensated by an additional noise term. For more details see Aarts (2012). Two prominent structures are the autoregressive model with extra (ARX) input term and the ARX model with moving average (ARMAX). The ARX model is the same as the least square method in sec. 3.2.1, however, this time with an explicit noise term added. Another prominent PEM structure is the output error (OE) model.

The different structures have advantages, disadvantages and specific characteristics. An ARX predictor model leads to a smaller prediction error  $\varepsilon(t, \Theta)$  in the high frequency range compared to an OE predictor. However, the OE predictor outperforms the ARX predictor in the low frequency range. These characteristics are easily understood when switching to the frequency-domain, see Aarts (2012). Pre-filtering of  $\varepsilon(t, \Theta)$  changes this general PEM structure related characteristics.

Assume a filter  $L$  applied to the prediction error, leading to the filtered prediction error

$$\varepsilon_F(t, \Theta) = L \varepsilon(t, \Theta). \quad (3.38)$$

This is the same as applying the same filter on the input and the output data. Again understanding the effect of the filter  $L$  requires switching to the frequency-domain interpretation of  $\varepsilon$ . It can be said that  $L$  enables a frequency depending weighting in eq. (3.37). This can be understood also in the sense that the filtering suppresses or enhances particular model properties. For example a suppression of high frequency fluctuations in  $\varepsilon$  is possible. With pre-filtering even for an ARX predictor small values for  $\varepsilon$  in the low frequency range become possible.

#### Estimation methods tailored to building modeling

The relevance of successful parameter estimation in the context of thermal building models has led to a few approaches tailored especially to the underlying predictive control task. These approaches may be subsumed under the term model predictive control relevant identification (MRI). Based on the work of Lauri et al. (2010), Žáčková et al. (2011) and Privara, Cigler, Váňa, et al. (2013) elaborated on methods which facilitate multi-step predictors within the PEM approach. These multi-step predictors lead to a slightly better model performance for the relevant prediction horizon of the MPC problem.

Another approach in contrast to a detailed physical model (Sturzenegger et al., 2012) in the context of thermal building models is a purely data driven approach, see for example Killian et al. (2014). Such approaches are especially famous due to the laborious process of manually generating a building model.

### 3. System identification and modeling

#### 3.3. Model performance and stability

The question whether a model performs good or bad, both, concerning the model structure and the set of parameters, requires the definition of a suitable measure. For general and abstract performance criteria see Ljung (1999) or Aarts (2012) and for thermal building model related performance criteria see Sturzenegger et al. (2012).

As a layman one may think of various measures to judge on the quality of a mathematical model. These measures must provide information on the likeness of a model output  $\hat{y}(t)$  compared to the real measured or simulated variable  $y(t)$  for a given input value  $u(t)$ . Given a thermal SISO model with  $y := \text{temperature } (\vartheta)$  it is obvious to apply some statistics on the residual or model error defined by eq. (3.39). However, for a MIMO model the situation becomes slightly more complicated.

In addition to the natural measure e.g. temperature deviation one must think of an abstract measure to describe and evaluate a MIMO models performance with a single, lucid quantity. This quantity is generally referred to as *model fitness* or short fit. In simple words, it describes the ability of a model to reproduce a time series of output data  $y(t)$  for a given time series of input data  $u(t)$ . A few physical error and model fitness measures will be defined and discussed in the following paragraphs. The term *physical* is motivated by the fact, that the according error measure for an output  $y$  is associated with a real physical quantity – in this work mostly temperature.

##### 3.3.1. Output trajectories and physical model errors

A brief look at the model output  $\hat{y}(t)$  in comparison to the experimental data  $y(t) \in \mathcal{D}^N$  is always necessary. The best is to plot the residual defined by eq. (3.39) as done in fig. 3.4 for the operative temperature in the first and the second floor ( $\vartheta_{op,1fl}, \vartheta_{op,2fl}$ ) and for the average TABS temperature ( $\vartheta_{ta}$ ). Fig. G.28 in Appendix shows the cross-validation results.

Consider a time series of a single model output  $\hat{y}(1), \hat{y}(2), \dots, \hat{y}(N)$  – generated with a model  $\mathcal{M}(\Theta^*)$  abbreviated simply with  $\Theta^*$  in the following because the model structure does not change. The corresponding experimental data – originating from simulations or a real experiment in response to a time series of input data  $u(1), u(2), \dots, u(N)$  – are given by  $y(1), y(2), \dots, y(N)$ . Then, the physical error or *residual* at instant  $t$ , is defined as

$$\boxed{\varepsilon(t, \Theta^*) = y(t) - \hat{y}(t, \Theta^*)}. \quad (3.39)$$

##### Correlation between errors and input variables

Linear models, which are assumed for the following, are generally a great simplification of a real process or plant. An analysis of the residuals as a function of a specific input

### 3.3. Model performance and stability

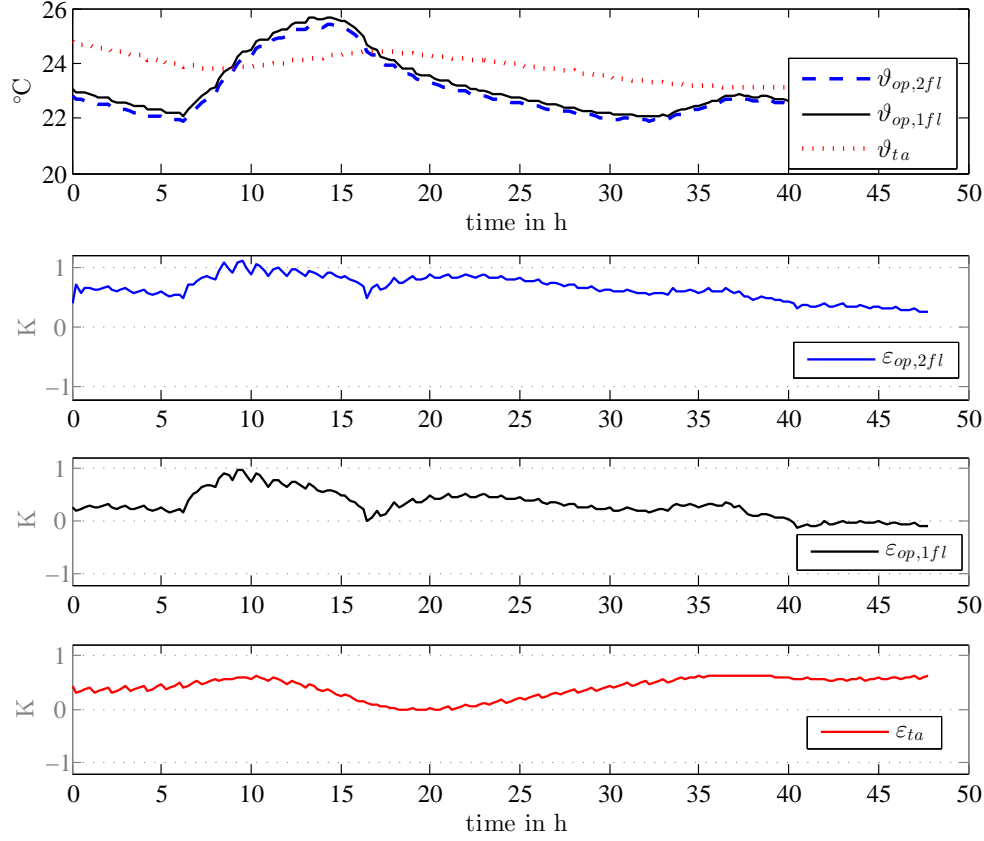


Figure 3.4.: Residuals for  $\mathcal{M}^{n4w}(\Theta_{wm}^a)$  validated with  $\mathcal{D}_{wm}$  for a typical prediction horizon of 48 h. More details on the TheBat TABS-MPC model are provided in sec. 4.3.3.

variable  $u \in \{\hat{q}_{ta2fl}, \hat{q}_{ta1fl}, \vartheta_{oa}, \dots\}$  is viable to explain increased residuals due to non-linear effects such as saturation, which would appear as an increasing residual for increasing input. Hence, it is reasonable to define an affine function to show possible correlations between a residual and a selected input variable  $u$ :

$$\hat{\varepsilon}(u) = a + b u \quad \text{and } a, b \text{ follow from a linear fit.} \quad (3.40)$$

The parameter  $a$  indicates the shift value wrt the origin and  $b$  gives the linear correlation. Residual-input correlations are given e.g. in the residual scatter plots for an MPC-Boxes model in fig. 4.2. The numbers in gray background provide information on the affine correlation according to eq. (3.40), except for the histograms where the numbers describe the bias and the empirical standard deviation of the residuals, see eq. (3.43). Appendix G includes residual scatter plots along with the residual histograms for a TheBat TABS-MPC model. For example fig. G.21 provides scatter plots where the residuals for TABS- and operative temperature are shown as a function of the various inputs.

### 3. System identification and modeling

Ideally, the histograms of the model residuals, especially for the self-validation, are all normally distributed – for the distinction between *self- and cross-validation* see sec. 3.4.3. Self-validation results with high bias and residual distributions far away from a bell-shaped curve indicate either a weakness of the model structure or a systematic problem in the estimation procedure (bad initial parameter, inappropriate constraints, etc.). A high linear correlation for a specific input according to eq. (3.40) may be an indicator where to start with the model redesign. In addition to structural redesign a suitable whitening-filter or noise model might improve the model if a residual distribution is far from a bell-shaped curve. The histograms are especially helpful for the cross-validation of a model in order to decide on the universality and applicability under different conditions.

#### Various mean error measures

The mean absolute error (MAE) for a model output is then defined as

$$MAE(\varepsilon) := \frac{1}{N} \sum_{t=1}^N |\varepsilon(t, \Theta^*)|. \quad (3.41)$$

Similarly the root mean square error (RMSE) of a model output is defined as

$$RMSE(\varepsilon) := \sqrt{\frac{1}{N} \sum_{t=1}^N \varepsilon(t, \Theta^*)^2}. \quad (3.42)$$

The RMSE is a progressive measure where single outliers become more relevant in the final result as compared to the MAE. In the given context the MAE is a suitable measure within the comfort range, but once this range is violated the RMSE is more appropriate, see OENORM (OENORM EN ISO 7730:2006), Herrmann et al. (1994) and Pichler et al. (2014). This is due to the adaptability within a range close to the so called physiological zero – a condition where neither warm nor cold is experienced.

#### Bias and spread of the physical errors (residuals)

The bias, which is simply the *time average* value of  $\varepsilon$  ( $\bar{\varepsilon}$ ), measures the systematic error and the empirical standard deviation  $s$  indicates the spread of the model error

$$s(\varepsilon) := \sqrt{\frac{1}{N-1} \sum_{t=1}^N (\varepsilon(t, \Theta^*) - \bar{\varepsilon})^2}, \quad \text{with} \quad \bar{\varepsilon} = \frac{1}{N} \sum_{t=1}^N \varepsilon(t). \quad (3.43)$$

Another indication for the spread of the model errors is provided by the maximum absolute error, expressed as maximum norm which identifies the worst case:

$$\|\mathcal{E}_N\|_{\infty} := \max(|\varepsilon(1)|, |\varepsilon(2)|, \dots, |\varepsilon(N)|). \quad (3.44)$$

As practiced in the last equation the dependence of  $\varepsilon$  on the model  $\Theta^*$  is, if not really relevant, often neglected for simplicity.

The strength of these physical measures is their close to reality property and the detailed information. Assume  $y := \vartheta$ , then the introduced measures MAE, RMSE describe an average temperature deviation from experimental data. Considering the MIMO case – a model with more than one output – it is desirable to have one performance measure for the model in addition to these physical measures for each output. Hence, an alternative to the physical quality measures is required.

Ideally, the performance of a model  $\mathcal{M}(\Theta^*)$  is expressed by a single quantity. In principal the physical measures may be extended to incorporate the evaluation of all output residuals, but since the physical meaning of such a measure is limited this approach is skipped in favor of an abstract quantity referred to as *model fitness* or *fit*.

#### 3.3.2. Model fitness value

The likeness of experimental data  $y(t)$ , and model-generated data  $\hat{y}(t)$  is expressed by the model fitness value. In this section a few suitable measures are defined and discussed with occasional reference to thermal models for heating and cooling purposes. The strength of the fitness value – in the sequel abbreviated as *fit* – is the characterization of the model performance in terms of a single value. The weakness of the fit is its abstract nature and loss of insight into individual performance measures if given as an average value for multiple output models.

#### Relative errors

The following two fit measures are defined using the MAE (eq. (3.41)), however, it may be replaced by the RMSE ((3.42)), which leads to more impact of large- and less influence of small residuals; for a mathematically profound definition see Appendix G.2.

$$fit_{MAE,H} := \left( 1 - \frac{\sum_{t=1}^N |\varepsilon(t)|}{\sum_{t=1}^N |y(t)|} \right) 100\% \quad (3.45)$$

$$fit_{MAE,L} := \left( 1 - \frac{1}{N} \sum_{t=1}^N \left| \frac{\varepsilon(t)}{y(t)} \right| \right) 100\% = \left( 1 - MAE \left( \frac{\varepsilon}{y} \right) \right) 100\% \quad (3.46)$$

The second term within the parenthesis of eq. (3.45) and eq. (3.46) represents always a relative error, which must be smaller than one for the definition to make sense. The quantity  $fit_{MAE,H}$  is calculated using one common denominator to be applied to the sum over all residuals, that is, each error is weighted with the same value to obtain an average relative error. By contrast, for the calculation of  $fit_{MAE,L}$  individual weighting is applied to obtain the relative errors which are consequently averaged. This individual weighting results in a higher average relative error, thus  $fit_{MAE,L} < fit_{MAE,H}$ .<sup>7</sup>

<sup>7</sup> The proof is straightforward by induction.

### 3. System identification and modeling

In the given context with models showing integral behavior and relatively high output mean values (close to the comfort temperature 20°C ) this simple relative error based fits are *too insensitive to be used*.

#### Relative variation errors

A simple extension to the relative error is the relative variation error, which are not calculated with respect to the whole experimental data level  $y$ , but with respect to the mean free value  $(y(t) - \bar{y})$  – this is the variation of  $y$  around its time average or simply the alternating part of  $y$ . Using the RMSE instead of the MAE and the variation of  $y$  in the denominator, eq. (3.46) may be modified to obtain

$$fit_{RMSE}^{var} = \left( 1 - \frac{1}{N} \sum_{t=1}^N \frac{\sqrt{\varepsilon(t)^2}}{\sqrt{(y(t) - \bar{y})^2}} \right) 100\%, \quad (3.47)$$

which is often found in literature, e.g. (Ljung, 1999), (Ljung, 2013). Extended to the multiple output case with  $\varepsilon$  being a vector one gets

$$fit_{RMSE}^{var} = \left( 1 - \frac{1}{N} \sum_{t=1}^N \frac{\|\varepsilon(t)\|_2}{\|\mathbf{y}(t) - \bar{\mathbf{y}}\|_2} \right) 100\%. \quad (3.48)$$

By contrast to the relative error from eq. (3.45) and (3.46) this relative error is very sensitive – sometimes too sensitive<sup>8</sup>.

Given the context of thermal models for buildings one may question whether the mean free value of  $y$  is a suitable measure to calculate a relative error. A relatively constant output with few variation – which happens for the temperature of a thermal building mass – has a small denominator and hence is likely to give a huge relative error even for a small absolute error. In addition, the variation of  $y$  alone in the context of thermal buildings has no meaning, the relevant ability of the model extends beyond a proper alternating part of  $y$ . A pure analysis of the alternating part makes sense for non integral model behavior only, then offset de-trending would also be allowed, which is not the case for the models considered herein.

#### Relative variation errors based on the maximum norm

A sensible modification of eq. (3.47) is to use a common denominator, namely the maximum norm as defined in eq. (3.44)

$$fit_{RMSE}^{max(var)} = \left( 1 - \frac{1}{N} \sum_{t=1}^N \frac{\sqrt{\varepsilon(t)^2}}{\|Y_N - \bar{y}\|_\infty} \right) 100\%. \quad (3.49)$$

<sup>8</sup> Even the version with the fraction of two sums, as in eq. (3.45), is very sensitive.

### 3.3. Model performance and stability

This way the calculation of all relative residual errors is based on a common denominator<sup>9</sup>, which represents the maximum variation of  $y$  with respect to its time average.

In this work the fitness measure from eq. (3.50) is used if not stated otherwise. Although, the definition in eq. (3.49) provides a more suitable model fitness measure than the other definitions introduced so far it is not very sensitive. Therefore a weighted sum of the maximum norm and a further reference value for relative error calculation is introduced. This could either be the individual variation as in eq. (3.47) or a value with common character such as the *sample median*<sup>10</sup> of the absolute variation:

$$fit = \left( 1 - \frac{1}{N} \sum_{t=1}^N \frac{\sqrt{\varepsilon(t)^2}}{a \cdot median(|Y_N - \bar{y}|) + b \cdot \|Y_N - \bar{y}\|_{\infty}} \right) 100\%. \quad (3.50)$$

The weighting quantities ( $a$ ,  $b$ ) are chosen to be in the *golden ratio*, that is  $a = 0.318$  and  $b = 0.682$ . A model fitness measure for a multiple output system is based on averaging over the individual outputs fit according to eq. (3.50). Although, the fit measure includes  $N$ , the length of the data interval, it may strongly depend on the evaluation horizon, especially for models with integral character. Fig. 3.5 illustrates a good and a bad *fit* in terms of a TABS and an operative (room) temperature.

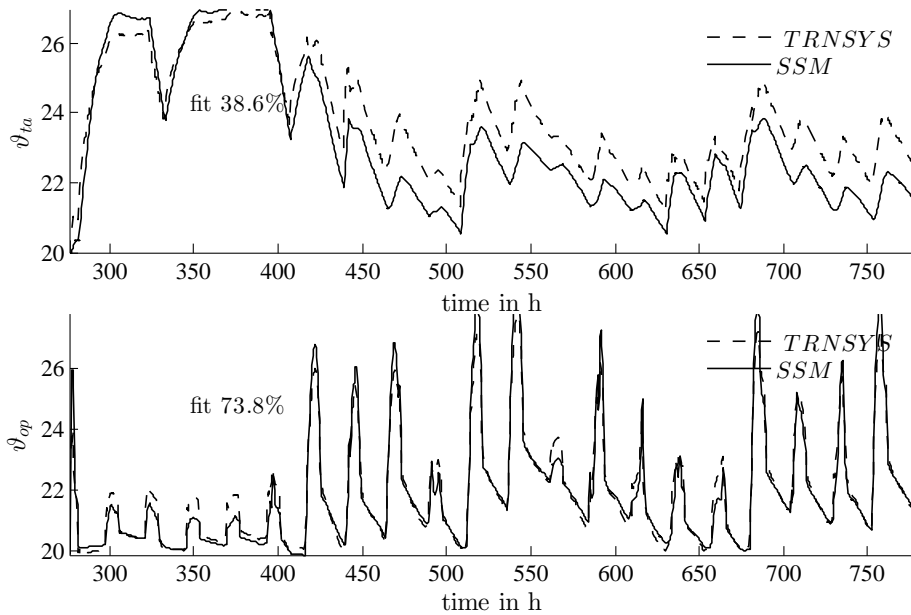


Figure 3.5.: Comparison of  $\vartheta_{ta}(t)$  and  $\vartheta_{op}(t)$  once generated with  $\mathcal{M}^{u3}$  and once with TRNSYS (dashed lines). Relatively bad agreement for  $\vartheta_{ta}(t)$ . The fit calculation was based on an interval of six weeks.

<sup>9</sup> The expression  $\|Y_N - \bar{y}\|_{\infty}$  is equivalent to  $\max(|y(1) - \bar{y}|, \dots, |y(N) - \bar{y}|)$ .

<sup>10</sup>The sample median is the middle value for a sorted set, e.g.  $median(1, 5, 3) \Leftrightarrow median(1, 3, 5) = 3$ , in case the number of elements is even it is the average of two values.

### 3. System identification and modeling

#### Evaluation interval

Another important aspect not mentioned so far is the length of the time series or the *evaluation interval*  $t = 1, 2, \dots, N$ . Assume a MPC with a prediction horizon of 72 h, and an assimilated initial model state based on experimental data. In this case the fit over the first 72 h is the most relevant. Now, if an evaluation interval is longer, i.e.  $N > 72$  h – to include a variety of excitations – and the model is only “suboptimal” for this long interval a bias ( $\bar{\epsilon}$  cf. eq. (3.43)) may rise. Given the “high” frequency part in the data is still represented sufficiently accurate, this bias contained in the residuals after 72 h leads to a bad fit result, although the first 72 h might be reproduced accurately enough. This insight underlines the importance of selecting a meaningful evaluation interval, and the relevance of the simple output- and residual trajectory analysis as shown in fig. 3.4. For further plots see Appendix G.4.1, fig. G.20 and fig. G.28.

### 3.4. Identification data and experiment design

This section deals with the generation and the selection of suitable data for model identification and model evaluation. Identification data (id-data) are used for the parameter estimation procedure, and validation data (valid-data) are used for the model evaluation. An evaluation may be conducted with the id-data itself (*self-validation*) or with a different set of data (*cross-validation*), more on this in 3.4.3. The keyword in context of data generation is *experiment design*. Insight from such an experiment often leads to a reformulation of e.g. the model structure. In the following the term measurement data is used for simulation data, when referring to real data it is explicitly noted.

In this thesis only *open loop identification* is discussed and only such experiments were conducted. This means, that the MPC for which the model is parametrized is not in operation for generation of the identification data (id-data); the plant operation is based on a simple rule based controller. The basics related to id-data generation derive from signal theory. The first question to answer relates to the time-constants or frequencies of interest. It is realistic to have some initial knowledge about the *smallest* relevant *time constant*  $\tau$  of the system of interest. Assume the smallest  $\tau$  is 1 h, then the famous *Nyquist-Shannon-Theorem* states that, in order to capture this frequency  $f_\tau$  the measured signal must be sampled with a frequency  $f_{\Delta ts}$  that is at least twice  $f_\tau$ :

$$f_{Nyquist} := 2 f_\tau \qquad f_{\Delta ts} > f_{Nyquist}. \qquad (3.51)$$

Given  $\Delta ts$  it is advisable to sample 10-times higher to allow for a good data quality even for occasional loss of data.

After specifying the signal sampling-time the question concerning the *lowest frequency* must be answered, and how many full periods  $\mathcal{T}$  of this frequency should be

### 3.4. Identification data and experiment design

contained in the id-data set. Relating to the predictive control task, it is reasonable to record over a time interval which is at least as long as the prediction horizon

$$\mathcal{T} \geq N_p \qquad N = \frac{\mathcal{T}}{\Delta t_s}. \qquad (3.52)$$

The longer  $\mathcal{T}$  the more information is potentially included in the id-data set. The natural number  $N$  in eq. (3.52) provides the length of the recorded data set in terms of the number of samples.

An *id-data* set of length  $N$  containing input and output data in the sense of fig. 3.3 and eq. (3.17) must be informative. This means, that the data provides enough system-characteristic information which must be learned or implemented by the model. The key to this are suitable input data which sufficiently excite the real system to estimate for example the parameter vector  $\Theta$  of a SSM as given in the box of fig. 3.3.

Data from real experiments are essential and desired, but simulation experiments are very helpful on the way to design a suitable model, which may be difficult based on real data only. In reality difficulties arise from sensor placement, noise, and other uncertainties typical for real environments. Simulation enables the generation of various id-data with sufficient *excitation* to drive the system in all relevant states.

#### 3.4.1. Properties of input and output data

The estimation of the model parameters  $\Theta$  requires a set of input ( $u$ ) and output ( $y$ ) measurement data with sufficient excitation. Input data are subdivided into manipulable input data – controlled heat-flux ( $\dot{q}_{ta}$ ) – and disturbance data such as weather data and internal gains ( $\vartheta_{oa}$ ,  $\dot{q}_{gs}$ ,  $\dot{q}_{gi}$ ). The origin of most of the disturbance data within this context does not allow for arbitrary chosen time series, although principally possible for simulation experiments; weather data are given by recorded data, because they can not be influenced in reality, and internal gains are assumed as (approximately) occurring in reality.

Input data i.e. a time series for  $\dot{q}_{ta}$  may be obtained via a hysteresis-controlled room-air temperature – the aim is to excite the system sufficiently. Concerning disturbance input data, the challenge is to select a suitable, informative time interval from the annual weather data, to be used as id-data. *Output data* are the TABS temperature and the room temperature ( $\vartheta_{ta}$ ,  $\vartheta_{ra}$ ). The higher the sensitivity of an output with respect to an input change the higher the chance to properly identify the relevant model parameters. Again, the excitation through the manipulable inputs and the selection of a *suitable interval* concerning disturbance inputs are the only levers in this matter.

### 3. System identification and modeling

#### Collinearity

Collinearity is an important and problematic aspect in experiment design and concerning modeling, it is explained by means of an example. Assume the first and the second floor of a single family house are heated by independently controlled TABS. Given the same  $\vartheta_{ra}$  set values, and thermal coupling through internal air exchange, naturally the actual temperatures will be very similar – this is collinearity. More strictly, collinearity refers to a linear relationship between two variables.

If independent controllers for the first and the second floor TABS exist, but demonstrate similar behavior for a certain heating interval, it is extremely difficult for an identification algorithm to discern whether the according room temperature increase (which is very likely similar in the first and the second floor) is due to heating in the first or in the second floor. This problem is encountered for the initial model  $\mathcal{M}^{n4}$  cf. fig. 4.10.

In system identification or regression the collinearity between two input or two output time series is problematic. Given two variables with strong positive or negative correlation coefficient it is sensible to exclude one of them from the id-data.

#### 3.4.2. Relevant temperature range – excitation

The relevant room temperature is approximately between 20 °C and 26 °C, see sec. 1.5. This temperature range and a dynamic typical for real operation should be included in any id-data set. The temperature range for the controlled variable ( $\vartheta_{ra}$ ) is met through an according control rule for a simple on/off controller switching the TABS operation on and off. The dynamic is met through applying real climate data.

On/off-thresholds of the  $\vartheta_{ra}$ -control are ideally such, to cover the whole relevant temperature range, however, this might cause very long heating up and floating intervals with few dynamic. On the one hand such an interval is likely to be relevant but on the other hand it requires long id-data intervals to capture also intervals with short heating and floating features. A compromise must be found, for id-data related to MPC-Boxes see tab. 4.5 or Pichler, Goertler, et al. (2016), for TheBat id-data see tab. 4.8.

The manipulated variable  $\dot{q}_{ta}$  may be adjusted through the flow temperature ( $\vartheta_{sw}$ ) and the mass flow rate ( $\dot{m}_{ta} = \text{const.}$  is assumed) given a certain return temperature. The lower bound of  $\vartheta_{sw}$  is determined by the dew point of the ambient temperature for an average cooling mode. According to the meteorological institute ZAMG the relative humidity (RH) barely increases 55% for  $\vartheta_{oa} \approx 30$  °C and 40% for  $\vartheta_{oa} \approx 35$  °C for the location Graz. Given a mean  $\vartheta_{oa}$  of 28 °C during cooling mode and  $\text{RH} \approx 55\%$  the lowest possible flow temperature is approximately 17 °C. The upper bound of the flow temperature is determined by the maximum heating load, the heat transfer coefficients

within the room, and the TABS design. This temperature is assumed not to increase 35 °C . In case  $\vartheta_{sw}(\vartheta_{oa})$  this should be taken into account also for the id-data.

#### 3.4.3. Model evaluation through self- and cross-validation

Data used for evaluation play an important role. Identification data (id-data) are data applied during the parameter estimation procedure, and validation data (valid-data) are data used for the model evaluation. A model evaluation may be conducted with the id-data itself (*self-validation*) or with a different set of data (*cross-validation*). Without detailed consideration one may think that the cross-validation performance is more important and more reliable than the self-validation performance.

However, both self- and cross-validation play an important role in an evaluation concept. Especially the self-validation is often underestimated. At an early stage of the system identification procedure the performance and the results obtained through self-validation should be given higher priority. This *self-validation* of a model with the *training data* is important to judge on the selected *model structure*, understand a good or bad choice of *initial parameters* and finally to see what can be expected for the cross-validation.

The successful *cross-validation* proves the versatility and robustness of a model and it plays an important role to judge on the overall performance of a model. It allows also to indirectly evaluate whether or not an id-data set includes a relevant range of excitations. Ideally, id-data include as much frequencies as possible with sufficient power, but the excitation is also practically restricted. The more similar a valid-data spectrum to the id-data spectrum the more likely the cross-validation results are similar to the self-validation results. Theoretically, the more similar the power spectrum of a valid-data and an id-data, the more likely a good performance for the cross-validation. Although, this comparison is theoretically possible, it might not be feasible in practice since the optimal spectrum is not available and hence, no reference exists.



## 4. Models for control purpose – system identification results

*This chapter summarizes and validates the final controller models, which are considered sufficiently accurate to be employed for a MPC scheme. These models were selected by means of extensive testing with respect to various criteria, most of which are represented in this chapter. The chapter starts with the most simple building model, followed by a 4th order building model employed in the project TheBat. The derivation of a non-linear TES-HP (thermal energy storage heat pump) model finishes the model-structure and -performance results presentation. Being familiar with the content of chapter 3 is advantageous when reading this chapter.*

### 4.1. MPC-Boxes linear building model

This section presents system identification results for the simple linear building model derived for the MPC-Boxes construction. The estimation of physical parameters for the model from first principles derived in sec. 3.1.1, has been investigated in a master thesis during the project MPC-Boxes, however, only a relatively narrow parameter range led to good results, see Gerstgrasser (2014). This, and the advantage of a simpler parameter estimation procedure in case of a S-SSM (structured state space model) led to the decision to use a S-SSM, which was already discussed in sec. 3.1.2.

The final model (structure) found, is selected by means of extensive testing. If a model structure performed badly in one test it was tried to improve the structure. The conducted tests comprise a detailed residual analysis, a versatility or robustness analysis by means of cross-validation and an inspection of the estimated parameters  $\Theta$  to mention only the most important. A few results obtained for models with significant weakness are documented in the Appendix G.4.2 – similar results are obtained when estimating the parameters with the least square approach (ARX-model) explained in sec 3.2.1.

The analysis on the most suitable model structure is based on simulation data. Finally, the best structure found is facilitated to estimate the parameters of the controller model by means of real measurement data.

## 4. Models for control purpose – system identification results

### 4.1.1. Final model structure and constraints

The final model structure is based on the SSM given in eq. (3.8) (but  $\mathbf{u}$  and  $\mathbf{u}_v$  combined to one vector) with the following state, input and output definitions

$$\mathbf{x} := [\vartheta_{ta}, \vartheta_{ra}, \vartheta_{fl}]^T, \quad \mathbf{u} := [\dot{q}_{ta}, \vartheta_{oa}, \dot{q}_{gs}, \dot{q}_{gi}, \dot{h}_{ven}, \vartheta_{grd}, \vartheta_{sky}]^T, \quad \mathbf{y} := \mathbf{x}.$$

With the possible parameter range instead of the numerical value (cf. tab. 4.1) for each matrix element, the final structure  $\mathcal{M}$  for the simple MPC-Boxes linear building model reads

$$\mathbf{A} = \begin{bmatrix} \mathbb{R} & \mathbb{R} & \mathbb{R} \\ \mathbb{R} & \mathbb{R} & \mathbb{R} \\ \mathbb{R} & \mathbb{R} & \mathbb{R} \end{bmatrix}, \quad \mathbf{B} = \begin{bmatrix} \mathbb{R}^+ & 0 & 0 & 0 & 0 & 0 & 0 \\ 0 & \mathbb{R}^+ & \mathbb{R}^+ & \mathbb{R}^+ & \mathbb{R}^+ & 0 & \mathbb{R}^+ \\ 0 & 0 & 0 & 0 & 0 & \mathbb{R}^+ & 0 \end{bmatrix}, \quad \mathbf{C} = \begin{bmatrix} 1 & 0 & 0 \\ 0 & 1 & 0 \\ 0 & 0 & 1 \end{bmatrix}. \quad (4.1)$$

As introduced in sec. 3.1.3 the  $\mathbf{A}$  and  $\mathbf{B}$  constituting values are summarized with  $\Theta$ . Precisely the model in eq. (4.1) is abbreviated as  $\mathcal{M}^{n3}(\Theta)$ , however, for the results analysis the MPC-Boxes building model is always *abbreviated as*  $\mathcal{M}(\Theta)$  or simply  $\mathcal{M}$ , to distinguish from any TheBat building model for which always some superscript is used ( $\mathcal{M}^{n4}$ ).

#### Interpretation of the constraints

The matrix  $\mathbf{A}$  which describes the thermal coupling between the three thermal nodes (TABS-, room air-, and floor-temperature, cf. 3.1) is considered unconstrained, although the estimated element values are finally checked in terms of physicality. With respect to  $\mathbf{A}$  *physicality* means, first, all diagonal elements having a negative sign and the rest being positive or close to zero for a weak coupling. In addition,  $\mathbf{A}$  is checked in terms of the *BIBO-stability*, that is, the real part of the eigenvalues must be negative, see Appendix B.1.3.

Concerning the input matrix, the parameter range for  $\mathbf{B}$  as indicated by eq. (4.1) represents a minimalist or the maximum constrained version. With *physicality* imposed on  $\mathbf{B}$  (only positive values are allowed, indicated by  $\mathbb{R}^+$ ) the most reliable model and the best performance is obtained. Variants with more relaxed constraints and input-coupling to more than one state are provided in the Appendix along with the according performance. Most investigated cases perform worse than the final model structure  $\mathcal{M}$  from eq. (4.1) and if the performance is similar the stringent single input coupling criteria for  $\mathbf{B}$  as in eq. (4.1) is preferred.

### 4.1.2. Parameter estimation and numerical results

Assume a time series  $i = 1, \dots, N$  of the output vector  $\mathbf{y}(i) = [\vartheta_{ta}, \vartheta_{ra}, \vartheta_{fl}]^T$  and similarly for all inputs  $\mathbf{u}(i)$  being available from simulation or a real experiment.

Elements of the dynamic matrix  $\mathbf{A}$  and the input matrix  $\mathbf{B}$  may be readily estimated using one of the methods described in sec. 3.2. The method actually used to obtain the parameters is a structured (S-SSM) gray box identification. The constraints on  $\mathbf{A}$  and  $\mathbf{B}$  are transferred to the discrete version of the S-SSM (by means of Euler). The discrete model is actually estimated using the command *ssest* cf. Ljung (2013) which facilitates a *pem*<sup>1</sup>. The

<sup>1</sup> The used method estimates the free elements of  $\mathbf{A}$ ,  $\mathbf{B}$  and the  $\mathbf{K}$  matrix of the so called innovations form:  $\dot{\mathbf{x}}(t) = \mathbf{A}\mathbf{x}(t) + \mathbf{B}\mathbf{u}(t) + \mathbf{K}\varepsilon(t)$ ,  $\mathbf{y}(t) = \mathbf{C}\mathbf{x}(t) + \varepsilon(t)$ , see Ljung (1999) p. 99.

detailed physical relations between the elements of a matrix as derived in sec. 3.1.1 are disregarded, the constraints are given only in terms of the restrictions of eq. (4.1), cf. with Pichler, Goertler, et al. (2016).

Tab. 4.1 lists the obtained parameter values transformed to the continuous time domain using the simple Euler approach, see Appendix eq. (B.7). The column  $\mathcal{M}(\Theta_{tf})$  refers to results from the simulation id-data set  $\mathcal{D}_{tf}$  also indicated by tf. All other columns concern the real experimental id-data set  $\mathcal{D}_{wcg}$ . These models differ in terms of the utilized sensor for the room temperature ( $\vartheta_{ra}$  versus  $\vartheta_{op}$ ) and concerning disturbances from the ventilation system. A graphical representation of the obtained parameter values from real measurement and simulation data is provided in the Appendix G.3. Interestingly, the elements of **A** estimated from *simulation data* are very similar for different id-data and the models differ mainly in the parametrization of **B**. For *real experimental data* also the elements of **A** differ from one data set to another. Finally, the maximum standard deviation of model parameters from real data is approximately an order of magnitude larger in comparison to the results from simulation data.

Table 4.1.: Estimated (time continuous) parameter values and uncertainties; MPC-Boxes; obtained with *ssest* command and LS (least square) initial model (options: DisturbanceModel: 'estimate', Focus: 'simulation', InitialState: 'backcast'), (Ljung, 2013). Elements without numerical value are zero.

data	$\mathcal{M}(\Theta_{tf})$ simulation <sup>a</sup>	$\mathcal{M}(\Theta_{wcg})$ real measurement	$\mathcal{M}(\Theta_{wcg})$ real measurement	$\mathcal{M}(\Theta_{wcg})$ real measurement
$\vartheta_{room}$	$\overline{\vartheta_{ra}}$	$\vartheta_{ra}$ at door <sup>b</sup>	$\vartheta_{op}$ at door	$\vartheta_{ra}$ at door
A(1,1)	-5.64e-02 ± 1e-03	-5.03e-02 ± 8e-04	-5.18e-02 ± 8e-04	-5.04e-02 ± 7e-04
A(1,2)	+3.39e-02 ± 1e-03	+3.09e-02 ± 2e-03	+3.10e-02 ± 2e-03	+3.13e-02 ± 2e-03
A(1,3)	+2.26e-02 ± 9e-04	+1.84e-02 ± 2e-03	+2.06e-02 ± 2e-03	+1.82e-02 ± 2e-03
A(2,1)	+6.53e-01 ± 3e-02	+8.47e-01 ± 5e-02	+6.31e-01 ± 3e-02	+7.97e-01 ± 4e-02
A(2,2)	-2.42e+00 ± 4e-02	-2.82e+00 ± 1e-01	-1.89e+00 ± 8e-02	-2.69e+00 ± 1e-01
A(2,3)	+1.64e+00 ± 4e-02	+1.81e+00 ± 9e-02	+1.11e+00 ± 5e-02	+1.74e+00 ± 7e-02
A(3,1)	-2.19e-03 ± 7e-04	+5.65e-04 ± 4e-04	-1.41e-03 ± 4e-04	+3.81e-04 ± 5e-04
A(3,2)	+5.68e-02 ± 1e-03	+4.05e-02 ± 2e-03	+4.34e-02 ± 1e-03	+4.03e-02 ± 2e-03
A(3,3)	-5.58e-02 ± 1e-03	-4.39e-02 ± 1e-03	-4.47e-02 ± 1e-03	-4.33e-02 ± 1e-03
B(1,1)	+7.03e-03 ± 1e-04	+7.41e-03 ± 6e-05	+7.45e-03 ± 6e-05	+7.42e-03 ± 6e-05
⋮	-	-	-	-
B(2,2)	+1.23e-01 ± 7e-03	+2.26e-01 ± 1e-02	+1.42e-01 ± 7e-03	+2.11e-01 ± 1e-02
B(2,3)	+4.78e-02 ± 1e-03	+6.10e-02 ± 3e-03	+4.19e-02 ± 2e-03	+5.65e-02 ± 2e-03
B(2,4)	+1.84e-01 ± 3e-03	+1.52e-01 ± 8e-03	+1.03e-01 ± 4e-03	+1.41e-01 ± 6e-03
B(2,5)	-	-	-	+4.01e+00 ± 2e-01
B(2,6)	-	-	-	-
B(2,7)	-4.44e-16 ± 3e-03	-1.33e-15 ± 5e-03	+2.79e-03 ± 2e-03	-1.33e-15 ± 4e-03
⋮	-	-	-	-
B(3,6)	+7.22e-04 ± 9e-05	+2.43e-03 ± 3e-04	+3.87e-03 ± 3e-04	+2.20e-03 ± 3e-04
B(3,7)	-	-	-	-

<sup>a</sup> with initial building model based on catalog material properties.

<sup>b</sup> "at door" specifies the exact (room temperature) sensor position; the other sensor is close to the south facing window.

<sup>c</sup> The model argument indicates the parametrization, e.g. in  $\mathcal{M}(\Theta_{wcg})$   $\Theta_{wcg}$  indicates that the parameters were obtained with the id-data abbreviated as *wcg*, cf. tab. 4.5.

#### 4. Models for control purpose – system identification results

The first, the second and the fourth column of tab. 4.1 are reproduced again in the eq. (4.3) - (4.7) in matrix form.

$$\mathbf{A}(\Theta_{tf}) = \begin{bmatrix} -0.056 & 0.034 & 0.023 \\ 0.65 & -2.4 & 1.64 \\ -0.0022 & 0.057 & -0.056 \end{bmatrix}, \quad (4.2)$$

$$\mathbf{B}(\Theta_{tf}) = \begin{bmatrix} 0.0070 & 0 & 0 & 0 & 0 & 0 & 0 \\ 0 & 0.12 & 0.048 & 0.18 & 0 & 0 & -4.4e - 16 \\ 0 & 0 & 0 & 0 & 0 & 0.00072 & 0 \end{bmatrix}. \quad (4.3)$$

$$\mathbf{A}(\Theta_{wcg}) = \begin{bmatrix} -0.050 & 0.031 & 0.018 \\ 0.85 & -2.8 & 1.8 \\ -0.00057 & 0.041 & -0.044 \end{bmatrix}, \quad (4.4)$$

$$\mathbf{B}(\Theta_{wcg}) = \begin{bmatrix} 0.0074 & 0 & 0 & 0 & 0 & 0 & 0 \\ 0 & 0.226 & 0.061 & 0.15 & 0 & 0 & -1.33e - 15 \\ 0 & 0 & 0 & 0 & 0 & 0.00243 & 0 \end{bmatrix}. \quad (4.5)$$

$$\mathbf{A}(\Theta_{wcg}) = \begin{bmatrix} -0.050 & 0.031 & 0.018 \\ 0.80 & -2.69 & 1.74 \\ 0.00038 & 0.040 & -0.043 \end{bmatrix}, \quad (4.6)$$

$$\mathbf{B}(\Theta_{wcg}) = \begin{bmatrix} 0.0074 & 0 & 0 & 0 & 0 & 0 & 0 \\ 0 & 0.21 & 0.057 & 0.14 & 4.01 & 0 & -1.33e - 15 \\ 0 & 0 & 0 & 0 & 0 & 0.0022 & 0 \end{bmatrix}. \quad (4.7)$$

Consulting the physical model from first principles meaningful physical properties may be assigned to specific variables based on the estimated parameters, compare with sec. 3.1.2. The estimated parameter value  $B(2,5)$ , describing the ventilation coupling for  $u(5) = \dot{H}(\dot{V} = 1 \text{ m}^3/h)/A_{ta}$  cf. tab. 3.1 and eq. (3.6), may be used to derive the actually identified ventilation  $\dot{V}_{ven} = n_{ven} \cdot V_{room}$ . Assuming  $\hat{\gamma}_{gi} = 1$  for the model from first principles one can see that  $\dot{V}_{ven}$  may be derived from the identified parameters  $B(2,4)$ , which gives  $c_{ra} \hat{\beta}_{ra}$ , and  $B(2,5)$ . With the values from the fourth column of tab. 4.1 one gets  $\dot{V}_{ven} \approx 20 \text{ m}^3/h$  or  $n_{ven} \approx 0.64/h$ . The required heating power to precondition the ventilation air is simply added to the internal gains input. Comparing the model output trajectories for the model with ventilation input  $u(5) \neq 0$  against those for which this input was neglected, one can see that the results became partly better but also partly worse. However, in case the preheating of the ventilation air is not adjusted to the current room air temperature the model with ventilation input  $\dot{h}_{ven}$ , is certainly a better choice than the other without.

## 4.1.3. Model performance and error analysis – based on simulation data

Fig. 4.1 illustrates the overall model performance for the structure  $\mathcal{M}$  in eq. (4.1) by means of the total height of a vertical bar (subdivided into three sections) – indicating the average model fit. The subdivision into three color coded sections is a measure for the fit with respect to the assigned output based on the definition of eq. (3.50). The bottom section indicates the fit of the air temperature ( $\vartheta_{ra}$ ) – the most important output variable. In case one color is missing the fit with respect to the related output is bad and the whole graphical representation contains limited information. However, this does not necessarily mean that the model is useless at all – in such case a detailed analysis of the residual for the individual outputs is required. The *parameter estimation* is conducted for six different id-data sets: winter cold (wc), winter moderate (wm), transition spring (ts), summer hot (sh), summer moderate (sm) and transition fall (tf); and the obtained models are sub-scripted with the id-data acronym. *The first group of six parallel bars above the label wc represents the fit values obtained with the model  $\mathcal{M}(\Theta_{wc})$  when tested with data wc, wm, ts, sh, sm, tf.* Obviously it is very likely that the best average model fit is obtained for the id-data itself, that is for the self-validation with the data wc (very first bar). The other bars of this group refer to cross-validation results with the data wm, ..., tf. For the model  $\mathcal{M}(\Theta_{wm})$  the second bar indicates the self-validation fit results and all other bars represent cross-validation results. Similarly for all remaining models. *The dash-dotted horizontal lines give the average model fit (over all validation data) with respect to the variable  $\vartheta_{ra}$  – the most important variable; e.g a perfect fit for a specific variable is represented by 33.3 %, hence, approximately 30 % as for the model identified with the data tf represent an excellent fit with respect to the considered variable.*

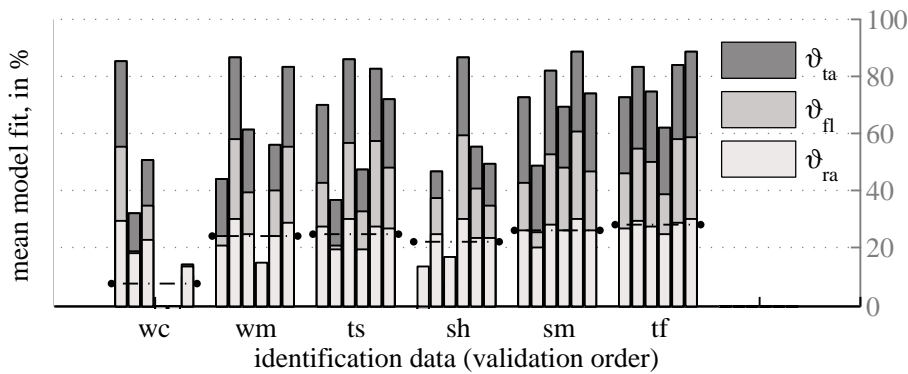


Figure 4.1.: Average model fits from simulation data, obtained for the MPC-Boxes model defined by eq. (4.1); method *ssest*,  $\Delta t_s = 0.25$  h, id-data interval 6 weeks, cf. tab 4.2.

A more detailed inspection represents a residual analysis such as demonstrated by fig. 4.2. The residual histograms of all model outputs ( $\vartheta_{ta}$ ,  $\vartheta_{ra}$  and  $\vartheta_{fi}$ ) demonstrate a close to normal distribution, which is a good sign concerning the model structure. Results for an *ill-structured model* are discussed and presented in Appendix G.4.2. The relatively nice residual (noise) distribution for the self-validation in fig. 4.2 is not

#### 4. Models for control purpose – system identification results

necessarily ensured for a cross-validation. An analysis with  $\mathcal{D}_{sh}$  (the id-data sh), which leads to moderate fit results in fig. 4.1 (the fourth bar in each group of six bars), shows still reasonable residual distributions, see histograms in fig. 4.3. However, all residuals develop a negative bias ranging from  $-0.33$  to  $-0.22$ , which is very likely caused by the ground temperature input variable<sup>2</sup>.

Table 4.2.: Characterization of MPC-Boxes simulation id- and valid-data ; Excitation realized with an on-off controller thresholds: heating  $20\text{ }^{\circ}\text{C}$  and  $24\text{ }^{\circ}\text{C}$ , cooling  $25.5\text{ }^{\circ}\text{C}$  and  $23.5\text{ }^{\circ}\text{C}$ ;  $\dot{q}_{ta}$  is evaluated for  $\dot{q}_{ta} \neq 0$  only, temperatures are in  $^{\circ}\text{C}$ .

data ( $\mathcal{D}^P$ ) $\rightarrow$	wc	wm	ts	sh	sm	tf
Start in h	606	7248	1698	4698	3246	6348
P in h	1008	1008	1008	1008	1008	1008
"inputs":						
$\bar{q}_{ta}$ , $\text{W}/\text{m}^2$	18	18	6	-15	-10	2
$\dot{q}_{ta}$ , $\text{W}/\text{m}^2$	$68 \pm 18$	$63 \pm 12$	$48 \pm 28$	$-60 \pm 9$	$-55 \pm 12$	$15 \pm 46$
$\vartheta_{oa}$	$3 \pm 6$	$4 \pm 5$	$8 \pm 5$	$21 \pm 5$	$18 \pm 5$	$11 \pm 5$
$\dot{q}_{gs}$ , $\text{W}/\text{m}^2$	$18 \pm 34$	$12 \pm 30$	$20 \pm 33$	$19 \pm 28$	$19 \pm 25$	$20 \pm 37$
$\dot{q}_{gi}$ , $\text{W}/\text{m}^2$	$7 \pm 10$	$7 \pm 10$				
$\vartheta_{grd}$	$2 \pm 1$	$4 \pm 2$	$8 \pm 2$	$20 \pm 1$	$19 \pm 1$	$11 \pm 2$
$\vartheta_{sky}$	$-6 \pm 9$	$-4 \pm 8$	$-0 \pm 7$	$14 \pm 5$	$11 \pm 5$	$2 \pm 8$
"outputs":						
$\vartheta_{ta}$	$24 \pm 1$	$24 \pm 1$	$23 \pm 1$	$22 \pm 1$	$22 \pm 1$	$23 \pm 1$
$\vartheta_{ra}$	$22 \pm 2$	$22 \pm 2$	$22 \pm 2$	$24 \pm 1$	$23 \pm 1$	$23 \pm 2$
$\vartheta_{fl}$	$22 \pm 1$	$21 \pm 1$	$22 \pm 1$	$24 \pm 0$	$23 \pm 0$	$22 \pm 1$

The influence of the  $\vartheta_{grd}$ -input is difficult to capture because a full period of  $\vartheta_{grd}$  lasts one year, that is any shorter data set will contain only a fraction of the whole period. This lack of dynamic in the input has an adverse effect on the robustness of the estimated parameter for another operating range.

Due to the integral character of the model and due to the relatively long interval of six weeks (cf. tab. 4.2), uncertainties (in the beginning) or minor deviations for input coupling may result in larger errors as the time proceeds see e.g. residuals in fig. 4.8 (cf. also Appendix G.4.1). However, the MPC relevant accuracy or MPC relevant fit (MRfit<sup>3</sup>) may still be good enough. That is, the short prediction horizon and the repeated alignment of the model with current measurements during MPC-operation allow to neglect a slowly developing bias (see also residuals for sh in fig. G.3 in Appendix).

Trajectories of the residuals for the best ( $\mathcal{M}(\Theta_{tf})$ ) and the worst ( $\mathcal{M}(\Theta_{wc})$ ) model according to fig. 4.1 are shown in fig. G.4 and fig. G.5 in Appendix. The residuals during the first 72 h for  $\mathcal{M}(\Theta_{wc})$  drawn in fig. G.3 put the results from fig. 4.1 in perspective. The conclusion is, that even the least parametrization may be suitable as controller model.

<sup>2</sup> The reason for a bias may be found in a potential correlation between a certain input value and the residuals.

<sup>3</sup> This measure is defined based on an evaluation interval starting at the beginning of the data and lasting as long as the maximum prediction horizon (72 h).

#### 4.1. MPC-Boxes linear building model

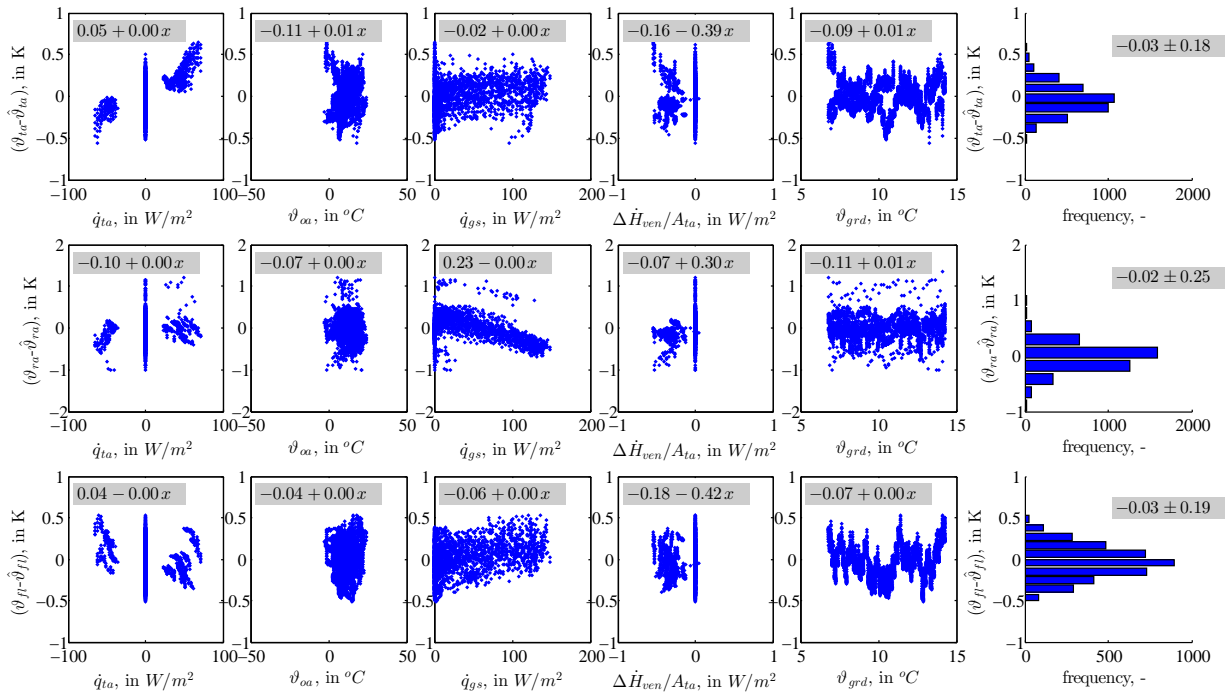


Figure 4.2.: Residual scatter-plots over relevant input variables and residual histograms for TABS-, air- and floor-temperature; S-SSM from eq. (4.1),  $\mathcal{M}(\Theta_{tf})$  self-validated against  $\mathcal{D}_{tf}$  over six weeks; numbers in gray background represent the residual as a function of the respective input variable for scatter plots ( $x$ ), cf. eq. (3.40), or the bias and the standard deviation for the histograms.

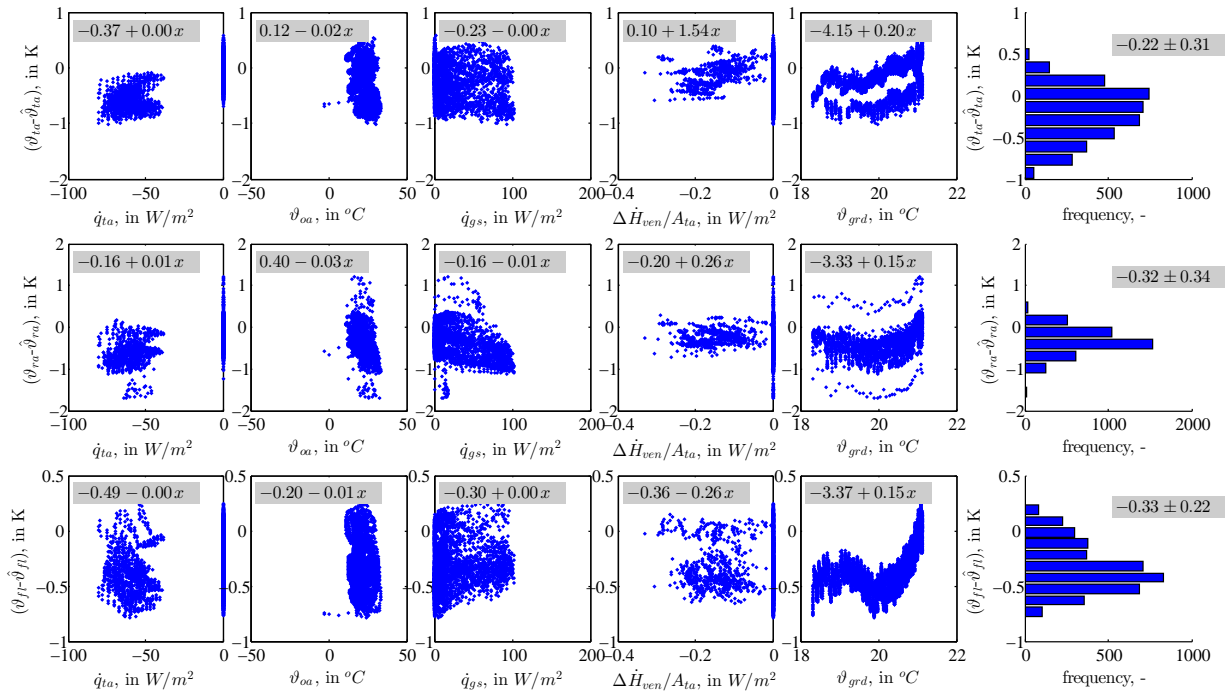


Figure 4.3.: Same as fig. 4.2 but now cross-validated against  $\mathcal{D}_{shl}$  over six weeks; numbers in gray background represent the residual as a function of the respective input variable for scatter plots ( $x$ ), cf. eq. (3.40), or the bias and the standard deviation for the histograms.

## 4.2. MPC-Boxes controller model based on real measurements

For the best structure found by means of simulations – see sec. 4.1 and eq. (4.1) – real measurement data are employed to identify the real controller model. In a first stage, id-data with internal gains being zero are used. Finally, the model parameters are estimated with excitation on all inputs.

### 4.2.1. Models from real measurement data with $\dot{q}_{gi} = 0$

The following analysis assumes internal gains being zero for all data, although this was not the case in reality. Table 4.3 characterizes the employed measurement data intervals. There are a few aspects to notice in these data. First, the interval length of the data sets is different ( $P$ ), and second, a dynamic external shading operation (1 :=closed, 0 :=open), is not included in all data. Finally, the disturbance from the ventilation is prevalent in the data but not modeled<sup>4</sup>. These data were generated with an on–off controller (20 °C , 24 °C ) for a mean room temperature.

The original data are recorded with a sampling interval of 1 or 2 min. Consequently, these data are post-processed applying the *median* over an interval of 10 min. The time spacing of these post-processed data is treated as 10 min<sup>5</sup>. For the parameter estimation procedure the id-data are linearly re-sampled depending on the desired model sampling time – finally  $\Delta t_s = 15$  min.

Table 4.3.: Characterization of real experimental data sets from MPC-Boxes; heating season with  $\dot{q}_{gi} = 0$ . Excitation is realized with an on–off controller (20 °C , 24 °C ) for a mean room temperature. The variables  $\dot{q}_{ta}$ ,  $\vartheta_{sw}$ ,  $\vartheta_{ret}$  and  $\dot{m}_{ta}$  are evaluated for  $\dot{m}_{ta} \neq 0$  only, temperatures are in °C .

data ( $D^P$ ) →	wc1	wc2	wc	wc1s	wc2s	wcs
P in h	384	240	672	72	72	72
shading <sup>a</sup>	1	0	1/0	1	0	1/0
"inputs":						
$\dot{q}_{ta}$ , W/m <sup>2</sup>	66 ± 18	84 ± 22	70 ± 21	73 ± 14	91 ± 32	71 ± 31
$\vartheta_{sw}$ (TABS)	34 ± 1	33 ± 2	34 ± 2	35 ± 2	32 ± 3	34 ± 3
$\vartheta_{ret}$ (TABS)	29 ± 2	28 ± 2	29 ± 2	30 ± 2	26 ± 2	29 ± 3
$\dot{m}_{ta}$ , kg/(h m <sup>2</sup> )	12 ± 1	13 ± 2	13 ± 1	13 ± 1	14 ± 2	13 ± 2
$\vartheta_{oa}$	1 ± 5	3 ± 4	2 ± 5	−5 ± 3	2 ± 2	2 ± 3
$\dot{q}_{gs}$ , W/m <sup>2</sup>	2 ± 4	16 ± 36	8 ± 24	2 ± 4	25 ± 46	21 ± 43
$\vartheta_{grad}$	12 ± 0	11 ± 0	11 ± 1	11 ± 0	11 ± 0	11 ± 0
$\vartheta_{sky}$	−11 ± 8	−6 ± 7	−9 ± 8	−17 ± 10	−11 ± 5	−11 ± 4
"outputs":						
$\vartheta_{ta}$	27 ± 2	26 ± 2	27 ± 2	28 ± 3	24 ± 1	26 ± 3
$\vartheta_{ra}$	21 ± 1	22 ± 3	22 ± 2	21 ± 1	22 ± 4	22 ± 3
$\vartheta_{fl}$	21 ± 0	21 ± 0	21 ± 0	21 ± 0	21 ± 0	21 ± 0

<sup>a</sup>) 1 means entirely closed = attenuation of  $\dot{q}_{gs}$  by 90%, compare with ESSO (2009).

Fig. 4.4 demonstrates the model performance for three relatively long and three relatively short id-data intervals. For all id-data the *operative room-temperature*<sup>6</sup> close to

<sup>4</sup> This has no particular adverse effect because the inlet air is heated to room-air conditions.

<sup>5</sup> In reality it may range from minimum 2 min to maximum 20 min in the worst case.

<sup>6</sup> This temperature is obtained with a globe thermometer.

## 4.2. MPC-Boxes controller model based on real measurements

the entrance door of the MPC-Box ( $\vartheta_{op-door}$ ) was used instead of the pure room air temperature (cf. fig. 4.5, 4.6, 4.2.4). At first sight the overall fit performance appears poor, however, one must take into account that data wc1 (winter cold 1), wc2 (winter cold 2), wc1s (winter cold 1 short) and wc2s (winter cold 2 short) do not include to whole operational range for the shading. Data including the whole range – wc (winter cold) and wcs (winter cold short)– perform well.

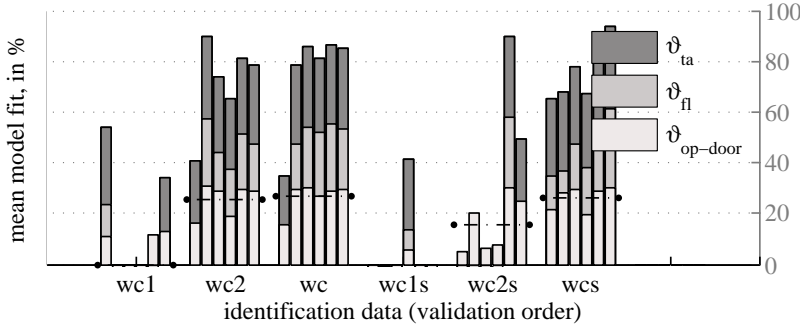


Figure 4.4.: Fit results from real experiment with  $\dot{q}_{gi} = 0$ , for  $\mathcal{M}$  with  $\Theta$  obtained from id-data wc1, wc2, wc where  $P = 240-672$  h and wc1s, wc2s, wcs where  $P = 72$  h.

Model parameters ( $\Theta$ ) corresponding to the results in fig 4.4 and a residual analysis for  $\mathcal{M}(\Theta_{wcs})$  are provided in Appendix G.5 .

### 4.2.2. Models from real measurement data with full excitation

Tab. 4.5 lists the temperature and heat flux ranges of the data employed for the estimation of  $\Theta^*$  – the “best” and final parametrization for  $\mathcal{M}$  according to eq. (4.1). The columns wc and wc2s refer to the same data as in tab. 4.3.

An analysis of the fit results in fig. 4.5 shows, that the model  $\mathcal{M}(\Theta_{wcg})$  performs best – for a quantitative residual analysis see tab. 4.4, for a graphical representation of the first 72 h see fig. G.17 in Appendix. Very likely the strength of this model is due to the long id-data interval along with the diverse excitation. In general the excitation of an id-data increases with the interval length – but not necessarily. However, an inspection of the residuals from validation of  $\mathcal{M}(\Theta_{wcgs})$  (where  $P(wcgs) = 72$  h only) shows, that  $\varepsilon$  for  $\vartheta_{ra}$  barely goes beyond  $\pm 2$  K in the first 48 h – see fig. G.18 in Appendix.

Table 4.4.: Cross- and self-validation analysis in terms of the model output residuals for  $\mathcal{M}(\Theta_{wcg})$ .

valid-data	$\vartheta_{ta}$ , in K residual $\pm s$	$\vartheta_{ra}$ , in K residual $\pm s$	$\vartheta_{fl}$ , in K residual $\pm s$
wcg1	$-0.03 \pm 0.09$	$0.05 \pm 0.23$	$0.01 \pm 0.12$
wcg2	$-0.34 \pm 0.27$	$-0.25 \pm 0.36$	$-0.15 \pm 0.14$
wcg	$0.02 \pm 0.13$	$0.02 \pm 0.23$	$0.01 \pm 0.12$
wc	$0.05 \pm 0.11$	$0.02 \pm 0.22$	$0.02 \pm 0.12$
wc2s	$0.01 \pm 0.09$	$0.12 \pm 0.34$	$0.01 \pm 0.09$
wcgs	$-0.39 \pm 0.22$	$-0.26 \pm 0.44$	$-0.1 \pm 0.13$
$\max( y )$	$0.39 \pm 0.27$	$0.26 \pm 0.44$	$0.15 \pm 0.14$

#### 4. Models for control purpose – system identification results

Models trained with the id-data  $wcg_1$  (winter cold gains 1),  $wcg_2$  (winter cold gains 2),  $wc_2s$  (winter cold 2) and  $wcgs$  (winter cold gains short) fail in terms of the fit-performance. One reason might be that e.g. data  $wc$  (winter cold) contain features which were not “learned” during the parameter estimation. A feature which is certainly not included in any of the id-data  $wcg_1$ ,  $wcg_2$ ,  $wc_2s$  and  $wcgs$  is the dynamic shading operation. However, since the shading operation is implemented directly through attenuation of the radiation itself, it would be surprising if the weakness came only from this data feature.

A weak performance of the models  $\mathcal{M}(\Theta_{wc})$  and  $\mathcal{M}(\Theta_{wc_2s})$  – not trained for internal gains – when cross-validated with the other data sets is not surprising.

##### 4.2.3. Investigation on the importance of selected disturbance variables

The influence of the disturbance inputs  $\vartheta_{sky}$  and  $\vartheta_{grd}$  on the overall model performance is discussed in the following. In general it is sensible to consider all available input variables. However, the parameter estimation problem becomes more complex with increasing number of inputs, and selected input variables must show enough dynamic within the selected identification interval to positively contribute to the model performance.

Hence, if a set of relevant input variables is selected, the question whether or not to include an additional variable depends on the according influence on the model performance. The variables  $\vartheta_{oa}$ ,  $\dot{q}_{gs}$ ,  $\dot{q}_{gi}$ , that is, the ambient temperature, solar- and internal gains are considered being essential variables. In practice, the estimation of  $\dot{q}_{gi}$  might be difficult, but there is promising research on human-building interaction, e.g. Langevin et al. (2015) under way.

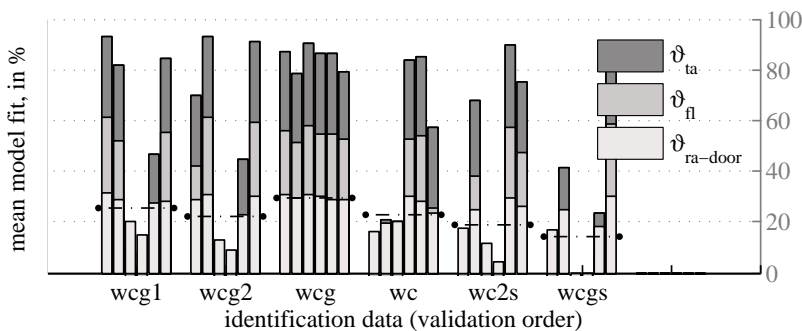


Figure 4.5.: Fit results from real experiment id-data ( $\Delta t_s = 0.25$  h) for  $\mathcal{M}$ .

The relevance of the input variables  $\vartheta_{grd}$  and  $\vartheta_{sky}$  may be questioned. Fig. 4.5 shows fit results obtained from six different id-data sets when validated against each other. The according results are now generated again once with  $\vartheta_{sky}$  being neglected and once with  $\vartheta_{grd}$  and  $\vartheta_{sky}$  being neglected.

## 4.2. MPC-Boxes controller model based on real measurements

Table 4.5.: Characterization of real experimental data sets from MPC-Boxes; Excitation during the heating season, realized with an on-off controller maintaining the mean air temperature between 20 °C and 24 °C. The variables  $\dot{q}_{ta}$ ,  $\vartheta_{sw}$ ,  $\vartheta_{ret}$  and  $\dot{m}_{ta}$  are evaluated for  $\dot{m}_{ta} \neq 0$  only, temperatures are in °C.

data ( $D^P$ ) →	wcg1	wcg2	wcg	wc	wc2s	wcgs
P in h	168	168	1008	672	72	72
shading <sup>a</sup>	0	0	0/1	0/1	0	0
"inputs":						
$\dot{q}_{ta}$ , W/m <sup>2</sup>	94 ± 22	90 ± 22	75 ± 23	70 ± 21	91 ± 32	90 ± 25
$\vartheta_{sw}$ (TABS)	32 ± 2	33 ± 2	33 ± 2	34 ± 2	32 ± 3	33 ± 2
$\vartheta_{ret}$ (TABS)	26 ± 2	27 ± 2	28 ± 2	29 ± 2	26 ± 2	27 ± 2
$\dot{m}_{ta}$ , kg/(h m <sup>2</sup> )	14 ± 3	13 ± 3	13 ± 2	13 ± 1	14 ± 2	14 ± 3
$\vartheta_{oa}$	4 ± 3	2 ± 3	2 ± 4	2 ± 5	2 ± 2	-1 ± 2
$\dot{q}_{gs}$ , W/m <sup>2</sup>	11 ± 27	13 ± 32	9 ± 25	8 ± 24	25 ± 46	17 ± 40
$\dot{q}_{gi}$ , W/m <sup>2</sup>	7 ± 10	7 ± 10	2 ± 7 <sup>b</sup>	0 ± 0	0 ± 0	7 ± 10
$\vartheta_{grd}$	10 ± 0	10 ± 0	11 ± 1	11 ± 1	11 ± 0	10 ± 0
$\vartheta_{sky}$	-3 ± 5	-8 ± 10	-7 ± 8	-9 ± 8	-11 ± 5	-14 ± 9
"outputs":						
$\vartheta_{ta}$	24 ± 1	25 ± 1	26 ± 2	27 ± 2	24 ± 1	26 ± 1
$\vartheta_{ra-door}$ <sup>c</sup>	22 ± 1	22 ± 1	22 ± 1	22 ± 1	22 ± 1	22 ± 2
$\vartheta_{fl}$	21 ± 0	21 ± 0	21 ± 0	21 ± 0	21 ± 0	21 ± 0

<sup>a</sup> 1 means entirely closed = attenuation of  $\dot{q}_{gs}$  by 90%, compare with ESSO (2009).

<sup>b</sup> contains times with gains switched off and times where gains are on.

<sup>c</sup> door indicates the sensor position near the door

Fit results with  $\vartheta_{sky}$  being *neglected* partly improve and partly get worse (fig. 4.6), it is difficult to judge based on the fits <sup>7</sup>. However, the extremely small input coupling for  $\vartheta_{sky}$  – cf.  $B(2,7)$  in tab. 4.1 – is an indicator that this variable may be neglected especially for short prediction horizons. With only  $\vartheta_{grd}$  being neglected, really good fit results get slightly worse, but intermediate and very bad results improve – it seems the model becomes more robust. If both inputs  $\vartheta_{sky}$  and  $\vartheta_{grd}$  are *neglected* (fig. 4.2.4), it is again difficult to say whether the overall performance improves. It is worth to notice, that results concerning negligence of certain inputs could not be reproduced with simulation data.

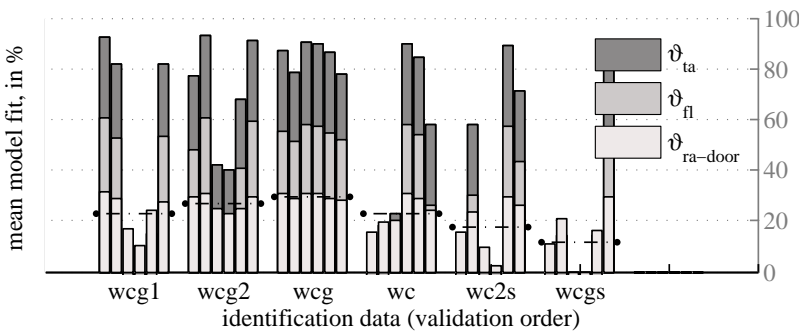


Figure 4.6.: Fit results from real experiment for  $\mathcal{M}$  ( $\vartheta_{sky}$  is neglected).

<sup>7</sup> This is probably due to the general identification problem complexity.

#### 4. Models for control purpose – system identification results

Table 4.6.: Average physical model errors in K according to eq. (3.39) for  $\mathcal{M}(\Theta_{wcgs})$ ; bias ( $\bar{\epsilon}$ ), empirical standard deviation ( $s$ ) and min and max values for P=72 h.

data → y↓	wcg1	wcg2	wcg	wc	wc2s	wcgs id-data
$\vartheta_{ta}$ $\bar{\epsilon} \pm s$	$-0.6 \pm -0.7$	$-0.6 \pm -0.7$	$-1.0 \pm -1.2$	$-0.9 \pm -1.0$	$-0.7 \pm -0.8$	$-0.1 \pm -0.1$
min/max	+1.4 / -0.1	+1.0 / -0.1	+2.1 / -0.2	+2.0 / -0.2	+1.2 / -0.1	+0.3 / -0.2
$\vartheta_{ra}$ $\bar{\epsilon} \pm s$	$-0.9 \pm -1.0$	$-0.8 \pm -0.8$	$-1.1 \pm -1.2$	$-1.0 \pm -1.1$	$-1.1 \pm -1.2$	$-0.2 \pm -0.3$
min/max	+1.7 / -0.0	+1.4 / +0.0	+2.2 / +0.1	+2.0 / -0.0	+2.9 / -0.2	+1.4 / -1.1
$\vartheta_{fl}$ $\bar{\epsilon} \pm s$	$-0.3 \pm -0.4$	$-0.4 \pm -0.5$	$-0.8 \pm -1.0$	$-0.7 \pm -0.8$	$-0.5 \pm -0.6$	$-0.1 \pm -0.1$
min/max	+0.8 / -0.1	+0.8 / -0.1	+1.6 / -0.2	+1.5 / -0.5	+1.0 / +0.1	+0.2 / -0.1
$\bar{\epsilon}(\bar{\vartheta})^a$	-0.6	-0.6	-1.0	-0.8	-0.8	-0.1

<sup>a</sup> average model bias over all outputs

#### 4.2.4. Reflection on the S-SSM for the MPC-Boxes

The minimum variant of parameters for  $\mathbf{B}$  – defined by eq. (4.1) with input coupling to only one model state – leads to very good or maybe even the best possible results for the controller model, cf. fig. 4.7 – for the extended version see fig. G.17 in Appendix. A sub-optimal model structure may be identified by a residual analysis as in fig. 4.3.

The cross-validation of  $\mathcal{M}(\Theta_{wcg})$  still reveals a bell shaped residual distribution, however, for long validation intervals a bias develops. Due to the relatively short prediction horizon during the control task (max. 72 h) even sub-optimal models, e.g. obtained from summer data or a relatively short (72 - 168 h) id-data, may probably be accurate enough for control purpose even in winter, cf. fig. 4.8.

Fig. 4.7 shows the reference trajectory and the model residuals defined by eq. (3.39) for all model outputs (left to right) and three data sets (top to bottom) – over the maximum MPC relevant horizon – for the parametrization  $\Theta_{wcg}$ . Tab. 4.7 provides quantitative measures for the validation of  $\mathcal{M}(\Theta_{wcg})$  by means of the first 72 h of all data sets in tab. 4.5.

The parametrization  $\Theta_{wcgs}$  performs poor according to fig. 4.5 but the fits refer to a conservative performance metric based on the whole data interval. Considering only the MPC relevant horizon, even  $\Theta_{wcgs}$  – based on a short interval with limited excitation (cf. tab. 4.5) – may lead to a sufficiently accurate prediction, see fig. 4.8. The rising bias for cross-validation

Table 4.7.: Average physical model errors in K according to eq. (3.39) for  $\mathcal{M}(\Theta_{wcg})$ ; bias ( $\bar{\epsilon}$ ), empirical standard deviation ( $s$ ) and min and max values for P=72 h; The last line is the average model bias over all outputs.

data → y↓	wcg1	wcg2	wcg id-data	wc	wc2s	wcgs
$\vartheta_{ta}$ $\bar{\epsilon} \pm s$	$-0.09 \pm -0.12$	$-0.10 \pm -0.12$	$-0.12 \pm -0.16$	$-0.11 \pm -0.13$	$-0.07 \pm -0.10$	$-0.37 \pm -0.41$
min/max	+0.24 / -0.29	+0.16 / -0.30	+0.32 / -0.29	+0.15 / -0.30	+0.32 / -0.25	+0.04 / -0.71
$\vartheta_{ra}$ $\bar{\epsilon} \pm s$	$-0.21 \pm -0.26$	$-0.18 \pm -0.20$	$-0.10 \pm -0.13$	$-0.24 \pm -0.26$	$-0.22 \pm -0.36$	$-0.32 \pm -0.42$
min/max	+1.18 / -1.21	+0.37 / -0.57	+0.44 / -0.46	+0.27 / -0.63	+1.45 / -1.10	+0.76 / -1.61
$\vartheta_{fl}$ $\bar{\epsilon} \pm s$	$-0.09 \pm -0.10$	$-0.09 \pm -0.11$	$-0.09 \pm -0.12$	$-0.30 \pm -0.32$	$-0.08 \pm -0.10$	$-0.11 \pm -0.13$
min/max	+0.16 / -0.20	+0.04 / -0.22	+0.04 / -0.26	-0.14 / -0.55	+0.24 / -0.19	+0.12 / -0.31
$\bar{\epsilon}(\bar{\vartheta})^a$	-0.13	-0.12	-0.10	-0.22	-0.12	-0.27

## 4.2. MPC-Boxes controller model based on real measurements

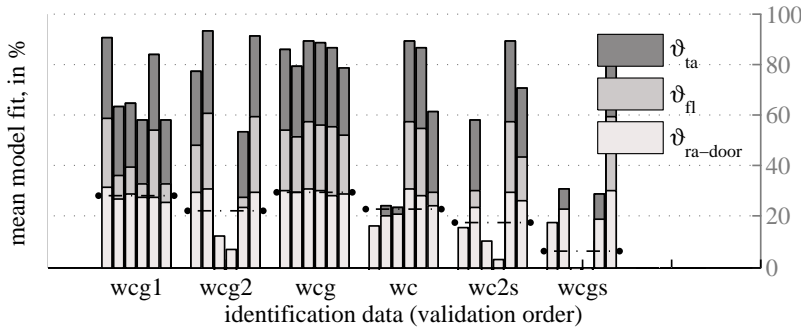


Figure 4.7.: Fit results from real experiment for  $\mathcal{M}$  ( $\vartheta_{sky}$  and  $\vartheta_{grd}$  being neglected).

with wcg in fig. 4.8 is likely to originate from the steady TABS heating phase. Such a feature is not included in the id-data showing only short on intervals for the TABS heating. A look on the quantitative results in tab. 4.6 clearly shows, that the residual average values are significantly higher compared to those in tab. 4.7 – the residuals stay within 2 K over the first 48 hours. Hence, a parametrization based on a longer id-data interval is clearly preferable.

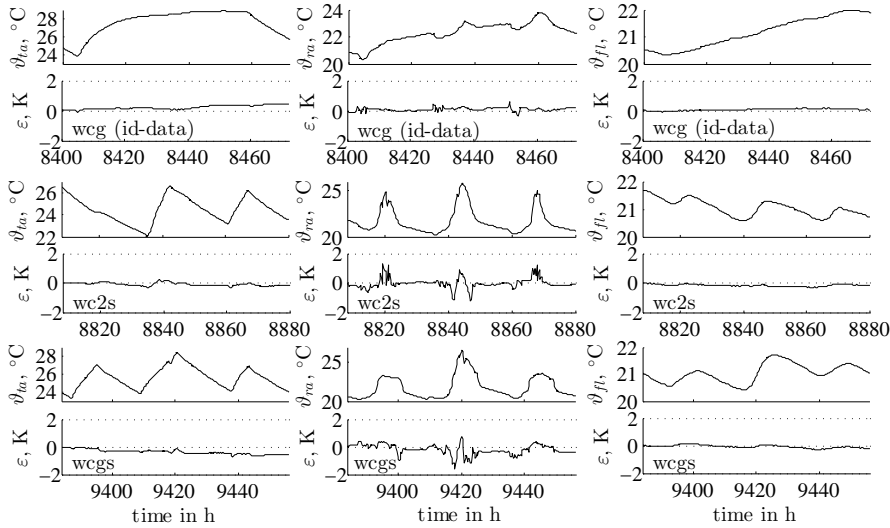


Figure 4.8.: Trajectories and model residuals for TABS-, room air and floor temperature over the first 72 h; id-data wcg from real measurements.

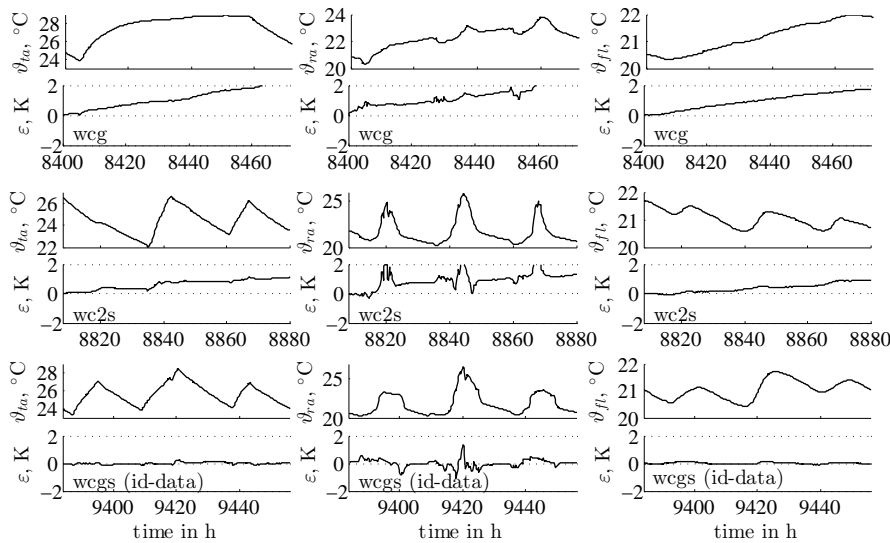


Figure 4.9.: Trajectories and model residuals for TABS-, room air and floor temperature over the first 72 h; id-data wcgs from real measurements.

## Other findings

A relaxation of the constraints on  $\mathbf{B}$  increases the diversity of the A-matrix parameters for varying id-data. A very general reason for this is, that, the more complex the parameter estimation space the more room for distinct solutions. This is a negative aspect from a system identification point of view. Parameter uncertainties are approximately an order of magnitude higher for estimations based on real measurement in comparison to simulation data. There is nothing significant observable wrt uncertainties in relation to varying constraints.

A detailed residual analysis reveals, that the disturbance  $\vartheta_{grd}$  is very difficult to capture. The reason is the period of one year for this signal. Concerning long intervals it is also a potential source for an increasing bias.

### 4.3. TheBat linear building model

The building within the context of TheBat is a single family house (cf. fig. 2.7) already explained in sec. 2.2. This building exist only as TRNSYS simulation, by contrast to the MPC-Boxes building which exists as TRNSYS simulation model and in reality.

A number of model structures were tested and evaluated with the six data sets characterized in tab. 4.8, before finally arriving at a suitable model of 4th order. The very first physical RC model approach is depicted in fig. 4.10. The conducted model identification process neglects ventilation and internal gains for simplicity. There is nothing particular about these disturbances, and it is clear that they couple directly to  $\vartheta_{ra}$ . Characteristics of the resulting S-SSM from fig. 4.10 ( $\mathcal{M}^{n4}$ ), a third order S-SSM ( $\mathcal{M}^{n3}$ ) and the best S-SSM found ( $\mathcal{M}^{n4w}$ ) are briefly outlined in this section.

Table 4.8.: Characterization of TheBat id-data; Excitation realized with an on-off controller maintaining the air temperature between 20 °C and 24 °C ;  $\dot{q}_{ta}$  is evaluated for  $\dot{q}_{ta} \neq 0$  only, temperatures are in °C .

data ( $\mathcal{D}^P$ ) →	wc	wm	ts	sh	sm	tf
Start in h	168	6912	2352	3939	2856	6216
P in h	1008	1008	1008	1008	1008	1008
"inputs":						
$\bar{q}_{ta}$ , W/m <sup>2</sup>	18	11	3	0	0	4
$\dot{q}_{ta}$ , W/m <sup>2</sup>	42 ± 11	28 ± 10	36 ± 10	0 ± 0	62 ± 4	30 ± 10
$\vartheta_{oa}$	-2 ± 5	6 ± 4	11 ± 5	19 ± 5	14 ± 5	10 ± 5
$\dot{q}_{gs2fl}$ , W/m <sup>2</sup>	15 ± 25	12 ± 21	17 ± 20	18 ± 19	17 ± 18	16 ± 24
$\dot{q}_{gs1fl}$ , W/m <sup>2</sup>	15 ± 25	12 ± 21	17 ± 20	18 ± 19	17 ± 18	16 ± 24
$\dot{q}_{gi}$ , W/m <sup>2</sup>	0 ± 0	0 ± 0	0 ± 0	0 ± 0	0 ± 0	0 ± 0
$\vartheta_{grd}$	0 ± 0	7 ± 2	10 ± 2	18 ± 1	13 ± 2	12 ± 2
$\vartheta_{sky}$	-14 ± 7	-4 ± 7	1 ± 8	9 ± 7	5 ± 7	-0 ± 8
"outputs":						
$\vartheta_{op,2fl}$	22 ± 1	22 ± 1	22 ± 1	23 ± 1	22 ± 1	22 ± 1
$\vartheta_{op,1fl}$	23 ± 1	23 ± 1	22 ± 1	23 ± 1	22 ± 1	22 ± 1
$\vartheta_{ta}$	26 ± 1	25 ± 2	22 ± 1	23 ± 0	22 ± 1	23 ± 2

As  $\bar{q}_{ta}$  – the average heat flux over the whole interval – indicates, the heating demand is highest for the data wc (winter cold) followed by wm (winter moderate). The summer intervals sh (summer hot) and sm (summer moderate) require practically no heating and the transition intervals ts (transition spring) and tf (transition fall) only little.

#### 4.3.1. Initial physical RC model structure – $\mathcal{M}^{n4}$

The very first S-SSM approach is based on the RC model depicted in fig. 4.10. By contrast to the MPC-Boxes building model (cf. 3.1), here the physical balance equations are not derived and the RC model serves merely as an aid to establish the model structure  $\mathcal{M}^{n4}$ . The four states represent room air- and TABS-core-temperature, for the 1st and the 2nd floor; the states-, the input- and the desired output-vector read

$$\begin{aligned} \mathbf{x} &:= [\vartheta_{ra2fl}, \vartheta_{ta2fl}, \vartheta_{ra1fl}, \vartheta_{ta1fl}]^T, & \mathbf{u} &:= [\dot{q}_{ta2fl}, \dot{q}_{ta1fl}, \vartheta_{oa}, \dot{q}_{gs2fl}, \dot{q}_{gs1fl}, \dot{q}_{gi}, \vartheta_{grd}, \vartheta_{sky}]^T, \\ \mathbf{y} &:= \mathbf{x}. \end{aligned} \quad (4.8)$$

The constrained prototype of this model is given in Appendix G.6.1 along with model fits, which are not too bad, but the model is excluded due to a specific weakness which is explained in the following.

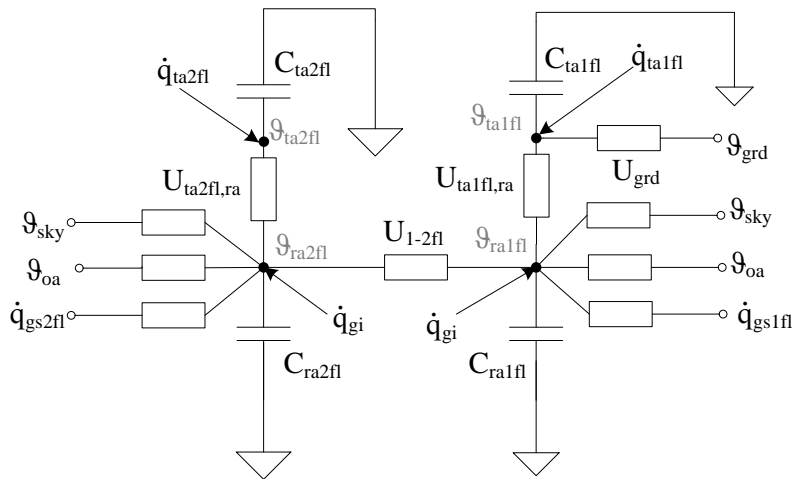


Figure 4.10.: RC representation of the initial four nodes ( $\mathcal{M}^{n4}$ ) model for the TheBat SFH, with two distinct temperatures for TABS- and room-temperature, for the first and second floor.

#### Poor model structure or insufficient model order

An important discovery relating to the initial structure was made while looking at the model outputs for room- and TABS-temperatures. Although, the model- and data-trajectories for the first floor were generally matching, either the room- or the TABS-temperature of the second floor was strongly damped for the self-validation.

#### 4. Models for control purpose – system identification results

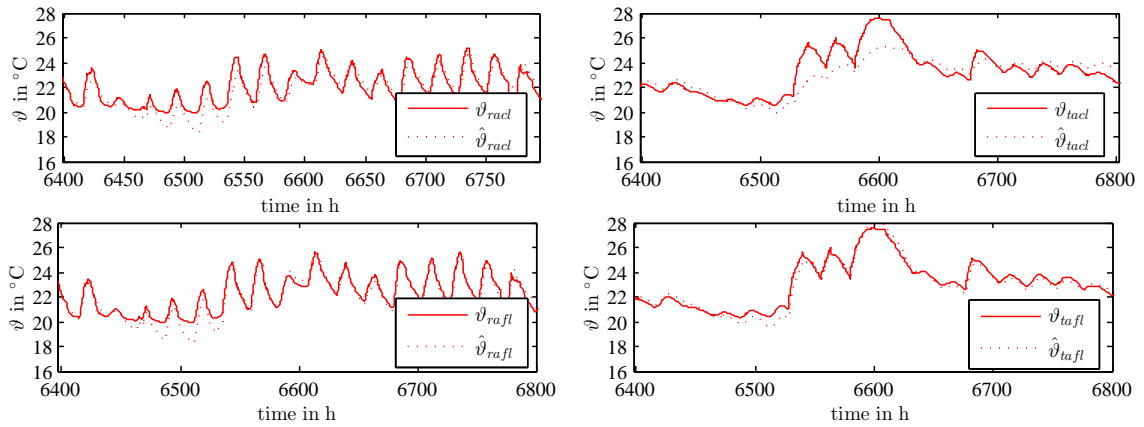


Figure 4.11.: Model- ( $\hat{\vartheta}$ ) and experimental- data ( $\vartheta$ ) trajectories for room- and TABS-temperatures for the model depicted in fig. 4.10 and  $\Theta$  estimated with id-data sh; top graphs 2nd- bottom graphs 1st floor.

Fig. 4.11 illustrates the damping for  $\hat{\vartheta}_{ta2fl} =: \hat{\vartheta}_{tacl}$  (TABS temperature of the ground floor ceiling); a similar illustration but with  $\hat{\vartheta}_{ta2fl}$  quite accurate and  $\hat{\vartheta}_{ra2fl} =: \hat{\vartheta}_{racl}$  (room air temperature in the second floor) strongly damped holds for the id-data ts. From a physical perspective this result could be explained with an additional thermal mass not explicitly incorporated in the model design. As a consequence it is either lumped to the room- or the TABS-temperature node during the parameter estimation. This interpretation led to the model  $\mathcal{M}^{n4w}$ , an alternative would be to increase the model order.

#### Physicality issues

A parameter estimation specific problem was also discovered for  $\mathcal{M}^{n4}$ . The coupling parameter ( $U_{1-2fl}$ ) between the room temperature nodes occurs more or less twice in the matrix  $\mathbf{A}$ , that is, if the data could be described with the given model structure it is expected to identify twice a similar parameter value.

However, the estimated parameters lead to coupling in one but not in the other direction ( $U_{1-2fl} = 0$ ), which is strange. In other words, from a physical structure point of view two independently estimated model parameters should be the same, but they are not.

Applying constraints on these physical parameters (reducing the two parameters to one which occurs twice), within a pure physical parameter estimation framework – as mentioned in sec. 4.1 – the ambiguity may be excluded but the final model performance is not better either. Finally, due to the similarity of the room temperature for the 1st- and the 2nd-floor also collinearity issues (cf. sec. 3.4.1) may be the reason for the non-physical parameter estimation results. The structure in fig. 4.10 is prone to collinearity issues during the parameter estimation, because  $\vartheta_{ra2fl} \approx \vartheta_{ra1fl}$ .

### 4.3.2. Third order models – $\mathcal{M}^{n3}$ S-SSM estimation

To avoid any collinearity issues – that might be the reason for the problems explained for  $\mathcal{M}^{n4}$  – it was tried to model only one room temperature which leads to a model for 3rd order.

The three states should represent an average operative room temperature and the TABS-core-temperature, for the 1st and the 2nd floor; the states- and the maximum input-, and the desired output-vector read

$$\begin{aligned} \mathbf{x} &:= [\vartheta_{ta2fl}, \vartheta_{op}, \vartheta_{ta1fl}]^T, & \mathbf{u} &:= [\dot{q}_{ta2fl}, \dot{q}_{ta1fl}, \vartheta_{oa}, \dot{q}_{gs2fl}, \dot{q}_{gs1fl}, \dot{q}_{gi}, \vartheta_{grd}, \vartheta_{sky}]^T, \\ \mathbf{y} &:= \mathbf{x}. \end{aligned} \quad (4.9)$$

Similarly as for  $\mathcal{M}^{n4}$ , the model- and data-trajectories for the first floor TABS temperature were generally matching but either the average operative- (wm) or the TABS-temperature (ts) of the second floor was strongly damped for the self-validation, compare with fig. 4.11. Appendix G.6.2 illustrates the trajectories for  $\mathcal{M}^{n3}(\Theta_{ts})$  with clearly visible damping of  $\vartheta_{ta2fl}$  (fig. G.20) and a detailed residual analysis shows that the residuals for  $\vartheta_{ta2fl}$  are far from being normally distributed (fig. G.21).

The limited accuracy already for the self-validation and the distorted residual distribution clearly indicate a weakness of the model structure. In addition to this third order model one similar to  $\mathcal{M}^{n4w}$  but with three states was investigated. That model ( $\mathcal{M}^{n3w}$ ) consists of the states for only one TABS- the room- and a virtual wall temperature – the results did not improve compared to  $\mathcal{M}^{n4}$  and  $\mathcal{M}^{n3}$ .

### 4.3.3. Fourth order model with virtual wall – $\mathcal{M}^{n4w}$

Based on the lessons learned from  $\mathcal{M}^{n4}$  and  $\mathcal{M}^{n3}$  another fourth order model is established. However, this model differs from the initial RC model in terms of state and output variables. The states represent a virtual wall-, two room air- and one TABS-temperature – first and second floor TABS are connected in series and have the same mass flow, cf. sec. 2.2. State-, input- and output-vector read

$$\begin{aligned} \mathbf{x} &:= [\vartheta_w, \vartheta_{ra2fl}, \vartheta_{ra1fl}, \vartheta_{ta}]^T, & \mathbf{u} &:= [\dot{q}_{ta}, \vartheta_{oa}, \dot{q}_{gs2fl}, \dot{q}_{gs1fl}, \dot{q}_{gi}, \vartheta_{grd}, \vartheta_{sky}]^T, \\ \mathbf{y} &:= [\vartheta_{op,2fl}, \vartheta_{op,1fl}, \vartheta_{ta}]^T. \end{aligned} \quad (4.10)$$

The general structure of the model  $\mathcal{M}^{n4w}$  is given by the set of real matrices  $\mathbf{A} \in \mathbb{R}^{4 \times 4}$ ,  $\mathbf{B} \in \mathbb{R}^{4 \times 7}$  and  $\mathbf{C} \in \mathbb{R}^{3 \times 4}$ , compare with sec. 3.1.2. The output matrix  $\mathbf{C}$  specifies the composition of the operative temperatures – each operative temperature is the average of an air- and the fictive wall-temperature:

$$\mathbf{C} := \begin{bmatrix} 0.5 & 0.5 & 0 & 0 \\ 0.5 & 0 & 0.5 & 0 \\ 0 & 0 & 0 & 1 \end{bmatrix} \Rightarrow \mathbf{y} = \begin{bmatrix} 0.5 & 0.5 & 0 & 0 \\ 0.5 & 0 & 0.5 & 0 \\ 0 & 0 & 0 & 1 \end{bmatrix} \begin{bmatrix} \vartheta_w \\ \vartheta_{ra2fl} \\ \vartheta_{ra1fl} \\ \vartheta_{ta} \end{bmatrix} = \begin{bmatrix} \frac{\vartheta_w + \vartheta_{ra2fl}}{0.5} \\ \frac{\vartheta_w + \vartheta_{ra1fl}}{0.5} \\ \vartheta_{ta} \end{bmatrix}. \quad (4.11)$$

#### 4. Models for control purpose – system identification results

##### Investigation of internal model structures

In the following a few variations of the *internal structure*, that is, the coupling between the states is investigated. Four internal structures:  $\Theta^a$ ,  $\Theta^b$ ,  $\Theta^c$  and  $\Theta^d$  are analyzed in detail. Given  $\mathbf{C}$  from eq. (4.11), the first prototypical parametrization  $\mathcal{M}^{n4w}(\Theta^a)$  – with  $\mathbf{B}$  established based on  $\mathbf{u} := [\dot{q}_{ta}, \vartheta_{oa}, \dot{q}_{gs2fl}, \dot{q}_{gs1fl}, \dot{q}_{gi}, \vartheta_{grd}, \vartheta_{sky}]^T$  and insight from sec. 4.1 (every input couples only to one state, here this is violated for the room air temperature state) – becomes complete with

$$\mathbf{A} := \begin{bmatrix} \mathbb{R}^- & \mathbb{R}^+ & \mathbb{R}^+ & 0 \\ \mathbb{R}^+ & \mathbb{R}^- & \mathbb{R}^+ & \mathbb{R}^+ \\ \mathbb{R}^+ & \mathbb{R}^+ & \mathbb{R}^- & \mathbb{R}^+ \\ 0 & \mathbb{R}^+ & \mathbb{R}^+ & \mathbb{R}^- \end{bmatrix}, \quad \mathbf{B} := \begin{bmatrix} 0 & 0 & 0 & 0 & 0 & 0 \\ 0 & \mathbb{R}^+ & \mathbb{R}^+ & 0 & X & 0 & \mathbb{R}^+ \\ 0 & \mathbb{R}^+ & 0 & \mathbb{R}^+ & X & 0 & \mathbb{R}^+ \\ \mathbb{R}^+ & 0 & 0 & 0 & 0 & \mathbb{R}^+ & 0 \end{bmatrix}. \quad (4.12)$$

The other structures for  $\mathcal{M}^{n4w} - \Theta^b$ ,  $\Theta^c$  and  $\Theta^d$  – are provided in Appendix G.6.3. The fit values obtained with this structure and constraints according to eq. (4.12) are relatively good. The damping effect as explained in sec. 4.3.1 vanished. Definitely  $\mathcal{M}^{n4w}$  outperforms the structures  $\mathcal{M}^{n3}$  and  $\mathcal{M}^{n4}$ .

All investigated internal structures  $\Theta^a$ ,  $\Theta^b$ ,  $\Theta^c$  and  $\Theta^d$  also referenced as structure a, b, c and d demonstrate similar performance, cf. G.6.3 in Appendix, and it is not straight forward to decide on the best model. To single out the most suitable variant for the MPC the eigensolutions of the dynamic matrix are analyzed.

##### Eigenvalues and eigensolutions – analysis

The eigensolution analysis of the excitation free system  $\mathbf{A}$  – all inputs and disturbances being zero – gives insight into fundamental model characteristics, as explained in Appendix B.1.2.

Fig. 4.12 on page 88 shows four windows corresponding to the variants a, b, c and d. Each window illustrates the eigenvalues of the *time continuous* matrix  $\mathbf{A}$  for a specific internal structure and six parametrizations based on six id-data, cf. tab. 4.8. One can see that all eigenvalues have a negative real part (the imaginary part is zero for all eigenvalues  $\lambda_i$ ). A negative real part is a "must" for a stable model, cf. Appendix B.1.3 BIBO criterion. Consulting a mechanical analogue for means of explanation such eigenvalues correspond to so called *over-damped solutions* of a free mass-spring system for which the dissipated energy flow – in this case heat flux – is so high that no oscillations occur. The dominating (greatest) eigenvalue ranges from  $-10^{-2}$  to  $-10^{-5}$ .

### 4.3. TheBat linear building model

Consulting the theory of Fourier analysis as a reminder and the topic eigensolutions discussed in B.1.3 in Appendix, it is clear that the number of distinct eigenvalues determines the possible variability for general solutions – the eigendirection is neglected. Actually, the maximum number of eigenvalues is  $n = 4$  and obviously the more distinct these values the higher the possibilities in terms of state trajectories. A question that follows is whether a full covering of the phase-space or partly covering of certain areas but with higher resolution lead to better results.

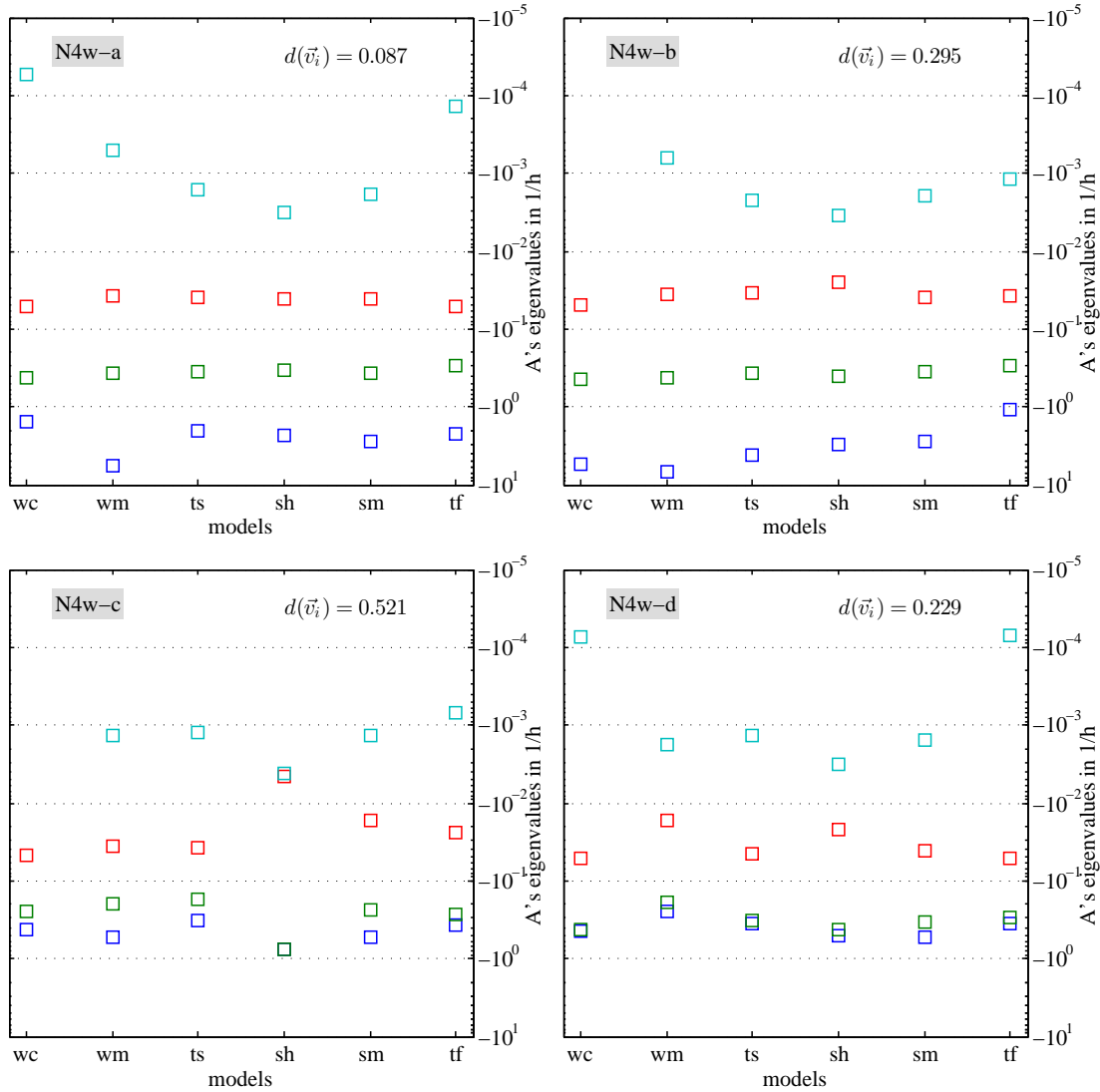


Figure 4.12.: Eigenvalue spectrum of  $A$  on a logarithmic scale, for four different internal model structures  $\{\mathcal{M}^{n4w}(\Theta^*) \mid * = a, b, c, d\}$  ( $N4w := n4w$ ) each of which is parametrized based on id-data wc, ...tf; missing values are smaller than  $-10^{-5}$ . The transformation  $A^d \rightarrow A$  is based on Euler – Tustin's method leads to very similar results.

#### 4. Models for control purpose – system identification results

##### Eigensolutions

Fig. 4.13 illustrates the *eigensolutions* for selected parameterizations. The trajectories in the right plot appear pair-wise whereas those in the left plot are more distinct. It is *assumed* that the accuracy of a model improves with the possibilities in terms of state trajectories. Consequently models with two or more similar eigenvalues should perform worse than models with four distinct values. A look at fig. 4.12 and the fits in Appendix G.6.3 shows that this definitely holds for  $\Theta^c(\text{sh})$ , but enough variation among the eigenvalues does not guarantee a high fit, compare results for  $\Theta^a(\text{sh})$  and  $\Theta^a(\text{sm})$ . Hence, the distinction of eigenvalues only does not seem to be a good and reliable indicator for the model performance.

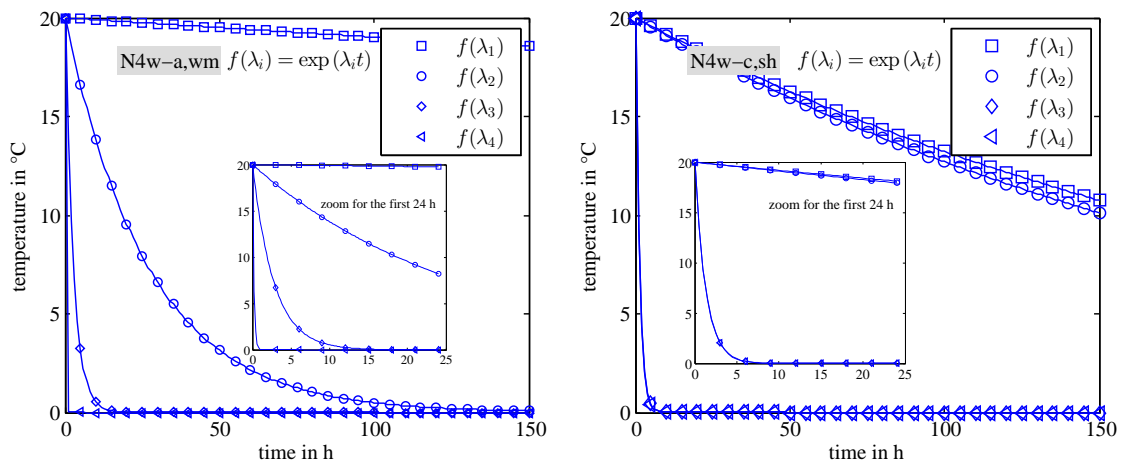


Figure 4.13.: Eigensolutions for the dynamic matrix (A) of the model  $\mathcal{M}^{n4w}$  and the parametrizations  $\Theta^a(\text{wm})$  (left) and  $\Theta^c(\text{sh})$  (right).

Finally, the direction of the dominating eigensolution  $\propto \exp(\lambda_1 t) \mathbf{v}_1$  is analyzed, cf. B.1.3 in Appendix. This direction is expected to relate to a physically relevant composition of the defined states. Among the different parametrizations (wc, wm, ...) of a specific variant (a, b, ...) the deviation between the eigendirections is measured according to eq. (B.22) given in Appendix. This distance measure is given in the right top corner of each window in fig. 4.12; the smaller the value the more like are the dominating eigendirections. Based on this criterion, variant a is the best or in other words the direction of the dominant solution is very similar for parametrizations obtained from different id-data. This may be interpreted as a sign for a good model structure, however, a detailed analysis should consider also the id-data property excitation. The individual components of the dominating eigendirection are given in tab. 4.9.

The average dominant eigendirections for the structures  $\Theta^a$ ,  $\Theta^b$ , ... are very similar as indicated by the similarity of the individual components in the last column of tab. 4.9. However, certain parametrizations show clearly a high deviation from the average

eigendirection, for example  $\Theta^b(wc)$  or  $\Theta^c(sh)$ ; comparing against the average component values, one could say that the parametrization ended at a different optimum; or is heavily distorted. Very likely the model  $\Theta^c(sh)$  performs bad when cross-evaluated with the other data sets even for a short horizon. This model is tailored to floating operation by means of one node only ( $\vartheta_w$ ), therefore it will fail for active TABS. A comparison of all average directions shows, that it is nearly evenly composed from all physical states – this is interpreted such that the interaction between the states plays an important role for the long term behavior which justifies and confirms the chosen model structure.

An analysis of the other eigensolutions – provided in Appendix G.6.4 – leads also to interesting findings. The eigensolutions  $f_3$  and  $f_4$  relate to the smallest eigenvalue – representing high damping or a small thermal mass – and the eigendirection is dominated by the room air temperature nodes which indicates *consistency* and is interpreted as a good sign in terms of model structure, because *the model node or state represents what it was designed for*.

Table 4.9.: Properties of the dominating eigensolutions  $f_1(\lambda_1, v_1)$ , obtained from the four structures  $\Theta^a$ ,  $\Theta^b$ ,  $\Theta^c$ ,  $\Theta^d$ , for all id-data wc, ... tf, respectively.

id-data	wc	wm	ts	sh	sm	tf	mean
normalized eigenvectors, and eigenvalue of the dominant eigensolution							
variant a	$dmax_{v_1} = 0.087$						
$v_{1,w}$	0.48	0.44	0.53	0.56	0.52	0.53	0.51
$v_{1,op2fl}$	0.52	0.54	0.50	0.50	0.48	0.49	0.50
$v_{1,op1fl}$	0.53	0.56	0.49	0.49	0.48	0.49	0.51
$v_{1,ta}$	0.47	0.46	0.47	0.43	0.51	0.50	0.48
$\lambda_1$	-5.4e-05	-5.0e-04	-1.6e-03	-3.3e-03	-1.9e-03	-1.4e-04	-1.2e-03
variant b	$dmax_{v_1} = 0.295$						
$v_{1,w}$	0.07	0.44	0.58	0.58	0.52	0.46	0.44
$v_{1,op2fl}$	0.65	0.54	0.48	0.51	0.48	0.53	0.53
$v_{1,op1fl}$	0.66	0.55	0.47	0.48	0.48	0.52	0.53
$v_{1,ta}$	0.37	0.46	0.47	0.41	0.52	0.49	0.45
$\lambda_1$	-7.4e-06	-6.2e-04	-2.2e-03	-3.5e-03	-1.9e-03	-1.2e-03	-1.6e-03
variant c	$dmax_{v_1} = 0.521$						
$v_{1,w}$	0.57	0.53	0.54	-1.00	0.54	0.46	0.61
$v_{1,op2fl}$	0.49	0.51	0.52	0.01	0.51	0.56	0.43
$v_{1,op1fl}$	0.41	0.47	0.44	0.01	0.45	0.50	0.38
$v_{1,ta}$	0.51	0.50	0.50	0.01	0.50	0.48	0.41
$\lambda_1$	0.0e-00	-1.4e-03	-1.3e-03	-4.1e-03	-1.3e-03	-7.1e-04	-1.5e-03
variant d	$dmax_{v_1} = 0.229$						
$v_{1,w}$	0.38	0.74	0.50	0.58	0.52	0.53	0.54
$v_{1,op2fl}$	0.55	0.38	0.51	0.49	0.49	0.49	0.48
$v_{1,op1fl}$	0.59	0.38	0.51	0.48	0.48	0.49	0.49
$v_{1,ta}$	0.45	0.40	0.48	0.44	0.51	0.49	0.46
$\lambda_1$	-7.4e-05	-1.8e-03	-1.4e-03	-3.2e-03	-1.6e-03	-7.1e-05	-1.4e-03

## 4. Models for control purpose – system identification results

### 4.3.4. Final model structure

The final model structure is given by eq. (4.10), eq. (4.11) and eq. (4.12). The model performance in terms of fits is provided in Appendix G.6.3. The selected model's ( $\mathcal{M}^{n4w}(\Theta_{wm}^a)$ ) performance when cross-evaluated is given by tab. 4.10. For trajectories demonstrating the performance over the first few days see fig. G.26 in Appendix. The final model structure was selected based on the *assumptions*, that

1. similar eigenvalue spectra for various id-data indicate a good model structure – *eigenvalue consistency*,
2. distinct eigenvalues are preferred over similar eigenvalues,
3. similar eigendirections for the dominating eigenvalue for different id-data are good.

A perturbation analysis for  $\mathbf{A}$  was not conducted, such an analysis would allow for a judgment on the robustness of the model as a function of the parametrization. For this analysis sequential perturbation of single elements of  $\mathbf{A}$  and the investigation of the model output allows for isolation of critical elements in  $\mathbf{A}$  or its *sensitivity*.

Table 4.10.: Evaluation results for  $\mathcal{M}^{n4w}(\Theta_{wm}^a)$  in terms of bias ( $\bar{\varepsilon}$ ) and empirical standard deviation ( $s$ ) in K, when tested with the six data sets for  $P = 6$  weeks.

data→	wc	wm	ts	sh	sm	tf
output↓	average residual or bias ( $\bar{\varepsilon}$ ) $\pm$ empirical standard deviation ( $s$ ) in K					
$\vartheta_{op2fl}$	$-0.08 \pm 0.38$	$0.03 \pm 0.32$	$-0.19 \pm 0.62$	$-0.17 \pm 1.12$	$-0.30 \pm 0.62$	$0.06 \pm 0.46$
$\vartheta_{op1fl}$	$0.04 \pm 0.45$	$-0.07 \pm 0.32$	$-0.64 \pm 0.64$	$-0.78 \pm 1.07$	$-0.81 \pm 0.69$	$-0.32 \pm 0.55$
$\vartheta_{ta}$	$-0.25 \pm 0.53$	$-0.07 \pm 0.40$	$-0.53 \pm 0.62$	$-0.95 \pm 0.99$	$-0.75 \pm 0.74$	$-0.22 \pm 0.47$

## 4.4. Thermal storage with heat pump – controller model

During preliminary work related to MPC a simple linear solar TES model has been suggested, cf. Pichler et al. (2014). For the research published in that article it was possible to utilize a linear model. However, the term *mini-simulation* defined in that work already points in the direction of a work-around concerning non-linear effects. This mini-simulation is only dealing with disturbance data (solar irradiance on a collector plane), which are translated into (auxiliary-) inputs that can be handled by a linear model. This kind of pre-processing of disturbance data is sometimes also termed disturbance simulation.

The non-linear effects which required the mini-simulation in Pichler et al. (2014) are due to a varying mass flow in the TES. Since the varying mass flow depended more or less only on the solar irradiance prediction, the mini-simulation provided a suitable work-around. Once a manipulated variable of the MPC scheme causes the mass flow to change, the situation becomes more complicated, and the mini-simulation approach

#### 4.4. Thermal storage with heat pump – controller model

gets very cumbersome as can be seen in an accompanying research to this doctoral thesis, see Arnitz (2014). The approach explained in that master thesis was not further elaborated for this thesis, instead a *hybrid approach* based on a linear and a non-linear model is worked out for the heat pump storage combination.

Consider the hydraulic scheme drawn in fig. 4.14. If the heat pump is switched off the thermal losses to the ambient may be modeled using a linear approach, compare with the model derived in Pichler et al. (2014). If the HP is switched on and operated such to assure  $\vartheta_{co} = 50$  °C the general controller model must be non-linear, since the water mass flow through the heat pump is a function of the compressor frequency and the condenser inlet temperature,  $\dot{m}(f, \vartheta_{ci})$ . However, this non-linear model is then *linearized* at an operating point, and the controller model finally becomes affine. The affine model may be treated as a linear model for the MPC routine. Depending on whether the HP is off or on, the *hybrid* model predictive controller must switch between, the originally linear ( $\mathcal{M}_1$ ), and the linearized model ( $\mathcal{M}_2$ ). The incorporation of the affine model and the switching between models is explained later in sec. 5.3. The sequel of this section deals with the derivation of the non-linear model and explains the “linearization” procedure. In addition, the performance of the hybrid model approach is evaluated.

##### 4.4.1. General non-linear storage model

Figure 4.14 shows a general TES modeled with three nodes, indicated by  $\vartheta_1$ ,  $\vartheta_2$  and  $\vartheta_3$ . The heat losses of each node to the environment are indicated by a heat transfer coefficient  $UA$ , the heat conduction and internal-mixing between the storage nodes is indicated by  $UA_\lambda$ . Heat may be supplied at the top of the storage, in terms of a mass flow  $\dot{m}$  at temperature  $\vartheta_{hp,o}$  – the same mass flow leaves the storage at the bottom. In this thesis, the external heat source which charges the storage, is a HP, compare with fig. 2.2.

A discharging of the TES for domestic hot water purposes (DHW) or space heating (SH) may be considered through any  $\dot{Q}_{aux,i}$ . In such case a negative heat-flux value is supplied to the model node or state  $i$ , which decreases the temperature of this node or state; this is only an approximation. However, considering a DHW draw off, in practice even the prediction is already difficult. In this research only a small amount of the really discharged DHW energy is provided to the MPC routine as predicted disturbance via  $\dot{Q}_{aux,i}$ . In principal, the discharging process by means of a mass flow may be implemented similarly to the charging process using a non-linear approach, compare with Berkenkamp and Gwerder (2014).

#### 4. Models for control purpose – system identification results

##### Derivation of the general model equations

Each node in fig. 4.14 has the thermal heat capacity  $C_i := m_i c_p$ . It is convenient to hide the mass flow  $\dot{m}$  in  $\dot{C} := \dot{m} c_p$  which is the heat capacity flow rate. Then, the energy balance of a thermal node  $i$  in interaction with an upper  $(i - 1)$  and a lower  $(i + 1)$  node, with a constant capacity flow rate entering and leaving, reads

$$C_i \frac{d\vartheta_i}{dt} = UA_i(\vartheta_{env} - \vartheta_i) + UA_{\lambda,i}(\vartheta_{i-1} - \vartheta_i) - UA_{\lambda,i+1}(\vartheta_i - \vartheta_{i+1}) + \dot{C}(\vartheta_{i-1} - \vartheta_i) + \dot{Q}_{aux,i} \quad \text{where } UA_\lambda = \lambda_z A / \Delta z. \quad (4.13)$$

The first term on the right hand side stands for energy losses against the environment, the second and the third term model the vertical mixing process to the upper and the lower node. The fourth term gives the energy change due to the heat capacity flow rate  $\dot{C}$ , and  $\dot{Q}_{aux,i}$  provides the option to consider an additional (electrical) energy source or a draw-off related to the  $i$ -th node only. Vertical mixing is expressed by means of a heat transfer per K ( $UA_\lambda$ ) which is determined by an average  $\lambda_z$ , the storage cross section  $A$  and the vertical distance of the considered nodes.

Considering a three-node thermal model the top- and the bottom-node do not include the upper and the lower mixing term. Further it is assumed, that the heat capacity rate enters the thermal storage at the top, at temperature  $\vartheta_{do}$ , and leaves the storage at the bottom node, at temperature  $\vartheta_3 =: \vartheta_{ci}$ . The complete thermal model becomes

$$\begin{aligned} C_1 \frac{d\vartheta_1}{dt} &= UA_1(\vartheta_{env} - \vartheta_1) - UA_{\lambda,2}(\vartheta_1 - \vartheta_2) + \dot{C}(\vartheta_{do} - \vartheta_1) + \dot{Q}_{aux,1} \\ C_2 \frac{d\vartheta_2}{dt} &= UA_2(\vartheta_{env} - \vartheta_2) + UA_{\lambda,2}(\vartheta_1 - \vartheta_2) - UA_{\lambda,3}(\vartheta_2 - \vartheta_3) + \dot{C}(\vartheta_1 - \vartheta_2) + \dot{Q}_{aux,2} \\ C_3 \frac{d\vartheta_3}{dt} &= UA_3(\vartheta_{env} - \vartheta_3) + UA_{\lambda,3}(\vartheta_2 - \vartheta_3) + \dot{C}(\vartheta_2 - \vartheta_3) + \dot{Q}_{aux,3}. \end{aligned} \quad (4.14)$$

If the mass flow through the storage is switched off then  $\dot{C} = 0$  and the model becomes linear  $\rightarrow \mathcal{M}_1$ . That is, the free *floating storage* – with external draw-offs being neglected – is a *linear* model. The non-linearity originates from the heat capacity rate, which is a general function  $\mathcal{F}$  of the condenser inlet-, the desuperheater outlet-, the source-temperature (evaporator), and the compressor frequency:

$$\dot{C} = \mathcal{F}(\vartheta_{ci}, \vartheta_{do}, \vartheta_{sc}, f). \quad (4.15)$$

Assuming a constant desuperheater outlet temperature  $\vartheta_{do}$  (e.g 50 °C), and a constant source temperature  $\vartheta_{sc}$  (e.g 0 °C), only the dependency on  $\vartheta_{ci}$  and  $f$  remains. Various approaches may be chosen to express  $\dot{C}$  as a function of  $\vartheta_{ci}$  and  $f$ , compare sec. 2.4.1.

It is only eq. (4.15) which represents the *HP part* in this non-linear model. Due to this "minor presence" of the HP in the storage heat pump (TES-HP) model it is often termed just storage model.

#### 4.4. Thermal storage with heat pump – controller model

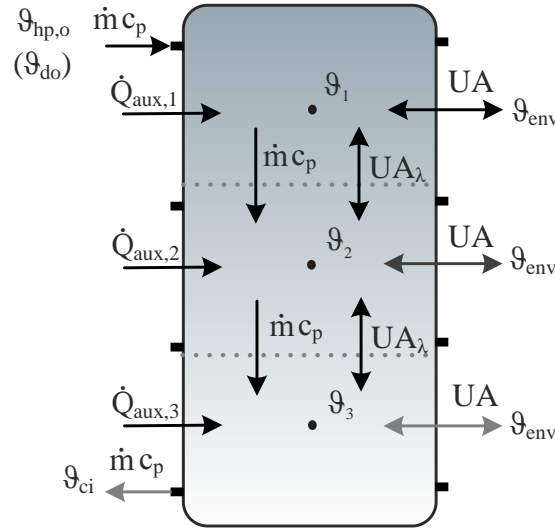


Figure 4.14.: Principle heat transfer mechanisms of the non-linear TES-HP model. Any draw-offs and redundant connections are neglected.

#### 4.4.2. Linearization of the general non-linear model

Assume a general vector valued function  $\mathbf{g}(\mathbf{x}, \mathbf{u})$  which describes the time development of  $\mathbf{x}$ . In this context, from a physical point of view the vector- $\mathbf{x}$  represents the storage temperatures, and the vector- $\mathbf{u}$  incorporates the manipulated variable (the HP frequency) and the estimated (predictable) disturbances (temperature of the environment, draw-off). Then, the the exact model equations may be written as

$$\dot{\mathbf{x}} = \mathbf{g}(\mathbf{x}, \mathbf{u}). \quad (4.16)$$

In order to facilitate this equation for the MPC, it must be linearized at a certain operating point (OP). This is realized by development of  $\mathbf{g}(\mathbf{x}, \mathbf{u})$  in a Taylor series up to the linear terms. That is, terms  $\mathcal{O}(x^2)$  and  $\mathcal{O}(u^2)$  are neglected. The general Taylor formula of a *scalar valued function*  $g(x, u)$  reads

$$\dot{x} = g(x_0, u_0) + \frac{\partial}{\partial x}g(x_0, u_0) (x - x_0) + \frac{\partial}{\partial u}g(x_0, u_0) (u - u_0) + \mathcal{O}(x^2) + \mathcal{O}(u^2). \quad (4.17)$$

Assume the OP  $(x_0, u_0)$  not to be a stationary or critical point, but rather a certain (the current) state of the plant. Then the Taylor expansion of  $g(x, u)$  at the OP  $(x_0, u_0)$  yields an affine function with respect to  $x$  and  $u$ . The partial derivatives give the linear proportionality constants with respect to changing  $x$  and  $u$ , and  $g$  evaluated at the OP gives a constant displacement. For a vector valued function these scalar expressions turn into two matrices and a vector.

The Taylor expansion for a *vector valued function* becomes more complex, with the simple partial derivatives turning into Jacobi-Matrices (see Appendix B), and the scalar

#### 4. Models for control purpose – system identification results

displacement becomes a displacement vector:

$$\dot{\mathbf{x}} = \mathbf{g}(\mathbf{x}_0, \mathbf{u}_0) + \frac{\partial}{\partial \mathbf{x}} \mathbf{g}(\mathbf{x}_0, \mathbf{u}_0) (\mathbf{x} - \mathbf{x}_0) + \frac{\partial}{\partial \mathbf{u}} \mathbf{g}(\mathbf{x}_0, \mathbf{u}_0) (\mathbf{u} - \mathbf{u}_0) + \mathcal{O}(x^2) + \mathcal{O}(u^2). \quad (4.18)$$

To identify the elements of the resulting affine model requires some rearrangement.

$$\dot{\mathbf{x}} \approx \underbrace{\frac{\partial}{\partial \mathbf{x}} \mathbf{g}(\mathbf{x}_0, \mathbf{u}_0)}_{\mathbf{A}(\mathbf{x}_0, \mathbf{u}_0)} \mathbf{x} + \underbrace{\frac{\partial}{\partial \mathbf{u}} \mathbf{g}(\mathbf{x}_0, \mathbf{u}_0)}_{\mathbf{B}(\mathbf{x}_0, \mathbf{u}_0)} \mathbf{u} + \underbrace{\mathbf{g}(\mathbf{x}_0, \mathbf{u}_0) - \frac{\partial}{\partial \mathbf{x}} \mathbf{g}(\mathbf{x}_0, \mathbf{u}_0) \mathbf{x}_0 - \frac{\partial}{\partial \mathbf{u}} \mathbf{g}(\mathbf{x}_0, \mathbf{u}_0) \mathbf{u}_0}_{\mathbf{r}(\mathbf{x}_0, \mathbf{u}_0)}. \quad (4.19)$$

The linearized affine SSM dynamic equation with the constant vector  $\mathbf{r}(\mathbf{x}_0, \mathbf{u}_0)$  finally reads

$$\dot{\mathbf{x}}(t) = \mathbf{A}(\mathbf{x}_0, \mathbf{u}_0) \mathbf{x}(t) + \mathbf{B}(\mathbf{x}_0, \mathbf{u}_0) \mathbf{u}(t) + \mathbf{r}(\mathbf{x}_0, \mathbf{u}_0). \quad (4.20)$$

Such a linearized model may be utilized by the MPC. Concerning the OP  $(\mathbf{x}_0, \mathbf{u}_0)$ , it must be decided whether one global linearization or repeated local linearization is conducted. Local linearization means, repeated linearization at the current OP when the MPC routine is called.

#### The linearization stages in detail – exemplification

With reference to the general storage model derived in sec. 4.4.1,  $\mathbf{g}(\mathbf{x}, \mathbf{u})$  from eq. (4.16) may be identified as the RHS of eq. (4.14) divided by the according thermal heat capacity. In the following the linearization of the first line of this general model is exemplified, which leads to the first line of the vector valued eq. (4.20). To this end a relatively simple function for  $\dot{C}$  and a constant compressor frequency  $f_0$  are assumed for simplicity, all *assumptions* made read:

$$\dot{C} := c_p (k_1 + k_2 \vartheta_{ci}), \quad \vartheta_{ci} = \vartheta_3, \quad f_0 = \text{const.}, \quad Q_{aux,1,0} = 0, \quad \vartheta_{do} = \vartheta_{do,0}, \quad C_1 = 1. \quad (4.21)$$

The first component of  $\mathbf{g}$  namely  $g_1$  is obtained by dividing the first line of eq. (4.14) by  $C_1 = 1$  (for simplicity). Inserting the expression for  $\dot{C}$  from eq. (4.21) into the resulting equation one gets:

$$g_1 = UA_1(\vartheta_{env} - \vartheta_1) - UA_{\lambda,2}(\vartheta_1 - \vartheta_2) + (c_p (k_1 + k_2 \vartheta_3))(\vartheta_{do} - \vartheta_1) + \dot{Q}_{aux,1}. \quad (4.22)$$

This expression evaluated at a specific OP  $(\mathbf{x}_0, \mathbf{u}_0)$ , leads to  $g_1(\mathbf{x}_0, \mathbf{u}_0)$  or short  $g_{1,0}$ :

$$g_{1,0} = UA_1(\vartheta_{env,0} - \vartheta_{1,0}) - UA_{\lambda,2}(\vartheta_{1,0} - \vartheta_{2,0}) + (c_p (k_1 + k_2 \vartheta_{3,0}))(\vartheta_{do,0} - \vartheta_{1,0}). \quad (4.23)$$

The next step is to apply the partial derivatives with respect to  $\vartheta_1, \vartheta_2$  and  $\vartheta_3$  on  $g_1$  from eq. (4.22) – this corresponds to the first line of the Jacobi-Matrix  $\mathbf{J}_x$ , compare eq. (B.27).

#### 4.4. Thermal storage with heat pump – controller model

Evaluation of the resulting row vector at the OP leads to the elements of the first row of  $\mathbf{A}(\mathbf{x}_0, \mathbf{u}_0)$

$$a_{11} = -UA_1 - UA_{\lambda,2} - k_1 - \vartheta_{3,0}k_2, \quad a_{12} = UA_{\lambda,2}, \quad a_{13} = -k_2(\vartheta_{1,0} - \vartheta_{do,0}). \quad (4.24)$$

Similarly the partial derivatives are applied with respect to all input or disturbance variables – here  $\mathbf{u} = [f, \vartheta_{env}, Q_{aux,1}, Q_{aux,2}, Q_{aux,3}]^T$  – and the resulting row vector must also be evaluated at the OP. This gives the elements of the first row of  $\mathbf{B}(\mathbf{x}_0, \mathbf{u}_0)$

$$b_{11} = 0, \quad b_{12} = UA_1, \quad b_{13} = 1, \quad b_{14} = 0, \quad b_{15} = 0. \quad (4.25)$$

The procedure explained in the last paragraph must be repeated for  $g_2$  and  $g_3$ , which are obtained from the second and the third row of eq. (4.14). This leads to all components of the dynamic matrix  $\mathbf{A}(\mathbf{x}_0, \mathbf{u}_0)$  and the input matrix  $\mathbf{B}(\mathbf{x}_0, \mathbf{u}_0)$ . To obtain the displacement vector  $\mathbf{r}(\mathbf{x}_0, \mathbf{u}_0)$  of the affine model it is necessary to evaluate the dynamic and the input matrix at  $\mathbf{x}_0$  and  $\mathbf{u}_0$  and subtract the resulting vectors from  $\mathbf{g}(\mathbf{x}_0, \mathbf{u}_0)$ , compare eq. (4.19).

#### 4.4.3. Hybrid approach for the TES-HP model

The term *hybrid* in this context refers to a combination of at least two models. Assume the whole operational range to be defined by all possible model states expressed as  $\mathbf{X}$  together with all possible model inputs  $\mathbf{U}$  – here input refers to the manipulated and the disturbance variables. A hybrid model approach switches between at least two *sub-models*  $\mathcal{M}_1, \mathcal{M}_2$  depending on the *current* operational conditions ( $\mathbf{x} \in \mathbf{X}, \mathbf{u} \in \mathbf{U}$ ).

The *free floating storage* may be modeled with a simple linear SSM which is obtained by setting  $\dot{C} = 0$  in eq. (4.14) as explained in sec. 4.4.1 – see also the derivation in Pichler et al. (2014). This linear model for the free-floating operation of the TES is indicated by  $\mathcal{M}_1$  in the following.

The operation where the *HP supplies* the thermal storage with heat requires initially a non-linear approach – the non-linearity in eq. (4.14) arises with  $\dot{C} > 0$ . This capacity flow rate may take a general form as indicated by eq. (4.15). Given a certain expression for  $\dot{C}$  as for example in eq. (4.21) and a linearization point in terms of  $\mathbf{x}_0$  and  $\mathbf{u}_0$ , the dynamic matrix  $\mathbf{A}$ , the input matrix  $\mathbf{B}$  and the affine displacement vector  $\mathbf{r}$  may be calculated. This is finally the *linearized* version of the non-linear model describing the storage heating by means of the HP, it is indicated by  $\mathcal{M}_2$  in the following.

The hybrid model results from the combination of the storage operational modes free floating:  $\mathcal{M}_1$ , and heating by means of the HP:  $\mathcal{M}_2$ . Depending on the current value of  $\dot{C}$  either  $\mathcal{M}_1$  or  $\mathcal{M}_2$  should be utilized. The realization of this switching between two different models is straight forward. In general the switching may be triggered through  $\mathbf{x}$  or through  $\mathbf{u}$ . We assume  $\mathbf{U} = \mathbf{U}_1 \cap \mathbf{U}_2$ , where  $\mathbf{U}_1$  includes all possible inputs with

#### 4. Models for control purpose – system identification results

$\dot{C} = 0$  and  $\mathbf{U}_2$  includes all possible inputs with  $\dot{C} > 0$ . Then the switching between the free-floating mode  $\mathcal{M}_1$  and the HP heating mode  $\mathcal{M}_2$  may be written as

$$\mathcal{M}_1 := [\dot{\mathbf{x}}(t) = \mathbf{A} \mathbf{x}(t) + \mathbf{B} \mathbf{u}(t)] \quad \text{use } \mathcal{M}_1 \text{ if } \mathbf{u} \in \mathbf{U}_1, \quad (4.26)$$

$$\mathcal{M}_2 := [\dot{\mathbf{x}}(t) = \mathbf{A}(\mathbf{x}_0, \mathbf{u}_0) \mathbf{x}(t) + \mathbf{B}(\mathbf{x}_0, \mathbf{u}_0) \mathbf{u}(t) + \mathbf{r}(\mathbf{x}_0, \mathbf{u}_0)] \quad \text{use } \mathcal{M}_2 \text{ if } \mathbf{u} \in \mathbf{U}_2. \quad (4.27)$$

#### 4.4.4. Discretization and valid model range

The sub-models  $\mathcal{M}_1$  and  $\mathcal{M}_2$  of the hybrid approach for the controller model are relatively simple in terms of modeling of the various physical phenomena. However, it is necessary to obey a few rules in order to obtain a reasonable model behavior and a suitable performance. In principle a model can be tailored to fit the requirements given by the control task, but it is important to consult theoretical limitations concerning temporal and spatial resolution when carrying out the discretization.

The hybrid storage model must capture heat conduction and forced flow for the inside medium, and natural flow and radiation to the environment. To be precisely it is also desirable to capture natural circulation in case of inversion of the thermal energy storage (water) stratification, however, in the given set-up a temperature inversion in the controller storage model is nearly impossible. This is why natural circulation is neglected. All heat transfer phenomena except for the forced circulation inside the storage are modeled by means of overall heat transfer coefficients ( $U$ ).

The temporal resolution for the hybrid model is naturally predefined by the minimum operation time of the HP, however, in principle a higher resolution is possible. With increasing temporal resolution the computational effort for the solution of the optimization problem increases. Hence, in order to solve this problem within a reasonable time it is important to chose a relatively high sampling time.

The spatial resolution is limited due to the forced circulation or convection and follows naturally from the temporal resolution given a certain flow rate inside the storage. Assume the sampling time  $\Delta t_s$  to be given, then the Courant-Friedrichs-Lewy (*CFL*)-number (Oertel et al., 2011) restrains the maximum spatial resolution. Assume only one spatial dimension  $z$ , and think of a specific mass flow rate  $\dot{m}_z$  (for simplicity instead of  $\dot{m}_z$ ,  $\dot{m}$  is written in context of the TES, cf. fig. 4.14). The *CFL*-number provides a measure for the *movement of the flow in terms of cells during one time step*

$$\boxed{CFL := \frac{w}{(\Delta z / \Delta t_s)} \leq 1 \quad \text{with} \quad w := \frac{\dot{m}_z}{r^2 \pi},} \quad (4.28)$$

with  $r$  being the radius of the cylindrical TES tank. If the condition  $CFL \leq 1$  is not met, the model will produce incorrect results. In other words, during one calculation step

#### 4.4. Thermal storage with heat pump – controller model

the maximum mass flow that can be captured is limited to the equivalent flow of one cell. Tab. 4.11 provides the *CFL*-numbers for a TES model with three and five nodes, as a function of the sampling time  $\Delta t_s$  for two different mass flow rates, respectively.

Table 4.11.: *CFL* numbers for different spatial- and temporal-discretizations for the hybrid TES-HP model. The bold *CFL* number relates to the higher mass flow rate.

No. of nodes	3 nodes ( $\Delta z = 0.6$ m)			5 nodes ( $\Delta z = 0.36$ m)		
$\dot{m}_z$	300 / <b>500</b> kg/h			300 / <b>500</b> kg/h		
$\Delta t_s$	10 min	20 min	30 min	10 min	20 min	30 min
<i>CFL</i>	0.3 / <b>0.5</b>	0.6 / <b>1.0</b>	0.9 / <b>1.5</b>	0.5 / <b>0.83</b>	1 / <b>1.67</b>	1.5 / <b>2.5</b>

As sampling time 20 min is chosen; with 10 min the computing time for a prediction horizon of 12 h increases enormously. Consulting fig. 2.13 it is reasonable to focus on the higher mass flow rate (500 kg/h) from tab. 4.11. However, only the simulation will show the occurring maximum  $\dot{m}_z$  during the loading process of the storage. Given these boundary conditions only the three nodes model with  $\Delta z = 0.6$  m is able to capture the desired flow rate from a theoretical point of view.

#### 4.4.5. Model performance and validation

A few model evaluation experiments are now presented to demonstrate the performance and the weakness of different forms of the hybrid model. The main variations between the selected examples refer to the linearization point (OP), the number of nodes and the temporal resolution. In all examples the hybrid controller model is compared against results from a TRNSYS simulation of a HP connected to a storage, compare with fig. 2.8. The used TRNSYS models are type887 (Dott et al., 2012), and type534 from the TESS library (TRNSYS 17), cf. sec. 2. The TRNSYS storage model has 30 nodes (states) and the simulation time step is 2 min (opposed to the TES-HP model which is discretized with 20 min sampling time).

The hybrid model TES-HP describes the physical behavior of the storage and the HP connected to it. The selected performance measures concern the storage temperatures, the total supplied energy and the mass flow rate. For each comparison-measure the *mean* and the *standard deviation* of the error

$$\varepsilon(y, t) = y_{NL-SSM}(t) - y_{TRNSYS}(t) \quad \text{with} \quad y \in \{\vartheta_i, \dot{m}, \dot{Q}_{HP}\} \quad (4.29)$$

are provided. That is, e.g. a mean negative error for a certain temperature node indicates that the hybrid non-linear SSM (NL-SSM) underestimates the node temperature if compared against the equivalent TRNSYS (representative mean) TES temperature. The interpretation of the error for the variables  $\dot{m}$  and  $\dot{Q}_{HP}$  is similar. In the following the acronym NL-SSM for  $n = 3$  is in principal equivalent to the final TES-HP model.

#### 4. Models for control purpose – system identification results

##### Free floating and auxiliary heating – exp.1

The first evaluation concerns auxiliary heating and free-floating. All heat transfer related parameters are the same for the TRNSYS storage model and the NL-SSM<sup>8</sup>. Fig. 4.15 shows the five temperatures of the NL-SSM in solid lines, the highest trajectory refers to  $\vartheta_1$ , the lowest trajectory to  $\vartheta_5$  (cf. fig. 4.14 and imagine the whole storage divided to 5 nodes). TRNSYS model average temperatures are depicted in dash-dotted lines.

After initialization with 20 °C the temperature stays the same for all nodes during the first hour, this is because the environment temperature is also constantly 20 °C. After that *auxiliary heating* is provided. During this stage each of the NL-SSM nodes  $n = 1, 2, \dots, 5$  is supplied with a certain auxiliary heating power  $Q_{aux,n}$ . At the same time selected nodes of the TRNSYS storage model – with the nodes  $m = 1, 2, \dots, 30$  from top to bottom – receive in total the same amount of heating energy. For example  $Q_{aux,1}$  is supplied at  $m = 4$ , and  $Q_{aux,2}$  is supplied at  $m = 10$  and so forth. The auxiliary heating stops at the fourth hour, leading again to free floating with losses against the environment.

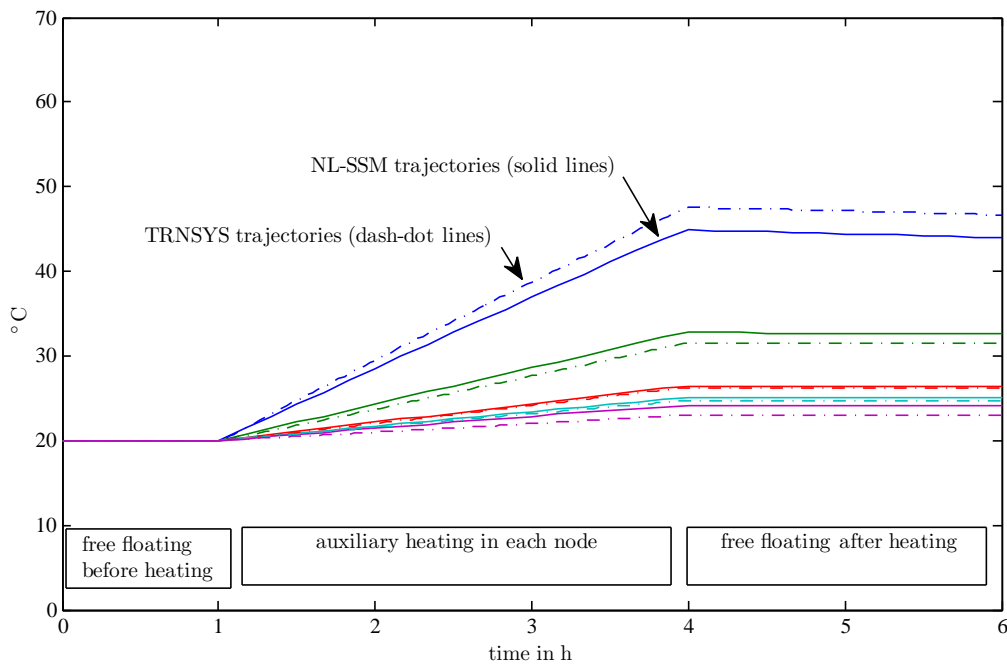


Figure 4.15.: Validation of auxiliary heating and free floating operation covered by  $\mathcal{M}_1$  of the hybrid approach from sec. 4.4.3, solid lines refer to the temperatures of the NL-SSM and dashed lines to the TRNSYS model equivalent temperatures with  $\vartheta_1$  from top to the bottom  $\vartheta_5$ , respectively;  $n = 5$  – exp.1.

<sup>8</sup> In principle it is possible to fit the NL-SSM parameters, potentially this leads to an improvement of the model.

#### 4.4. Thermal storage with heat pump – controller model

For the *temperature evaluation* over all six hours the temperature of say node  $n = 5$  is compared against the average temperature of the TRNSYS nodes extending over the same vertical section, in this case the nodes  $m = 25, \dots 30$ . Quantitative results for this experiment (exp.1) are listed in tab. 4.12. The NL-SSM underestimates the temperature in the top node, but overestimates the temperatures for all other nodes. However, the average temperature of the fully mixed storage ( $\bar{\theta}_i$ ) is nearly the same for the NL-SSM and the TRNSYS model cf. row six in tab. 4.12.

#### Free floating and HP operation

The main challenge concerning the hybrid model, composed by the free-floating model  $\mathcal{M}_1$  and  $\mathcal{M}_2$ , poses the HP operation mode  $\mathcal{M}_2$ . It was demonstrated that the pure free floating operation is quite similar to TRNSYS, however, such a result is not expected for  $\mathcal{M}_2$ . For the following simulation experiments *the quadratic mass flow model* depicted in fig. 2.21 was facilitated for  $\mathcal{M}_2$ , compare with eq. (4.15). The temperature linearization points were chosen 20 °C for every node or model state.

#### Operation close to the linearization frequency – exp.2

Fig. 4.18 demonstrates the performance of the NL-SSM when operating close to the frequency linearization point being 60 Hz. During the first half hour after switching on the HP the temperature of the top node deviates only slightly to the TRNSYS average temperature of the same vertical section. The individual NL-SSM temperature trajectories clearly show deviations up to 5 K to the TRNSYS average temperatures, however, the fully mixed storage temperature is nearly the same as for the TRNSYS storage model. In addition, the amount of energy supplied to the storage over the six hours deviates only by 7%. Also the mass flow is very accurate compared to TRNSYS. Tab. 4.12 provides more quantitative details to exp.2.

#### Operation further away from the linearization frequency – exp.3

The similarity of the NL-SSM temperatures and the TRNSYS average temperatures diminishes with increasing deviation of the actual compressor frequency from the linearization frequency. This is demonstrated by fig. 4.19. However, the difference between the fully mixed storage temperatures is still only 0.7 K, and the energy supply to the storage over the six hours deviates also only by 5% with respect to the totally supplied amount of energy during this six hours, compare with tab. 4.12. The mass flow error slightly increases compared to exp.2.

## 4. Models for control purpose – system identification results

### Operation close to the linearization frequency, three nodes – exp.4

Fig. 4.16 demonstrates the results for the hybrid (linearized) NL-SSM with three nodes (=TES-HP) for a sampling time of  $\Delta t_s = 20$  min. The results for a temporal resolution of  $\Delta t_s = 10$  min and  $\Delta t_s = 30$  min are very similar. In comparison to fig. 4.18 showing the results for five thermal nodes, the difference of the top temperature to the TRNSYS average value is higher for the three node model, and the bottom temperature is significantly overestimated. However, during the first hour of HP operation the similarity for the top and the bottom node between the hybrid NL-SSM (TES-HP) and the average TRNSYS temperatures is very good, especially during the first 45 min. The top and the bottom node are the most important, because the top temperature will be the controlled variable later, and the bottom temperature is a significant variable in the derivation of the mass flow rate or the capacity flow rate, compare with eq. (4.15). Tab. 4.12 provides further quantitative evaluation measures.

### Repetition of exp.4 with $\mathcal{M}_2$ only – exp.5

To investigate the relevance of a hybrid approach the six hour interval was repeated making use of  $\mathcal{M}_2$  only, that is it is not switched to a different model during the free floating operation. A good performance would allow to put aside the hybrid approach, which leads to a substantial reduction of the computing time during the optimization runs. However, as fig. 4.17 demonstrates, the performance of  $\mathcal{M}_2$  during the floating periods is really not sufficient.

#### 4.4.6. Linearization point and $\dot{C}$ -model

The linearization point or OP of the NL-SSM, which is the necessary consequence to arrive at a linear model for the MPC, may have an impact on the final performance of the hybrid model. Consulting sec. 4.4.2 one finds that the linearization is conducted around the compressor frequency  $f_0$ , around all storage temperatures  $\vartheta_{i,0}$  and around the HP outlet temperature  $\vartheta_{do,0}$  which was assumed to be constant anyway.

Concerning this linearization no rigorous analysis was conducted. A few experiments concerning the frequency and the storage temperatures provided some insight. There is a natural tendency, that linearization close to the operation frequency leads to the best results. As the frequency is significantly above the linearization frequency and in parallel the HP thermal output, the very top temperatures in the storage are clearly overestimated. The reason may either be the  $\dot{C}$ -model or something else (e.g. the limited spatial discretization which causes the lowest storage temperature to increase faster and hence the HP output temperature is too high).

#### 4.4. Thermal storage with heat pump – controller model

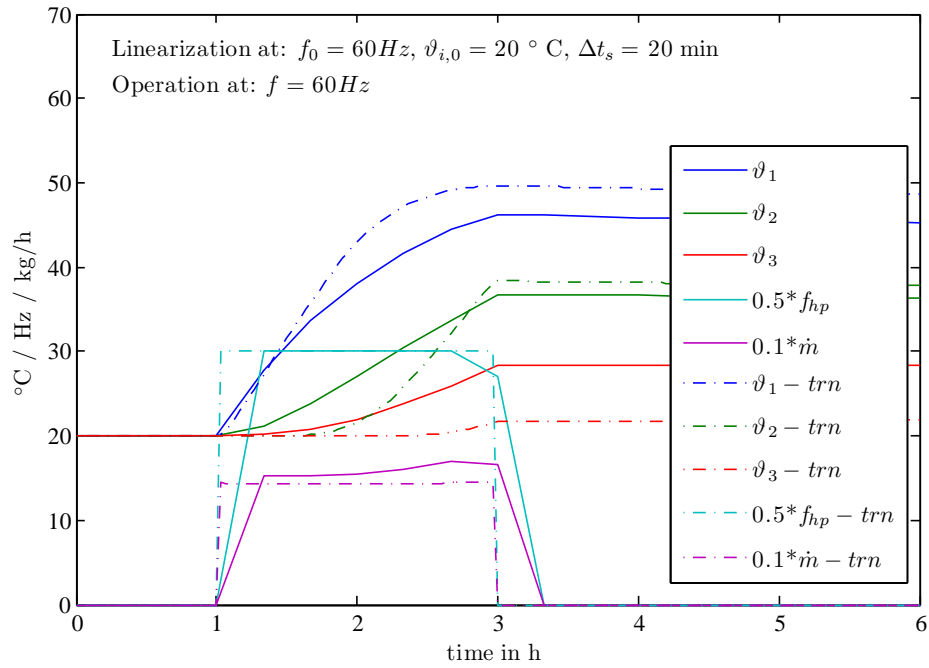


Figure 4.16.: TES-HP model, validation of HP operation at 60 Hz and free floating modeled by means of the hybrid approach according to sec. 4.4.3 with  $n = 3$  - exp.4.

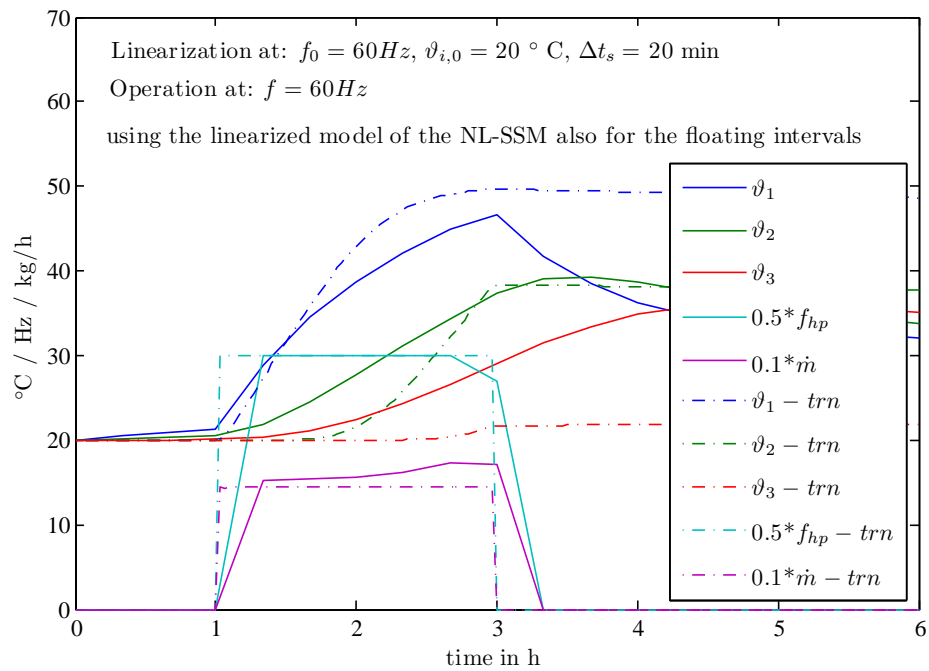


Figure 4.17.: Validation of HP operation at 60 Hz and free floating modeled by  $\mathcal{M}_2$  only, see sec. 4.4.3 with  $n = 3$  - exp.5.

#### 4. Models for control purpose – system identification results

Observance of the facts learned from the frequency linearization, and using average prediction interval temperatures – resulting from a first trial with 20 °C as initial temperatures – as linearization point, an improvement in terms of the energy accuracy or mean temperature deviation is possible. However, single temperatures such as the top or the bottom temperature may show increased errors. Especially for the five node model the performance improves when the model is linearized around the average temperatures, but for the three node model the improvement is not significant.

Concerning the  $\dot{C}$ -model approach as given by eq. (4.15), the pure bi-linear model (investigated initially but not documented herein) is worse compared to a *quadratic approach*. The  $\dot{m}$  errors from tab. 4.12 more than doubles and the standard deviation increases by approximately a factor of 1.5 – for operation close to the frequency linearization point. However, it is difficult to say whether this performance difference will have an impact on the final operation performance of the MPC, to judge on this simulations are required. The advantage of the simplified  $\dot{C}$ -model is more than two times less computation time required for the optimization runs.

Finally, 60 Hz and 20 °C for all nodes were selected as linearization point. The 20 °C proved to be the most suitable value from an overall perspective. Higher linearization temperatures caused MPC parametrization problems, because with a higher linearization temperature there was a tendency visible that the TES temperatures reached too high values over the prediction horizon. The following gives a vague first assumption for this. It is assumed, that the 20 °C opposed to a higher linearization temperature bring "additional numerical diffusion" into the model, which stabilizes the model or makes it "slower" in terms of heating up. This assumption is borrowed from theory on numerical schemes in context of more dimensional heat conduction, where (numerical) diffusion leads to stabilization and eases convergence.

Table 4.12.: Quantitative evaluation of the hybrid controller model performance. Mean ( $\bar{\epsilon}$ ) and empirical standard deviation ( $s$ ) of the calculated error according to eq. (4.29); for the quadratic mass flow model cf. fig. 2.21.

exp. No $f / \Delta t_s$	Linearization conditions $\vartheta_{i,0} = 20 \text{ }^\circ\text{C}$ , $f_0 = 60 \text{ Hz}$			
	exp.1 0 Hz / 10 min	exp.2 58.5 Hz / 10 min	exp.3 80 Hz / 10 min	exp.4 60 Hz / 20 min
$\bar{\epsilon}(\vartheta_1) \pm s, \text{ K}$	$-1.6 \pm 1.1$	$-1.8 \pm 1.5$	$5.0 \pm 3.9$	$-2.7 \pm 1.8$
$\bar{\epsilon}(\vartheta_2) \pm s, \text{ K}$	$0.8 \pm 0.5$	$-2.1 \pm 2.9$	$1.4 \pm 2.0$	$0.1 \pm 2.2$
$\bar{\epsilon}(\vartheta_3) \pm s, \text{ K}$	$0.1 \pm 0.1$	$0.7 \pm 1.9$	$-2.1 \pm 2.5$	$4.1 \pm 2.9$
$\bar{\epsilon}(\vartheta_4) \pm s, \text{ K}$	$0.2 \pm 0.1$	$3.8 \pm 2.6$	$-1.6 \pm 2.4$	-
$\bar{\epsilon}(\vartheta_5) \pm s, \text{ K}$	$0.7 \pm 0.5$	$3.0 \pm 2.4$	$1.0 \pm 0.8$	-
$\bar{\epsilon}(\bar{\vartheta}_i) \pm s, \text{ K}$	$0.1 \pm 0.0$	$0.7 \pm 0.4$	$0.7 \pm 0.4$	$0.5 \pm 0.3$
$\Delta Q, \text{ kWh}$	0	0.4 or 7%	0.4 or 5%	0.3 or 5%
$\bar{\epsilon}(\dot{m}) \pm s, \text{ kg/h}$	-	$7.0 \pm 21.8$	$10.1 \pm 33.9$	$12.4 \pm 37.1$

#### 4.4. Thermal storage with heat pump – controller model

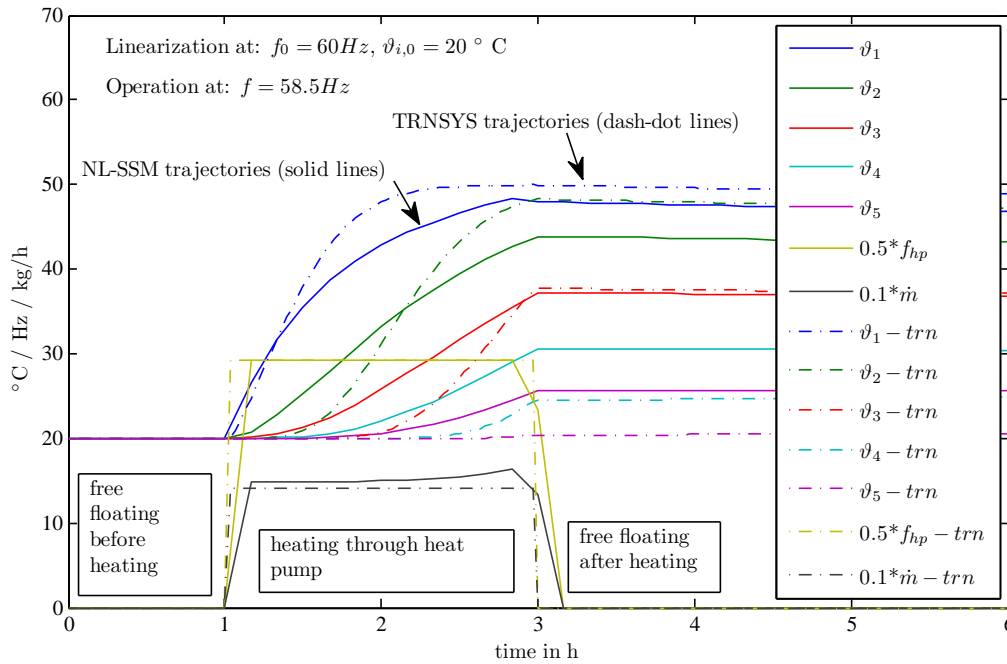


Figure 4.18.: Validation of HP operation at 58.5 Hz and free floating modeled by means of the hybrid approach according to sec. 4.4.3;  $n = 5 - \text{exp.2}$ .

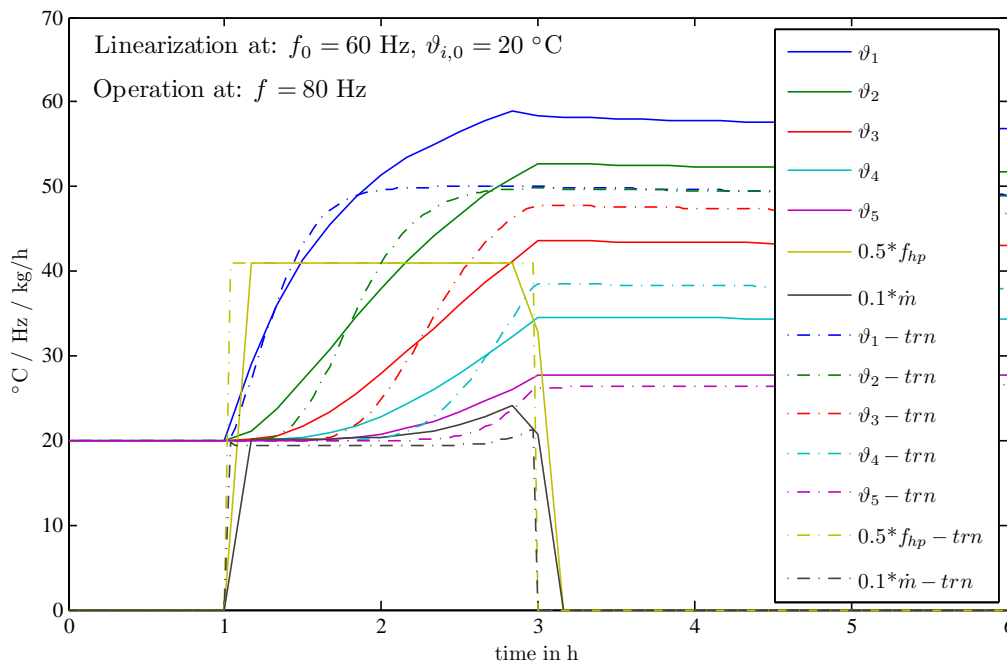


Figure 4.19.: Validation of HP operation at 80 Hz and free floating modeled by means of the hybrid approach according to sec. 4.4.3;  $n = 5 - \text{exp.3}$ .



## 5. Model predictive control

*A general introduction to MPC was already provided in ch. 1. The three main ingredients from a methodological point of view are: a model, a suitable objective or cost function and an optimization algorithm. The best models found for the MPC-Boxes- and the TheBat-building are given in ch. 4, as well as the controller model derived for the TES of the TheBat reference system.*

*This chapter deals with the formulation and explanation of the objective function. Further, it introduces the subject state estimation, which may be required to initialize the optimization if specific states of the controller model are not directly measurable. The topic optimization is only briefly touched towards the end of this chapter.*

### 5.1. Simple temperature control – MPC-Boxes

A room temperature control by means of a model predictive controller (MPC) consists of a simple optimization problem with only one manipulated variable  $u$ , representing e.g. the heat flux to the TABS for the project MPC-Boxes. For the current example the controller model is that from sec. 4.1.1. This model describes the thermal dynamic by means of three states: the ceiling concrete temperature (which is the TABS), the room-air and the floor (concrete)-temperature. In this context all non-controllable inputs are isolated from  $\mathbf{u}$  and treated as disturbances summarized in  $\mathbf{v}$ . The objective function which builds upon the controller model, together with further constraints, is given in eq. (5.1), compare with Cigler et al. (2013).

The receding finite horizon implementation is realized by continuously searching for the minimum of the objective function  $J$ . This is an open-loop optimization problem, however, the feedback is introduced by means of the initial state  $\mathbf{x}_1$  which is repeatedly updated with real measurement values<sup>1</sup> before every optimization run. The *prediction horizon*  $N_p$  is the forecast in terms of calculation steps for the system states and outputs, cf. fig. 1.3. The *control horizon*  $N_c$  is the time window for which the manipulated variable changes dynamically subject to specific constraints or rules. Hence, a sensible problem requires  $N_p > N_c$ .

---

<sup>1</sup> In case not for every single state a measurement value exists, a state estimator is required – this topic is elaborated on in sec. 5.4.

## 5. Model predictive control

### 5.1.1. Objective function and constraints

The objective function<sup>2</sup> for the simple temperature control with two comfort zones (funnels) and the required constraints are given by eq. (5.1). The constraint formulation is written down twofold, on the left with abstract canonical terms and on the right with physical terms relating to the control of the MPC-Boxes building.

$$\min_{\mathbf{u}, \mathbf{e}, \mathbf{e}^c} J(\mathbf{u}, \mathbf{e}, \mathbf{e}^c) = \sum_{i=1}^{N_C < N_P} \underbrace{R |u_i| + S |u_i|^2}_{\text{energy terms}} + \sum_{i=1}^{N_P-1} \underbrace{Q |e_{i+1}|^2 + Q^c |e_{i+1}^c|^2}_{\text{comfort terms}}, \quad (5.1)$$

subject to

$\mathbf{x}_{i+1} := \mathbf{A}\mathbf{x}_i + \mathbf{B}_u u_i + \mathbf{B}_v \mathbf{v}_i,$ <p>abstract formulation:</p> $\mathbf{y}_i = [0 \ 1 \ 0] \mathbf{x}_i$ $u_{min} \leq u_i \leq u_{max}$ $y_{min} - e_i \leq y_i \leq y_{max} + e_i$ $y_{min}^c - e_i^c \leq y_i \leq y_{max}^c + e_i^c$ $0 \leq e_i$ $0 \leq e_i^c$	$\mathbf{x}_1 \text{ is given from "measurements"}$ <p>or in terms of the physical pendants:</p> $\vartheta_{ra,i} = 0 \cdot \vartheta_{ta,i} + 1 \cdot \vartheta_{ra,i} + 0 \cdot \vartheta_{fl,i}$ $\dot{q}_{ta,min} \leq \dot{q}_{ta,i} \leq \dot{q}_{ta,max}$ $\vartheta_{ra,min} - e_i \leq \vartheta_{ra,i} \leq \vartheta_{ra,max} + e_i$ $\vartheta_{ra,min}^c - e_i^c \leq \vartheta_{ra,i} \leq \vartheta_{ra,max}^c + e_i^c$ $0 \leq e_i$ $0 \leq e_i^c.$
---	--

The weights  $R$ ,  $S$ ,  $Q$  and  $Q^c$  refer to the individual costs for the linear energy term, the smoothing term  $S |u_i|^2$  and the violation of the inner and the outer comfort zone. The smoothing term weight must be much smaller than  $R$  and  $Q^c \gg Q$ . The building dynamic for the simple MPC-Boxes building is incorporated by means of a SSM, that is described in sec. 4.1.1. The thermal comfort is assured through an inner and an outer (comfort) zone, each indicated by an upper and a lower limit, compare dotted lines in fig. 5.2. The inner limits should not be violated and the outer limits must not be violated. These comfort zones are implemented by means of *slack variables* ( $e$ ,  $e^c$ ) which relax or expand the parametrized limits, however, this relaxation increases the value of the cost function  $J$ , as is explained in detail in the following.

The implementation is rather simple and the computational effort to solve the minimization task for the given objective function is comparable low. As discussed in sec. 5.5 the minimization requires the solution of a constrained quadratic program (QP) see e.g. Maciejowski (2002).

<sup>2</sup> Because  $J$  is a function of functions, the precise mathematical term should be *functional*, but for sake of simplicity this subtlety is neglected.

### 5.1.2. An optimization run in slow motion

To understand the objective function with its constraints it is sensible to use a supportive example with practical reference. By contrast to the detailed description of single steps during the solving process, the flow chart in fig. 5.1 explains the contextual boundaries. Lets start with the MPC operation of a building at some winter day at 12:00 noon. Before starting an optimization run the currently available and required temperature measurement values are provided as initial conditions  $\mathbf{x}_1$ . Lets further assume a prediction ( $N_p$ ) horizon of 24 h and a control horizon ( $N_c$ ) of (24-1) h, and for simplicity a sampling time of 1 h. This implies the availability of disturbance data  $\mathbf{v}$  (outside ambient temperature, solar radiation, etc.) for the next (24-1) h. The term *limits* in the flow chart in fig. 5.1, summarizes those inputs to the MPC routine which represent variable constraints that may change from one call to another (e.g. heating power limits, comfort limits).

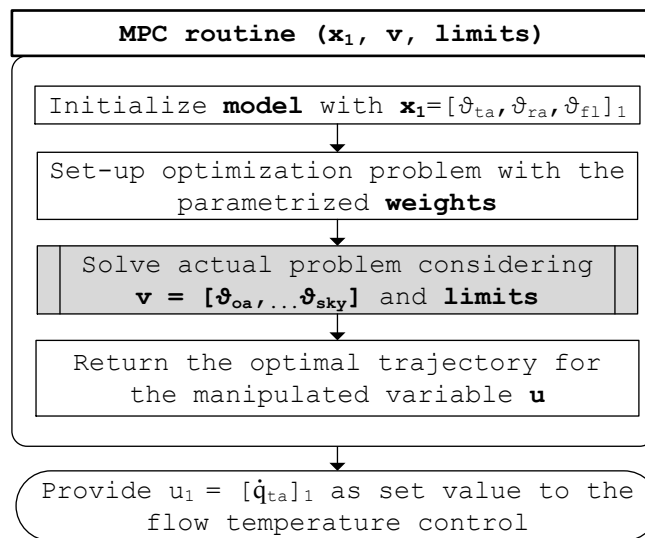


Figure 5.1.: Flow chart describing the principal steps of the MPC routine for a simple model predictive control with the task to maintain the room air temperature by adjusting the heating power; to distinguish the disturbances ( $\mathbf{v}$ ) from the manipulated variable ( $\dot{q}_{ta}$ ),  $\mathbf{u}$  as defined in sec. 4.1.1 is split into  $\mathbf{v}$  and  $\dot{q}_{ta}$ .

Now, the task for the MPC is to find the currently optimal value for the manipulated variable ( $u_1$ ) – the heat flux supplied to the TABS – under the perspective of looking 24 h ahead. Lets focus on solving a specific problem and what is happening in the gray box in fig. 5.1. To this end, the attention is given to a certain time step  $i$  of the prediction horizon. The most important is the value of the controlled variable  $y_i$  referring to the room air temperature  $\vartheta_{ra,i}$ . The aim is to keep this temperature within the inner comfort zone defined by  $y_{min}$  and  $y_{max}$ . If the temperature lies e.g. 2 K below  $y_{min}$ , the variable  $e_i$  must relax the comfort zone by 2 K in order to meet the constraint

## 5. Model predictive control

$y_{min} - e_i \leq y_i \leq y_{max} + e_i$ . However, this increases the objective function value by  $Q|2|^2$ . The only possible counteraction to this violation, is to increase the manipulated variable<sup>3</sup>  $u_i$  ( $\dot{q}_{ta,i}$ ), but in parallel the linear energy term increases. The challenge lies in the proper adjustment of the weights such that the comfort is sustained with minimum energy utilization.

The characteristic controller behavior related to the second, outer comfort zone with the weight  $Q^c$  is the same, however, a relaxation of the zone limits  $y_{min}^c$  and  $y_{max}^c$  costs much more and is thus very unlikely. The quadratic energy term  $S|u_i|^2$  is optional. It may be added with very low weight in order to smooth the manipulated variable, that is, to avoid a highly fluctuating manipulated variable. Finally, roughly speaking the optimal trajectory for the heating power  $\mathbf{u}$  results from the result of 23 decisions as explained in the last paragraph.

Fig. 5.2 shows exemplary heating simulation results over one week. The upper graph depicts the trajectories for the ceiling-TABS (5 cm layer depicted in fig. D.3), the room air and the floor (concrete) temperatures. The dotted lines indicate the inner and outer comfort zone. The room air temperature (black line), peaking during the day due to the external solar and the internal gains, barely goes below the inner comfort zone – which is desired. The only exception are the first 10 h, where the temperature lies below both comfort zones, during these hours the controller reacts with the maximum available power.

### 5.2. PV-led heat pump control for space heating (TABS-MPC)

In the last section the task of the simple model predictive temperature controller was, to sustain the thermal comfort with utilization of a minimum amount of energy. The possible values for the manipulated variable – the supplied heat flux – ranged from zero to a maximum value which is determined by the highest possible/allowed flow-temperature. The control task in this section incorporates also characteristics of the heat generation system (a HP) and an additional objective is the forced operation of this system at times where solar radiation is available. This objective originates from the requirement to maximize the PV self consumption, that is, PV electricity generated on site should not be feed into the grid but consumed by the HP.

Assume a HP with variable compressor speed within a certain range  $f_{min}, \dots, f_{max}$ , then the possible variable range for the thermal output  $\dot{Q}_{HP}$ , being a function of the compressor speed  $f$  and the (water) condenser inlet temperature  $\vartheta_{ci}$ , becomes

$$\dot{Q}_{HP} \in \{0, \dot{Q}_{min}(f_{min}, \vartheta_{ci}), \dots, \dot{Q}_{max}(f_{max}, \vartheta_{ci})\}. \quad (5.2)$$

<sup>3</sup> Precisely, only  $u_{i-1}$  is viable to increase the controlled variable  $y_i$ .

## 5.2. PV-led heat pump control for space heating (TABS-MPC)

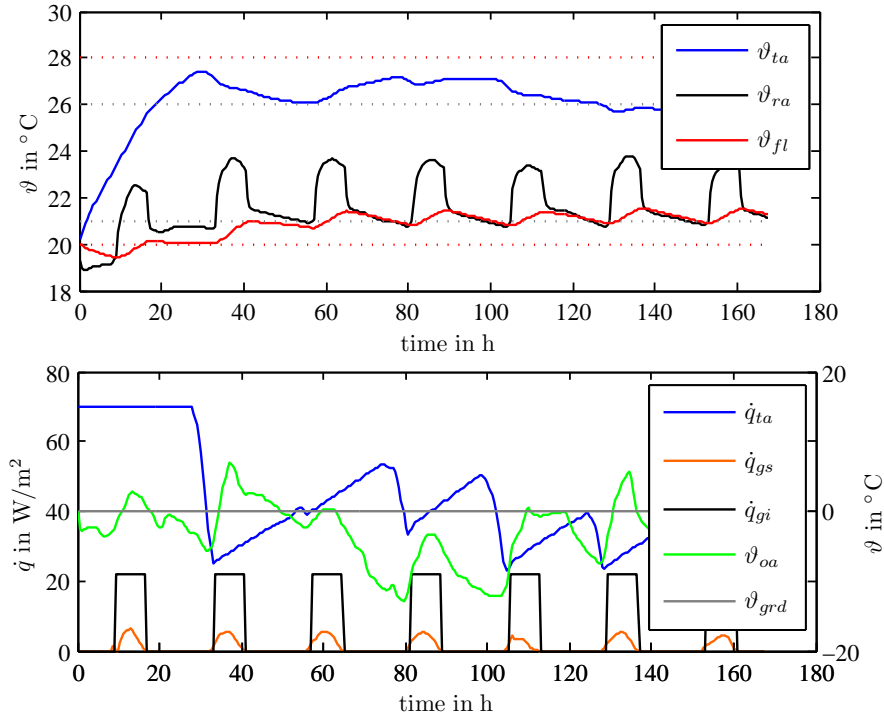


Figure 5.2.: Exemplary heating simulation trajectories for MPC operation obtained with eq. (5.1); top graph: relevant model temperatures (cf. sec. 4.1.1) and minimum and maximum values (dotted lines) defining the inner and outer  $\vartheta_{ra}$  comfort zone, lower graph: manipulated variable and disturbances.

This set is discontinuous, since it includes also the value 0 in addition to the continuous range. The upper limit is indirectly determined by the maximum compressor speed and the condenser inlet temperature. Consideration of this simple fact for the minimization problem requires a leap in terms of the optimization problem class.

Instead of a constrained QP (quadratic problem), which is required to solve the optimization in sec. 5.1, the PV-led HP control task with the restricted range from eq. (5.2) demands a more sophisticated program, which is viable to deal also with logical expressions, see Bemporad and Morari (1999). The class of programs which are able to solve the current problem is called mixed integer quadratic program (MIQP), more on this class in sec. 5.5.

### 5.2.1. Objective function and constraints

The objective function from eq. (5.3) of this MIQP differs to that given in eq. (5.1) mainly by the term with the weight  $R_{s,i}$  accounting for deviations of  $u_i$  from the reference value  $u_{ref,i}$  – thinking in physical terms this reference value is responsible to lead  $\dot{q}_{ta}$  such that as much as possible PV-generated electricity is utilized by the HP. The reference

## 5. Model predictive control

function is discussed later in this section. In addition, the weight  $R_{u,i}$  of the linear energy term is now variable over the control horizon, which is indicated by the index  $i$ . This allows the controller to consider a varying energy price, for example it makes sense to reduce this weight, or set it even to zero, if PV-electricity is available. Further, the optional smoothing term with the weight  $S$  is neglected for simplicity. The controller model is the  $\mathcal{M}^{n4w}$  from sec. 4.3.3.

In comparison to the constraints added to eq. (5.1) those related to eq. (5.3) have the additional slack variable inequality  $u_{ref,i} - s_i \leq u_i \leq u_{ref,i} + s_i$  and a further constraint on  $u_i$  to meet the heating power operation range restrictions from eq. (5.2).

$$\min_{\mathbf{u}, \mathbf{s}, \mathbf{e}, \mathbf{e}^c} J(\mathbf{u}, \mathbf{s}, \mathbf{e}, \mathbf{e}^c) = \sum_{i=1}^{N_C < N_P} R_{u,i} |u_i| + R_{s,i} |s_i|^2 + \sum_{i=1}^{N_P-1} Q |e_{i+1}|^2 + Q^c |e_{i+1}^c|^2, \quad (5.3)$$

subject to

$\mathbf{x}_{i+1} := \mathbf{A}\mathbf{x}_i + \mathbf{B}_u u_i + \mathbf{B}_v \mathbf{v}_i,$ abstract formulation: $y_i = [0.5 \ 0.25 \ 0.25 \ 0] \mathbf{x}_i$ $u_{min} \leq u_i \leq u_{max}, \quad 0 \leq u_{min}$ $u_{ref,i}^L - s_i \leq u_i \leq u_{ref,i} + s_i, \quad 0 \leq s_i$ $y_{min} - e_i \leq y_i \leq y_{max} + e_i$ $y_{min}^c - e_i^c \leq y_i \leq y_{max}^c + e_i^c$ $0 \leq e_i$ $0 \leq e_i^c$	$\mathbf{x}_1$ is given from measurements or in terms of the physical pendants: $\vartheta_{op,i} = 0.5\vartheta_{w,i} + 0.25\vartheta_{ra2fl,i} + 0.25\vartheta_{ra1fl,i}$ $\dot{q}_{ta,min} \leq \dot{q}_{ta,i} \leq \dot{q}_{ta,max}, \quad 0 \leq \dot{q}_{ta,min}$ $\dot{q}_{ta,ref,i}^L - s_i \leq \dot{q}_{ta,i} \leq \dot{q}_{ta,ref,i} + s_i, \quad 0 \leq s_i$ $\vartheta_{op,min} - e_i \leq \vartheta_{op,i} \leq \vartheta_{op,max} + e_i$ $\vartheta_{op,min}^c - e_i^c \leq \vartheta_{op,i} \leq \vartheta_{op,max}^c + e_i^c$ $0 \leq e_i$ $0 \leq e_i^c.$
---	---

The objective function comfort terms with the weights  $Q$  and  $Q^c$  have the same function as already explained in sec. 5.1. However, this time they compete with more energy related terms. Concerning the reference building (cf. fig. 2.1 and 2.7), two room or better zone temperatures are available (the first floor and the second floor temperature). Hence, each zone could have extra comfort terms and the related slack variable inequality constraints, however, for simplicity the objective function is formulated using a mean room temperature.

### 5.2.2. Reference function for tracking a certain PV power

The inequality constraints  $u_{ref,i}^L - s_i \leq u_i \leq u_{ref,i} + s_i$  need further explanations. Assume the HP to be switched off, in this case there should not be additional costs due to a high slack variable, which is why the lower reference value  $u_{ref,i}^L = 0$  if the HP is down. In

### 5.3. PV-led heat pump control for TES heating (TES-MPC)

case the HP operates and PV-electricity is available  $u_{ref,i}^L = u_{ref,i}$ , that is, any deviation of  $u_i$  from  $u_{ref,i}$  is penalized in terms of the slack variable  $s_i$ . This way it should be guaranteed to utilize as much as possible of the generated PV power.

To make sure the HP operates such to demand the generated PV power, it is necessary to provide a value to  $u_{ref,i}$  such that the electricity consumption of the HP matches the PV-generated amount. Hence, the specific heating power  $\dot{q}_{ta,i}$  supplied to the TABS should follow the value of a reference function

$$u_{ref,i} = g_{ref}(P_{PV,i}, A_{ta}). \quad (5.4)$$

A deviation from this reference value is considered in the objective function eq. (5.3) by means of the quadratic term with the slack variable  $s_i$ . For example, a deviation may arise if the heating power to meet the thermal comfort is higher than the heating power corresponding to the current electricity generation  $P_{PV,i}$  according to eq. (5.4), then the slack variable term  $R_{s,i} |s_i|^2$  has to compete against the comfort terms in the objective function. Since only very limited comfort violations are tolerated, the slack variable  $s_i$  will increase and such  $u_{ref,i} + s_i$  the upper limit for  $u_i$ , and thus the heating power increases to meet the comfort.

If  $P_{PV} < P_{PV,min}$  the tracking term is externally switched to efficiency tracking, cf. fig. 2.17;  $P_{PV,min}$  for the given PV-system was between 500 and 700 W.

### 5.3. PV-led heat pump control for TES heating (TES-MPC)

The PV-led HP operation for TES heating is slightly more involved than the PV-led space heating operation of the HP as explained in sec. 5.2. The reason is, that the controller model – in comparison to the building model used in eq. (5.3) – is a hybrid model. The hybrid model approach relies on two sub-models a *free floating* for the stratified TES and a *linearized model* able to model TES heating by means of a HP; these two sub-models exclude each other, only one model may be active at a time. More details on the hybrid approach are explained in sec. 4.4.3.

#### 5.3.1. Objective function and constraints

The discontinuous operation range of the HP according to eq. (5.2) applies also to this control task. The major difference to the PV-led space heating is the hybrid model. The hybrid model approach relies on the free floating model  $\mathcal{M}_1$  for the stratified TES and the linearized model  $\mathcal{M}_2$  able to model TES heating by means of the HP. Two binary switching variables (being constituted by the optimal controller decision) decide which of the two models is active. The optimization problem arising for this control task is also a MIQP but this time the computation time is larger compared to eq. (5.3), due to the hybrid nature of the model.

## 5. Model predictive control

$$\min_{\mathbf{u}, \mathbf{s}, \mathbf{e}, \mathbf{e}^c} J(\mathbf{u}, \mathbf{s}, \mathbf{e}, \mathbf{e}^c) = \sum_{i=1}^{N_c < N_p} R_{u,i} |u_i| + R_{s,i} |s_i|^2 + \sum_{i=1}^{N_p-1} Q |e_{i+1}|^2 + Q^c |e_{i+1}^c|^2, \quad (5.5)$$

subject to

$$\begin{aligned} \delta_{1,i} &\Leftrightarrow (u_i < u_{min}), \quad \delta_{2,i} \Leftrightarrow (u_i \geq u_{min}) & \sum_{k=1}^2 \delta_{k,i} &= 1 \\ \mathbf{x}_{i+1} &= \mathcal{M}_1^d(\mathbf{x}_i, \mathbf{v}_i) \delta_{1,i} + \mathcal{M}_2^d(\mathbf{x}_i, u_i, \mathbf{v}_i) \delta_{2,i} & \text{and } \mathbf{x}_1 &\text{ is given} \\ &\text{abstract formulation:} & \text{or in terms of the physical pendants:} & \\ & \mathbf{y}_i = [1 \ 0 \ 0] \cdot \mathbf{x}_i & \vartheta_{1,i} &= \vartheta_{1,i} + 0 \cdot \vartheta_{2,i} + 0 \cdot \vartheta_{3,i} \\ & (\delta_{2,i} \cdot u_{min}) \leq u_i \leq u_{max}, & (\delta_{2,i} \cdot f_{min}) \leq f_i \leq f_{max}, & \\ & (\delta_{2,i} \cdot u_{ref,i}) - s_i \leq u_i \leq u_{ref,i} + s_i, \quad 0 \leq s_i & (\delta_{2,i} \cdot f_{ref,i}) - s_i \leq f_i \leq f_{ref,i} + s_i, \quad 0 \leq s_i & \\ & y_{min} - e_i \leq y_i \leq y_{max} + e_i & \vartheta_{1,min} - e_i \leq \vartheta_{1,i} \leq \vartheta_{1,max} + e_i & \\ & y_{min}^c - e_i^c \leq y_i \leq y_{max}^c + e_i^c & \vartheta_{1,min}^c - e_i^c \leq \vartheta_{1,i} \leq \vartheta_{1,max}^c + e_i^c & \\ & 0 \leq e_i & 0 \leq e_i & \\ & 0 \leq e_i^c & 0 \leq e_i^c. & \end{aligned}$$

The constraint formulation along with the minimization problem given in eq. (5.5) is conducted in a quite abstract manner. The hybrid model approach is denoted with two binary decision variables to stress the hybrid nature of the MPC problem. All other constraints may be similarly interpreted as those from eq. (5.1) and eq. (5.3).

Here, the reference function  $u_{ref,i}$  refers to a frequency function. If the PV power is high enough to operate the HP above the minimum frequency  $f_{min}$ , this reference function must provide a frequency value such to adjust the HP electricity consumption to the current PV-generated electricity. In case no PV power is available the reference frequency provided is a function considering the maximum COP values, cf. fig. 2.18.

Fig. 5.3 depicts the main steps of the MPC routine for the PV-led HP control for TES heating. In comparison to fig. 5.1 the light gray blocks were added. These blocks refer to the linearization of the non-linear model and the decision which model to use while solving the problem.

### MPC parameters

The most important MPC parameters are briefly discussed. Both, the TABS-MPC and the TES-MPC use a model discretization time of 20 min (for the MPC-Boxes project 15 min are used). The prediction horizon  $N_p$  for the pure TABS-MPC tasks was taken 48 h, which is reasoned with the acceptable accuracy of weather forecast data up to  $\approx 48$  h. The TES-MPC uses  $N_p = 8$  h, because the underlying optimization problem is computationally more challenging higher values cause very high computation times. For both MPC tasks the control horizon  $N_c$  was set  $N_p - 1$ .

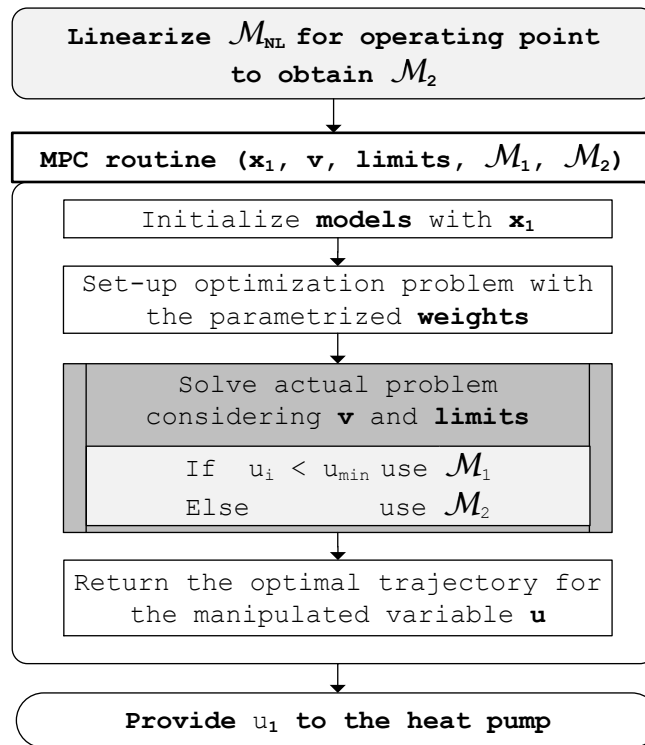


Figure 5.3.: Flow chart showing the principal steps of the MPC routine for a temperature MPC of a TES with energy supply from a HP (TES-HP model).

Sundström et al. (2016) report on significant *energy cost reductions* already for a relatively short  $N_p$  of 5 h. Optimal energy cost savings for a 500 L TES are obtained with a  $N_p$  of approximately 12 h – a higher  $N_p$  does not lead to increased savings unless the TES is also increased in parallel. This is probably explained by the ratio between the potential energy supply to the storage and the heat draw off from the thermal storage (within the 12 h). Concerning *peak power reduction* Sundström et al. (2016) found that a  $N_p$  of 5 h in combination with a TES of 500 L has already a significant impact, however, increasing the horizon to 23 h reduces the peak power further.

## 5.4. State estimation – Kalman Filter

State estimation is a topic taught or included in every course of a study or curriculum related to control theory. It is an extremely useful and essential topic. Although, common in control theory, it remains a mysterious subject to people outside of this field who come to it the very first time. This holds especially for the famous *Kalman Filter* named after its co-inventor Rudolf Emil Kalman (1960). Reflecting on the practical relevance of the Kalman Filter today, it must be said, that it is implemented in every

## 5. Model predictive control

global positioning system (gps). Hence, everybody using a modern smart phone or any kind of navigation system is accompanied by the Kalman Filter and makes use of this famous equations. The Kalman Filter's (first) most popular implementation was probably the Apollo Program of the NASA in the sixties.

In this thesis the subject *state estimation* is required for the TheBat building model, since not all states of the derived building model  $\mathcal{M}^{n4w}$  are directly measurable. However, before going deeper and introducing the recursive filter equations which are implemented as part of the TABS-MPC, the concept of the Kalman Filter is explained heuristically.

### 5.4.1. Heuristic explanation and basic examples

The following explanations are based on a teaching video from Sebastian Thrun "Artificial Intelligence for Robotics"<sup>4</sup> from UDACITY, the first pure online University. Another good online lecture for introduction is "What is a Kalman Filter?"<sup>5</sup> from Michel van Biezen from Loyola Marymount University. Both videos take only 10 minutes.

The Kalman Filter is based on a *two-step procedure*. The first step is a *prediction step* and the second step is an *update or filtering step*. This principle procedure will be explained with the aid of a very simple heuristic example sketched in fig. 5.4. Assume a localization problem with a Robot and a very simple world or landscape – this example is taken from an online lecture of Sebastian Thrun.

Robot, drawn with three wheels in fig. 5.4, stands somewhere in the landscape and is desperate. He is familiar with the map of his world – a simple white wall with three doors – but has no idea about his position. In probabilistic terms this may be expressed with a uniform probability density function (pdf). That is, Robots initial belief (1. in fig. 5.4) tells him that there is not any position which is more likely than any other. He uses his only sensor, his electronic eye and sees a door in front of him (2. in fig. 5.4). Based on his internal map and this additional information he updates his belief and thinks now that he must be in front of any of the three doors (3. in fig. 5.4). Mathematically this is expressed by an increased probability for positions  $x$  nearby a door. He does not hesitate and moves further to the right (4. in fig. 5.4). Robot is aware of his movement and knows roughly how far he moved. He knows, that if he was in front of door 1, he will now be somewhere right to door 1, that is his belief after the first measurement (3. in fig. 5.4) must shift to the right. During the movement some accuracy is lost, the shifted belief has flatter bumps (5. in fig. 5.4), since he has only an approximate idea how far he moved. After the movement he senses once more, and again gets a picture of a door (6. in fig. 5.4). Combining the information where he could be – based on the internal map – with his prior belief, gives him a good estimate of his current position (7. in fig. 5.4).

4 <https://www.youtube.com/watch?v=n1EacrqyCs8&list=PLAwxTw4SYaPkCSYXw6-a.aAoXVKLDwnHK&index=3> available on the 04.03.2016.

5 <https://www.youtube.com/watch?v=CaCcOwJPytQ> available on the 04.03.2016

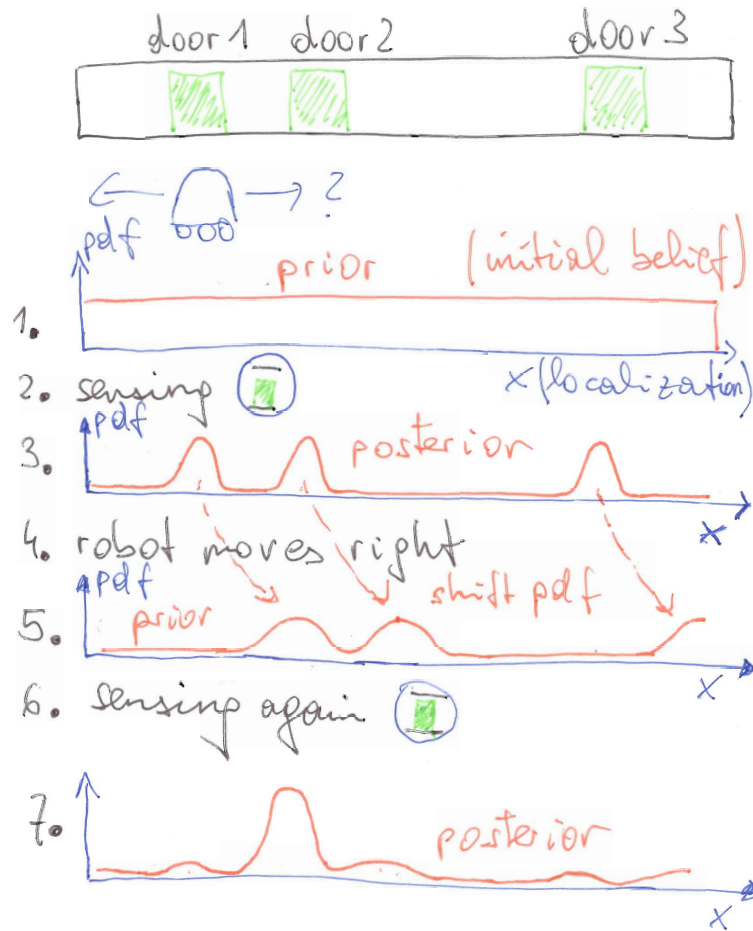


Figure 5.4.: Heuristic explanation of the Kalman Filter and the predictor-update principle.

### 5.4.2. Kalman Filter equations and explanations

The following interpretations of the recursive Kalman Filter equations try to explain the Kalman Filter without going into mathematical details. The vector and matrix notation with bold letters is neglected temporary for readability, but finally used again in the summary of the equations. For a rigorous treatment of this topic see e.g Papoulis (1991).

Now the focus is on eq. (5.6), a SSM representation of a real process or plant. This model looks very similar to the discrete time SSM in eq. (B.3) with 1 subtracted from all indices, however, this time  $x_k$  expresses the *real state* and  $y_k$  stands for the *real output*.

$$x_k = A^d x_{k-1} + B^d u_{k-1} + w_{k-1} \quad y_k = C x_k + v_k. \quad (5.6)$$

The purpose of the model is to reconstruct  $x_k$  based on  $x_{k-1}$ ,  $u_{k-1}$ , and  $y_k$ , this is

## 5. Model predictive control

different to eq. (B.3), which is used to obtain the output value given the former state and the input value.

Two *new variables* are included in eq. (5.6) in comparison to eq. (B.3). The variable  $w_{k-1}$  expresses the model deficiency and is needed on the RHS (right hand side) to make the equation correct by compensating for the inaccuracy (notice that the real state  $x_{k-1}$  and the real input  $u_{k-1}$  are used, though) of our model  $A^d, B^d$ . Similarly for  $y_k$ , we want it to be the real (measured) output value and since  $C x_k$  is only an estimate for this value we need the auxiliary error variable  $v_k$  to make this output equation correct.

Initially we do not know the exact values of the state and the output error. The only information we have on the nature of  $w$  and  $v$  are a few statistical properties described by  $W$  and  $V$ . Both error variables have a bell shaped probability distribution with zero mean and a certain variance.

### The prediction step

Recalling Robot's localization problem there is a pattern when his belief changes, after a movement (prediction step) and after sensing (update step). This subsection deals with the prediction step.

It is assumed that the values of the past state  $\hat{x}_{k-1}$  and input  $u_{k-1}$  are known. The general question we are asking refers to the state variable "what is the best estimate ( $x_k^*$ ) for the actual state based on  $\hat{x}_{k-1}$  and  $u_{k-1}$ ?" Thinking of the heuristic Robot example state corresponds to the belief on the position or localization.

Let's start at 3. in fig. 5.4. The (belief of the) current state estimate is written as  $\hat{x}_{k-1} \pm \sqrt{P_{k-1}}$ <sup>6</sup> with  $P_{k-1}$  containing the uncertainty information of the belief. With  $u_{k-1}$  being the known input action (Robot's movement which is the prediction step and requires a model) the *predicted* belief  $x_k^*$  may be expressed with the dynamic matrix  $A^d$  and the input matrix  $B^d$  as

$$x_k^* = A^d \hat{x}_{k-1} + B^d u_{k-1}. \quad (5.7)$$

The error of this predicted value is  $x_k - x_k^*$  and the question remaining refers to how to obtain this error with the given information. Intuitively one may guess that this error should depend on the uncertainty of  $\hat{x}_{k-1}$  on the one hand, that is on  $P_{k-1}$ , and on the basic model error measure  $W$  on the other hand. The error propagation follows the transformation rule

$$P_k^* = (A^d) P_{k-1} (A^d)^T + W. \quad (5.8)$$

This equation provides information on the accuracy of the predicted state. With reference to fig. 5.4 we are now at 5.

---

<sup>6</sup> For readability  $P$  is denoted like a scalar variance, although it might be a matrix.

### The update step

For the update step we do it as Robot, take a measurement  $y_k$  and utilize it to improve our belief. That is, the second question is "what is the best estimate ( $\hat{x}_k$ ) or *posterior belief* after conducting the measurement".

The update step is slightly more involved and it is lengthy to derive the required equations which is why they are just stated and interpreted. The complete update step comprises a few *sub-steps*: measurement prediction, estimation of the filtered state and update of the uncertainty variable  $P$ . The *measurement prediction* is easily understood, it refers to the prediction of the expected measurement result based on  $x_k^*$

$$\hat{y}_k = C x_k^* \quad (5.9)$$

Now the measurement data  $y_k$  is incorporated for the estimation of the *filtered state*,

$$\hat{x}_k = x_k^* + K_k(y_k - \hat{y}_k) \quad \text{with } K_k = P_k^* C^T (C P_k^* C^T + V)^{-1}. \quad (5.10)$$

Based on  $x_k^*$  from the prediction step the filtered state  $\hat{x}_k$  is obtained with  $K_k$  which weights the influence of the error between the real and the predicted measurement data. The Kalman gain  $K_k$  is a function of the state uncertainty information  $P$ , the output matrix  $C$  and the output error information  $V$ . With increasing output error  $V$  the Kalman gain gets smaller. Concerning the state uncertainty it is not so straight forward to judge on its influence on the Kalman gain. From a pure causal understanding more emphasis should be put on the measurement result with increasing uncertainty  $P_k^*$  for  $x_k^*$ , hence,  $K_k$  ought to increase with  $P_k^*$ .

Finally only the *update of the uncertainty* information after conducting the measurement step is left

$$P_k = (\mathbf{I} - K_k C) P_k^*. \quad (5.11)$$

#### 5.4.3. Summary of the Kalman Filter equations and recursion

Assume the discrete dynamic system given in eq. (5.12) with  $\mathbf{A}^d$ ,  $\mathbf{B}^d$  and  $\mathbf{C}$  describing the model and  $\mathbf{W}$  and  $\mathbf{V}$  providing additional statistical properties for the state ( $\mathbf{w}_{k-1}$ ) and the output error  $\mathbf{v}_k$ . It is assumed that both errors are bell shaped with zero mean. In addition it must be ensured, that the system is observable, see Appendix B.

$$\mathbf{x}_k = \mathbf{A}^d \mathbf{x}_{k-1} + \mathbf{B}^d \mathbf{u}_{k-1} + \mathbf{w}_{k-1} \quad \mathbf{y}_k = \mathbf{C} \mathbf{x}_k + \mathbf{v}_k \quad (5.12)$$

## 5. Model predictive control

In eq. (5.13) all equations required for the recursive implementation of the Kalman Filter are summarized.  $\mathbf{P}_k^*$  provides prior (to the measurement step) information and  $\mathbf{P}_k$  provides posterior information concerning the state estimation accuracy.

Prediction step: i) $\mathbf{x}_k^* = \mathbf{A}^d \hat{\mathbf{x}}_{k-1} + \mathbf{B}^d \mathbf{u}_{k-1}$ ii) $\mathbf{P}_k^* = (\mathbf{A}^d) \mathbf{P}_{k-1} (\mathbf{A}^d)^T + \mathbf{W}$ Update step: iii) $\mathbf{K}_k = \mathbf{P}_k^* \mathbf{C}^T (\mathbf{C} \mathbf{P}_k^* \mathbf{C}^T + \mathbf{V})^{-1}$ iv) $\hat{\mathbf{x}}_k = \mathbf{x}_k^* + \mathbf{K}_k (\mathbf{y}_k - \hat{\mathbf{y}}_k)$ with $\hat{\mathbf{y}}_k = \mathbf{C} \mathbf{x}_k^*$ v) $\mathbf{P}_k = (\mathbf{I} - \mathbf{K}_k \mathbf{C}) * \mathbf{P}_k^*$	(5.13)
--	--------

### Initiate the recursion

It was not stressed so far, that the Kalman filter operates in a recursive manner, that is, it generates new results based on given past results. This feature makes it numerically very efficient. The question is how to set the sub-steps (i) to (v) from eq. (5.13) with mutual reference in motion.

The recursion starts with an assumption<sup>7</sup> for the initial (belief) state  $\mathbf{x}_0^*$ , in order to fulfill (i). For (ii) the uncertainty information concerning  $\mathbf{x}_0^*$  is needed, since the initial belief was estimated it is likewise possible to estimate the assigned uncertainty information. More rigorous

$$\begin{aligned} \mathbf{x}_0^* &= E[\mathbf{x}_0] \\ \mathbf{P}_0^* &= E[(\mathbf{x}_0^* - \mathbf{x}_0)(\mathbf{x}_0^* - \mathbf{x}_0)^T] \end{aligned} \quad (5.14)$$

with  $E$  standing for the expectation value. Based on eq. (5.14) the sub-steps (iii) to (v) may be conducted and the recursive scheme is set in motion.

Finally, it is possible to solve the sub-steps (ii), (iii) and (v) beforehand and anticipate the *steady state* for the Kalman gain and the state estimation uncertainty. This is not possible for a non-stationary noise or a time dependent model, however, in this context a stationary noise and a time-invariant model are given.

The consequence of using the steady state Kalman gain from the beginning is an initially suboptimal operation of the Kalman Filter which is demonstrated by fig. 5.5. For the model  $\mathcal{M}^{n4w}(\Theta_{wm})$  it takes approximately a day until the Kalman Filter states have converged to an optimum – this is the price, which is clearly visible by the diminishing residuals.

<sup>7</sup> For the TheBat building model the initial state was chosen [17; 20; 20; 20].

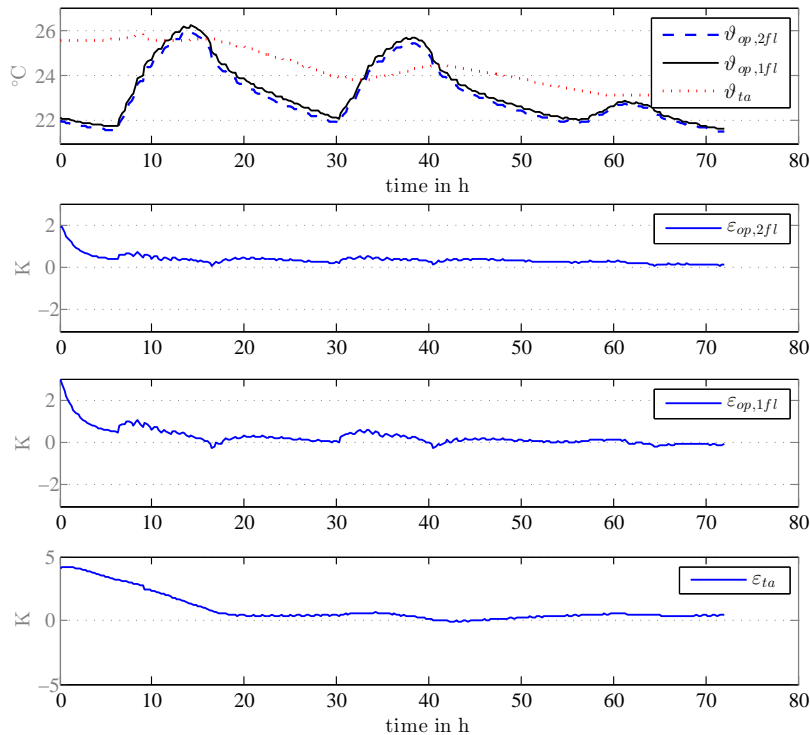


Figure 5.5.: Exemplification of the suboptimal operation of the Kalman Filter and the consequence on the initial estimation errors ( $\epsilon_{op,2fl}, \epsilon_{op,1fl}, \epsilon_{ta}$ ).

## 5.5. Optimization problem

This section discusses only the basics on solution-finding ( $\mathbf{u}_0, \mathbf{u}_1, \mathbf{u}_2, \dots$ ) given a SSM and a problem specific quadratic cost function  $J(\mathbf{u})$  with additional constraints. For a general introduction on optimization methods see Fletcher (2007), or Boyd and Vandenberghe (2009) for convex optimization, and from an MPC point of view see e.g. Maciejowski (2002). For mixed logical dynamical systems (MLD) and MIQP problems and their solution see chapter 10 in Camacho and Bordons (2004).

Before presenting the solution to a prototypical quadratic MPC problem – very similar to that in sec. 5.1 – practical aspects dealing with the successful operation of an implemented MPC are put forward.

### 5.5.1. General aspects

In the following especially problems encountered during the research activities are discussed.

## 5. Model predictive control

The MIQP (mixed integer quadratic problem) as formulated in sec. 5.3 is in general non-polynomial (NP)-hard, which means that it is not even possible to derive a formula for the time it will take to converge to a solution. That is, such problems are *really hard* from an optimization point of view. Convergence to a feasible solution, even when it exists, cannot be guaranteed. When it comes to a practical implementation that fact, the complexity of the employed model and the accompanying risk of not finding a solution for specific parameters, together with the uncertainties of the necessary external forecast data ask for a strategy to assure a reasonable set of control variables for the next time step. Such a *back-up strategy* is always required. Most of the annual simulations, each of which requires 26280 calls of the TABS-MPC and 26280 calls of the TES-MPC, were conducted without a back-up strategy. This way it was possible to “filter” problematic input variable-scenarios and think of an improvement for the parametrization or the MPC concept as such. In every call the MPC *input variables*<sup>8</sup> are more or less unique. However, finally a back-up strategy was implemented, which relies on the last successful optimization run, allowing three successive times an infeasibility or a numerical problem. After exploiting the first four trajectory values<sup>9</sup> of the last successful optimization run an error is generated.

To increase the solution-feasibility hard constraints on the outputs must be avoided. Concerning the inputs, hard constraints are normally not a problem. In addition, any weight or disturbance modification towards the end of the prediction horizon that has a positive effect on the convergence behavior represents a suitable remedy. The reason is simply that nearly always only the first value of the optimal manipulated variables trajectory is really facilitated, and all other values are disposed.

The computation time in context of building automation and control is generally not so critical, because the systems are relatively slow with huge time constants. However, operation with sub-optimal solutions should be considered. Unfortunately, within the toolbox YALMIP (release 20150918) see Löfberg (release 20150918) no way was found to control the used solver Gurobi (2015) such that it stops after a certain time even if the optimum has not been found. This is why the optimizer tried to converge to the optimum solution in the sense of closing the gap between the *primal-problem* and the *dual-problem*. Practically it is sensible to break and exit an iterative optimization run after a certain time, even if this gap  $\neq 0$ . The required optimization or convergence time for the hybrid TES-MPC ranged between 1 s and extremely seldom 2-10 minutes on a standard office PC.

---

8 In this context “input variables” refers to the state feedback variable, the set of predicted disturbance variables and all constant and variable constraints and the MPC parameters.

9 Finally, this was relaxed to maximum 15 values (5 h) to avoid continuous repetition of simulations in case of an error. However, during annual simulations the maximum number of 3 required trajectory values is typical and it was observed, that in total between 60 and 400 times past trajectory results were supplied due to a numerical optimization problem.

### 5.5.2. A prototypical MPC problem solved with a QP

Lets assume a relatively simple cost functional eq. (5.15) with a linear term for the heating energy costs ( $\mathbf{u} := [\dot{q}_{ta}, 0, 0]^T$  for a model of 3rd order or simply  $u := \dot{q}_{ta}$ ) and a quadratic term penalizing the deviation from a desired reference value (e.g. room air set temperature  $y^{ref} := \vartheta_{ra,set}$ ,  $\hat{y} := \vartheta_{ra}$ ). This functional<sup>10</sup> is even simpler than (5.1), however, it is a prototype suitable to describe the basic concept behind finding a solution in form of a time series for  $\mathbf{u}$ .

$$\min_{\mathbf{u}} J(\mathbf{u}) = \sum_{i=k}^{k+N-1} \underbrace{R_i u_i}_{\text{energy term}} + \underbrace{Q_{i+1} \|y_{i+1}^{ref} - \hat{y}_{i+1}\|^2}_{\text{comfort term}} \quad (5.15)$$

Assuming  $k = 0$  and reducing the norm to a simple square for a scalar model output  $\hat{y}$ , the extended version of the sum  $J(\mathbf{u})$  reads:

$$J(\mathbf{u}) = R_0 u_0 + Q_1 (y_1^{ref} - \hat{y}_1)^2 + R_1 u_1 + Q_2 (y_2^{ref} - \hat{y}_2)^2 \dots + R_{N-1} u_{N-1} + Q_N (y_N^{ref} - \hat{y}_N)^2. \quad (5.16)$$

The aim is to find the predicted trajectory for the current instant in time ( $k$ ), given a linear SSM for the building eq. (5.17) and disturbance data  $\mathbf{v}$  predicting the outside ambient temperature, solar irradiance etc. By contrast to the discrete model from eq. (B.3) the superscript  $d$  is skipped for readability and the manipulated input variable  $\mathbf{u}$  is isolated from the disturbance input variables  $\mathbf{v}$ :

$$\mathbf{x}_{k+1} = \mathbf{A}\mathbf{x}_k + \mathbf{B}_u \mathbf{u}_k + \mathbf{B}_v \mathbf{v}_k \quad \hat{y}_k = \mathbf{C} \mathbf{x}_k \quad \mathbf{x}_k \text{ is given.} \quad (5.17)$$

The concept of the receding horizon means that the optimization problem defined by eq. (5.15) is repeated for the instants  $k = 0, 1\Delta t_s, 2\Delta t_s, \dots$ , with  $\Delta t_s$  being the sampling time or the discretized time steps. For readability  $k = 0$  is convenient to demonstrate the solution process.

For each selected control action  $\mathbf{u}_i$  the model from eq. (5.17) is used to calculate the output value  $\hat{y}_i$  representing the room air temperature. Assume  $\mathbf{x}_k = \mathbf{x}_0$ , and  $\mathbf{v}_0, \mathbf{v}_1, \dots, \mathbf{v}_{N-1}$  then the new state  $\mathbf{x}_1$  and the output  $\hat{y}_1$  as a consequence of the manipulated variable  $\mathbf{u}_0$  are determined through

$$\mathbf{x}_1 = \mathbf{A}\mathbf{x}_0 + \mathbf{B}_u \mathbf{u}_0 + \mathbf{B}_v \mathbf{v}_0 \quad \hat{y}_1 = \mathbf{C} \mathbf{x}_1 \quad (5.18)$$

Moving one step ahead and applying the input variable  $\mathbf{u}_1$  we get

$$\begin{aligned} \mathbf{x}_2 &= \mathbf{A}\mathbf{x}_1 + \mathbf{B}_u \mathbf{u}_1 + \mathbf{B}_v \mathbf{v}_1 & \hat{y}_2 &= \mathbf{C} \mathbf{x}_2, \text{ or} \\ \mathbf{x}_2 &= \mathbf{A}^2 \mathbf{x}_0 + \mathbf{A}\mathbf{B}_u \mathbf{u}_0 + \mathbf{A}\mathbf{B}_v \mathbf{v}_0 + \mathbf{B}_u \mathbf{u}_1 + \mathbf{B}_v \mathbf{v}_1 & \hat{y}_2 &= \mathbf{C} \mathbf{x}_2, \end{aligned} \quad (5.19)$$

<sup>10</sup>The prediction horizon  $N_p$  is denoted simply with  $N$  to be able to fit equations in one line.

## 5. Model predictive control

where  $\mathbf{x}_1$  was replaced with the expression from (5.18). Continuing this scheme and always replacing the current state by that from a step before we finally get:

$$\begin{aligned}
 \mathbf{x}_1 &= \mathbf{A}\mathbf{x}_0 + \mathbf{B}_u\mathbf{u}_0 + \mathbf{B}_v\mathbf{v}_0 & \hat{y}_1 &= \mathbf{C}\mathbf{x}_1, \\
 \mathbf{x}_2 &= \mathbf{A}^2\mathbf{x}_0 + \mathbf{A}\mathbf{B}_u\mathbf{u}_0 + \mathbf{A}\mathbf{B}_v\mathbf{v}_0 + \mathbf{B}_u\mathbf{u}_1 + \mathbf{B}_v\mathbf{v}_1 & \hat{y}_2 &= \mathbf{C}\mathbf{x}_2, \\
 \mathbf{x}_3 &= \mathbf{A}^3\mathbf{x}_0 + \mathbf{A}^2\mathbf{B}_u\mathbf{u}_0 + \mathbf{A}^2\mathbf{B}_v\mathbf{v}_0 + \mathbf{A}\mathbf{B}_u\mathbf{u}_1 + \mathbf{A}\mathbf{B}_v\mathbf{v}_1 + \mathbf{B}_u\mathbf{u}_2 + \mathbf{B}_v\mathbf{v}_2 & \hat{y}_3 &= \mathbf{C}\mathbf{x}_3, \\
 &\vdots & & \\
 \mathbf{x}_N &= \mathbf{A}^N\mathbf{x}_0 + \mathbf{A}^{N-1}\mathbf{B}_u\mathbf{u}_0 + \mathbf{A}^{N-1}\mathbf{B}_v\mathbf{v}_0 + \dots + \mathbf{A}\mathbf{B}_u\mathbf{u}_{N-2} + \mathbf{A}\mathbf{B}_v\mathbf{v}_{N-2} + \mathbf{B}_u\mathbf{u}_{N-1} + \mathbf{B}_v\mathbf{v}_{N-1} & \hat{y}_N &= \mathbf{C}\mathbf{x}_N.
 \end{aligned} \tag{5.20}$$

With a few definitions the eq. (5.20) can be written compact in vector notation as

$$\boxed{\mathbf{X} = \mathcal{A}\mathbf{x}_0 + \mathcal{B}_u\mathbf{U} + \mathcal{B}_v\mathbf{V} \qquad \hat{\mathbf{Y}} = \mathbf{C}\mathbf{X}} \tag{5.21}$$

with the following definitions, for which the scalar output  $y$  is replaced by a general output vector  $\mathbf{y}$ ,

$$\begin{aligned}
 \mathbf{X} &:= \begin{bmatrix} \mathbf{x}_1 \\ \mathbf{x}_2 \\ \vdots \\ \mathbf{x}_N \end{bmatrix} & \mathbf{Y} &:= \begin{bmatrix} \mathbf{y}_1 \\ \mathbf{y}_2 \\ \vdots \\ \mathbf{y}_N \end{bmatrix} & \mathbf{U} &:= \begin{bmatrix} \mathbf{u}_0 \\ \mathbf{u}_1 \\ \vdots \\ \mathbf{u}_{N-1} \end{bmatrix} & \mathbf{V} &:= \begin{bmatrix} \mathbf{v}_0 \\ \mathbf{v}_1 \\ \vdots \\ \mathbf{v}_{N-1} \end{bmatrix} & \mathcal{A} &:= \begin{bmatrix} \mathbf{A} \\ \mathbf{A}^2 \\ \vdots \\ \mathbf{A}^N \end{bmatrix} & \mathcal{C} &:= \begin{bmatrix} \mathbf{C} & & 0 \\ & \ddots & \\ 0 & & \mathbf{C} \end{bmatrix} \\
 \mathcal{B}_u &:= \begin{bmatrix} \mathbf{B}_u & 0 & \dots & 0 \\ \mathbf{A}\mathbf{B}_u & \mathbf{B}_u & \dots & 0 \\ \vdots & \vdots & \ddots & \vdots \\ \mathbf{A}^{N-1}\mathbf{B}_u & \mathbf{A}^{N-2}\mathbf{B}_u & \dots & \mathbf{B}_u \end{bmatrix} & \mathcal{B}_v &:= \begin{bmatrix} \mathbf{B}_v & 0 & \dots & 0 \\ \mathbf{A}\mathbf{B}_v & \mathbf{B}_v & \dots & 0 \\ \vdots & \vdots & \ddots & \vdots \\ \mathbf{A}^{N-1}\mathbf{B}_v & \mathbf{A}^{N-2}\mathbf{B}_v & \dots & \mathbf{B}_v \end{bmatrix}. \tag{5.22}
 \end{aligned}$$

The cost function eq. (5.15) may be written as

$$\begin{aligned}
 J(\mathbf{u}) &= \begin{bmatrix} \hat{\mathbf{y}}_1 - \mathbf{y}_1^{ref} \\ \hat{\mathbf{y}}_2 - \mathbf{y}_2^{ref} \\ \vdots \\ \hat{\mathbf{y}}_N - \mathbf{y}_N^{ref} \end{bmatrix}^T \underbrace{\begin{bmatrix} Q_1 & & 0 \\ & \ddots & \\ 0 & & Q_N \end{bmatrix}}_{=: \mathbf{Q}} \begin{bmatrix} \hat{\mathbf{y}}_1 - \mathbf{y}_1^{ref} \\ \hat{\mathbf{y}}_2 - \mathbf{y}_2^{ref} \\ \vdots \\ \hat{\mathbf{y}}_N - \mathbf{y}_N^{ref} \end{bmatrix} + \underbrace{[R_0 \ R_1 \ \dots \ R_{N-1}]}_{=: \mathbf{R}} \begin{bmatrix} \mathbf{u}_0 \\ \mathbf{u}_1 \\ \vdots \\ \mathbf{u}_{N-1} \end{bmatrix} \tag{5.23}
 \end{aligned}$$

and making use of the definitions from eq. (5.22) this simplifies to

$$\boxed{J(\mathbf{u}) = [\hat{\mathbf{Y}} - \mathbf{Y}^{ref}]^T \mathbf{Q} [\hat{\mathbf{Y}} - \mathbf{Y}^{ref}] + \mathbf{R}\mathbf{U}.} \tag{5.24}$$

Substituting  $\hat{\mathbf{Y}}$  with the definitions made in eq. (5.21) we get

$$\begin{aligned}
 J(\mathbf{u}) &= [\mathbf{C}\mathbf{X} - \mathbf{Y}^{ref}]^T \mathbf{Q} [\mathbf{C}\mathbf{X} - \mathbf{Y}^{ref}] + \mathbf{R}\mathbf{U} \tag{5.25} \\
 &= [\mathbf{C}(\mathcal{A}\mathbf{x}_0 + \mathcal{B}_u\mathbf{U} + \mathcal{B}_v\mathbf{V}) - \mathbf{Y}^{ref}]^T \mathbf{Q} [\mathbf{C}(\mathcal{A}\mathbf{x}_0 + \mathcal{B}_u\mathbf{U} + \mathcal{B}_v\mathbf{V}) - \mathbf{Y}^{ref}] + \mathbf{R}\mathbf{U}
 \end{aligned}$$

Conducting the multiplications – for which the non- $\mathbf{U}$  dependent part is lumped in a constant term – we get

$$J(\mathbf{u}) = \left[ \mathcal{C}(\mathcal{A}\mathbf{x}_0 + \mathcal{B}_u\mathbf{U} + \mathcal{B}_v\mathbf{V}) - \mathbf{Y}^{ref} \right]^T \mathbf{Q} [\mathcal{C}\mathcal{B}_u\mathbf{U}] + \mathbf{R}\mathbf{U} + const.$$

Separating the orders of  $\mathbf{U}$  we finally get<sup>11</sup>

$$J(\mathbf{U}) = \mathbf{U}^T \underbrace{\left[ \mathcal{B}_u^T \mathcal{C}^T \mathbf{Q} \mathcal{C} \mathcal{B}_u \right]}_{=: \mathcal{H}} \mathbf{U} + \underbrace{\left( \left[ \mathcal{C}(\mathcal{A}\mathbf{x}_0 + \mathcal{B}_v\mathbf{V}) - \mathbf{Y}^{ref} \right]^T \mathbf{Q} \mathcal{C} \mathcal{B}_u + \mathbf{R} \right)}_{=: \mathcal{G}} \mathbf{U} + const.$$

from which the prototypical quadratic program may be written as

$$\begin{array}{l} \min_{\mathbf{U}} J(\mathbf{U}) = \mathbf{U}^T \mathcal{H} \mathbf{U} + \mathcal{G} \mathbf{U} \\ \text{subject to} \\ \Omega \mathbf{U} \geq \mathbf{c} \end{array} \quad (5.26)$$

with  $\mathcal{H}$  being the Hessian of  $J(\mathbf{U})$ ,  $\mathcal{G}$ <sup>12</sup> characterizing the linear dependency in  $J(\mathbf{U})$  and  $\Omega$  and  $\mathbf{c}$  defining the valid linear constraints on  $\mathbf{U}$ . For the solution of this class of programs see e.g. Fletcher (2007) Ch. 7, but see also Maciejowski (2002) Ch. 3 and Wimmer (2004) Ch. 6 p. 66 for the derivation. For MIQP which incorporate logical switching variables into the QP see Bemporad and Morari (1999).

### 5.5.3. Numerical complexity

The numerical complexity of the TABS-MPC problem described in section 5.2 is approximately estimated as follows. Assume a discretization time of 20 min and a prediction and control horizon ( $N_p = N_c$  is assumed for simplicity) of 24 h. This gives 72 numerical values for each continuous variable involved. The building model is of forth order and the cost function from eq. (5.3) has four degrees of freedom – this gives 8 continuous variables per time step. For the complete horizon one gets 576 continuous variables to be found numerically to solve the ordinary quadratic problem.

The situation gets much more complex with binary switching variables being involved as for the TES-MPC problem described in section 5.3. The discretization time is the same as for the TABS-MPC but the prediction and the control horizon are much smaller than for the TABS-MPC, lets assume 8 h. This gives 24 numerical values for each variable involved. In this case the controller model is of third order and the cost function from (5.5) has four degrees of freedom, which means 7 continuous variables per time step. For the complete horizon one gets 168 continuous variables to be found. From the perspective of continuous variables the problem is relatively cheap, however, it gets

<sup>11</sup>Including  $\mathcal{C}$  in the definition of  $\mathcal{A}, \mathcal{B}_u, \mathcal{B}_v$  this expression simplifies to  $\mathbf{U}^T [\tilde{\mathcal{B}}_u^T \mathbf{Q} \tilde{\mathcal{B}}_u] \mathbf{U} + \left( [\tilde{\mathcal{A}}\mathbf{x}_0 + \tilde{\mathcal{B}}_v\mathbf{V} - \mathbf{Y}^{ref}]^T \mathbf{Q} \tilde{\mathcal{B}}_u + \mathbf{R} \right) \mathbf{U} + const.$

<sup>12</sup>In optimization books one can find the term *gradient vector* for  $\mathcal{G}$  although it is a matrix.

## 5. Model predictive control

more involved taking into account the binary switching variables, which are also part of the cost function. Although 2 binary variables are defined for the cost function, the problem requires essentially only one binary variable. The complete horizon comprises 24 steps or in terms of the binary variable 24 decisions are required over the complete horizon. This gives  $2^{24} \approx 17 \cdot 10^6$  possible combinations. Each binary combination requires theoretically to solve one quadratic problem with 168 continuous variables. Hence, the number of continuous variables to be evaluated to achieve a global optimum is approximately  $2.8 \cdot 10^9$ .

This brief calculation shows, that the numerical complexity of the mixed integer quadratic problem is huge. In practice there exist optimization algorithms which do not require to solve the quadratic problem for every single binary combination. These algorithms partly relax the binary nature caused by the switching variable and solve the problem approximately but much more efficiently. For more details see Camacho and Bordons (2004). In this research the full version of Gurobi 6.5 was facilitated (Gurobi, 2015) to solve all MPC problems. Annual simulations took between one and three days on a standard office PC. Typically the TES-MPC failed in 0.3 – 1.4% of the total number of calls. In such cases values from past result trajectories were used as backup.

### 5.6. The complete MPC control task – overview

Fig. 5.6 illustrates the complete control task from a control structure point of view. The system simulation is conducted with TRNSYS with a time step of 15 minutes. This simulation includes the incorporation of the weather data, the thermal building simulation, the domestic hot water demand profile, the simulation of the heat pump, the PV panel and the periodic call of the embedded MATLAB (cf. fig. 5.7). The TRNSYS simulation provides the feedback to the controllers in terms of the current temperatures in the building (cf.  $\mathbf{y}$  in eq. (4.10)) and in terms of the current temperatures in the stratified thermal storage (cf. fig. 4.14). To assimilate the current system state of the MPC building dynamic model (TABS-MPC) from the available building temperatures a Kalman Filter is required, because the virtual wall temperature (cf. eq. (4.10),  $\vartheta_w \in \mathbf{x}$ ) is not directly provided as TRNSYS output. The temperatures required by the thermal energy storage controller model are directly available from TRNSYS. The thermal heat pump may either heat the TES (thermal energy storage) or the TABS (thermally activated building system), in case both MPCs output a control action at the same time, priority is given to TES heating or the frequency signal from the TES-MPC.

Fig. 5.7 illustrates the essential elements of the TRNSYS simulation including the embedded MATLAB environment. By contrast to fig. 5.6 this figure shows the interaction and the structural set-up of the involved software tools to realize the investigation by means of simulations. The MATLAB environment Type155-control is directly embedded in TRNSYS, scheduled to be called always at the end of each

## 5.6. The complete MPC control task – overview

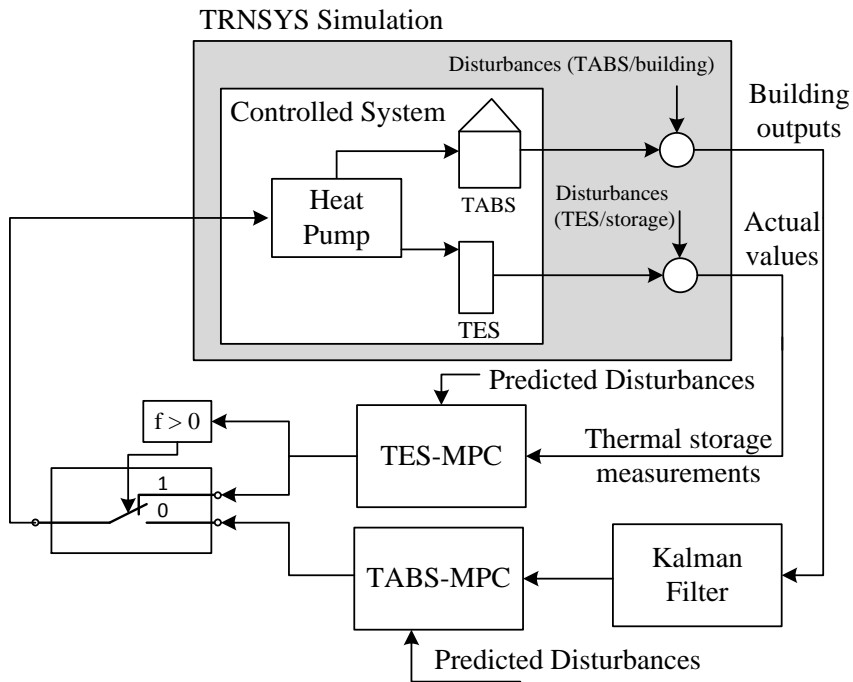


Figure 5.6.: Illustration of the complete control task for the system described in Ch. 2

TRNSYS time step, and it provides a flexible (to be defined once) input and output array. Type155-control represents a single MATLAB script file, in which the common MATLAB commands and functions may be called and executed. More on the implementation or coding of the model predictive controllers is described in the next subsection.

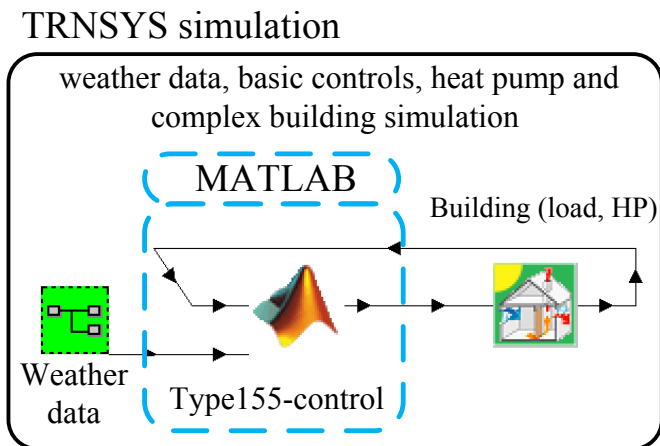


Figure 5.7.: Illustration of the principal elements of the TRNSYS simulation.

## 5. Model predictive control

Fig. 5.8 shows the principal elements and data interfaces of an MPC on behalf of the TABS-MPC. Actual sensor data stands for the feedback from the controlled system, reference values indicate set-values and constraints on the controlled variables and prediction data stands for the weather forecast data and load estimations (in this case internal building loads, for the TES-MPC domestic hot water loads). Because the main aim is to operate the heat pump as a function of the generated PV power, only the solar irradiance is mentioned explicitly as input to the MPC, although also the ambient temperature from the weather forecast data and other disturbance related forecasts are used. With the controller dynamic model and suitable MPC cost function parameters it is finally possible to find an optimal control trajectory  $\dot{Q}_{TABS}$  that may be translated to a compressor frequency based on the required heat pump characteristic (map).

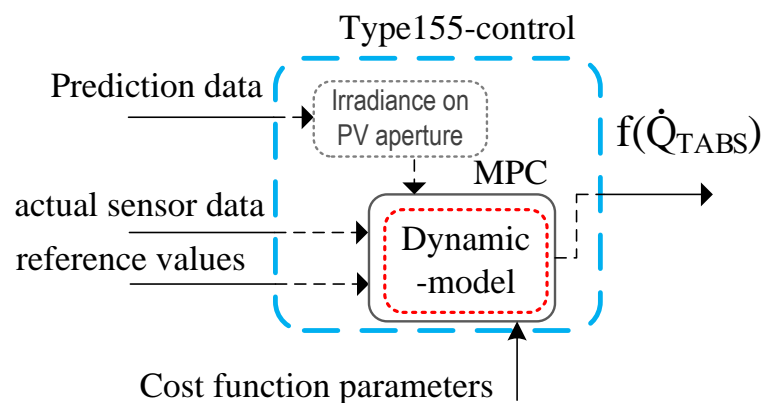


Figure 5.8.: Illustration of the principal elements for each MPC on behalf of the TABS-MPC.

### 5.6.1. Realization and coding of the MPC

As mentioned earlier in this work a number of tools are utilized to implement the model predictive controllers. The basic programming environment and language is MATLAB. A MATLAB script file may be directly called by the TRNSYS simulation, cf. fig. 5.7. However, MATLAB itself makes use of various functions provided by the YALMIP toolbox cf. Löfberg (release 20150918).

YALMIP provides a function to directly implement the cost function in terms of symbolic variables. In addition to this, all cost function constraints, the inputs (disturbance data, dynamic model) and the outputs (control trajectory, forecast simulation data) must be defined. Finally, a suitable optimizer algorithm must be defined, which can cover the underlying or resulting optimization problem. Throughout the conducted research Gurobi 6.5 was used (Gurobi, 2015).

## 6. Results and controller performance

*Results presented in this chapter refer mainly to the heat pump PV-system (HP-PV-system) described in Ch. 2. These results are obtained by means of TRNSYS simulations and the MPC relies on ideal weather forecast data. The outcome for base case (BC) and MPC scenarios is reported. In addition to a BC versus MPC comparison, especially different MPC scenarios are compared against each other. Occasionally, real measurement results referring to the MPC-Boxes project will be reported to justify a specific idealization or underline the reliability of simulation results.*

### 6.1. Evaluation strategy and performance indicators

In principal, the fact to obtain annual simulation results for the MIQP MPC for the heat pump PV system speaks for itself, that is annual simulation results are already a great success due to the computational complexity of the underlying MIQP being NP-hard, cf. sec. 5.5.3. However, a few case scenarios for the developed MPC will be compared against each other and related to the base case results obtained with hysteresis controllers. Results for simple (pseudo model) predictive approaches have been elaborated by Kofler (2016), and also within the project TheBat.

The reliability of the simulation results is validated by means of various *energy balances* proofing the energy conservation, for the following sub-systems: the HP itself, the TES, the TES and the distribution system, and finally the building, though, the results will not be provided explicitly for every simulation. The most important results for each scenario are presented in this chapter an extensive outline of the results is given in Appendix H or especially H.5 for the most realistic and relevant MPC-scenario. The principal characteristic behavior of the developed MPC is explained along with supporting graphical illustrations. In addition, annual results for various total energy amounts and temperatures are presented along with a few performance indicators provided for means of comparison of the different scenarios.

#### 6.1.1. Penalties for comfort violation

Penalties are required to account for any comfort violation. Comfort violations may occur wrt DHW provision if the TES top-temperature is too low or wrt the SH, if the

## 6. Results and controller performance

room temperature leaves the defined comfort range. The penalty definitions used herein are based on those given in Haller (2013).

The comfort violations are quantified by means of a temperature. The penalty calculations related to the DHW supply and SH rely on the following temperature differences:

$$\begin{aligned}\Delta\vartheta_{DHW} &:= \max(0, \vartheta_{DHW,set} - \vartheta_{DHW,act}) \\ \Delta\vartheta_{SH,1fl} &:= \max(0, \vartheta_{op,min} - \vartheta_{op,1fl,act}) \cdot CF_{heating} \\ \Delta\vartheta_{SH,2fl} &:= \max(0, \vartheta_{op,min} - \vartheta_{op,2fl,act}) \cdot CF_{heating}.\end{aligned}\quad (6.1)$$

The *penalty definitions* deviate from a pure energy compensation term. This is to punish a bad controller behavior. For the DHW penalties, the punishment factor is 1.5, and it is assumed that the missing share of thermal energy is provided directly through an electric immersion heater, cf. eq. (6.2). SH penalties are considered through an average  $UA$  value for the whole building ( $UA_{bui} = 168 \text{ W/m}^2$ ). The progressive character of this penalty in case of comfort violations is realized by means of a three-fold linear consideration of  $\Delta\vartheta_{SH}$  added to a quadratic term of  $\Delta\vartheta_{SH}$ , cf. eq. (6.3).

$$P_{pen,DHW} := 1.5 \dot{m}_{DHW} c_p \Delta\vartheta_{DHW} \quad (6.2)$$

$$\begin{aligned}P_{pen,SH,1fl} &:= UA_{bui} \left( 3 \Delta\vartheta_{SH,1fl} + \Delta\vartheta_{SH,1fl}^2 \right) \\ P_{pen,SH,2fl} &:= UA_{bui} \left( 3 \Delta\vartheta_{SH,2fl} + \Delta\vartheta_{SH,2fl}^2 \right)\end{aligned}\quad (6.3)$$

The total (electrical) energy penalty term constitutes of the DHW-penalty and the SH-penalties for the first and the second floor. This electrical energy term is introduced as an additional *pseudo consumption* term for the calculation of performance indicators including the comfort violation penalties:

$$P_{pen,\Sigma} = P_{pen,DHW} + P_{pen,SH,1fl} + P_{pen,SH,2fl} \quad (6.4)$$

### 6.1.2. Heat pump- and system-performance indicators

The actual performance or efficiency of the HP at instant  $t$  is expressed by the coefficient of performance (COP), relating the generated thermal energy flux or capacity of the HP  $\dot{Q}_c(t) + \dot{Q}_d(t)$  to the electrical power supplied to the HP  $P_{HP,comp}(t) + P_{HP,aux}(t)$ , where  $P_{HP,aux} := 50 \text{ W}$  (considering the required pump capacity from the thermal heat reservoir and the pump capacity to feed into the TES):

$$COP_{HP} := \frac{\dot{Q}_c + \dot{Q}_d}{P_{HP,comp} + P_{HP,aux}} \quad (6.5)$$

## 6.1. Evaluation strategy and performance indicators

The performance of the HP or the whole system over a specific interval is expressed by the seasonal performance factor (SPF), which is the pendant to the  $COP$  at an energy-base:

$$\begin{aligned} SPF_{HP} &:= \frac{\int (\dot{Q}_c + \dot{Q}_d) dt}{\int (P_{HP,comp} + P_{HP,aux}) dt} \\ SPF_{sys} &:= \frac{\int (\dot{Q}_{DHW} + \dot{Q}_{SH}) dt}{\int (P_{HP,comp} + P_{HP,aux} + P_{sys,aux}) dt}. \end{aligned} \quad (6.6)$$

$SPF_{HP}$  relates the HP-generated total amount of thermal energy to the total electricity consumption of the HP during the same time-interval.  $SPF_{sys}$  is a slightly more conservative measure than  $SPF_{HP}$ . It relates the useful energy which is finally consumed, to the total electricity consumption of the whole system, where  $P_{sys,aux} = (25 \cdot (\text{TABS on}) + 25 \cdot (\text{FWS on}))$  W incorporates the pump capacity for the TABS hydraulic loop and the pump capacity for the FWS (fresh water station), if in operation respectively.

Finally, each performance indicator may be re-defined by including the electrical energy penalty term, to obtain the performance indicators with penalties:

$$COP_{HP}^{pen} := \frac{\dot{Q}_c + \dot{Q}_d}{P_{HP,comp} + P_{HP,aux} + P_{pen,\Sigma}} \quad (6.7)$$

$$SPF_{HP}^{pen} := \frac{\int (\dot{Q}_c + \dot{Q}_d) dt}{\int (P_{HP,comp} + P_{HP,aux} + P_{pen,\Sigma}) dt'} \quad (6.8)$$

$$SPF_{sys}^{pen} := \frac{\int (\dot{Q}_{DHW} + \dot{Q}_{SH}) dt}{\int (P_{HP,comp} + P_{HP,aux} + P_{sys,aux} + P_{pen,\Sigma}) dt}. \quad (6.9)$$

### 6.1.3. Control related performance indicators

In addition to the defined seasonal performance factors from above a grid-consumption related performance indicator may be defined. This SPF is sub-scripted with  $ctr$ , that is, related to the control, because a reduction of the grid-consumption may be directly attributed to the MPC performance; compare also Young (2013) which introduced a seasonal primary energy efficiency factor (SPEEF):

$$SPF_{HP,ctr} := \frac{\int (\dot{Q}_c + \dot{Q}_d) dt}{\int (P_{HP,comp} + P_{HP,aux} - P_{PV})_{>0} dt'} \quad (6.10)$$

$$SPF_{sys,ctr} := \frac{\int (\dot{Q}_{DHW} + \dot{Q}_{SH}) dt}{\int (P_{HP,comp} + P_{HP,aux} + P_{sys,aux} - P_{PV})_{>0} dt}. \quad (6.11)$$

Including the  $P_{pen,\Sigma}$  in the denominator of  $SPF_{HP,ctr}$  and  $SPF_{sys,ctr}$  leads to the related performance factors considering also the penalty energy terms.

## 6. Results and controller performance

### 6.2. PV yield and boundary conditions

Tab. 6.1 summarizes the results obtained for the PV system and provides the most relevant simulation boundary conditions on a monthly and annual base for the simulation climate data set (Innsbruck cf. Appendix C.2). These data hold for all simulation scenarios except for the MPC-Boxes related investigations.

The last three columns in tab. 6.1 provide the area specific irradiation on the PV array, the PV-yield on a per  $m^2$  basis and the average cell temperature. This PV yield is obtained with the four-parameter model described in Appendix C.4.2, a  $\tau\alpha$  of 0.85 and incidence angle corrections for the module Solarwatt 60P with 250 W rated power, cf. data sheet in Appendix H, p. 267. The annual yield ( $183 \text{ kWh}/m^2$ ) is relatively high, which is due to the high module efficiency. The 0.85 for  $\tau\alpha$  represent a realistic value where moderate soiling of the panels is already considered<sup>1</sup>.

The cell temperature average values together with the empirical standard deviation allow for an estimation of the expected temperature range. Taking the region of two sigma (two standard deviations left and right from the mean which represent 95.4% of all values),  $45^\circ\text{C}$  are obtained as the maximum cell temperature in summer, which is relatively low. In winter the temperature stays below  $30^\circ\text{C}$ .

Table 6.1.: Boundary conditions holding for all scenarios; temperatures, solar radiation and PV yield.

	$\vartheta_{oa}$ $^\circ\text{C}$	$RH_{oa}$ %	$\vartheta_{grad}$ $^\circ\text{C}$	$H_{tot,hor}$ $\text{kWh}/m^2$	$H_{PV}$ $\text{kWh}/m^2$	$W_{PV}$ $\text{kWh}/m^2$	$\vartheta_{cell,>15W}$ $^\circ\text{C}$
Jan	$-1.8 \pm 4.8$	$83.8 \pm 11.8$	$0.3 \pm 0.2$	45.5	99.3	12.5	$10.0 \pm 7.4$
Feb	$0.9 \pm 4.7$	$78.2 \pm 14.0$	$0.8 \pm 0.5$	64.0	105.6	13.1	$11.8 \pm 7.5$
Mar	$5.1 \pm 5.3$	$73.9 \pm 17.5$	$3.5 \pm 1.1$	108.3	145.7	17.6	$17.8 \pm 8.1$
Apr	$9.8 \pm 5.4$	$70.0 \pm 18.8$	$7.7 \pm 1.3$	135.0	147.7	17.5	$21.9 \pm 8.7$
May	$15.1 \pm 5.4$	$69.3 \pm 20.0$	$12.4 \pm 1.3$	172.2	159.8	18.5	$27.2 \pm 8.5$
Jun	$17.4 \pm 5.2$	$72.7 \pm 18.3$	$16.2 \pm 0.9$	172.5	150.9	17.3	$28.6 \pm 8.0$
Jul	$18.5 \pm 5.0$	$72.9 \pm 18.8$	$18.1 \pm 0.3$	176.1	159.4	18.2	$29.8 \pm 7.8$
Aug	$18.2 \pm 4.7$	$74.5 \pm 16.6$	$17.7 \pm 0.5$	148.1	150.6	17.3	$29.9 \pm 7.5$
Sep	$13.8 \pm 4.6$	$77.9 \pm 15.0$	$14.9 \pm 1.1$	111.8	135.8	15.9	$25.4 \pm 7.3$
Oct	$9.9 \pm 4.8$	$80.0 \pm 14.5$	$10.6 \pm 1.4$	81.6	126.1	15.1	$21.4 \pm 7.1$
Nov	$3.9 \pm 4.3$	$82.9 \pm 12.0$	$6.0 \pm 1.3$	45.4	82.0	10.1	$13.3 \pm 6.7$
Dec	$-0.4 \pm 4.4$	$84.4 \pm 11.5$	$2.2 \pm 0.9$	35.5	80.1	10.1	$9.4 \pm 6.5$
annual	$9.2 \pm 8.7$	$76.7 \pm 16.8$	$9.2 \pm 6.5$	1296.1	1542.8	183.3	$20.5 \pm 7.6$

### 6.3. DHW(TEs) and SH(TABS) – BC results, scenario 0.0

The results provided in this section refer to the initial BC scenario 0.0; the respective non-predictive control rules are described in sec. 2.2. The evaporator inlet temperature is constantly  $\vartheta_{sc} = 0^\circ\text{C}$ , no separate  $\vartheta_{ra}$ -control is implemented and the internal gains of the building are neglected for simplicity.

<sup>1</sup> For conservative estimations  $\tau\alpha = 0.75$  is advised.

### 6.3. DHW(TES) and SH(TABS) – BC results, scenario 0.0

Fig. 6.1 shows the overview of the most relevant energy flows for the initial BC scenario, which gives an approximate idea on the magnitude of the individual quantities. Fig. 6.2 provides a more detailed representation on the shares and the path of the PV-generated electricity and the total electricity consumption of the HP. The relatively low fraction (19.5 %) of electricity with PV origin directly consumed by the HP stands out – this holds if coincidence rules. Hence, if no measures are taken most of the PV-generated electricity is fed into the grid. Although, grid-parity is actually already reached in Austria, due to the low feed-in tariffs this is a disadvantage, see Fechner et al. (2016).

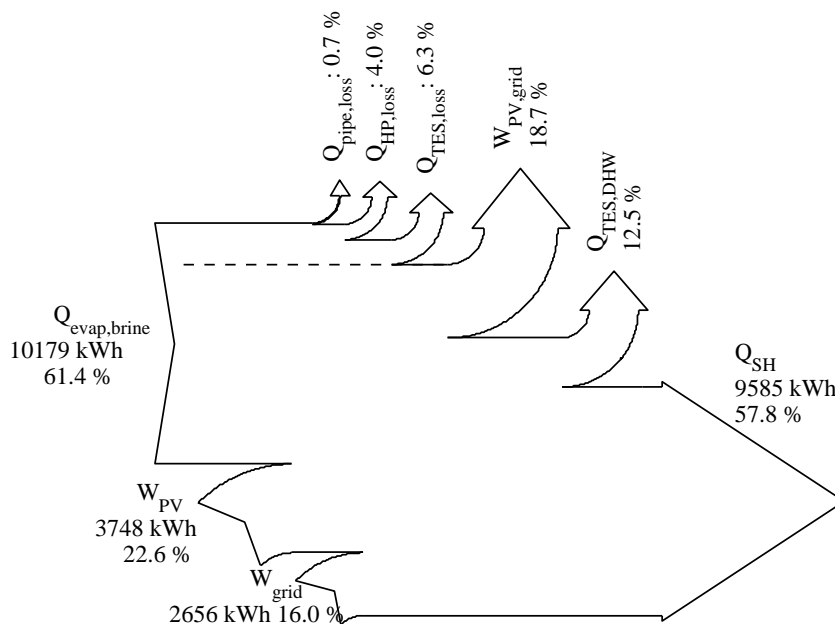


Figure 6.1.: Total annual energy flow overview;  $\vartheta_{sc} = 0^{\circ}\text{C}$  – BC scenario 0.0.

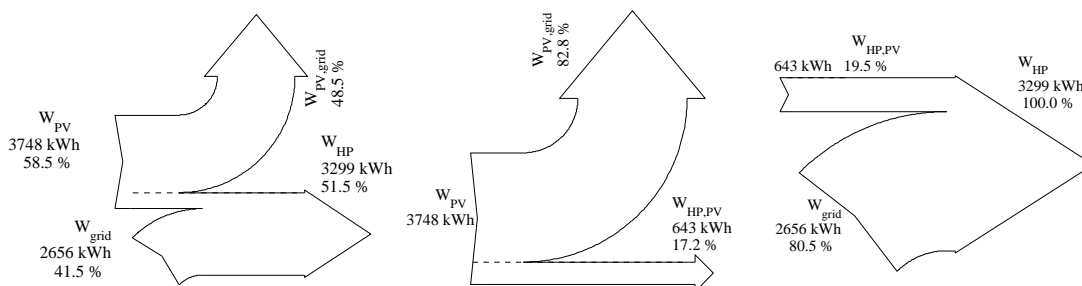


Figure 6.2.: Electrical annual energy; overview (left), split of the PV-generated related to the utilization (middle) and split of the total HP consumption related to the origin (right);  $\vartheta_{sc} = 0^{\circ}\text{C}$  – BC scenario 0.0.

## 6. Results and controller performance

Simulation result details are provided in Appendix H.1. With 9585 kWh/a useful SH energy consumption the specific SH demand calculates to 68 kWh/(m<sup>2</sup> a) which is relatively high, considering the original design SH demand of 45 kWh/(m<sup>2</sup>a). One main reason for this difference is the negligence of the internal gains due to occupancy (1270) and electrical equipment (1875) resulting in 3146 kWh total or 22 kWh/m<sup>2</sup> per year (cf. Dott et al. (2013)). The annual TES losses are 1040 kWh and the overall HP losses (start and stop and thermal) are 664 kWh.

During the heating season, the average room temperature is approximately 23 °C, which is caused by the strict ambient temperature led HP operation without any feedback from the actual room temperature – for a base case results with feedback see scenario BC 0.1 sec. 6.7. Due to the generally high room temperatures the SH penalties are nearly zero; the annual DHW penalties (88 kWh) are also very low. A detailed picture on the comfort relevant variables is given in fig. 6.11. Fig. 6.16 gives detailed information on the TABS supply- and return-water temperatures and the specific heating power.

Tab. H.5 in Appendix lists the interesting performance indicators for the initial BC scenario. All indicators are defined in sec. 6.1. The last line provides the most significant annual value. Due to the assumption  $\vartheta_{sc} = 0^\circ\text{C}$ , the *SPF* is relatively low.

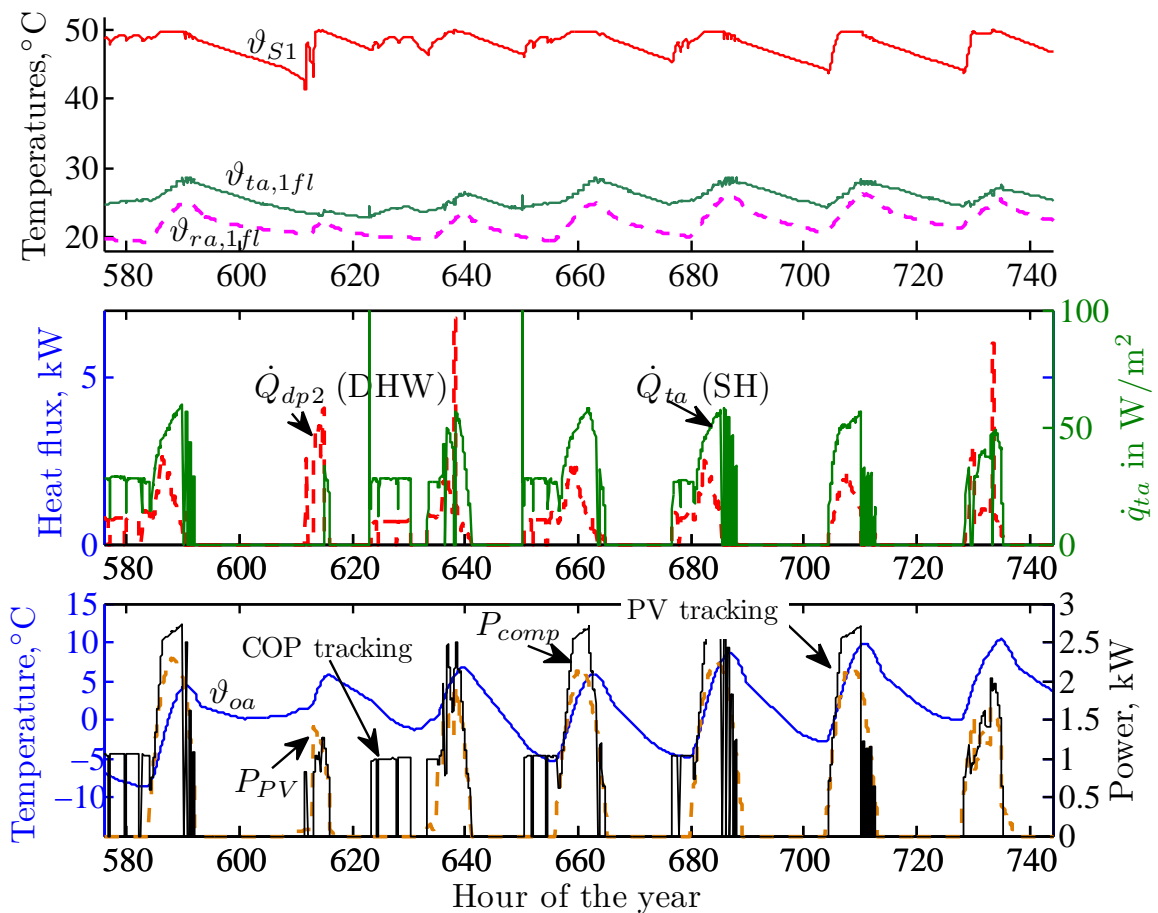


Figure 6.3.: MPC in winter, typical  $\vartheta$ - and  $\dot{Q}$ -trajectories over a week (generated from scenario 1.4 results but holds in principal also for scenario 1.0 except for the level of  $\vartheta_{S1}$ ).

## 6.4. DHW(TES) and SH(TABS) – MPC results, scenario 1.0

This section presents graphical and numerical results for the parallel operation of the TES-MPC and the TABS-MPC. In principal these two control tasks may be formulated as one MPC problem leading to a relatively complex optimization problem. However, the assumption is, that the outcome is not significantly different from a separate implementation with parallel operation of the TES-MPC and the TABS-MPC. For details on the cost functions of the underlying control problems see sec. 5.3 and sec. 5.2.

Important simulation *boundary conditions* which may be different for other scenarios are, a constant brine source temperature  $\vartheta_{sc} = 0$  °C and overheating of the TES is activated to 65 °C to maximally exploit the thermal storage capacity.

The parallel operation of the TES-MPC and the TABS-MPC requires a *prioritization* to decide which manipulated variable to provide to the HP; the following rule is implemented: if the TES-MPC outputs a value for the manipulated variable different from zero  $u_{TES-MPC} \neq 0$ , then the operation of the HP is determined by this value, which in this case is the compressor frequency. Should there be a SH demand at the same time, that is  $u_{TABS-MPC} \neq 0$ , then this value is ignored until  $u_{TES-MPC} = 0$ . The simple reason for this is, that the room-temperature in the building changes slower than the temperature in the TES, and the required time-interval for bringing the TES temperature back into the comfort band is short in general.

### 6.4.1. Control system trajectories

The figures 6.3 and 6.6 provide typical trajectories for HP operation by means of an MPC. The top graph in fig. 6.3 shows the top-sensor TES-temperature ( $\vartheta_{s1}$ ), the average TABS temperature ( $\vartheta_{ta,1fl}$ ) at pipe layer level in the center of area and the room air temperature. For  $\vartheta_{s1}$  it is clearly visible, that the temperature reaches its lowest value frequently just before PV power is available. The same holds for  $\vartheta_{ra,1fl}$  and this is exactly what is required to maximally exploit all available thermal storage capacity. The temperatures for the second floor are nearly the same as for the first floor. Occasionally as  $\vartheta_{oa}$  tends to or below  $\approx -5$  °C the MPC is forced to switch on the HP to sustain the thermal comfort, at such times (cf. bottom graph of fig. 6.3 at 625 h, 655 h) the HP operates in COP-tracking or efficiency tracking mode (cf. 5.2.2). In winter, the extended SH operation with parallel TES heating through the desuperheater ( $\dot{Q}_{dp2}$  see fig. 2.3) barely requires pure direct TES heating (cf.  $CF_1$ ) such as at 625 h. The middle graph of fig. 6.3 provides the total heat flux supplied to the building in kW (left axis) and in  $W/m^2$  (right axis), and also the heat flux supplied to the TES  $\dot{Q}_{dp2}$ .

The absent SH demand in summer (cf. fig. 6.6) leads to pure TES heating at times where PV power is available. The shown figure relates to MPC scenario 1.4 and not to scenario 1.0 which is why the upper part of the TES is not heated up to 65 °C. However, as can be seen in the figure this temperature is already enough to ensure the thermal supply until the next PV power peak is available. This probably explains why the overheating to 65 °C is not really an advantage. Very rarely the HP operation is *not* led by the PV power. The repeated on/off switching at e.g. 3950 h results from the fact, that the TES top temperature is very close to the parametrized maximum temperature (50 °C). Assume the temperature is 50 °C and as a result the HP is off, that is no direct PV consumption is possible. If a DHW draw-off occurs, and the top TES temperature slightly decreases the HP may be switched on again, this leads to intermittent HP operation.

## 6. Results and controller performance

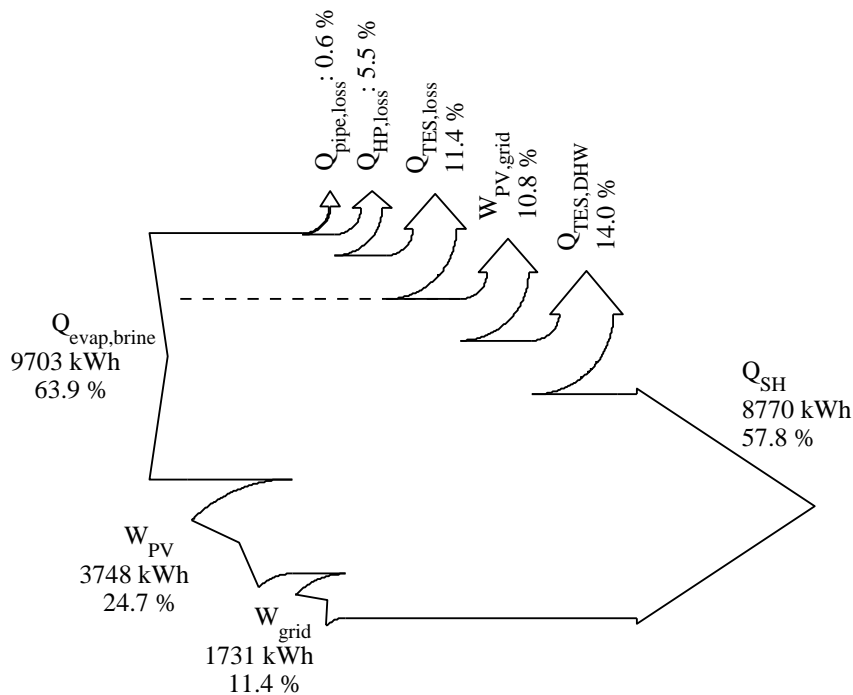


Figure 6.4.: Total annual energy flow overview;  $\vartheta_{sc} = 0^{\circ}\text{C}$  – MPC scenario 1.0.

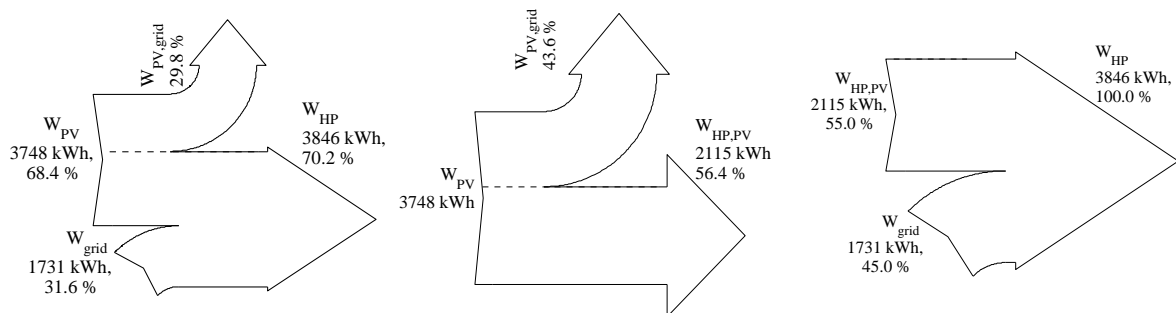


Figure 6.5.: Electrical annual energy; overview (left), split of the PV-generated related to the utilization (middle) and split of the total HP consumption related to the origin (right);  $\vartheta_{sc} = 0^{\circ}\text{C}$  – MPC scenario 1.0.

### 6.4.2. Energy flow and induced PV self consumption

Fig. 6.4 demonstrates the overall energy flow into the system, the losses of the system and the useful energies being outputs of the system. Compared to BC 0.0 the TES losses increased (1724 kWh), which is very probably due to the increased storage temperature ( $65^{\circ}\text{C}$ , cf. fig. 6.12) at times with PV being available, and the fact, that the SH supply from the storage is deactivated ( $CF_5 = 0$  for the whole simulation, which means no SH directly from the TES). If the TES is located such to indirectly support the SH in reality through its losses, this issue must not be given too much attention. However, the overheating in summer must be questioned for this system. The total SH energy consumption is slightly below the consumption for the BC scenario 0.0, but also the average room temperatures are approximately 0.5 K below those of the BC scenario.

Fig. 6.5 illustrates the electrical energy flows into the system, the split of the generated PV electricity related to the utilization and the origin of the electricity consumed by the HP. The PV plant with approximately 20 m<sup>2</sup> module or 18 m<sup>2</sup> net cell area may supply more than 56% of its generation directly to the HP and the rest is fed into the grid. From an origin perspective, 55% of the total HP-consumed electricity is directly generated by the PV. Comparison against the base case scenario results from fig. 6.2 shows, that the grid consumption is drastically reduced and the PV self-consumption is significantly increased, from 19.5% to 55.0%. However, with 1731 kWh the grid consumption of the HP is still relatively high.

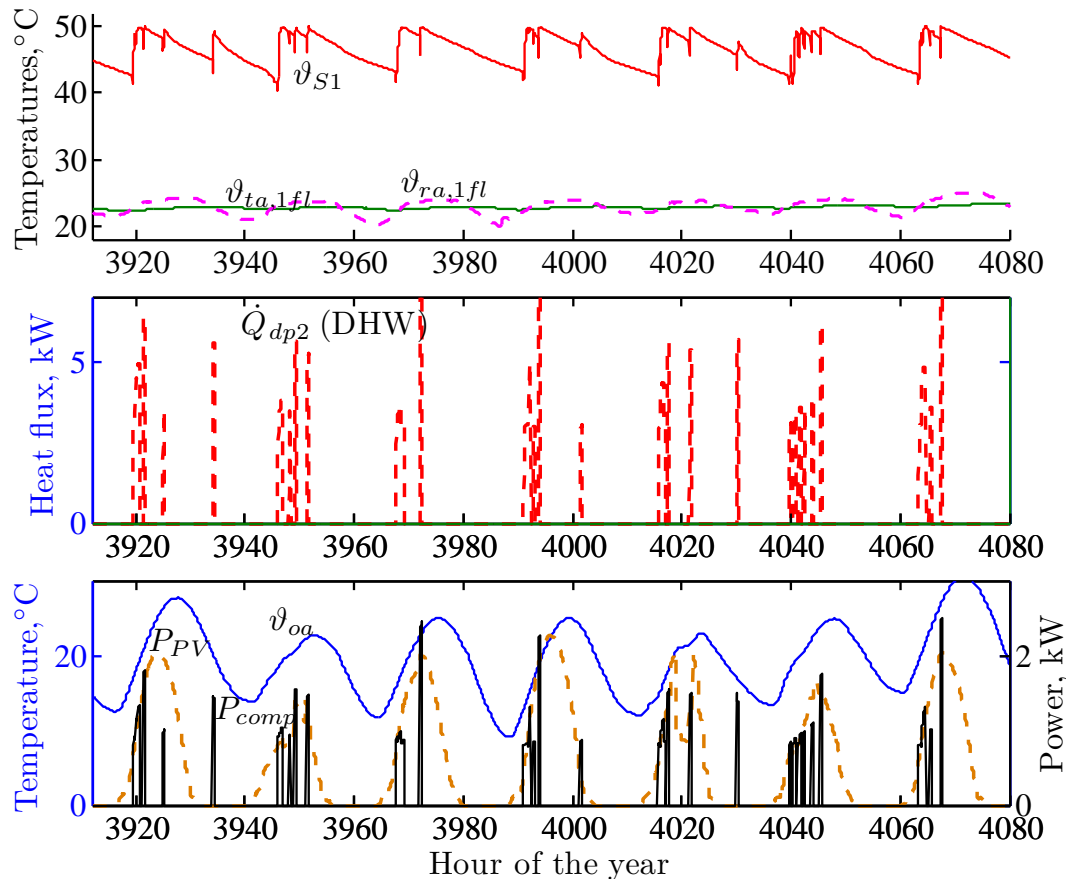


Figure 6.6.: MPC in *summer*, typical  $\vartheta$ - and  $\dot{Q}$ -trajectories over a week (generated from scenario 1.4 results but holds in principal also for scenario 1.0 except for the level of  $\vartheta_{S1}$ ).

A monthly break down with average room air- and operative temperatures among other variables is given in Appendix H.3. The *SPF* is 3.44 cf. tab. 6.2 which is below that of the BC scenario 0.0 (3.74). This is reasoned by the tracking of the generated PV-electricity, which causes the HP operation to be not very efficient sometimes. The diverse range of *COP* values for MPC operation of the HP is also visible through the 3-fold increased empirical standard deviation (see tab. 6.2) compared to the BC scenario 0.0 (see tab. H.5). The indicator  $SPF_{sys}^{pen}$  (2.8) is clearly below that of the BC scenario 0.0 (3.25). The reason for this is the clearly increased total electrical energy demand of the HP (3846 kWh) compared to the BC scenario (3299 kWh) and less thermal energy supplied for space heating at the same

## 6. Results and controller performance

Table 6.2.: Performance indicators overview for monthly and annual results – MPC scenario 1.0.

	$SPF$	$SPF_{ctr}$	$SPF_{sys}$	$SPF_{sys,ctr}$	$COP$	$SPF_{sys}^{pen}$	$SPF_{sys,ctr}^{pen}$	$\eta_{PV}$
	–	–	–	–	–	–	–	–
Jan	3.46	5.63	3.13	5.05	$3.56 \pm 0.74$	2.95	4.61	$12.30 \pm 0.01$
Feb	3.42	7.28	3.07	6.44	$3.52 \pm 0.82$	2.97	6.05	$12.20 \pm 0.01$
Mar	3.36	11.09	2.93	9.47	$3.46 \pm 0.89$	2.86	8.85	$11.88 \pm 0.01$
Apr	3.49	14.60	3.00	12.23	$3.60 \pm 0.99$	2.93	11.32	$11.57 \pm 0.01$
May	2.83	8.95	1.50	4.74	$2.86 \pm 0.63$	1.42	4.12	$11.30 \pm 0.01$
Jun	3.00	8.69	1.62	4.67	$3.05 \pm 0.69$	1.52	4.09	$11.20 \pm 0.01$
Jul	3.05	8.63	1.62	4.56	$3.10 \pm 0.68$	1.52	4.01	$11.16 \pm 0.01$
Aug	2.99	8.68	1.59	4.61	$3.03 \pm 0.68$	1.50	4.03	$11.17 \pm 0.01$
Sep	3.11	9.49	2.01	6.08	$3.16 \pm 0.97$	1.90	5.38	$11.41 \pm 0.01$
Oct	3.51	14.33	2.98	11.82	$3.62 \pm 1.04$	2.91	10.90	$11.72 \pm 0.01$
Nov	3.76	7.12	3.35	6.26	$3.89 \pm 0.96$	3.28	6.02	$11.99 \pm 0.01$
Dec	3.64	5.46	3.32	4.94	$3.73 \pm 0.77$	3.23	4.75	$12.25 \pm 0.01$
annual	3.44	7.56	2.91	6.30	$3.54 \pm 0.88$	2.80	5.88	$11.59 \pm 0.01$

time. The increased total electrical energy demand of the HP is a result of PV tracking, which occasionally leads to unfavorable HP operating conditions. However, in terms of the electricity consumption from the grid the situation improves for scenario 1.0 compared to BC scenario 0.0, which is reflected in the increased  $SPF_{sys,ctr}$  (scenario 1.0: 6.3 versus BC scenario 0.0: 4.31).

Fig. 6.17 on page 143 relates to the TABS and illustrates the frequencies of the supply water, the TABS- and the return-temperature and the specific heating power occurring during one year. Compared to all base case scenarios the temperature histograms are shifted to the left by  $\approx 3$  K for this and the other MPC scenarios.

### 6.5. DHW(TES) and SH(TABS) – scenario overview

Scenario 0.0 represents the initial base case (BC) scenario with constant source temperature ( $\vartheta_{sc} = 0$  °C) and maximum TES temperature set to 65 °C. The improved and more realistic BC scenario is BC scenario 0.1 for which the source temperature is modeled according to Kasudas formula cf. eq. (6.12), and the maximum TES temperature is set to 50 °C.

Scenario 1.0 represents the basic MPC scenario. Based on this scenario a number of variations led to the scenarios 1.1-1.3 and finally to scenario 1.4 which represents the most realistic and most relevant results. For the scenarios 1.1, 1.3a and 1.5 PV-tracking is either partly or completely deactivated, to investigate the performance of the MPCs with respect to efficiency tracking.

#### 6.5.1. Scenarios 1.1 - 1.3

The following discussion deals with the modifications with respect to scenario 1.0 (the basic MPC scenario), the most important results for these modifications may be seen in tab. 6.5.

For scenario 1.1 PV tracking for the TES was deactivated (this means also no overheating to 65 °C) which significantly increased the  $SPF_{sys}$  but at the same time the fraction of directly

used PV decreases by  $\approx 14$  pp. However, a positive side effect is that  $Q_{TES,loss}$  and  $W_{comp}$  decrease significantly. This scenario and the increase of the  $SPF$  gives already a flavor in which direction a pure  $COP$  tracking operation goes, which is finally realized for MPC scenario 1.5.

For scenario 1.2 TABS heating directly from the TES was enabled every time when the HP is in operation to heat up the TES. This slightly increased the  $SPF_{sys}$  and decreased  $Q_{TES,loss}$  by  $\approx 300$  kWh. However, the fraction of  $Q_d$ , the energy supplied into the TES via the desuperheater during SH operation, decreased significantly. This indicates, that “emptying” the TES for SH purpose causes an increase of pure TES heating cycles. From an exergetical point of view this is a disadvantage because the TES temperatures must be mixed down for SH. In parallel, the high allowed TES temperature promotes the heating from the TES because the criteria  $C_B$  is frequently fulfilled, cf. 2.3.1. These results indicate the problems involved in space heating from the TES.

For scenario 1.3 SH heating from the TES was enabled every time before the HP is switched on after a longer break. This way it should be ensured, that energy stored in the TES during a sunny interval is used for SH before switching on the HP for this purpose. It was expected, that  $Q_{TES,loss}$  decreases through this measure, however, the whole picture of performance figures (cf. tab. 6.5) did not change noticeable, which was the motivation for MPC scenario 1.3a.

## 6.6. DHW(TES) and SH(TABS) – MPC results 1.3a

For scenario 1.3a the maximum desuperheater outlet temperature  $\vartheta_{do}$  is reduced to  $50$  °C to decrease the average TES temperature. This led to a significant reduction of  $Q_{TES,loss}$  by  $\approx 600$  kWh (to 1020 kWh), in parallel the required compression work  $W_{comp}$  reduced significantly. In addition, all system performance indicators increased significantly, but the fraction of directly consumed PV electricity slightly decreased. Compared to MPC scenario 1.0 the scenario 1.3a consumes significantly less energy from the grid (1274 kWh) cf. fig. 6.7 against fig. 6.4 (1731 kWh), although, the thermal comfort is the same. The fraction of PV energy directly consumed by the HP is slightly smaller for scenario 1.3a (fig. 6.8) than for scenario 1.0 (fig. 6.5), but also the total electricity consumption of the HP is significantly smaller. The share of PV self-consumption is 50% for MPC scenario 1.3a.

MPC scenario 1.3a makes also more extensive use of the desuperheater (1631 kWh) compared to MPC scenario 1.0 (1447 kWh), but slightly less than BC scenario 0.0 (1983 kWh), see tab. H.17, H.12, H.3 in Appendix.

Tab. H.23 provides the main performance indicators and shows that the system performance improved significantly compared to the MPC scenario 1.0, although the comfort did not change noticeable. With 1022 kWh the TES losses are approximately the same as for the BC scenario 0.0, but significantly less than for MPC scenario 1.0 (1724 kWh). One reason for this may be the occasional heating from the TES enabled every time before the HP is switched on after a longer break. This way energy stored in the TES during a sunny interval is used before switching on the HP.

## 6. Results and controller performance

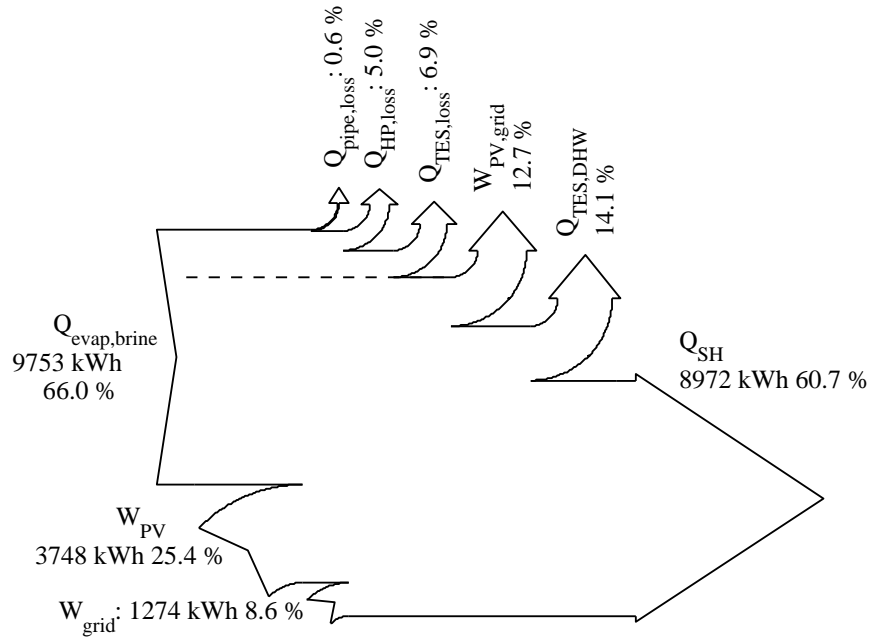


Figure 6.7.: Total annual energy flow overview;  $\vartheta_{sc} = 0^\circ\text{C}$  – MPC scenario 1.3a.

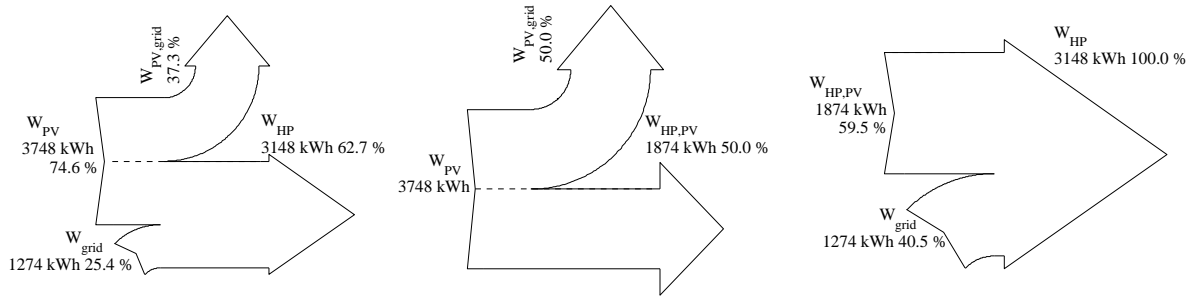


Figure 6.8.: Electrical annual energy; overview (left), split of the PV-generated related to the utilization (middle) and split of the total HP consumption related to the origin (right);  $\vartheta_{sc} = 0^\circ\text{C}$  – MPC scenario 1.3a.

### 6.7. DHW(TES) and SH(TABS) – base case results 0.1

The BC scenario 0.1 is very similar to scenario 0.0 but this time the HP source temperature  $\vartheta_{sc}$  is variable. The model for this temperature is based on the Kasuda model cf. eq. (D.6) in Appendix. Precisely the ground source temperature is a function the ground temperature in 2 m depth ( $\vartheta_{2m,t}$ ):

$$\vartheta_{sc}(t) = \vartheta_{2m,t} - 4K. \quad (6.12)$$

Due to the increased brine temperature, compare column 7 in tab. 6.3, all performance figures slightly improved in comparison to BC scenario 0.0. One must be aware, that after switching off the HP for a while the initial temperature supplied to the evaporator when switching on again is higher than  $\vartheta_{sc}$  because of the pipe connection between the source and the HP. The detailed simulation results are provided in Appendix H.2.

## 6.8. DHW(TES) and SH(TABS) – MPC results 1.4

Table 6.3.: Performance indicators overview for monthly and annual results – BC scenario 0.1.

	$SPF$	$SPF_{ctr}$	$SPF_{sys}$	$SPF_{sys,ctr}$	$COP$	$\vartheta_{sc}$	$SPF_{sys}^{pen}$ °C	$SPF_{sys,ctr}^{pen}$	$\eta_{PV}$
	–	–	–	–	–	–	–	–	–
Jan	3.77	4.76	3.53	4.46	$3.82 \pm 0.30$	0.7	3.49	4.40	$12.30 \pm 0.01$
Feb	3.81	5.05	3.51	4.65	$3.83 \pm 0.21$	-0.4	3.46	4.57	$12.20 \pm 0.01$
Mar	3.83	5.24	3.46	4.74	$3.85 \pm 0.26$	0.0	3.39	4.63	$11.88 \pm 0.01$
Apr	3.92	5.43	3.42	4.73	$3.95 \pm 0.35$	1.9	3.32	4.60	$11.57 \pm 0.01$
May	3.41	5.10	2.38	3.58	$3.41 \pm 0.46$	4.5	2.16	3.30	$11.30 \pm 0.01$
Jun	3.58	6.05	2.43	4.14	$3.57 \pm 0.48$	7.4	2.20	3.77	$11.20 \pm 0.01$
Jul	3.70	5.36	2.51	3.65	$3.70 \pm 0.52$	9.7	2.26	3.36	$11.16 \pm 0.01$
Aug	3.77	5.49	2.57	3.75	$3.77 \pm 0.53$	10.8	2.31	3.44	$11.17 \pm 0.01$
Sep	4.01	6.02	3.02	4.54	$4.20 \pm 0.71$	10.3	2.75	4.15	$11.41 \pm 0.01$
Oct	4.47	6.15	3.91	5.38	$4.55 \pm 0.45$	8.6	3.77	5.22	$11.72 \pm 0.01$
Nov	4.35	5.37	4.00	4.93	$4.38 \pm 0.27$	5.8	3.93	4.85	$11.99 \pm 0.01$
Dec	4.01	5.05	3.73	4.69	$4.05 \pm 0.26$	2.8	3.68	4.62	$12.25 \pm 0.01$
annual	3.95	5.20	3.53	4.65	$4.01 \pm 0.42$	5.2	3.44	4.53	$11.59 \pm 0.01$

## 6.8. DHW(TES) and SH(TABS) – MPC results 1.4

The MPC scenario 1.4 is very similar to 1.3a but this time the HP source temperature  $\vartheta_{sc}$  is variable according to eq. (6.12), based on the Kasuda model cf. eq. (D.6) in Appendix.

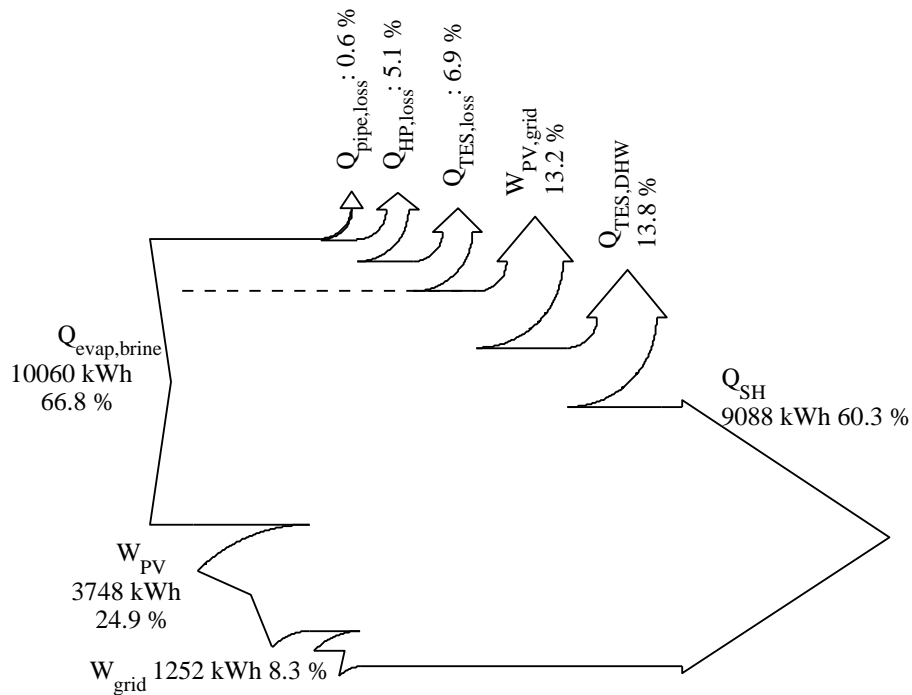


Figure 6.9.: Total annual energy flow overview;  $\vartheta_{sc} = 0^\circ\text{C}$  – MPC scenario 1.4.

Tab. 6.4 shows that the non-control related mean performance indicators are better than those for the BC scenario 0.1. Fig. 6.9 and fig. 6.10 show what can be expected in terms of energy for a realistic variable annual brine source temperature. The split of the HP power

## 6. Results and controller performance

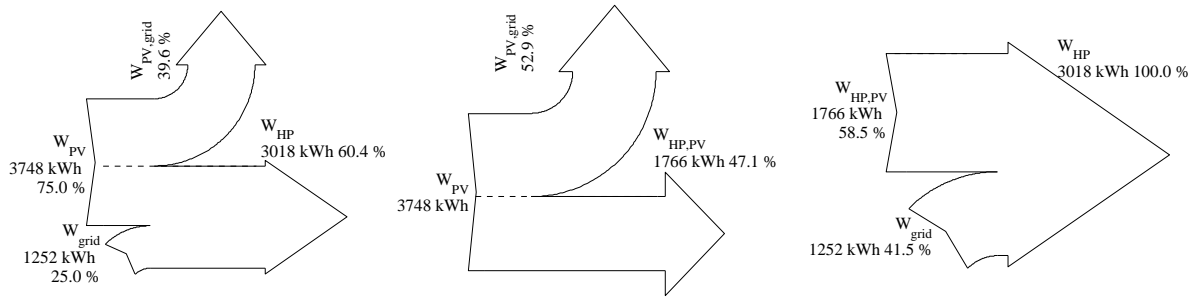


Figure 6.10.: Electrical annual energy; overview (left), split of the PV-generated related to the utilization (middle) and split of the total HP consumption related to the origin (right);  $\vartheta_{sc}$  is variable – MPC scenario 1.4.

consumption as a function of the origin (fig. 6.10 right sankey) looks very similar to the result of scenario 1.3a with constant  $\vartheta_{sc}$ .

The slightly increased exploitation of the source reservoir may be reasoned with the PV power staying the same and the increased  $COP$ . This allows for slightly increased overheating of the building during PV-led operation, which can be seen by the marginally right shifted return temperatures in fig. 6.20 compared to 6.18. Further simulation results are given in Appendix H.5.

Table 6.4.: Performance indicators overview for monthly and annual results – MPC scenario 1.4.

	$SPF$	$SPF_{ctr}$	$SPF_{sys}$	$SPF_{sys,ctr}$	$COP$	$\vartheta_{sc}$	$SPF_{sys}^{pen}$	$SPF_{sys,ctr}^{pen}$	$\eta_{PV}$	$F_{PV}^{use}$	$F_{HP}^{PV}$
	–	–	–	–	–	–	°C	–	% <sup>a</sup>	%	%
Jan	3.95	6.97	3.68	6.40	$4.0 \pm 0.5$	0.7	3.51	5.90	12.30	92	43
Feb	3.85	9.35	3.54	8.39	$3.9 \pm 0.5$	-0.4	3.41	7.67	12.20	90	59
Mar	3.68	14.61	3.34	12.70	$3.7 \pm 0.5$	0.0	3.25	11.58	11.88	75	75
Apr	3.71	21.21	3.31	17.86	$3.8 \pm 0.6$	1.9	3.23	16.03	11.57	66	83
May	3.11	15.47	2.05	10.14	$3.1 \pm 0.6$	4.5	1.89	7.79	11.30	18	80
Jun	3.23	14.42	2.14	9.51	$3.2 \pm 0.7$	7.4	1.96	7.46	11.20	17	78
Jul	3.36	16.82	2.23	11.08	$3.4 \pm 0.7$	9.7	2.03	8.43	11.16	17	80
Aug	3.41	14.56	2.26	9.56	$3.4 \pm 0.7$	10.8	2.06	7.49	11.17	17	77
Sep	3.68	15.80	2.74	11.56	$3.7 \pm 0.9$	10.3	2.53	9.28	11.41	22	77
Oct	4.36	23.45	3.89	19.69	$4.4 \pm 0.7$	8.6	3.79	17.51	11.72	69	81
Nov	4.35	8.70	3.99	7.82	$4.4 \pm 0.7$	5.8	3.90	7.50	11.99	84	50
Dec	4.16	6.70	3.87	6.16	$4.2 \pm 0.5$	2.8	3.73	5.81	12.25	95	38
Year	3.92	9.83	3.49	8.56	$4.0 \pm 0.7$	5.2	3.35	7.85	11.59	50	60

<sup>a)</sup> The empirical standard deviation over all months is 0.01.

## 6.9. Results overview and histograms

The histograms on page 142 and 143 provide details on the thermal comfort and the thermal storage capacity management – operation of the TES and the TABS. Except for  $\vartheta_{TES,z>0.8}$  all histograms are the result of SH-windowed variables. This means values where SH is inactive are disregarded for the histograms, by contrast to the values in the tables in Appendix which represent e.g. real annual averages. However, the representation for  $\vartheta_{TES,z>0.8} \propto \vartheta_{S1}$  in the tables is based on the whole year data.

The histograms in e.g. fig. 6.12 show the frequencies of the room air temperatures for the 1st and the 2nd floor and the TES temperature above a relative height of  $z=0.8$ . The histograms in e.g. fig. 6.17 show the frequencies for the most important TABS variables. A monthly break down with average room air- and operative temperatures among other temperatures and comfort relevant variables is given in Appendix H.

### Room- and TES temperatures

The histograms on page 142 (e.g. fig. 6.11) provide also the total number of SH operating hours (2307 h), the comfort violation in terms of Kh (71 Kh and 70 Kh), the number of desuperheater operating hours<sup>2</sup> (2304 h) and finally the hours during which the TES is supplied with heat (2654 h). The shown temperatures are preselected through the condition, that the space heating pump must be switched on.

In general the  $\vartheta_{ra}$  histograms are clearly different for the BC and the MPC scenarios. While the BC scenarios lead to a close to bell-shaped temperature distribution, the MPC scenarios have clear peaks at the lower end of the comfort range. The fact, that the MPC scenarios show slightly too much comfort violations for the second floor is very likely due to the average room temperature approach within the cost function defined in eq. (5.3). If the MPC would get information on the room air temperature in the ground floor zone and in the zone on the upper floor, very likely the comfort violations would not be that high. The comfort violations in Kh may be expressed in kWh considering the average  $UA$  value of the building (for 600 Kh with  $UA_{bui} = 168 \text{ W/K}$  one gets 100.8 kWh of additional heating demand to compensate the violations). However, increasing the lower temperature limits by  $\approx +0.5 \text{ K}$  should remedy this problem and bring the  $\vartheta_{ra}$  comfort violations back into the acceptable range being maximum 200 Kh<sup>3</sup>. As commented earlier, the high TES temperatures in fig. 6.12 are the reason for the relatively high TES losses.

### TABS related temperatures and heat flux

The histograms on p. 143 show less outstanding features compared to the comfort related histograms. In general all temperature distributions for the MPC scenarios are shifted a few K to the left compared to the BC scenarios. The temperatures shown are preselected through the condition, that the space heating pump must be on.

The obtained distributions for  $\vartheta_{ta}$  and  $\vartheta_{ret}$  may also be interpreted from a different point of view. Assume the MPC demonstrates a desired control behavior, now the obtained distributions can be taken as some supportive reference when trying to implement a pseudo MPC. Although a rule based approach will probably require much more information (than given here) and a clear concept what to look at and what to adjust, but the outcome from an MPC scenario is likely to provide useful information for the design of such a rule based controller.

<sup>2</sup> That means, hours where the desuperheater operates in desuperheater mode.

<sup>3</sup> It was found, that the violations with respect to  $19.5 \text{ }^\circ\text{C}$  are  $\approx 200 \text{ Kh}$  instead of 600 Kh for scenario 1.0.

## 6. Results and controller performance

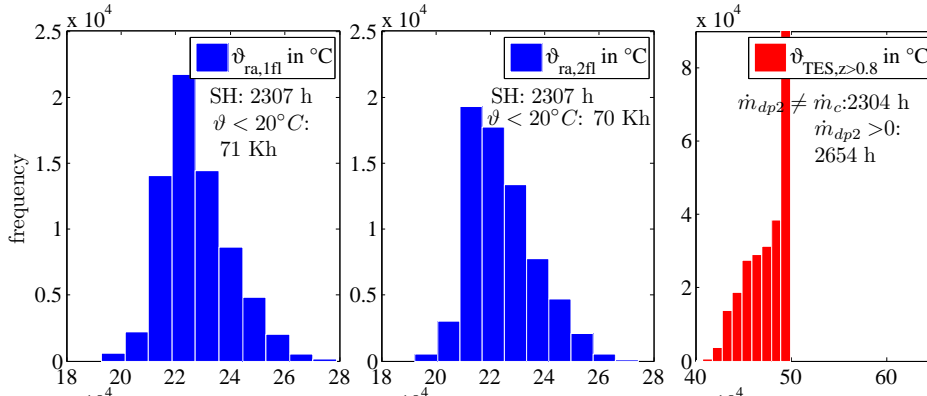


Figure 6.11.: BC scenario 0.0,  $\vartheta_{sc} = 0$  °C ; to obtain hours from absolute frequency divide by 3.

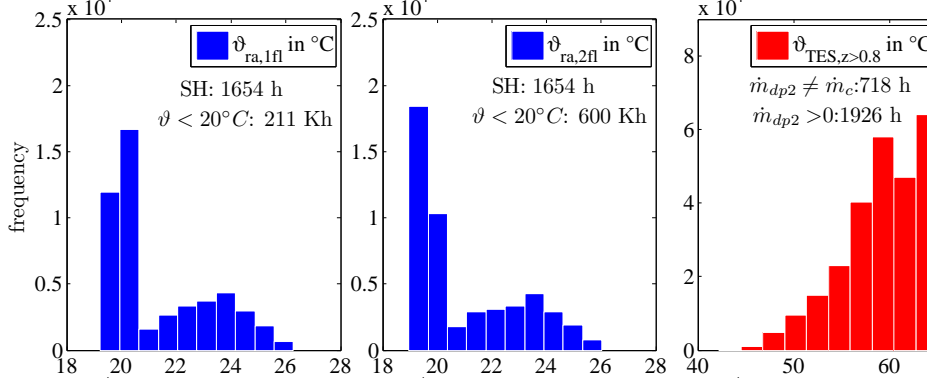


Figure 6.12.: MPC scenario 1.0,  $\vartheta_{sc} = 0$ , TES heating to 65 °C ; to obtain hours from absolute frequency divide by 3.

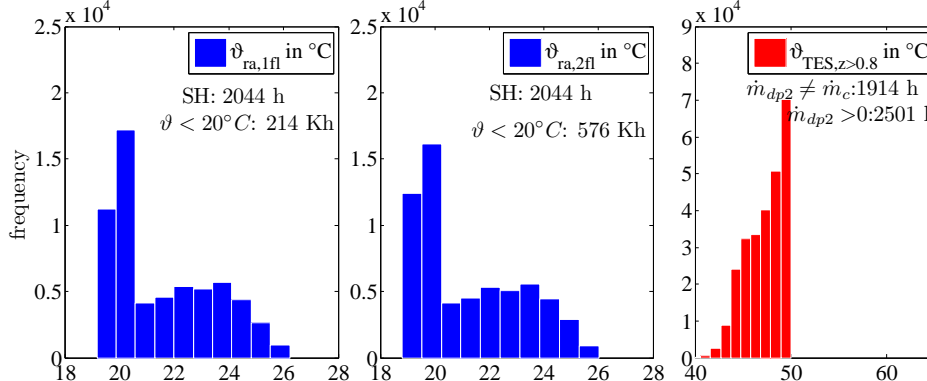


Figure 6.13.: MPC scenario 1.3a,  $\vartheta_{sc} = 0$ , SH from TES after heating was off for longer interval, TES heating to 50 °C ; to obtain hours from absolute frequency divide by 3.

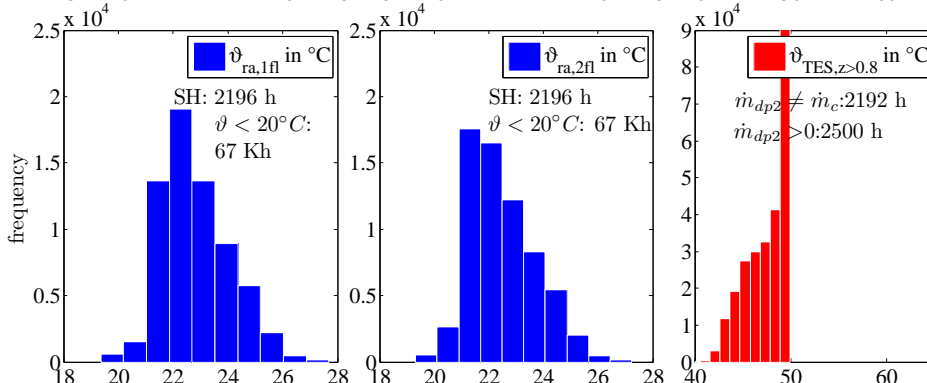


Figure 6.14.: BC scenario 0.1,  $\vartheta_{sc}$  variable; to obtain hours from absolute frequency divide by 3.

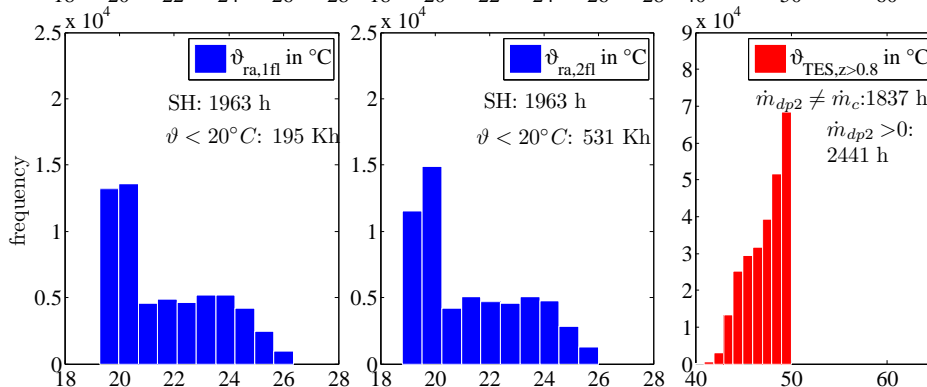


Figure 6.15.: MPC scenario 1.4, like scenario 1.3a but  $\vartheta_{sc}$  variable; to obtain hours from absolute frequency divide by 3.

## 6.9. Results overview and histograms

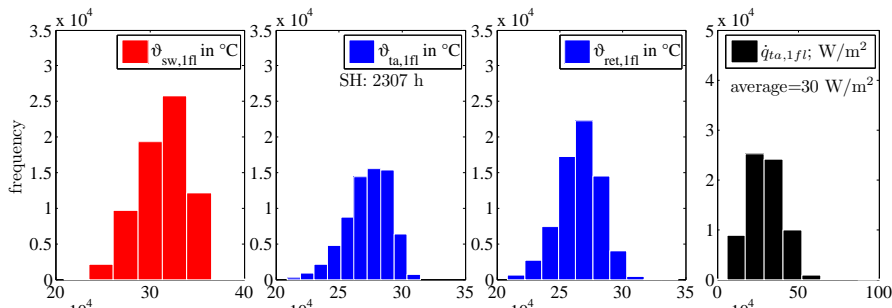


Figure 6.16.: BC scenario 0.0

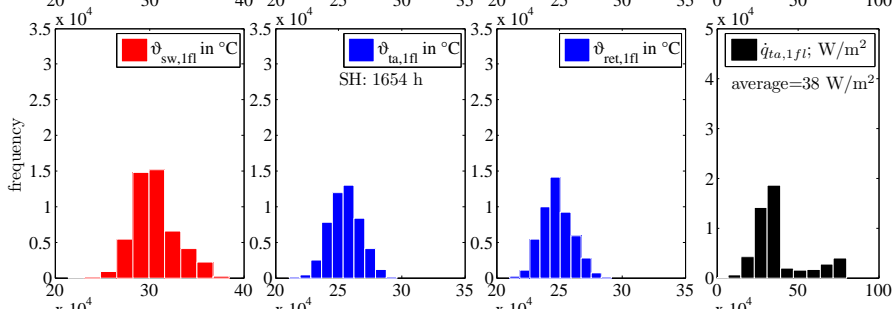


Figure 6.17.: MPC scenario 1.0

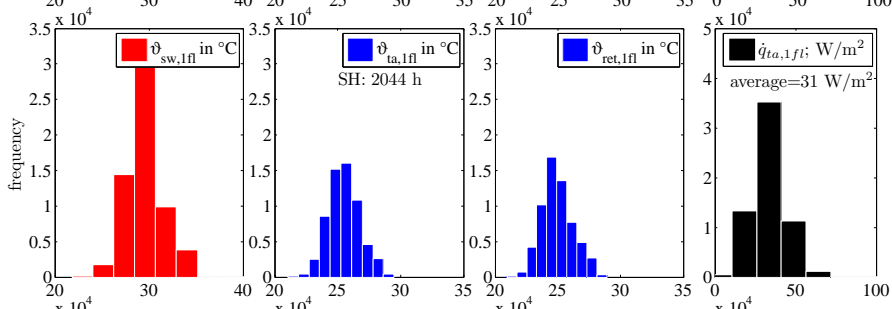


Figure 6.18.: MPC scenario 1.3a

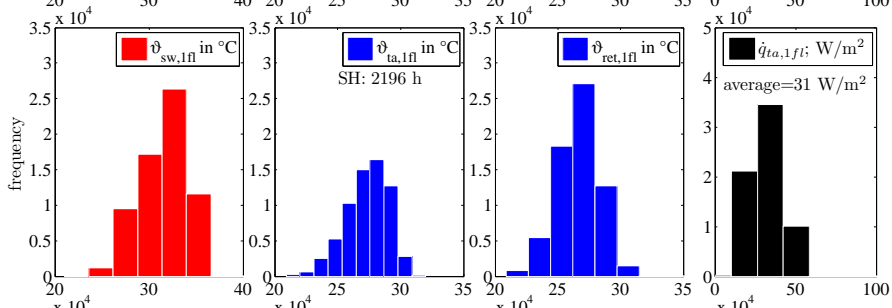


Figure 6.19.: BC scenario 0.1

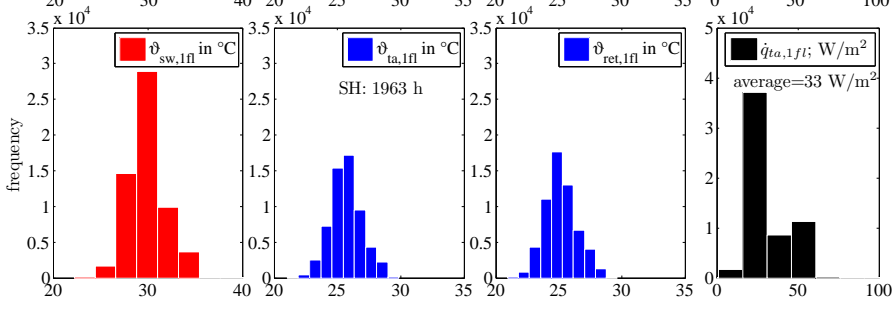


Figure 6.20.: MPC scenario 1.4

## 6. Results and controller performance

### Results overview

Tab. 6.5 provides an overview on the most relevant annual simulation results for all investigated scenarios. The very first line of the table with variable  $F_{PV,use}$  describes the *fraction of PV-generated electricity directly used* by the HP – the HP consumption is composed by the compressor and the pump (sink and source) auxiliary consumption. The numbers here are slightly larger (e.g. 20.70 %) than those given in the sankey diagrams cf. fig 6.2 (against 17.2 %) which is due to the inclusion of the auxiliary consumption, which is neglected in the diagrams. For the MPC scenarios with PV tracking (MPC 1.0 - MPC 1.4)  $F_{PV,use}$  ranges between 46 % and 62 %. If one includes also a base load<sup>4</sup> for the household consumption these numbers increase by 13 pp for a simultaneity factor<sup>5</sup> of 0.5 or by 26 pp for a simultaneity factor of 1 (which is not realistic and just a theoretical number).

Table 6.5.: Results overview for all simulated scenarios

Variable	Scenario #	BC 0.0	MPC 1.0	MPC 1.1	MPC 1.2	MPC 1.3	MPC 1.3a	BC 0.1	MPC 1.4	MPC 1.5
$F_{PV,use}$	%	20.70	60.24	45.98	61.60	60.67	53.34	20.85	50.38	17.39
$SPF_{sys}$	-	3.33	2.70	3.34	2.79	2.71	3.32	3.53	3.49	3.68
$SPF_{sys}^{pen}$	-	3.25	2.62	3.23	2.70	2.59	3.18	3.44	3.35	3.43
$SPF_{sys,ctr}^{pen}$	-	4.21	5.76	6.45	6.23	5.75	7.64	4.53	7.85	4.54
$\vartheta_{ra,avg}$	°C	22.6	22.0	22.2	22.1	21.9	22.1	22.7	22.2	21.4
$\sigma$		±1.3	±1.5	±1.6	±1.6	±1.6	±1.6	±1.3	±1.6	±1.4
$\vartheta_{S1}$	°C	47.5	59.2	47.4	55.5	58.9	47.3	47.5	47.3	47.4
		±2.0	±3.9	±1.6	±4.2	±4.1	±1.8	±2.0	±1.9	±1.4
$Q_{HP,loss}$	MWh	0.66	0.83	0.80	0.80	0.88	0.75	0.66	0.77	0.81
$Q_{TES,loss}$	MWh	1.04	1.72	1.03	1.43	1.64	1.02	1.04	1.05	0.89
$Q_c$	MWh	10.84	11.28	10.63	11.96	11.24	10.53	10.95	10.78	9.63
$Q_d$	MWh	1.98	1.45	1.74	0.60	1.29	1.63	1.87	1.54	0.98
$Q_{e,brine}$	MWh	10.18	9.70	9.97	9.59	9.61	9.75	10.34	10.06	8.96
$W_{comp}$	MWh	3.30	3.85	3.18	3.76	3.80	3.15	3.12	3.02	2.46
$Q_{in} + W_{in}$	MWh	16.58	15.18	15.29	14.93	15.02	14.77	16.56	15.06	14.63
$W_{grid}$	MWh	2.66	1.73	1.58	1.59	1.67	1.27	2.47	1.25	1.92

BC 0.0:  $\vartheta_{sc} = 0$  °C , TES heating to 50 °C ;

MPC 1.0:  $\vartheta_{sc} = 0$  °C , TES heating to 65 °C ;

MPC 1.1:  $\vartheta_{sc} = 0$  °C , TES heating to 65 °C , PV-tracking is deactivated for TES heating.

MPC 1.2:  $\vartheta_{sc} = 0$  °C , TES heating to 65 °C , SH from the TES if HP is on for TES heating.

MPC 1.3:  $\vartheta_{sc} = 0$  °C , TES heating to 65 °C , SH from the TES before HP is turned on for SH.

MPC 1.3a:  $\vartheta_{sc} = 0$  °C , TES heating to 50 °C , SH from the TES before HP is turned on for SH.

BC 0.1: variable  $\vartheta_{sc} = 0$  °C , TES heating to 50 °C ;

MPC 1.4: like MPC 1.3a but with variable  $\vartheta_{sc}$ .

MPC 1.5: like MPC 1.4 but PV-tracking is completely deactivated, i.e. pure COP-tracking

<sup>4</sup> A total household consumption of 3500 kWh is assumed over one year. The HP operation hours for an MPC scenario are approximately 2500 h.

<sup>5</sup> This simultaneity factor stands for simultaneity of household consumption and PV generation; e.g. 0.5 means that 50% of the household consumption occurs at times where sufficient PV is available to cover this household consumption.

The two base case scenarios BC 0.0 and BC 0.1 rely on the control rules defined in sec. 2.3. The difference between the scenarios is the source temperature  $\vartheta_{sc}$  which is constant 0 °C for BC 0.0 and variable according to eq. (6.12) for BC 0.1. Changing this boundary condition leads to a decreased  $W_{comp}$  and an increased  $SPF$  for BC 0.1. Apart from this, the changes of result variables are not outstanding.

Among the simulated MPC scenarios with  $\vartheta_{sc}=0$  °C (1.0 – 1.3a) scenario 1.3a performs best in terms of  $SPF_{sys,ctr}^{pen}$  and  $W_{grid}$ . Although  $F_{PV,use}$  is higher for the scenarios with increased TES heating to 65 °C in case of PV radiation, the TES losses are very high in these cases. Providing a variable  $\vartheta_{sc}$  for the setting of MPC 1.3a leads to the results given under MPC scenario 1.4. The performance figures slightly improve compared to  $\vartheta_{sc} = 0$  °C .

MPC scenario 1.5 is the same as scenario 1.4 but with PV-tracking being deactivated, that is, the MPC strives to operate the HP at maximum efficiency. This is successfully achieved, proved in terms of the highest  $SPF_{sys}$ . Due to the high comfort violations, the penalties-including  $SPF$  is not so high, but it is expected that an increased minimum set-value with less comfort violations leads to an  $SPF_{sys}^{pen}$  for scenario 1.5 which is clearly higher than for all other scenarios. An analysis of the detailed results shows supply water temperatures reduced by  $\approx 2$  K and and return temperatures reduced by  $\approx 1$  K compared to the other MPC scenarios. Tab. 6.5 demonstrates this temperature reduction – implicitly realized by the MPC to increase the efficiency – also for  $\vartheta_{ra}$ . Due to the negligence of the expected PV power within the MPC framework, the grid consumption is higher compared to the other MPC scenarios.

## Practical experience

The model sampling time  $\Delta t_s$  (1/3 h in this work) has an influence on the maximum allowed permanent control deviation. The larger the sampling time the greater the control deviation. This happens if the controlled variable, say the temperature lies outside the inner set-temperature band and the applied heating power in the first time step of the MPC simulation is enough to bring the (model) temperature into the inner band during one time-step; however, due to model inaccuracy the power might not be enough so there is a remaining deviation. Only a decrease of the controller model sampling time (e.g. 1/4 h is used for the project MPC-Boxes) lowers this permanent error or control deviation.

The evaluation of the real measurement data over almost a year from the project MPC-Boxes showed, that for pure SH control the MPC clearly outperforms the rule based control. The energy consumption of the rule based control is  $\approx 26$  % higher. Interestingly simulation results based on ideal prediction data indicate only  $\approx 12$  % savings. Another strength of the MPC compared to the rule based controller concerns overheating. In winter, for the rule based control the room air temperature repeatedly shoots over 28 °C ; this happens at days with high solar radiation. The MPC is able

## 6. Results and controller performance

to foresee such situations and turns off the TABS well in advance to prevent the overheating. Another practical aspect which was analyzed during the project MPC-Boxes relates to the temperature measurements in concrete, once directly in the concrete and once with a sensor being placed in a thermometer pocket – the measurement results were the same. For more results on the Project MPC-Boxes see Pichler and Schranzhofer (2016).

## 7. Summary and conclusion

The aim for this thesis was the development of a model predictive control (MPC)-scheme for a heat pump (HP) with variable speed compressor supplying a thermal energy storage (TES) for domestic hot water (DHW) purpose and the space heating (SH) system of a single family house. In addition, the MPC approach has to incorporate electricity generation from a PV-system installed on the roof of the house. One research question was the achievable annual fraction of PV electricity self-consumption with such an MPC. The answer to this question is given by the values for the variable  $F_{PV,used}$ . For the scenario (1.4) with the best performance from a broader perspective this number is 50%. This means, that 50% of the annual generated PV-electricity is directly consumed by the HP. If one includes also the household electricity demand an approximate estimation leads to self-consumption of 63%.

The thermal comfort related implications owing to MPC in comparison to a rule based control were investigated by means of histograms (cf. p. 142). For all MPC scenarios the room temperature frequency peaks around the minimum allowed room temperature whereas for the rule based control the temperature distribution is more bell-shaped like. An evaluation of the comfort violations shows that the number of Kh stays below the acceptable threshold of 200 Kh for the 1st floor but is more than twofold higher for the 2nd floor. The reason for this relatively high number of comfort violations on the 2nd floor is likely due to the simple representation of the room air temperature in the cost function of the MPC. Within the MPC only an average room temperature approach (for the 1st and the 2nd floor) is used within the comfort term of the cost function. The number of comfort violations may be improved through a slightly higher allowed minimum temperature in the cost function or separate consideration of the two temperatures within the MPC cost function.

For the complete MPC approach the control of the temperature in TES and the room temperature control were split into to separate MPC tasks, with higher priority for the TES controlling MPC (TES-MPC) and lower priority for the MPC in charge of the SH (TABS-MPC). The optimization problem which arose within the MPC's is either a constrained quadratic (TABS-MPC) or a mixed integer quadratic problem (TES-MPC). Hence, the TABS-MPC is computationally less involved than the TES-MPC. Typically the TES-MPC failed in 0.3 – 1.4 % of the total number of calls. In such cases values from past result trajectories were used as backup. Annual simulations for MPC scenarios took between 1.5 and 2.5 days on a standard office desktop with a time step of 20 min and a prediction horizon of 48 h for the TABS-MPC and 8 h for the TES-MPC; the

## 7. Summary and conclusion

control horizon was only one hour shorter than the prediction time step, respectively. The base case simulations took less than an hour for a simulation time step of 2 min.

The model developed for the TABS-MPC is a relatively simple linear model. For one thermal zone a model of 3rd order proved accurate enough to capture the important dynamics. For the single family house with two stores it was necessary to increase the order to 4. In terms of modeling it was started with a white box physical model, however, since this approach was not robust enough wrt different identification data it was finally replaced by a gray box approach or precisely a structured state space model (SSM). The white box approach has been investigated by Gerstgrasser (2014); the developed models require very narrow constraints for different identification data to obtain a similar parametrization, which is unwanted. Structured SSM with constraints on the matrix elements mark a robust and reliable approach well suitable for parameter estimation in context of thermal building models, and a white box physical model serves as a starting point to derive the structure of such a model. The structured SSM approach is very similar to the white box approach, but the pure physically motivated interactions of the white box model are slightly relaxed. The final model selection procedure – which was based on insight in terms of eigenvalues and the dominating eigendirection of the dynamic matrix – seems to be a reliable and versatile method to globally determine model properties and compare models from different buildings against each other. The model error within the relevant prediction horizon is barely larger than  $\pm 1$  K and never above  $\pm 2$  K.

As was explained in sec. 5.4 it is not necessary that all internal states of the thermal building model of the controller are directly measurable. By means of a Kalman Filter missing measurements may be “re-constructed”. The Kalman Filter was heuristically explained to demonstrate its intrinsic logic and operation.

The model developed for the TES-MPC required a hybrid non-linear approach. This hybrid model is composed of a linear SSM for free floating operation of the TES and a linearized general model describing the heat supply into the TES by means of the HP. An alternative to this approach is an iterative framework based on a linear model, which is documented in Arnitz (2014). That approach was not further investigated because it becomes very lengthy in terms of coding, requires also a few additional workarounds and finally is not as flexible as the approach employed herein.

The features of the developed MPC approach are HP operation according to the (future) solar irradiance or predicted PV generation (PV-tracking) and maximization of the HP operation efficiency (COP-tracking). Through PV-tracking a PV self-consumption of 50% may be achieved and COP tracking can increase the  $SPF_{sys}$  by 5%. These two features require specific characteristics of the operated HP being provided to the MPC. The basis for these characteristic functions was documented in chapter 2. Practically it is thinkable to measure these characteristics on a HP testbed. In addition, the PV-tracking of the MPC requires the determination of the expected PV power based on solar irradiance forecasts. To this end a simple efficiency curve model for the PV system

was facilitated. This model is not as accurate as the 4-parameter PV-model but accurate enough for the purpose in this work.

### 7.1. What can be learned from the MPC

When it comes to the implementation of the developed MPC in practice one may ask, whether it is really necessary to implement an MPC as opposed to imitating the behavior of the MPC by means of a complex a rule based approach. The main disadvantage of such a rule based approach is a loss of flexibility in terms of parametrization and reference values. The requirements on a rule based approach originate from the features demonstrated by the MPC. In the following paragraphs the outstanding features of the investigated MPCs are reflected.

A main requirement to maximally exploit the available thermal storage capacity of a building as thermal battery, is an empty storage at times where PV power is available. This behavior is nicely demonstrated by the MPC for the top part of the TES ( $\vartheta_{S1}$ ), but also for the building ( $\vartheta_{ra,1fl}$ ). For  $\vartheta_{S1}$  it is clearly visible, that the temperature reaches its lowest value frequently just before PV power is available. The same holds for  $\vartheta_{ra,1fl}$  and this is exactly what is required to maximally exploit all available thermal storage capacity. The remaining question is the rule-based implementation of this characteristic behavior, but this lies outside the scope of this research.

Concerning the TES for DHW purpose it was found, that heating up the TES to 65 °C is not really sensible due to highly increased storage losses. The absent SH demand in summer (cf. fig. 6.6) together with the available thermal storage capacity of the 500 L tank, leads to pure TES heating nearly only at times where PV power is available. The graphical evaluation shows that with a 500 L storage the 50 °C are already enough to ensure the thermal supply until the next PV power "peak". This probably explains why the overheating above 65 °C is not really an advantage. However, for longer periods without sun or very small TES capacities it might be sensible to overheat the TES above 50 °C .

Extensive utilization of the lower part of the TES for SH seems to be disadvantageous. The reason is, that the fraction of  $Q_d$ , the energy supplied into the TES via the desuperheater during SH operation, was found to decrease significantly if SH from the TES happens more often. This indicates, that "emptying" the TES for SH purpose causes an increase of pure TES heating cycles. That is, the utilization of the desuperheater strongly depends on sensible settings for SH from the TES. Shooting from the hip one could say deactivation of SH from the TES is the most sensible.

Another aspect concerning the HP operation is the variability of the COP. The diverse range of COP values for MPC operation of the HP is visible through the 3-fold increased empirical standard deviation (see tab. 6.2) compared to the BC scenario 0.0 (see tab. H.5).

## 7. Summary and conclusion

### 7.2. Possible future work

Practically it is thinkable to apply two times the 3rd order model but this was not investigated.

Various identification data sets (with resulting model parameters) could be used to conduct investigations on the values for the inner and the outer comfort band temperatures. On top of this different MPC cost function parameters could be tested for various model parametrizations.

The thermal output  $\dot{Q}_d$  of the desuperheater during SH operation represents a disturbance for the TES-MPC and the TES. So far this disturbance was not considered. This variable can be approximately derived from the predicted trajectories of the TABS-MPC and utilized as disturbance prediction for the TES-MPC. Probably, this way  $Q_d$  can be further increased.

So far a very simple DHW load prediction concept is used, actually 40% of the DHW demand are used and distributed over the three nodes or states of the TES model as predicted disturbance. Concerning load prediction Pedersen et al. (2016) suggests an oscillator based model with two modes, in connection with a Kalman Filter for prediction of the uncontrollable consumer load profiles. Such an approach could also be interesting for implementation.

Finally, the practical experimental investigation of the developed MPC approach or a rule based pseudo MPC, mark an interesting subject of investigation.

## Bibliography

- Aarts, R. (2012). *Course: System Identification and Parameter Estimation*. University of Twente (cit. on pp. 43, 50, 57, 58).
- Abdelrahman, H., F. Berkenkamp, J. Poland, and A. Krause (2016). "Bayesian Optimization for Maximum Power Point Tracking in Photovoltaic Power Plants." In: *European Control Conference*. IEEE, pp. 2078–2083 (cit. on p. 185).
- Ahmad, M., M. Eftekhari, T. Steffen, and A. Danjuma (2013). "Investigating the performance of a combined solar system with heat pump for houses." In: *Energy and Buildings* 63. cited By (since 1996)0, pp. 138–146 (cit. on p. 6).
- ANSI/ASHRAE Standard 55, *Thermal Environmental Conditions for Human Occupancy* (2004). American Society of Heating, Refrigeration and Airconditioning Engineers, Inc. (cit. on p. 12).
- Arnitz, A. (2014). "Model based predictive control of a heat pump system." MA thesis. Graz University of Technology, Institut für Wärmetechnik (cit. on pp. 91, 148, 165).
- Becquerel, E. (1839). "Mémoire sur les effets électriques produits sous l'influence des rayons solaires." In: *Comptes Rendus* 9, pp. 561–567 (cit. on p. 181).
- Beigelboeck, B. (2009). "Abschaetzung des Energieeinsparungspotentials durch Simulation einer Raumtemperaturregelung mit Hilfe von modellbasierten praediktiven Regelalgorithmen unter Verwendung einer idealen Wettervorhersage." MA thesis. FH-Pinkafeld (cit. on pp. 3, 8, 9).
- Bemporad, A. and M. Morari (1999). "Control of systems integrating logic, dynamics, and constraints." In: *Automatica* 35.3, pp. 407–427 (cit. on pp. 109, 123).
- Bemporad, A., M. Morari, and N. L. Ricker (2010). *Model Predictive Control Toolbox 3.2, Manual* (cit. on p. 4).
- Berkenkamp, F. and M. Gwerder (2014). "Hybrid model predictive control of stratified thermal storages in buildings." In: *Energy and Buildings* 84, pp. 233–240 (cit. on p. 91).
- Bianchi, M. A. (2006). "Adaptive Modellbasierte Praediktive Regelung einer Kleinwaermepumpenanlage." PhD thesis. ETH Zuerich (cit. on pp. 5, 6).
- Bishop, C. M. (2006). *Pattern Recognition and machine learning*. Ed. by M. Jordan, J. Kleinberg, and B. Schoelkopf. Springer (cit. on p. 236).
- Boyd, S. and L. Vandenberghe (2009). *Convex Optimization*. Cambridge University Press (cit. on p. 119).
- Bradley, D. and M. Kummert (2004). *CONVERGING ON A RECOMMENDED SET OF INTERPRETATIONS AND ASSUMPTIONS IN APPLYING STANDARD TESTS TO ENERGY ANALYSIS TOOLS*. Tech. rep. Proceedings of the IBPSA-Canada Bi-Annual Conference, eSIM 2004. IBPSA. (cit. on p. 213).

## Bibliography

- Bradley, D., M. Kummert, and T. McDowell (2004). *EXPERIENCES WITH AND INTERPRETATION OF STANDARD TEST METHODS OF BUILDING ENERGY ANALYSIS TOOLS*. Tech. rep. Proceedings of the IBPSA-Canada Bi-Annual Conference, eSIM 2004. IBPSA. (cit. on p. 213).
- Brandemuehl, M. and W. Beckman (1980). "Transmission of diffuse radiation through CPC and flat plate collector glazings." In: *Solar Energy* 24.5, pp. 511–513 (cit. on p. 187).
- Buck, A. L. (1981). "New Equation for Computing Vapor Pressure and Enhancement Factor." In: *Journal of applied meteorology* 20, pp. 1527–1532 (cit. on p. 207).
- Buck, A. L. (2012). *MODEL CR-1A HYGROMETER WITH AUTOFILL – OPERATING MANUAL*. Buck Research Instruments, LLC. PO Box 19498, Boulder, CO 80308 (cit. on p. 207).
- Camacho, E. F. and C. Bordons (2004). *Model Predictive Control*. second Edition. Springer (cit. on pp. 4, 119, 124).
- Candanedo, J., V. Dehkordi, and M. Stylianou (2013). "Model-based predictive control of an ice storage device in a building cooling system." In: *Applied Energy* 111, pp. 1032–1045 (cit. on pp. 8, 9).
- Cigler, J., J. Siroky, M. Korda, and C. N. Jones (2013). "On the Selection of the Most Appropriate MPC Problem Formulation for Buildings." In: *Congress Clima 2013* (cit. on p. 105).
- Clark, J. A. (2001). *Energy simulation in building design*. Butterworth-Heinemann (cit. on p. 217).
- Coninck, R. D. (2015). "Grey-Box Based Optimal Control for Thermal Systems in Buildings – Unlocking Energy Efficiency and Flexibility." PhD thesis. Arenberg Doctoral School Faculty of Engineering: KU LEUVEN (cit. on pp. 5, 7, 8, 189).
- Croitoru, C., I. Nastase, F. Bode, A. Meslem, and A. Dogeanu (2015). "Thermal comfort models for indoor spaces and vehicles – Current capabilities and future perspectives." In: *Renewable and Sustainable Energy Reviews* 44, pp. 304–318 (cit. on p. 13).
- Danny, G., J. Wapler, and M. Miara (May 2014). "SIMULATION AND ANALYSIS OF DEMAND SIDE MANAGEMENT EFFECTS ON OPERATING BEHAVIOUR AND EFFICIENCY OF HEAT PUMP SYSTEMS." In: *11th IEA Heat Pump Conference 2014, May 12-16 2014, Montreal (Quebec) Canada*. KN.2.3.1 (cit. on p. 7).
- Delcroix, B., M. Kummert, A. Daoud, and M. Hiller (2012). "CONDUCTION TRANSFER FUNCTIONS IN TRNSYS MULTIZONE BUILDING MODEL: CURRENT IMPLEMENTATION, LIMITATIONS AND POSSIBLE IMPROVEMENTS." In: *IBPSA-USA Journal* (cit. on p. 213).
- Dott, R., T. Afjei, A. Dalibard, D. Carbonell, A. Heinz, M. Haller, and A. Witzig (2012). *Models of Sub-components and Validation for the IEA SHC Task 44/HPP Annex 38, Part C: Heat Pump Models, A Technical Report of Sub-task C, Deliverable C2.1 Part C*. Tech. rep. (cit. on pp. 18, 97).
- Dott, R., M. Y. Haller, J. Ruschenburg, F. Ochs, and J. Bony (2013). *The Reference Framework for System Simulations of the IEA SHC Task 44 / HPP Annex 38 Part A*:

- General Simulation Boundary Conditions; Part B: Buildings and Space Heat Load*. Tech. rep. IEA (cit. on pp. 22, 23, 25, 27, 132).
- Duffie, J. A. and W. A. Beckman (2006). *Solar Engineering of Thermal Processes*. Wiley (cit. on pp. 41, 181, 187).
- Ebert, M., H. Stascheit, I. Hädrich, and U. Eitner (2014). "THE IMPACT OF ANGULAR DEPENDENT LOSS MEASUREMENT ON PV MODULE ENERGY YIELD PREDICTION." In: *29th European PV Solar Energy Conference and Exhibition, Amsterdam, The Netherlands* (cit. on p. 186).
- Eckstein, J. H. (1990). "Detailed modelling of photovoltaic system components." MA thesis. University of Wisconsin - Madison (cit. on pp. 40, 41, 182, 183, 185).
- Electronic, T. (2015). *Platin Temperatur Sensoren, Ueberischt zu linearen Sensoren, Eigenerwärmung, Telemeter Electronic GmbH* (cit. on p. 194).
- ESSO (2009). *Energieeffiziente Gebaeude mit nachhaltigem Komfort Passives Kuehlen Solare Raumwaerme Tageslichtbeleuchtung PRODUKTBLAETTER SONNENSCHUTZSYSTEME*. Tech. rep. European solar shading organization (cit. on pp. 76, 79).
- Fanger, P. O. (1981). "Indoor Climate, D.A. McIntyre. Applied Science Publishers, London (1980)." In: *Journal of Environmental Psychology* 1.3, pp. 259–260 (cit. on pp. 12, 209, 215).
- Fanger, P., B. Ipsen, G. Langkilde, B. Olessen, N. Christensen, and S. Tanabe (1985). "Comfort limits for asymmetric thermal radiation." In: *Energy and Buildings* 8.3, pp. 225–236 (cit. on pp. 13, 210, 211).
- Fechner, H., C. Mayr, A. Schneider, M. Rennhofer, and G. Peharz (2016). *Technologie-Roadmap für Photovoltaik in Österreich*. Tech. rep. Bundesministerium für Verkehr, Innovation und Technologie (cit. on p. 131).
- Fletcher, R. (2007). *Practical methods of OPTIMIZATION*. Wiley (cit. on pp. 119, 123).
- Fry, B. (1998). "Simulation of grid tied building integrated photovoltaic systems." MA thesis. University of Wisconsin - Madison (cit. on pp. 40, 183).
- Gaehler, C., M. Gwerder, R. Lamon, and J. Toedtli (2007). "Optimal Control of Cogeneration Building Energy Systems, Proceedings of Clima 2007 WellBeing Indoors, REHVA." In: (cit. on pp. 9, 10).
- Garcia, C. E., D. M. Prett, and M. Morari (1989). "Model predictive control: Theory and practice – a survey." In: *Automatica* 25.3, pp. 335–348 (cit. on p. 5).
- Garcia, M., L. Marroyo, E. Lorenzo, and M. Perez (2011). "Soiling and other optical losses in solar-tracking PV plants in navarra." In: *Progress in Photovoltaics: Research and Applications* 19.2, pp. 211–217 (cit. on p. 186).
- Gerstgrasser, D. (2014). "Modellprädiktive Regelung für Klimatisierungseinrichtungen." MA thesis. Graz University of Technology, Institut für Regelungstechnik (cit. on pp. 69, 148, 165).
- Glueck, B. (1994). "Zulaessige Strahlungstemperatur-Asymmetrie." In: *Gesundheits-Ingenieur* 6, pp. 285–344 (cit. on pp. 210, 211).
- Glueck, B. (1990). *Bausteine der Heizungstechnik – Waermeuebertragung, Waermeabgabe von Heizflaechen und Rohren*. Verlag fuer Bauwesen (cit. on pp. 204, 215).

## Bibliography

- Glueck, B. (1999). *Thermische Bauteilaktivierung*. Tech. rep. Rud. Otto Meyer-Umwelt-Stiftung (cit. on pp. 205, 206).
- Grondzik, W. T. (2009). *ASHRAE Handbook Fundamentals (SI Edition)*. Ed. by M. S. Owen. W. Stephen Comstock (cit. on p. 215).
- Gruenenfelder, W. J. and J. Toedtli (1985). "The Use of Weather predictions and dynamic programming in the control of solar domestic hot water systems." In: *Melecon'85, Madrid, Spain* (cit. on p. 1).
- Gurobi (2015). "Gurobi Optimizer 6.5." In: *www.gurobi.com*. Free Academic License (cit. on pp. 120, 124, 126).
- Gwerder, M., D. Gyalistras, F. Oldewurtel, B. Lehmann, K. Wirth, V. Stauch, and J. Toedtli (2010). "Potential Assessment of Rule-Based Control for Integrated Room Automation." In: *10th REHVA World Congress – Clima 2010* (cit. on p. 8).
- Gwerder, M., D. Gyalistras, C. Sagerschnig, R. Smith, and D. Sturzenegger (2013). *Final Report: Use of Weather And Occupancy Forecasts For Optimal Building Climate Control – Part II: Demonstration (OptiControl-II)*. Tech. rep. (cit. on pp. 1, 5, 8, 189).
- Gyalistras, D. and M. Gwerder (2010). *Use of Weather and Occupancy Forecasts for Optimal Building Climate Control (OptiControl): Two Years Progress Report*. Tech. rep. Terrestrial Systems Ecology ETH Zurich, Building Technologies Division, Siemens Switzerland Ltd., Zug, Switzerland (cit. on pp. 3, 8, 10).
- Haller, M. Y. (2013). *Intercomparison of System Simulation Results for the IEA SHC Task 44 / HPP Annex 38 – A technical report of subtask C, Deliverable C4.2*. Tech. rep. IEA (cit. on p. 128).
- Halvgaard, R., P. Bacher, B. Perers, E. Andersen, S. Furbo, J. B. Jorgensen, N. K. Poulsen, and H. Madsen (2012). "Model Predictive Control for a Smart Solar Tank Based on Weather and Consumption Forecasts." In: *Energy Procedia* 30, pp. 270–278 (cit. on p. 8).
- Hengel, F., A. Heinz, and R. Rieberer (2014). "ANALYSIS OF AN AIR SOURCE HEAT PUMP SYSTEM WITH SPEED CONTROLLED COMPRESSOR AND VAPOR INJECTION." In: *Proceedings of 11th IEA Heat Pump Conference 12-16 May, Montreal, Canada* (cit. on pp. 18, 30).
- Hengel, F., A. Heinz, and R. Rieberer (2016). "Performance analysis of a heat pump with desuperheater for residential buildings using different control and implementation strategies." In: *Applied Thermal Engineering* 105, pp. 256–265 (cit. on pp. 18, 30).
- Herrmann, C., V. Candás, A. Hoeft, and I. Garreaud (Nov. 1994). "Humans under showers: Thermal sensitivity, thermoneutral sensations, and comfort estimates." In: *Physiology & Behavior* 56.5, pp. 1003–1008 (cit. on pp. 13, 60).
- Heusden, K. van, A. Karimi, and T. Söderström (2010). "On identification methods for direct data-driven controller tuning." In: *INTERNATIONAL JOURNAL OF ADAPTIVE CONTROL AND SIGNAL PROCESSING* (cit. on p. 55).
- Horn, M. and N. Dourdoumas (2004). *Regelungstechnik: Rechnerunterstützter Entwurf zeitkontinuierlicher und zeitdiskreter Regelkreise*. Pearson Studium (cit. on p. 174).
- Hundy, G., A. Trott, and T. Welch (2016). "Chapter 3 - Refrigerants." In: *Refrigeration, Air Conditioning and Heat Pumps (Fifth Edition)*. Ed. by G. Hundy, A. Trott, and

- T. Welch. Fifth Edition. Butterworth-Heinemann, pp. 41–58. ISBN: 978-0-08-100647-4 (cit. on p. 18).
- Kalman, R. E. (1960). "A New Approach to Linear Filtering and Prediction Problems." In: *Transactions of the ASME—Journal of Basic Engineering* 82, pp. 35–45 (cit. on p. 113).
- Karlsson, H. and C.-E. Hagentoft (2011). "Application of model based predictive control for water-based floor heating in low energy residential buildings." In: *Building and Environment* 46.3, pp. 556–569 (cit. on pp. 8, 43, 189).
- Karlsson, H. (2010). "Thermal Modelling of Water-Based Floor Heating Systems - supply temperature optimisation and self-regulating effects." Professor Bjarne Olesen, Technical University of Denmark. PhD thesis. Chalmers University of Technology (cit. on pp. 1, 5, 8).
- Kasten, F. and G. Czeplak (1980). "Solar and terrestrial radiation dependent on the amount and type of cloud." In: *Solar Energy* 24.2, pp. 177–189 (cit. on p. 226).
- Kasuda, T. and P. Archenbach (1965). "Earth Temperature and Thermal Diffusivity at Selected Stations in the United States." In: *ASHRAE Transactions* 71, Part 1 (cit. on p. 201).
- Keller, B. (1997). *Klimagerechtes Bauen: Grundlagen - Dimensionierung - Beispiele*. Vieweg und Teubner Verlag (cit. on p. 215).
- Killian, M., B. Mayer, and M. Kozek (2014). "Hierarchical Fuzzy MPC Concept for Building Heating Control." In: *Preprints of the 19th World Congress The international Federation of Automatic Control* (cit. on p. 57).
- King, D. L., A. J. Kratochvil, and W. E. Boyson (Sept. 1997). "Measuring the Solar Spectral and Angle-of-Incidence Effects on Photovoltaic Modules and Irradiance Sensors." In: *Proceedings of the 1994 IEEE Photovoltaics Specialists Conference*, pp. 1113–1116 (cit. on p. 186).
- Klein, S. et al. (2010). *A TRaNsient SYstems Simulation Program, Vol.5 Multizone Building modeling with Type56 and TRNBuild*. TRNSYS Coordinator Thermal Energy System Specialists. LLC 22 North Carroll Street – suite 370 Madison, WI 53703 – U.S.A. (cit. on p. 204).
- Klein, S. et al. (2013). *A TRaNsient SYstems Simulation Program – TRNSYS 17.00.0019, Manual*. Solar Energy Laboratory, University of Wisconsin-Madison (cit. on pp. ix, 15, 23, 97, 204, 215, 216).
- Kofler, D. (2016). "Untersuchung von "einfachen" Ansätzen zur prädiktiven Regelung von Wärmepumpen." MA thesis. Graz University of Technology, Institut für Wärmetechnik (cit. on pp. 24, 27, 127).
- Kolokotsa, D., A. Pouliezos, G. Stavrakakis, and C. Lazos (2009). "Predictive Control techniques for energy and indoor environmental quality management in buildings." In: *Building and Environment* 44.9, pp. 1850–1863 (cit. on p. 8).
- Korkas, C. D., S. Baldi, I. Michailidis, and E. B. Kosmatopoulos (2015). "Intelligent energy and thermal comfort management in grid-connected microgrids with heterogeneous occupancy schedule." In: *Applied Energy* 149, pp. 194–203 (cit. on p. 5).

## Bibliography

- Koschenz, M. and V. Dorer (1999). "Interaction of an air system with concrete core conditioning." In: *Energy and Buildings* 30.2, pp. 139–145 (cit. on p. 22).
- Koschenz, M. and B. Lehmann (2000). *Thermoaktive Bauteilsysteme TABS*. Ed. by M. Koschenz. EMPA (cit. on p. 22).
- Laenderexpertengruppe (2011). *OIB Richtlinie 6*. Austrian Institute of Construction Engineering (cit. on p. 190).
- Langevin, J., P. L. Gurian, and J. Wen (2015). "Tracking the human-building interaction: A longitudinal field study of occupant behavior in air-conditioned offices." In: *Journal of Environmental Psychology* 42, pp. 94–115 (cit. on p. 78).
- Lauri, D., J. Salcedo, S. Garca-Nieto, and M. Martinez (Sept. 2010). "Model predictive control relevant identification: multiple input multiple output against multiple input single output." English. In: *IET Control Theory & Applications* 4 (9), 1756–1766(10) (cit. on pp. 8, 57).
- Lechner, T. (1992). *Berechnung des Waermestromes durch ebene geschichtete Waende, Mathematische und physikalische Grundlagen der Transfer Function - Methode*. Tech. rep. Institut fuer Thermodynamik und Waermetechnik Universitaet Stuttgart (cit. on p. 213).
- Lehmann, B., V. Dorer, and M. Koschenz (2007). "Application range of thermally activated building systems tabs." In: *Energy and Buildings* 39.5, pp. 593–598 (cit. on p. 22).
- Li, S., J. Joe, J. Hu, and P. Karava (2015). "System identification and model-predictive control of office buildings with integrated photovoltaic-thermal collectors, radiant floor heating and active thermal storage." In: *Solar Energy* 113, pp. 139–157 (cit. on pp. 7, 8).
- Ljung, L. (1999). *System Identification – Theory for the User*. Ed. by T. Kailath. Prentice Hall (cit. on pp. 43, 49, 50, 52, 55, 56, 58, 62, 70, 236).
- Ljung, L. (2002). "Prediction Error Estimation Methods." In: *Circuits Systems Signal Processing* 21, pp. 11–21 (cit. on pp. 55, 56).
- Ljung, L. (2013). *MATLAB R2013b, System Identification Toolbox – Manual*. The MathWorks GmbH (cit. on pp. 62, 70, 71).
- Löfberg, J. (2004). "YALMIP : A Toolbox for Modeling and Optimization in MATLAB." In: *Proceedings of the CACSD Conference, Taipei, Taiwan* (cit. on pp. 120, 126).
- Maciejowski, J. M. (2002). *Predictive Control with Constraints*. Pearson Education (cit. on pp. 4, 9, 106, 119, 123).
- Malkawi, A. M. and G. Augenbroe (2004). *Advanced Building Simulation*. Ed. by A. M. Malkawi and G. Augenbroe. Spon Press (cit. on pp. 213, 225).
- Martin, M. and P. Berdahl (1984). "Characteristics of Infrared Sky Radiation in the United States." In: *Solar Energy* 33. Lawrence Berkeley Laboratory, University of California, pp. 321–336 (cit. on pp. 23, 206, 226).
- Martin, N. and J. Ruiz (2005). "Annual angular reflection losses in PV modules." In: *Prog. Photovolt: Res. Appl.* 13, pp. 75–84 (cit. on p. 187).

- Mayer, B., M. Killian, and M. Kozek (2015). "Management of hybrid energy supply systems in buildings using mixed-integer model predictive control." In: *Energy Conversion and Management* 98, pp. 470–483 (cit. on p. 1).
- Morari, M. and J. H. Lee (1999). "Model predictive control: past, present and future." In: *Computers & Chemical Engineering* 23.4-5, pp. 667–682 (cit. on pp. 3–6).
- OENORM (2003a). *Dateblatt- und Typschildangaben von Photovoltaik-Modulen*. Österreichischer Verband für Elektrotechnik (cit. on p. 184).
- OENORM (2003b). *Heizungsanlagen in Gebaeuden - Verfahren zur Berechnung der Normheizlast*. Oesterreichisches Normungsinstitut (cit. on p. 197).
- OENORM (2006a). *OENORM EN ISO 7730, Ergonomie der thermischen Umgebung - Analytische Bestimmung und Interpretation der thermischen Behaglichkeit durch Berechnung des PMV- und des PPD-Indexes und Kriterien der lokalen thermischen Behaglichkeit*. Oesterreichisches Normungsinstitut (cit. on pp. 12, 13, 60, 209).
- OENORM (2006b). *OENORM Vornorm H 7500, Heizungssystem in Gebaeude - Verfahren zur Berechnung der Normheizlast*. Oesterreichisches Normungsinstitut (cit. on p. 197).
- OENORM (2006c). *Waermeschutz im Hochbau; Teil 6: Grundlagen und Nachweisverfahren Heizwaermebedarf und Kuehlbedarf* (cit. on pp. 197, 215).
- OENORM (2007). *OENORM EN 15251, Eingangsparameter fuer das Raumklima zur Auslegung und Bewertung der Energieeffizienz von Gebaeuden – Raumluftqualitaet, Temperatur, Licht und Akustik*. Oesterreichisches Normungsinstitut (cit. on pp. 12, 14, 209).
- OENORM (Jan. 2008a). *Lueftung von Nichtwohngebaeuden - Allgemeine Grundlagen und Anforderungen fuer Lueftungs- und Klimaanlagen und Raumkuehlssysteme OENORM EN 13779*. ON Oesterreichisches Normungsinstitut (cit. on p. 12).
- OENORM (2008b). *ÖNORM EN 15377, Heizungsanlagen in Gebaeuden – Planung von eingebetteten Flaechenheiz- und -kuehlssystemen mit Wasser als Arbeitsmedium Teil 1-3* (cit. on p. 204).
- OENORM (2008c). *Waermetechnisches Verhalten von Bauteilen - Dynamisch-thermische Kenngroessen - Berechnungsverfahren*. OENORM 2008 (cit. on p. 204).
- OENORM (2010). *Waermeschutz im Hochbau; Teil 5: Klimamodell und Nutzungsprofile* (cit. on p. 190).
- Oertel, H., M. Böhle, and T. Reviol (2011). *Strömungsmechanik – Grundlagen - Grundgleichungen - Lösungsmethoden - Softwarebeispiele*. Springer Vieweg (cit. on p. 96).
- Oldewurtel, F., D. Gyalistras, M. Gwerder, C. N. Jones, A. Parisio, V. Stauch, B. Lehmann, and M. Morari (2010). "Increasing Energy Efficiency in Building Climate Control using Weather Forecasts and Model Predictive Control." In: *Clima 2010 - REHVA World Congress* (cit. on pp. 8, 11, 14, 225).
- Oldewurtel, F., A. Parisio, C. N. Jones, D. Gyalistras, M. Gwerder, V. Stauch, B. Lehmann, and M. Morari (2012). "Use of model predictive control and weather forecasts for energy efficient building climate control." In: *Energy and Buildings* 45, pp. 15–27 (cit. on pp. 8, 14).
- Oldewurtel, F., A. Parisio, C. N. Jones, M. Morari, D. Gyalistras, M. Gwerder, V. Stauch, B. Lehmann, and K. Wirth (June 2010). "Energy Efficient Building Climate Control

## Bibliography

- using Stochastic Model Predictive Control and Weather Predictions." In: *American Control Conference*. Baltimore, USA (cit. on p. 8).
- Papoulis, A. (1991). *Probability, Random Variables, and Stochastic Processes*. Ed. by S. W. Director. 3rd. McGraw-Hill, Inc. (cit. on p. 115).
- Pedersen, R., C. Sloth, and R. Wisniewski (2016). "Active Power Management in Power Distribution Grids: Disturbance Modeling and Rejection." In: *European Control Conference*. IEEE, pp. 1782–1787 (cit. on p. 150).
- Perez, R., P. Ineichen, R. Seals, J. Michalsky, and R. Stewart (1990). "Modeling daylight availability and irradiance components from direct and global irradiance." In: *Solar Energy* 44, pp. 271–289 (cit. on p. 23).
- Pichler, M. F., A. Arnitz, M. Brychta, A. Heinz, and R. Rieberer (2016). "Small Scale PV-Power – On Site Use Maximization through Smart Heat Pump Control." In: *International Journal of Contemporary Energy* 2, pp. 22–30 (cit. on p. 165).
- Pichler, M. F., A. Droescher, H. Schranzhofer, G. K. and G.I. Giannakis, E. Kosmatopoulos, and D. Rovas (2011). "Simulation-Assisted Building Energy Performance Improvement Using Sensible Control Decisions." In: *BuildSys'11 Proceedings*, Seattle, WA, USA, (cit. on pp. 5, 10).
- Pichler, M. F., G. Goertler, and H. Schranzhofer (June 2016). "Test buildings with TABS for MPC-performance evaluation – Comparability and System Identification." In: *Europe Control Conference (ECC16) Aalborg* (cit. on pp. 66, 71, 165, 197, 238).
- Pichler, M. F. and A. Heinz (2016). *TheBat – Die Thermische Batterie im Smart Grid in Kombination mit Wärmepumpen – eine Interaktionsoptimierung*. Tech. rep. (interner Bericht IWT). Graz University of Technology (cit. on p. 165).
- Pichler, M. F., A. Heinz, and R. Rieberer (2016). "Modellprädiktive Regelung eines Wärmepumpen-PV-Systems für ein Einfamilienhaus." In: *DKV-Tagung 2016, Kassel* (cit. on p. 165).
- Pichler, M. F., A. Heinz, and R. Rieberer (2017). "MODEL PREDICTIVE HP- AND BUILDING CONTROL TO MAXIMIZE PV-POWER ON SITE USE." In: *12th IEA Heat Pump Conference* (cit. on p. 165).
- Pichler, M. F., W. Lerch, A. Heinz, G. Goertler, H. Schranzhofer, and R. Rieberer (2014). "A novel linear predictive control approach for auxiliary energy supply to a solar thermal combistorage." In: *Solar Energy* 101, pp. 203–219 (cit. on pp. 60, 90, 91, 95).
- Pichler, M. F. and H. Schranzhofer (2016). *Model Predictive Control von aktiven Bauteilen und Messungen in zwei Test-BOXen*. Tech. rep. TU Graz, interner Bericht (cit. on p. 146).
- Pichler, M. F., H. Schranzhofer, and G. Goertler (2016). *Model Predictive Control von aktiven Bauteilen und Messungen in zwei Test-BOXen*. Tech. rep. Projektbericht im Rahmen des Programms Haus der Zukunft plus - Entwurf (cit. on p. 165).
- Privara, S. (2013). "BUILDING MODELING AND IDENTIFICATION FOR PREDICTIVE CONTROL." PhD thesis. Department of Control Engineering Faculty of Electrical Engineering Czech Technical University in Prague (cit. on pp. 1, 5, 189).

- Privara, S., J. Cigler, V. Zdenek, F. Oldewurtel, C. Sagerschnig, and Z. Eva (2013). "Building modeling as a crucial part for building predictive control." In: *Energy and Buildings* 56, pp. 8–22 (cit. on pp. 8, 43).
- Privara, S., J. Cigler, Z. Váňa, F. Oldewurtel, and E. Žáčková (2013). "Use of partial least squares within the control relevant identification for buildings." In: *Control Engineering Practice* 21.1, pp. 113–121 (cit. on p. 57).
- Privara, S., Z. Vana, E. Žáčková, and J. Cigler (2012). "Building modeling: Selection of the most appropriate model for predictive control." In: *Energy and Buildings* 55. Cool Roofs, Cool Pavements, Cool Cities, and Cool World, pp. 341–350 (cit. on p. 8).
- Qin, S. and T. A. Badgwell (2003). "A survey of industrial model predictive control technology." In: *Control Engineering Practice* 11.7, pp. 733–764 (cit. on p. 4).
- Rana, R., B. Kusy, R. Jurdak, J. Wall, and W. Hu (2013). "Feasibility analysis of using humidex as an indoor thermal comfort predictor." In: *Energy and Buildings* 64, pp. 17–25 (cit. on p. 13).
- Recknagel Sprenger, S. (2013/2014). *Taschenbuches fuer Heizung und Klimatechnik*. Oldenbourg Industrieverlag GmbH (cit. on pp. 18, 204).
- Reiner, G., E. Shafai, R. Wimmer, D. Zogg, H. Gabathuler, H. Mayer, and H. Bruderer (1998). *Kurztestmethode fuer Wärmepumpenanlagen. Phase 1 bis 3: Messung, Modellierung und Erprobung der Parameteridentifikation*. Tech. rep. Forschungsprogramm UAW des Bundesamtes fuer Energie, Bern (cit. on pp. 6, 43).
- Richalet, J., A. Rault, J. L. Testud, and J. Papon (Sept. 1978). "Paper: Model Predictive Heuristic Control." In: *Automatica* 14.5, pp. 413–428 (cit. on p. 5).
- Rovas, D. (2011). *PEBBLE Deliverable 3.2: PEBBLE Building Optimization and Control System*. Tech. rep. Technical University of Crete (cit. on pp. 5, 9, 10).
- Sarver, T., A. Al-Qaraghuli, and L. L. Kazmerski (2013). "A comprehensive review of the impact of dust on the use of solar energy: History, investigations, results, literature, and mitigation approaches." In: *Renewable and Sustainable Energy Reviews* 22, pp. 698–733 (cit. on p. 186).
- Schaefer, A., H. Schuster, U. Kasper, and A. Moser (2015). *Electrochemical Energy Storage for Renewable Sources and Grid Balancing – Ch.3*. Ed. by P. T. Mosely and J. Garche. Elsevier (cit. on p. 15).
- Schuss, M. (2011). "Implementation of a predictive simulation-based controller for environmental systems in buildings." PhD thesis. Vienna University of Technology (cit. on pp. 5, 10).
- Seem, J. E. (1987). "Modeling of heat transfer in buildings." PhD thesis. University of Wisconsin-Madison (cit. on pp. 213, 214).
- Shockley, W. (1956). "Transistor technology evokes new physics." In: *Nobel Lecture, December 11*, pp. 344–374 (cit. on p. 182).
- Snoek, C. W. and S. C. Kluiters (2011). "THERMAL STORAGE OPTIONS FOR SOLAR HEATED BUILDINGS." In: *Proceedings of Building Simulation 2011*, pp. 138–145 (cit. on pp. 8, 10).

## Bibliography

- Soto, W. D., S. Klein, and W. Beckman (2006). "Improvement and validation of a model for photovoltaic array performance." In: *Solar Energy* 80.1, pp. 78–88 (cit. on pp. 40, 181).
- Sourbron, M., C. Verhelst, and L. Helsen (2013). "Building models for model predictive control of office buildings with concrete core activation." In: *Journal of Building Performance Simulation* 6.3, pp. 175–198 (cit. on pp. 5, 8, 43, 189, 209).
- Sourbron, M. and L. Helsen (2011). "Evaluation of adaptive thermal comfort models in moderate climates and their impact on energy use in office buildings." In: *Energy and Buildings* 43, pp. 423–432 (cit. on p. 13).
- Stephenson, D. and G. Mitalas (1971). "Calculation of heat conduction transfer functions for multi-layer slabs." In: *ASHRAE Transactions* 77(2), pp. 117–126 (cit. on p. 213).
- Sturzenegger, D., D. Gyalistras, M. Morari, and R. S. Smith (2012). "Semi-Automated Modular Modeling of Buildings for Model Predictive Control." In: *Buildsys'12 Proceedings*, Toronto, ON, Canada. (cit. on pp. 1, 5, 8, 43, 57, 58).
- Sundström, C., D. Jung, and A. Blom (2016). "Analysis of Optimal Energy Management in Smart Homes Using MPC." In: *European Control Conference*. IEEE (cit. on p. 113).
- Tanner, C. (2004). *Luftdichtigkeits-Messungen: Bitte besser... !* Tech. rep. EMPA (cit. on p. 197).
- Thornton, J., D. Bradley, T. McDowell, N. Blair, M. Duffy, N.D.LaHam, and A. Naik (2012). *TESSLibs 17 – Component Libraries for the TRNSYS Simulation Environment*. Thermal Energy System Specialists, LLC of Madison, Wisconsin, USA (cit. on p. 22).
- Toedtli, J. (2011). "Praediktive Regelungen und Wetterprognosen in der Gebaudeautomation – Ueberlegungen im Vorfeld zweier Forschungsprojekte." In: *SGA – ASSPA – SSAC BULLETIN* 59, pp. 2–12 (cit. on p. 189).
- Toedtli, J., M. Gwerder, B. Lehmann, F. Renggli, and V. Dorer (2009). *TABS Control - Steuerung und Regelung von thermoaktiven Bauteilsystemen*. Faktor Verlag Zuerich (cit. on pp. 13, 194).
- Townsend, T. (1989). "A Method for Estimating the Long-Term Performance of Direct-Coupled Photovoltaic Systems." MA thesis. University of Wisconsin – Madison (cit. on pp. 40, 181, 182).
- Wallace, M., R. McBride, S. Aumi, P. Mhaskar, J. House, and T. Salsbury (2012). "Energy efficient model predictive building temperature control." In: *Chemical Engineering Science* 69.1, pp. 45–58 (cit. on p. 6).
- Wimmer, R. W. (2004). "Regelung einer Waermepumpenanlage mit Model Predictive Control." PhD thesis. ETH Zuerich (cit. on pp. 3, 5, 6, 123).
- Yang, L., H. Yan, and J. C. Lam (2014). "Thermal comfort and building energy consumption implications – A review." In: *Applied Energy* 115, pp. 164–173 (cit. on p. 12).
- Young, J. Y. (Aug. 2013). "DEMAND-SIDE-MANAGEMENT WITH HEAT PUMPS FOR SINGLE FAMILY HOUSES." In: *Proceedings of BS2013, 13th Conference of International Building Performance Simulation Association, Chambéry, France* (cit. on pp. 7, 129).

- Žáčková, E., S. Privara, and Z. Vana (2011). "Model predictive control relevant identification using partial least squares for building modeling." In: *Australian Control Conference, Melbourne* (cit. on pp. 8, 57).
- Žáčková, E., Z. Váňa, and J. Cigler (2014). "Towards the real-life implementation of MPC for an office building: Identification issues." In: *Applied Energy* 135, pp. 53–62 (cit. on pp. 5, 8, 43, 189).



# Appendix



## Appendix A.

### Overview on related publications

The following excerpt provides an overview on related publications elaborated on during the genesis of this work. The Master-thesis of Gerstgrasser (2014) focuses on the derivation of a pure physical white box model for a simple building construction (cf. 3rd order model for a Test-Box within the project MPC-Boxes). The finally successful 3rd order, structured state space model, which is closely related to the pure physical model is outlined and investigated by means of real measurement data in Pichler, Goertler, et al. (2016). The report by Pichler, Schranzhofer, and Goertler (2016) – related to the project MPC-Boxes – provides detailed information on energy savings and implications on the thermal comfort for a model predictive control tested in a real building object.

The Master-thesis of Arnitz (2014) deals with a preliminary (MPC-concept) investigation within the framework of the project TheBat. In that thesis an iterative MPC-approach for the PV-led heat pump operation was investigated, which was finally replaced by a non-linear hybrid MPC-approach as is reported in this thesis. Results of the preliminary study are published in Pichler, Arnitz, et al. (2016). A selection of results from this thesis is published in Pichler et al. (2016) and in Pichler et al. (2017). Finally, all relevant results in the context PV-led heat pump operation are provided in the "TheBat" project report cf. Pichler and Heinz (2016).



## Appendix B.

### Mathematical preliminaries

#### B.1. State space model representation

Any linear homogeneous ordinary (one variable) differential equation with constant coefficients of  $n$ -th order (e.g.  $n=3$ :  $a \partial_t^3 z(t) + b \partial_t^2 z(t) + c \partial_t z(t) + d z(t) = 0$ ) may be written as a system of first order linear differential equations. This is done by defining *state variables* ( $x_1 := \partial_t^2 z$ ,  $x_2 := \partial_t z$ ,  $x_3 := z$ ) for each degree of derivative smaller than  $n$ . A systematic approach of writing the new system of  $n$  equations is to use a matrix  $\mathbf{A}$  which is composed by the new constant coefficients

$$\dot{\mathbf{x}}(t) = \mathbf{A}\mathbf{x}(t). \quad (\text{B.1})$$

Inhomogeneous terms, which stand for some kind of excitations, may be added to the RHS of eq. (B.1) via an *input* vector  $\mathbf{u}(t)$ ; the matrix  $\mathbf{B}$  determines the coupling of the inputs to the states. This leads to the standard dynamic equation in continuous state space representation with *dynamic-matrix*  $\mathbf{A}$  and *input-matrix*  $\mathbf{B}$

$$\dot{\mathbf{x}}(t) = \mathbf{A}\mathbf{x}(t) + \mathbf{B}\mathbf{u}(t). \quad (\text{B.2})$$

By combining certain state variables in a linear manner to form a model *output* it is obvious to define also an *output-matrix*  $\mathbf{C}$ . The complete canonical<sup>1</sup> continuous time state space model (SSM) and its discrete time representation read

$$\dot{\mathbf{x}}(t) = \mathbf{A}\mathbf{x}(t) + \mathbf{B}\mathbf{u}(t) \quad \mathbf{x}_{k+1} = \mathbf{A}^d \mathbf{x}_k + \mathbf{B}^d \mathbf{u}_k \quad (\text{B.3})$$

$$\mathbf{y}(t) = \mathbf{C}\mathbf{x}(t) \quad \mathbf{y}_k = \mathbf{C}^d \mathbf{x}_k \quad (\text{B.4})$$

where the discrete formalism is denoted using superscripts  $d$ , to clearly distinguish from the continuous version. To refine the description:  $\mathbf{A} \in \mathbb{R}^{n \times n}$  with  $n$  being the number of state variables,  $\mathbf{B} \in \mathbb{R}^{n \times m}$  with  $m$  being the number of input variables, and  $\mathbf{C} \in \mathbb{R}^{p \times n}$  with  $p$  being the number of output variables.

---

<sup>1</sup> Often the canonical representation includes an additional term  $\mathbf{D}\mathbf{u}(t)$  in the output equation  $\mathbf{y}(t) = \mathbf{C}\mathbf{x}(t) + \mathbf{D}\mathbf{u}(t)$ , however, feed-through is neglected in this context.

### Quick and dirty – from the continuous to the discrete representation

The discretization method demonstrated in the following is called after Leonhard Euler. Although it is risky to use this calculation in numerical practice it is provided due to its simplicity.

The finite difference representation of the continuous state space dynamic eq. (B.3) is used to derive the innovation term  $\Delta \mathbf{x}$ :

$$\frac{\Delta \mathbf{x}(t)}{\Delta t} = \mathbf{A}\mathbf{x}(t) + \mathbf{B}\mathbf{u}(t) \quad \Rightarrow \Delta \mathbf{x}(t) = \Delta t \mathbf{A}\mathbf{x}(t) + \Delta t \mathbf{B}\mathbf{u}(t) \quad (\text{B.5})$$

Thinking discrete,  $\mathbf{x}_{k+1}$  may be obtained from  $\mathbf{x}_k$  and the innovation term  $\Delta \mathbf{x}$  (for which  $\mathbf{x}(t) \rightarrow \mathbf{x}_k$ ,  $\mathbf{u}(t) \rightarrow \mathbf{u}_k$ , with  $k$  indicating the discrete time instant) through

$$\begin{aligned} \mathbf{x}_{k+1} &= \mathbf{x}_k + \Delta \mathbf{x} & \Rightarrow \mathbf{x}_{k+1} &= \mathbf{x}_k + \Delta t \mathbf{A}\mathbf{x}_k + \Delta t \mathbf{B}\mathbf{u}_k \\ & & \Leftrightarrow \mathbf{x}_{k+1} &= (\mathbf{I}^{n \times n} + \Delta t \mathbf{A})\mathbf{x}_k + (\Delta t \mathbf{B})\mathbf{u}_k. \end{aligned} \quad (\text{B.6})$$

Comparing the last eq. (B.6) against the discrete representation in eq. (B.3) one finds the expressions

$$\Rightarrow \mathbf{A}^d = \mathbf{I}^{n \times n} + \Delta t \mathbf{A} \quad \Rightarrow \mathbf{B}^d = \Delta t \mathbf{B}. \quad (\text{B.7})$$

This simple discretization has the main drawback, that it has a small stability region. Its stability region in the complex plane is the unit circle shifted by  $-1$ , hence  $\{(\Delta t \mathbf{A}) \in \mathbb{C} \mid |\Delta t \mathbf{A} + 1| \leq 1\}$ . Assuming only real eigenvalues  $\lambda_i$  of  $\mathbf{A}$  for all these values  $-2 < \lambda_i \Delta t < 0$  must hold. From this criterion the maximum stable discretization time  $\Delta t$  can be derived. A more accurate and less problematic calculation for the dynamic- and input-matrix of the discrete time SSM is given in the sequel section.

#### B.1.1. Solution for $\mathbf{x}$ in the time domain and discrete time SSM

The general solution of  $\mathbf{x}(t)$  for the continuous SSM in the time domain is given by

$$\mathbf{x}(t) = \Phi(t) \mathbf{x}(t=0) + \int_0^t \Phi(t-\tau) \mathbf{B} \mathbf{u}(\tau) d\tau \quad (\text{B.8})$$

with  $\Phi(t) := \exp(\mathbf{A}t)$  being the transition matrix.

The exponential function of the matrix in the definition of  $\Phi(t)$  must be understood in terms of the series expansion, that is  $\exp(\mathbf{A}t) = \mathbf{I} + \mathbf{A}t + (\mathbf{A}t)^2/2! + \dots$ . The most important properties of the transition matrix are

$$\begin{aligned} \Phi(0) &= \mathbf{I} & \Phi(t_1 + t_2) &= \Phi(t_1) \Phi(t_2) \\ \Phi^{-1}(t) &= \Phi(-t) & \frac{\partial}{\partial t} \Phi(t) &= \mathbf{A}\Phi(t) \end{aligned} \quad (\text{B.9})$$

### Accurate SSM transformation from the continuous to the discrete time

A quick but dirty solution for  $\mathbf{x}$  in the discrete time representation of the SSM in eq. (B.3) is given by eq. (B.7). An accurate solution may be obtained by repeatedly conducting eq. (B.8). Assume  $\mathbf{x}_k$  to be given, then the value of the state variable after the next time-step ( $\Delta t$ ) reads

$$\mathbf{x}_{k+1} = \Phi(\Delta t) \mathbf{x}_k + \int_0^{\Delta t} \Phi(\Delta t - \tau) \mathbf{B} \mathbf{u}(\tau) d\tau. \quad (\text{B.10})$$

Assume  $\mathbf{u}(t)$  to be piecewise constant, that is for the duration of the time step it may be treated as a constant value  $\mathbf{u}_k$ . Since  $\mathbf{B}$  is also assumed constant, for an invertible matrix  $\mathbf{A}$  the solution of the integral term reduces to the integral of the transition matrix<sup>2</sup>

$$\left( \int_0^{\Delta t} \Phi(\Delta t - \tau) d\tau \right) \mathbf{B} \mathbf{u}_k = \mathbf{A}^{-1} (\Phi(\Delta t) - \mathbf{I}) \mathbf{B} \mathbf{u}_k. \quad (\text{B.11})$$

The final solution for  $\mathbf{x}_{k+1}$ , bringing forth the expressions for  $\mathbf{A}^d$  and  $\mathbf{B}^d$  in the discrete SSM representation, becomes

$$\boxed{\mathbf{x}_{k+1} = \underbrace{\Phi(\Delta t)}_{\mathbf{A}^d} \mathbf{x}_k + \underbrace{\mathbf{A}^{-1} (\Phi(\Delta t) - \mathbf{I}) \mathbf{B}}_{\mathbf{B}^d} \mathbf{u}_k.} \quad (\text{B.12})$$

#### B.1.2. Properties of the dynamic matrix $\mathbf{A}$

The following content is a discussion of square matrix- and linear operator properties. This theory is important to follow the analysis for  $\mathbf{A}$  obtained from a S-SSM parameter estimation, see sec. 4.3.3. Everything is treated from a practical user oriented perspective and restricted to  $\mathbf{A} \in \mathbb{R}$ .

Assume a SSM as given in eq. (B.2) or eq. (B.3) with  $\mathbf{C}$  being equal to  $\mathbf{1}$  in a matrix sense; the full discrete form of this model for  $n = 2$  may be seen in eq. (3.21). Actually, the focus is on the *excitation free continuous model*, that is the input matrix  $\mathbf{B}$  is neglected, which leads to a system of linear first-order differential equations

$$\dot{\mathbf{x}} = \mathbf{A} \mathbf{x} \quad \text{explicitly for } n=2: \quad \begin{bmatrix} \dot{x}_1 \\ \dot{x}_2 \end{bmatrix} = \begin{bmatrix} a_{11} & a_{12} \\ a_{21} & a_{22} \end{bmatrix} \begin{bmatrix} x_1 \\ x_2 \end{bmatrix} \quad a_{ij} \dots \text{phys. parameters.} \quad (\text{B.13})$$

The general solution<sup>3</sup> may be given analog to the scalar version of the equation as

$$\mathbf{x}(t) = \sum_{i=1}^n c_i \exp(\mathbf{A} t) \mathbf{v}_i \quad \text{for } n=2: \quad \mathbf{x}(t) = c_1 \exp(\mathbf{A} t) \mathbf{v}_1 + c_2 \exp(\mathbf{A} t) \mathbf{v}_2, \quad c_i \in \mathbb{R}. \quad (\text{B.14})$$

<sup>2</sup> The integral over  $\Phi(\Delta t - \tau)$  simplifies by applying a variable substitution  $\bar{\tau} := \Delta t - \tau$ .

<sup>3</sup> Precisely  $c_i \in \mathbb{C}$ , but we assume all eigenvalues being real for simplicity.

## Appendix B. Mathematical preliminaries

Here the exponential function must be understood as series expansion<sup>4</sup>. For  $n = 2$ , clearly  $\mathbf{x}(t)$  has two components  $x_1(t)$ ,  $x_2(t)$  which may be interpreted as air- and TABS-temperature for example. The vectors  $\mathbf{v}_i$  must be linearly independent.

The representation of the matrix  $\mathbf{A}$  in eq. (B.13) by means of the four elements  $a_{ij}$ ,  $i, j = 1, 2$  is only one possible *representation* depending on the basis system. Taking the example from above with  $x_1 := \vartheta_{ra}$  and  $x_2 := \vartheta_{ta}$ , the first *basis vector*  $\mathbf{b}_1 := [1, 0]^T$  represents  $\vartheta_{ra}$  and  $\mathbf{b}_2 := [0, 1]^T$  represents  $\vartheta_{ta}$ . Applying the matrix-multiplication it becomes clear, that the elements  $a_{11}$ ,  $a_{12}$  determine the influence of  $\vartheta_{ra}$  and  $\vartheta_{ta}$  on  $\dot{x}_1$  and similarly for the second row of  $\mathbf{A}$  and  $\dot{x}_2$ . Interchanging the assignment ( $:=$ ) of physical temperatures between  $x_1$  and  $x_2$  would require to interchange also the lines of  $\mathbf{A}$  in eq. (B.13) to describe the same physics as before.

Looking at eq. (B.14) with  $\mathbf{A}$  in the exponent and recalling that  $\exp(\cdot)$  must be understood as its series expansion one may ask for a simpler version of this equation. Consulting linear algebra this boils down to finding the so called *eigendirections*. For eigendirections represented by eigenvectors  $\mathbf{v}$

$$\mathbf{A} \mathbf{v} = \lambda \mathbf{v} \quad (\text{B.15})$$

holds. This means, that  $\mathbf{A}$  acting on  $\mathbf{v}$  does not change the direction<sup>5</sup> of  $\mathbf{v}$ , it is only a multiplication by a certain factor  $\lambda$  – the *eigenvalue*. Eigenvalues and eigenvectors are obtained from solving

$$(\mathbf{A} - \lambda \mathbf{I}) \mathbf{v} = 0, \quad \mathbf{v} \neq \mathbf{0} \quad \Leftrightarrow \quad \det(\mathbf{A} - \lambda \mathbf{I}) = 0. \quad (\text{B.16})$$

That is, the bracketed term's *determinant* must be equal to zero; for  $n = 2$  it reads

$$(a_{11} - \lambda)(a_{22} - \lambda) - (a_{21}a_{12}) = 0 \quad \Leftrightarrow \quad \lambda^2 - (a_{11} + a_{22})\lambda + (a_{11}a_{22} - a_{21}a_{12}) = 0, \quad (\text{B.17})$$

hence, the (two) solutions of this quadratic equation give the eigenvalues  $\lambda_1$  and  $\lambda_2$ . Assuming  $\lambda_1 \neq \lambda_2$ , two independent eigenvectors  $\mathbf{v}_1$ ,  $\mathbf{v}_2$  may be constructed from solving eq. (B.15) for  $\lambda_1$  and  $\lambda_2$ . Given these eigenvalues and the dedicated eigenvectors eq. (B.14) may be written – compare with eq. (B.15) – as

$$\mathbf{x}(t) = \sum_{i=1}^n c_i \exp(\lambda_i t) \mathbf{v}_i \quad \text{for } n=2: \quad \mathbf{x}(t) = \underbrace{c_1 \exp(\lambda_1 t) \mathbf{v}_1}_{\mathbf{f}_1} + \underbrace{c_2 \exp(\lambda_2 t) \mathbf{v}_2}_{\mathbf{f}_2}, \quad c_i \in \mathbb{R}. \quad (\text{B.18})$$

The *eigensolutions*  $\mathbf{f}(\lambda_i, \mathbf{v}_i)$  decouple, hence it is interesting to analyze the directional component ( $\mathbf{v}_i$ ) of these solutions in the representation of the original basis e.g.  $\mathbf{b}_1$ ,  $\mathbf{b}_2$ . More on the *representation* of  $\mathbf{A}$  in different basis systems is given in Appendix B.1.4.

<sup>4</sup>  $\exp(\mathbf{A}) = \mathbf{I} + \mathbf{A}t + \frac{(\mathbf{A}t)^2}{2!} + \dots$

<sup>5</sup> Commonly squared matrices describe general rotations.

### B.1.3. Interpretation of the eigensolutions – eigenvalues and -directions

The eigenvalues  $\lambda_i$  describe the asymptotic behavior of each eigensolution. Given for example an initial temperature of 20°C for both states in eq. (B.18) it is expected that the free solution (all inputs are zero) returns to the origin  $\mathbf{x}(t) \rightarrow \mathbf{x}_0 = \mathbf{0}$  for  $t \rightarrow \infty$ , clearly this requires  $\lambda_i < 0$  for all  $i$ . More generally this is required from the asymptotic stability criterion, which is assured given the real part of all eigenvalues  $\lambda_i$  of  $\mathbf{A}$  is negative<sup>6</sup>. If all  $\lambda_i < 0$  and real (which is the case in this context), one may interpret their inverse value as a *time constant* of an exponential damping term.

If there is no repeated eigenvalue then there exists a basis which enables to represent any state-trajectory by a linear combination of the eigenvectors. More precisely, any solution to  $\dot{\mathbf{x}} = \mathbf{A} \mathbf{x}$ , may be written in terms of the eigensolutions  $\mathbf{f}(\lambda_i, \mathbf{v}_i)$  cf. eq. (B.18) – an intrinsic property of a linear operator. Hence once  $\lambda_i$  and  $\mathbf{v}_i$  are known all possible trajectories are predetermined. The  $\lambda$ 's describe the dynamics, that is, if real and negative, the damping and the corresponding  $\mathbf{v}_i$  denote the "directions" in which the system evolves with this damping. An analysis with respect to the eigensolutions is given on behalf of a SSM with  $n = 4$  in sec. 4.3.3 – fig. 4.13 for example shows the dynamic for different  $\lambda$ 's.

Concerning the eigendirections,  $\mathbf{v}_1$  is the most interesting to look at given  $\lambda_1 > \lambda_2 > \dots > \lambda_n$ . The reason is, that the greatest eigenvalue determines the long term behavior. This is why only  $\mathbf{v}_1$  is analyzed in detail. Assume the original basis representation for this vector and recall the example given for  $n = 2$

$$\mathbf{v}_1 = \begin{bmatrix} v_{11} \\ v_{12} \end{bmatrix} \propto \begin{bmatrix} \vartheta_{ra} \\ \vartheta_{ta} \end{bmatrix}. \quad (\text{B.19})$$

This shows that the first component stands for the "relevance" of  $\vartheta_{ra}$  and the second one stands for that of  $\vartheta_{ta}$  concerning the long term behavior. A good balance for the numbers  $v_{11} \cong 0.3$ ,  $v_{12} \cong 0.7$ , would be considered reasonable, whereas  $v_{11}/v_{12} \cong 10^{\pm 3}$  would be seen as imbalance. Such an imbalance expresses that asymptotically one state dominates, however, this implicitly means, that the internal state interaction is very loose, this in turn may indicate a suboptimal model or an unreasonable high model order.

Eigendirections of all but the dominant eigensolution may be used to evaluate the model *consistency*, which is understood as follows. Recall the example model with  $n = 2$  states, with the first state describing  $\vartheta_{ra}$ . Clearly, in the context of thermal building models, this model node (state) usually has the least heat capacity, in other words – if imagined in a single node model – the damping is high opposed to that of a TABS node. Now, if an eigensolution analysis leads to  $\lambda_2 = -10^{-3}$ ,  $v_{21} = 0.7$ ,  $v_{22} = 1$  and

<sup>6</sup> For any (real) quadratic matrix  $\mathbf{A}$  the eigenvalues may be obtained either from its equivalent diagonal form or if not available from a Schur factorization which leads to an upper triangle matrix. In the context of this thesis  $\mathbf{A}$  must have this property –  $\mathbf{x}_0$  represents an asymptotically stable point.

## Appendix B. Mathematical preliminaries

$\lambda_1 = -10^{-2}$ ,  $v_{1_1} = 1$ ,  $v_{1_2} = 0$  and  $\lambda_1 \gg \lambda_{ra}$ , with  $\lambda_{ra}$  standing for a room air node's typical eigenvalue, then the model (structure) approach must be questioned. Here  $\mathbf{v}_2$  consists of a  $\vartheta_{ra}$ -component only, but the dynamic it has does not at all fit to the physical understanding underlying the model approach<sup>7</sup>. Such an analysis is conducted in sec. 4.3.3.

### The dominant eigendirection – comparison between different models

As explained in the previous paragraphs the dominant eigensolution, that with  $\lambda_1$  the largest eigenvalue, determines the long term behavior in the superposition of eigensolutions:

$$\mathbf{x}(t) = \sum_{i=1}^n c_i \exp(\lambda_i t) \mathbf{v}_i \xrightarrow{t \gg |\lambda_1|} \mathbf{x}(t) \approx c_1 \exp(\lambda_1 t) \mathbf{v}_1; \quad c_i \in \mathbb{R}. \quad (\text{B.20})$$

This fact is the reason why special attention is given to the dominant eigendirection, obtained for different model structures. Minor changes of the internal structure of a general 4<sup>th</sup> order model  $\mathcal{M}^{n4}$  mean different models at first sight, however, if the dominant eigensolution of these models is approximately the same, one could claim that the models are approximately equal from a mathematical point of view, although their parameters are different. The same holds for one and the same model structure but varying parametrizations obtained from a different id-data.

The comparison of dominant eigenvalues  $\lambda_1$  from different models is straight forward, however, to measure the similarity of the dedicated eigendirections requires the definition of a *distance* measure. The *euclidean distance* metric can be applied to *compare* the eigendirections  $\mathbf{v}_1$  of *two dominating eigensolutions* from different parametrizations  $\mathcal{M}_1^n, \mathcal{M}_2^n$

$$dmax_{\mathcal{V}_2} := \sqrt{\sum_{i=1}^n (v_{1,i}(\mathcal{M}_1^n) - v_{1,i}(\mathcal{M}_2^n))^2}. \quad (\text{B.21})$$

Given, for example a set of six parametrizations a measure for the variation of the dominant eigensolution among these parametrizations is:

$$dmax_{\mathcal{V}_i} := \sqrt{\sum_{i=1}^n (\max(\mathcal{V}_i) - \min(\mathcal{V}_i))^2} \quad \text{with} \quad \mathcal{V}_i := \{v_{1,i}(\mathcal{M}_1^n), \dots, v_{1,i}(\mathcal{M}_6^n)\}. \quad (\text{B.22})$$

This definition means that from a set  $\mathcal{V}$  of 6 dominating eigendirections – each from a corresponding model of order  $n$  – the RMSE of the maximum difference over all  $n$  components is calculated.

<sup>7</sup> A two node model is not really a good example, since low order models are more likely to show such a phenomenon, but it is well suited for explanation.

### B.1.4. Matrix algebra

Assume  $n$  distinct eigenvalues  $\lambda_i$  and  $n$  associated linear independent eigenvectors  $\mathbf{v}_i$  were obtained for the matrix  $\mathbf{A}$ , then it may be diagonalized. The *similarity-transformation* that does this job is defined by the obtained eigenvectors  $\mathbf{v}_i$ . This transformation takes the form

$$\mathbf{\Lambda} = \mathbf{P}^{-1}\mathbf{A}\mathbf{P} \quad \text{where the transformation matrix is } \mathbf{P} := [\mathbf{v}_1, \dots, \mathbf{v}_n], \quad (\text{B.23})$$

and  $\mathbf{A}$  and  $\mathbf{\Lambda}$  are similar to each other. Similar matrices mathematically describe the same mapping.

Consider now a SSM of third order, with three different eigenvalues  $\lambda_1, \lambda_2, \lambda_3$  and associated eigenvectors which define the transformation matrix  $\mathbf{P} := [\mathbf{v}_1, \mathbf{v}_2, \mathbf{v}_3]$ . The general model reads

$$\begin{aligned} \dot{\mathbf{x}} &= \mathbf{A}\mathbf{x} + \mathbf{B}\mathbf{u}, \quad \text{left multiplication by } \mathbf{P}^{-1} \text{ and inserting } \mathbf{P}\mathbf{P}^{-1} \text{ leads to} \\ \underbrace{\mathbf{P}^{-1}\dot{\mathbf{x}}}_{\mathbf{z}} &= \underbrace{\mathbf{P}^{-1}\mathbf{A}\mathbf{P}}_{\mathbf{\Lambda}} \underbrace{\mathbf{P}^{-1}\mathbf{x}}_{\mathbf{z}} + \underbrace{\mathbf{P}^{-1}\mathbf{B}\mathbf{P}}_{\tilde{\mathbf{B}}} \underbrace{\mathbf{P}^{-1}\mathbf{u}}_{\tilde{\mathbf{u}}} \quad \text{the SSM transformed into the eigenspace} \\ \Rightarrow \begin{bmatrix} \dot{z}_1 \\ \dot{z}_2 \\ \dot{z}_3 \end{bmatrix} &= \begin{bmatrix} \lambda_1 & 0 & 0 \\ 0 & \lambda_2 & 0 \\ 0 & 0 & \lambda_3 \end{bmatrix} \begin{bmatrix} z_1 \\ z_2 \\ z_3 \end{bmatrix} + \tilde{\mathbf{B}} \tilde{\mathbf{u}}. \end{aligned} \quad (\text{B.24})$$

In eq. (B.24) we can see that the eigenstates  $z_1, z_2$  and  $z_3$  decouple. The free solution for the transformed SSM and for  $n = 3$ , with  $c_i \in \mathbb{R}$  reads

$$\mathbf{z}(t) = \sum_{i=1}^n c_i \exp(\lambda_i t) z_i(0), \quad \mathbf{z}(t) = c_1 \exp(\lambda_1 t) z_1(0) + c_2 \exp(\lambda_2 t) z_2(0) + c_3 \exp(\lambda_3 t) z_3(0). \quad (\text{B.25})$$

Looking at the transformation rule for  $\mathbf{x} \rightarrow \mathbf{z}$  one may understand the nature of these (new) states in terms of the original state vector  $\mathbf{x}$ . The question how the eigenstates look in the original basis  $\mathcal{B}$  of  $\mathbf{A}$  is answered by applying the transformation to the new basis  $\tilde{\mathcal{B}}$  vectors  $\tilde{\mathbf{b}}_1, \tilde{\mathbf{b}}_2, \tilde{\mathbf{b}}_3$  in canonical representation

$$\mathbf{z} = \mathbf{P}^{-1} \mathbf{z}_{\mathcal{B}} \quad \Rightarrow \quad \mathbf{P} \tilde{\mathbf{b}} = \tilde{\mathbf{b}}_{\mathcal{B}} \quad \Leftrightarrow \quad [\mathbf{v}_1, \mathbf{v}_2, \mathbf{v}_3] \tilde{\mathbf{b}}_i = [\tilde{\mathbf{b}}_i]_{\mathcal{B}}. \quad (\text{B.26})$$

Since for example  $\tilde{\mathbf{b}}_1 = [1, 0, 0]^T$  we see that the decoupled eigenstates of the transformed model represented in the old basis  $\mathcal{B}$  are given by the eigenvectors of  $\mathbf{A}$ . That is, the eigenvector  $\mathbf{v}_1$  corresponding to the largest eigenvalue gives the representation of  $z_1$  in the original basis  $\mathcal{B}$ .

## B.2. Jacobi-matrix

The Jacobi-matrix  $\mathbf{J}_x$  of a vector valued function with three components  $\mathbf{g} = [g_1, g_2, g_3]^T$ , evaluated at  $(\mathbf{x}_0, \mathbf{u}_0)$  reads

$$\frac{\partial}{\partial \mathbf{x}} \mathbf{g}(\mathbf{x}_0, \mathbf{u}_0) := \begin{bmatrix} \partial_{x_1} g_1(\mathbf{x}_0, \mathbf{u}_0) & \partial_{x_2} g_1(\mathbf{x}_0, \mathbf{u}_0) & \partial_{x_3} g_1(\mathbf{x}_0, \mathbf{u}_0) \\ \partial_{x_1} g_2(\mathbf{x}_0, \mathbf{u}_0) & \partial_{x_2} g_2(\mathbf{x}_0, \mathbf{u}_0) & \partial_{x_3} g_2(\mathbf{x}_0, \mathbf{u}_0) \\ \partial_{x_1} g_3(\mathbf{x}_0, \mathbf{u}_0) & \partial_{x_2} g_3(\mathbf{x}_0, \mathbf{u}_0) & \partial_{x_3} g_3(\mathbf{x}_0, \mathbf{u}_0) \end{bmatrix}, \text{ with } \partial_{x_i} := \frac{\partial}{\partial x_i}. \quad (\text{B.27})$$

## B.3. Observability and controllability

A system  $(\mathbf{A}, \mathbf{C})$  is observable if it is possible to back-calculate the initial state  $\mathbf{x}(t_0)$ , given  $\mathbf{y}(t)$  and  $\mathbf{u}(t)$  for the finite time interval  $t_0 \leq t \leq t_1$ , see for example Horn and Dourdoumas (2004). A system in the sense of Kalman is observable, if the so called *observability matrix*  $\mathbf{S}_O$  defined by eq. (B.29) fulfills the rank condition

$$\text{rank}(\mathbf{S}_O) = n \quad \text{with } n \text{ being the number of states.} \quad (\text{B.28})$$

$$\mathbf{S}_O := \begin{bmatrix} \mathbf{C} \\ \mathbf{CA} \\ \mathbf{CA}^2 \\ \vdots \\ \mathbf{CA}^{n-1} \end{bmatrix} \quad (\text{B.29})$$

For the time discrete analogous of eq. (B.29)  $\mathbf{A}$  must be replaced with the transition matrix  $\Phi(\Delta t)$ .

A system fulfills the *controllability* property if a suitable input time-series may be found to move the system from an arbitrary initial state  $\mathbf{x}(t_0)$  to any other state  $\mathbf{x}(t_{final})$  in the entire configuration space. Similarly as for the concept of observability a *controllability matrix*  $\mathbf{S}_C$  exists which must obey to following property to meet controllability:

$$\text{rank}(\mathbf{S}_C) = n \quad \text{with } n \text{ being the number of states.} \quad (\text{B.30})$$

$$\mathbf{S}_C := [B \quad AB \quad A^2B \quad \dots \quad A^{n-1}B] \quad (\text{B.31})$$

The time discrete analogue looks exactly the same.

## B.4. Positive and semi-positive definiteness

$\mathcal{H} \in \mathbb{R}^{n \times n}$ , symmetric,  $\mathbf{U} \in \mathbb{R}^n$ :

$$\mathbf{U}^T \mathcal{H} \mathbf{U} > 0, \forall \mathbf{U} \neq \mathbf{0} \Leftrightarrow \mathcal{H} \text{ positive definite (p.d.)} \quad (\text{B.32})$$

$$\mathbf{U}^T \mathcal{H} \mathbf{U} \geq 0, \forall \mathbf{U} \neq \mathbf{0} \Leftrightarrow \mathcal{H} \text{ semi-positive definite (s.p.d.)} \quad (\text{B.33})$$



## Appendix C.

### HP PV system and building

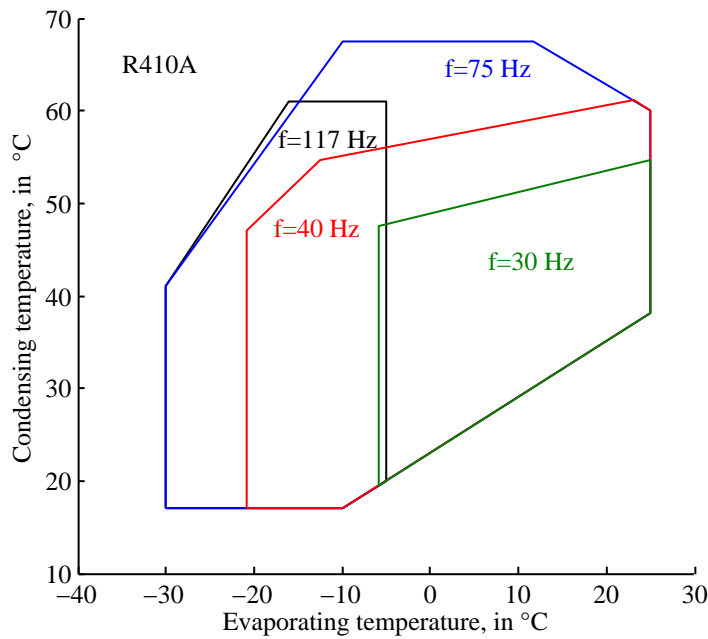


Figure C.1.: Heat pump scroll compressor operating limits.

#### C.1. Control of V4 and V4a

Mixing valve V<sub>4</sub> in fig. 2.3 has two distinct functions. During direct space heating (CF<sub>4</sub>) it assures a total TABS loop mass flow greater than 700 kg/h. This may be realized through a simple temperature mixing strategy with set temperature according to eq. (C.1). The pump P<sub>3</sub> together with the distribution valve V<sub>4a</sub> have to ensure  $\dot{m}_{ta} \geq 700$  kg/h. If P<sub>1</sub> would always drive a mass flow being greater than 700 kg/h P<sub>3</sub>, V<sub>4</sub> and V<sub>4a</sub> would not be necessary.

$$\tilde{\vartheta}_{sw} = \frac{\vartheta_{V1,A} \dot{m}_{V1,A} + \vartheta_{ret} \max(700 \text{ kg/h} - \dot{m}_{V1,A}, 0)}{700 \text{ kg/h}}$$

$$\vartheta_{sw} = \min(\vartheta_{V1,A}, \tilde{\vartheta}_{sw}) \quad (\text{C.1})$$

During heating from the TES V<sub>4</sub> is adjusted such, that  $\vartheta_{AB} = \vartheta_{ret} + 5$  K given a constant mass flow  $\dot{m}_{AB} = 1031$  kg/h maintained by P<sub>3</sub>. The distribution valve V<sub>4a</sub> has to ensure  $\dot{m}_{V4a,B} = 1031$  kg/h.

## Appendix C. HP PV system and building

Table C.1.: Specification of physical constants and model parameters for simulation purpose, Ch. 2.

Variable	Description	Value
<i>Physical properties</i>		
$c_{p,b}$	specific heat brine	3.8 kJ/(kgK)
$c_p$	specific heat water	4.19 kJ/(kgK)
$\rho_w$	density water	1000 kg/m <sup>3</sup>
$\rho_b$	density brine	1000 kg/m <sup>3</sup>
<i>Thermal energy storage</i>		
V	volume	0.5 m <sup>3</sup>
h	effective thermal storage height	1.81 m
$\lambda_z$	"internal mixing" in the TES	2.0 W/(m K)
U	U value of top/medium/bottom node	1.45 W/(m <sup>2</sup> K)
<i>Heat pump (refrigerant cycle)</i>		
$\tau_{start}$	PT1 characteristic start losses	0.0167 h
$\tau_{stop}$	PT1 characteristic stop losses	0.167 h
$\eta_{eco,HX}$	economizer efficiency, from measurements	<sup>b</sup> 0.94, [0.6 – 1.0]
$\eta_{is,HP}$	isentropic efficiency of the high pressure part	[0.2 – 0.9]
$\eta_{vol,HP}$	volumetric efficiency <sup>a</sup> of the high pressure part	<sup>b</sup> 0.93, [0.2 – 1.0]
$\eta_{is,lp}$	isentropic efficiency of the low pressure part	<sup>b</sup> 0.6, [0.2 – 0.9]
$\eta_{vol,lp}$	volumetric isentropic efficiency of the low pressure part	<sup>b</sup> 0.87, [0.2 – 1.0]
$\vartheta_{c,max}$	maximum condensing temperature	65 °C
$\dot{V}_{swept,tot}$	total swept volume	6.55 m <sup>3</sup> /h
$\dot{V}_{swept,high}$	high pressure (2 <sup>nd</sup> stage) swept volume	4.67 m <sup>3</sup> /h
$\Delta T_{sup}$	superheating at evaporator	5 K
$\Delta T_{sup,eco}$	superheating at economizer	5 K
$\Delta T_{sub}$	subcooling at condenser	0 K

<sup>a</sup>  $\dot{V}_{real}/\dot{V}_{ideal}$ .

<sup>b</sup> This value holds for BoW30/35, f= 90 Hz.

## C.2. Climate data

Table C.2.: Overview on the climate data set (Innsbruck) used for all TheBat simulations, ch. 6.

	$H_{tot,hor}$ kWh/m <sup>2</sup>	$G_{tot,max}$ W/m <sup>2</sup>	$H_{dif,hor}$ kWh/m <sup>2</sup>	$G_{dif,max}$ W/m <sup>2</sup>	$\vartheta_{oa}$ °C	$\vartheta_{oa,min}$ °C	$\vartheta_{oa,max}$ °C	RH %	$RH_{min}$ %	$RH_{max}$ %
Jan	45.5	420	18.7	191	-1.8	-13.7	12	83.81	47	100
Feb	64	588	31.4	290	0.86	-10.5	13.4	78.25	38	100
Mar	108.3	794	46.9	350	5.13	-6.7	20.3	73.94	29	100
Apr	135	903	56.8	407	9.83	-2	24.1	70.07	31	100
May	172.2	988	74	430	15.09	3.6	29.3	69.33	24	100
Jun	172.5	1033	78.7	448	17.43	6.4	30.6	72.74	34	100
Jul	176.1	972	75.5	419	18.49	8	33.8	72.9	30	100
Aug	148.1	933	68	419	18.24	7.4	31.1	74.53	35	100
Sep	111.8	852	51.9	384	13.78	4.1	27.1	77.93	40	100
Oct	81.6	648	36.8	295	9.85	-1.4	22.5	79.97	43	100
Nov	45.4	444	25	232	3.91	-5.1	15.9	82.93	43	100
Dec	35.5	352	17	163	-0.44	-11.9	12	84.37	42	100
annual	1296.1	1033	580.8	448	9.24	-13.7	33.8	76.73	24	100

### C.3. CF minimal terms based on Karnaugh maps

	$C_A=1$	$C_A=1$	$C_A=0$	$C_A=0$	
$C_B=1$	1	1	0	0	$C_D=1$
$C_B=1$	1	1	0	0	$C_D=0$
$C_B=0$	1	1	0	0	$C_D=0$
$C_B=0$	1	1	0	0	$C_D=1$
	$C_C=1$	$C_C=0$	$C_C=0$	$C_C=1$	

Result:  $CF_1 = C_A$

Figure C.2.: Karnaugh map and minimal term result for  $CF_1$ .

	$C_A=1$	$C_A=1$	$C_A=0$	$C_A=0$	
$C_B=1$	1	0	0	1	$C_D=1$
$C_B=1$	1	0	0	1	$C_D=0$
$C_B=0$	1	0	0	1	$C_D=0$
$C_B=0$	1	0	0	1	$C_D=1$
	$C_C=1$	$C_C=0$	$C_C=0$	$C_C=1$	

Result:  $CF_3 = C_C$

Figure C.3.: Karnaugh map and minimal term result for  $CF_3$ .

	$C_A=1$	$C_A=1$	$C_A=0$	$C_A=0$	
$C_B=1$	0	0	1	1	$C_D=1$
$C_B=1$	0	0	0	0	$C_D=0$
$C_B=0$	0	0	0	0	$C_D=0$
$C_B=0$	0	0	1	1	$C_D=1$
	$C_C=1$	$C_C=0$	$C_C=0$	$C_C=1$	

Result:  $CF_4 = \overline{C_A} \wedge C_D$

Figure C.4.: Karnaugh map and minimal term result for  $CF_4$ .

	$C_A=1$	$C_A=1$	$C_A=0$	$C_A=0$	
$C_B=1$	0	0	0	0	$C_D=1$
$C_B=1$	0	0	0	0	$C_D=0$
$C_B=0$	0	0	0	0	$C_D=0$
$C_B=0$	1	1	0	0	$C_D=1$
	$C_C=1$	$C_C=0$	$C_C=0$	$C_C=1$	

Result:  $CF_5 = C_A \wedge \overline{C_B} \wedge C_D$

Figure C.5.: Karnaugh map and minimal term result for  $CF_5$ .

Appendix C. HP PV system and building

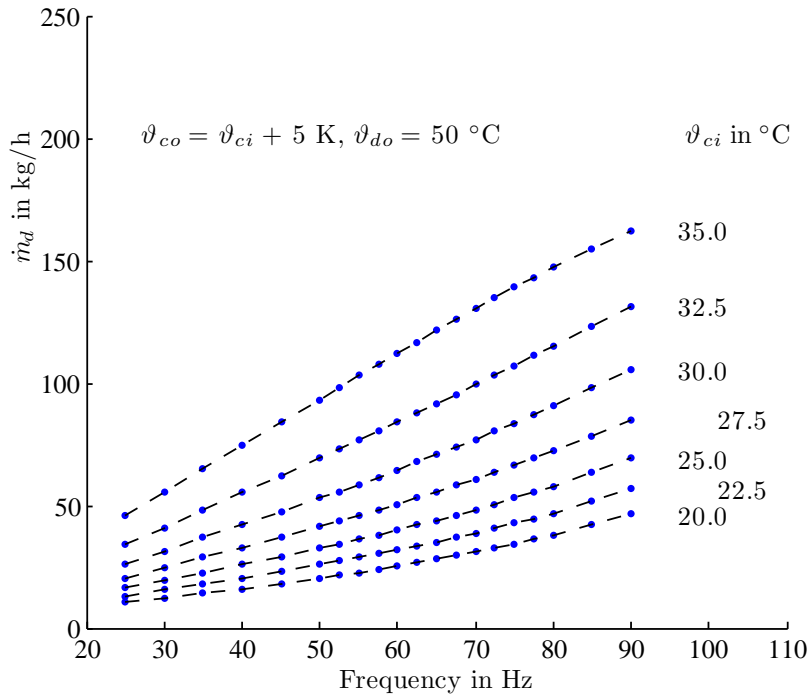


Figure C.6.: Desuperheater mass flow rate ( $\dot{m}_d$ ) for TABS mode.

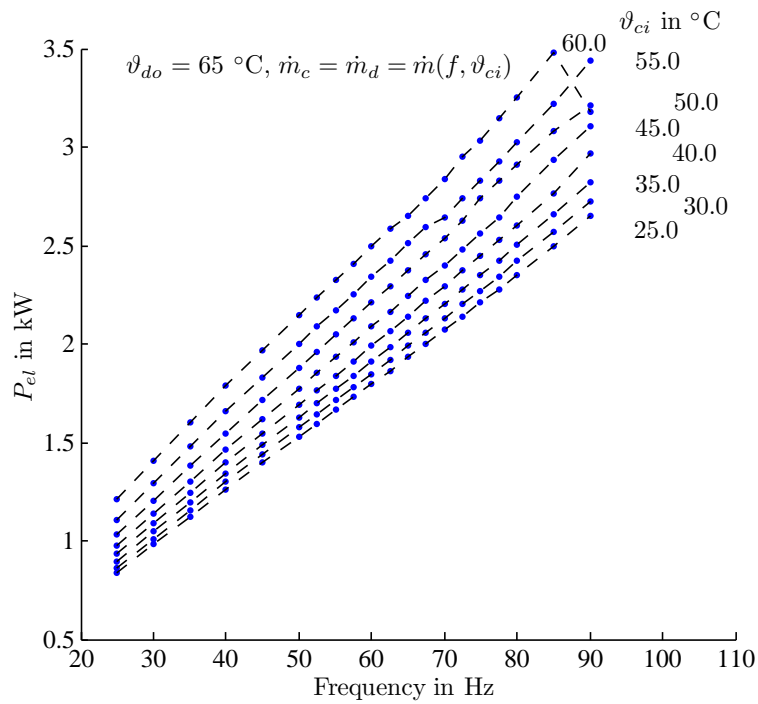


Figure C.7.: HP, power consumption  $P_{el}$  for TES heating for DHW purpose with  $\vartheta_{do} = 65 \text{ }^{\circ}\text{C}$ .

## C.4. Modelling of photovoltaic components

The following subsections provide physical details required to understand the four-parameter PV model.

### Semiconductor properties

The heart of a polycrystalline PV cell consists of a p-type and a n-type semiconductor. At thermodynamic equilibrium these materials have *differing* Fermi levels. The Fermi level ( $E_F$ ) expresses the highest occupied energy level at a certain temperature. Above  $E_F$  no electrons are assumed to be found. Bringing the two semiconductor types together, the individual Fermi levels adopt one common  $E_F$ . This requires free electrons to move towards the p doped region. The transit stops until the resulting electric force balances the original driving potential. Finally, at the interface, the p-n junction is empty of free charge carriers (depletion zone). The build up electric force constitutes the built-in voltage barrier.

Light induced electron/whole-pair generation within the depletion zone leads to charge carrier separation due to the built-in voltage. Recombination of these pairs becomes possible through an external circuit. This essentially describes the function of a PV cell.

### C.4.1. PV equivalent circuit diagram

Throughout this thesis a simple silicon based semiconductor PV cell is considered. The heart of a PV cell is a p-n junction. The electric field at this p-n junction leads to the separation of light induced electron-hole-pairs. The detailed physics is described by the *photovoltaic effect*, discovered by the French physicist Edmond Becquerel in 1839 (Becquerel, 1839). Although slightly different to the photoelectric effect, it was not until Einsteins discovery in 1905<sup>1</sup> that the photovoltaic effect was completely understood.

An equivalent circuit diagram of a PV cell is depicted in fig. C.8. This circuit neglects an optional shunt resistance in parallel with the diode, see e.g. Soto et al. (2006) or Duffie and W. A. Beckman (2006). Hence, this PV cell equivalent circuit does not directly account for internal leakage losses due to electron-hole recombination, however, the *ideality factor*, later introduced to alter the ideal diode equation, does. Townsend (1989) has shown that the effect of the shunt resistance on the generated power is negligible.

The very left symbol in fig. C.8 represents the current source – its current  $I_L$  is a function of the actual irradiance onto the PV cell. The diode describes the properties

<sup>1</sup> For this discovery Einstein was rewarded the Nobel Prize in 1921.

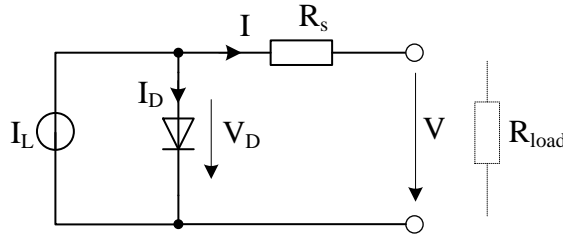


Figure C.8.: Equivalent circuit for a PV cell, four parameter model according to Townsend (1989) see also Eckstein (1990). A series connection of this circuit yields the module equivalent circuit.

of the p-n junction and the serial resistance ( $R_s$ ) models internal ohmic losses of the PV cell. Ohmic losses – dissipated as heat – originate from the semiconductor material itself and various contact interfaces.

The shape of the I-V characteristic of a PV cell (see left graph in fig. C.9) is dominated by a flipped diode I-V characteristic. The *Shockley diode equation* (Shockley, 1956) reads

$$I_D = I_S \left( \exp \left( \frac{qV_D}{nV_T} \right) - 1 \right), \quad \text{with} \quad V_T = kT_c, \quad (\text{C.2})$$

with  $I_S$  being the (negative) reverse saturation current,  $q$  being the elementary charge ( $1.602 \cdot 10^{-19}$  C),  $V_D$  being the diode voltage,  $V_T$  being the thermal voltage (approximately 26 mV) – defined as the Boltzmann constant ( $k = 1.381 \cdot 10^{-23}$  J/K) times the cell temperature in Kelvin –, and  $n \approx (1 - 2)$  being the *ideality factor* for shaping the diode characteristic<sup>2</sup>. The exponential term in eq. (C.2) dominates for forward bias voltages and the  $-1$  may be neglected, whereas for reverse bias voltages the  $-1$  term dominates and the exponential term may be neglected. The reverse saturation current as a function of the current cell temperature  $T_c$  in Kelvin is given as

$$I_S = DT_c^3 \exp \left( \frac{-q\epsilon_G}{nkT_c} \right), \quad (\text{C.3})$$

where  $D$  is the diode diffusion factor,  $\epsilon_G$  is the semiconductor material bandgap energy (1.12 eV for Si and 1.35 eV for GaAs), and the other parameters as described for eq. (C.2).

#### C.4.2. Four-parameter model

The four-parameter model with an equivalent circuit as in fig. C.8 will be used in this thesis. The model (type 94) has been implemented in TRNSYS by Eckstein (1990). This

<sup>2</sup> The original Shockley equation is obtained for  $n = 1$ , this factor was introduced later to account for imperfect junctions, recombination and generation of charge carriers.

model reliably predicts the whole operational range of mono- and polycrystalline PV cells.<sup>3</sup> The related physical basics are described next, followed by an outline dealing with the determination of the relevant model parameters.

The current-voltage (I-V) relation of the PV cell in fig. C.8 at a fixed cell temperature is obtained through applying Kirchoff's laws. First the voltage law leads to the expression  $V_D = IR_s + V$  which is substituted in eq. (C.2). This equation and the current law applied to the upper node leads to:

$$I = I_L - I_S \left( \exp \left( \frac{q(IR_s + V)}{nV_T} \right) - 1 \right), \quad (\text{C.4})$$

which provides an *implicit solution* for the I-V characteristic of the PV cell. To obtain I and V from this equation for various irradiance and cell temperature values, two further expressions are required, one for  $I_L$  and one for  $I_S$ .

The light current  $I_L$ , as a function of the total irradiance and the cell temperature ( $G, T_c$ ) may be calculated based on reference data ( $G_{ref}, I_{L,ref}, T_{c,ref}$ ) and the temperature coefficient at short circuit condition ( $\mu_{sc}$ , defined in eq. (2.23)):

$$I_L = \frac{G}{G_{ref}} (I_{L,ref} + \mu_{sc}(T_c - T_{c,ref})), \quad (\text{C.5})$$

The first term describes the linear dependence on the total radiation and the second term describes a correction due to a change of the cell temperature.

The reverse saturation current cannot be directly derived from (C.3) since  $D$  is unknown, however, taking the ratio of this equation for two different operating conditions one finds

$$I_S = I_{S,ref} \left( \frac{T_c}{T_{c,ref}} \right)^3 \exp \left( \frac{q\epsilon_G}{nk} \left( \frac{1}{T_{c,ref}} - \frac{1}{T_c} \right) \right), \quad (\text{C.6})$$

which allows for calculation of  $I_S$  for any condition given a reference operating condition.

The equations (C.4)–(C.6) are sufficient to describe the relevant operational range of a single PV cell. However, manufacturers do not provide the required model parameters  $I_{L,ref}$ ,  $I_{S,ref}$ , and the cell specific parameters  $n$  and  $R_s$ . Since the manufacturer data usually do not refer to a single solar cell, but to one *solar module* usually assembled of a series connection of single cells, the cell specific ideality factor<sup>4</sup>  $n$  in eq. (C.4) must be extended to a module specific *shape factor*  $\gamma = n \cdot NCS$ , where  $NCS$  is the number of serial cells. Finally,  $I_{L,ref}$ ,  $I_{S,ref}$ ,  $\gamma$  and  $R_s$  must be derived from available standard test condition (STC) data.

<sup>3</sup> For amorphous photovoltaics the assumption of a flat slope at the short circuit condition does not hold, which is why simulations of amorphous PV cells require the five-parameter model, see Fry (1998).

<sup>4</sup>  $n$  corresponds to  $A$  in Eckstein (1990).

### Determination of $I_{L,ref}$ , $I_{S,ref}$ , $\gamma$ and $R_s$ from STC data

In practice, manufacturers typically provide only limited electrical parameters. In general, the given operational data for a PV module are the open circuit voltage ( $V_{oc}$ ), the short circuit current ( $I_{sc}$ ), the maximum power current ( $I_{MP}$ ) and voltage ( $V_{MP}$ ) and the temperature coefficients at  $V_{oc}$  and  $I_{sc}$ . The following paragraphs explain the determination of the required equivalent circuit physical- and empirical-parameters based on available manufacturers catalog (STC) data according to OENORM (OENORM EN 50380:2003).

Eq. (C.4) for a whole PV module assembled of  $N_{SC}$  serial cells reads:

$$I = I_L - I_S \left( \exp \left( \frac{q(IR_s + V)}{\gamma k T_c} \right) - 1 \right) \quad (C.7)$$

Assume  $R_s$  to be known one may insert the module specific I-V STC data for the open circuit, the short circuit and the maximum power (MP) point. This leads to three algebraic equations:

$$\begin{aligned} \text{open circuit:} \quad & 0 = I_{L,ref} - I_{S,ref} \left( \exp \left( \frac{qV_{oc,ref}}{\gamma k T_{c,ref}} \right) - 1 \right) \\ \text{short circuit:} \quad & I_{sc,ref} = I_{L,ref} - I_{S,ref} \left( \exp \left( \frac{qI_{sc,ref}R_s}{\gamma k T_{c,ref}} \right) - 1 \right) \\ \text{MP point :} \quad & I_{MP,ref} = I_{L,ref} - I_{S,ref} \left( \exp \left( \frac{q(I_{MP,ref}R_s + V_{MP,ref})}{\gamma k T_{c,ref}} \right) - 1 \right) \end{aligned}$$

As explained in sec. C.4.1 for forward biased voltage the  $-1$  term may be dropped. Since  $I_{S,ref} \propto \mathcal{O}(10^{-10})$  and  $R_s$  is very small, from eq. (C.7) at short circuit conditions we find

$$\text{short circuit:} \quad I_{L,ref} \approx I_{sc,ref}. \quad (i)$$

With this solving eq. (C.7) at open circuit conditions for  $I_{S,ref}$  one finds

$$\text{open circuit:} \quad I_{S,ref} = \frac{I_{sc,ref}}{\exp(qV_{oc,ref}/(\gamma k T_{c,ref}))}, \quad (ii)$$

substituting this into the MP point version of eq. (C.7), after some rearrangement one finds:

$$\text{MP point : (iii)} \quad \gamma = \frac{q(I_{MP,ref}R_s + V_{MP,ref} - V_{oc,ref})}{kT_{c,ref} \ln(1 - I_{MP,ref}/I_{sc,ref})} \quad (iii).$$

The last three equations (i)-(iii) are suitable to calculate three out of the four required parameters analytically, however, a prerequisite to obtain numerical values is the value of  $R_s$ , which is still missing.

#### C.4. Modelling of photovoltaic components

The value of  $R_s$  cannot be determined directly, although, a necessary condition to arrive at  $R_s$  is as follows. The open circuit data expression for eq. (C.7) may be solved for  $V_{oc,ref}$ , and the reverse saturation current is substituted by eq. (C.3) to achieve temperature dependence. This expression differentiated with respect to  $T_{c,ref}$  leads to a *conditional equation* to find  $R_s$  together with the equations (i)-(iii) through a numerical scheme. The conditional equation reads:

$$\frac{\partial V_{oc,ref}}{\partial T_{c,ref}} = \frac{\gamma k}{q} \left[ \ln \left( \frac{I_{sc,ref}}{I_{s,ref}} \right) + \frac{T_{c,ref} \mu_{sc}}{I_{sc,ref}} - \left( 3 + \frac{qE_G}{nkT_{c,ref}} \right) \right]. \quad (C.8)$$

The temperature coefficient  $\mu_{oc}$  is included in the provided manufacturer STC data, thus a convergent solution is achieved with respect to a suitable positive  $\delta$  if

$$\mu_{oc} - \delta < \frac{\partial V_{oc,ref}}{\partial T_{c,ref}} < \mu_{oc} + \delta \quad \text{holds.} \quad (C.9)$$

As numerical scheme, *Newton's method* is implemented in TRNSYS, for more details see Eckstein (1990).

#### Calculation stages during TRNSYS simulations

The initial stage comprises the determination of all required model parameters. The four parameter simulation model requires all reference STC data required to determine the equivalent model parameters as explained in sec. C.4.2. The cell temperature model requires the nominal cell temperature operating conditions (NOCT) data. That is, the user must provide all relevant STC and NOCT data.

Given the model parameters  $I_{L,ref}$ ,  $I_{S,ref}$ ,  $\gamma$  and  $R_s$ , equations (C.7), (C.5) and (C.6) are sufficient to calculate the I-V characteristic of a single PV module at a certain cell temperature and for a given irradiance value. The single cell ideality parameter is  $n = \gamma/NCS$ . During the simulation scheme the current cell temperature  $T_c$  is continuously updated according to eq. (2.27) – more details on the cell temperature evaluation are given in sec. 2.5.2.

In practice it is desired to maximize the power of the PV source for given external conditions – see fig. C.9 for the module power as a function of I and V. This is possible through a *maximum power point tracker* (MPPT) – for the most recent developments on MPPT see Abdelrahman et al. (2016). Operation at maximum power point is also assumed for the TRNSYS simulation. The current PV power reads

$$P = V \cdot I. \quad (C.10)$$

This product must be maximized to operate the PV plant at the maximum possible power for given external conditions. The maximum power point tracking is realized through a continuous alteration of the load resistance. This is done through an electronic device switched between the PV modules and the AC converter – in practice the solar converter includes the MPPT. More details may be found in Eckstein (1990).

## Appendix C. HP PV system and building

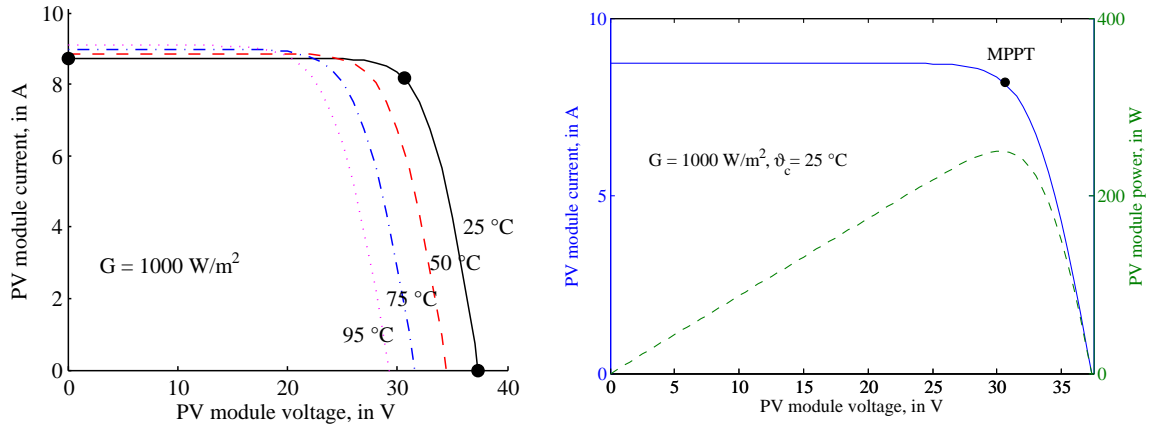


Figure C.9.: Left graph: I-V curves for the PV module for four different cell operating temperatures, and right graph: I-V curve and PV power (dashed line) as a function of the operating point; the black dots indicate the given STC data.

### Incident angle modifier

The current solar irradiance value ( $G$ ) and the current ambient temperature  $\vartheta_{oa}$  provide the main input variables for the PV model. The optical efficiency is considered through the average *transmittance-absorptance product*,  $(\tau\alpha) = 0.9$  is a commonly used value for *attenuation* of the normal incidence, that is for  $\theta_s = 0$ . However, using only this factor will lead to an overestimation of the PV-yield for annual simulations, especially for highly inclined PV array cf. Ebert et al. (2014). In practice  $(\tau\alpha)$  is obtained as the ratio of the absorbed to the incident normal solar radiation. If *soiling and dust* should be included in the optical efficiency factor  $(\tau\alpha) = 0.85$  is more appropriate see M. Garcia et al. (2011) or for an extensive review Sarver et al. (2013).

A further refinement concerning optical effects and the absorbed radiation is provided by the *incidence angle modifier*<sup>5</sup>, which provides a measure to define  $(\tau\alpha)$  as a function of the actual incident angle  $\theta_s$ :

$$K_{\tau\alpha}(\theta_s) = \frac{\tau\alpha(\theta_s)}{\tau\alpha(0)}, \quad \text{with } \tau\alpha(0) := \tau\alpha(\theta_s = 0). \quad (\text{C.11})$$

This factor explains the optical effects of a module, such as reflexion for increasing incident angles<sup>6</sup>. Up to  $\theta_s \approx 60^\circ$   $K_{\tau\alpha}(\theta_s) \approx 1$ , but for  $\theta_s > 60^\circ$  it decreases quickly, reaching 0 at an incident angle of  $90^\circ$ . The empirical expression which has been found by King et al. (1997) reads

$$K_{\tau\alpha}(\theta_s) = 1 - (1.098 \cdot 10^{-4})\theta_s - (6.267 \cdot 10^{-6})\theta_s^2 + (6.583 \cdot 10^{-7})\theta_s^3 - (1.4272 \cdot 10^{-8})\theta_s^4. \quad (\text{C.12})$$

<sup>5</sup> The incident angle modifier is often abbreviated as IAM( $\theta_s$ ) or just IAM.

<sup>6</sup> The incident angle  $\theta_s$  is measured with respect to the normal on the PV module surface.

For an alternative approach the author relates to the research of N. Martin and Ruiz (2005)<sup>7</sup>

Concerning *beam radiation* (C.12) may be directly facilitated to obtain  $K_{\tau\alpha}(\theta_{s,beam})$  given  $\theta_{s,beam}$ , which may be calculated from the known geometrical Earth-Sun relations, (Duffie and W. A. Beckman, 2006, pg.12). However, wrt the *diffuse* and the *reflected* radiation empirical correlations describing an effective incidence angle are needed see Brandemuehl and W. Beckman (1980) or Duffie and W. A. Beckman (2006), pg. 214. The correlations read

$$\hat{\theta}_{s,diff} = 59.7 - 0.1388\beta + 0.001497\beta^2 \quad \hat{\theta}_{s,grd-refl} = 90 - 0.5788\beta + 0.002693\beta^2 \quad (C.13)$$

where  $\beta$  stands for the slope of the PV surface in *degrees*. Based on these equations  $K_{\tau\alpha}(\hat{\theta}_{s,diff})$  and  $K_{\tau\alpha}(\hat{\theta}_{s,grd-refl})$  may be calculated.

Finally, the total effective irradiance on the PV cell p-n junction is given by

$$G_{K\tau\alpha} = (K_{\tau\alpha}(\theta_s) G_{beam} + K_{\tau\alpha}(\hat{\theta}_{s,diff}) G_{diff} + K_{\tau\alpha}(\hat{\theta}_{s,grd-refl}) G_{grd-refl}) \tau\alpha(0). \quad (C.14)$$

For consideration of the incidence angle modifier in the calculation of the light current  $G$  in eq. (C.5) must be replaced by  $G_{K\tau\alpha}$ . Concerning the *cell temperature* calculations outlined in sec. 2.5.2,  $\tau\alpha$  must be interpreted as the angle dependent, average transmittance-absorptance product. That is

$$(\tau\alpha) = \overline{\tau\alpha} \quad \text{and} \quad \overline{\tau\alpha} := \frac{G_{K\tau\alpha}}{G_T}. \quad (C.15)$$

---

<sup>7</sup> Have a look also to the web site of the "PVPerformance Modeling Collaborative".



## Appendix D.

### The Project MPC-Boxes

Model predictive control (MPC) for heating or cooling of buildings, especially by means of TABS, is a famous topic. A few research projects have been conducted in recent years, (Karlsson and Hagetoft, 2011; Gwerder et al., 2013; Sourbron et al., 2013; Privara, 2013; Žáčková et al., 2014; Coninck, 2015) but representative<sup>1</sup> results from real experiments on comfort- or energy demand-improvement are rare. MPC in this context has already found its way into practice even before reliable simulation results with respect to these topics were available, (compare Toedtli, 2011). The research project MPC-Boxes was established with the challenge to partly fill the gap of real representative experimental results on comfort and energy related improvements, owing to MPC.

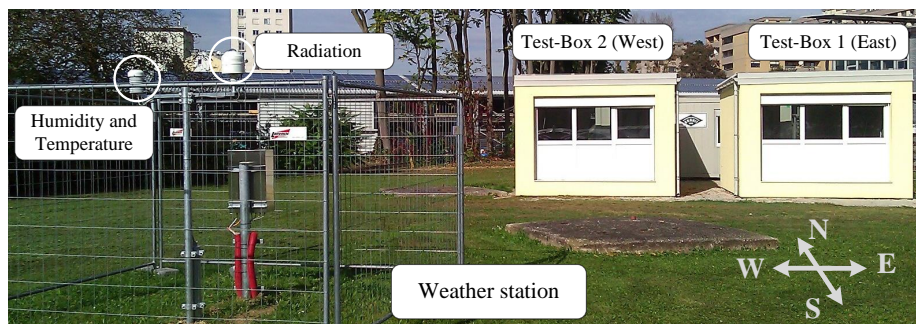


Figure D.1.: Photo of the experimental set-up, weather station and the two Test-Boxes; S-view.

Two Test-Boxes each with the approximate size of a garage were designed and constructed at Graz Inffeldgasse with the purpose to enable tests for residential and office buildings. Figure D.1 shows a photo of the experimental set-up: the two built Test-Boxes and the weather station. Both, heating and cooling by means of thermally activated building systems (TABS) are to be investigated with a Test-Box. One Test-Box is operated by a standard controller and the other is operated by means of a MPC. A local weather station was erected and used to record the ambient conditions and to obtain accurate weather forecast data at the site, which improves the performance of the

<sup>1</sup> In practice even two similar buildings do not share the same boundary conditions due to the variance of user behavior and occupancy, which makes it nearly impossible to compare a standard control against an MPC approach.

predictive controller. Heating or cooling energy is generated by means of a reversible heat pump feeding into a thermal storage. The buffer storage is situated northern of the two Test-Boxes in a trailer which incorporates the hydraulic distributor and all required building automation devices.

The physical construction should be similar to the the most recent construction standards, given in Tab. D.1, and it should be possible to adapt the Test-Boxes according to the intended investigation. An adaption of the heating or cooling demand may be obtained through additional ventilation and or internal energy gains, see Appendix D.4.

## D.1. Test-Box construction and thermal characteristics

The valid heating and cooling demand limits for new buildings in Austria are given in Table D.1. The values rely on certain standard internal load profiles<sup>2</sup>. These values for new buildings served as a guideline at the construction-design stage of the project.

Table D.1.: Heating and cooling demand limits of new buildings according to OIB 6 (2011), with standard internal load profile given in OENORM B 8110-5:2010 and  $n_{inf}=0.15$ .

Usage	Heating, (max)	Cooling, (max)
Residential building	$16 (1 + 3.0 A/V)$ , (54.4) kWh/(m <sup>2</sup> a)	–
Office building	$5.5 (1 + 3 A/V)$ , (18.7) kWh/(m <sup>3</sup> a)	1.0 kWh/(m <sup>3</sup> a)

### D.1.1. Detailed geometry and material properties

Fig. D.2 provides the inner dimensions of a Test-Box. Together with the layer constructions depicted in Fig. D.3 the outer dimensions may readily be derived. Figures in this section refer to the real objects and to the simulation model (the segmentation of the TABS refers only to the simulation). The numbers drawn on the outer (left) and inner (right) wall segments in white background indicate the wall number of the TRNSYS model. The ceiling and the floor segments constitute the ceiling and the floor TABS, respectively. The detailed *real pipe layer scheme* is depicted in Fig. D.4. For the TRNSYS model the ceiling is divided in lengthy N-S-direction segments, whereas the floor is divided in lengthy E-W-direction segments. In general N-S-direction segments are needed to approximate the real design and operation – as for the ceiling, which is the prior TABS of investigation. However, the E-W-segments on the floor allow for different temperatures in N-S-direction which is wanted to see the effect of solar radiation heating the floor. That is, external effects on the passive TABS are better modeled with

<sup>2</sup> Internal loads are assumed  $3.75 \text{ W/m}^2$  and  $0 \text{ W/m}^2$  for the heating and cooling season, respectively.

## D.1. Test-Box construction and thermal characteristics

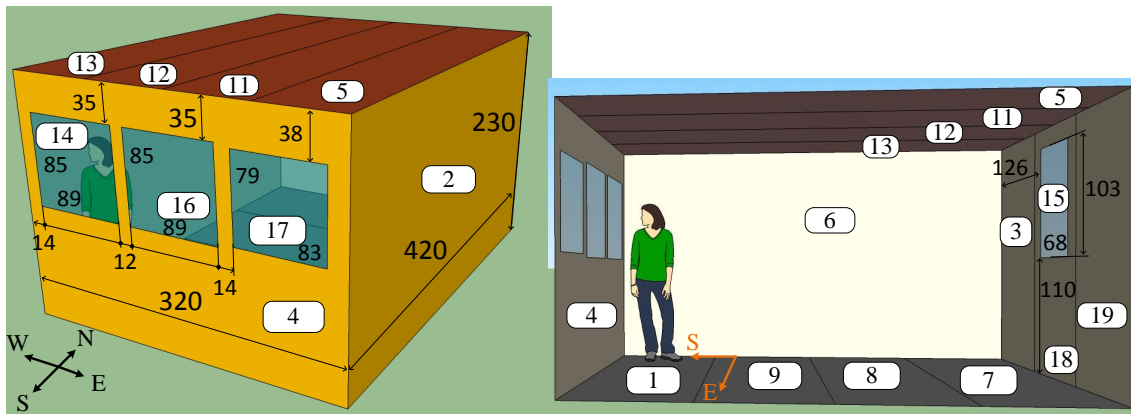


Figure D.2.: Test-Box inner dimensions in cm and TRNSYS wall segmentation numbers in white background; outside SE-view (left) and inside E-view (right). All measures are in cm.

E-W-segments, and the active TABS is better modeled using N-S-segments. The entire S-wall consists of one portal window only, compare Tab. D.3.

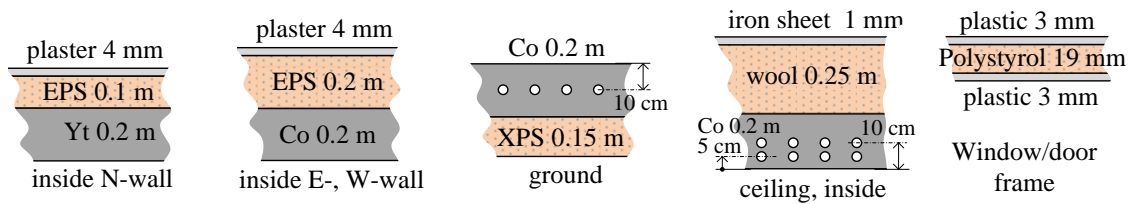


Figure D.3.: Layer construction overview for walls, ground floor and ceiling. The active layer horizontal pipe-distance in the ground floor and the ceiling is 0.15 m. The entire S-wall is a portal-window. With cold-bridge correction in terms of altered U- and cp-values, the insulation layer thicknesses become 0.104, 0.16, 0.121 and 0.2 m, and the cp of concrete is increased to 1.23 kJ/(kg K).

Tab D.2 provides the physical material properties of the construction materials. The range after the forward dash – which is provided for a few parameters – indicates the possible values, however, the first value is chosen for the simulation, respectively. Tab. D.3 lists the properties of the entrance door and the south-facing window. The window and door parameters given in the first five columns (the parameters without asterisk) are those provided by the manufacturer, calculated according to OENORM EN ISO 10077-1. The quantities with an asterisk are finally used for the simulation, for which the door and the window element are split into a wall- and a glass-section. The wall section properties consider first, the “gaps” between the walls and the element, and second, integration characteristics such as the external insulation cover of the frame.

The window represents an entire wall in TRNSYS (cf. segment 4 in fig. D.2) and in reality, that is the whole area of 3.2 m x 2.3 m is filled by the portal window element. By contrast, the entrance door (wall segment 18) represents only one of the three wall

## Appendix D. The Project MPC-Boxes

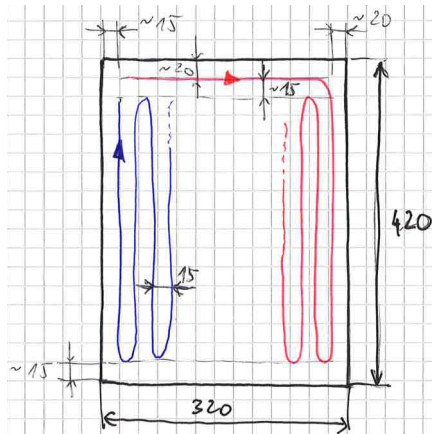


Figure D.4.: Real pipe layer scheme for Test-Box +So2 (East). The pipes are layed in meander shape with the first straight flow section (hot when heating) close to and parallel to the "middle" wall where the two Test-Boxes face each other. All measures are in cm. The scheme is similar for Test-Box +So3 (West) but mirrored at the longitudinal (central) axis;  $L_{total} \approx 84$  m.

Table D.2.: Test-Box construction – material parameters used in TRNSYS simulations.

Material	Thermophysical properties			Optical properties	
	$\lambda$ W/(m K)	$\rho$ kg/m <sup>3</sup>	$c_p$ kJ/(kg K)	$\alpha_{SW}$	$\epsilon_{LW}$
Concrete (Co)	2.5/2.3-2.5	2.4/2.3-2.4, t/m <sup>3</sup>	1.08	0.8/0.65-0.8	0.9/0.85-0.95
Ytong (Yt)	0.11	400	1.00	0.56/0.56-0.69	0.94
XPS	0.036	35	1.45	-	-
EPS	0.039	20	1.45	-	-
Min. wool	0.032	32	1.03	-	-
Polystyrol	0.031	20	1.25	-	-
Plastic	0.231	1500	1.00	0.6	0.9
Plaster	0.7	1400	1.00	0.4/0.3-0.5	0.91
Painted iron	15	7800	1.80	0.4/0.3-0.55	0.5/0.27-0.67
Pipes (Rautherm S)	$d_{outer}=17$ mm, $s_{wall}=2$ mm, roughness coef. 0.007 mm, $L_{total} \approx 84$ m				
	0.35	0.93 g/cm <sup>3</sup>	0.55	-	-

segments (3,18,19) forming the N-wall. Concerning the Window the wall segment 4 has three embedded glasses with segment number 14, 16 and 17, these segments are represented by one entry only in Tab. D.3. Concerning the Door the wall segment 18 has assigned the glass area with segment number 15.

Table D.3.: Test-Box construction – wall (embedded) elements;  $\alpha_{SW} = 0.6$  and  $\epsilon_{LW} = 0.9$  for both wall sides, inside and outside, respectively.

Property	$A_{gla}$	g	$U_g$	$U_w$	$A_w$	$A_{gla}^*$	$U_g^*$	$g^*$	$A_{w,TRN}^*$	$U_w^*$
Unit	m <sup>2</sup>	-	W/m <sup>2</sup>	W/m <sup>2</sup>	m <sup>2</sup>	m <sup>2</sup>	W/m <sup>2</sup>	-	m <sup>2</sup>	W/m <sup>2</sup>
Door	0.84	0.62	1.1	1.3	2.23	0.70	1.06	0.626	1.69	1.223
Window	2.17	0.62	1.1	1.25	7.01	2.17	1.1	0.609	5.19	1.223

### D.1.2. TRNSYS building model deficiency – compensation

The building model Type 56 in TRNSYS does not consider a thickness for any material layer of a wall, ceiling, or floor. This causes an error where one such element connects to another. This error is significant for small surfaces. Adjusting the physical parameters provided in Tab. D.2 and Tab. D.3 is one option to compensate for the neglected lateral heat flux. The altered thicknesses of the insulation layers are given in the caption of Fig. D.3. The detailed procedure, how to obtain the according correction factors for U- and  $c_p$ -values is described in Appendix E.2.

The Test-Box building model with *corrected* physical parameters (U- and  $c_p$ -values) is considered as the final advanced or corrected building model. This model represents the base case. One level higher in terms of performance is only the validated building model for which the model dynamic is compared against measurement values and, if required, parameters are adjusted to increase the agreement between model generated and real (measurement) data.

### D.1.3. Heating and cooling demand

The initial construction based TRNSYS simulation model with cold-bridge corrections (see Appendix E.2), yields an annual heating and cooling demand of 64 kWh/m<sup>2</sup> and 16 kWh/m<sup>2</sup>, respectively<sup>3</sup>. These results are obtained with the data set Graz-TRY1990-2012, the ground temperature model from Kasuda, an infiltration ( $n_{inf}$ ) of 0.11, constant internal loads of 3.75 W/m<sup>2</sup> and no shading function. The actual heating or cooling demand of a Test-Box may be altered by playing with the ventilation system, the external shading and the load dummy, dedicated to simulate internal energy gains. Tab. D.4 provides results for different boundary conditions.

Fig. D.5 illustrates the specific heating and cooling powers by means of a scatter plot obtained for the construction with cold-bridge-correction already implemented.

### D.1.4. Maximum heating and cooling load

The values from Fig. D.5 sorted in ascending or descending order yield the cooling- and heating-power duration curves, drawn in Fig. D.6. The extrema of these two design parameters are obtained when analyzing ideal heating and cooling powers with TRNSYS for boundary conditions (occupancy, equipment) characterizing the most extreme cases. The maximum heating power is obtained for a minimum of internal loads and the maximum cooling power for internal loads reaching a maximum. Typical

---

<sup>3</sup> These values are obtained using ideal heating and cooling to hold the temperature between 20°C and 26°C. When neglecting the radiation losses against the virtual sky temperature  $\vartheta_{sky}$  the according values become 59 kWh/(m<sup>2</sup> a) and 19 kWh/(m<sup>2</sup> a).

## Appendix D. The Project MPC-Boxes

Table D.4.: Test-Box space heating (SH) and cooling demand (CD) for different boundary conditions; four weeks pre-simulation. Shading (shad.) on means a reduction of solar gains by a factor of 2/3 if the shading position is down, the shading goes down if  $I_{g,horizontal} > 400 \text{ W/m}^2$  and goes up again if  $I_{g,horizontal} < 300 \text{ W/m}^2$ .  $\vartheta_{sky}$ -model: *on* indicates consideration of long wave losses to the sky.

Boundary conditions				Heating		Cooling	
$n_{inf}$ $h^{-1}$	int. gains $\text{W/m}^2$	shad. -	$\vartheta_{sky}$ - model	SH $\text{kWh}/(\text{m}^2\text{a})$	$\dot{Q}_{max}$ $\text{W/m}^2$	CD $\text{kWh}/(\text{m}^2\text{a})$	$\dot{Q}_{max}$ $\text{W/m}^2$
<b>0.5</b>	3.75 (0-24 h)	off	on	89.1	55	11.3	29
<b>0.2</b>	3.75 (0-24 h)	off	on	69.7	46	14.5	27
0.11	3.75 (0-24 h)	off	on	64.0	44	15.7	27
0.11	<b>0</b>	off	on	81.5	48	7.2	23
0.11	<b>34 (9-17 h)</b>	off	on	39.5	44	41.6	47
0.11	3.75 (0-24 h)	<b>on</b>	on	74.5	44	4.5	15
0.11	3.75 (0-24 h)	off	<b>off</b>	59	43	18.6	28

values for an office building are  $8 \text{ W/m}^2$  (persons),  $16 \text{ W/m}^2$  (equipment),  $10 \text{ W/m}^2$  (lightening); compare with Toedtli et al. (2009) p.73.

Fig.D.6 depicts duration curves for various boundary conditions – compare Tab. D.4. The case with low internal gains requires a SH demand of  $64 \text{ W/m}^2$  and a CD of  $15.7 \text{ W/m}^2$ . Assuming increased internal gains (office building,  $34 \text{ W/m}^2$  9-17 h) and given a set value  $\vartheta = 24^\circ\text{C}$  the Test-Box's maximum cooling power reaches  $59 \text{ W/m}^2$ .

## D.2. Measurement equipment and accuracy

### D.2.1. Temperature sensors

The employed temperature sensors for air-, surface-, flow-medium- and concrete-temperature measurement are Pt1000, IP67 – this protection standard against splashing water allows also to place the sensors in concrete. All sensors are calibrated and tested in the lab. Finally it turned out, that with these kind of sensors the only element in the measurement chain which is prone to inaccuracy is the analog input of the I/O bus units as part of the building automation system. These I/O channels must be calibrated ideally with a simple highly accurate ohmic resistance.

Due to the relatively low permanent current<sup>4</sup> in the 2-wire circuit one may neglect the self-heating of the sensor. A rule of thumb is, that any measurement current below  $3 \text{ mA}$  mostly leads to negligible self-heating Telemeter Electronic (2014) .

<sup>4</sup>  $5\text{V}/(10\text{k}+1\text{k}) = 0.454 \text{ mA}$ ; 10 000 ohm from the inner resistance of the I/O unit and 1000 ohm from the Pt1000

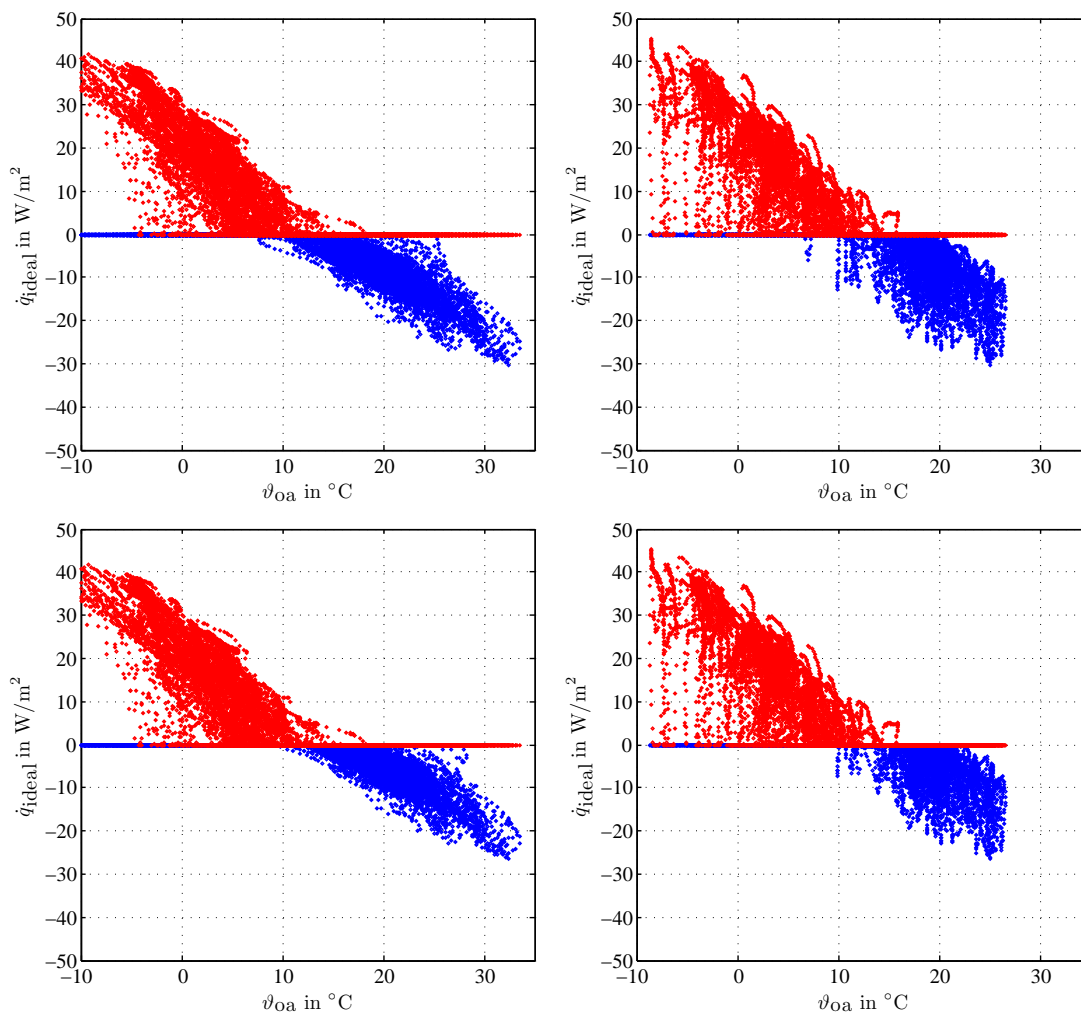


Figure D.5.: Heating (positiv) and cooling power (negative) as a function of the outside ambient temperature. Top graphs for a comfort range of  $20^{\circ}\text{C} - 24^{\circ}\text{C}$ , and lower graphs for a comfort range of  $20^{\circ}\text{C} - 26^{\circ}\text{C}$ . The left graphs refer to the current ambient temperature and the right graphs refer to the smoothed (24 h moving average) ambient temperature.

### D.2.2. Heat meter

The applied heat meter Kamstrup MC402 is based on an ultrasonic flow measurement in connection with two pairwise selected Pt500 sensors.

Appendix D. The Project MPC-Boxes

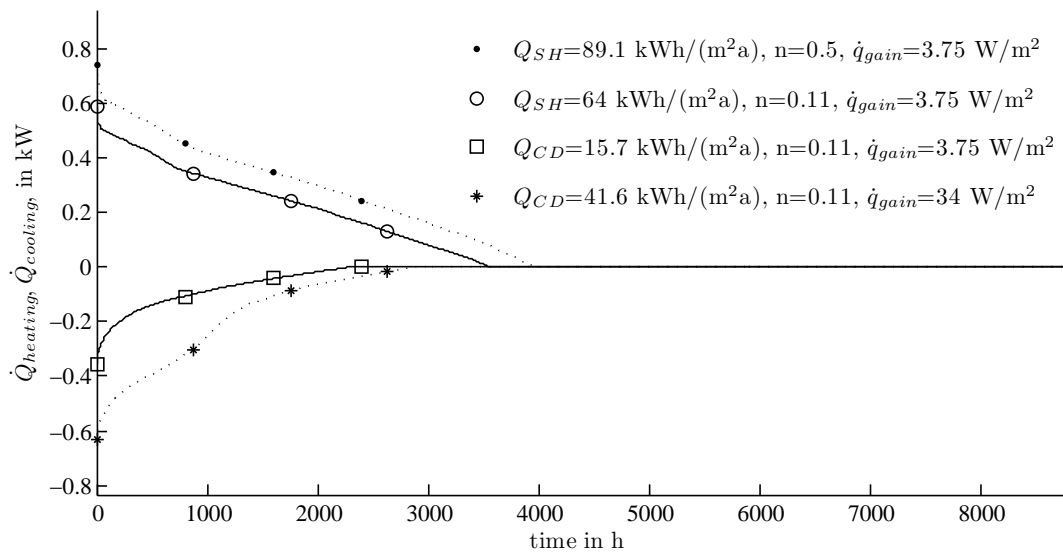


Figure D.6.: Heating and cooling power duration curve for the Test-Box and different boundary conditions, compare Tab. D.4.

### D.3. Evaluation and comparison of the two real Test-Boxes

Given the overall research task it is important to evaluate to which degree the Test-Boxes are equal, or termed negatively what is the deviation for measured temperatures and powers given the same operation (plan) and the same real ambient conditions for the Boxes +So<sub>2</sub> (East) and +So<sub>3</sub> (West), respectively.

The whole chain of elements – construction, actuator, sensor, PLC- and measurement hardware, with potential errors for each – makes it difficult to guess a degree of results-similarity for the experimental setup, if both Boxes +So<sub>2</sub> and +So<sub>3</sub> are operated in the same way. Potential deviations may originate from the (concrete) construction, inhomogeneous material properties, inaccurate sensor placement, calibration errors or hardware temperature errors and so forth.

To evaluate the construction and especially leakage, a so called Blower Door Test is conducted for both Test-Boxes. In a second stage, temperature and power measurements for the two constructions are compared, given an equal excitation. Excitation means heating or cooling with a certain flow temperature, at a constant water volume flow. The answer to the question of equality is astonishing, for a concise report see Pichler, Goertler, et al. (2016).

#### D.3.1. Comparison by means of a Blower Door Test

In order to examine the construction of the two Test-Boxes and to assure equality from an infiltration point of view a *blower door test* is conducted for both Test-Boxes. This test pressurizes and depressurizes the objects to determine the leakage characteristics of the building envelope. The exact procedure of the test is described in DIN EN 13829.

The quantity  $n_{50}$ , which is measured during this test, gives the air change during one hour with respect to the volume of the building when applying a pressure difference of 50 Pa between outside and inside. At this pressure difference the measurement is least sensitive to the influence of wind variation during the test, however, it does not reflect the real natural air change rate ( $n_x$ ) and it must be used with caution when compared for different constructions in terms of size and shape, compare Tanner (2004).

Long term infiltration rates  $n_x$  may be estimated through down scaling of the  $n_{50}$  value to 4 Pa – which is a suitable annual average pressure difference. Rules for down scaling are given in OENORM B 8110-6:2010 or in OENORM Vornorm H 7500:2006 in connection with OENORM EN 12831:2003. According to OENORM B 8110-6:2010 a good estimate for the real air change rate, given  $n_{50} > 1.5 h^{-1}$  is

$$n_x = 0.11. \quad (D.1)$$

### Experimental set up and measurement results

Fig. D.7 shows the experimental set-up for the depressurization (vacuum) and the pressurization – the ventilator is flipped between the two measurements.



Figure D.7.: Blower door depressurization (left) and pressurization (right) test.

The measured average leakage volume flow rate at 50 Pa is  $49 \text{ m}^3/\text{h}$  for the Box +S<sub>02</sub>, and  $47 \text{ m}^3/\text{h}$  for the Box +S<sub>03</sub>, which correspond to an  $n_{50}$ -value of 1.58 1/h and 1.51 1/h, respectively.

#### D.3.2. Comparison by means of measurement data

Measurement data for temperature and power are available from conducted system identification experiments. For both Test-Boxes, the recorded data are used to evaluate the thermo-physical similarity. Since both Boxes are situated at the same site, with the only window facade oriented towards South, the ambient conditions are considered exactly the same.

Fig. D.8 shows an exemplary interval with the TABS- ( $\vartheta_{ta}$ ), the room air- ( $\vartheta_{ra}$ ), and the ground temperature ( $\vartheta_{grd}$ ) and the specific TABS power ( $\dot{q}_{ta}$ ) trajectories for the Boxes +S<sub>2</sub> (East) and +S<sub>3</sub> (West), respectively – the bottom window shows also the ambient

### D.3. Evaluation and comparison of the two real Test-Boxes

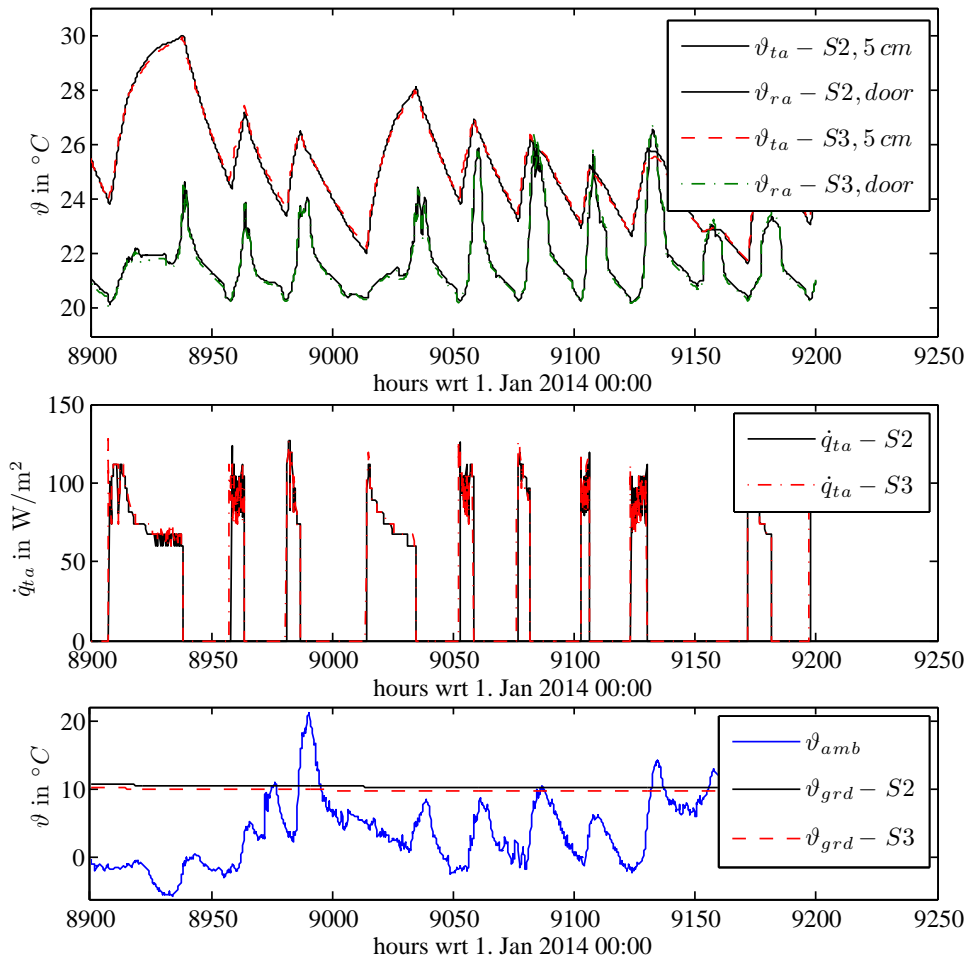


Figure D.8: Exemplary temperature and TABS power trajectories.

temperature. The pure visual inspection of the graphs leads to the conclusion that the measurement data are very similar, nearly equal, except for the ground temperature.

Table D.5.: MPC-Boxes, Test-box measurement results comparison, interval 8700 h - 9590 h,  $A=4.2 \text{ m} \times 3.2 \text{ m}$ ; 1. Jan 2014 00:00 := 0 h.

variables	evaluation measures				
	$\sum y_{S3} / \sum y_{S2}$ %	$\overline{\Delta y}$ K or W/m <sup>2</sup>	$\sigma_{\Delta y}$ K or W/m <sup>2</sup>	$\min \{ \Delta y \}$ K or W/m <sup>2</sup>	$\max \{ \Delta y \}$ K or W/m <sup>2</sup>
$\vartheta_{ta}$	100.30	0.07	0.16	-0.47	0.90
$\vartheta_{ra}$	100.00	0.00	0.16	-2.43	1.30
$\vartheta_{grd}$	95.15	-0.50	0.04	-0.59	-0.37
$\dot{q}_{ta}$	102.89	0.86	14.19	-133.93	136.27

## Appendix D. The Project MPC-Boxes

Table D.6.: MPC-Boxes, Test-Box measurement results comparison, interval 9900 h - 10840 h; A=4.2 m x 3.2 m; 1.Jan 2014 00:00 := 0 h .

variables		evaluation measures			
$y$	$\sum y_{S3} / \sum y_{S2}$	$\overline{\Delta y}$	$\sigma_{\Delta y}$	$\min \{ \Delta y \}$	$\max \{ \Delta y \}$
$\downarrow$	%	K or W/m <sup>2</sup>			
$\vartheta_{ta}$	99.66	-0.08	0.16	-0.45	0.18
$\vartheta_{ra}$	99.52	-0.10	0.18	-0.90	1.30
$\vartheta_{grd}$	94.09	-0.57	0.03	-0.66	-0.52
$\dot{q}_{ta}$	100.47	0.08	13.39	-160.19	208.64

Table D.3.2 and Tab. D.3.2 provide quantitative evaluation measures for two intervals each longer then the one depicted in Fig. D.8. Relevant measures for the evaluation are defined in Eq. . The results are very satisfying. The mean deviation for the room air temperature is  $0.00 \pm 0.16$  K and  $-0.10 \pm 0.18$  K. The highest difference occurs for the ground temperature  $-0.50 \pm 0.04$  K and  $-0.57 \pm 0.03$  K which is an external variable that cannot be influenced. This difference can be reasoned with a different ground, and the tendency of slightly higher heating power during the interval evaluated in Tab. D.8 confirms this assumption, hence it is assumed that this difference does not originate from e.g. a calibration error.

$$\frac{\sum y_{S3}}{\sum y_{S2}} := \frac{\sum_{t=1}^N y_{S3}(t)}{\sum_{t=1}^N y_{S2}(t)} \quad (D.2)$$

$$\Delta y := y_{S3} - y_{S2}$$

### D.3.3. Calibration and validation of the TRNSYS simulation

Based on the TRNSYS model with cold-bridge-correction simulation and real (measurement) data (wcg) are compared against each other, given equal "input" variables. The simulation input variables relate to the TABS, the ambient (weather) and to internal gains:

$$\text{TABS :} \quad \dot{m}_{ta}, \vartheta_{sw} \quad (D.3)$$

$$\text{ambient :} \quad \vartheta_{oa}, I_{beam, horizontal}, I_{dif, horizontal}, RH_{oa}, \vartheta_{grd} \quad (D.4)$$

$$\text{internal gains :} \quad \dot{Q}_{gi}, n_{vent}, \dot{Q}_{vent}. \quad (D.5)$$

A first comparison of measurement and simulation data showed, that the coupling to the ambient and the ground is much stronger for the real object than for the TRNSYS simulation model. This is also evident from the parameters B(2,2), B(2,3) and B(3,6) in tab. 4.1. Comparing these parameters for  $\mathcal{M}_{gray}(\Theta_{tf})$  and  $\mathcal{M}_{gray}(\Theta_{wgc})$  a much stronger ambient-coupling is noticeable for the real model. The SSM parameter values

### D.3. Evaluation and comparison of the two real Test-Boxes

obtained with the real measurement data are 1.72, 1.16 and 3.05 times greater than those obtained with simulation data from the initial (base case) model. The fact, that the ground coupling is such strong is very probably due to a modeling deficiency of the ground temperature within the TRNSYS simulation.

The ground temperature  $\vartheta_{grd}$  for the TRNSYS simulation, applied to the XPS surface facing the ground, is obtained from the simple Kasuda equation according to Kasuda and Archenbach, 1965:

$$\vartheta(d, t) = \bar{\vartheta} - A \exp(-\kappa) \cos\left(\frac{2\pi}{365}\left(t - \Delta t - \frac{\kappa}{2\pi}\right)\right) \quad (D.6)$$

where  $\bar{\vartheta} := \text{mean}(\vartheta_{oa})$ ,  $A := \max(|\vartheta_{oa}|) - \bar{\vartheta}_{oa}$   
and  $\kappa := d \sqrt{\frac{\pi}{365 a}}$ .

Here,  $\vartheta(d, t)$ , indicates the undisturbed ground temperature as a function of the desired depth  $d$  and the day of the year  $t$ . It is a function of the outside air ambient temperature  $\vartheta_{oa}$  in °C and  $\Delta t$ , which is the day of the year with the minimum of  $\vartheta_{oa}$ . The parameter  $a$  in m<sup>2</sup>/day stands for the thermal diffusivity of the ground. Based on the Graz-TRY1990-2012 data one gets  $\bar{\vartheta} = 10.5$  K,  $A = 10.8$  °C and  $\Delta t = 11.1$  d for the location Graz, assuming  $\kappa = 0$ . Applying eq. (D.6) with a thermal diffusivity<sup>5</sup> of  $a = 3.24 \cdot 10^{-3}$  m<sup>2</sup>/h one may calculate the ground temperature at a certain depth e.g. 0.05 m. The major shortcoming of this model is, that the real interaction, that is the heating of the ground or the ground response due to heat absorption is not considered, the temperature represents a rigid boundary.

For the real building, the ground temperature  $\vartheta_{grd}$  is measured in the center of the fundament, directly underneath the XPS insulation. However, this temperature seems not to be representative for the whole ground surface. This is why the ground is split into three patches as depicted in fig. D.9. Finally, the measured temperature is only applied for the inner patch. For the other two patches the ground temperature model according to eq. (D.6) is facilitated for two "depths". The required parameters are adjusted based on the available ambient data for the location Graz St. Peter in 2015 and the thermal diffusivity<sup>6</sup>  $a$  is calibrated by means of the measured ground temperature  $\vartheta_{grd}$ . The obtained parameters are  $\bar{\vartheta} = 11.8$  °C,  $A = 10.3$  K and  $\Delta t = 15.6$  d; and the (lateral) diffusivity<sup>7</sup> is  $a = 0.93 \cdot 10^{-3}$  m<sup>2</sup>/h.

Based on the described ground temperature modeling approach the cold-bridge-corrected TRNSYS model is now further adjusted by means of the available data wcg,

5 The assumed soil parameters are  $\lambda = 8.72$  kJ/(hmK) – this is relatively high –  $\rho = 3200$  kg/m<sup>3</sup> and  $cp = 0.84$  kJ/(kgK).

6 This diffusivity describes rather a lateral than a vertical diffusion. In fact, it represents the thermal diffusivity from the ground exposed to ambient conditions, towards the ground underneath the XPS insulation.

7 The soil parameters are  $\lambda = 2.5$  kJ/(hmK),  $\rho = 3200$  kg/m<sup>3</sup> and  $cp = 0.84$  kJ/(kgK)

## Appendix D. The Project MPC-Boxes

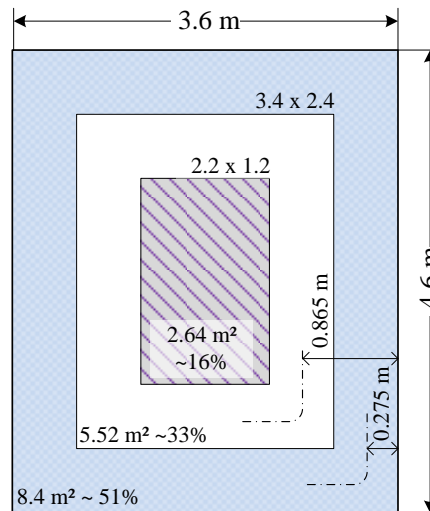


Figure D.9.: Sections for the ground coupling.

which represents measurement data from mid December 2014 to mid February 2015. After discovering that the temperature levels of the simulation are too high, the heat conductivity for all insulation layers (except the door) was increased by 15%. After that, the residuals between measurement and model data for concrete, surface, operative and air temperatures are inspected in detail and the heat conductivities are further adjusted to minimize the residuals. Finally it turned out, that a total increase of all U-values, except that of the door, by a factor of approximately 1.21 is required to obtain a good match between the measurement and the simulation data. This is realized by means of increased  $\lambda$ 's. The final  $\lambda$  values in TRNSYS in kJ/(hmK) are: XPS: 0.17, EPS: 0.2124, Min. wool: 0.115, polystyrol: 0.145, Yt: 0.45. In order to improve the match between the measured and the simulated return temperature, it was also necessary to lower the TABS pipe thermal conductivity from 1.26 to 0.9 kJ/(hmK) and the supply water inlet temperature by 0.05 K. One parameter referring to the ventilation was also adjusted, the final outcome confirms the assumed air-exchange rate of 0.9 for the ventilation system. The effective shading factor for the state entirely closed was found to be 0.963. Finally the infiltration was increased to 0.15 and the fraction of internal gains released through radiation was adjusted to 0.2 (originally 0.5).

After the calibration of the TRNSYS model a simulation with a time step of 10 min is conducted for the whole interval of the data wcg. The first week (168 h) is considered as natural settling of the model and are therefore neglected for the evaluation. Tab. D.7 provides quantitative results for the validation of the calibrated TRNSYS model. As a basis the residual  $\varepsilon$  according to eq. (3.39) is determined for each time instance between the real data and the model output and the *mean*, the standard deviation ( $\sigma$ ) and the minimum and the maximum error are calculated. Positive numbers indicate too small simulation results and negative numbers stand for too big simulation results. The sum

### D.3. Evaluation and comparison of the two real Test-Boxes

Table D.7.: MPC-Boxes, wcg (real) versus TRNSYS data after model calibration.

variables ( $y$ )	evaluation criteria for $\varepsilon = y_{real} - y_{TRNSYS}$				unit
	$mean(\varepsilon)$	$\sigma(\varepsilon)$	$min(\varepsilon)$	$max(\varepsilon)$	
$\vartheta_{si,N}$	-0.88	0.53	-5.13	0.02	K
$\vartheta_{si,E}$	-0.09	0.29	-0.85	2.63	K
$\vartheta_{si,S}$	0.04	0.71	-3.47	1.84	K
$\vartheta_{si,W}$	-0.08	0.24	-0.80	0.94	K
$\vartheta_{ra,N}$	0.50	0.48	-1.74	2.63	K
$\vartheta_{ra,S}$	0.74	1.22	-1.87	9.57	K
$\vartheta_{op,N}$	0.28	0.35	-1.50	1.75	K
$\vartheta_{op,S}$	0.19	1.36	-1.77	9.97	K
$\vartheta_{si,ceil}$	0.05	0.30	-1.12	0.64	K
$\vartheta_{si,floor}$	-0.27	0.22	-0.84	0.21	K
$\vartheta_{ta,ceil,5cm}$	-0.07	0.38	-1.64	0.66	K
$\vartheta_{Co,floor,10cm}$	-0.02	0.21	-0.43	0.52	K
$\dot{Q}_{ta,ceil,5cm}$	-11.89	44.53	-244.63	435.26	W
$\vartheta_{so,N}$	0.87	0.93	-3.22	4.00	K
$\vartheta_{so,E}$	0.07	1.44	-7.24	6.21	K
$\vartheta_{so,S}$	-0.36	1.82	-14.39	5.47	K
$\vartheta_{so,W}$	0.51	1.15	-9.37	5.43	K
$\vartheta_{so,roof}$	-1.35	2.45	-9.52	5.06	K

over the bias values ( $mean(\epsilon)$ ) of all evaluated temperature variables turns out to be 0.12 K which is within the measurement accuracy of 0.2 K.

As a summary it may be stated, that it is difficult to calibrate the TRNSYS simulation based on the available measurement data. One problem is, that at site only the global solar radiation is measured. The split into beam and diffuse radiation is based on meteorological measurements a few kilometers away. What complicates the model calibration further is the fact, that at the time of data acquisition the building contained still large amounts of construction moisture. At that stage the thermal properties alter continuously and in addition continuous condensation and vaporization occurs, which increases or lowers the temperature and leads to a distortion of the measurement, since latent heat processes are neglected for the TRNSYS simulation.

### D.3.4. Thermally Activated Building System (TABS)

Tab. D.3 lists the physical properties of the pipe layer<sup>8</sup>. Each Test-Box has three pipe layers in total. Two layers are in the ceiling, one in the middle of the 20 cm thick ceiling, and the second with a distance of 5 cm to the inner ceiling surface. Another layer is situated in the middle of the 20 cm thick floor. The pipes are laid in meander-shape with a center-center distance of 15 cm.

TABS transfer heat to other walls or surfaces and finally to the room air by means of radiation and convection. Heat transfer due to *radiation* is modeled using the detailed *Gebhart method*, see Klein et al. (TRNSYS 17) and Klein et al. (TRNSYS Type56) for more details.

The convective heat transfer coefficients<sup>9</sup> for *inner wall surfaces* in TRNSYS are modeled dependent on the temperature gradient<sup>10</sup> ( $\vartheta_{surface} - \vartheta_{roomair}$ ) according to (Glueck, 1990, p 120 foll.) see also (Recknagel, 2013/2014, p. 214). For heat transfer downwards  $\alpha_c = 2.0 |\Delta\vartheta|^{0.31}$ , upwards  $\alpha_c = 1.08 |\Delta\vartheta|^{0.31}$ , and for vertical surfaces  $\alpha_c = 1.6 |\Delta\vartheta|^{0.30}$ . The coefficients for *outer wall surfaces* are assumed constant 17.8 W/(m<sup>2</sup>K)<sup>11</sup>. For the outer (back) side of the ground floor surface, which faces earth, the convective heat transfer coefficients is set < 0.001 kJ/(h m<sup>2</sup>) which indicates direct contact in TRNSYS – to avoid convective heat transfer. For models applied for heat transfer calculations through construction layers in buildings see also OENORM (EN ISO 13786:2008).

---

8 Common design parameters are  $d_a=17$  mm with 2 mm pipe wall thickness or  $d_a=20$  mm with 2 mm wall thickness; and a pipe to pipe distance of 15 cm. Such designs are operated at flow rates between 12 and 16 kg/(h m<sup>2</sup>). To assure turbulent flow the speed of the medium should not go below 0.2 m/s.

9 For standard average values see also OENORM (EN 15377:2008), part 1 p. 15.

10TRNSYS provides also the option to use a constant convective transfer coefficient.

11Changing this value by even one order of magnitude does not change the results significantly.

### D.3. Evaluation and comparison of the two real Test-Boxes

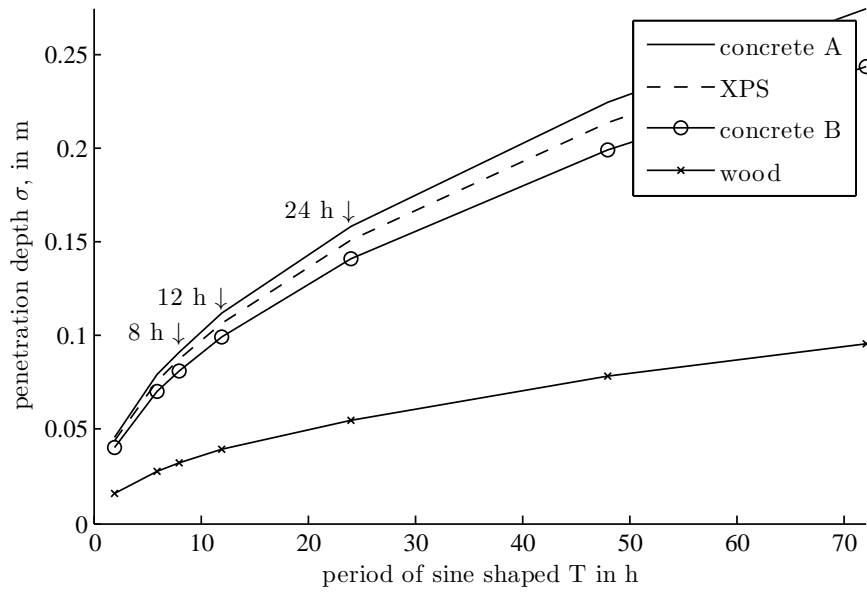


Figure D.10.: Penetration depth for different materials, with sinusoidal wave applied on one surface.

#### Motivation for TABS

In context of heating and cooling applications by means of a compression heat pump or cooling unit the physical quantity *exergy* is of particular importance. Loosely speaking exergy quantifies the *technical working ability* of a substance. Electrical energy is pure exergy, whereas thermal energy consists also of a fraction energy which is technically not useful. Rather than asking for the technical working ability in heating and cooling applications the question is how much exergy is required for heating or cooling.

The Carnot-factor provides a metric to determine the required exergy demand during a heat transfer process from one reservoir to another. For simplicity lets assume one reservoir being at ambient temperature  $\vartheta_{oa}$ . Eq. (D.7) provides the implicit definition for the Carnot factor, compare with Glueck (1999).

$$\dot{E}_{12} = \underbrace{\frac{T_m - T_{oa}}{T_m}}_{\text{Carnot-factor, } \eta_c} \dot{Q}_{12} \qquad \dot{E}_{12} = 1 - \frac{T_{oa}}{T_m} \dot{Q}_{12} \qquad (D.7)$$

For heating and cooling applications  $T_m$  may be replaced by the average supply- and return-water temperature.  $\dot{E}_{12}$  expresses the theoretically required minimum amount of exergy which is required to supply e.g. the heating energy amount given by  $\dot{Q}_{12}$  at temperature  $T_m$  by means of a heat pump which uses the ambient air as energy reservoir. The eq. (D.7) shows, that the smaller  $T$ , the smaller the Carnot factor and thus the smaller the required exergy demand. The differences for various supply water temperatures are quite significant: Assume an ambient temperature of 10 °C and

## Appendix D. The Project MPC-Boxes

$T_m = 40\text{ }^\circ\text{C}$ , than  $\eta_c = 0.096$  by contrast for  $T_m = 25\text{ }^\circ\text{C}$   $\eta_c = 0.05$ . That means, a reduction of the average heating temperature (in this case by 15 K) reduces the required exergy demand by nearly 50 %, which directly corresponds to a significant reduction of the electricity demand, although the supplied heating energy stays the same.

Standard cooling applications with high air flow rates operate at minimum temperatures of  $\approx 6\text{ }^\circ\text{C}$  and the resulting return temperatures are  $\approx 12\text{ }^\circ\text{C}$ , this results in an average temperature of  $9\text{ }^\circ\text{C}$ . The Carnot factor in this case for a constant ambient temperature of  $30\text{ }^\circ\text{C}$  becomes -0.074. The average temperatures of TABS during cooling operation are approximately  $18\text{ }^\circ\text{C}$  which results in a Carnot factor of -0.041. This means a reduction of the electricity demand for cooling by 45 % compared to the standard air flow cooling application.

These short calculations demonstrate the strengths of TABS for heating and cooling applications with respect to the (exergy) electricity demand, which is only one aim in any optimization in heating and cooling applications. Another advantage of TABS which is linked to this moderate heating and cooling temperatures concerns the thermal comfort. Low heating-, and high cooling temperatures are more comfortable than high heating- and low- cooling temperatures.

Concerning the aspect of storage capacity: based on a simple calculation in 0.3 m thick concrete theoretically  $630\text{ Wh/m}^2$  can be stored through TABS assuming  $\Delta T=3\text{ K}$ , however, practically only 60 % of this value  $378\text{ Wh/m}^2$  are feasible. For more details on TABS and the related advantages and disadvantages, heating and cooling powers etc. Glueck (1999) is highly recommended (e.g. page 16).

### D.3.5. TRNSYS-model interior – air-node

The density of air is assumed as  $\rho_{air} = 1.2\text{ kg/m}^3$ . This together with the thermal heat capacity of air  $c_{p,air} = 1.0\text{ kJ/kgK}$  leads to the thermal heat capacity of the room or the thermal zone of the building. The total air-node heat capacity may be increased to incorporate the heat capacity of e.g. furniture (typical values are table 70 kJ/K cupboard 150 kJ/K).

The virtual sky temperature  $T_{sky}(\varepsilon_0, C_C)$  in K, which models the long-wave radiation exchange between the building's envelope and the atmosphere, is obtained as a function of the emittance of the clear sky ( $\varepsilon_0$ ) and the cloud cover ( $C_C$ ) according to M. Martin and Berdahl, 1984:

$$T_{sky} = T_{oa} (\varepsilon_0 + 0.8 (1 - \varepsilon_0) C_C)^{0.25}. \quad (\text{D.8})$$

Formulas for  $\varepsilon_0$  and  $C_C$  are provided in the appendix. If neglecting the losses against the sky the according values for the heating and the cooling demand change to 59 kWh/(m<sup>2</sup>a) and 19 kWh/(m<sup>2</sup>a).

## D.4. Mechanical ventilation and related disturbance variables

The weather data used for simulation, but also measurement and forecast data (within the project MPC-Boxes) include the ambient temperature ( $\vartheta_{oa}$ ), solar radiation on the horizontal and the relative humidity. Incorporation of a mechanical ventilation system and all related heat fluxes into the framework of a building model, entails the inclusion of the change of enthalpy – finally, only the sensible heat part will be facilitated within the MPC framework. This requires the saturation pressure of air, not available in the weather (forecast) data. However, Buck (1981) has found an empirical correlation between the saturation vapor pressure  $p_s$  and the temperature of moist air.

The saturation pressure of water in *hPa* (mbar) as a function of the air temperature in °C taken from Buck (2012) reads

$$p_s = 6.1121 \exp \left( \left( 18.678 - \frac{\vartheta}{234.5} \right) \frac{\vartheta}{257.14 + \vartheta} \right). \quad (\text{D.9})$$

Based on eq. (D.9) the calculation of enthalpy change is straight forward by means of the provided data, a few basic equations and a simple balance under the assumption of ideal mixing.

The mass mixing ratio ( $x$ ) for moist air, relating the mass of water vapor to the mass of dry air may be calculated from

$$x = 0.622 \frac{RH \cdot p_s}{p_s - RH \cdot p_s}. \quad (\text{D.10})$$

The specific enthalpy of moist air, with respect to the mass of dry air ( $h_{1+x}$ )<sup>12</sup>, as a function of the air temperature and the mass mixing ratio is given as

$$h_{1+x} = c_{p,air} \cdot \vartheta + x (r_0 + c_{p,vap} \cdot \vartheta), \quad (\text{D.11})$$

where temperature values must be provided in °C, since the enthalpy of dry air and vapor is defined zero for  $\vartheta = 0$  °C. The first term gives the internal energy of dry air and the second and the third term account for the vaporization and the internal energy of the vapor.

Based on the equations (D.9), (D.10) and (D.11), and given a certain ventilation mass flow rate  $\dot{m}_{air}$  the enthalpy change of a thermal zone (a room) may be calculated. This calculation assumes ideal mixing, which means that the same amount of supplied (heated) ambient air ( $\dot{m}_{air,in}$ ) is forced out at room conditions ( $\dot{m}_{air,out}$ ). Finally, the following parameters are facilitated for the calculation:

$$\begin{array}{lll} \rho_{air} = 1.204 \text{ kg/m}^3 & c_{p,air} = 1.006 \text{ kJ/(kgK)} & c_{p,vap} = 1.86 \text{ kJ/(kgK)} \\ r_0 = 2502.6 \text{ kJ/kg} & p_{oa} = 1000 \text{ mbar} & p_{ra} = 1000 \text{ mbar}. \end{array}$$

<sup>12</sup>Since  $m_{air,moist} = m_{air} + m_{vap} = m_{air}(1 + x)$  and  $h_{1+x} = H/m_{air}$  the specific enthalpy with respect to the moist air is simply calculated through dividing  $h_{1+x}$  by  $(1 + x)$ .

## Appendix D. The Project MPC-Boxes

Equation (D.11) applied once for outside (ventilation) air and once for inside (room) air and establishing a balance (*incoming – outgoing*) the following three components are obtained. These specific values  $\Delta h$ , each indicating the enthalpy change for the exchange of 1 kg of air, are finally summed up and multiplied with the according mass flow rate of air to obtain the net enthalpy flux. When relying on the given physical parameters from above, and  $\dot{V}$  being in  $\text{m}^3/\text{h}$  to obtain  $\dot{H}$  in Watt eq. (D.12) must be divided by 3.6.

$$\Delta h_{\Delta\theta} = c_{p,air} (\vartheta_{oa} - \vartheta_{ra}) \quad \Delta h_{\Delta\theta x} = c_{p,vap} (\vartheta_{oa} x_{oa} - \vartheta_{ra} x_{ra}) \quad \Delta h_{\Delta x} = r_0 (x_{oa} - x_{ra})$$

$$\dot{H} = \dot{V} \rho_{air} (\Delta h_{\Delta\theta} + \Delta h_{\Delta\theta x} + \Delta h_{\Delta x}), \quad \Delta h_{\Delta x} \text{ is neglected for the SSM.} \quad (\text{D.12})$$

Fig. D.11 exemplifies the (negative) gains in  $\text{W}/\text{m}^2$  per each  $\text{m}^3$  of room air replaced by 1  $\text{m}^3$  of ambient air during one hour. The measurement data relate to the turn of the year (2014/2015). Clearly  $\Delta H_{\Delta\theta}$  has the biggest share on the total sum followed by  $\Delta H_{\Delta x}$ . The contribution from  $\Delta H_{\Delta\theta x}$  is very low. For example, an air exchange rate of  $20 \text{ m}^3/\text{h}$  for the box with  $A_{ta} = 13.44 \text{ m}^2$  leads to equivalent gains of approximately  $-20 \text{ W}/\text{m}^2$  or when given with respect to the whole box approximately  $-269 \text{ W}$ . This power is required to sustain the air room temperature at the original level ( $\approx 20 \text{ }^\circ\text{C}$ ).

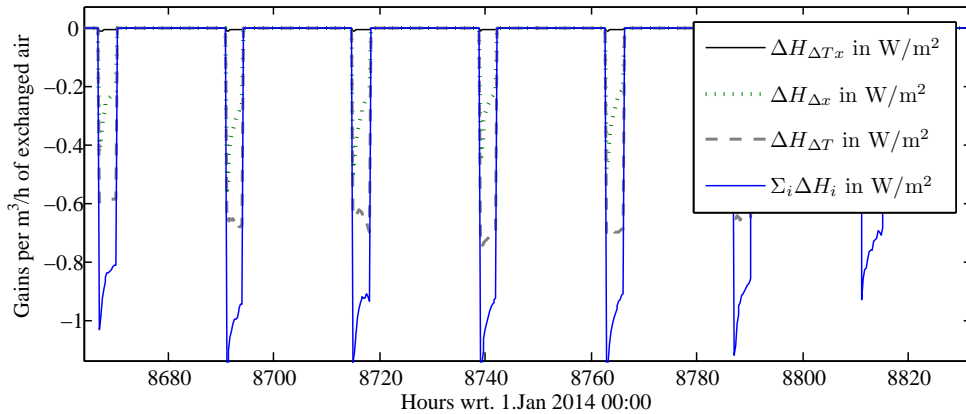


Figure D.11.: Exemplification of the (negative) gains per each  $\text{m}^3$  of exchanged room air with ambient air during one hour, for a winter week.

### Incorporation in the MPC-framework

Finally, the latent heat part of the enthalpy change ( $\Delta h_{\Delta x}$ ) will be neglected because only the sensitive heat is considered for the thermal building model within the MPC framework. This is common practice found in related literature. Accept for evaporation

of water drops from the ventilation air, or vapor condensation inside a room this approximation has no consequences on the model accuracy. However, it means that humidity is not available for comfort evaluation in terms of P. O. Fanger (1981).

For  $\dot{H}$  to be facilitated as a heat flux SSM-input (disturbance) all required variables must be either forecast data or deducible from model states. As demonstrated eq. (D.12) may be calculated from  $\vartheta_{ra}$ ,  $RH_{ra}$ ,  $\vartheta_{oa}$  and  $RH_{oa}$ . The last two values are available from forecast data,  $\vartheta_{ra}$  is a model state of the building model, but  $RH_{ra}$  is not part of the model. Hence an estimate is required for  $RH_{ra}$  and to make things simpler also  $\vartheta_{ra}$  is replaced by an estimated value – therefore these variables are starred in tab. 3.1. A reasonable assumption is to use the according set value for  $\vartheta_{ra}^*$  and an estimation for  $RH_{ra}^* = 50\%$  or a current value if available.

## D.5. Further details on comfort models

Concerning the cooling season [OENORM EN 15251:2007](#) distinguishes between mechanically chilled buildings and non-mechanically<sup>13</sup> chilled buildings. For mechanically chilled buildings the set-points and limits from [OENORM EN ISO 7730:2006](#) may directly be applied. For the other class of buildings adaptability theory is facilitated to justify rather relaxed limits during summer. In Appendix A.2 of this standard the upper and lower limit for summer is given according to eq. (D.13). Heating season values are relevant for  $\vartheta_{rm} < 10\text{ }^\circ\text{C}$  and the cooling season values are relevant for  $\vartheta_{rm} > 15\text{ }^\circ\text{C}$ , compare with Sourbron et al. (2013).

$$\begin{aligned}\vartheta_{max} &= 0.33 \vartheta_{rm} + 18.8 + (cat + 1), \quad \text{with } cat \in \{1, 2, 3\} \\ \vartheta_{min} &= 0.33 \vartheta_{rm} + 18.8 - (cat + 1).\end{aligned}\tag{D.13}$$

The classification A, B, C in [OENORM EN ISO 7730:2006](#) corresponds to categories (*cat*) 1, 2, 3 in [OENORM EN 15251:2007](#), hence *cat* = 2 must be selected. The resulting temperature limits as a function of the reference outdoor temperature, composed from the limits of a class B building for winter and eq. D.13 for summer are represented by fig. D.12.

The reference outdoor temperature according to [OENORM EN 15251:2007](#) is calculated as

$$\vartheta_{rm} = (1 - \alpha)\vartheta_{ed-1} + \alpha\vartheta_{rm-1},\tag{D.14}$$

with  $\vartheta_{rm}$  being the running mean temperature of the considered day,  $\vartheta_{ed-1}$  being the average ambient temperature of the day before and  $\vartheta_{rm-1}$  being the running mean temperature of the day before. The recommended value for the weighting factor  $\alpha$  is 0.8. The higher  $\alpha$  the more important are past values. Due to the recursive definition the

<sup>13</sup>Concerning the definition whether a building belongs to the mechanically chilled buildings or not, [OENORM EN 15251:2007](#), which is especially interesting for buildings with TABS for heating and cooling, gives a few explanations, some of which are vague.

## Appendix D. The Project MPC-Boxes

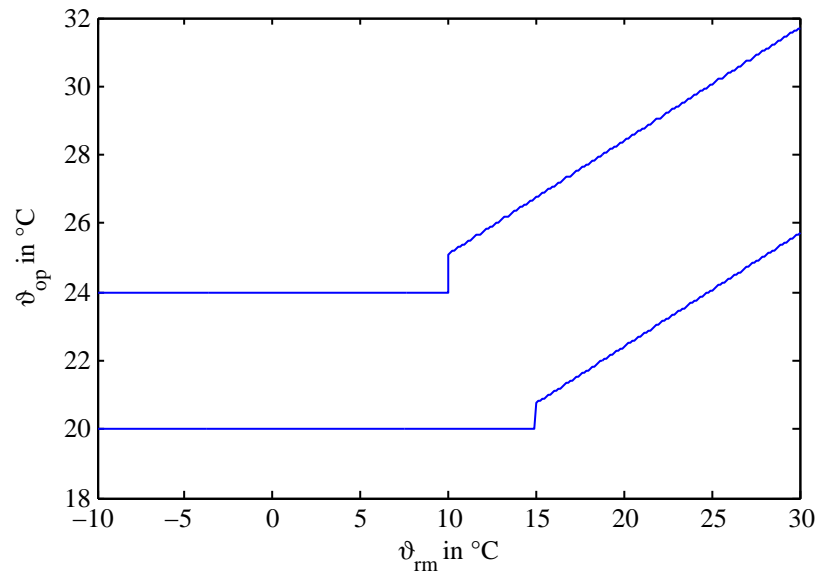


Figure D.12.: Operative temperature range as a function of the reference outdoor temperature for class B/category II buildings with adaptability-theory being applied for the summer limits, which remain constant above  $\vartheta_{rm} > 30$  °C .

first few days of an evaluation interval do not provide a running mean in the intended sense.

### Radiation asymmetry and other aspects

Comfort violation due to radiation temperature asymmetry is an important aspect with heating or cooling through TABS. The reason is, that an asymmetric heat flux between the human body and its surrounding may result in uncomfortable feelings. For the sake of completeness local discomfort due to draught and the increased heat sensitivity for high relative humidity are mentioned, but these aspects are not analyzed.

Radiation asymmetry is described on behalf of an example. Heat radiated away from the face against a wall and heat received at the back of the head from another wall stimulates the according thermal-receptors in one and the other direction. If this opposed stimulation gets to large it is perceived as local discomfort (Glueck, 1994). The limiting values to prevent this perception are maximum radiant temperature values (differences) with respect to two opposite surfaces. The human sensation in this matter has been investigated by P. Fanger et al. (1985) through experimental research and the results have been exploited in many standards.

Glueck (1994) analyzed these prominent results with respect to the experimental set up, the used extrapolation of measurements and concerning a few statistical indicators.

He resumes minor flaws and reworks different steps based on certain premisses. His recalculation of the limiting values incorporates not only the experimental results from Fanger but also from former research on this topic. The results are presented by the solid lines in fig. D.13 along with those of P. Fanger et al. (1985). Summing up, the analysis of Glueck allows higher radiation temperature asymmetry compared to P. Fanger et al. (1985). Especially for a heated ceiling the asymmetry according to Glueck may be approximately 4 K higher.

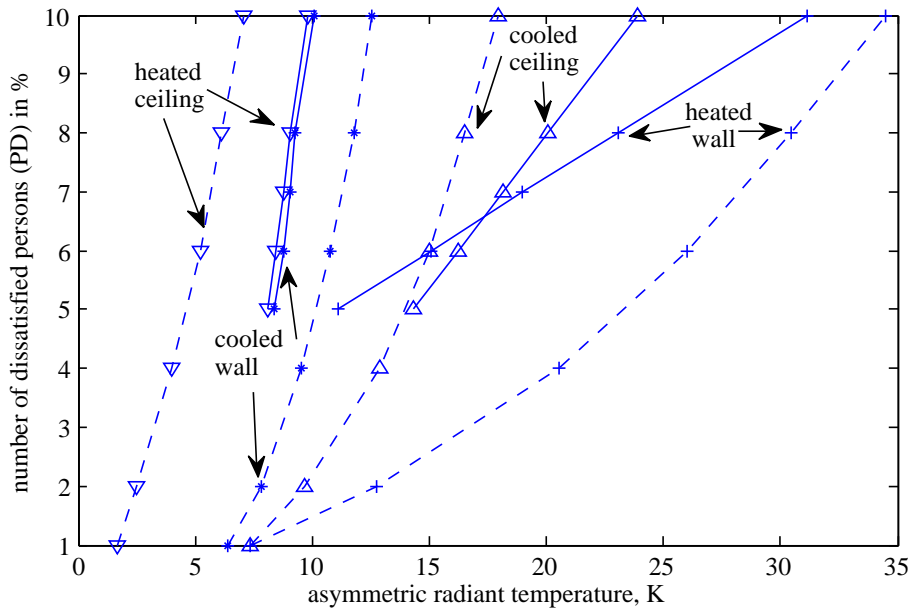


Figure D.13.: Illustration of the expected number of dissatisfied as a function of the asymmetric radiant temperature. Dashed lines (P. Fanger et al., 1985), solid lines (Glueck, 1994).



## Appendix E.

# Selected TRNSYS models and simulation details

### E.1. Building simulation

Bradley et al. (2004) separately apply ANSI/ASHRAE Standard 140-2001 to the simulation program TRNSYS, comparing both, their results and the individual interpretation of this standard. The authors main choice is given in terms of the diffuse sky model, convective heat transfer coefficients, ground coupling, simulation time step to mention but a few. Although there is a great assumption leeway within the standard the results do not diverge tremendously and one has confidence with respect to the results. In a follow-up work Bradley and Kummert (2004) agreed on a set of recommended practices and repeated the comparison of simulation results, which were much closer and fall well within the range of acceptable answers with respect to the standard. "Building simulation suit very well to answer *what if* questions in the context of building simulation." Malkawi and Augenbroe (2004), Ch. 2.

The heat conduction in TRNSYS is modeled using the transfer function mechanism (see Seem, 1987; Lechner, 1992) or the primary source Stephenson and Mitalas (1971). This mechanism requires the definition of a wall-timebase, representing the sampling time for discretization. In general, the wall-timebase should be chosen as small as possible. The smaller the timebase, the more coefficients are calculated. Limitations of this method and workarounds applied for TRNSYS are discussed in Delcroix et al. (2012).

#### E.1.1. Long-wave radiation exchange

Actually TRNSYS provides three modes for long-wave radiation exchange. The *simple* mode making use of a one node model with combined heat transfer coefficients, the *standard* mode or star network approach, and the *detailed* mode based on view factors. The standard and the detailed mode are briefly described in the following.

### Standard mode – star network approach

The star network approach has been developed by Seem (1987). The core of this approach is an *artificial* node (*temperature*) through which combined (convective and radiative) heat transfer between the walls is considered. The coupling between the inside of a thermal zone and the attributed air-node is solely described through convective heat transfer between the star node and the air node.

### Detailed mode – Gebhart method

The detailed mode for long-wave (LW) radiation exchange separates convective and radiative heat transfer. The walls of a thermal zone are assumed perfect opaque for LW radiation, isothermal and diffuse gray, that is emissivity and absorptivity are isotropic and wavelength independent. The LW radiation exchange between all surfaces of the thermal zone is based on the dimensionless Gebhart-factor. The Gebhart-factor mechanism describes radiative heat exchange between two surfaces which may be realized through any imaginable path between the two surfaces. That is, it is a property of geometry (view factor) and material (emissivity, reflectivity).

#### E.1.2. Short-wave radiation distribution

Short-wave (SW) radiation is divided into direct and diffuse radiation. For each fraction TRNSYS provides a *standard* and a *detailed* distribution mode.

##### Standard mode

In standard mode direct SW radiation entering a thermal zone may be distributed to the inside surfaces according to a value defining the fraction attributed to each surface respectively. The diffuse radiation is distributed between the surfaces according to a transmission-absorption weighted area factor for each surface. Transmission losses are only considered for windows.

##### Detailed mode

In detailed mode direct sunlight (SW) radiation entering a thermal zone is distributed depending on the geometric relation between the sun and the internal surface. The distribution of diffuse radiation is similar to the distribution of LW radiation in detailed mode.

### E.1.3. Convective heat transfer

Convective heat transfer coefficients are to be defined for each wall for the inside and the outside surface separately. The coefficients may be set to a constant value, or alternatively an internal calculation can be selected. The internal calculation relies on a constant coefficient  $\alpha_{c,0}$  which is scaled with a function of the form  $f(\Delta\vartheta) = |\Delta\vartheta|^{exp}$ , where  $\Delta\vartheta$  is the temperature difference between the surface and the surrounding air, and  $exp$  is a constant exponent. The constants  $\alpha_{c,0}$  and  $exp$  must be defined for vertical and horizontal surfaces, flow direction dependent, i.e. for heating and cooling, respectively. For more details on the used settings see sec. D.3.4, for additional material on heat transfer coefficients for TABS see OENORM (OENORM B 8110-6:2010) page 15, Keller (1997) page 29 ff and Glueck (1990) page 120 (3.43).

### E.1.4. Operative temperature

The operative or effective room temperature in TRNSYS is a measure for the comfort relevant temperature, and it is defined as:

$$\vartheta_{op} = \frac{\alpha_c \vartheta_{air} + \alpha_{rad} \vartheta_{rad}}{\alpha_c + \alpha_{rad}}, \quad (\text{E.1})$$

or, equivalently as:

$$\vartheta_{op} = a \vartheta_{air} + (1 - a) \vartheta_{rad} \quad \text{with} \quad a = \frac{\alpha_c}{\alpha_c + \alpha_{rad}}. \quad (\text{E.2})$$

A relative air velocity below 0.2 m/s and a difference wrt the mean radiant temperature below  $< 4$  °C allows for an approximation of the operative temperature by the mean of air- and radiative temperature (acc. to. EN ISO 7726:2001), see also Klein et al. (TRNSYS 17) p 5-207.

### E.1.5. Mean radiant temperature

The mean radiant temperature  $T_{rad}$  was originally introduced by P. O. Fanger (1981). It is the uniform temperature of an imaginary enclosure in which radiant heat transfer from the human body equals the radiant heat transfer in the actual non-uniform enclosure. (see Grondzik, 2009, Chapter 9)

Neglecting reflection,  $T_{rad}$  with respect to a person – in relation to the  $n$  surface temperatures of an enclosure – is calculated according to

$$T_{rad}^4 = T_1^4 F_1 + T_2^4 F_2 + \dots + T_n^4 F_n \quad (\text{E.3})$$

where  $T_i$  is the mean surface temperature in K and  $F_i$  is the angular factor between the person and the surface  $i$ . This equation may be approximated by replacing the power of "4" with "1" for similar surface temperatures  $T_i$ .

The *standard comfort model* in TRNSYS approximates  $T_{rad}$  by the area weighted mean surface temperature of all the surfaces of a thermal zone:

$$T_{rad} = \frac{T_1 A_1 + T_2 A_2 + \dots + T_n A_n}{A_1 + A_2 + \dots + A_n}. \quad (\text{E.4})$$

The *detailed comfort model* in TRNSYS calculates  $T_{rad}$  by means of a model for a globe thermometer, which represents a sensor to measure  $T_{rad}$ . The surface temperature of the sphere of the globe thermometer is calculated using convective heat transfer coefficients for forced or free convection, an emissivity  $\epsilon = 0.82$  of the sphere (standard value of the human body) and the dimensionless Gebhart-factor. This factor describes the interaction of two surfaces incorporating emissivity, reflectivity and the according view factor between two surfaces. *A typical physical assumption is that a surface's spectral emissivity and absorptivity do not depend on wavelength, so that the emissivity is a constant. This is known as the "gray body assumption".* (TRNSYS 17)

### E.2. U value error in TRNSYS – 'Cold-bridge correction'

The building model (Type 56) in TRNSYS does not consider a thickness for any material layer of a wall, ceiling, or floor. This causes an error where one such element connects to another. The error may be negligible for large surfaces, however, it is investigated and correction factors are derived for the MPC-box simulation by means of FEM simulations.

Walls, ceilings and floors – generally termed as *walls* in TRNSYS – are modeled by means of transfer functions. A wall may be built up of several layers, each of which contributes to this transfer function. However, the thickness of a layer and finally the wall is not considered. This state, calculated with Type 56 in TRNSYS, is illustrated by Fig. E.1 showing a 3D object with dilated faces. The area of each face is drawn according to the size appearing inside of the object – these geometric data are normally parametrized in TRNSYS. The heat transfer calculation error results from disregarding the interconnection of the walls. An extended wall with adiabatic lateral surfaces, which are indicated by wiggly lines in Fig. E.1, represents the construction calculated by TRNSYS. Hence, the lateral heat flux, existing in reality at the joints of two or more walls, is neglected.

One option to compensate for this shortcoming is to enlarge the surface area, but this is associated with an extension of the inside-volume. Another possible compensation for the neglected lateral heat flux is to define additional cold-bridges or to increase the heat transfer characterizing quantities by a certain factor. This factor may be estimated through detailed FEM simulations for a stationary case.

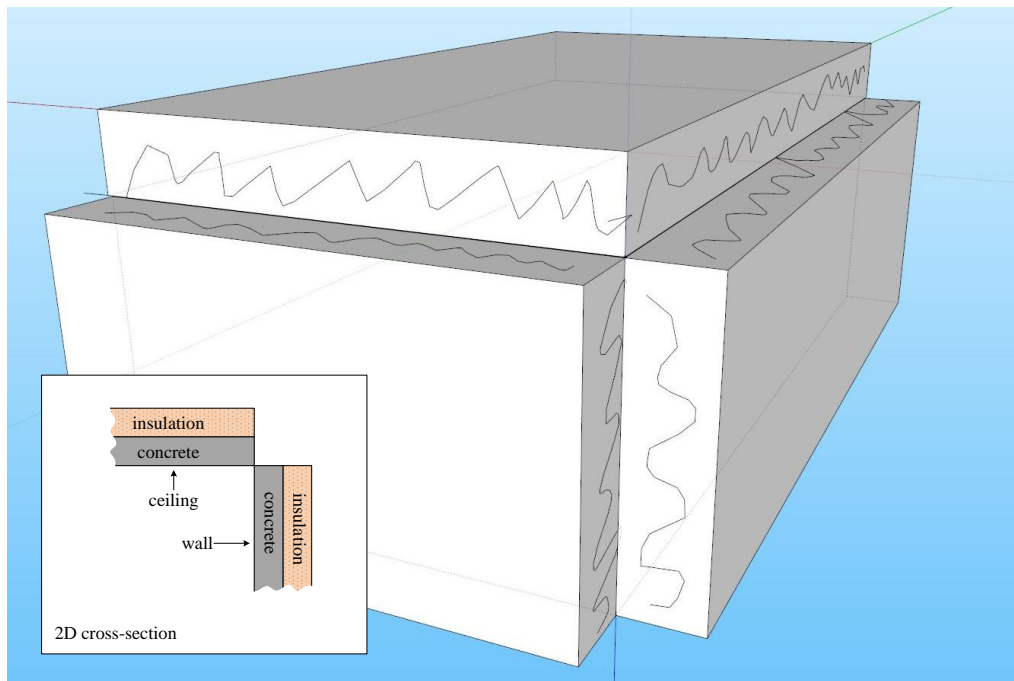


Figure E.1.: Illustration of the error-origin due to the assumption of layers with no thickness.

### E.2.1. FEM-simulations for the TRNSYS layer construction

The simplification calculated by TRNSYS Type 56, using the transfer-function method (see e.g. Clark, 2001) neglects the region where walls join each other. In the current situation it is assumed that the inside geometry must stay the same. This leaves the option to alter the heat transfer properties in TRNSYS<sup>1</sup>. To estimate the required correction the TRNSYS layer construction and the real construction are compared against each other with respect to the stationary heat flux for certain boundary conditions (BC).

Solving the stationary heat equation for the 2D cross section with suitable BC, using finite element method (FEM), allows for an emulation of the calculations in TRNSYS Type 56. The simulated construction consists of two elements joining at an angle of 90°. Each element is built up of two layers, an inner layer (0.2 m concrete or Ytong) and an outer insulation layer (0.2 m or 0.1 m EPS). A depth of 1 m is assumed for the L-shaped cross section, that is, the inner surface area is one m<sup>2</sup>. Fig. E.2 shows the geometry and the resulting temperature profile for the given boundary conditions for two concrete+EPS walls.

Fig. E.3 shows the results for a concret+EPS wall joining a Ytong+EPS wall. The lower thermal conductivity of Ytong in comparison to concrete is clearly visible. In

<sup>1</sup> Defining a coldbridge is not possible in detailed radiation mode in connection with preserving Google SketchUp compatibility.

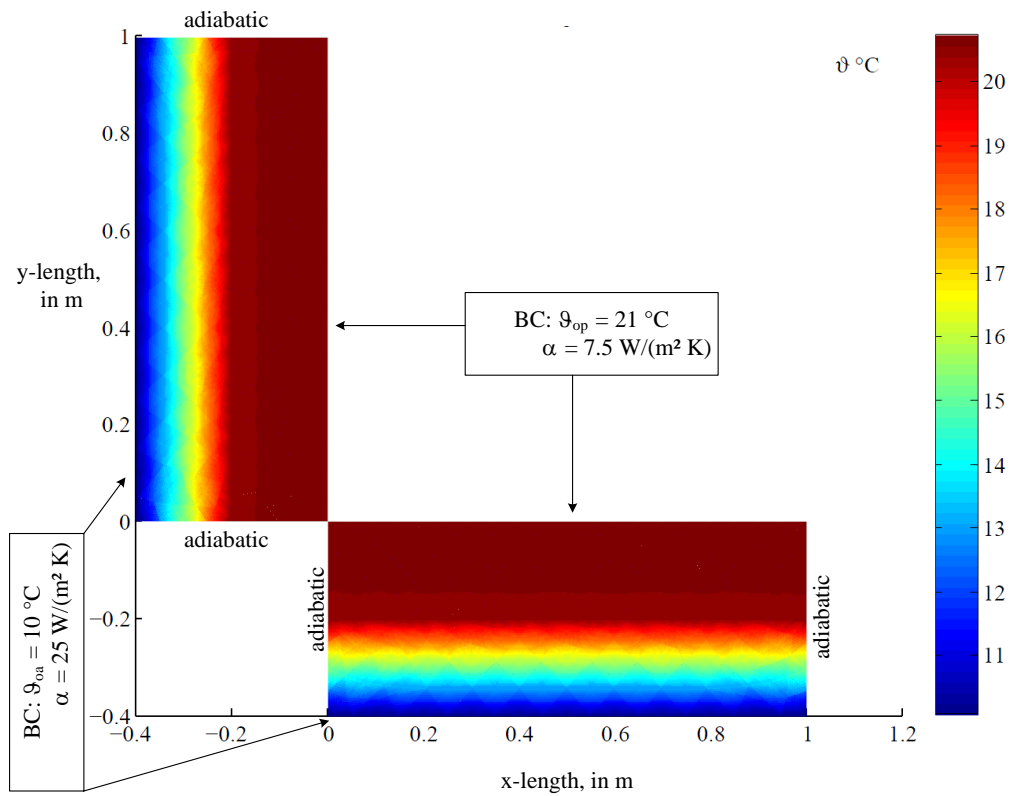


Figure E.2.: Temperature profile of joining concrete+EPS TRNSYS-like walls – simulated with FEM. The heat flux with respect to inside is  $2.04 \text{ W}/\text{m}^2$  for each wall.

the concrete wall the temperature is nearly homogeneous in the concrete layer and reduces within the isolation, but for the Ytong wall a clear temperature gradient is visible already in the Ytong layer. This justifies also the decision to reduce the isolation layer to  $0.1 \text{ m}$ . The heat flux for the two different joints is entirely homogeneous either in x- or in y-direction.

Results for the obtained specific heat transfer ( $\dot{q}$ ) are listed in tab. E.1. The table summarizes the TRNSYS-like results for three different joints in the first two columns. The rows refer to the considered wall, that is  $\dot{q}$  for a concrete wall joining<sup>2</sup> a Ytong wall is  $2.04 \text{ W}/\text{m}^2$  and  $\dot{q}$  for a Ytong wall joining a concrete wall is  $2.44 \text{ W}/\text{m}^2$ . To judge on the discussed TRNSYS error additional FEM simulations for the real construction are required.

<sup>2</sup> Due to the simplified joint the joining the result is independent of the joining wall material.

## E.2. U value error in TRNSYS – 'Cold-bridge correction'

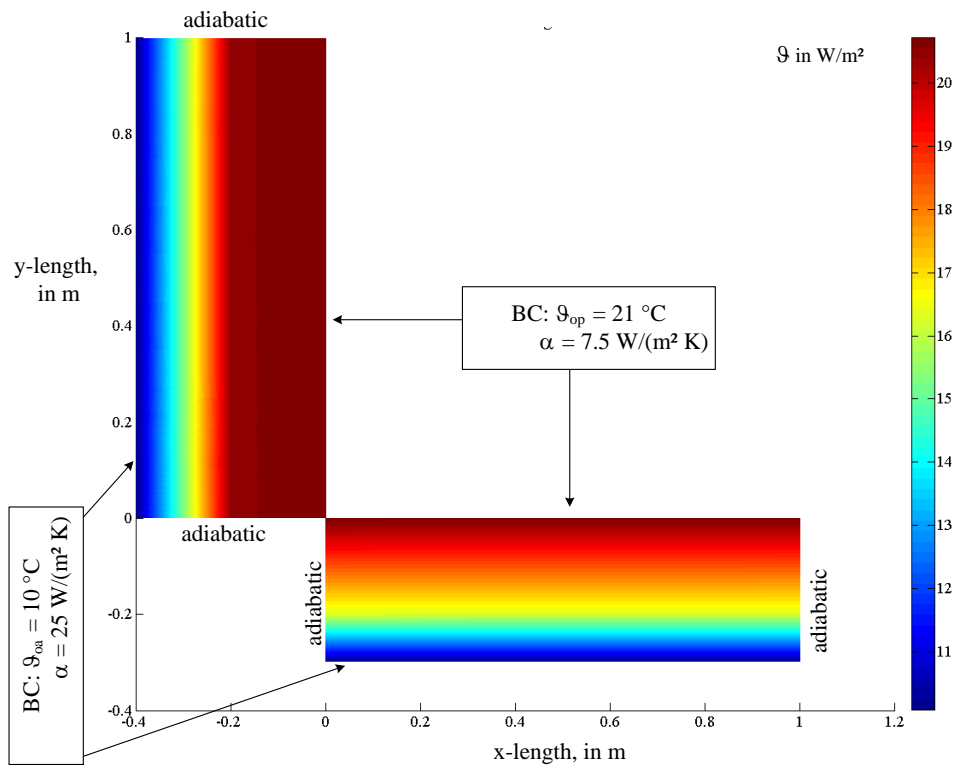


Figure E.3.: Temperature profile of a concrete+EPS TRNSYS-like wall joining a Ytong+EPS TRNSYS-like wall – simulated with FEM. The heat flux with respect to inside is  $2.04 \text{ W/m}^2$  for the vertical (Concrete) section and  $2.44 \text{ W/m}^2$  for the horizontal (Ytong) section.

### E.2.2. FEM-simulations for a real construction

The FEM simulations are now repeated with the same inside-BCs as before, but this time the walls connect as in reality, adding additional outer surface for heat transfer. Fig. E.4 depicts the temperature profile of a real cross-section.

Fig. E.5 illustrates the absolute value for the specific heat flux, showing a clear maximum in the corner. The average values for each wall are  $2.49 \text{ W/m}^2$  – see Tab. E.1. The heat flux and the temperature profile for a concrete Ytong joint are not as symmetric as for a concrete concrete one. Fig. E.6 shows the real temperature profile for a concrete+EPS wall joining a Ytong+EPS wall and Fig. E.7 provides the according heat flux. The average values are  $3.26 \text{ W/m}^2$  for the concrete wall and  $2.38 \text{ W/m}^2$  for the Ytong wall – see Tab. E.1.

## Appendix E. Selected TRNSYS models and simulation details

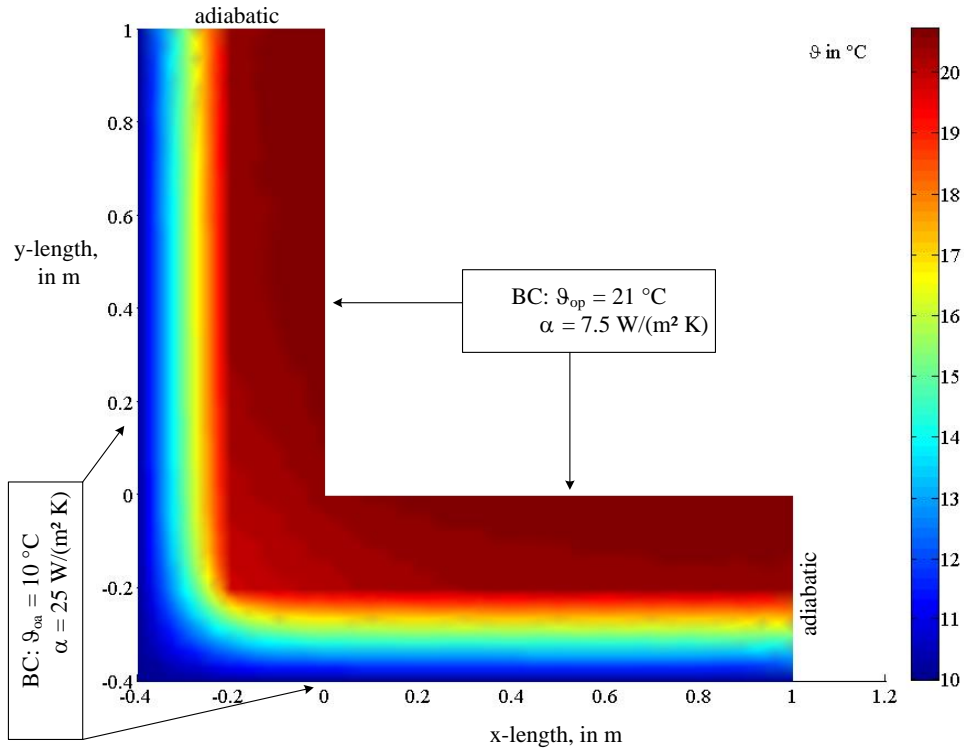


Figure E.4.: Real temperature profile of two joining concrete+EPS walls – simulated with FEM.

### E.2.3. Increased heat flux near an edge

FEM simulations conducted for the TRNSYS-like and the reality-like construction of the walls are now used to derive correction factors to compensate for the shortcoming of the transfer function method in TRNSYS concerning heat transfer along the edges of a building construction.

Let us assume a TRNSYS-like wall patch with vertical cross-section and constant boundary conditions in terms of operative and ambient temperature ( $\vartheta_{op}$ ,  $\vartheta_{oa}$ ) and concerning the heat transfer cf. fig. E.2. The U value of this wall patch is given by

$$U = \frac{1}{1/\alpha_i + d_1/\lambda_1 + d_2/\lambda_2 + 1/\alpha_{oa}}. \quad (\text{E.5})$$

This U-value allows for calculation of the total heat flux e.g. in x-direction through a wall with surface area A according to

$$\dot{Q} = U A (\vartheta_{op} - \vartheta_{oa}). \quad (\text{E.6})$$

The inner surface area is the same for the TRNSYS-like and the reality-like FEM simulations, however, the outer surface area changes. Using the results for the inner specific heat flux values in x-direction, from sections E.2.1 and E.2.2, a ratio  $\dot{q}_{TRNSYS}/\dot{q}_{reality}$

## E.2. U value error in TRNSYS – 'Cold-bridge correction'

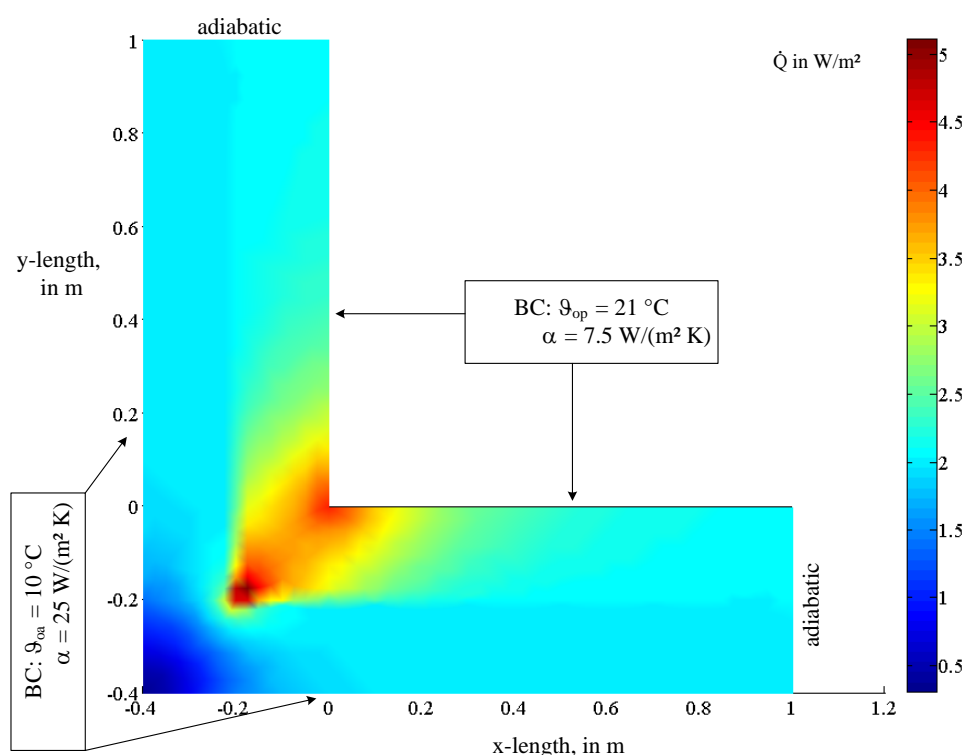


Figure E.5.: Real heat flux for joining concrete+EPS walls, cf. Fig. E.4 – simulated with FEM. The heat flux with respect to inside is  $2.49 \text{ W/m}^2$  for both sections.

may be calculated. This number is an estimate to account for the lateral heat transfer due to the overlap with the horizontal wall in reality. Given eq. (E.6) and the constant area it is possible to interpret this ratio as a scaling for the U-value or for a  $\lambda$ . The same procedure may be applied for the heat flux in y-direction.

Tab. E.1 summarizes the obtained heat flux results and the derived ratios. Each row stands for a certain wall construction and the effect of a joining wall is given in different columns. For example, the heat flux of a concrete+EPS wall increases by a factor of 1.6 from 2.04 to 3.26 if the connection to the joining Ytong+EPS wall is properly modeled.

Table E.1.: FEM results for the specific heat flux at two joining walls; Ratios indicate the required scaling of the heat flux to obtain close to reality results at the joints.

Wall ↓	$\dot{q}$ in $\text{W/m}^2$				$\dot{q}$ -Ratio	
	Construction		Reality-like		Reality-like/ TRNSYS-like	
joining →	TRNSYS-like Concr.	Ytong	Concr.	Ytong	Concr.	Ytong
Concr.	2.04	2.04	2.49	3.26	1.22	1.60
Ytong	2.44	-	2.38	-	0.98	-

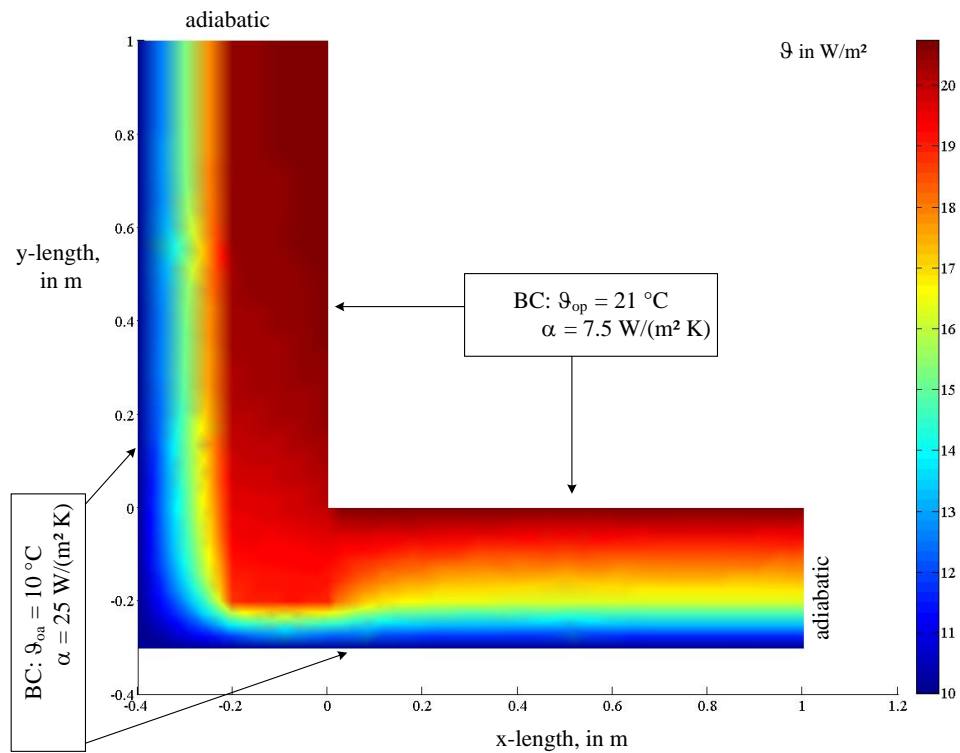


Figure E.6.: Real temperature profile of a concrete+EPS wall joining a Ytong+EPS wall – simulated with FEM.

#### E.2.4. Weighting scheme to obtain correction factors

Given the results of the last two columns in tab. E.1 – which are valid only near to an edge – the necessary correction factors for a whole wall may be derived applying an according weighting scheme. To this end the whole wall area is divided into patches. The area of the patches are lumped together depending on the category a patch belongs to.

For example, the ceiling is treated as a concrete+EPS wall, the joining east and west walls are also concrete+EPS walls but the northern wall is a Ytong+EPS wall. That is, the north-south edges belong to the category concrete+EPS-concrete+EPS (CoCo) and the northern east-west edge belongs to the category (CoYt), the southern east-west edge is also treated as (CoCo). The northern corners of the ceiling are divided half to belong to CoCo and half to belong to CoYt. Finally, the rest of the ceiling area is treated as a TRNSYS-like wall. Fig. E.8 illustrates this division into patches.

Multiplying the lumped area of a category with the according ratio and summing up these products leads to the intended U-value correction factor ( $f_{cor}^{UL}$ ), this procedure

## E.2. U value error in TRNSYS – 'Cold-bridge correction'

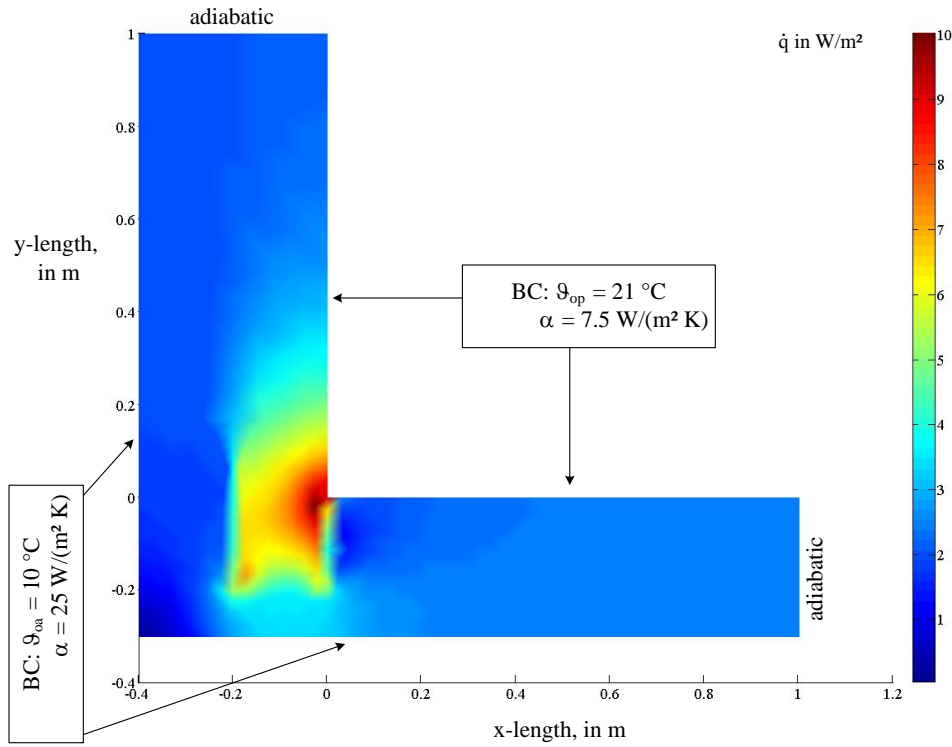


Figure E.7.: Real heat flux for a concrete+EPS wall joining a Ytong+EPS wall, cf. Fig. E.6 – simulated with FEM. The heat flux with respect to inside is 3.26 W/m<sup>2</sup> for the vertical (Concrete) section and 2.38 W/m<sup>2</sup> for the horizontal (Ytong) section.

is indicated by arrows in tab. E.2. The procedure is formalized by

$$f_{cor}^U = \frac{\sum_{i=1}^{i=4} \dot{q}\text{-Ratio}_i A_i}{\sum_{i=1}^{i=4} A_i}, \quad (\text{E.7})$$

with  $A_i$  indicating the area of the patches and  $\dot{q}\text{-Ratio}_i$  the relevant Ratio in tab. E.2, respectively. Here for  $A_i$  the outer areas were used.

To account for additional thermal mass at the joints, which is also neglected for the TRNSYS-like representation, an influence factor  $f_{cp}$  due to the massive material joining the wall is calculated – the isolation layer is neglected this time. The calculation is as follows

$$f_{cp} = 0.5 \left( \frac{A_{tot}^{outer}}{A_{tot}^{inner}} - 1 \right). \quad (\text{E.8})$$

The 0.5 in this equation indicates that the additional cp-value is split among the considered wall and the joining wall, however, this is only exact if the considered area has joining walls at all four sides and the cp values of the joining materials is similar. This geometry-dependent factor may now be used to scale the cp-value using the size

## Appendix E. Selected TRNSYS models and simulation details

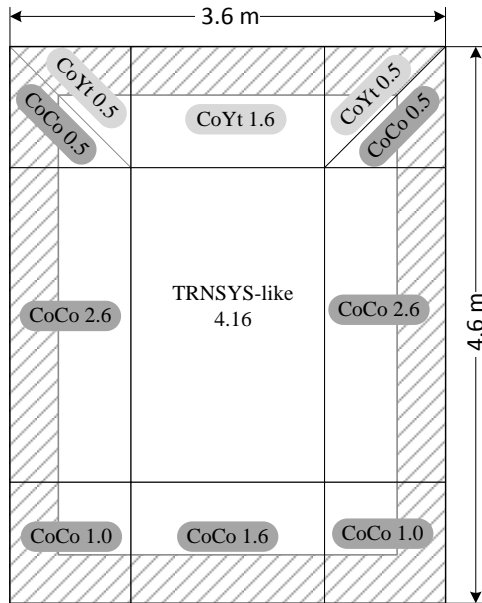


Figure E.8.: Division of the total "outer" ceiling surface into patches belonging to different categories depending on the material of the joining wall. The strip at the boundary has a width of 1 m.

and the material property of the joint.

$$cp_{cor} = cp + f_{cp} \frac{\sum_{i=1}^4 cp_i L_i}{\sum_{i=1}^4 L_i}, \quad (\text{E.9})$$

with  $cp_i$  being the heat capacity of the dominating joint material and  $L_i$  being the length of the considered edge. The results presented in tab. E.3 are relatively simple, the situation may be more difficult for walls with different thickness and a complex joint.

Table E.2.: Derivation of the correction factors for TRNSYS walls based on a division of each wall and weighting with the according  $\dot{q}$ -Ratio.

Surface	Area in m <sup>2</sup>		Area of patches in m <sup>2</sup>				$f_{cor}^U$
	$A_{tot}^{inner}$	$A_{tot}^{outer}$	$A_{CoCo}$	$A_{CoYt}$	$A_{YtCo}$	$A_{rest}$	
E,W-wall	9.66	11.5	8.70	1.50	0.00	1.3	→ 1.24
Ceil,floor	13.44	16.56	9.80	2.60	0.00	4.16	→ 1.22
N-wall	7.36	9.0	0.00	0.00	8.20	0.8	→ 0.98
$\dot{q}$ -Ratio			↑	↑	↑	↑	
			1.22	1.60	0.98	1.0	

### E.2.5. Facilitation of the correction factors

The corrected cp-value may be readily used as an input parameter for the simulation – in the simulation the cp-value of concrete is collectively increased by a factor of 1.14

Table E.3.: Calculation of the corrected cp values to account for addition thermal mass due to the joints of the walls.

Surface	Length of inner edges in m				$cp_{cor}$
	$L_{tot}$	$L_{CoCo}$	$L_{CoYt}$	$L_{YtCo}$	
E,W-wall	13.00	13.00	0	0	$cp_{Co} + 0.13 cp_{Co}$
Ceil,floor	14.80	14.80	0	0	$cp_{Co} + 0.14 cp_{Co}$
N-wall	11.00	0	0	11.00	$cp_{Yt}$

giving a cp of 1.23. The U-value correction factor  $f_{cor}^U$  must be interpreted in terms of the material properties from the denominator in (E.5). An objective for this procedure may be to preserve the thermal diffusivity  $a = \lambda / (\rho cp)$  of the original problem, in order to keep the dynamic behavior. The U value correction is implemented by means of a reduced isolation layer thickness. The corrected isolation layer thicknesses become 0.104 m for the N-wall, 0.16 m for the E- and the W-wall, 0.121 m for the ground floor and 0.2 m for the ceiling.

### E.3. Uncertainty

Modeling and simulation of buildings and thermal plants involves uncertainties from various sources, see e.g. Malkawi and Augenbroe, 2004. In general design *specifications* give room for a number of materials with different physical properties. The modeling itself requires assumptions and physical simplifications resulting in *modeling* uncertainties. The mathematical representation of a model on a computer entails truncation and round-off (discretization) errors which propagate over a simulation; their cumulative impact is termed *numerical* uncertainty. Finally, every simulation is characterized by initial and exogenous conditions – weather data, load profiles, disturbance – determining a scenario over the whole simulation time. Variations due to changes of these boundary conditions are named *scenario* uncertainties.

#### Assessment of uncertainty

The analysis of model parameters is an iterative process which initiates with a first screening process ranking the importance of the different parameters. This *importance* of a certain parameter gives the relative sensitivity of a model output. The relative sensitivity allows to establish a ranking indicating how crucial a parameter is. Following this crude first stage more elaborated techniques are applied to analyze the model uncertainty Malkawi and Augenbroe (2004). Results for robustness in building simulation for the OptiControl project analysis can be found in Oldewurtel, Gyalistras, et al. (2010).

## E.4. Climate data

Since 2001 the standard ÖNORM EN ISO 15927-4<sup>3</sup> provides a uniform European framework for climate data facilitated for thermal- and humidity-related calculations and simulations. Throughout this work, for the project MPC-Boxes the climate data Test Reference Year (TRY) Graz-TRY1990-2012 is used for thermal simulations. Within the project TheBat climate data for Innsbruck are used. The data are read with a specific weather data reader, which has various possibilities to process and extend the original weather data, based on physical relations.

### E.4.1. virtual sky temperature

The virtual sky temperature  $T_{sky}(\varepsilon_0, C_C)$  in K, which models the long-wave radiation exchange between the building's envelope and the atmosphere, is obtained as a function of the emittance of the clear sky ( $\varepsilon_0$ ) and the cloud cover ( $C_C$ ) according to M. Martin and Berdahl (1984):

$$T_{sky} = T_{oa} (\varepsilon_0 + 0.8 (1 - \varepsilon_0) C_C)^{0.25}. \quad (\text{E.10})$$

Formulas for  $\varepsilon_0$  and  $C_C$  are provided in the following. If neglecting the losses against the sky the heating demand for the MPC-Box decreases by 8.5 % and the cooling demand increases by 19 %, cf. Appendix D.1.

### E.4.2. Effective sky temperature

The cloud cover  $C_C$  can be calculated according to Kasten and Czeplak (1980) as a function of the diffuse ( $I_{diffuse}$ ) and the global irradiance ( $I_{global}$ ) on the horizontal

$$C_C = \sqrt{\left(1.4286 \frac{I_{diffuse}}{I_{global}} - 0.3\right)}. \quad (\text{E.11})$$

The emittance  $\varepsilon_0$  of the clear sky can be calculated according to M. Martin and Berdahl (1984) from the dew point temperature  $\vartheta_{sat}$  at given ambient pressure  $p_{amb}$  and temperature  $\vartheta_{oa}$

$$\begin{aligned} \varepsilon_0 = & 0.711 + 0.005 \vartheta_{sat} + 7.3 \cdot 10^{-5} \vartheta_{sat}^2 \\ & + 0.013 \cos\left(2\pi \frac{t}{24}\right) + 12 \cdot 10^{-5} (p_{amb} - p_0). \end{aligned} \quad (\text{E.12})$$

Time  $t$  in this equation is the time of the day in hours,  $p_{amb}$  may be obtained from the barometric height formula and  $p_0$  is the reference pressure at sea level.

<sup>3</sup> Wärme- und feuchtetechnisches Verhalten von Gebäuden - Berechnung und Darstellung von Klimadaten - Teil 4: Daten zur Abschätzung des Jahresenergiebedarfs für Kühl- und Heizsysteme

## E.5. TRNSYS results interpretation

TRNSYS uses the general convention that any results of variables exchanged between types are averaged over the simulation time-step, e.g. an output or recorded value  $\dot{Q}_k$  represents the average from the converged results at instant  $k$  and  $k - 1$ , i.e.  $\dot{Q}_k = (\dot{Q}_{k-1}^{converged} + \dot{Q}_k^{converged})/2$ . This means that annual results obtained with a time-step of 1 h comprise 8760 meaningful values.

## E.6. Further details on the TRNSYS simulation

The start time must be a natural multiple of the wall-time-base. This prevents from very strange initializations of the AL elements. The simulation report of TRNSYS states that the simulation did not converge in 32 time steps. This is a very good number. Depending on the complexity of the simulation for annual simulations up convergence issues up to 1.5 % of the total simulation time may be acceptable.



## **Appendix F.**

### **Blower door test – complete measurement protocols**

The following pages provide the complete measurement protocols for both Test-Boxes. Each measurement procedure consists of a pressurization- and depressurization-run.

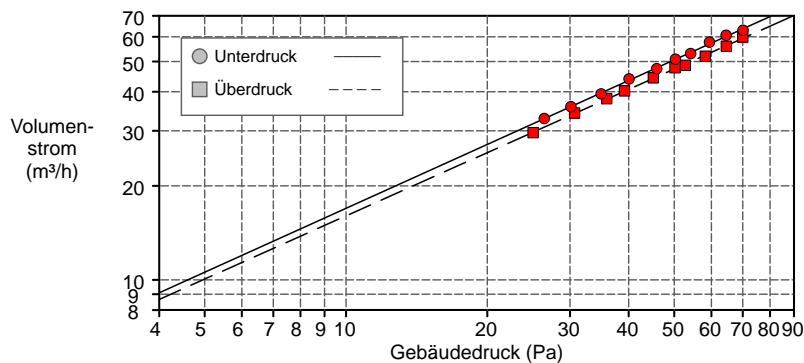
## Appendix F. Blower door test – complete measurement protocols

### BlowerDoor-Messung Seite 1

Techn. Universität Graz  
 Labor für Bauphysik  
 Inffeldgasse 24  
 - 8010 Graz  
 Tel.: 0316/873-1300  
 Fax: 0316/873-1320

Datum: 10.11.2014 Prüfer/in: Mosing  
 Dateiname: B14-215-075001-430  
 Name: IWT Gebäudestandort: +S02  
 Pichler Inffeldgasse  
 Tel.:  
 Fax:

	<u>Unterdruck</u>	<u>Überdruck</u>	<u>Mittelwerte</u>
<b>Messergebnisse bei 50 Pascal:</b>			
V50: Leckagestrom (m³/h)	51 (+/- 0.3 %)	47 (+/- 0.2 %)	49
n50: 1/h Luftwechselrate	1.64	1.53	1.58
w50: m³/(h*m² Nettogrundfläche)	3.77	3.52	3.64
q50:			
<b>Leckagefläche:</b>			
Canadian EqLA @ 10 Pa (cm²)	18.9 (+/- 1.8 %)	17.9 (+/- 1.4 %)	18.4
LBL ELA @ 4 Pa (cm²)	9.8 (+/- 2.8 %)	9.3 (+/- 2.2 %)	9.6
<b>Leckageparameter:</b>			
Strömungskoeffizient (Cenv)	3.5 (+/- 4.4 %)	3.4 (+/- 3.4 %)	
Leckagekoeffizient (CL)	3.5 (+/- 4.4 %)	3.4 (+/- 3.4 %)	
Leckageexponent (n)	0.680 (+/- 0.011)	0.673 (+/- 0.009)	
Korrelations-Koeffizient	0.99894	0.99932	
Messnorm:	EN 13829	Anforderungen nach:	
Verfahren:	B		
Gerät:	Modell 4 (230V) Minneapolis Blower Door		
Innen-Temperatur:	17 °C	Volumen:	31 m³
Außen-Temperatur:	11 °C	Gebäudehüllfläche:	
Barometrischer Druck:	101325 Pa	Gebäudegrundflächen:	13 m²
Windstärke nach Beaufort:	0 Still	Unsicherheit	
Windschutzklasse:	Sehr exponiertes Gebäude	der Bezugsgrößen:	%
Art der Heizungsanlage:		Baujahr:	2014
Art der Klimaanlage:			
Art der Lüftungsanlage:	Keine		



## BlowerDoor-Messung Seite 2

Datum: 10.11.2014 Dateiname: B14-215-075001-430

### Bemerkungen

#### Messungen: Unterdruck:

Gemessener Gebäude Druck (Pa)	Gebläse Druck (Pa)	Gemessener Volumenstrom (m³/h)	Temperatur korrigierter Volumenstrom (m³/h)	% Fehler	Blende
-0.3	n/a				
-70.5	26.5	64	63	-1.1	Blende D
-64.9	24.6	62	61	0.8	Blende D
-59.8	22.2	59	58	1.3	Blende D
-54.6	18.8	54	53	-0.9	Blende D
-50.7	17.3	52	51	0.1	Blende D
-46.3	88.4	48	47	-0.7	Blende E
-40.5	76.4	45	44	1.0	Blende E
-35.3	61.6	40	39	-0.8	Blende E
-30.5	51.3	36	36	-0.1	Blende E
-26.8	43.4	33	33	0.0	Blende E
-0.5	n/a				

Messung 1 Natürliche Druckdifferenz (Pa): p01- = -0.3 p01+ = 0.0 p02- = -0.5 p02+ = 0.0

#### Messungen: Überdruck:

Gemessener Gebäude Druck (Pa)	Gebläse Druck (Pa)	Gemessener Volumenstrom (m³/h)	Temperatur korrigierter Volumenstrom (m³/h)	% Fehler	Blende
-0.1	n/a				
69.9	132.3	59	60	0.9	Blende E
64.5	115.9	55	56	-0.5	Blende E
58.2	100.5	52	52	-1.0	Blende E
52.7	88.3	48	49	-1.1	Blende E
50.1	85.4	47	48	0.6	Blende E
45.1	73.9	44	44	0.2	Blende E
39.1	61.3	40	40	0.1	Blende E
35.9	54.8	38	38	0.1	Blende E
30.6	44.8	34	34	0.3	Blende E
25.0	33.8	29	30	-0.6	Blende E
-0.0	n/a				

Messung 1 Natürliche Druckdifferenz (Pa): p01- = -0.2 p01+ = 0.1 p02- = -0.1 p02+ = 0.2

## Appendix F. Blower door test – complete measurement protocols

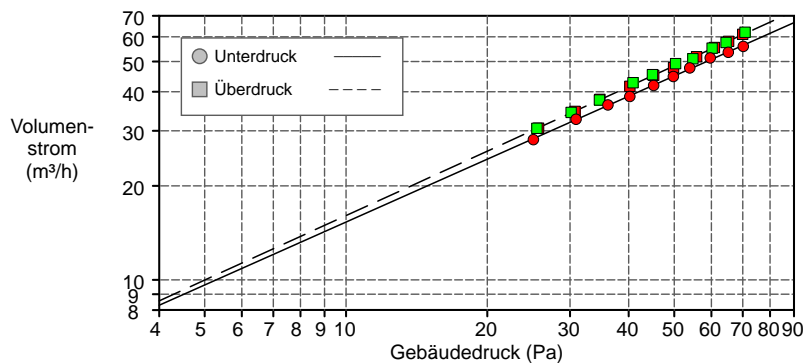
### BlowerDoor-Messung Seite 1

Techn. Universität Graz  
 Labor für Bauphysik  
 Inffeldgasse 24  
 - 8010 Graz  
 Tel.: 0316/873-1300  
 Fax: 0316/873-1320

Datum: 10.11.2014 Prüfer/in: Mosing  
 Dateiname: B14-215-075002-430  
 Name: IWT Gebäudestandort: +S03  
 Pichler Inffeldgasse  
 Tel.:  
 Fax:

	<u>Unterdruck</u>	<u>Überdruck</u>	<u>Mittelwerte</u>
<b>Messergebnisse bei 50 Pascal:</b>			
V50: Leckagestrom (m³/h)	45 ( +/- 0.3 %)	48 ( +/- 0.2 %)	47
n50: 1/h Luftwechselrate	1.45	1.57	1.51
w50: m³/(h*m² Nettogrundfläche)	3.34	3.60	3.47
q50:			
<b>Leckagefläche:</b>			
Canadian EqLA @ 10 Pa (cm²)	17.1 ( +/- 1.6 %)	17.9 ( +/- 0.9 %)	17.5
LBL ELA @ 4 Pa (cm²)	8.9 ( +/- 2.5 %)	9.2 ( +/- 1.4 %)	9.1
<b>Leckageparameter:</b>			
Strömungskoeffizient (Cenv)	3.3 ( +/- 3.8 %)	3.3 ( +/- 2.2 %)	
Leckagekoeffizient (CL)	3.3 ( +/- 3.8 %)	3.3 ( +/- 2.2 %)	
Leckageexponent (n)	0.669 ( +/- 0.010 )	0.686 ( +/- 0.006 )	
Korrelations-Koeffizient	0.99916	0.99941	
Messnorm:	EN 13829	Anforderungen nach:	
Verfahren:			
Gerät:	Modell 4 (230V) Minneapolis Blower Door		

Innen-Temperatur:	19 °C	Volumen:	31 m³
Außen-Temperatur:	14 °C	Gebäudehüllfläche:	
Barometrischer Druck:	101325 Pa	Gebäudegrundflächen:	13 m²
Windstärke nach Beaufort:	0 Still	Unsicherheit	
Windschutzklasse:	Sehr exponiertes Gebäude	der Bezugsgrößen:	%
Art der Heizungsanlage:		Baujahr:	2014
Art der Klimaanlage:			
Art der Lüftungsanlage:	Keine		



## BlowerDoor-Messung Seite 2

Datum: 10.11.2014 Dateiname: B14-215-075002-430

### Bemerkungen

#### Messungen: Unterdruck:

Gemessener Gebäude Druck (Pa)	Gebläse Druck (Pa)	Gemessener Volumenstrom (m³/h)	Temperatur korrigierter Volumenstrom (m³/h)	% Fehler	Blende
0.1	n/a				
-70.2	20.7	57	56	-0.9	Blende D
-65.3	19.0	54	54	-0.3	Blende D
-59.7	17.5	52	51	1.5	Blende D
-54.0	88.7	48	48	0.8	Blende E
-49.9	78.4	45	45	-0.2	Blende E
-45.3	68.9	42	42	-0.3	Blende E
-40.3	58.9	39	39	-0.6	Blende E
-36.2	52.3	37	36	0.4	Blende E
-31.0	42.6	33	33	0.3	Blende E
-25.1	31.8	28	28	-0.8	Blende E
-0.2	n/a				

Messung 1 Natürliche Druckdifferenz (Pa): p01- = -0.1 p01+ = 0.1 p02- = -0.2 p02+ = 0.0

#### Messungen: Überdruck:

Gemessener Gebäude Druck (Pa)	Gebläse Druck (Pa)	Gemessener Volumenstrom (m³/h)	Temperatur korrigierter Volumenstrom (m³/h)	% Fehler	Blende
-0.2	n/a				
69.9	137.5	61	61	0.1	Blende E
65.3	124.4	58	58	-0.3	Blende E
60.9	114.0	55	55	-0.0	Blende E
55.8	99.9	51	52	-0.9	Blende E
49.8	85.6	47	48	-1.1	Blende E
45.2	76.7	45	45	-0.1	Blende E
40.2	65.5	41	42	-0.2	Blende E
34.7	54.3	37	38	0.2	Blende E
30.7	45.8	34	35	-0.3	Blende E
25.7	36.1	30	31	-0.4	Blende E
0.0	n/a				

Messung 1 Natürliche Druckdifferenz (Pa): p01- = -0.2 p01+ = 0.2 p02- = -0.1 p02+ = 0.1

-0.1	n/a				
70.7	141.5	61	62	0.8	Blende E
64.4	122.3	57	57	-0.4	Blende E
60.2	113.0	55	55	0.2	Blende E
54.8	97.1	51	51	-1.2	Blende E
50.3	90.6	49	49	1.0	Blende E
44.9	77.4	45	45	0.7	Blende E
40.8	68.9	42	43	1.3	Blende E
34.6	53.9	37	38	-0.2	Blende E
30.1	45.1	34	34	0.1	Blende E
25.5	36.0	30	31	-0.1	Blende E
0.0	n/a				

Messung 2 Natürliche Druckdifferenz (Pa): p01- = -0.1 p01+ = 0.0 p02- = -0.1 p02+ = 0.1



## Appendix G.

### System identification

#### G.1. Comments on the physical model from first principles

Instead of  $\vartheta_{oa}$  a fictive ambient temperature may be used for the model derived in sec. 3.1.1. This temperature is suggested as weighted average derived from the sky temperature and the ambient temperature.

$$\vartheta_{ia}^* = (1 - Fsky) \vartheta_{oa} + Fsky \vartheta_{sky}$$

where  $Fsky = 0.14 \pm 0.06$  for the MPC-Boxes geometry – this value is derived from simulation experiments. However, the improvement is not significant and relevant only for long horizons ( $\gg 72$  h) and hence practically not relevant in this context. Instead of this weighted approach, the virtual sky temperature could be included as an additional variable, as in sec. 3.1.4, but this means an extended SSM.

#### G.2. Multiple correlation coefficient

The fit measures in eq. (3.45) and eq. (3.46) may be readily defined based on intuition and a physical perspective. However, a very similar expression as eq. (3.45) with MAE replaced by the RMSE follows also from a detailed residual analysis.

Consider a model resulting from a LSE as given def. by eq. (3.19) and eq. (3.23). The regressors<sup>1</sup>  $\varphi$  in that cost function may be interpreted as the spanning set from which the estimation  $\hat{y}$  is constructed. The optimum estimate for  $\Theta$  in eq. (3.23) may be understood as tuning of the parameters  $\theta_1, \theta_2, \dots$  such that the distance (the error) between  $y$  and  $\hat{y} = \varphi^T(t)\Theta$  becomes a minimum. Assume only two regressors (a plane in 2D) from which  $\hat{y}$  must be constructed, that is  $\hat{y}$  must lie in this plane. Then the minimum distance from any point in the plane to a vector  $y$  outside the spanning set is found through orthogonal projection of  $y$  onto the plane. Hence, the error  $\varepsilon$  between  $y$  and  $\hat{y}$  is orthogonal to  $\hat{y}$ . In this case Pythagoras' theorem may be used  $y^2 = \hat{y}^2 + \varepsilon^2$ , and since it holds for any error, given a time series with  $N$  values one may write

<sup>1</sup> A regressor  $\varphi := [\mathbf{xu}]^T$ , compare eq. (3.32).

$$\begin{aligned} \sum_{t=1}^N y^2(t) &= \sum_{t=1}^N \hat{y}^2(t) + \sum_{t=1}^N \varepsilon^2(t) \\ \Leftrightarrow 1 &= \frac{\sum_{t=1}^N \hat{y}^2(t)}{\underbrace{\sum_{t=1}^N y^2(t)}_{=:R_y^2}} + \frac{\sum_{t=1}^N \varepsilon^2(t)}{\sum_{t=1}^N y^2(t)}. \end{aligned} \quad (\text{G.1})$$

The second term on the right hand side is ideally zero and the first term measures how well experimental data are reproduced by the model.  $R_y$  is known as the *multiple correlation coefficient*. For more details on this and on the geometric interpretation of the errors the author refers to Ljung (1999), App.II or Bishop (2006), sec.3.

Rewriting eq. (G.2) shows the mathematical origin of eq. (3.45) and eq. (3.46).

$$R_y^2 = 1 - \frac{\sum_{t=1}^N \varepsilon^2(t)}{\sum_{t=1}^N y^2(t)}. \quad (\text{G.2})$$

Testing a model with other data sets – one major reason why fit measures are defined – may change conditions, used during the derivation of a fit measure (orthogonality), which may lead to non-meaningful fit values. This fact highlights the difficulty of right interpretations of a fit result and it shows that certain information may be contained in one fit measure but not in another.

### G.3. Model parameter values – MPC-Boxes

Fig. G.1 and fig. G.2 graphically represent the parameter values and the standard deviations obtained from the parameter estimation procedure. Interestingly, the dynamic matrix elements estimated from simulation data are nearly the same for different id-data and the models differ mainly in the parametrization of the input matrix  $\mathbf{B}$ . For real experimental data also the dynamic matrix elements differ from one data set to another. Finally, the standard deviation of model parameters from real data is approximately an order of magnitude larger in comparison to the results from simulation data.

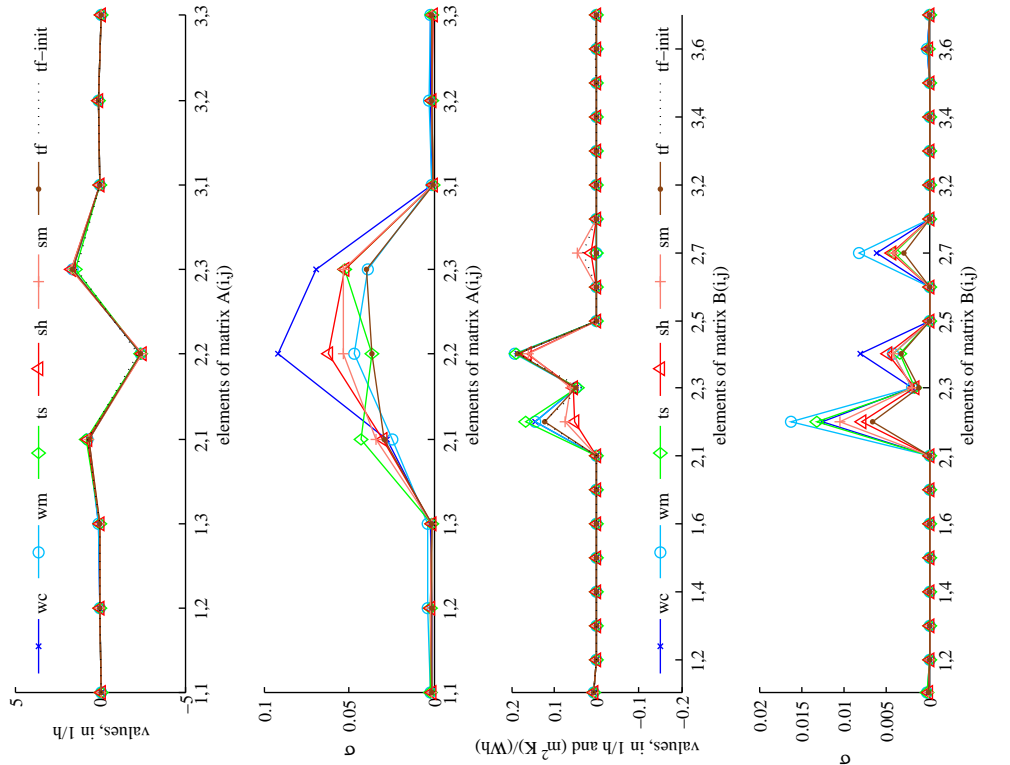


Figure G.1.: Parameter values and uncertainties for **A** and **B**, obtained with the method *ssst* and constraints according to 4.1; LSQ initial model – simulation data.

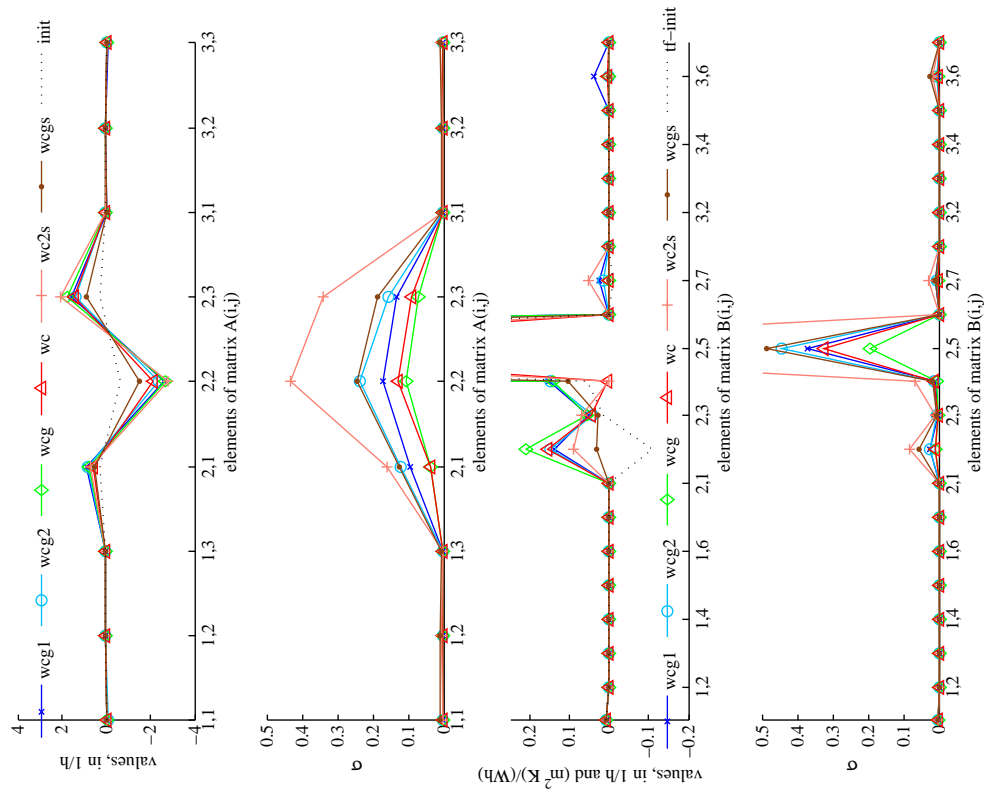


Figure G.2.: Similar to fig. G.1 but this time based on real measurement data.

## G.4. MPC-Boxes results based on simulation data

### G.4.1. Residual analysis – MPC-Boxes

Trajectories of the residuals for the best ( $\mathcal{M}_{tf}$ ) and the worst ( $\mathcal{M}_{wc}$ ) model according to fig. 4.1 are shown in fig. G.4 and fig. G.5. The first 72 h for  $\mathcal{M}_{wc}$  are also shown in fig. G.3, which puts the results from fig. 4.1 into perspective. For a complete and concise discussion on the building model in context of the project MPC-Boxes see Pichler, Goertler, et al. (2016).

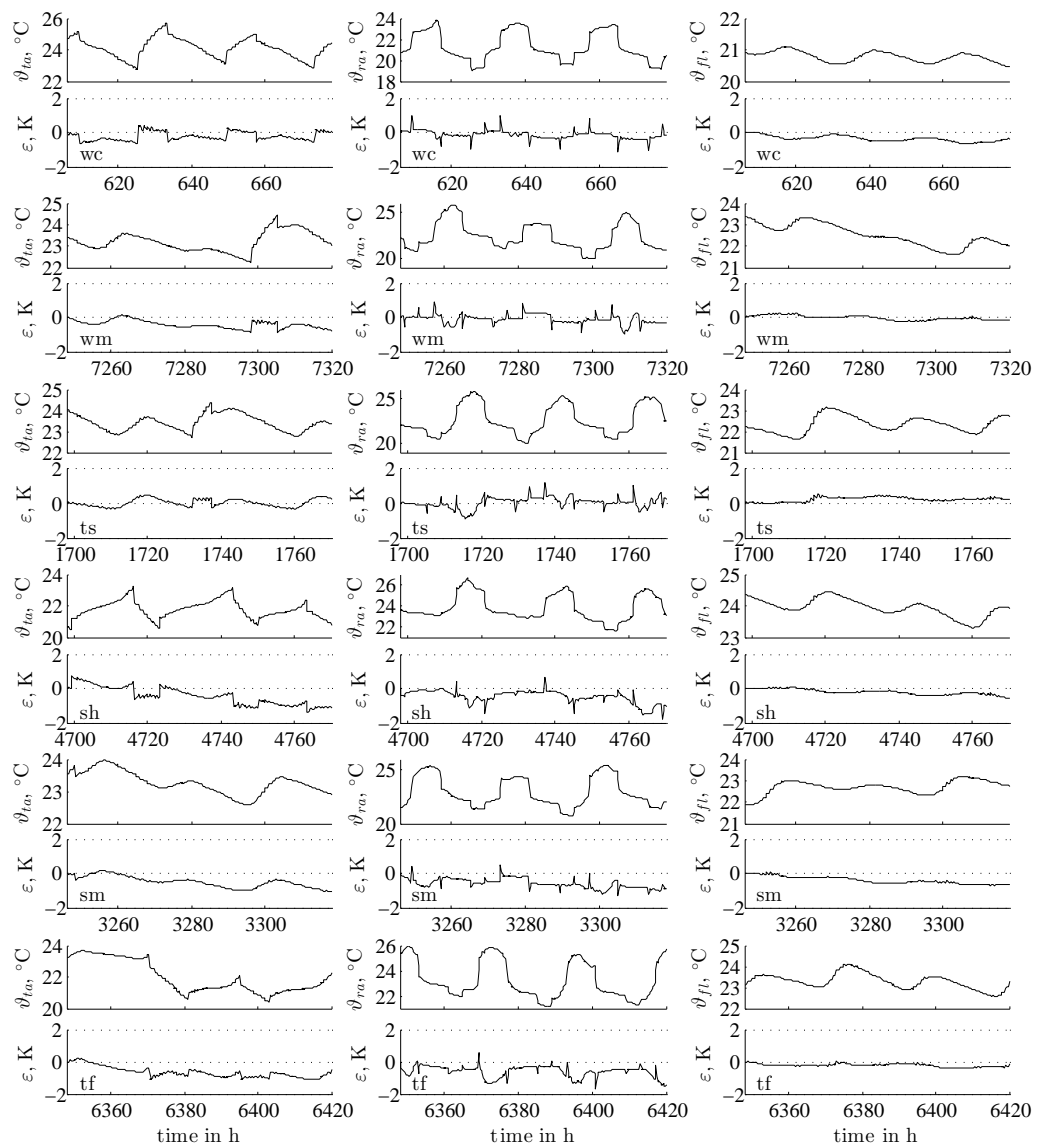


Figure G.3.: Same as fig. G.5 evaluation over 3 days only – MPC-Boxes.

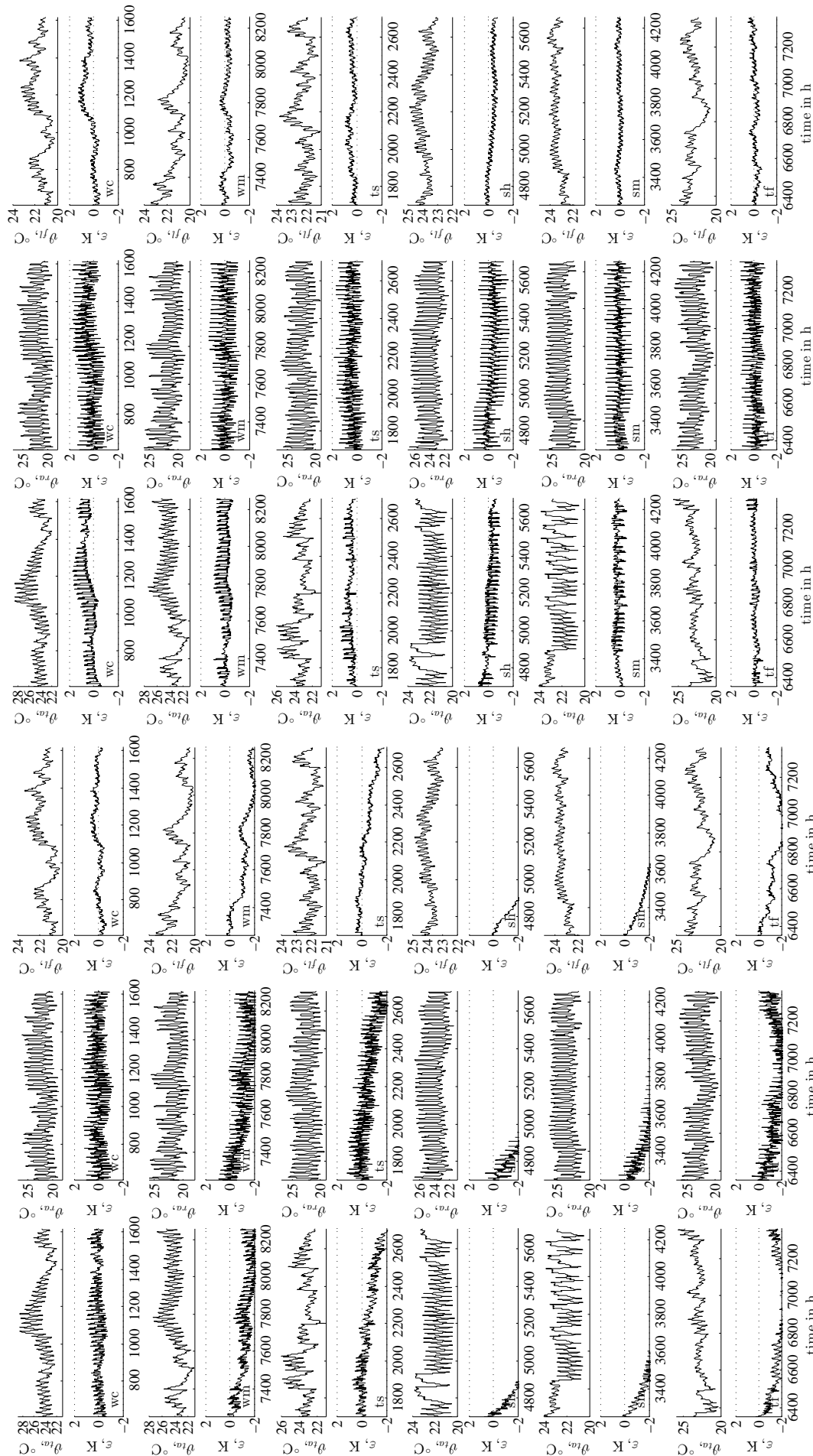


Figure G.4.: Reference trajectories and residual analysis for the model  $\mathcal{M}_{tf}$  validated against data  $wc$  (top),  $wm$ , ...,  $tf$ (bottom); horizon: six weeks – MPC-Boxes.

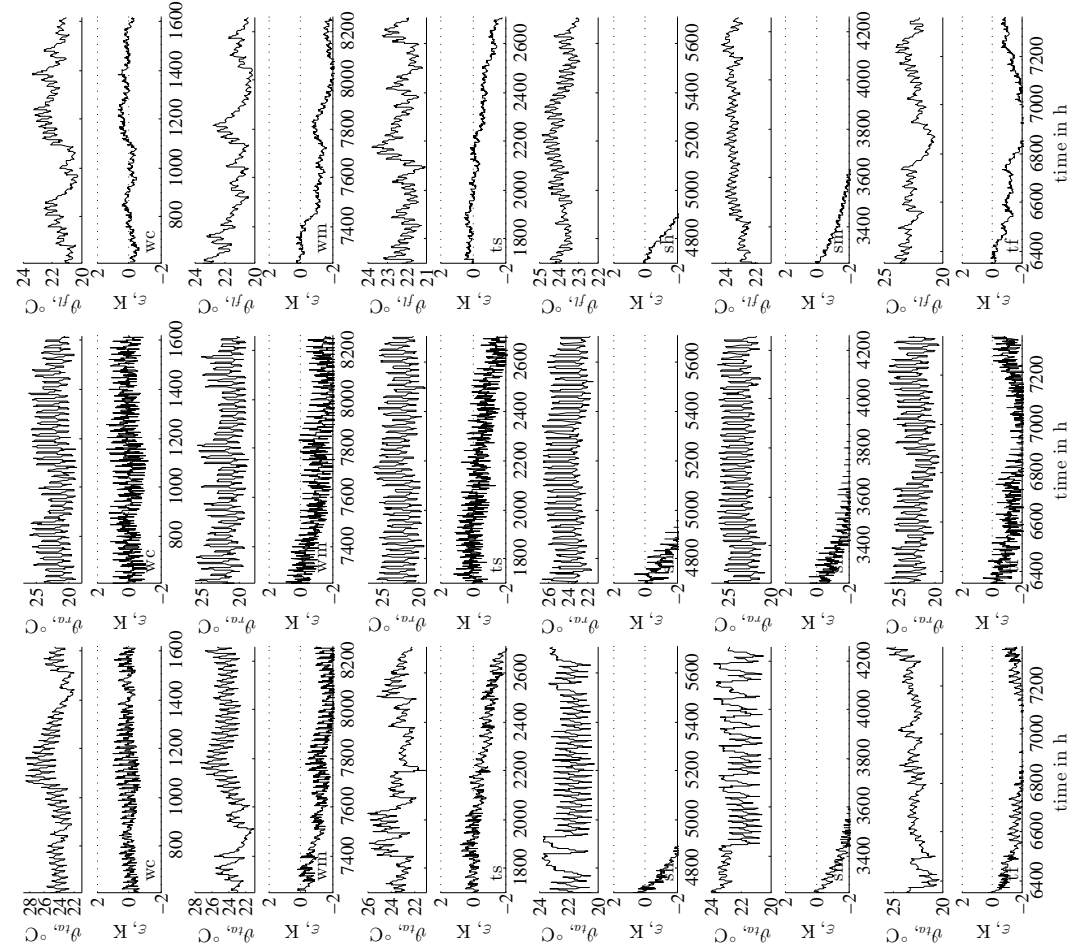


Figure G.5.: Same as fig. G.4 but for the model  $\mathcal{M}_{wc}$  – MPC-Boxes.

### G.4.2. III-structured SSM from simulation – MPC-Boxes

The following results refer to a really bad model structure<sup>2</sup>. Except for the output matrix ( $\mathbf{C} = \mathbf{1}$ ) all elements of  $\mathbf{A}$  and  $\mathbf{B}$  where *unconstrained* for the parameter estimation, compare eq. (G.3). For this structure it was tried to use the TABS-, the room air- and the mean inner (boundary) surface-temperature as model states and outputs ( $y(i) = [\vartheta_{ta}, \vartheta_{air}, \vartheta_{bs}]^T$ , with  $\vartheta_{bs} = 2\vartheta_{op} - \vartheta_{air}$ ), concerning  $u$  internal- and ventilation gains are neglected ( $\mathbf{u} := [\dot{Q}_{ta}, \vartheta_{oa}, \dot{I}_g, \vartheta_{grd}, \vartheta_{sky}]^T$ ).

$$\mathbf{A} = \begin{bmatrix} \mathbb{R} & \mathbb{R} & \mathbb{R} \\ \mathbb{R} & \mathbb{R} & \mathbb{R} \\ \mathbb{R} & \mathbb{R} & \mathbb{R} \end{bmatrix}, \quad \mathbf{B} = \begin{bmatrix} \mathbb{R} & \mathbb{R} & \mathbb{R} & \mathbb{R} & \mathbb{R} \\ \mathbb{R} & \mathbb{R} & \mathbb{R} & \mathbb{R} & \mathbb{R} \\ \mathbb{R} & \mathbb{R} & \mathbb{R} & \mathbb{R} & \mathbb{R} \end{bmatrix}, \quad \mathbf{C} = \begin{bmatrix} 1 & 0 & 0 \\ 0 & 1 & 0 \\ 0 & 0 & 1 \end{bmatrix}. \quad (\text{G.3})$$

Fig. G.6 shows the performance of the unfavorable model structure by means of a comparison of the model outputs against simulation data. Although the self-validation (top row plots) seems qualitatively good, the model fails completely when cross-validated.

An analysis of the residuals for the *self-validation* (see fig. G.7), indicates already a weakness of the structure. This can be seen from the distorted  $\vartheta_{bs}$ -residuals histogram, which should be bell shaped as for the other two ( $\vartheta_{ta}$  and  $\vartheta_{ra}$ ) histograms. Hence, the state  $\vartheta_{bs}$  can not be reproduced properly by the model structure.

Analyzing the residuals for *cross-validation* with  $D_{shr}$ , depicted in fig. G.8, one gets further insight about possible reasons why the structure fails. The scatter plots of all residuals over the input  $\vartheta_{grd}$  show a strong correlation between this input variable and the residuals. With increasing input variable, the residuum values increase. This indicates that the coupling of the input into the model structure must be changed.

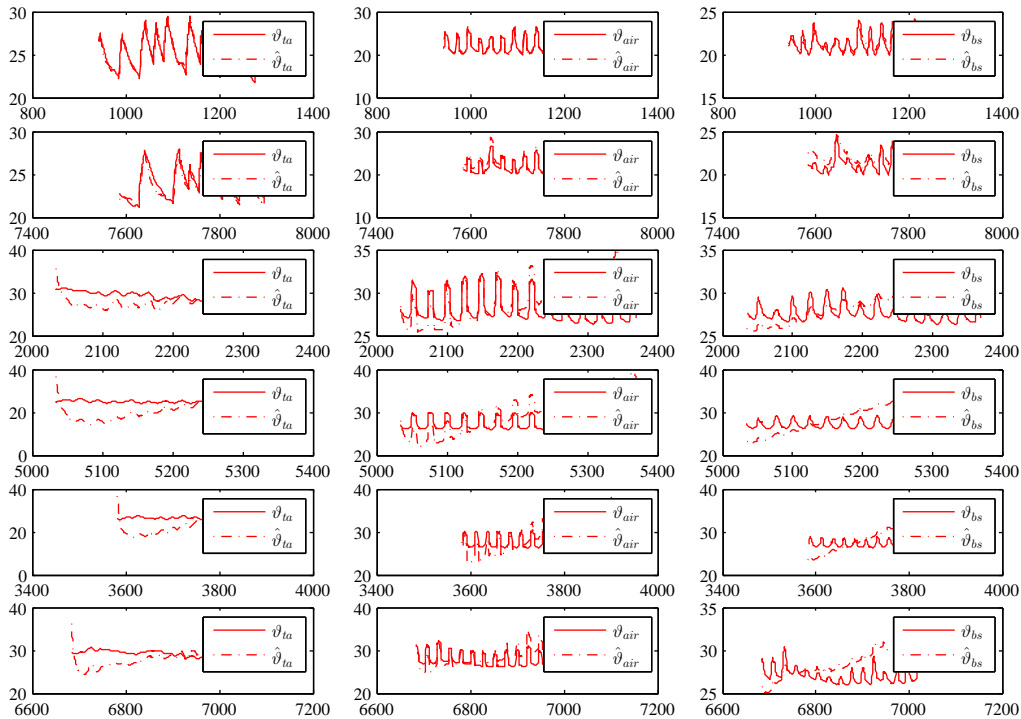


Figure G.6.: Temperature trajectories for a bad model structure. The first row plots show the self-validation against  $D_{wc}$ , rows two to six refer to cross-validation with  $D_{wm}$ ,  $D_{ts}$ ,  $D_{shr}$ ,  $D_{sm}$  and  $D_{tf}$ ; plot horizon: two weeks.

<sup>2</sup> This section shows early results where a different nomenclature was used; the following equivalents hold:  $\dot{Q}_{ta} \equiv \dot{q}_{ta}$ ,  $I_g \equiv \dot{q}_{gs}$ ,  $\vartheta_{air} \equiv \vartheta_{ra}$ .

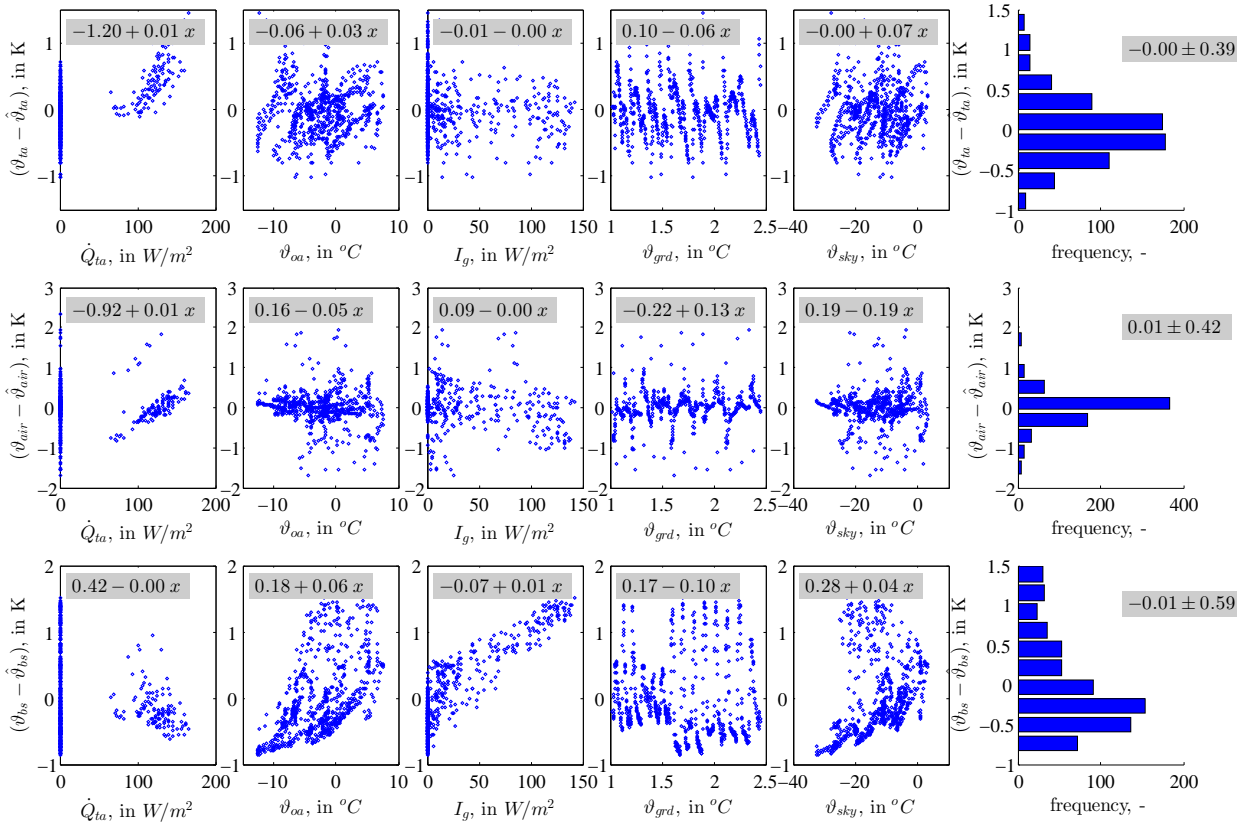


Figure G.7.: Residual scatter-plots for relevant input variables and histograms for the model outputs. Self-validation of unconstrained S-SSM with  $\mathcal{D}_{wc}$ , horizon: two weeks.

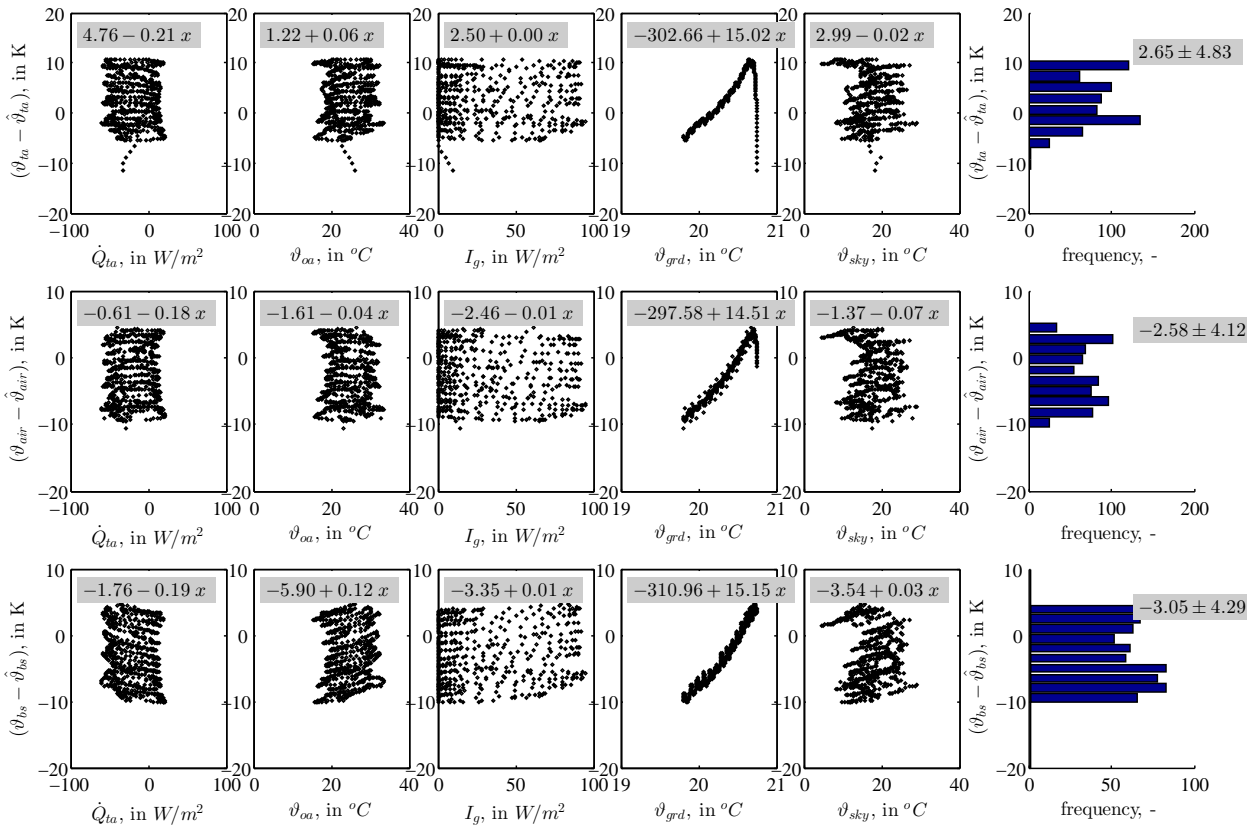


Figure G.8.: Residual scatter-plots for relevant input variables and histograms for the model outputs. Cross-validation of unconstrained S-SSM from id-datal against  $\mathcal{D}_{sh}$ , horizon: two weeks.

G.4.3. Unconstrained case – MPC-Boxes

For the unconstrained case the parameter values of the input matrix may take any value, indicated by  $\mathbb{R}$  in the following  $\mathbf{B}$  matrix<sup>3</sup>,  $\mathbf{A}$  and  $\mathbf{C}$  are given for the sake of completeness

$$\mathbf{A} = \begin{bmatrix} \mathbb{R} & \mathbb{R} & \mathbb{R} \\ \mathbb{R} & \mathbb{R} & \mathbb{R} \\ \mathbb{R} & \mathbb{R} & \mathbb{R} \end{bmatrix}, \quad \mathbf{B} = \begin{bmatrix} \mathbb{R} & \mathbb{R} & \mathbb{R} & \mathbb{R} & X & \mathbb{R} & \mathbb{R} \\ \mathbb{R} & \mathbb{R} & \mathbb{R} & \mathbb{R} & X & \mathbb{R} & \mathbb{R} \\ \mathbb{R} & \mathbb{R} & \mathbb{R} & \mathbb{R} & X & \mathbb{R} & \mathbb{R} \end{bmatrix}, \quad \mathbf{C} = \begin{bmatrix} 1 & 0 & 0 \\ 0 & 1 & 0 \\ 0 & 0 & 1 \end{bmatrix}. \quad (\text{G.4})$$

Figure G.9 represents the estimated parameter values for  $\mathbf{A}$  and  $\mathbf{B}$  for all six ( $\mathcal{D}_{wm}, \dots \mathcal{D}_{tf}$ ) identification data sets<sup>4</sup>. The two top graphs refer to matrix  $\mathbf{A}$ , where the first one provides the parameter values and the second one the uncertainty of the parameter. Similarly for the lower two graphs. What is special for these parameter values is the fact that a few  $\mathbf{B}$ -elements are negative, which is not physical. The model fits are quite good, compare fig. G.10. However, the obtained models are not necessarily physical and stability issues were also neglected so far.

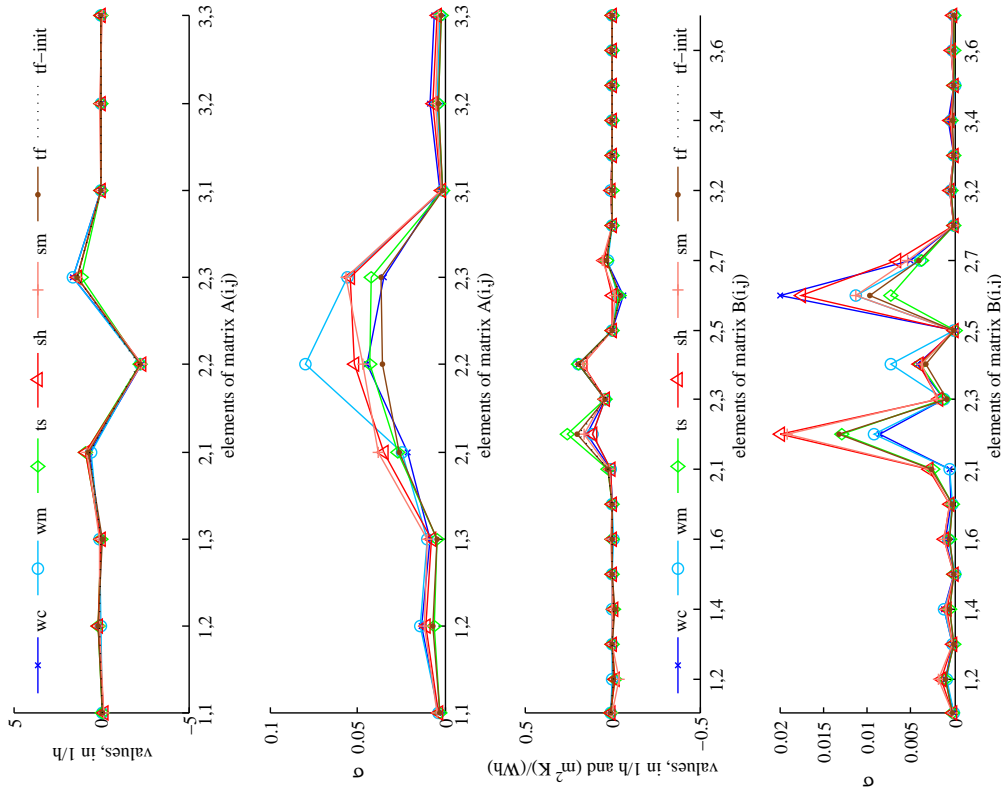


Figure G.9.: Estimated values and parameter uncertainties for  $\mathbf{A}$  and  $\mathbf{B}$ , unconstrained estimation for the S-SSM given in eq. (G.4); *ssest* results, MPC-Boxes.

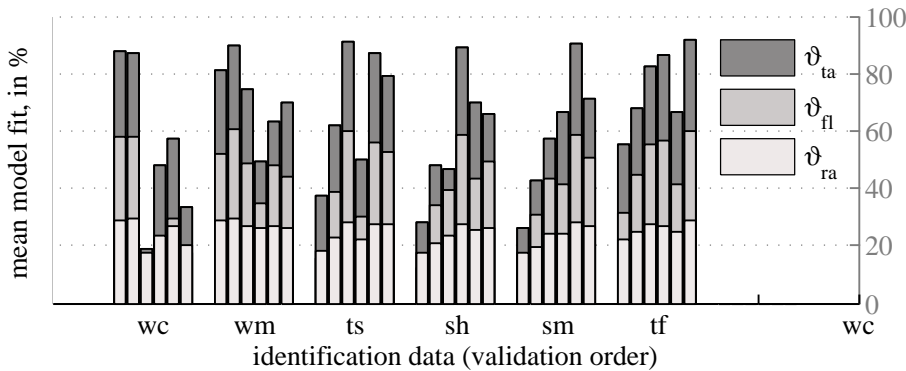


Figure G.10.: Average model fits obtained for the S-SSM given in eq. (G.4) identified with MPC-Boxes simulation data; *ssest* results.

<sup>3</sup> X means that a parameter value is not relevant since the input values are disregarded.

<sup>4</sup> In addition the "initial values" obtained from a LSQ fit, that is the ARX model for the data tf (tf-init) is given.

## G.4.4. Parameters from another season – MPC-Boxes

The model defined in eq. 4.1 with parameters obtained from a summer data set –  $\mathcal{M}(\Theta_{sh})$  – performs sufficiently for a short interval in winter as can be seen in fig. G.11. Something similar shows the model  $\mathcal{M}(\Theta_{wc})$  when tested with summer data, see fig. G.3.

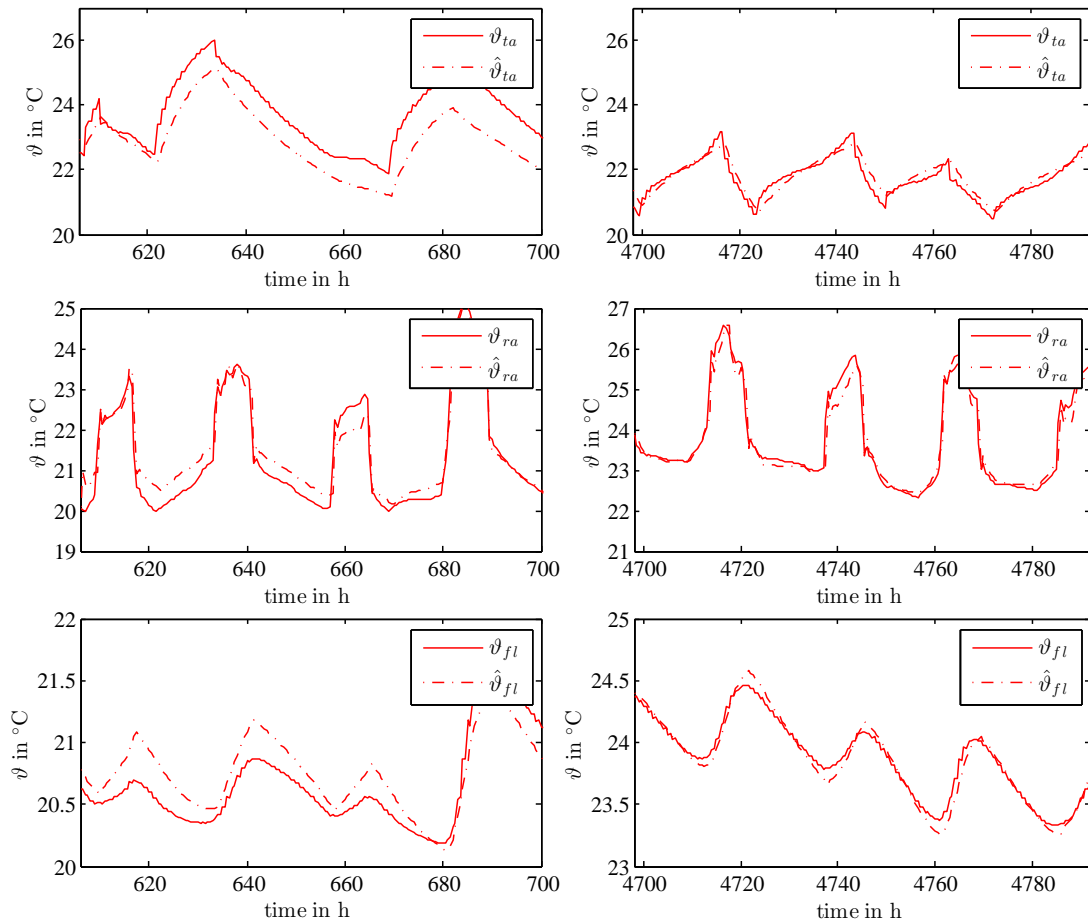


Figure G.11.: Temperature trajectories for  $\mathcal{M}(\Theta_{sh})$  when cross-validated with winter data (left hand side graphs) and self-validated with summer data (right hand side graphs).

G.4.5. Further results of sub-optimal model structures – MPC-Boxes

For the following results, the matrix  $\mathbf{A}$  and  $\mathbf{C}$  is according to eq. (4.1) and  $\mathbf{B}$  is altered.

$$\mathbf{B} = \begin{bmatrix} \mathbb{R} & 0 & 0 & 0 & X & 0 & 0 \\ 0 & \mathbb{R} & \mathbb{R} & \mathbb{R} & X & 0 & \mathbb{R} \\ 0 & 0 & 0 & 0 & X & \mathbb{R} & 0 \end{bmatrix}$$

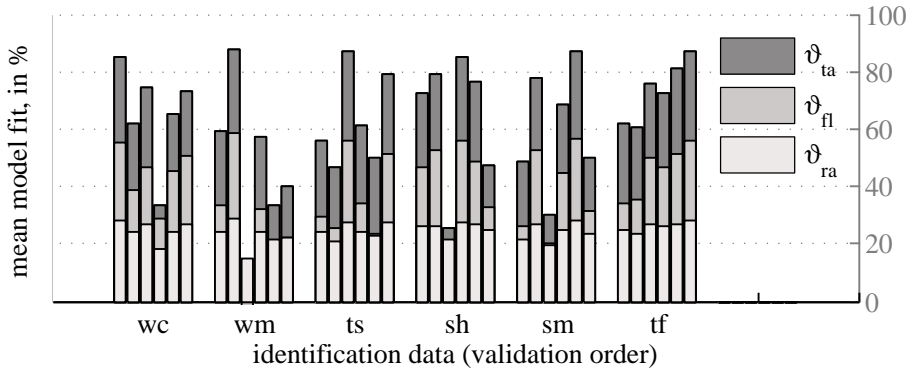


Figure G.12.: Average fits for constrained estimation  $\mathbf{A}$ ,  $\mathbf{C}$  as in the main text and  $\mathbf{B}$  from above.

$$\mathbf{B} = \begin{bmatrix} \mathbb{R} & \mathbb{R} & 0 & \mathbb{R} & X & 0 & \mathbb{R} \\ 0 & \mathbb{R} & \mathbb{R} & \mathbb{R} & X & 0 & \mathbb{R} \\ 0 & \mathbb{R} & \mathbb{R} & \mathbb{R} & X & \mathbb{R} & \mathbb{R} \end{bmatrix}$$

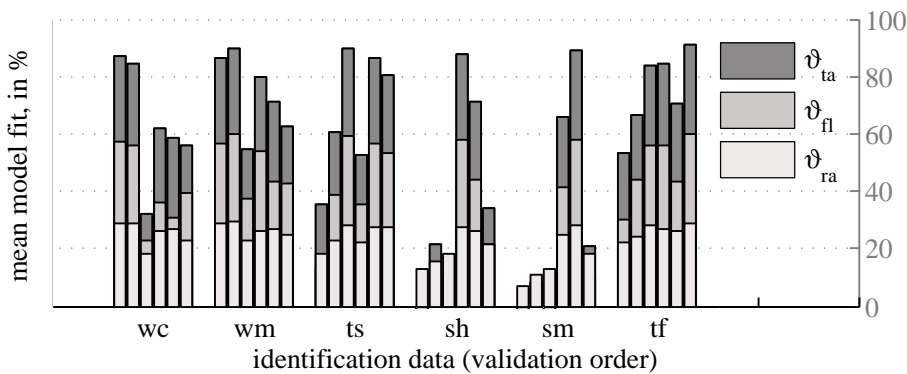


Figure G.13.: Average fits for constrained estimation  $\mathbf{A}$ ,  $\mathbf{C}$  as in the main text and  $\mathbf{B}$  from above.

$$\mathbf{B} = \begin{bmatrix} \mathbb{R} & \mathbb{R} & 0 & \mathbb{R} & X & 0 & \mathbb{R} \\ \mathbb{R} & \mathbb{R} & \mathbb{R} & \mathbb{R} & X & \mathbb{R} & \mathbb{R} \\ 0 & \mathbb{R} & \mathbb{R} & \mathbb{R} & X & \mathbb{R} & \mathbb{R} \end{bmatrix}$$

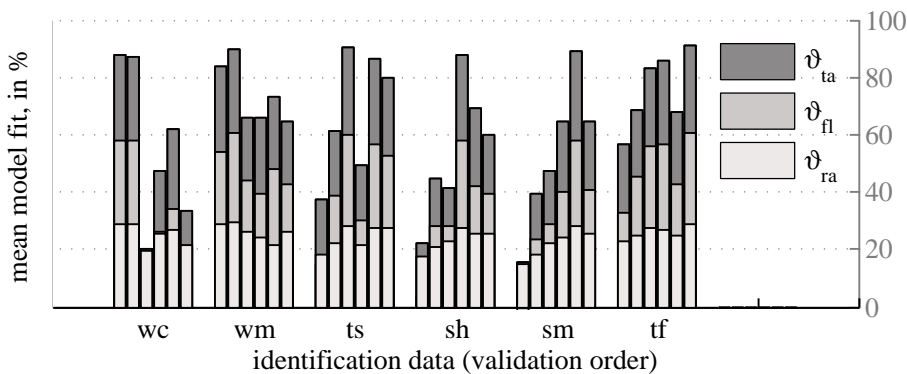


Figure G.14.: Average fits for constrained estimation  $\mathbf{A}$ ,  $\mathbf{C}$  as in the main text and  $\mathbf{B}$  from above.

### G.5. MPC-Boxes results based on real measurement data

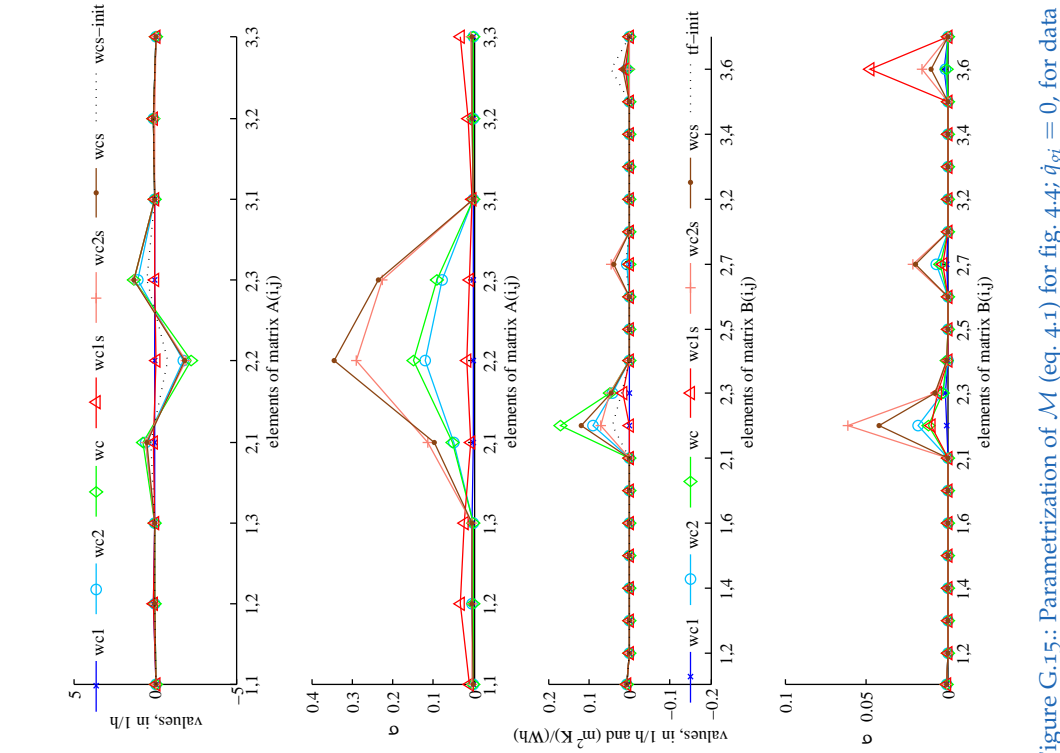


Figure G.15.: Parametrization of  $\mathcal{M}$  (eq. 4-1) for fig. 4-4;  $\hat{q}_{gf} = 0$ , for data see tab. 4-3, obtained with *ssest* and LSQ initial model.

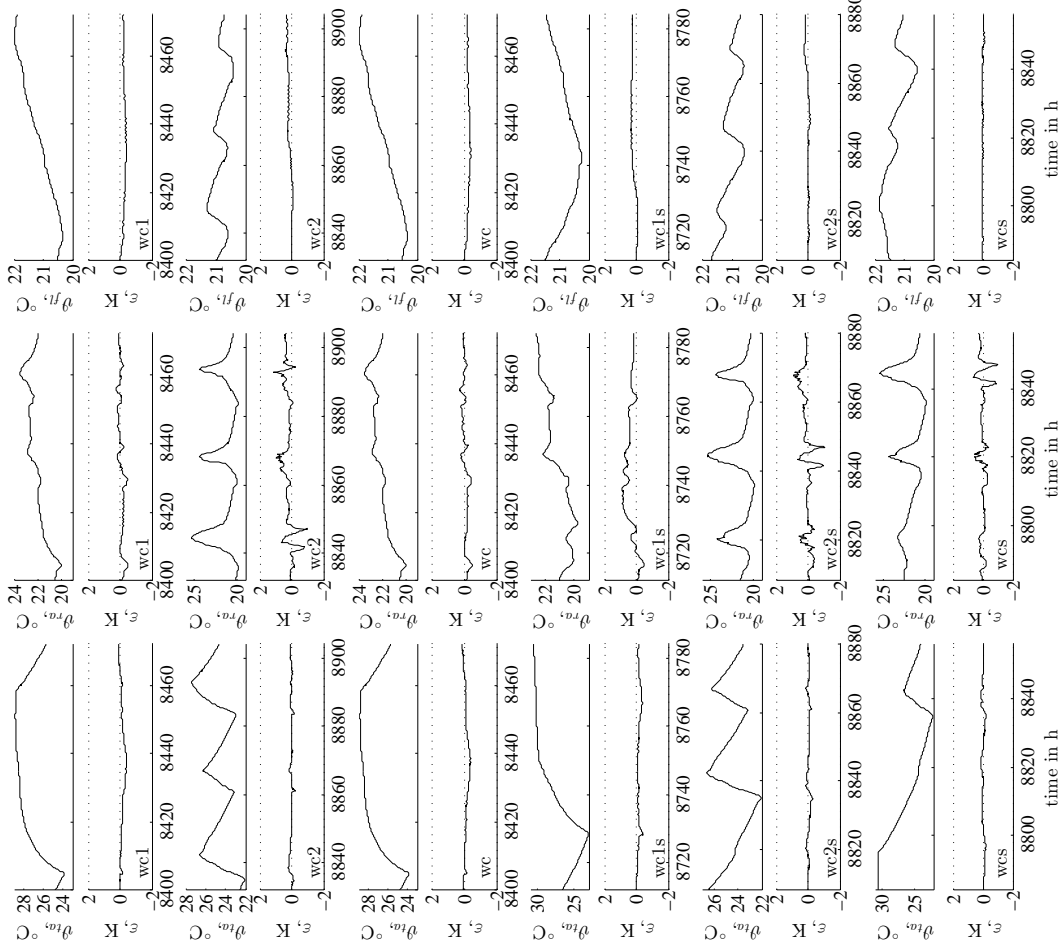


Figure G.16.: Reference trajectories and residual analysis for  $\mathcal{M}(\Theta_{wcs})$  validated against data  $D_{wc1}$  (top),  $D_{wc2}, \dots, D_{wcs}$  (bottom) see tab. 4-3; horizon: 7z h.

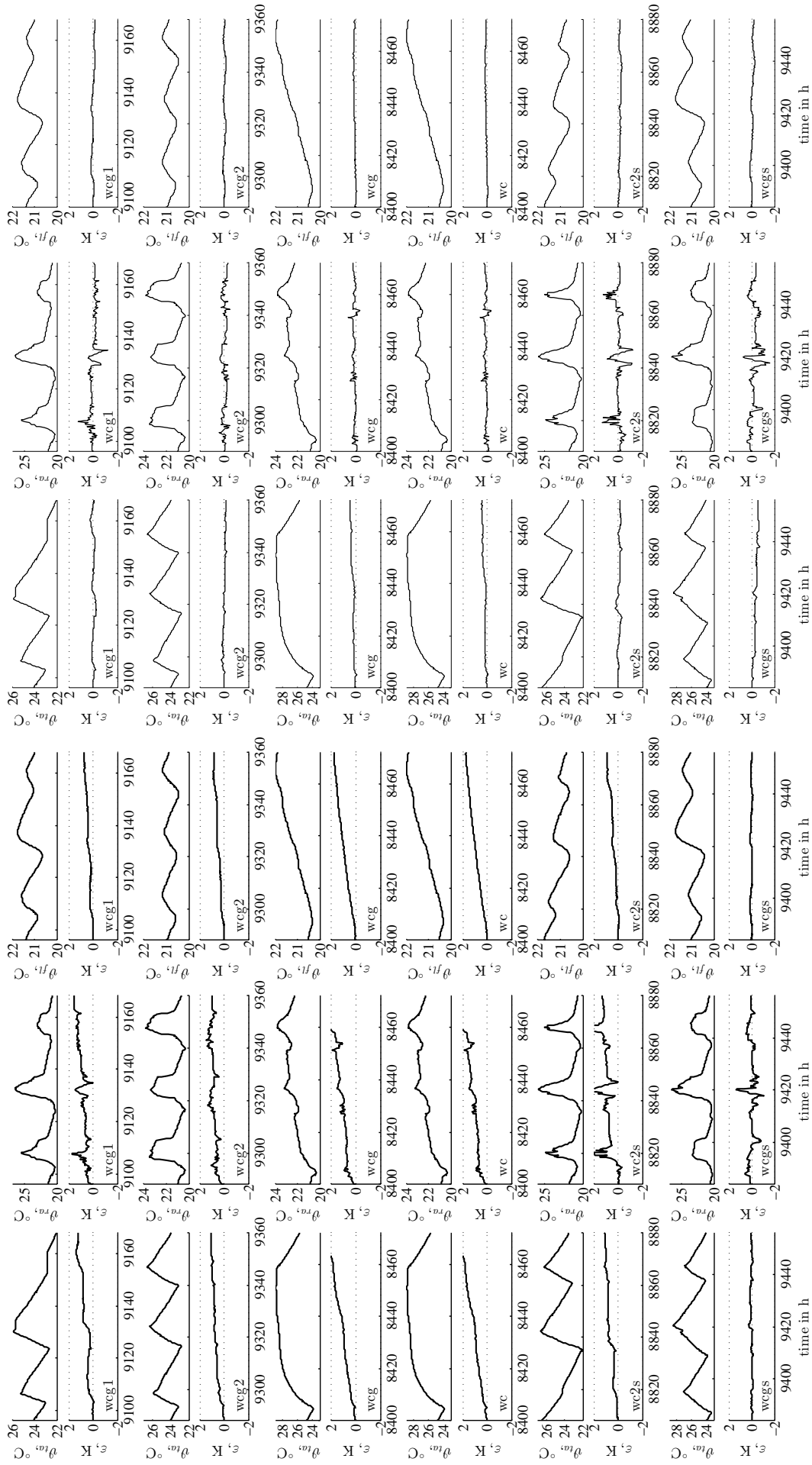


Figure G.17: Reference trajectories and residual analysis for the model  $\mathcal{M}(\Theta_{wcg1})$  validated against data  $wcg1$  (top),  $wcg2$ , ...,  $wcgs$ (bottom); horizon: 72 h.

## G.6. TheBat – model structures and results

### G.6.1. The model $\mathcal{M}^{n4}$

The S-SSM relating to fig. 4.10 and defined by eq. (G.5) indicates the very first model approach. The performance shown by fig. G.19 is not too bad, except for (cross-) validation where the data sh is involved. The reason why sh is problematic is due to the fact that the TABS are never in operation for this data, that is, the excitation is very different to the other data. An analysis of  $\Theta$  shows also exceptionally high uncertainty for specific elements for the model identified with sh.

$$\mathbf{x} := [\vartheta_{ra2fl}, \vartheta_{ta2fl}, \vartheta_{ra1fl}, \vartheta_{ta1fl}]^T, \quad \mathbf{u} := [\dot{q}_{ta2fl}, \dot{q}_{ta1fl}, \vartheta_{oa}, \dot{q}_{gs2fl}, \dot{q}_{gs1fl}, \dot{q}_{gi}, \vartheta_{grd}, \vartheta_{sky}]^T, \\ \mathbf{y} := \mathbf{x}.$$

$$\mathbf{A} = \begin{bmatrix} \mathbb{R}^- & \mathbb{R}^+ & \mathbb{R}^+ & 0 \\ \mathbb{R}^+ & \mathbb{R}^- & 0 & 0 \\ \mathbb{R}^+ & 0 & \mathbb{R}^- & \mathbb{R}^+ \\ 0 & 0 & \mathbb{R}^+ & \mathbb{R}^- \end{bmatrix}, \quad \mathbf{B} = \begin{bmatrix} 0 & 0 & \mathbb{R}^+ & \mathbb{R}^+ & 0 & X & 0 & \mathbb{R}^+ \\ \mathbb{R}^+ & 0 & 0 & 0 & 0 & 0 & 0 & 0 \\ 0 & 0 & \mathbb{R}^+ & 0 & \mathbb{R}^+ & X & 0 & \mathbb{R}^+ \\ 0 & \mathbb{R}^+ & 0 & 0 & 0 & 0 & \mathbb{R}^+ & 0 \end{bmatrix}, \quad \mathbf{C} = \begin{bmatrix} 1 & 0 & 0 & 0 \\ 0 & 1 & 0 & 0 \\ 0 & 0 & 1 & 0 \\ 0 & 0 & 0 & 1 \end{bmatrix}. \quad (\text{G.5})$$

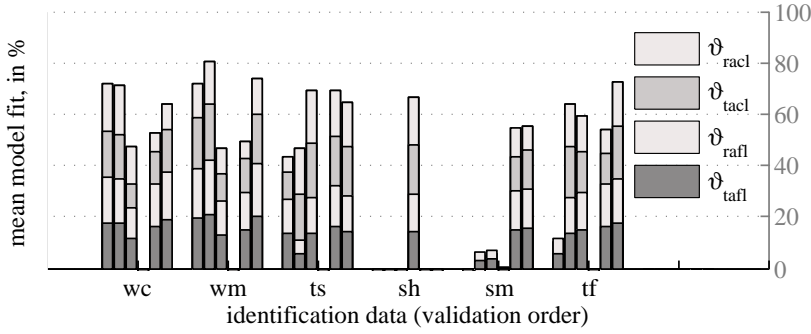


Figure G.19.: Fit results for  $\mathcal{M}^{n4}$  (see fig. 4.10), fl := 1fl and cl := 2fl; ,  $\dot{q}_{gi}$  is neglected.

### G.6.2. The model $\mathcal{M}^{n3}$

Definitions for the third order model with results in fig. G.20 and fig. G.21 read

$$\mathbf{x} := [\vartheta_{ta2fl}, \vartheta_{op}, \vartheta_{ta1fl}]^T, \quad \mathbf{u} := [\dot{q}_{ta2fl}, \dot{q}_{ta1fl}, \vartheta_{oa}, \dot{q}_{gs2fl}, \dot{q}_{gs1fl}, \dot{q}_{gi}, \vartheta_{grd}, \vartheta_{sky}]^T, \\ \mathbf{y} := \mathbf{x}.$$

$$\mathbf{A} = \begin{bmatrix} \mathbb{R}^- & \mathbb{R}^+ & 0 \\ \mathbb{R}^+ & \mathbb{R}^- & \mathbb{R}^+ \\ 0 & \mathbb{R}^+ & \mathbb{R}^- \end{bmatrix}, \quad \mathbf{B} = \begin{bmatrix} \mathbb{R}^+ & 0 & 0 & 0 & 0 & 0 & 0 & 0 \\ 0 & 0 & \mathbb{R}^+ & \mathbb{R}^+ & \mathbb{R}^+ & X & 0 & \mathbb{R}^+ \\ 0 & \mathbb{R}^+ & 0 & 0 & 0 & 0 & \mathbb{R}^+ & 0 \end{bmatrix}, \quad \mathbf{C} = \begin{bmatrix} 1 & 0 & 0 \\ 0 & 1 & 0 \\ 0 & 0 & 1 \end{bmatrix}. \quad (\text{G.6})$$

## Appendix G. System identification

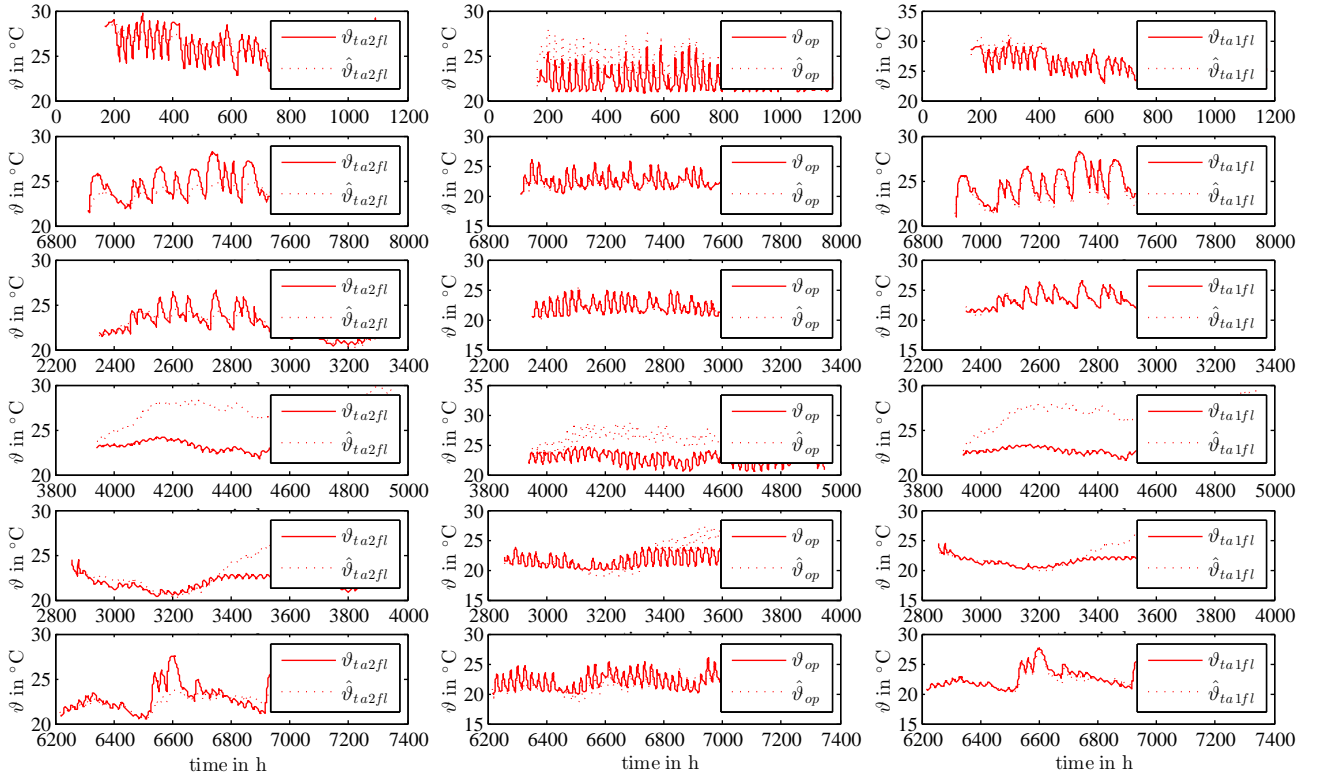


Figure G.20.: Output trajectories obtained with  $\mathcal{M}^{n3}(\Theta_{ts})$  in comparison to experimental data from simulation; validation with data wc (top), wm, ts, sh, sm and tf (bottom).

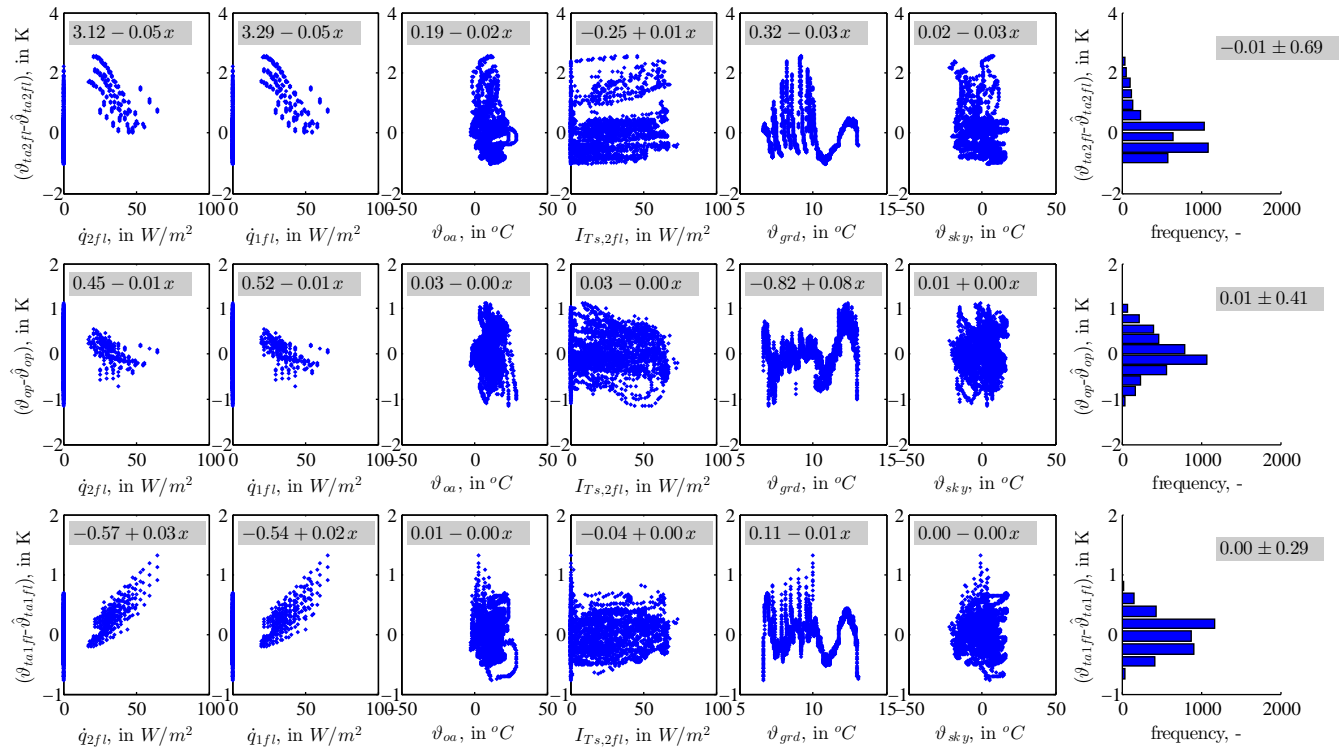


Figure G.21.: Residuals for  $\vartheta_{ta2fl}$ ,  $\vartheta_{op}$ ,  $\vartheta_{ta1fl}$  as a function of the input data and residual-histograms obtained with  $\mathcal{M}^{n3}(\Theta_{ts})$ ; results for input data  $I_{Ts,1fl} := \dot{q}_{gs1fl}$  are  $\approx$  those obtained with  $I_{Ts,2fl}$  and  $I_{Ts,2fl} := \dot{q}_{gs2fl}$ .

### G.6.3. The model $\mathcal{M}^{n4w}$ – further internal parametrizations

For the parametrization  $\Theta^b$  cf. eq. (G.7) the coupling between  $\vartheta_w$  and  $\vartheta_{ra1fl}$  is deleted, hence  $\vartheta_w$  couples only to  $\vartheta_{ra2fl}$  – which was a problematic node in  $\mathcal{M}^{n4}$  – for **B** and **C** see eq. (4.12) and (4.11) in the main text. The fits are especially good for identification with id-data ts.

$$\mathbf{A} := \begin{bmatrix} \mathbb{R}^- & \mathbb{R}^+ & 0 & 0 \\ \mathbb{R}^+ & \mathbb{R}^- & \mathbb{R}^+ & \mathbb{R}^+ \\ 0 & \mathbb{R}^+ & \mathbb{R}^- & \mathbb{R}^+ \\ 0 & \mathbb{R}^+ & \mathbb{R}^+ & \mathbb{R}^- \end{bmatrix}. \quad (\text{G.7})$$

In the parametrization  $\Theta^c$  cf. eq. (G.8) also the coupling between  $\vartheta_{ra1fl}$  and  $\vartheta_{ra2fl}$  is deleted, hence  $\vartheta_{ra1fl}$  and  $\vartheta_{ra2fl}$  decouple. Compared to  $\Theta^b$  the fits did not change significantly.

$$\mathbf{A} = \begin{bmatrix} \mathbb{R}^- & \mathbb{R}^+ & 0 & 0 \\ \mathbb{R}^+ & \mathbb{R}^- & 0 & \mathbb{R}^+ \\ 0 & 0 & \mathbb{R}^- & \mathbb{R}^+ \\ 0 & \mathbb{R}^+ & \mathbb{R}^+ & \mathbb{R}^- \end{bmatrix} \quad (\text{G.8})$$

For the last variation  $\Theta^d$  cf. eq. (G.9), the coupling between  $\vartheta_w$  and  $\vartheta_{ra1fl}$  is recovered which allows indirect coupling between  $\vartheta_{ra2fl}$  and  $\vartheta_{ra1fl}$  through the virtual wall node. Except for summer id-data, the fits are fairly good.

$$\mathbf{A} = \begin{bmatrix} \mathbb{R}^- & \mathbb{R}^+ & \mathbb{R}^+ & 0 \\ \mathbb{R}^+ & \mathbb{R}^- & 0 & \mathbb{R}^+ \\ \mathbb{R}^+ & 0 & \mathbb{R}^- & \mathbb{R}^+ \\ 0 & \mathbb{R}^+ & \mathbb{R}^+ & \mathbb{R}^- \end{bmatrix} \quad (\text{G.9})$$

The fit results for the individual structures are shown in the fig. G.6.3 to fig. G.6.3. The bad fit results for (cross-) validation where the data sh is involved are due to the fact that this data set includes free floating only, cf. sec. 4.3.1.

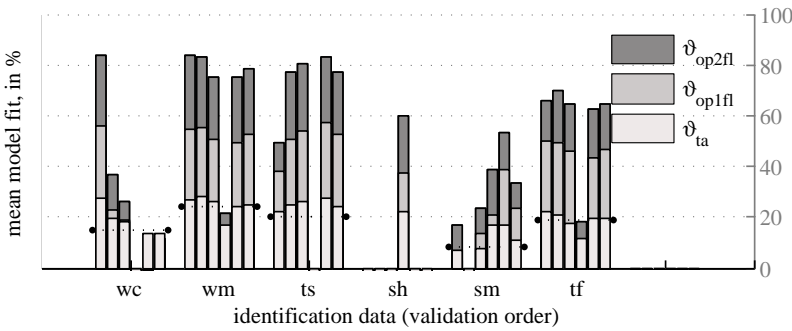


Figure G.22.: Fit results for  $\mathcal{M}^{n4w}(\Theta^a)$ ;  $P=6$  weeks,  $\Delta t=0.25$  h,  $\dot{q}_{gi}$  is neglected.

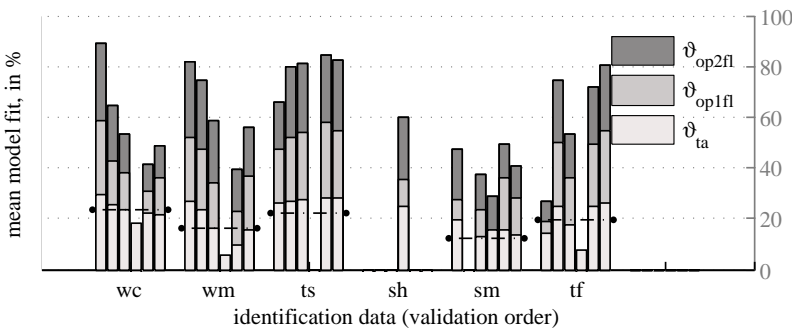


Figure G.23.: Fit results for  $\mathcal{M}^{n4w}(\Theta^b)$ ;  $P=6$  weeks,  $\Delta t=0.25$  h,  $\dot{q}_{gi}$  is neglected.

## Appendix G. System identification

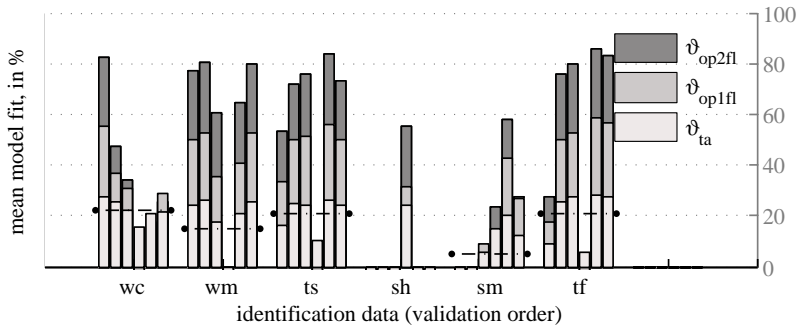


Figure G.24.: Fit results for  $\mathcal{M}^{n4w}(\Theta^c)$ ;  $P=6$  weeks,  $\Delta t=0.25$  h,  $\dot{q}_{gi}$  is neglected.

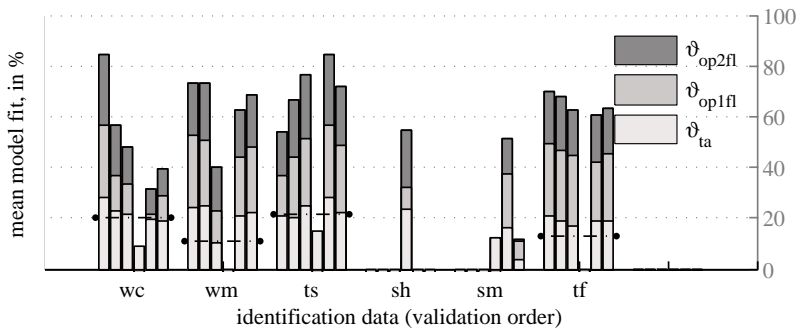


Figure G.25.: Fit results for  $\mathcal{M}^{n4w}(\Theta^d)$ ;  $P=6$  weeks,  $\Delta t=0.25$  h,  $\dot{q}_{gi}$  is neglected.

### G.6.4. The other eigensolutions of $\mathcal{M}^{n4w}$

The eigensolution  $\mathbf{f}_2$  is dominated by the TABS node with minor influence from the room temperature node and less influence from the virtual wall node. The corresponding eigenvalue is of the order  $-10^{-2}$ . Further  $\mathbf{f}_3$  is dominated by the room temperature node with an eigenvalue of the order  $-10^{-1}$ , similarly for  $\mathbf{f}_4$  with the smallest eigenvalue of the order  $-10^0$ . The correspondence of a small eigenvalue – representing high damping or a small thermal mass – and an eigendirection dominated by the room air temperature nodes indicates *consistency*, that is the model node represents what it was designed for.

Table G.1.: Properties of the eigensolutions  $f_2(\lambda_2, \mathbf{v}_2)$ , obtained from the four parametrizations  $\Theta^a, \Theta^b, \Theta^c, \Theta^d$ , for all id-data wc, ... tf, respectively. Eigendirections were adjusted with the dominating component to be positive.

id-data	wc	wm	ts	sh	sm	tf	mean
normalized eigenvectors $\mathbf{v}_2$ and corresponding eigenvalues							
variant a							$dmax_{\gamma_2} = 0.306$
$v_{2,w}$	0.00	-0.02	-0.09	-0.17	-0.20	-0.01	-0.08
$v_{2,op2fl}$	0.08	0.39	0.22	0.03	-0.01	-0.01	0.12
$v_{2,op1fl}$	0.20	0.47	0.26	0.11	0.08	0.10	0.20
$v_{2,ta}$	0.98	0.79	0.94	0.98	0.98	1.00	0.94
$\lambda_2$	-5.1e-02	-3.7e-02	-3.9e-02	-4.0e-02	-4.1e-02	-5.2e-02	-4.4e-02
variant b							$dmax_{\gamma_2} = 0.342$
$v_{2,w}$	0.00	-0.03	-0.15	-0.25	-0.32	-0.06	-0.13
$v_{2,op2fl}$	0.40	0.40	0.29	0.12	-0.02	0.12	0.22
$v_{2,op1fl}$	0.55	0.49	0.37	0.23	0.13	0.29	0.34
$v_{2,ta}$	0.74	0.78	0.87	0.93	0.94	0.95	0.87
$\lambda_2$	-4.9e-02	-3.5e-02	-3.4e-02	-2.5e-02	-4.0e-02	-3.7e-02	-3.7e-02
variant c							$dmax_{\gamma_2} = 0.686$
$v_{2,w}$	0.00	-0.07	-0.02	0.99	0.00	-0.05	0.14
$v_{2,op2fl}$	0.04	0.28	0.03	-0.09	0.00	0.33	0.10
$v_{2,op1fl}$	0.71	0.72	0.75	-0.09	0.70	0.71	0.58
$v_{2,ta}$	0.71	0.63	0.66	-0.11	0.72	0.62	0.54
$\lambda_2$	-4.6e-02	-3.5e-02	-3.8e-02	-4.5e-03	-1.7e-02	-2.4e-02	-2.8e-02
variant d							$dmax_{\gamma_2} = 0.467$
$v_{2,w}$	0.00	-0.15	-0.02	-0.43	0.00	0.00	-0.10
$v_{2,op2fl}$	0.15	0.55	0.04	0.11	0.00	0.00	0.14
$v_{2,op1fl}$	0.19	0.51	0.06	0.06	0.09	0.00	0.15
$v_{2,ta}$	0.97	0.64	1.00	0.89	1.00	1.00	0.92
$\lambda_2$	-5.2e-02	-1.7e-02	-4.5e-02	-2.2e-02	-4.1e-02	-5.2e-02	-3.8e-02

Table G.2.: Properties of the eigensolutions  $f_3(\lambda_3, \mathbf{v}_3)$ , obtained from the four parametrizations  $\Theta^a, \Theta^b, \Theta^c, \Theta^d$ , for all id-data wc, ... tf, respectively. Eigendirections were adjusted with the dominating component to be positive.

id-data	wc	wm	ts	sh	sm	tf	mean
normalized eigenvectors $\mathbf{v}_3$ and corresponding eigenvalues							
variant a							$dmax_{\gamma_3} = 0.104$
$v_{3,w}$	0.00	0.00	-0.02	-0.07	-0.10	-0.01	-0.04
$v_{3,op2fl}$	0.65	0.63	0.71	0.66	0.72	0.74	0.67
$v_{3,op1fl}$	0.76	0.76	0.70	0.74	0.68	0.65	0.70
$v_{3,ta}$	-0.09	-0.15	-0.11	-0.08	-0.09	-0.16	-0.09
$\lambda_3$	-4.3e-01	-3.6e-01	-3.5e-01	-3.4e-01	-3.8e-01	-2.9e-01	-3.5e-01
variant b							$dmax_{\gamma_3} = 0.088$
$v_{3,w}$	0.00	0.00	-0.02	-0.03	-0.10	-0.03	-0.03
$v_{3,op2fl}$	0.62	0.62	0.71	0.71	0.71	0.68	0.67
$v_{3,op1fl}$	0.78	0.78	0.70	0.71	0.69	0.72	0.72
$v_{3,ta}$	-0.10	-0.09	-0.10	-0.04	-0.10	-0.10	-0.07
$\lambda_3$	-4.5e-01	-4.3e-01	-3.7e-01	-4.1e-01	-3.6e-01	-2.9e-01	-3.8e-01
variant c							$dmax_{\gamma_3} = 0.071$
$v_{3,w}$	0.00	0.00	0.00	0.00	0.00	0.00	0.00
$v_{3,op2fl}$	0.00	0.00	0.00	0.00	0.00	0.00	0.00
$v_{3,op1fl}$	1.00	1.00	1.00	1.00	0.99	1.00	0.99
$v_{3,ta}$	0.00	0.00	0.00	0.00	-0.14	0.00	-0.01
$\lambda_3$	-2.5e-01	-2.0e-01	-1.8e-01	-7.6e-01	-2.4e-01	-2.7e-01	-3.1e-01
variant d							$dmax_{\gamma_3} = 0.709$
$v_{3,w}$	0.00	-0.01	0.00	-0.04	0.00	0.00	-0.01
$v_{3,op2fl}$	-0.13	0.00	0.97	0.99	0.00	0.98	0.46
$v_{3,op1fl}$	0.99	1.00	-0.17	-0.15	1.00	0.00	0.44
$v_{3,ta}$	-0.04	0.00	-0.16	-0.01	-0.09	-0.19	-0.06
$\lambda_3$	-4.6e-01	-1.9e-01	-3.2e-01	-4.3e-01	-3.5e-01	-3.0e-01	-3.3e-01

## Appendix G. System identification

Table G.3.: Properties of the eigensolutions  $\mathbf{f}_4(\lambda_4, \mathbf{v}_4)$ , obtained from the four parametrizations  $\Theta^a, \Theta^b, \Theta^c, \Theta^d$ , for all id-data wc, ... tf, respectively. Eigendirections were adjusted with the dominating component to be positive.

id-data	wc	wm	ts	sh	sm	tf	mean
normalized eigenvectors $\mathbf{v}_4$ and corresponding eigenvalues							
variant a							$dmax_{\nu_4} = 0.707$
$v_{4,w}$	0.00	0.00	0.00	-0.01	0.00	0.00	-0.01
$v_{4,op2fl}$	-0.19	1.00	0.71	0.74	-0.28	0.00	0.38
$v_{4,op1fl}$	0.98	0.00	-0.70	-0.68	0.96	1.00	0.32
$v_{4,ta}$	0.00	0.00	-0.02	0.00	-0.01	0.00	-0.02
$\lambda_4$	-1.6e+00	-5.7e+00	-2.0e+00	-2.3e+00	-2.8e+00	-2.2e+00	-2.4e+00
variant b							$dmax_{\nu_4} = 0.618$
$v_{4,w}$	0.00	0.00	0.00	0.00	0.00	0.00	0.00
$v_{4,op2fl}$	0.96	0.97	-0.57	-0.40	-0.29	-0.01	0.19
$v_{4,op1fl}$	-0.28	-0.22	0.82	0.92	0.96	1.00	0.56
$v_{4,ta}$	0.00	-0.01	0.01	0.00	-0.01	0.00	-0.01
$\lambda_4$	-5.5e+00	-7.0e+00	-4.2e+00	-3.0e+00	-2.8e+00	-1.1e+00	-3.4e+00
variant c							$dmax_{\nu_4} = 0.343$
$v_{4,w}$	0.00	-0.01	-0.04	0.00	-0.09	-0.01	-0.02
$v_{4,op2fl}$	0.98	0.99	0.98	0.76	1.00	0.94	0.81
$v_{4,op1fl}$	0.15	0.07	0.14	0.65	0.02	0.32	0.33
$v_{4,ta}$	-0.13	-0.12	-0.13	-0.01	-0.04	-0.11	-0.08
$\lambda_4$	-4.3e-01	-5.3 e-01	-3.2e-01	-7.7e-01	-5.3e-01	-3.7e-01	-4.6e-01
variant d							$dmax_{\nu_4} = 0.654$
$v_{4,w}$	0.00	-0.01	-0.03	0.00	-0.09	-0.01	-0.02
$v_{4,op2fl}$	0.98	0.25	0.29	0.05	0.98	0.07	0.44
$v_{4,op1fl}$	0.20	0.90	0.96	1.00	0.15	1.00	0.66
$v_{4,ta}$	-0.09	-0.36	-0.04	-0.03	-0.04	-0.03	-0.09
$\lambda_4$	-4.4e-01	-2.4e-01	-3.5e-01	-5.2e-01	-5.3e-01	-3.5e-01	-3.9e-01

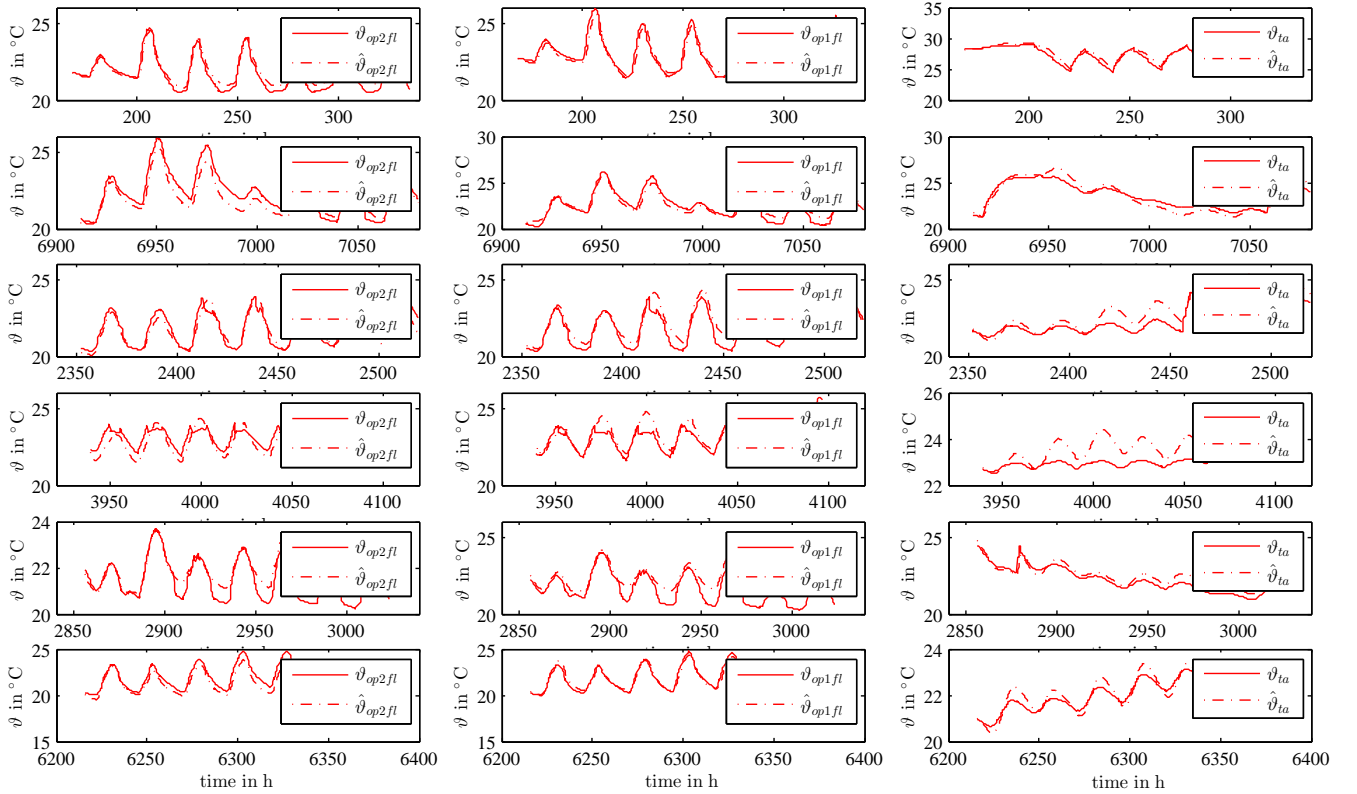


Figure G.26.: Output trajectories obtained with  $M^{n4w}(\Theta^a(wm))$  in comparison to experimental data from simulation; evaluation with data wc (top), wm, ts, sh, sm and tf (bottom).

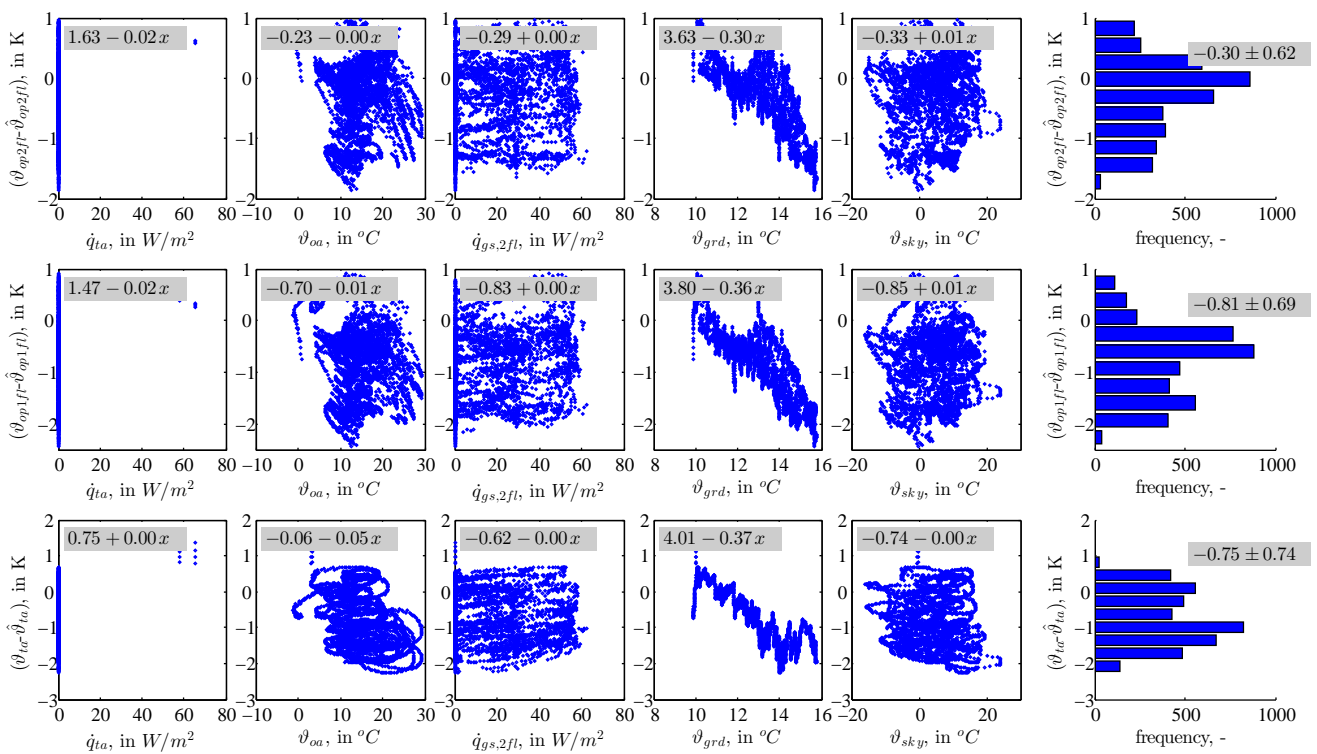


Figure G.27.: Residuals for  $\theta_{op2fl}$ ,  $\theta_{op1fl}$ ,  $\theta_{ta}$  as a function of selected input data and residual-histograms obtained with  $\mathcal{M}^{N4w}(\Theta_{wm}^a)$  for  $\mathcal{D}_{sm}$  (6 weeks cross-validation).

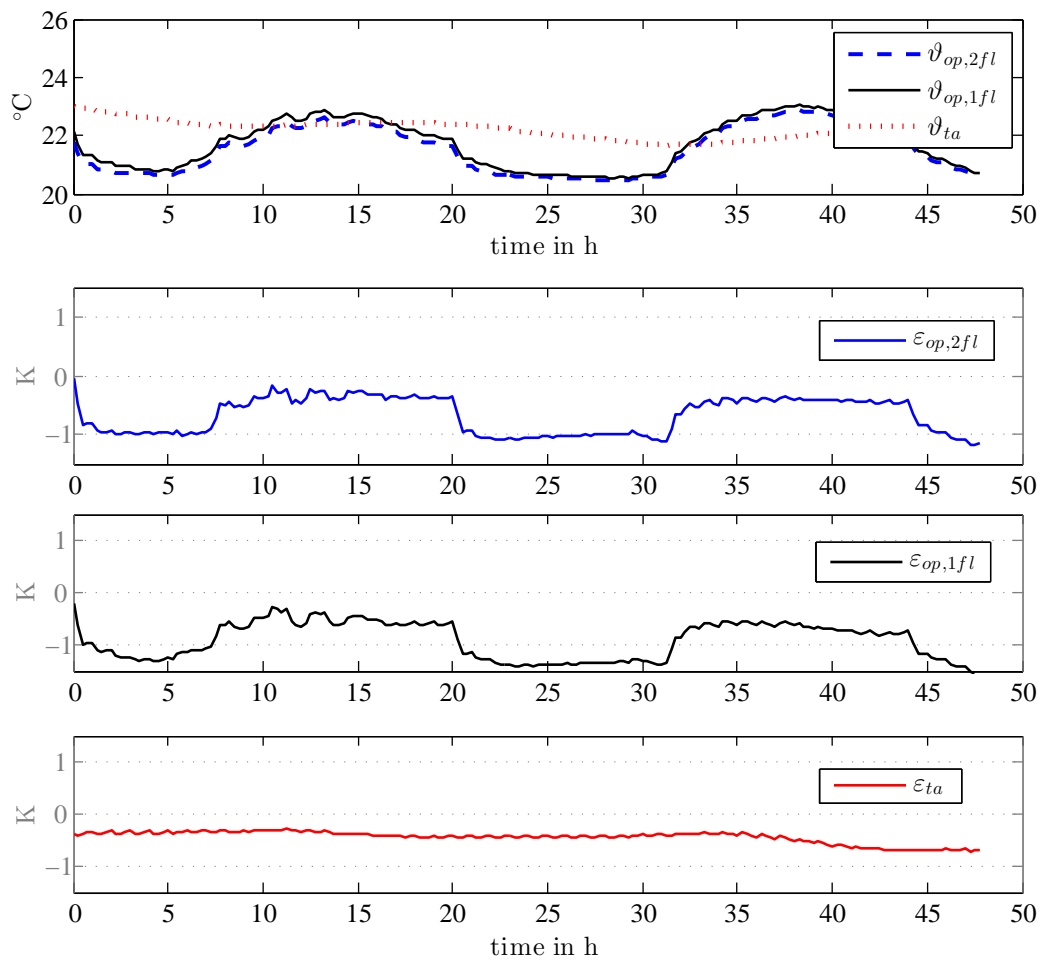


Figure G.28.: Residuals for  $\mathcal{M}^{n4w}(\Theta_{sm}^a)$  cross-validated with  $\mathcal{D}_{wm}$  for a typical prediction horizon of 48 h.

### G.6.5. Parameter inspection

An additional criterion for the four variants may be the inspection of the individual parametrization (see fig. G.29) in light of physics.

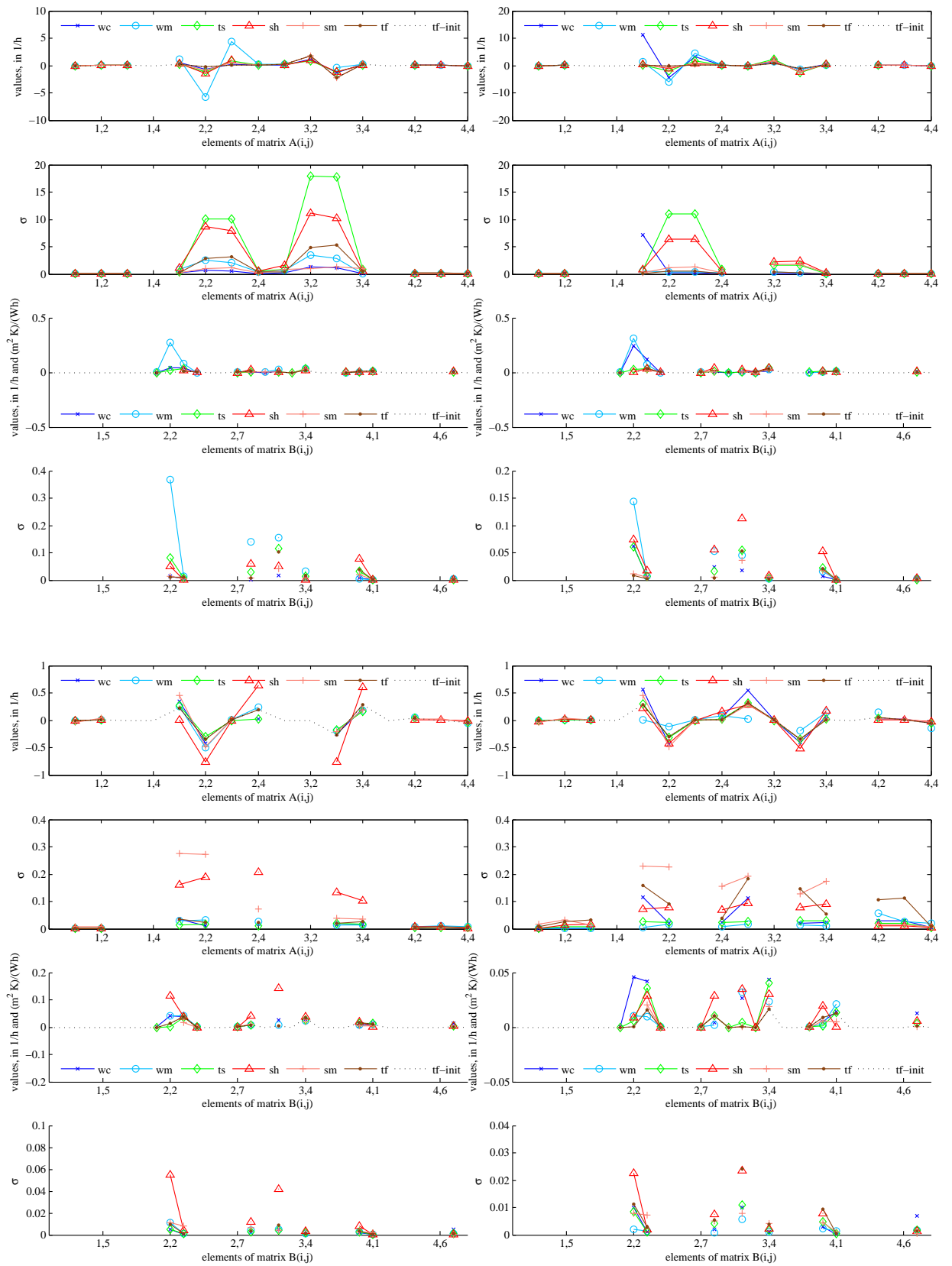
$\Theta^a$ : On a uniform parameter scale for the id-data wc, ... tf, the greatest internal coupling is given for  $\Theta^a(wm)$ , which couples also much stronger to  $\vartheta_{oa}$  than the others. For  $\Theta^a(ts,sh)$  the coupling parameters for  $\vartheta_{op2fl} \leftrightarrow \vartheta_{op1fl}$  have high uncertainties (collinearity).

$\Theta^b$ : The coupling between  $\vartheta_w \leftrightarrow \vartheta_{op1fl}$  is more or less deleted. As a consequence the parameter uncertainty for the coupling  $\vartheta_{op2fl} \leftrightarrow \vartheta_{op1fl}$  decreases.

$\Theta^c$ : The parameter values are much smaller, and the uncertainties as well, however, uncertainties are higher for summer id-data.

$\Theta^d$ : Compared to variant a the direct coupling between  $\vartheta_{op2fl} \leftrightarrow \vartheta_{op1fl}$  is deleted, however it is still possible indirectly over  $\vartheta_w$ . Compared to the variants a and b the uncertainties decrease significantly for both, A and B parameters.

## Appendix G. System identification



256 Figure G.29.: TheBat,  $\mathcal{M}^{n^{4w}}(\Theta^*)$ ,  $*$  = a, b, c, d: left-, right-top and left-, right-bottom four graphs; be aware of the scaling.

## Appendix H.

### Detailed simulation results

#### H.1. DHW(TES) and SH(TABS) results – BC scenario 0.0

Table H.1.: Comfort related variables and results – BC scenario 0.0.

	$\vartheta_{ra,1fl}$ °C	$\vartheta_{op,1fl}$ °C	$\vartheta_{ra,2fl}$ °C	$\vartheta_{op,2fl}$ °C	$RH_{avg}$ %	$\vartheta_{TES,z>0.8}$ °C
Jan	23.0 ± 1.3	23.8 ± 1.2	22.6 ± 1.2	23.1 ± 1.2	16.2 ± 4.9	48.7 ± 1.5
Feb	23.1 ± 1.2	23.8 ± 1.1	22.7 ± 1.1	23.2 ± 1.1	18.1 ± 4.2	48.2 ± 1.8
Mar	23.3 ± 1.3	23.9 ± 1.2	23.0 ± 1.3	23.5 ± 1.2	22.5 ± 5.1	47.7 ± 2.1
Apr	22.7 ± 1.3	23.1 ± 1.2	22.6 ± 1.2	23.0 ± 1.1	30.8 ± 9.3	47.5 ± 2.0
May	21.8 ± 1.4	22.1 ± 1.3	21.9 ± 1.4	22.2 ± 1.3	43.5 ± 7.5	46.8 ± 2.1
Jun	22.6 ± 1.3	22.9 ± 1.1	22.7 ± 1.3	23.0 ± 1.2	50.9 ± 8.1	46.8 ± 2.1
Jul	22.9 ± 1.1	23.1 ± 0.9	23.0 ± 1.1	23.2 ± 0.9	53.9 ± 8.9	46.8 ± 2.0
Aug	22.6 ± 1.2	22.9 ± 1.0	22.7 ± 1.2	23.0 ± 1.0	55.6 ± 10.1	46.8 ± 2.1
Sep	21.8 ± 1.2	22.1 ± 1.1	21.8 ± 1.2	22.1 ± 1.1	46.9 ± 9.2	46.9 ± 2.0
Oct	22.6 ± 1.3	23.0 ± 1.3	22.4 ± 1.2	22.8 ± 1.2	36.0 ± 9.2	47.4 ± 2.1
Nov	22.6 ± 1.1	23.2 ± 1.1	22.2 ± 1.1	22.7 ± 1.0	25.2 ± 7.1	48.1 ± 2.0
Dec	22.7 ± 1.0	23.4 ± 0.9	22.2 ± 1.0	22.7 ± 0.9	18.5 ± 5.4	48.6 ± 1.7
annual	22.6 ± 1.3	23.1 ± 1.3	22.5 ± 1.3	22.9 ± 1.2	35.0 ± 16.2	47.5 ± 2.0

Table H.2.: TABS and DHW control relevant variables and results – BC scenario 0.0.

	$\vartheta_{ra,avg}$ °C	$\vartheta_{sw}$ °C	$\vartheta_{ta}$ °C	$\vartheta_{ret}$ °C	$\vartheta_{ret,SHon}$ °C	$\dot{q}_{ta}$ W/m <sup>2</sup>	$\vartheta_{TES,z>0.8}$ °C
Jan	23.0 ± 1.3	33.1 ± 2.1	28.0 ± 1.5	27.2 ± 1.4	27.5 ± 1.6	36.5 ± 9.8	48.7 ± 1.5
Feb	23.1 ± 1.2	32.3 ± 1.9	27.3 ± 1.4	26.5 ± 1.2	27.0 ± 1.2	33.1 ± 9.7	48.2 ± 1.8
Mar	23.3 ± 1.3	30.7 ± 2.1	26.1 ± 1.6	25.6 ± 1.3	26.3 ± 1.2	26.3 ± 9.0	47.7 ± 2.1
Apr	22.7 ± 1.3	28.5 ± 1.8	24.5 ± 1.6	24.2 ± 1.4	25.2 ± 1.1	19.2 ± 7.1	47.5 ± 2.0
May	21.8 ± 1.4	–	22.3 ± 1.1	22.3 ± 1.0	–	–	46.8 ± 2.1
Jun	22.6 ± 1.3	–	23.0 ± 0.8	23.0 ± 0.8	–	–	46.8 ± 2.1
Jul	22.9 ± 1.1	–	23.3 ± 0.4	23.3 ± 0.4	–	–	46.8 ± 2.0
Aug	22.6 ± 1.2	–	23.1 ± 0.5	23.1 ± 0.5	–	–	46.8 ± 2.1
Sep	21.8 ± 1.2	26.1 ± 1.0	22.4 ± 0.7	22.4 ± 0.7	23.0 ± 1.1	17.8 ± 5.6	46.9 ± 2.0
Oct	22.6 ± 1.3	28.8 ± 2.1	24.4 ± 1.8	24.1 ± 1.5	25.4 ± 1.5	19.8 ± 7.3	47.4 ± 2.1
Nov	22.6 ± 1.1	31.1 ± 1.9	26.3 ± 1.7	25.7 ± 1.5	26.3 ± 1.4	28.8 ± 7.3	48.1 ± 2.0
Dec	22.7 ± 1.0	32.8 ± 1.6	27.7 ± 1.4	26.8 ± 1.3	27.3 ± 1.3	35.0 ± 8.1	48.6 ± 1.7
annual	22.6 ± 1.3	31.4 ± 2.6	24.9 ± 2.4	24.5 ± 2.0	26.6 ± 1.6	29.7 ± 10.5	47.5 ± 2.0

## Appendix H. Detailed simulation results

Table H.3.: Overview on annual supplied-, generated- and utilized energy amounts – BC scenario 0.0.

	$Q_{e,brine}$ kWh	$Q_{gi}$ kWh	$W_{comp}$ kWh	$W_{PV}$ kWh	$Q_c$ kWh	$Q_d$ kWh	$Q_{HP,loss}$ kWh	$Q_{TES,in}$ kWh	$Q_{TES,o}$ kWh	$Q_{TES,loss}$ kWh	$Q_{SH}$ kWh
Jan	1944	0	637	256	1997	464	122	300	193	107	2144
Feb	1416	0	450	269	1468	317	84	255	165	90	1514
Mar	1039	0	325	361	1095	207	63	267	177	92	1025
Apr	715	0	224	357	767	128	45	257	172	83	630
May	192	0	75	378	245	0	22	245	174	77	0
Jun	192	0	75	354	246	0	22	245	169	75	0
Jul	197	0	77	373	252	0	22	252	176	77	0
Aug	201	0	78	353	257	0	23	256	174	77	0
Sep	242	0	89	325	295	12	24	246	171	76	60
Oct	708	0	222	309	762	125	45	257	175	86	623
Nov	1418	0	436	207	1481	293	81	271	174	94	1489
Dec	1916	0	611	206	1978	438	113	297	189	104	2101
annual	10179	0	3299	3748	10842	1983	664	3149	2108	1040	9585

Table H.4.: Overview on thermal energies and energy penalty terms – BC scenario 0.0.

	$Q_{HP,tot}$ kWh	$Q_{HP,loss}$ kWh	$Q_{dp1,in}$ kWh	$Q_{dp2,in}$ kWh	$Q_{dp3,o}$ kWh	$Q_{dp4,o}$ kWh	$Q_{TES,loss}$ kWh	$Q_{SH}$ kWh	$P_{pen,DHW}$ kWh	$P_{pen,SH}$ kWh
Jan	2461	122	−0	300	179	15	107	2144	7	0
Feb	1784	84	−0	255	161	4	90	1514	7	0
Mar	1302	63	−0	267	176	1	92	1025	7	0
Apr	895	45	−0	257	172	0	83	630	7	0
May	245	22	−0	245	174	0	77	0	7	0
Jun	246	22	−0	245	169	0	75	0	7	0
Jul	252	22	−0	252	176	0	77	0	7	0
Aug	257	23	−0	256	174	0	77	0	7	0
Sep	307	24	−0	246	171	0	76	60	7	1
Oct	886	45	−0	257	175	0	86	623	7	0
Nov	1774	81	−0	271	172	2	94	1489	7	0
Dec	2416	113	−0	297	181	8	104	2101	7	0
annual	12825	664	−0	3149	2078	30	1040	9585	88	1

Table H.5.: Performance indicators overview for monthly and annual results – BC scenario 0.0.

	$SPF$	$SPF_{ctr}$	$SPF_{sys}$	$SPF_{sys,ctr}$	$COP$	$SPF_{sys}^{pen}$	$SPF_{sys,ctr}^{pen}$	$\eta_{PV}$
Jan	3.74	4.83	3.47	4.47	$3.78 \pm 0.24$	3.43	4.42	$12.30 \pm 0.01$
Feb	3.82	4.69	3.52	4.32	$3.84 \pm 0.22$	3.47	4.26	$12.20 \pm 0.01$
Mar	3.83	5.24	3.46	4.72	$3.84 \pm 0.27$	3.39	4.62	$11.88 \pm 0.01$
Apr	3.78	5.38	3.29	4.69	$3.80 \pm 0.31$	3.20	4.55	$11.57 \pm 0.01$
May	3.17	4.64	2.23	3.28	$3.16 \pm 0.40$	2.04	3.05	$11.30 \pm 0.01$
Jun	3.17	4.66	2.16	3.18	$3.17 \pm 0.40$	1.98	2.96	$11.20 \pm 0.01$
Jul	3.17	4.91	2.19	3.41	$3.17 \pm 0.40$	2.00	3.15	$11.16 \pm 0.01$
Aug	3.17	4.46	2.13	3.01	$3.17 \pm 0.40$	1.95	2.80	$11.17 \pm 0.01$
Sep	3.32	4.73	2.46	3.52	$3.41 \pm 0.49$	2.25	3.24	$11.41 \pm 0.01$
Oct	3.77	5.31	3.30	4.65	$3.80 \pm 0.32$	3.20	4.53	$11.72 \pm 0.01$
Nov	3.90	4.75	3.57	4.34	$3.91 \pm 0.20$	3.52	4.28	$11.99 \pm 0.01$
Dec	3.82	4.55	3.54	4.21	$3.85 \pm 0.20$	3.50	4.17	$12.25 \pm 0.01$
annual	3.74	4.83	3.33	4.31	$3.77 \pm 0.33$	3.25	4.21	$11.59 \pm 0.01$

## H.2. DHW(TEs) and SH(TABS) results – BC scenario 0.1

Table H.6.: Comfort related variables and results – BC scenario 0.1.

	$\vartheta_{ra,1fl}$ °C	$\vartheta_{op,1fl}$ °C	$\vartheta_{ra,2fl}$ °C	$\vartheta_{op,2fl}$ °C	$RH_{avg}$ 1	$\vartheta_{TES,z>0.8}$ °C
Jan	23.0 ± 1.3	23.8 ± 1.2	22.5 ± 1.2	23.1 ± 1.2	16.3 ± 4.9	48.6 ± 1.6
Feb	23.1 ± 1.1	23.8 ± 1.1	22.8 ± 1.1	23.2 ± 1.1	18.0 ± 4.2	48.3 ± 1.8
Mar	23.3 ± 1.3	23.9 ± 1.3	23.0 ± 1.3	23.5 ± 1.2	22.6 ± 5.2	47.6 ± 2.1
Apr	22.6 ± 1.3	23.1 ± 1.2	22.6 ± 1.2	23.0 ± 1.1	30.9 ± 9.3	47.5 ± 2.1
May	21.9 ± 1.5	22.2 ± 1.3	22.0 ± 1.5	22.2 ± 1.3	43.4 ± 7.5	46.8 ± 2.1
Jun	22.6 ± 1.3	22.9 ± 1.1	22.7 ± 1.3	23.0 ± 1.2	50.9 ± 8.1	46.8 ± 2.0
Jul	22.9 ± 1.1	23.1 ± 0.9	23.0 ± 1.1	23.2 ± 0.9	53.9 ± 8.9	46.8 ± 2.1
Aug	22.6 ± 1.2	22.9 ± 1.0	22.7 ± 1.2	23.0 ± 1.0	55.6 ± 10.1	46.8 ± 2.0
Sep	21.8 ± 1.2	22.1 ± 1.1	21.8 ± 1.2	22.1 ± 1.1	46.8 ± 9.2	46.9 ± 2.0
Oct	22.5 ± 1.3	23.0 ± 1.2	22.4 ± 1.2	22.8 ± 1.2	36.1 ± 9.2	47.2 ± 2.1
Nov	22.6 ± 1.1	23.2 ± 1.0	22.3 ± 1.0	22.7 ± 1.0	25.1 ± 6.8	47.9 ± 2.0
Dec	22.7 ± 1.0	23.5 ± 0.9	22.3 ± 1.0	22.7 ± 0.9	18.5 ± 5.3	48.6 ± 1.6
annual	22.7 ± 1.3	23.1 ± 1.3	22.5 ± 1.3	22.9 ± 1.2	34.9 ± 16.2	47.5 ± 2.0

Table H.7.: TABS and DHW control relevant variables and results – BC scenario 0.1.

	$\vartheta_{ra,avg}$ °C	$\vartheta_{sw}$ °C	$\vartheta_{ta}$ °C	$\vartheta_{ret}$ °C	$\vartheta_{ret,SHon}$ °C	$\dot{q}_{ta}$ W/m <sup>2</sup>	$\vartheta_{TES,z>0.8}$ °C
Jan	23.0 ± 1.3	33.1 ± 2.1	28.0 ± 1.5	27.2 ± 1.4	27.5 ± 1.6	37.7 ± 10.8	48.6 ± 1.6
Feb	23.1 ± 1.1	32.2 ± 1.8	27.3 ± 1.4	26.5 ± 1.2	27.0 ± 1.2	32.1 ± 9.0	48.3 ± 1.8
Mar	23.3 ± 1.3	30.8 ± 2.1	26.1 ± 1.6	25.6 ± 1.3	26.3 ± 1.2	26.5 ± 8.8	47.6 ± 2.1
Apr	22.6 ± 1.3	28.9 ± 1.8	24.5 ± 1.6	24.2 ± 1.4	25.3 ± 1.2	20.5 ± 7.6	47.5 ± 2.1
May	21.9 ± 1.5	–	22.5 ± 1.2	22.4 ± 1.1	–	–	46.8 ± 2.1
Jun	22.6 ± 1.3	–	23.0 ± 0.8	23.0 ± 0.8	–	–	46.8 ± 2.0
Jul	22.9 ± 1.1	–	23.3 ± 0.4	23.3 ± 0.4	–	–	46.8 ± 2.1
Aug	22.6 ± 1.2	–	23.1 ± 0.5	23.1 ± 0.5	–	–	46.8 ± 2.0
Sep	21.8 ± 1.2	27.3 ± 1.3	22.4 ± 0.7	22.4 ± 0.7	23.5 ± 1.3	22.3 ± 6.6	46.9 ± 2.0
Oct	22.5 ± 1.3	29.2 ± 2.3	24.4 ± 1.6	24.0 ± 1.3	25.1 ± 1.4	24.5 ± 9.3	47.2 ± 2.1
Nov	22.6 ± 1.1	31.4 ± 1.9	26.4 ± 1.5	25.7 ± 1.3	26.3 ± 1.3	31.8 ± 8.5	47.9 ± 2.0
Dec	22.7 ± 1.0	33.0 ± 1.7	27.7 ± 1.3	26.9 ± 1.3	27.4 ± 1.3	36.5 ± 9.0	48.6 ± 1.6
annual	22.7 ± 1.3	31.6 ± 2.5	24.9 ± 2.4	24.5 ± 2.0	26.6 ± 1.6	31.3 ± 10.8	47.5 ± 2.0

## Appendix H. Detailed simulation results

Table H.8.: Overview on annual supplied-, generated- and utilized energy amounts – BC scenario o.1.

	$Q_{e,brine}$ kWh	$Q_{gi}$ kWh	$W_{comp}$ kWh	$W_{PV}$ kWh	$Q_c$ kWh	$Q_d$ kWh	$Q_{HP,loss}$ kWh	$Q_{TES,in}$ kWh	$Q_{TES,o}$ kWh	$Q_{TES,loss}$ kWh	$Q_{SH}$ kWh
Jan	1936	0	625	256	1980	453	130	292	186	106	2140
Feb	1416	0	451	269	1467	317	84	255	164	91	1516
Mar	1037	0	325	361	1093	208	62	264	177	92	1026
Apr	737	0	220	357	791	122	45	260	171	84	646
May	198	0	70	378	247	0	22	246	174	78	0
Jun	199	0	66	354	244	0	21	244	168	76	0
Jul	212	0	67	373	257	0	23	256	176	78	0
Aug	210	0	65	353	253	0	22	252	174	78	0
Sep	267	0	77	325	311	10	23	245	170	76	75
Oct	742	0	188	309	794	94	42	261	175	83	622
Nov	1461	0	391	207	1523	255	74	267	173	92	1499
Dec	1930	0	578	206	1986	414	110	294	189	105	2089
annual	10345	0	3123	3748	10945	1873	659	3137	2097	1038	9612

Table H.9.: Overview on thermal energies and energy penalty terms – BC scenario o.1.

	$Q_{HP,tot}$ kWh	$Q_{HP,loss}$ kWh	$Q_{dp1,in}$ kWh	$Q_{dp2,in}$ kWh	$Q_{dp3,o}$ kWh	$Q_{dp4,o}$ kWh	$Q_{TES,loss}$ kWh	$Q_{SH}$ kWh	$P_{pen,DHW}$ kWh	$P_{pen,SH}$ kWh
Jan	2433	130	-0	292	179	8	106	2140	7	0
Feb	1784	84	-0	255	161	2	91	1516	7	0
Mar	1300	62	-0	264	176	1	92	1026	7	0
Apr	913	45	-0	260	171	0	84	646	7	0
May	247	22	-0	246	174	0	78	0	7	0
Jun	244	21	-0	244	168	0	76	0	7	0
Jul	257	23	-0	256	176	0	78	0	7	0
Aug	253	22	-0	252	174	0	78	0	7	0
Sep	321	23	-0	245	170	0	76	75	7	1
Oct	888	42	-0	261	175	0	83	622	7	0
Nov	1778	74	-0	267	171	2	92	1499	7	0
Dec	2400	110	-0	294	181	9	105	2089	7	0
annual	12818	659	-0	3137	2076	22	1038	9612	88	1

### H.3. DHW(TES) and SH(TABS) results – MPC scenario 1.0

Table H.10.: Comfort related variables and results – MPC scenario 1.0.

	$\vartheta_{ra,1fl}$ °C	$\vartheta_{op,1fl}$ °C	$\vartheta_{ra,2fl}$ °C	$\vartheta_{op,2fl}$ °C	$RH_{avg}$ 1	$\vartheta_{TES,z>0.8}$ °C
Jan	21.0 ± 1.3	21.7 ± 1.3	20.6 ± 1.3	21.1 ± 1.3	18.2 ± 5.1	57.4 ± 4.6
Feb	21.3 ± 1.3	22.0 ± 1.3	21.0 ± 1.3	21.5 ± 1.3	20.0 ± 4.6	58.5 ± 3.7
Mar	22.3 ± 1.7	22.9 ± 1.6	22.1 ± 1.7	22.6 ± 1.6	23.7 ± 4.8	59.3 ± 3.4
Apr	23.2 ± 1.4	23.7 ± 1.2	23.1 ± 1.4	23.5 ± 1.2	29.9 ± 9.0	58.5 ± 4.4
May	21.8 ± 1.4	22.1 ± 1.3	21.9 ± 1.4	22.2 ± 1.3	43.6 ± 7.4	60.6 ± 3.8
Jun	22.6 ± 1.3	22.9 ± 1.1	22.7 ± 1.3	23.0 ± 1.2	50.9 ± 8.1	60.7 ± 3.7
Jul	22.9 ± 1.1	23.1 ± 0.9	23.0 ± 1.1	23.2 ± 0.9	53.9 ± 8.9	60.8 ± 3.5
Aug	22.6 ± 1.2	22.9 ± 1.0	22.7 ± 1.2	23.0 ± 1.0	55.6 ± 10.1	60.7 ± 3.6
Sep	21.8 ± 1.2	22.1 ± 1.1	21.8 ± 1.2	22.1 ± 1.1	46.8 ± 9.2	60.4 ± 3.7
Oct	22.7 ± 1.4	23.2 ± 1.3	22.5 ± 1.4	22.9 ± 1.3	35.5 ± 8.1	59.6 ± 3.1
Nov	20.9 ± 1.1	21.5 ± 1.1	20.6 ± 1.1	21.0 ± 1.0	27.8 ± 7.1	56.5 ± 5.2
Dec	20.7 ± 1.0	21.4 ± 0.9	20.3 ± 1.0	20.7 ± 0.9	20.9 ± 6.2	57.0 ± 4.6
annual	22.0 ± 1.5	22.4 ± 1.4	21.9 ± 1.6	22.2 ± 1.5	35.7 ± 15.4	59.2 ± 3.9

Table H.11.: TABS and DHW control relevant variables and results – MPC scenario 1.0.

	$\vartheta_{ra,avg}$ °C	$\vartheta_{flow}$ °C	$\vartheta_{ta}$ °C	$\vartheta_{ret}$ °C	$\vartheta_{ret,SHon}$ °C	$\dot{q}_{ta}$ W/m <sup>2</sup>	$\vartheta_{TES,z>0.8}$ °C
Jan	21.0 ± 1.3	30.9 ± 1.9	25.5 ± 1.2	24.5 ± 1.1	25.1 ± 1.1	37.0 ± 13.8	57.4 ± 4.6
Feb	21.3 ± 1.3	30.6 ± 2.2	25.0 ± 1.3	24.2 ± 1.2	24.8 ± 1.2	38.2 ± 15.0	58.5 ± 3.7
Mar	22.3 ± 1.7	31.1 ± 2.4	25.1 ± 1.2	24.4 ± 1.1	25.0 ± 1.2	43.7 ± 19.0	59.3 ± 3.4
Apr	23.2 ± 1.4	31.9 ± 2.8	25.4 ± 1.2	24.8 ± 1.0	25.8 ± 1.2	46.0 ± 21.6	58.5 ± 4.4
May	21.8 ± 1.4	–	22.3 ± 1.0	22.3 ± 0.9	–	–	60.6 ± 3.8
Jun	22.6 ± 1.3	–	23.0 ± 0.8	23.0 ± 0.8	–	–	60.7 ± 3.7
Jul	22.9 ± 1.1	–	23.3 ± 0.4	23.3 ± 0.4	–	–	60.8 ± 3.5
Aug	22.6 ± 1.2	–	23.1 ± 0.5	23.1 ± 0.5	–	–	60.7 ± 3.6
Sep	21.8 ± 1.2	29.9 ± 3.2	22.5 ± 0.9	22.4 ± 0.8	23.7 ± 2.1	44.2 ± 19.2	60.4 ± 3.7
Oct	22.7 ± 1.4	31.2 ± 2.7	24.8 ± 1.2	24.3 ± 1.1	25.1 ± 1.3	45.2 ± 20.9	59.6 ± 3.1
Nov	20.9 ± 1.1	29.2 ± 2.1	24.2 ± 1.1	23.4 ± 1.0	23.8 ± 1.0	33.6 ± 13.6	56.5 ± 5.2
Dec	20.7 ± 1.0	30.3 ± 1.8	25.2 ± 1.1	24.3 ± 1.1	24.8 ± 1.0	34.1 ± 11.4	57.0 ± 4.6
annual	22.0 ± 1.5	30.5 ± 2.3	24.1 ± 1.6	23.7 ± 1.2	24.8 ± 1.2	37.9 ± 15.9	59.2 ± 3.9

## Appendix H. Detailed simulation results

Table H.12.: Overview on annual supplied-, generated- and utilized energy amounts – MPC scenario 1.0.

	$Q_{e,brine}$ kWh	$W_{comp}$ kWh	$W_{PV}$ kWh	$Q_c$ kWh	$Q_d$ kWh	$Q_{HP,loss}$ kWh	$Q_{TES,in}$ kWh	$Q_{TES,o}$ kWh	$Q_{TES,loss}$ kWh	$Q_{SH}$ kWh
Jan	1707	594	256	1882	303	117	331	180	145	1836
Feb	1243	454	269	1398	210	90	296	164	134	1300
Mar	1032	417	361	1189	177	84	330	180	149	1026
Apr	791	340	357	926	136	70	313	177	137	740
May	232	139	378	333	0	39	332	180	150	0
Jun	221	133	354	317	0	37	316	175	144	0
Jul	235	142	373	337	0	40	335	182	150	0
Aug	229	139	353	329	0	39	328	180	149	0
Sep	289	156	325	391	14	40	320	177	144	83
Oct	772	335	309	915	125	67	330	180	147	702
Nov	1216	417	207	1359	187	88	306	174	131	1228
Dec	1736	579	206	1904	294	118	324	182	144	1855
annual	9703	3845	3748	11280	1447	829	3860	2133	1724	8770

Table H.13.: Overview on thermal energies and energy penalty terms – scenario 1.0.

	$Q_{HP,tot}$ kWh	$Q_{HP,loss}$ kWh	$Q_{dp1,in}$ kWh	$Q_{dp2,in}$ kWh	$Q_{dp3,o}$ kWh	$Q_{dp4,o}$ kWh	$Q_{TES,loss}$ kWh	$Q_{SH,tot}$ kWh	$P_{pen,dhw}$ kWh	$P_{pen,SH}$ kWh
Jan	2185	117	-0	331	180	0	145	1836	7	16
Feb	1608	90	-0	296	164	0	134	1300	7	7
Mar	1366	84	-0	330	180	0	149	1026	7	4
Apr	1062	70	-0	313	177	0	137	740	7	0
May	333	39	-0	332	180	0	150	0	7	0
Jun	317	37	-0	316	175	0	144	0	7	0
Jul	337	40	-0	335	182	0	150	0	7	0
Aug	329	39	-0	328	180	0	149	0	7	0
Sep	405	40	-0	320	177	0	144	83	7	1
Oct	1040	67	-0	330	180	0	147	702	7	0
Nov	1546	88	-0	306	174	0	131	1228	7	3
Dec	2198	118	-0	324	182	0	144	1855	7	8
annual	12727	829	-0	3860	2133	0	1724	8770	88	38

Table H.14.: Performance indicators overview for monthly and annual results – MPC scenario 1.0.

	$SPF$	$SPF_{ctr}$	$SPF_{sys}$	$SPF_{sys,ctr}$	$COP$	$SPF_{sys}^{pen}$	$SPF_{sys,ctr}^{pen}$	$\eta_{PV}$
Jan	3.55	5.93	3.22	5.33	3.66 ± 0.77	3.11	5.03	12.30 ± 0.01
Feb	3.41	7.31	3.06	6.45	3.53 ± 0.83	2.97	6.09	12.20 ± 0.01
Mar	3.17	10.48	2.76	8.93	3.25 ± 0.84	2.70	8.32	11.88 ± 0.01
Apr	3.02	13.91	2.58	11.55	3.07 ± 0.76	2.53	10.68	11.57 ± 0.01
May	2.31	8.34	1.25	4.47	2.34 ± 0.47	1.18	3.91	11.30 ± 0.01
Jun	2.29	7.76	1.26	4.24	2.32 ± 0.46	1.20	3.73	11.20 ± 0.01
Jul	2.28	7.51	1.23	4.03	2.31 ± 0.44	1.17	3.57	11.16 ± 0.01
Aug	2.29	7.72	1.25	4.19	2.33 ± 0.45	1.19	3.68	11.17 ± 0.01
Sep	2.51	8.67	1.60	5.47	2.55 ± 0.70	1.52	4.80	11.41 ± 0.01
Oct	3.01	13.25	2.53	10.79	3.06 ± 0.81	2.47	9.95	11.72 ± 0.01
Nov	3.56	6.43	3.17	5.66	3.67 ± 0.86	3.10	5.45	11.99 ± 0.01
Dec	3.65	5.48	3.32	4.95	3.74 ± 0.77	3.24	4.78	12.25 ± 0.01
annual	3.19	7.35	2.70	6.13	3.29 ± 0.91	2.62	5.76	11.59 ± 0.01

## H.4. DHW(TES) and SH(TABS) results – MPC scenario 1.3a

Table H.15.: Comfort related variables and results – MPC scenario 1.3a.

	$\vartheta_{ra,1fl}$ °C	$\vartheta_{op,1fl}$ °C	$\vartheta_{ra,2fl}$ °C	$\vartheta_{op,2fl}$ °C	$RH_{avg}$ 1	$\vartheta_{TES,z>0.8}$ °C
Jan	21.2 ± 1.4	21.9 ± 1.4	20.8 ± 1.5	21.3 ± 1.4	18.1 ± 5.0	48.3 ± 1.4
Feb	21.6 ± 1.4	22.2 ± 1.4	21.2 ± 1.4	21.7 ± 1.4	19.7 ± 4.3	47.9 ± 1.7
Mar	22.6 ± 1.7	23.2 ± 1.6	22.4 ± 1.7	22.8 ± 1.6	23.3 ± 4.7	47.5 ± 1.8
Apr	23.3 ± 1.4	23.8 ± 1.2	23.2 ± 1.4	23.7 ± 1.2	29.6 ± 8.9	47.2 ± 1.9
May	21.9 ± 1.4	22.2 ± 1.3	21.9 ± 1.4	22.2 ± 1.3	43.4 ± 7.4	46.6 ± 2.1
Jun	22.6 ± 1.3	22.9 ± 1.1	22.7 ± 1.3	23.0 ± 1.2	50.9 ± 8.1	46.7 ± 2.1
Jul	22.9 ± 1.1	23.1 ± 0.9	23.0 ± 1.1	23.2 ± 0.9	53.9 ± 8.9	46.6 ± 2.1
Aug	22.6 ± 1.2	22.9 ± 1.0	22.7 ± 1.2	23.0 ± 1.0	55.6 ± 10.1	46.5 ± 2.2
Sep	21.8 ± 1.2	22.1 ± 1.1	21.8 ± 1.2	22.1 ± 1.1	46.8 ± 9.2	46.7 ± 2.1
Oct	22.9 ± 1.4	23.4 ± 1.3	22.8 ± 1.4	23.2 ± 1.3	35.0 ± 8.1	47.1 ± 2.0
Nov	21.1 ± 1.2	21.6 ± 1.2	20.8 ± 1.2	21.2 ± 1.1	27.5 ± 6.9	47.8 ± 1.5
Dec	20.8 ± 1.1	21.5 ± 1.0	20.3 ± 1.0	20.8 ± 1.0	20.9 ± 6.2	48.4 ± 1.2
annual	22.1 ± 1.6	22.6 ± 1.4	22.0 ± 1.6	22.4 ± 1.5	35.5 ± 15.5	47.3 ± 1.8

Table H.16.: TABS and DHW control relevant variables and results – MPC scenario 1.3a.

	$\vartheta_{ra,avg}$ °C	$\vartheta_{flow}$ °C	$\vartheta_{ta}$ °C	$\vartheta_{ret}$ °C	$\vartheta_{ret,SHon}$ °C	$\dot{q}_{ta}$ W/m <sup>2</sup>	$\vartheta_{TES,z>0.8}$ °C
Jan	21.2 ± 1.4	30.0 ± 1.7	25.7 ± 1.2	24.9 ± 1.2	25.2 ± 1.1	31.9 ± 10.2	48.3 ± 1.4
Feb	21.6 ± 1.4	29.7 ± 1.8	25.3 ± 1.3	24.6 ± 1.2	25.0 ± 1.2	31.5 ± 10.9	47.9 ± 1.7
Mar	22.6 ± 1.7	29.8 ± 1.9	25.4 ± 1.1	24.8 ± 1.1	25.1 ± 1.2	33.3 ± 12.9	47.5 ± 1.8
Apr	23.3 ± 1.4	30.1 ± 2.1	25.7 ± 1.2	25.2 ± 1.0	25.6 ± 1.2	32.4 ± 13.8	47.2 ± 1.9
May	21.9 ± 1.4	–	22.4 ± 1.0	22.3 ± 1.0	–	–	46.6 ± 2.1
Jun	22.6 ± 1.3	–	23.0 ± 0.8	23.0 ± 0.8	–	–	46.7 ± 2.1
Jul	22.9 ± 1.1	–	23.3 ± 0.4	23.3 ± 0.4	–	–	46.6 ± 2.1
Aug	22.6 ± 1.2	–	23.1 ± 0.5	23.1 ± 0.5	–	–	46.5 ± 2.2
Sep	21.8 ± 1.2	28.9 ± 2.7	22.5 ± 0.9	22.5 ± 0.8	23.9 ± 2.1	37.7 ± 13.1	46.7 ± 2.1
Oct	22.9 ± 1.4	29.7 ± 2.1	25.2 ± 1.2	24.7 ± 1.0	25.1 ± 1.2	32.7 ± 13.4	47.1 ± 2.0
Nov	21.1 ± 1.2	28.6 ± 1.9	24.4 ± 1.2	23.7 ± 1.2	24.1 ± 1.2	29.8 ± 10.6	47.8 ± 1.5
Dec	20.8 ± 1.1	29.4 ± 1.7	25.3 ± 1.2	24.6 ± 1.1	24.9 ± 1.1	29.6 ± 9.0	48.4 ± 1.2
annual	22.1 ± 1.6	29.6 ± 1.9	24.3 ± 1.6	23.9 ± 1.4	25.0 ± 1.2	31.4 ± 11.2	47.3 ± 1.8

## Appendix H. Detailed simulation results

Table H.17.: Overview on annual supplied-, generated- and utilized energy amounts – MPC scenario 1.3a.

	$Q_{e,brine}$ kWh	$W_{comp}$ kWh	$W_{PV}$ kWh	$Q_c$ kWh	$Q_d$ kWh	$Q_{HP,loss}$ kWh	$Q_{TES,in}$ kWh	$Q_{TES,o}$ kWh	$Q_{TES,loss}$ kWh	$Q_{SH}$ kWh
Jan	1736	532	256	1819	335	116	404	316	90	1870
Feb	1265	391	269	1338	236	84	314	232	81	1318
Mar	1057	342	361	1122	208	71	290	201	90	1053
Apr	837	279	357	885	168	63	262	177	86	785
May	204	86	378	259	0	30	258	174	84	0
Jun	197	83	354	251	0	29	250	169	82	0
Jul	205	87	373	261	0	31	260	176	84	0
Aug	204	86	353	258	0	31	258	173	85	0
Sep	268	106	325	324	16	33	257	175	82	86
Oct	837	276	309	893	161	59	270	180	88	777
Nov	1203	362	207	1285	201	81	329	249	83	1222
Dec	1741	518	206	1839	306	116	443	356	87	1860
annual	9753	3148	3748	10534	1631	745	3596	2578	1022	8972

Table H.18.: Overview on thermal energies and energy penalty terms – MPC scenario 1.3a.

	$Q_{HP,tot}$ kWh	$Q_{HP,loss}$ kWh	$Q_{dp1,in}$ kWh	$Q_{dp2,in}$ kWh	$Q_{dp3,o}$ kWh	$Q_{dp4,o}$ kWh	$Q_{TES,loss}$ kWh	$Q_{SH,tot}$ kWh	$P_{pen,dhw}$ kWh	$P_{pen,SH}$ kWh
Jan	2154	116	-0	404	178	138	90	1870	7	21
Feb	1573	84	-0	314	161	71	81	1318	7	9
Mar	1330	71	-0	290	176	25	90	1053	7	3
Apr	1053	63	-0	262	172	4	86	785	7	0
May	259	30	-0	258	174	0	84	0	7	0
Jun	251	29	-0	250	169	0	82	0	7	0
Jul	261	31	-0	260	176	0	84	0	7	0
Aug	258	31	-0	258	173	0	85	0	7	0
Sep	341	33	-0	257	171	4	82	86	7	1
Oct	1054	59	-0	270	176	4	88	777	7	0
Nov	1486	81	-0	329	172	77	83	1222	7	4
Dec	2145	116	-0	443	181	175	87	1860	7	14
annual	12165	745	-0	3596	2079	499	1022	8972	88	52

Table H.19.: Performance indicators overview for monthly and annual results – MPC scenario 1.3a.

	$SPF$	$SPF_{ctr}$	$SPF_{sys}$	$SPF_{sys,ctr}$	$COP$	$SPF_{sys}^{pen}$	$SPF_{sys,ctr}^{pen}$	$\eta_{PV}$
Jan	3.90	6.90	3.64	6.34	$3.99 \pm 0.46$	3.46	5.83	$12.30 \pm 0.01$
Feb	3.87	9.40	3.57	8.44	$3.95 \pm 0.49$	3.44	7.74	$12.20 \pm 0.01$
Mar	3.75	14.63	3.40	12.70	$3.82 \pm 0.52$	3.31	11.57	$11.88 \pm 0.01$
Apr	3.64	19.86	3.26	16.72	$3.71 \pm 0.55$	3.18	15.14	$11.57 \pm 0.01$
May	2.90	22.05	1.93	14.53	$2.86 \pm 0.53$	1.78	10.86	$11.30 \pm 0.01$
Jun	2.90	19.76	1.93	13.13	$2.86 \pm 0.52$	1.79	10.15	$11.20 \pm 0.01$
Jul	2.87	21.95	1.92	14.56	$2.84 \pm 0.52$	1.77	10.86	$11.16 \pm 0.01$
Aug	2.88	23.31	1.92	15.29	$2.85 \pm 0.53$	1.77	11.15	$11.17 \pm 0.01$
Sep	3.10	16.98	2.32	12.38	$3.06 \pm 0.67$	2.16	9.94	$11.41 \pm 0.01$
Oct	3.69	20.40	3.28	16.94	$3.75 \pm 0.55$	3.20	15.17	$11.72 \pm 0.01$
Nov	3.93	7.89	3.61	7.10	$3.99 \pm 0.54$	3.51	6.75	$11.99 \pm 0.01$
Dec	3.97	6.25	3.70	5.76	$4.02 \pm 0.47$	3.56	5.43	$12.25 \pm 0.01$
annual	3.72	9.55	3.32	8.32	$3.76 \pm 0.64$	3.18	7.64	$11.59 \pm 0.01$

## H.5. DHW(TES) and SH(TABS) results – MPC scenario 1.4

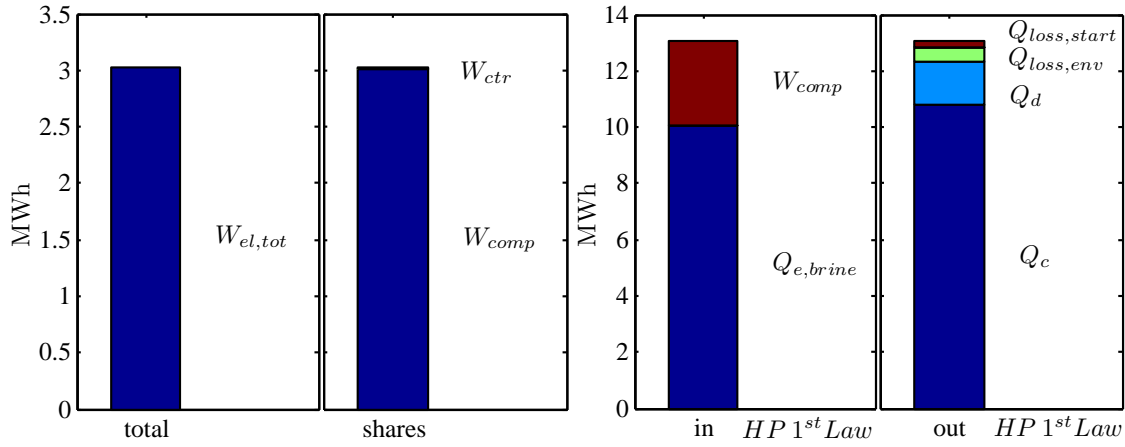


Figure H.1.: Energy balance HP electrical consumption (left), HP 1st Law – MPC scenario 1.4.

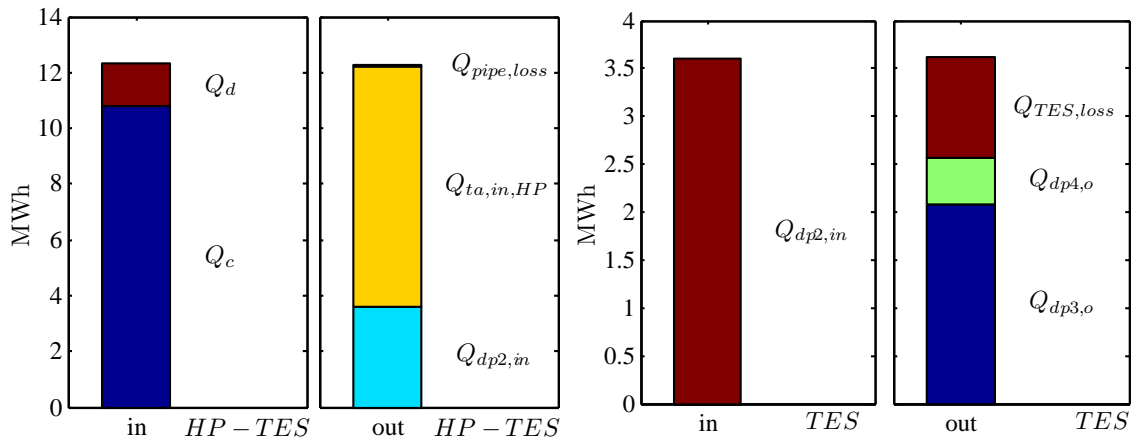


Figure H.2.: Energy balance HP-TES, TABS (left) and TES alone (right) MPC scenario 1.4.

Figure H.3.: Comfort related variables and results – MPC scenario 1.4.

	$\vartheta_{ra,1fl}$ °C	$\vartheta_{op,1fl}$ °C	$\vartheta_{ra,2fl}$ °C	$\vartheta_{op,2fl}$ °C	$RH_{avg}$ 1	$\vartheta_{TES,z>0.8}$ °C
Jan	21.2 ± 1.5	21.9 ± 1.4	20.8 ± 1.5	21.3 ± 1.4	18.0 ± 5.0	48.3 ± 1.4
Feb	21.6 ± 1.4	22.2 ± 1.4	21.2 ± 1.4	21.7 ± 1.4	19.7 ± 4.3	47.9 ± 1.6
Mar	22.6 ± 1.7	23.2 ± 1.6	22.4 ± 1.7	22.8 ± 1.6	23.3 ± 4.7	47.5 ± 1.8
Apr	23.4 ± 1.4	23.9 ± 1.2	23.3 ± 1.4	23.7 ± 1.2	29.5 ± 8.9	47.2 ± 1.9
May	21.9 ± 1.4	22.2 ± 1.3	21.9 ± 1.4	22.2 ± 1.3	43.4 ± 7.4	46.7 ± 2.1
Jun	22.6 ± 1.3	22.9 ± 1.1	22.7 ± 1.3	23.0 ± 1.2	50.9 ± 8.1	46.6 ± 2.2
Jul	22.9 ± 1.1	23.1 ± 0.9	23.0 ± 1.1	23.2 ± 0.9	53.9 ± 8.9	46.8 ± 2.1
Aug	22.6 ± 1.2	22.9 ± 1.0	22.7 ± 1.2	23.0 ± 1.0	55.6 ± 10.1	46.7 ± 2.1
Sep	21.8 ± 1.2	22.1 ± 1.1	21.8 ± 1.2	22.1 ± 1.1	46.8 ± 9.2	46.7 ± 2.1
Oct	23.2 ± 1.4	23.8 ± 1.3	23.1 ± 1.4	23.5 ± 1.3	34.3 ± 8.0	47.2 ± 1.9
Nov	21.5 ± 1.4	22.0 ± 1.4	21.1 ± 1.4	21.6 ± 1.3	26.8 ± 6.7	47.7 ± 1.7
Dec	20.8 ± 1.1	21.5 ± 1.0	20.4 ± 1.1	20.8 ± 1.0	20.8 ± 6.2	48.4 ± 1.3
annual	22.2 ± 1.6	22.6 ± 1.4	22.0 ± 1.6	22.4 ± 1.5	35.4 ± 15.5	47.3 ± 1.9

## Appendix H. Detailed simulation results

Table H.20.: TABS and DHW control relevant variables and results – MPC scenario 1.4.

	$\vartheta_{ra,avg}$ ° C	$\vartheta_{sw}$ ° C	$\vartheta_{ta}$ ° C	$\vartheta_{ret}$ ° C	$\vartheta_{ret,SHon}$ ° C	$\dot{q}_{ta}$ W/m <sup>2</sup>	$\vartheta_{TES,z>0.8}$ ° C
Jan	21.2 ± 1.5	30.0 ± 1.7	25.7 ± 1.2	25.0 ± 1.1	25.2 ± 1.1	32.0 ± 10.4	48.3 ± 1.4
Feb	21.6 ± 1.4	29.6 ± 1.8	25.3 ± 1.3	24.6 ± 1.2	25.0 ± 1.2	31.3 ± 10.9	47.9 ± 1.6
Mar	22.6 ± 1.7	30.1 ± 2.0	25.4 ± 1.2	24.8 ± 1.1	25.2 ± 1.2	35.3 ± 14.7	47.5 ± 1.8
Apr	23.4 ± 1.4	30.6 ± 2.2	25.7 ± 1.2	25.2 ± 1.0	25.8 ± 1.2	36.3 ± 16.0	47.2 ± 1.9
May	21.9 ± 1.4	–	22.4 ± 1.0	22.4 ± 1.0	–	–	46.7 ± 2.1
Jun	22.6 ± 1.3	–	23.0 ± 0.8	23.0 ± 0.8	–	–	46.6 ± 2.2
Jul	22.9 ± 1.1	–	23.3 ± 0.4	23.3 ± 0.4	–	–	46.8 ± 2.1
Aug	22.6 ± 1.2	–	23.1 ± 0.5	23.1 ± 0.5	–	–	46.7 ± 2.1
Sep	21.8 ± 1.2	29.5 ± 2.8	22.5 ± 0.9	22.5 ± 0.8	24.2 ± 2.2	42.8 ± 14.5	46.7 ± 2.1
Oct	23.2 ± 1.4	30.7 ± 1.8	25.7 ± 1.1	25.1 ± 1.0	25.8 ± 1.1	38.1 ± 13.8	47.2 ± 1.9
Nov	21.5 ± 1.4	29.4 ± 2.1	24.8 ± 1.6	24.2 ± 1.5	24.7 ± 1.5	32.4 ± 11.3	47.7 ± 1.7
Dec	20.8 ± 1.1	29.7 ± 1.7	25.3 ± 1.2	24.6 ± 1.2	25.0 ± 1.1	31.3 ± 10.5	48.4 ± 1.3
annual	22.2 ± 1.6	29.9 ± 1.9	24.3 ± 1.7	24.0 ± 1.4	25.1 ± 1.3	33.1 ± 12.2	47.3 ± 1.9

Table H.21.: Overview on annual supplied-, generated- and utilized energy amounts – MPC scenario 1.4.

	$Q_{e,brine}$ kWh	$Q_{gi}$ kWh	$W_{comp}$ kWh	$W_{PV}$ kWh	$Q_c$ kWh	$Q_d$ kWh	$Q_{HP,loss}$ kWh	$Q_{TES,in}$ kWh	$Q_{TES,o}$ kWh	$Q_{TES,loss}$ kWh	$Q_{SH}$ kWh
Jan	1747	0	526	256	1831	329	115	401	313	90	1876
Feb	1261	0	393	269	1333	239	84	313	232	81	1316
Mar	1056	0	350	361	1126	208	73	291	199	93	1053
Apr	845	0	276	357	900	159	62	266	178	89	787
May	217	0	81	378	262	0	36	261	174	87	0
Jun	215	0	75	354	254	0	36	253	170	84	0
Jul	225	0	75	373	265	0	36	265	177	87	0
Aug	227	0	73	353	262	0	38	261	175	87	0
Sep	296	0	90	325	334	12	40	260	175	84	88
Oct	946	0	251	309	1001	135	61	279	187	91	856
Nov	1259	0	333	207	1340	173	80	329	246	84	1247
Dec	1766	0	495	206	1869	281	113	430	342	89	1864
annual	10060	0	3018	3748	10775	1535	774	3610	2568	1046	9088

Table H.22.: Overview on thermal energies and energy penalty terms – MPC scenario 1.4.

	$Q_{HP,tot}$ kWh	$Q_{HP,loss}$ kWh	$Q_{dp1,in}$ kWh	$Q_{dp2,in}$ kWh	$Q_{dp3,o}$ kWh	$Q_{dp4,o}$ kWh	$Q_{TES,loss}$ kWh	$Q_{SH}$ kWh	$P_{pen,DHW}$ kWh	$P_{pen,SH}$ kWh
Jan	2160	115	–0	401	178	135	90	1876	7	20
Feb	1571	84	–0	313	161	71	81	1316	7	10
Mar	1334	73	–0	291	176	23	93	1053	7	3
Apr	1059	62	–0	266	173	5	89	787	7	0
May	262	36	–0	261	174	0	87	0	7	0
Jun	254	36	–0	253	170	0	84	0	7	0
Jul	265	36	–0	265	177	0	87	0	7	0
Aug	262	38	–0	261	175	0	87	0	7	0
Sep	346	40	–0	260	172	3	84	88	7	1
Oct	1136	61	–0	279	177	10	91	856	7	0
Nov	1512	80	–0	329	171	75	84	1247	7	1
Dec	2149	113	–0	430	180	162	89	1864	7	13
annual	12311	774	–0	3610	2084	484	1046	9088	88	48

## H.6. DHW(TES) and SH(TABS) results – MPC scenario 1.5

Table H.23.: Performance indicators overview for monthly and annual results – MPC scenario 1.5.

	$SPF$	$SPF_{ctr}$	$SPF_{sys}$	$SPF_{sys,ctr}$	$COP$	$\theta_{sc}$	$SPF_{sys}^{pen}$ °C	$SPF_{sys,ctr}^{pen}$	$\eta_{PV}$ % <sup>a</sup>	$F_{PV,use}$ %	$F_{HP,PV}$ %
Jan	4.18	5.58	3.91	5.21	4.2 ± 0.4	2.3	3.61	4.69	12.30	47	25
Feb	4.12	5.70	3.82	5.27	4.2 ± 0.5	1.6	3.55	4.79	12.20	38	28
Mar	3.99	5.44	3.62	4.92	4.1 ± 0.7	2.7	3.38	4.55	11.88	19	27
Apr	3.78	4.90	3.22	4.17	4.0 ± 0.9	4.7	2.92	3.78	11.57	9	23
May	3.17	4.77	2.12	3.21	3.2 ± 0.7	7.5	1.95	2.93	11.30	7	34
Jun	3.31	5.00	2.24	3.40	3.3 ± 0.8	10.0	2.04	3.12	11.20	7	34
Jul	3.45	5.20	2.33	3.53	3.4 ± 0.8	11.9	2.12	3.24	11.16	7	34
Aug	3.50	5.27	2.37	3.58	3.5 ± 0.8	12.8	2.15	3.27	11.17	7	34
Sep	3.60	5.11	2.56	3.64	3.7 ± 1.0	12.3	2.32	3.32	11.41	7	30
Oct	4.31	5.65	3.71	4.86	4.6 ± 1.1	10.3	3.47	4.58	11.72	11	24
Nov	4.68	5.89	4.33	5.44	4.7 ± 0.6	7.2	4.14	5.18	11.99	32	21
Dec	4.41	5.63	4.12	5.25	4.4 ± 0.4	4.3	3.92	4.93	12.25	50	22
Year	4.13	5.53	3.68	4.92	4.2 ± 0.7	7.3	3.43	4.54	11.59	17	25

<sup>a</sup>) The empirical standard deviation over all months is 0.01.

## H.7. PV module data

NEW NEU NOUVEAU NUOVO

# SOLARWATT 60P



**EASY-ON SYSTEM  
PRIVAT**



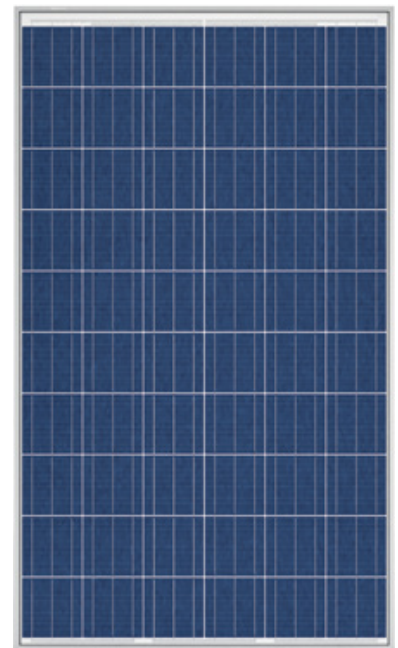
**EASY-ON SYSTEM  
GEWERBE**

DATENBLATT – SOLARWATT 60P | DE

### DIE INNOVATIVE GLAS-GLAS GENERATION

- ▶ Super-Leichtgewicht durch 2mm dünnes Glas
- ▶ Höchste Ertragszuverlässigkeit
- ▶ Höhere mechanische Belastbarkeit
- ▶ 100% Schutz gegen PID
- ▶ Höhere Brandsicherheit
  
- ▶ 30 Jahre Produktgarantie
- ▶ 30 Jahre lineare Leistungsgarantie

Gemäß „Besondere Garantiebedingungen für SOLARWATT-Solarmodule.“



### SOLARWATT QUALITÄT

- |   |   |   |
|---|---|---|
|  Langlebig |  Ertragreich |  Innovativ |
|  Belastbar |  Sicher      |  Blendarm  |

#### Beständigkeit gegenüber:

- |  |   |   |
|--|---|---|
|  Ammoniak |  Salznebel |  Hagel |
|--|---|---|



### SOLARWATT SERVICE

- |   |  |
|---|--|
| <ul style="list-style-type: none"> <li>▶ SOLARWATT Komplettschutz inklusive (bis 1000 kWp)</li> <li>▶ Einfache Finanzierung ohne zusätzliche Sicherheitsnachweise</li> <li>▶ Kompetente Beratung vor Ort</li> <li>▶ Unkomplizierte Rücknahme</li> </ul> | <ul style="list-style-type: none"> <li>▶ SOLARWATT 60P</li> <li>▶ Polykristalline Solarzellen</li> <li>▶ 250 Wp - 260 Wp*</li> </ul> |
|---|--|

\*100% Plussortierung

### SOLARWATT LÖSUNGEN

PRIVAT						GEWERBE			
EASY-IN SYSTEM	EASY-ON SYSTEM	EASY-FLAT SYSTEM	CARPORT SYSTEM	VERANDA SYSTEM	FACADE SYSTEM	EASY-IN SYSTEM	EASY-ON SYSTEM	EASY-FLAT SYSTEM	FACADE SYSTEM
●	●	●	●	●	●	●	●	●	●



**SOLARWATT GmbH**  
 Maria-Reiche-Str. 2a  
 01109 Dresden, Germany  
 Tel.+49 351 8895-0  
 Fax+49 351 8895-111  
 info@solarwatt.de  
 www.solarwatt.de

**Zertifiziert nach**  
 DIN EN ISO 9001 und 14001  
 BS OHSAS 18001:2007

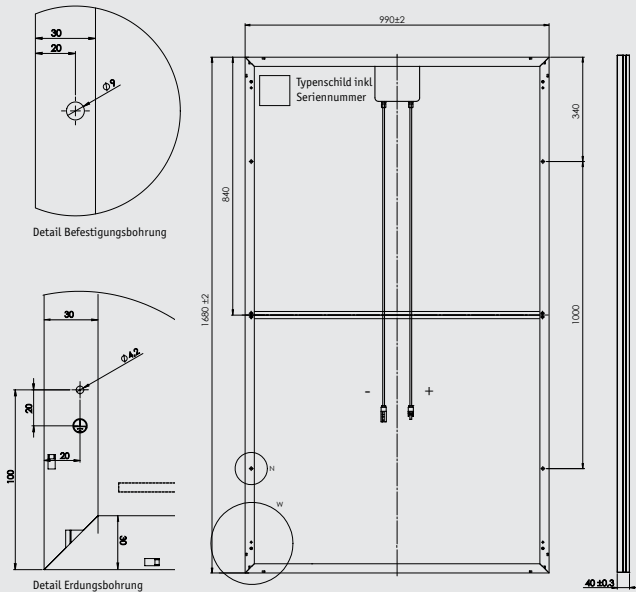


# SOLARWATT 60P

## Technische Daten

Änderungen vorbehalten.

### ABMESSUNGEN



### ALLGEMEINE DATEN

<b>Modultechnologie</b>	Glas-Glas-Laminat; Aluminiumrahmen, natur eloxiert
<b>Deckmaterial</b>	Hochtransparentes Solarglas, 2 mm
<b>Verkapselung</b>	EVA-Solarzellen-EVA, weiß
<b>Rückseitenmaterial</b>	Rückseitenglas, 2 mm
<b>Solarzellen</b>	60 kristalline Solarzellen
<b>Maße der Zellen</b>	156 x 156 mm
<b>LxBxD</b>	1680 x 990 x 40 mm
<b>Anschlusstechnik</b>	Kabel 2 x 1,0 m/4 mm <sup>2</sup> , MC4/PV4-Steckverbinder
<b>Gewicht</b>	ca. 24 kg
<b>Bypass-Dioden</b>	3 Stück
<b>Anwendungsklasse</b>	Application class A (nach IEC 61730)
<b>Max. Systemspannung</b>	1000 V
<b>Freigegebene Belastungen</b>	Soglast bis 2400 Pa Prüfbedingungen: nach IEC 61215 Ed.2 Auflast bis 5500 Pa (bei Quermontage*) Testbedingungen: Schrägbelastung mit 9000 Pa (Die Bedingungen berücksichtigen Sicherheitsfaktoren für Schneeeinlagerung und Eislast gem. Eurocode 1)
<b>Qualifikationen</b>	IEC 61215 Ed.2 IEC 61730 (inkl. Schutzklasse II)

\* Beachten Sie hierzu bitte die Angaben in der Montageanleitung.

### ELEKTRISCHE EIGENSCHAFTEN BEI STC

STC: Standard Test Conditions: Bestrahlungsstärke 1000 W/m<sup>2</sup>, Spektrale Verteilung AM 1,5, Temperatur 25±2 °C, entsprechend EN 60904-3

<b>Nennleistung P<sub>N</sub></b>	250 Wp	255 Wp	260 Wp
<b>Nennspannung U<sub>mpp</sub></b>	30,6 V	30,9 V	31,2 V
<b>Nennstrom I<sub>mpp</sub></b>	8,18 A	8,26 A	8,34 A
<b>Leerlaufspannung U<sub>OC</sub></b>	37,4 V	37,7 V	38,0 V
<b>Kurzschlussstrom I<sub>SC</sub></b>	8,73 A	8,81 A	8,88 A
<b>Rückstrombelastb. IR*</b>		20 A	

Messtoleranzen bezogen auf P<sub>max</sub> ±5 %;

\* Rückstrombelastbarkeit: Betrieb der Module mit eingespeisten Fremdstrom ist nur bei Verwendung einer Strangsicherung mit Auslösestrom < 20 A zulässig.

Reduktion des Modulwirkungsgrades bei Rückgang der Bestrahlungsstärke von 1000 W/m<sup>2</sup> auf 200 W/m<sup>2</sup> (bei 25 °C): 4±2% (relativ) / -0,6±0,3% (absolut).

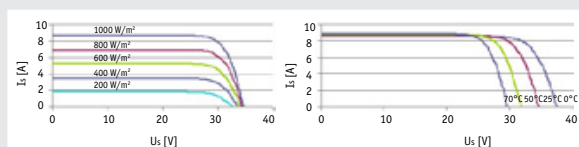
### ELEKTRISCHE EIGENSCHAFTEN BEI NOCT

NOCT: Normal Operation Cell Temperature: Bestrahlungsstärke 800 W/m<sup>2</sup>, AM 1,5, Temperatur 20 °C, Windgeschwindigkeit 1m/s, elektrischer Leerlauf

<b>Nennleistung P<sub>N</sub></b>	186 W	190 W	194 W
<b>Nennspannung U<sub>mpp</sub></b>	28,4 V	28,6 V	28,9 V
<b>Leerlaufspannung U<sub>OC</sub></b>	35,2 V	35,4 V	35,7 V
<b>Kurzschlussstrom I<sub>SC</sub></b>	7,07 A	7,13 A	7,19 A

### KENNLINIEN

Strom-Spannung bei versch. Einstrahlungen und Temperaturen



Leistungsklasse 260 Wp

### THERMISCHE EIGENSCHAFTEN

<b>Betriebstemperaturbereich</b>	-40 ... +80 °C
<b>Umgebungstemperaturbereich</b>	-40 ... +45 °C
<b>Temperaturkoeffizient von P<sub>N</sub></b>	-0,34%/K
<b>Temperaturkoeffizient von U<sub>OC</sub></b>	-0,30%/K
<b>Temperaturkoeffizient von I<sub>SC</sub></b>	0,06%/K
<b>NOCT</b>	45 °C

[Diese Datenblatt entspricht den Vorgaben der DIN EN 50380:2003] REV 10/2013